

Durham E-Theses

Monogenetic basaltic edifices: their architecture, volcanology and importance in hydrocarbon basins

REYNOLDS, PETER, WILLIAM

How to cite:

REYNOLDS, PETER, WILLIAM (2015) *Monogenetic basaltic edifices: their architecture, volcanology and importance in hydrocarbon basins*, Durham theses, Durham University. Available at Durham E-Theses Online: <http://etheses.dur.ac.uk/11369/>

Use policy

The full-text may be used and/or reproduced, and given to third parties in any format or medium, without prior permission or charge, for personal research or study, educational, or not-for-profit purposes provided that:

- a full bibliographic reference is made to the original source
- a [link](#) is made to the metadata record in Durham E-Theses
- the full-text is not changed in any way

The full-text must not be sold in any format or medium without the formal permission of the copyright holders.

Please consult the [full Durham E-Theses policy](#) for further details.

Monogenetic basaltic edifices: their architecture, volcanology and importance in hydrocarbon basins

Peter William Reynolds

A thesis submitted for the degree of
Doctor of Philosophy

**Department of Earth Sciences
Durham University**

2015

Monogenetic basaltic edifices: their architecture, volcanology and importance in hydrocarbon basins

Peter W. Reynolds

Abstract

Flood basalt provinces host significant hydrocarbon reserves. The provinces are produced during fissure eruptions which construct volcanic edifices atop an erupting dyke. The edifices are important components of volcanic-affected hydrocarbon basins; they provide insights into the underlying structural and magmatic plumbing systems, as well as acting as fluid migration pathways after burial. Furthermore, the edifices host a wealth of volcanological evidence that can be used to derive information relating to eruption dynamics such as eruption column height, mass flux and duration; as well as providing insights into the effects of eruptions on the environment. However, the location of the fissures in many hydrocarbon basins is poorly constrained. Furthermore, few studies have characterised the internal architecture of the edifices produced during fissure eruptions. This thesis uses field, seismic and well data to characterise the architecture of monogenetic basaltic edifices and understand their temporal and spatial evolution.

Field studies along a dissected Holocene fissure, Northeast Iceland, reveal that a scoria-agglutinate cone, spatter ramparts and a scoria rampart were constructed during Hawaiian-style lava fountaining. These edifices are analogous to those formed in the 1783 Laki eruption. Data gathered in this study can be used to recognise fissure-derived edifices in other volcanic provinces. I then contrast these dyke-fed edifices with rootless cones; a morphologically similar volcanic edifice produced during explosive interaction between inflating pāhoehoe lava and unconsolidated sediment. This thesis reveals that rootless cones can be distinguished from dyke-fed edifices on the basis of their juvenile clast morphology and clast density. This allows us to better recognise dyke-proximal locations. Lastly, I use exceptional quality 3D seismic and well data to show how a series of submarine monogenetic volcanoes evolved; progressing from a maar-forming stage, to a pillow volcano and tuff-cone-building stage as the confining pressure decreased above the growing edifices. These insights allow us to distinguish volcanic edifices from similar non-volcanic edifices in other seismic data sets, and also indicates that our understanding of submarine volcanism has previously been biased towards recognition of constructional features.

Copyright © by Peter W Reynolds

The copyright of this thesis rests with the author. No quotation from it should be published without prior written consent and information derived from it should be acknowledged.

Acknowledgements

With thanks to:

Uncle Hess
Rich Brown
Nick Schofield
Simon Holford
Thor Thordarson
Ed Llewelin
Kevin Fielding
Davie Brown
Brian Bell
Douglas Halliday
Colin MacPherson
Claire Horwell
Paula Elliott
Karen Atkinson
April Furnal
Ian Chaplin
Dave Stevenson
Mat Hepburn
Cat Hirst
Sam Clark
Bob Jamieson
Alex Peace
Clayton Grove
Tim Watton
Heather Rawcliffe
Kirsty Wright
Tim Dempster
Gia Pendred
Nick Crabtree
Alwyn Ross
Dougal Jerram
Sverre Planke
John Millett

and especially

Charlotte Simmons

and

Susan Reynolds

Table of Contents

Abstract	i
Acknowledgements	iii
Chapter 1: Introduction	1
1.1 Flood basalt volcanism and hydrocarbon exploration	1
1.2 The importance of fissure volcanism	2
1.3 The importance of volcanic edifices	2
1.4 The problem: identifying volcanic edifices and constraining their architecture	3
1.4.1 Identifying volcanic edifices in remote datasets	3
1.4.2 Characterising the architecture of volcanic edifices in the field	5
1.5 Aims	6
1.6 Thesis Outline	7
1.7 References	8
Chapter 2: Background Information	12
2.1 Introduction	12
2.2 The North Atlantic Igneous Province	12
2.2.1 The Faroe Shetland Basin	13
2.3 The eruption of basaltic magma	16
2.3.1 Feeder dykes for monogenetic eruptions	17
2.3.2 Eruption styles	19
2.3.2.1 Physical processes governing eruption style	20
2.3.2.2 Hydromagmatic eruptions	20
2.3.2.3 Magmatic volatile-driven eruptions	21
2.3.2.3.1 Fissure eruptions	22
2.3.3 Pyroclast accumulation and lava fountains	23
2.4. Basaltic lavas	24
2.4.1 Definition of terms	24
2.4.2 Emplacement	27
2.4.2.1 Inflation of pāhoehoe lavas	29
2.4.3 Types of pāhoehoe lavas	30
2.4.4 Physical features of lava flow fields	33
2.4.4.1 Rootless eruptions	34
2.4.5 Internal features of lava flows	35

2.4.5.1 Crustal structure	35
2.4.5.2 Cooling joints	36
2.5 Volcanic edifices	38
2.5.1 Monogenetic volcanoes	38
2.5.1.1 Spatter cones and ramparts	42
2.5.1.2 Scoria cones	42
2.5.1.3 Shield volcanoes	44
2.5.1.4 Agglutinate cones	45
2.5.1.5 Tuff cones	46
2.5.1.6 Tuff rings	47
2.5.1.7 Maars	47
2.5.2 Polygenetic volcanoes	48
2.5.2.1 Seamounts	49
2.6 The identification and importance of volcanic features in hydrocarbon basins	50
2.6.1 Lavas	50
2.6.1.1 Basaltic lavas in seismic data	51
2.6.1.2 Basaltic lavas in well data	51
2.6.2 Volcanic edifices	52
2.6.2.1 Volcanic edifices in seismic data	52
2.6.2.1.1 Monogenetic volcanoes	52
2.6.2.1.2 Polygenetic volcanoes	53
2.6.2.1.3 Seamounts	54
2.6.2.2 Volcanic edifices in well data	57
2.7 Non-volcanic edifices found in hydrocarbon basins	57
2.7.1 Mud volcanoes	58
2.7.2 Hydrothermal vents	62
2.7.3 Comparison between types of sedimentary edifices	64
2.8 Summary	65
2.9 References	65
Chapter 3: The Evolution of the 6–8 kyr R-K Basaltic Fissure Eruption, Northeast Iceland	79
3.1 Introduction	79
3.2 Geological setting	80

3.3 Methods	87
3.4 Pyroclastic lithofacies	89
3.4.1 Lithofacies descriptions	100
3.4.2 Distribution of the pyroclastic lithofacies	108
3.4.3 Temporal variations in pyroclast welding intensity, bedding and contacts	109
3.4.4 Variations in componentry	109
3.5 Lava flow field architecture	112
3.6 Sedimentary lithofacies	132
3.7 Architecture of the pyroclastic deposits	136
3.7.1 The R-K feeder dykes	145
3.7.2 Rootless cones	148
3.7.3 Scoria ramparts	151
3.7.4 Sheet-like fall deposits	157
3.7.5 Scoria-agglutinate cone	158
3.7.6 The spatter ramparts	162
3.8 Evolution of the fissure	173
3.9 Discussion	176
3.9.1 Feeder dyke and conduit morphology	176
3.9.2 Rootless eruption mechanisms	177
3.9.3 Scoria ramparts	177
3.9.4 Scoria-agglutinate cone	178
3.9.5 Spatter ramparts	179
3.9.6 Comparison with high-volume fissure eruptions	180
3.10 Summary	184
3.11 References	184
Chapter 4: Rootless Cone Processes Informed from Dissected Vent and Tephra Deposits	191
4.1 Introduction	191
4.2 Geological setting of the Columbia River Basalt Province	193
4.3 Method	195
4.4 Ice Harbor rootless cone field	196
4.4.1 Volcanic ash substrate	196
4.4.2 Ice Harbor lava flows	197
4.4.3 Rootless cone conduits	197

4.4.4 Rootless cone tephra deposits	200
4.4.4.1 Juvenile pyroclast types	200
4.4.4.2 Pyroclastic lithofacies	205
4.4.4.3 Lava-silicic volcanic ash interaction textures in tephra deposits	211
4.5 Emplacement of the Ice Harbor rootless cones	213
4.6 Comparison with other rootless cones	216
4.7 Conclusions	220
4.8 References	220
Chapter 5: The Construction of Submarine Volcanoes: Insights from 3D	224
Seismic Data	
5.1 Introduction	224
5.1.1 Aims	225
5.2 Geological setting	225
5.3 Dataset and methodology	227
5.3.1 Seismic and well data	224
5.3.2 Composition of the edifices	235
5.3.3 Calculating edifice dimensions	235
5.3.4 Seismic facies analysis	237
5.4 Edifice characteristics	240
5.4.1 Pit craters	240
5.4.2 Cone-shaped edifices	240
5.4.2.1 Pointed edifices	240
5.4.2.2 Flat-topped edifices	240
5.4.2.3 Cratered edifices	241
5.4.3 Edifice distribution	243
5.5 Discussion	247
5.5.1 Physical volcanology of the edifices	248
5.5.2 Temporal and spatial evolution of the Bass Basin volcanic field	249
5.5.3 Comparison with other volcanoes in seismic data	252
5.5.4 Implications for the identification of submarine volcanoes	253
5.5.5 Edifice Preservation	253
5.5.6 Limitations of the study	254
5.6 Conclusion	254
5.7 References	254

Chapter 6: Discussion	261
6.1 Introduction	261
6.2 Fissure-eruption derived volcanoes	261
6.3 Rootless cones	263
6.4 Monogenetic edifices in seismic data	265
6.5 References	266
Chapter 7: Summary	270
7.1 Summary and conclusions	270
Chapter 8: Future Work	272
8.1 Directions for future work	272
8.2 References	273
Appendix 1: Support Material for Chapter 3	275
Appendix 2: Support Material for Chapter 4	381
Appendix 3: Support Material for Chapter 5	422
Appendix 4: Material Published in Support of the Thesis	425

List of Figures

Figure 1.1.	Map showing the distribution of Large Igneous Provinces and basins that are the sites of current hydrocarbon exploration. Modified from Coffin and Eldholm (1992), Coffin and Eldholm (1994), Courtillot et al. (1999), Sheth (1999), Jerram and Widdowson (2005), Ross et al. (2005), Rohrman (2007), Bryan and Ernst (2008) and Wright (2013).	1
Figure 1.2.	Seismic section from offshore Norway illustrating the sub-basalt imaging problem – notice that the stratigraphy is obscured beneath the basalt cover. Taken from Jerram (2002).	5
Figure 2.1.	Location, structure and volcanic features of the Faroe-Shetland Basin. Modified from Stoker et al. (1993), Ritchie et al. (1996, 1999), Sørensen (2003), Ellis et al (2009), Moy and Imber (2009) and Wright (2013).	16
Figure 2.2.	Factors controlling lava fountain structure. Modified from Head and Wilson (1989).	24
Figure 2.3.	Schematic diagram illustrating the difference between lava flows, lobes and flow fields. The lava lobe shown is 300 cm wide. Individual lava flows are shaded. The lava flow field ranges in size from tens to hundreds of kilometres. Photograph from Swanson (1974). Diagram modified from Self et al. (1998).	26
Figure 2.4.	Tabular classic (A) and Compound braided flow facies (B) found within flood basalt provinces. Modified from Jerram (2002).	27
Figure 2.5.	Cross section of an ‘a’ā lava. The flow has a massive core with irregular vesicles and an upper and lower crust composed of clinker.	28
Figure 2.6.	Schematic diagram illustrating how pāhoehoe lava transitions to ‘a’ā as a function of strain rate and viscosity. Modified from Peterson and Tilling (1980).	29
Figure 2.7.	Photographs showing (A) P-type, (B) S-type, (C) silvery (D) blue glassy and (E) shelly pāhoehoe. Photograph C is from Leverington (2002) and D is from Wilch (2011). The ruler in A is	32

	10 cm long and the scale card in E is 10 cm long.	
Figure 2.8.	Photographs showing spiny (A), rubbly (B), entrail (C) and clastogenic (D) pāhoehoe. Photograph C from Pendred (2011).	33
Figure 2.9.	Schematic cross section through P-type pāhoehoe. The lobe has a tripartite structure defined by variations in vesicularity, crystallinity and jointing. The basal crust is 20–100 mm thick regardless of lobe thickness and is hypohyaline – hypocrystalline. Cooling joints are sparse. The core of the flow is non-vesicular and holocrystalline. Columnar jointing may penetrate the core. Vesicle cylinders (VCs) and vesicle sheets (VSs) are found. The upper crust comprises 40–60% of the lobe thickness. It is vesicular and hypohyaline – hypocrystalline. It may contain prismatic or irregular joints and numerous horizontal vesicle zones (VZs). Modified from Self et al. (1998).	36
Figure 2.10.	Jointing styles in lavas. (A) The colonnade of a lava flow with regular, columnar jointing. These joints form due to thermal contraction during cooling. (B) The entablature of a lava flow with characteristic wavy-shaped joints. These joints form due to percolation of water through the cooling lava. (C) A tiered lava flow, displaying both an entablature and colonnade. This style of jointing develops due to intermittent flooding and dry periods.	37
Figure 2.11.	Schematic cross section of the Rothenburg scoria cone. Taken from Houghton and Schmincke (1989).	44
Figure 2.12.	Profiles of shield volcanoes in Iceland. The dark column represents the feeder dyke. Taken from Rossi (1996).	45
Figure 2.13.	Schematic cross section of an agglutinate cone. Modified from Brown et al. (2014).	46
Figure 2.14.	Schematic cross section of a tuff cone. (1) Explosion breccia, (2) thinly bedded deposits (3) thickly bedded, massive deposits. Adapted from Wohletz and Sheridan (1983).	46
Figure 2.15.	Schematic cross section of a tuff ring. (1) Explosion breccia, (2) thinly bedded deposits. Adapted from Wohletz and Sheridan (1983).	47

Figure 2.16.	Schematic cross section of a maar and underlying diatreme. UD=Upper diatreme; LD=Lower Diatreme, RZ=root zone. Taken from White and Ross (2011).	48
Figure 2.17.	Schematic cross section of a polygenetic seamount. The seamount is ≥ 5 km in diameter and several hundred metres in height. Modified from Schnur (2007).	50
Figure 2.18.	A comparison of the volcanoes currently recognised in seismic data. (A) Shield volcano, taken from Magee et al. (2013). (B) Maar crater, described by Wall et al. (2010). (C) Seismic line from Jólnir (left) and Stóra-Hraun (right) in the vicinity of Surtsey. Modified from Thors and Jakousson (1982). (D) Seamount in the Faroe-Shetland Basin, modified from Bell and Butcher (2002). (E) Kora andesitic stratovolcano, offshore New Zealand, modified from Bergman et al. (1991).	55
Figure 2.19.	Schematic cross section of a mud volcano. The vertical scale varies from hundreds to thousands of metres. Modified from Evans et al. (2007).	61
Figure 2.20.	Seismic cross section of Lich mud volcano. Modified from Kopf (2002).	61
Figure 2.21.	Schematic cross section of a hydrothermal vent. Vent formation is linked to the heating of pore fluids adjacent to the sill. Modified from Jamtveit et al. (2004).	63
Figure 2.22.	Seismic cross section of an eye-type hydrothermal vent. Modified from Svensen et al. (2003).	64
Figure 3.1	Location of the Sveinar graben in the Holocene rift zone of Northern Iceland. Inset map shows the location of the study area outlined in red and the Tjörnes Fracture Zone (TFZ). Adapted from Gudmundsson et al. (2008).	82
Figure 3.2	Regional geology map of the Rauduborgir-Kvensödul fissure. See Figure 3.1 for location. Lavas produced during the eruption pond in the Sveinar graben towards the south.	83
Figure 3.3	Geological map of the study area. See Figure 3.2 for location.	84
Figure 3.4	Map of faults in the study area. The faults are coloured to indicate	85

	formation prior to, during, or post eruption. Black outline indicates the limit of the R-K stratigraphy. See text for details. See Figure 3.2 for location.	
Figure 3.5	Google Earth image showing the change in strike of the R-K fissure as it is captured by the Sveinar graben. Pyroclastic edifices are shown; not all edifices are numbered for clarity. Note the large (3.5 km) gap between edifices 29 and 30, perhaps resulting from post-eruption erosion. Edifice 35 is located at the end of this section of the fissure.	86
Figure 3.6	Pyroclast types identified in the study area. (A) Spindle-shaped and (B) ragged clast typical of Hawaiian and Strombolian activity. (C) Clast with a brittle rind (outlined) extruding melt from its interiors (arrowed). (D) Fluid clasts that agglutinate, produced from the inner part of the lava fountain or a low fountain. (E) Fluid clasts that coalesce, produced from the inner lava fountain or a low fountain. (F) Cored bombs produced by the recycling of clasts within an edifice. They have a core of cognate lithic clasts and a 10 mm thick coating of lava. (G) An armoured clast with an accidental or cognate lithic core and a partial coating of lava. (H) Scoria lapilli produced from a rootless lava fountain. Notice the furrows in the crust, similar to those in breadcrust bombs.	90
Figure 3.7	Pyroclastic lithofacies observed in the study area. (A) Non-welded scoria lapilli. Inter-clast cavities are visible (outlined). Note the absence of clast flattening. (UTM 557085/7264940). (B) Incipiently welded scoria. Inter-clast cavities are visible (outlined) and clasts are sintered at contacts. Minor clast flattening is observed. (UTM 557442/7264902). (C) Moderately welded scoria. Clast outlines are visible (dashed outline) and some inter-clast cavities (circled) remains. Sub-horizontal clast flattening is parallel to the dashed lines. (UTM 557356/7265748). (D) Densely welded scoria. Flattened clasts (dashed outline) are visible. Small (<1 cm diameter) inter-clast cavities remain. (UTM 563879/7301531). (E) Incipiently welded spatter. Resinous clast rinds are visible (arrowed). (UTM 557433/7264891). (F)	91

	<p>Moderately welded spatter. Vesicular cores of clasts remain (dashed outline) and define the bedding. (UTM 557442/7264902).</p> <p>(G) Densely welded spatter. Thin relict vesicular cores (dashed outline) are visible between densely welded zones. The ghost clasts dip $\sim 10^\circ$. (UTM 557356/7265748). (H) Massive scoria lapilli and bombs. The clasts are incipiently welded. Armoured clasts with an accidental lithic core are common in these deposits. (UTM: 557790/7264865).</p>	
Figure 3.8	<p>Thin section images of pyroclastic lithofacies (plane polarised light). (A) Non-welded scoria lapilli. Note the sphericity of the vesicles compared to the other lithofacies. (B) Incipiently welded scoria. The dashed line indicates an inferred contact between welded clasts. (C) Moderately welded scoria. Domains of less vesicular scoria (dashed outline) are inferred to represent welded clasts. (D) Densely welded scoria. The lithofacies appears texturally similar to clast-supported moderately welded scoria lapilli and bombs (mwSc). (E) Incipiently welded spatter. The dashed line indicates a clast rind folded into the clast core. (F) Moderately welded spatter. Note the increasing crystal content relative to (D) and (E). (G) Densely welded spatter. Note the laminated appearance of the groundmass. The crystal-rich groundmass contains a band of vesicles and is interpreted as the relict core of a spatter bomb. (H) Massive scoria lapilli and bombs. Note the thick bubble septae relative to A and B.</p>	93
Figure 3.9	<p>Density histograms for the pyroclastic lithofacies. (A) Scoria lapilli. (B) Incipiently welded scoria. (C) Moderately welded scoria. (D) Densely welded scoria. (E) Incipiently welded spatter. (F) Moderately welded spatter. (G) Densely welded spatter. (H) Graph showing that clast aspect ratio increases with density for the pyroclastic lithofacies (average of 50; see Table. 3.2).</p>	95
Figure 3.10	<p>Stratigraphic logs showing variations in grain size (black line) and clast aspect ratio (red line); each the average of 10 measurements. Abbreviations for lithofacies are given in Table 3.1. Note the restriction of the lithic clasts to within the crater.</p>	96

Figure 3.11	Stratigraphic logs showing variations in grain size (black line) and clast aspect ratio (red line); each the average of 10 measurements. Abbreviations for lithofacies are given in Table 3.1. Note the restriction of the lithic clasts to within the crater.	97
Figure 3.12	Dispersal and welding characteristics of the tephra and lavas. (A) Graph to show the relationship between distance from the fissure (m) and pyroclast size (mm). Pyroclasts decrease in size with distance. (B) Graph to show the relationship between distance from the fissure (m) and pyroclast lithofacies thickness (m). Deposits thin with distance. (C) Graph to show the relationship between distance from the fissure (m) and aspect ratio. Clast aspect ratio (i.e. welding intensity) decreases with distance. For descriptions of lithofacies see Tables 3.1 and 3.2.	111
Figure 3.13	Lavas observed in the study area. (A) Hummocky lava (Hu) with little erosional dissection. Tumuli and squeeze outs (arrowed) create the hummocky topography. The contact with pre-existing topography is marked by the dashed line. (UTM 556219/7266138). (B) Lava-like agglutinate. Tension gashes (dashed outline) are sub-parallel to the basal contact (UTM 557447/7264902). (C) Clastogenic pāhoehoe (Cl). Gas blisters (outlined) are common. Ghost clasts are identified by intensely deformed non- and incipiently vesicular patches (dashed outline). (UTM 556985/7264113). (D) Crust of spiny pāhoehoe (dashed outline). The crust dips 30° toward the viewer. Spines on the surface of the crust are oriented parallel to the solid white lines. Hammer for scale. (UTM 557457/7265092). (E) Hyaloclastite. The pillow lava (dashed outline) occurs in a matrix of palagonitised pillow fragments. (UTM 558272/7263904). (F) Shelly pāhoehoe. The crusts and internal cavity is visible. The resinous interior surface is thought to be caused by draining of lava from the lobe (UTM 557463/7264067).	113
Figure 3.14	Thin section images of lavas (plane polarised light). (A) Shelly pāhoehoe. Note the large vesicles. (B) Clastogenic pāhoehoe. (C) Lava-like agglutinate. (D) Hyaloclastite. The thin section is taken	114

	from the palagonite matrix. Vesicles are labelled v; sideromelane fragments are labelled s and palagonite is labelled p.	
Figure 3.15	Density histograms for lava lithofacies with a pyroclastic origin. (A) Lava-like agglutinate. (B) Clastogenic lava.	115
Figure 3.16	Features of the columnar-jointed pāhoehoe. (A) Alternating beds of sheet-like columnar-jointed pahoehoe (Cp) and clast-supported weakly agglutinated scoria lapilli and bombs (waSc) (UTM 557469/7264936). (B) Hummocky morphology flow (sensu Self et al. 1998); Cr: crust, Co: core, Ca: cavity. The hammer (circled) is 30 cm long. (UTM 557145/7265409). (C) Megavesicle in the flow core. Graticules on the scale card are 10 cm. (UTM 557772/7265756). (D) Platy fabric observed towards the base of the flow. The scale on the ruler is mm. (UTM 557772/7265756). (E) Vesicle cylinder in the core of a flow. Graticules on the scale card are 1 cm. (UTM 557544/72651054).	119
Figure 3.17	Features of the clastogenic lava. (A) Photograph showing the internal texture of the clastogenic flows, with highly deformed ghost clasts and a suture between lobes towards the base. Hammer for scale. (B) Clastogenic lava with a break out of shelly lava. The shelly lava has been subsequently covered by later clastogenic breakouts. Hammer for scale. (UTM 556985/7264113). (UTM 557465/7266307). (C) Clastogenic lava that has been flooded with water during cooling. The lava has a distinctive entablature comprised of two dominant sets of joints, in which the subsidiary set radiate from the master set. (UTM 556935/7263621).	122
Figure 3.18	Hummocky lava features. (A) A tumulus, with the upper crust partially eroded and the core exposed. Hammer for scale. (UTM 556481/7266232). (B) A lava channel on the surface of the flow field. The channel has resinous walls with vertical striations caused by the draining of lava within the channel. Direction of flow is inferred from the slope (toward viewer). The channel is ~3 m wide. (UTM 547155/7208827). (C) An elongate squeeze out at the margin of the flow field. The squeeze out is composed of numerous crusts that dip radially from the centre of the structure.	124

	Hammer for scale. (UTM 556215/7266339). (D) Photograph of the inside of a lava tube. Backpack for scale. (UTM 557462/7265995).	
Figure 3.19	Features of the lava-like agglutinate (l-l Agg). (A) Tension gashes at the top of unit 5 in log 81. Graticules on the scale card are 1 cm, the arrow indicates up. (UTM 557442/7264902). (B) Intrusion of lava-like agglutinate (l-l Agg) into overlying clast-supported weakly agglutinated scoria lapilli and bombs (waSc). Dashed line indicates contact. (UTM 557442/7264902). (C) Ghost clasts (outlined) in lava-like agglutinate (l-l Agg), overprinted by a spherical vesicle (arrowed). These spherical vesicles suggest post depositional vesiculation of the lava. (UTM 557772/7265756). (D) Equant ghost clast (outlined) interpreted to represent a lava crust lithic. Compare this ghost clast with those in C and clast-supported moderately welded spatter bombs (mwSp; Figure 3.7). (UTM 557772/7265756). (E) Cored bomb with a rind of vesicular juvenile magma. The core is composed of dense agglutinate. (UTM 557442/7264902).	126
Figure 3.20	Figure 3.20. Features of the hyaloclastite. (A) Photograph showing the stratigraphic relationship of hyaloclastite and pillow lavas (Hy) with clastogenic pāhoehoe (Cl) and fSxb (UTM 557949/7263864). (B) Vertical section through the pillow-dominated and fragmental hyaloclastite. This section is also represented in log 7; Figure 3.10 (UTM 557908/7263830). (C) Detail of a pillow lava. The chilled rinds have spalled or been abraded from the majority of the pillow. The aligned vesicles occur in a zone 5 cm wide. The core has large, irregular vesicles (UTM 558272/7263904).	129
Figure 3.21	Panoramic photos of the western wall of the graben formed by faults F9 and F12. The photos show that the area is dominantly composed of clastogenic lavas underlain by lobate beds of clast-supported weakly agglutinated scoria lapilli and bombs (waSc) <0.5 m in thickness. 3 m wide flows of shelly pāhoehoe are also observed. Hyaloclastite thickens towards the southwest (Figure	130

	3.3) and is inferred to be underlain by fSxb, as observed on the east of the graben (Figure 3.22). (A: UTM557585/7264214; B: UTM557595/7264181; C: UTM557601/7264125; D: UTM557616/7264059; E: UTM557649/726; F: UTM 557656/7263914).	
Figure 3.22	Panoramic photos of the eastern wall of the graben formed by faults F9 and F12. The photos show that the area is composed of clastogenic and hummocky lavas underlain by lobate beds of clast-supported weakly agglutinated scoria lapilli and bombs (waSc) <0.5 m in thickness. The contacts between the hummocky and clastogenic lavas are unclear. Numerous lobes 1–5 m thick are observed within the clastogenic lavas. Hyaloclastite thickens towards the southwest (Figure 3.3) and is underlain by fSxb. Note the absence of Clast-supported weakly agglutinated scoria lapilli and bombs (waSc) at the base of the stratigraphy in (A), suggesting either that this section of the fissure was dominated by effusive activity, or that the pyroclasts coalesced to form lava which subsequently interacted with surface water (forming hyaloclastite). (A: UTM 557934/7263920; B: UTM 558083/7264079; C: UTM 557849/7264219).	131
Figure 3.23	Photograph showing shelly pāhoehoe at the opening of a horseshoe-shaped scoria cone (UTM 557647/7265074).	132
Figure 3.24	Sedimentary lithofacies observed in the study area. (A) Fine, diffusely bedded volcanoclastic pebbly sandstone (pebbles are outlined). See log 16 for stratigraphic position. (UTM 557437/7263977). (B) Inverse-graded cobble breccia. See log 16 for stratigraphic position. (UTM 557437/7263977). (C) Fine, cross bedded volcanoclastic sandstone with gravel, pebbles and cobbles. See log 81 for stratigraphic position. (UTM 557495/7265751). (D) Fine, hummocky cross-stratified pebbly sandstone. Sub-horizontal diffuse beds ~10 cm thick are marked by dashed lines. See log 81 for stratigraphic position. (UTM 557442/7264902). See Tables 3.1 and 3.2 for lithofacies descriptions.	133

Figure 3.25	<p>Photographs of the canyon walls. (A) Cross section of a scoria-agglutinate cone (location 289; edifice 26) and scoria rampart (location 280). Crater 2 of an overlapping edifice is also shown. (UTM 557542/7264269). (B) Photograph of the canyon wall north of image A. The R-K volcanic sequence is composed of sheet-like fall deposits, scoria ramparts and lava flows of columnar-jointed pāhoehoe (Cp) and clastogenic pāhoehoe (Cl). Numerous faults are visible with throws of ~1 m. The northwestern bounding fault of the Sveinar graben is ~20 m left of the image. (UTM 557617/7265642). (C) Photograph of the western canyon wall. A scoria rampart (Location 477) is observed and has anticlinal bedding at its base. Clastogenic lavas onlap the rampart towards the southeast. Contacts beneath the rampart within crystalline and clastic successions are gradational and beds may pinch-out laterally. The graben bounding fault (F33) is visible toward the southeast. The northwest graben fault is not visible from this location. (UTM 557356/7265748). (D) Photograph of the western canyon wall. The volcanoclastic sandstone with planar bedding (vSpb) is observed at the base of the R-K volcanic sequence. Faults are numbered according to Figure 3.4. (UTM 557617/7265642).</p>	137
Figure 3.26	<p>Location and orientation of faults associated with edifice 26 and the scoria rampart (location 280). Faults are labelled according to Figure 3.4 and are indicated by the dashed line. Arrows indicate the direction of downthrown. The contact between the underlying stratigraphy and the R-K stratigraphy is indicated. (A) F10 is exploited by the R-K feeder dyke. Throw is observed to be ~3 m southeast. (UTM 557542/7264269). (B) Numerous faults in the scoria rampart (location 280). Note the throw in the upper pyroclastic units (stippled lines). (UTM 557465/7264189). Images C–F show deformed blocks of clast-supported densely welded spatter bombs (dwSp) located at the top of normal faults (UTM 564033/7302375). Ghost clasts indicate the original depositional fabric, whilst tension gashes that intersect the bedding suggest</p>	138

	ductile deformation in a viscous deposit. Movement was not along the depositional planes, nor confined to the margins of the clast-supported densely welded spatter bombs (dwSp). Ghost clasts are downthrown towards the west (indicated by the dashed line) and suggest extensional deformation. The ruler in C is 70 cm. The block in E is 20 mm wide. Similar features are observed in the clast-supported densely welded spatter bombs (dwSp) at the top of F2. Deformation is interpreted to be the result of syn-eruptive faulting. (G) Map showing location of the faults.	
Figure 3.27	Location and orientation of selected faults (dashed lines). Faults are labelled according to Figure 3.4. Arrows indicate direction of downthrown. The contact between the underlying stratigraphy and the R-K stratigraphy is indicated. (A) F6 forms the margin of an inlet and offsets the upper clastogenic pāhoehoe (Cl). (UTM 557601/7265530). (B) Syn-eruptive slip along F17 is inferred to have resulted in the ductile deformation of the upper agglutinated pyroclastic units resulting in a break in slope at the surface. (UTM 557772/7265756). (C) Fault 21 forms an inlet on the river and forms a gully. There is no topographic expression of the fault in the uppermost lavas. (UTM 557772/7265756). (D) Faults 19 and 20. Columnar-jointed pāhoehoe (Cp) occurs within the graben formed by these faults. (UTM 557601/7265530). (E) Map showing location of the faults.	140
Figure 3.28	Location and orientation of the Sveinar graben bounding faults and stereonet data. Faults are labelled according to Figure 3.4 and are indicated by the dashed line. Arrows indicate direction of downthrown. The contact between the underlying stratigraphy and the R-K stratigraphy is indicated. (A) Segmented graben bounding faults (F31–33) east of the river. (UTM 557432/7264244). (B) Graben bounding fault west of the river. The lava-like agglutinate (l-l Agg) terminates against the footwall of the graben. The contact between the lava-like agglutinate (l-l Agg) and clastogenic pāhoehoe (Cl) is shown as a stippled line. Note the absence of faulting in the hummocky pāhoehoe (Hu),	141

	<p>indicating that the fault existed prior to the eruption. (UTM 563879/7301531). (C) Google Earth image showing F33 (arrowed) faulting the uppermost clastogenic lavas, indicating that the fault had several stages of growth. The fault is concealed further north by scoria (dashed outline). (D) F9 forming the margin of an inlet. The clastogenic pāhoehoe (Cp) is offset by the fault. (UTM 557617/7265642). (E) Pole to plane plot showing the orientation of faults XA, F0,1,4–6,9,13,17, 19–21, 31–33 and 38. (F) Google Earth image showing that F33 (the eastern Sveinar graben bounding fault) does not have a scarp east of the river. This suggests that either: the fault is segmented and slip did not occur on this section of the fault; and/or the eruption continued after faulting. (G) Map showing location of the faults.</p>	
Figure 3.29	Google Earth image showing the extent and bedding of the pyroclastic constructs. See text for details.	143
Figure 3.30	<p>Figure 3.30 (overleaf). Architectural features of the dyke. (A) Thin section image of the dyke (plane polarised light). The sample is taken 30 cm from the country rock contact. (B) View toward the conduit from the west of the canyon. The underlying plagioclase porphyritic lava flows are the source of the lithic clasts in log 29 (Figure 3.12). Note the scalloped contacts between the dyke and country rock and the numerous intrusions into the overlying pyroclasts. (UTM 557617/7265642). (C) Plot of depth from the top of the canyon vs. conduit radius. The flaring hinge is located at a depth of 40 m at the base of the porphyritic lavas. (D) An effusive dyke on the west of the canyon feeding overlying lava-like agglutinate (l-l Agg). Dashed lines indicate cooling joint orientations. See Figure 3.25 for location. (UTM 557460/7264234). (E) A section of the dyke adjacent to the river on the west of the canyon. Dashed lines indicate cooling joint orientations. The solid line indicates the contact with the country rock. Bag (circled) is ~0.5 m. See Figure 3.25 for location. (UTM 557510/7264268). (F) Multiple chilled margins at the dyke/country rock contact. The scale card is 10 cm long. Dashed</p>	147

	lines indicate laminations spaced ~ 2 cm. See (D) for location. (UTM 557510/7264268). (G) Arrested dyke intruding into overlying pyroclastics west of the river. See Figure 3.25 for location. Lithofacies codes are as Figs. 3.8 and 3.13. (UTM 557519/7264280).	
Figure 3.31	Comparison between rootless vents at Hjalparfoss (UTM 402187/7098548) and those along the R-K fissure (UTM 557772/7265756). Images A and C show the vents and the host lavas flows along the R-K fissure and at Hjalparfoss respectively, images B and D show the contact between the columnar jointed pāhoehoe (Cp) lava and massive scoria lapilli and bombs (mSc). Notice the colonnade (CN) and entablature (EN) of the lava flows with cooling joints that radiate from the hummocky, bowl-shaped upper contact. The ruler in B and D is 25 cm.	150
Figure 3.32	Photograph (A) and a reconstruction of the geometry of the pyroclastic constructs immediately after the eruption (B). Truncated beds are visible in the NW margin of the scoria rampart (location 280) and in the crater of cone 26. Field observations suggest ~10 m of stratigraphy is has been eroded from the cone and the rampart. (A: UTM 557542/7264269).	155
Figure 3.33	Google Earth image showing the inferred location of paleo-channels, contemporary channels and the outcrops of sedimentary lithofacies.	156
Figure 3.34	Scoria ramparts adjacent to the Laki fissure. (A) Google earth image showing that the ramparts are linear and crescent-shaped, elongated parallel to the fissure. They occur on the outer margin of the cones. (B) Photo of scoria ramparts, showing that they are asymmetric and larger than the adjacent cones. The ramparts decrease in thickness towards and with distance from the fissure. Photo: Nick Crabtree.	157
Figure 3.35	Photographs showing the architecture of edifice 26. (A) The rosette structure is located above the feeder dyke. The cooling joints at the top of the rosette are more closely spaced and shorter than those at the base, implying that the rosette cooled from the	161

	<p>top downwards. (UTM 557498/7264870). (B) A lobate lense of clast-supported weakly agglutinated scoria lapilli and bombs (waSc) within the lava-like agglutinate (l-l Agg). The lava-like agglutinate (l-l Agg) has distinct contacts with the clast-supported weakly agglutinated scoria lapilli and bombs (waSc) and is interpreted to be part of a lava sill/dyke network. (UTM 557447/7264902). (C) View of the northern crater rim showing the outwardly dipping units of lava-like agglutinate (l-l Agg) which merge further west. Inverse-graded cobble breccia (cPi) and fine, diffusely bedded volcanoclastic pebbly sandstone (fSdb) are visible inside the crater. (UTM 557438/7264880). (D) Photo of the outwardly dipping lithofacies on the crater rim. (UTM 557447/7264902).</p>	
Figure 3.36	<p>Orientation and onlap relationships of the spatter ramparts. (A) Google Earth image showing that some spatter ramparts are oriented perpendicular to the strike of the fissure. (B) Google Earth image of eroded spatter ramparts that are oriented parallel to the strike of the fissure. (C) Photograph of the spatter ramparts shown in B. (D) Google Earth image of scoria cone 22 overprinting adjacent spatter ramparts. The onlapping relationship of the edifices cannot be used to constrain the direction in which the fissure propagated.</p>	165
Figure 3.37	<p>Figure 3.37. Google earth image (A), geological map (B) of the spatter ramparts west of the river. See Figure 3.3 for location.</p>	166
Figure 3.38	<p>Features and measurements associated with location Y29. (A) Scoured agglutinate slab with adjacent sections missing, exposing underlying rubbly agglutinate. The slab has detached from the upper section (arrowed) where the dip of the outcrop changes. The tape measure (arrowed) is 1 m long. (UTM 564346/7301822). (B) Close up of the scours overprinted by tension gashes (outlined), indicating deformation of the agglutinate after the external surface was scoured. Graticules on the scale card are 1 cm. (UTM 564346/7301822). (C) Stereonet plot to show orientation of bedding (black) and scours (purple) on</p>	167

	<p>the southwest face of location Y29. The scour plunges are not parallel to the bedding dip direction suggesting that sliding from the outer face occurred in numerous directions with a component of lateral movement. (D) Cross sectional view of the snout of an agglutinate bed. The tension gashes (dashed lines) on the crust (Cr) are perpendicular to the scours (sub vertical striations) and give the snout a rugose texture. The core of the bed (Co) is also exposed (see Figure 3.39 for details). The tape measure is 1 m long. (UTM 564346/7301822). (E) A rugose textured surface, showing irregular protrusions separated by tension gashes. The ruler is 10 cm long. (UTM 557584/72664247). (F) Graph showing that tension gashes are most abundant towards the snout of the agglutinate sheets, where 0 = the snout tip. (G) Graph showing that crenulation width tends to decrease with distance from the snout of agglutinate beds, where 0 = the snout tip. Graphs F and G suggest that strain is greatest towards the snout of the beds.</p>	
Figure 3.39	<p>Stratigraphic log showing the internal componentry of location Y29. The outcrop is composed of numerous discordant slabs of agglutinate. The upper unit of agglutinate is shown in Figure 3.38D. See Figure 3.37 for the location.</p>	169
Figure 3.40	<p>Photographs and measurements associated with location Y28. (UTM 564390/7301820). (A) Cross section of the agglutinate, with clast-supported incipiently welded spatter bombs (waSp) beneath. The agglutinate becomes more vesicular with height and has a 70 mm thick platy crust. Tension gashes occur at the base (arrowed) and in the incipiently vesicular agglutinate in the upper 0.5 m. The tape measure is 50 cm long. (B) Log showing the internal stratigraphy of A. Clast aspect ratio is shown in red, juvenile clast size in black. (C) Details of the ghost clasts (solid lines). Graticules on the scale card are 1 cm. (D) Stereonet to show the orientation of the crust (great circles) tension gashes (black) and ghost clasts (purple). The tension gashes are approximately perpendicular to the outer crust. (E) Photo of the upper crust showing the jigsaw-fit plates. The tape measure is 25</p>	170

	cm long.	
Figure 3.41	<p>Schematic diagram to show the development of Location Y29. Images A and B show the accumulation and coalescence of constituent spatter bombs during Hawaiian-style activity. Images C–E show the evolution of the south face, whilst images F–H show the evolution of the north face of the rampart. (C) Agglutinate slides down the rampart, scouring the underlying face. The material that causes the scouring is not observed. (D) Continued lava fountaining deposits spatter bombs atop the scoured surface. (E) The spatter bombs coalesce forming a slab of agglutinate, on which a crust develops. This crust is deformed by tension gashes (found dominantly towards the snout of the slab) during clastogenic flow. This slab has scours on its outer surface, suggesting repeating episodes of deposition and flow (not shown). The absence of material at the toe of the slab may suggest collapse of the slab in stages. (F) On the northern slope scouring occurs due to sliding of material down the outer rampart face. (G) The scours are preserved as the rampart cools and a brittle crust develops. (H) Fractures form at the change in dip amplitude and sections of the outer crust collapse due to gravitational instability.</p>	171
Figure 3.42	<p>Interpretive picture to show the development of location Y28. (A) High rate accumulation of spatter bombs during lava fountaining. Welding intensity is greatest beneath the dashed line. (B) Agglutination and coalescence of pyroclasts. Ghost clasts remain in the upper part of the deposit. (C) Bubbles migrate upwards in the deposit and a crust forms. (D) Gravitational spreading is initiated along the basal lubricating layer. The crust is fractured into numerous plates. Note that stages A and B are contemporaneous: welding and coalescence occurring during deposition.</p>	172
Figure 3.43	<p>Schematic diagram to show the development of the R-K fissure. (A) Phase 0: The Sveinar graben pre-dates the fissure. Drainage patterns are controlled by pre-existing faults. (B) Phase I: The dyke fed numerous en-echelon fissure segments that propagated</p>	175

	north-south. (C) Phase II: Lava flows buried scoria ramparts. The fissure began to evolve to numerous point sources due to thermal instabilities. (D) Phase III: Low fountains ≤ 100 m in height constructed edifice 26 (location 289). (E) Phase IV: In the north of the study area, hummocky lava was emplaced. (F) Phase V: Pyroclastic constructs were deformed by slip along faults. Post-eruption faulting associated with the Sveinar graben continued. Diagram not to scale.	
Figure 4.1	Generalised structure of a rootless cone. The cones form on active lava flows. The conduits in the host lava flow are irregular funnels that widen upwards. The upper parts of the conduits are filled with tephra. Cooling joints in the host lava flow radiate from the conduit. Cone forming deposits are composed of lapilli- to bomb-sized material that is often reversely graded and formed by fallout. Platform and sheet deposits are formed by fallout and deposition from pyroclastic density currents. Adapted from Hamilton et al. (2010a).	193
Figure 4.2	Location of the study area. (A) The CRFBP in the NW USA, adapted from Brown et al. (2014). (B) Map of the area showing the Ice Harbor fissure as described by Swanson et al. (1975) and the field area on the banks of the Snake River. (C) Sites of the tephra and conduit deposits described in this study.	195
Figure 4.3	Field photographs and schematic diagrams showing the varying geometries of rootless conduits. (A) Field sketch showing the upper part of a funnel-shaped conduit at location 6 (UTM Nad83 zone 11T, 359 987 E/5 126 647 N). View to the southwest. (B) Field photograph of massive spatter (mSp) within the conduit in a, composed of spatter bombs, silicic volcanic ash and hypocrySTALLINE lapilli. (C) Irregular lower part of a conduit in the lava flow at location 22 (UTM Nad83 zone 11T, 359 724 E/5 128 162 N) with cooling joints (white) radiating from the conduit/lava core contact (outlined). The ruler is 1 m. Inset D shows a close up of the conduit inner wall with embedded juvenile and lava crust lithic clasts. The ruler is 25 cm. Image E shows a cross section	199

	through the conduit wall, with hypohyaline lapilli embedded into the surface. (F) Interpretive sketch of E. (G) Plan view of a section of conduit wall, approximately 100 mm across, showing clasts that are inferred to have become embedded in the conduit wall during explosions (dashed outlines).	
Figure 4.4	Clast types recognised in this study. (A) Folded spatter bomb with embedded lapilli (dashed outline). Graticules on the scale card are 1 cm (UTM Nad83 zone 11T, 359 942 E/5 126 519 N). (B) Ventricular clast (outlined). The clast has an amoeboid shape with a hypohyaline rind approx. 10 mm thick that grades inwards into the core. Vesicles up to 8 cm in diameter (dashed outline) have angular shapes and give clasts their characteristic ventricular morphology (UTM Nad83 zone 11T, 359 942 E/5 126 519 N). (C) Globular bomb (outlined). The bombs have a sub-spherical shape and a black hypohyaline rind ~1 cm thick that becomes more orange in colour toward the core. Sub angular, dull black coloured basaltic lapilli (arrowed) are contained within the cores of the bombs. Cooling joints (dashed lines) penetrate from the clast margin up to 10 mm towards the core (UTM Nad83 zone 11T, 359 942 E/5 126 519 N). (D) Armoured bomb (solid outline) with 1 cm thick dense rind and vesicular core (dashed outline) (UTM Nad83 zone 11T, 360 015 E/5 126 664 N). (E) Sideromelane clast (arrowed) formed by fragmentation in a brittle state (arrowed). (F) Sideromelane clast (arrowed) formed by ductile disruption of molten lava.	202
Figure 4.5	Lithofacies found in the study area. (A) mL A with ventricular bomb (outlined) enclosing laminated silicic volcanic ash. Graticules on the scale card are 1 cm (UTM Nad83 zone 11T, 359 881 E/5 126 506 N) (B) lensLA with hypocrySTALLINE lapilli-rich lenses. Dashed white outlines indicate lenses (UTM Nad83 zone 11T, 359 868 E/5 126 485 N) (C) lensLA with silicic ash-rich lenses. White outlines indicate lenses (UTM Nad83 zone 11T, 359 868 E/5 126 485 N) (D) xsLA, white outlines indicate beds. The ruler is 25 cm long (UTM Nad83 zone 11T, 359 868 E/5 126	206

	485 N) (E) //bSp, showing bedded spatter bombs. The ruler is 50 cm (UTM Nad 83 zone 11T, 359 942 E/5 126 519 N).	
Figure 4.6	Lithofacies logs of tephra deposits south of the river. Clast size is shown on the top axis with divisions at 32, 64, 128 and 256 mm (Location 9 uses 32, 64, 128, 256 and >1000 mm divisions). Silicic volcanic ash abundance (black squares; %) is shown across the bottom axis in 25% graticules. Logs are shown at relative altitudes. For locations of the sections see Fig. 4.2.	209
Figure 4.7	Photographs and interpretive pictures of Location 9 (UTM Nad 83 zone 11T, 359 942 E/5 126 519 N). a, b Outcrop of platform-forming admixed tephra and silicic volcanic ash. c,d Outcrop of cone-forming tephra composed of lithofacies //bSp.	210
Figure 4.8	Peperite-like textures produced by the interaction of juvenile clasts and silicic volcanic ash. (A) Fluidal peperite with elongate and globular clasts in lithofacies //bSp (UTM Nad 83 zone 11T, 359 942 E/5 126 519 N). (B) Blocky peperite with jigsaw-fit fractures (circled). Graticules are 1 cm (UTM Nad 83 zone 11T, 360 014 E/5 126 649 N). Thin section C and interpretive sketch D shows section of mingled spatter and silicic volcanic ash. The spatter clasts exhibit elongate and globular morphologies. The silicic ash is thermally altered and contains vesicles. Vesicles within the spatter clasts enclose silicic volcanic ash. Section of a ventricular bomb E and interpretive sketch F are also shown. The hypohyaline rind is spalling from the core and has encapsulated a domain of silicic volcanic ash. Fluidal basalt clasts are found within the silicic ash domain (arrowed) indicating that the core of the bomb was molten when the sediment was encapsulated.	212
Figure 4.9	Inferred eruption chronology for the cones. (A) Lava flow traverses wet ground and subsides heterogeneously into the underlying silicic volcanic ash. (B) Initial mingling of lava with the silicic ash results in the formation of globular and ventricular juveniles and peperite-like textures. (C) Interaction between molten lava and water saturated silicic volcanic ash results in explosive brecciation of the host lava flow and fragmentation of	215

	<p>the globular and ventricular juveniles into lapilli and ash sized clasts. Episodic eruptions and dilute PDC's deposit poorly sorted juveniles and clasts sourced from the host lava flow, forming sheet and platform deposits (lithofacies m/nLA(f), lensLA, xsLA). Minor clast recycling may occur, producing armoured bombs. Substrate pore water is gradually depleted beneath the lava flow. (D) Decreasing water availability results in less efficient fragmentation and lava fountains are generated. These fountains produce lithofacies //bSp that builds a cone. Lapilli are also impacted into the cooling conduit walls. (E) With time water availability decreases and eruptions cease. The lava flow may continue to inflate and deform the conduit. Post-eruption cooling of the lava promotes the formation of cooling joints that radiate from the conduit.</p>	
Figure 4.10	<p>Photographs of Leitin and Búrfell rootless cones in southern Iceland (UTM Nad 83, zone 27, 500 000 E/7 097 014 N; 402 187 E/7 098 548 N respectively). (A) Overlapping cone stratigraphies composed of crudely bedded spatter and scoria bombs and lapilli and clastogenic lava. The sequence is ~6 m thick. (B) Bomb-sized clast of sediment (outlined) within a sequence of scoria and spatter. The ruler is 40 cm long. (C) Sediment-rich pyroclastic density current deposit at the base of the cone forming stratigraphy. The reddish colour is given by the agglutinated sediment (inferred to be a lacustrine siltstone), not oxidation of the pyroclasts. The scale card is 120 mm long. (D) Bomb-sized, ventricular-type pyroclast (outlined) within the bedded spatter and scoria. The ruler is ~25 cm long. (E) Initial cone-forming fall deposit, composed of scoria lapilli. Beds often form inversely-graded couplets. The bed indicated is ~6 cm thick. Beds thickness and clast size increases up-section. (F) Cross section of the conduit wall, with lapilli sized pyroclasts agglutinated to the outer wall. Cooling joints (dashed lines) radiate from the contact and are perpendicular to the conduit contact. The arrow points towards the core of the lava flow. The</p>	217

	ruler is 30 cm long. (G) A lava flow affected by rootless cone formation. The lava flow can be divided into a colonnade (CN) and an entablature (EN), and has an irregular upper contact that forms the rootless conduit. The lava is ~10 m thick.	
Figure 5.1.	Location of the study area. The Bass Basin is shown in green, the red outline delimits the Labatt survey and the yellow delimits Yolla survey. Bass-1, King-1, Yolla-1 and Cormorant-1 wells are also shown. A 2D seismic line (A–A'; Fig. 5.2) between the surveys is shown. A simplified stratigraphy of the Bass Basin is also shown. Modified from Boral Energy Resources Ltd. (1998).	226
Figure 5.2.	Seismic line A–A' and interpretation intersecting the Cormorant-1, Bass-1 and Yolla-1 wells. Correlated horizons are also shown.	229
Figure 5.3.	Well logs for King-1, Cormorant-1, Bass-1 and Yolla-1. Seismic horizons are also shown: LMM=Lower Mid Miocene, TV=Top Volcanic, BV=Base Volcanic, OH=Oligocene, Demons Bluff=DB, EVCM=Eastern View Coal Measures, LV=Lower Volcanic, TA=Top Aroo and BA=Base Aroo. Adapted from Trigg et al. (2003).	230
Figure 5.4.	Time (A) and amplitude (B) maps of the TV horizon in the Labatt survey. The edifices (dashed outline) are numbered in B. See Fig. 5.5 for cross section.	232
Figure 5.5.	Seismic line B–B' and interpretation in the Labatt survey. See Fig. 5.4 for location.	228
Figure 5.6.	Time (A) and amplitude (B) maps of the TV horizon in the Yolla survey. The edifices (dashed outline) are numbered in B. See Fig. 5.7 for cross section.	233
Figure 5.7.	Seismic line C–C' and interpretation in the Yolla survey. See Fig. 5.6 for location.	234
Figure 5.8.	Seismic line X–Y showing that the basal diameter of the edifices (A–B) is calculated from the change in seismic facies and amplitude of the edifice. See Fig. 5.4 for location.	236
Figure 5.9.	Seismic sections showing the seismic facies of the pit craters (A), pointed (B), flat-topped (C) and cratered (D) edifices. The	242

	location of the sections is shown in the time map of the Labatt survey (E).	
Figure 5.10.	Features associated with the pointed edifices. Seismic line (A). Horizons V1 and V2 are shown in B and C respectively. See Fig. 5.9 for location. (B) Concentric faulting (dashed lines) in horizon V1 around the underlying conduit. (C) Concentric faulting (dashed lines) in horizon V2 around the underlying conduit. (D) Time slice at 0.63 s TWTT beneath the edifice showing an onion-ring structure.	243
Figure 5.11.	Seismic line (A) and interpretation (B) showing that the edifices in linear clusters young towards the south.	245
Figure 5.12.	Seismic section (A) and time map (B) of a flat-topped edifice fed by a sill/dyke system. See Fig. 5.4 for location.	246
Figure 5.13.	Amplitude map of the LV horizon. Inset B shows a RGB decomposition image of the lava flows.	247
Figure 5.14.	Schematic diagram to show the evolution of a submarine monogenetic volcano. (A) Submarine maar-diatreme complexes form during Taalian-style activity. Syn- and post-eruptional sediments fill the Continued activity results in the submarine effusion of lavas, building pillow volcanoes. These are represented by the pointed edifices. (C) Tuff cones, represented by the flat-topped and cratered edifices, are formed during Surtseyan activity. Ponding of lavas within the crater resulted in the formation of flat-topped volcanoes. These edifices may have been emergent. Image (D) shows the location of diagrams A–C.	251
Figure A.1.	Seismic section (A) and interpretations (B and C) of the cone-shaped edifice observed on the 2D seismic line between the Yolla and Labatt surveys. The edifice has identical internal facies to the edifices observed in the Labatt and Yolla surveys, although its morphology is somewhat different. Well data from King-1 indicates that the edifice is composed of volcanic rock. LMM=Lower Mid Miocene, TV= Top Volcanic.	422
Figure A2.	Amplitude map of the Lower Volcanic Horizon in the Labatt survey.	423

List of Tables

Table 2.1	Summary of volcanic edifice morphology. Data from Waters and Fisher (1971); Wood (1980); Head et al. (1981); Wilson and Head (1981); Thors and Jakousson (1982); Wohletz and Sheridan (1983); Gatliff et al. (1984); Ross (1986); Rossi (1996); Vespermann and Schmincke (2000); White and Ross (2011); Grosse et al. (2009); Mitchell et al. (2012) and (Brown et al., 2014).	40
Table 2.2	Table 2.2. Summary of volcanic edifice architecture (*water depth to summit). Data from Macdonald (1972); Wohletz (1983); Lorenz (1986); Rossi (1996); Riedel et al. (2003); Grosse et al. (2009); White and Ross (2011); Mitchell et al. (2012); Magee et al. (2013) and Brown et al. (2014).	41
Table 2.3	Summary of the seismic characteristics of volcanic edifices in seismic section. Data from Thors and Jakousson (1982); Bergman et al. (1991); Bell and Butcher (2002); Thomson (2005); Wall et al. (2010) and Magee et al. (2013).	56
Table 2.4	Summary of the morphology of sedimentary edifices. Data from Kopf et al. (1998); Yusifov and Rabinowitz (2004); Davies and Stewart (2005); Planke et al. (2005); MØller Hansen (2006); Svensen et al. (2006); Svensen et al. (2007); Huuse et al. (2010); Grove (2013).	58
Table 2.5	Summary of the seismic characteristics of sediment type vents in seismic section. Data from Kopf et al. (1998); Davies and Stewart (2005) Stewart and Davies (2006); Evans et al. (2007) and Roberts (2011).	59
Table 3.1	Terminology and definitions.	88
Table 3.2	Summary descriptions of pyroclastic lithofacies.	98
Table 3.3	Summary of the texture, distribution and petrography of the pyroclastic lithofacies	99
Table 3.4	Summary table of lavas and dyke (* sample depth 80 m beneath paleo-surface)	116

Table 3.5	Summary of sedimentary lithofacies. All lithofacies are interpreted as fluvial deposits, possibly related to glacial floods.	134
Table 3.6	Summary features of pyroclastic deposits. *shortest axis	144
Table 4.1	Summary descriptions of pyroclast types.	204
Table 4.2	Summary descriptions of cone-forming and conduit deposits.	208
Table 4.3	Comparison of rootless and littoral cone structures using data from Simpson and McPhie (2001); Mattox and Mangan (1997); Moore and Ault (1965); Fisher (1968); Hamilton et al. (2010a); Melchior Larsen et al. (2006); Jurado-Chichay et al. (1996); and this study.	219
Table 5.1	Summary characteristics and interpretation of seismic facies.	235
Table A1.1	Orientations of faults	275
Table A1.2	Point count data for lithofacies.	276
Table A1.3	Measurements of platy zone in columnar basalt, log 14, unit 4	276
Table A1.4	Measurements of platy zone in columnar basalt, Log 30, unit 1.	276
Table A1.5	Measurements of platy zone in columnar basalt, Log 12, unit 11.	277
Table A1.6	Density measurements for waSp.	278
Table A1.7	Density measurements for mwSp.	280
Table A1.8	Density measurements for l-l Agg.	282
Table A1.9	Density measurements for dwSp.	286
Table A1.10	Density measurements for ScL.	287
Table A1.11	Density measurements for waSc.	289
Table A.1.12	Density measurements for mwSc.	292
Table A1.13	Density measurements for Cl.	293
Table A1.14	Density measurements for dwSc.	295
Table A1.15	Bedding measurements for edifices.	296
Table A1.16	Dispersal characteristics for the tephra.	298
Table A1.17	Bedding measurements in scoria rampart.	301
Table A1.18	Stratigraphic log measurements from 2012.	303
Table A1.19	Stratigraphic log measurements from 2013.	335
Table A1.20	Measurements of lithic clasts.	338
Table A1.21	Measurements of scours at location y29.	366

Table A1.22	Measurements of tension gashes at location y26.	367
Table A1.23	Measurements of scours at location Y29.	368
Table A1.24	Measurements of tension gashes at location y26.	368
Table A1.25	Measurements of tension gashes at location y28.	370
Table A1.26	Measurements of tension gashes at location y28.	371
Table A1.27	Measurements of tension gashes at location y29.	372
Table A1.28	Measurements of tension gash distribution at Location Y29.	372
Table A1.29	Measurements of tension gash lengths at location y29.	373
Table A1.30	Measurements of tension gashes at location y29.	374
Table A1.31	Measurements of tension gashes at location y27.	375
Table A1.32	Measurements of tension gashes at location y29.	376
Table A1.33	Measurements if tension gashes at location y35.	377
Table A1.34	Measurements of tension gashes at location y37.	377
Table A1.35	Measurements of tension gashes at location y37.	378
Table A1.36	Measurements of tension gashes at Location Y42.	379
Table A2.1	Measurements of the lapilli impacted into the conduit walls.	381
Table A2.2	Measurements of juvenile clast sizes and lithofacies type.	395
Table A2.3	Summary of unit thickness, average maximum clast size and Silicic volcanic ash abundance.	400
Table A2.4	Spacing of cooling joints in host lava flows.	401
Table A2.5	Juvenile abundance calculated using IJ.	402
Table A2.6	Point count measurements of pyroclasts. Glass content corrected for vesicles and Silicic volcanic ash. Point counts conducted at 20X mag.	403
Table A2.7	Image analysis measurements of sideromelane ash.	406
Table A2.8	UTM coordinates of study locations.	408
Table A2.9	Sorting of Silicic volcanic ash calculated by sieving.	408
Table A2.10	Measurements of largest clasts in lithofacies mSp.	409
Table A2.11	Density measurements for the Ice Harbor lava core. Weight is in g, density in kg m^{-3} , vesicularity in %.	410
Table A2.12	Density measurements for the spatter bombs. Weight is in g, density in kg m^{-3} , vesicularity in %.	412
Table A2.13	Density measurements for the armoured bombs. Weight is in g,	414

	density in kg m ⁻³ , vesicularity in %.	
Table A2.14	Density measurements for the hypocrystalline lapilli. Weight is in g, density in kg m ⁻³ , vesicularity in %.	417
Table A2.15	Measurements of ventricular and globular bomb fragments in lithofacies lensLA, mSp and mLA.	419
Table A3.1	Summary of measurements for vents described in this study. Vents 1–28 are found within the Labatt survey, 29 – 34 are within the Yolla survey.	424

Chapter 1: Introduction

1.1 Flood basalt volcanism and hydrocarbon exploration

Flood basalt volcanism has produced the largest and most extensive lava flow fields in Earth's history, covering areas 10^6 km^2 in size (Jerram and Stollhofen 2002; Bryan and Ernst 2008; Bryan et al. 2010). The products of this volcanism provide information on the timing of major mantle melting events and may be linked to mass extinctions (e.g. Thordarson et al. 1996; Wignall 2001; Jerram 2002; Thordarson et al. 2009). Since flood basalt emplacement is associated with continental breakup (Courtilot et al. 1999), many flood basalt provinces are located in oceanic basins. These basins are frontier regions for hydrocarbon exploration (Fig. 1.1). The Faroe Shetland Basin (FSB) in the North Atlantic Igneous Province (NAIP) is one such basin and provides the motivation for this research.

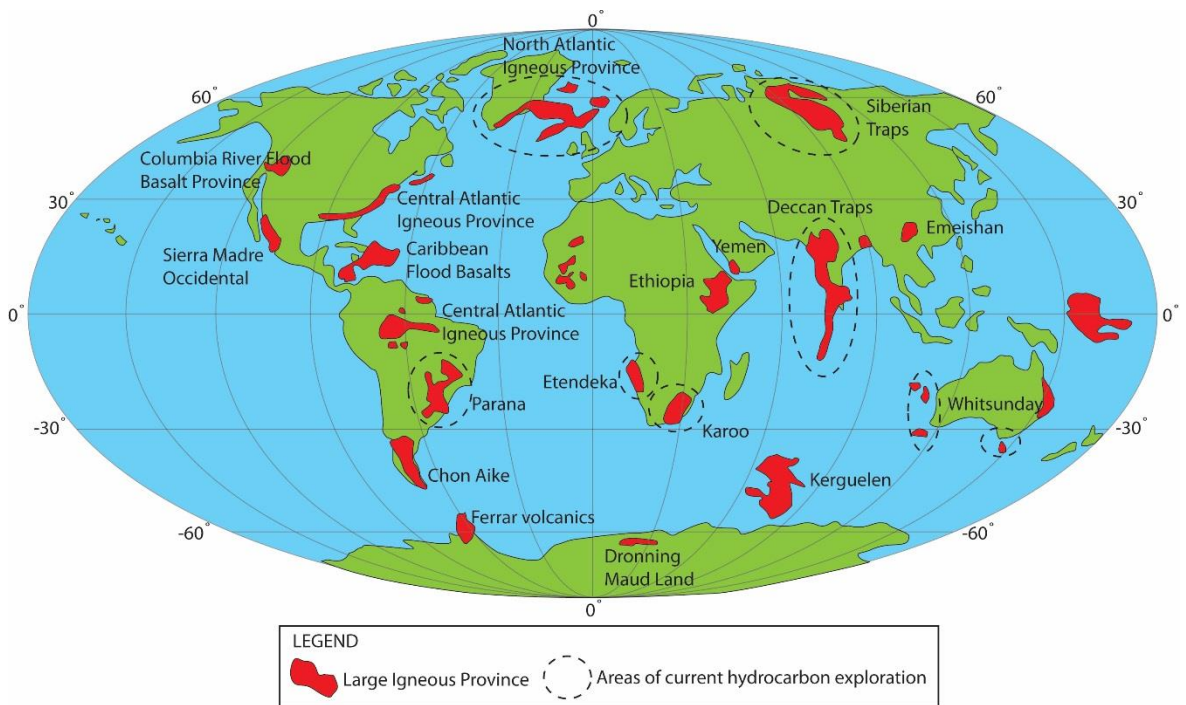


Figure 1.1. Map showing the distribution of Large Igneous Provinces and basins that are the sites of current hydrocarbon exploration. Modified from Coffin and Eldholm (1992), Coffin and Eldholm (1994), Courtilot et al. (1999), Sheth (1999), Jerram and Widdowson (2005), Ross et al. (2005), Rohrman (2007), Bryan and Ernst (2008) and Wright (2013).

1.2 The importance of fissure volcanism

Flood basalts are inferred to have been erupted from fissures (e.g. Swanson et al. 1975; Reidel and Tolan 1992; Thordarson and Self 1998; Kent et al. 1998; Hooper 2000; Walker 2000; Bondre et al. 2004a; Passey and Bell 2007; White et al. 2009; Brown et al. 2014). Fissure eruptions are monogenetic events that are the starting point for most continental basaltic eruptions (Valentine and Gregg 2008). They are linear vents that produce lavas and a variety of pyroclastic edifices; most of which are magmatic (e.g. Swanson et al. 1975; Fedotov et al. 1980; Karhunen 1988; Carracedo et al. 1992; Thordarson and Self 1993; Walker 1993; Valentine and Cortés 2013; Brown et al. 2014). Magmatic edifices include agglutinate cones, spatter ramparts and Earth's most abundant volcanic landform: the scoria cone (Riedel et al. 2003). Despite the abundance of these magmatic edifices, they have remained elusive in many, if not all volcanic-affected hydrocarbon basins.

1.3 The importance of volcanic edifices

The location and development of monogenetic volcanic edifices has important implications for hydrocarbon basin architecture. Edifices partly determine lava flow field morphology as lava production is commonly focused from particular edifices (e.g. Karhunen 1988; Valentine and Cortés 2013). The lava flow field then determines the development of overlying sedimentary systems, which are potential hydrocarbon reservoirs (e.g. Schofield and Jolley 2013). Volcanic edifices also indicate underlying dyke and sill systems (e.g. Bell and Butcher 2002) which can compartmentalise and metamorphose underlying reservoirs, reducing their porosity (e.g. Girard et al. 1989; Doyle 2001; McKinley et al. 2001; Rateau et al. 2013; Grove 2014). Alternatively, underlying dykes and sills may focus fluid flow (e.g. Rateau et al. 2013). Thus, edifices and their plumbing systems can act as fluid migration pathways long after burial (e.g. Holford et al. 2012). The pyroclasts of which edifices are composed may also act as fluid reservoirs, similar to the vesicular flow tops of lava flows (e.g. Cukur et al. 2010; Burns et al. 2014; Holford and Schofield in review). Volcanic edifices can also be used to identify structural trends (e.g. Connor and Conway 2000) concealed by poor imaging in underlying stratigraphy (e.g. Jerram 2002). Moreover, edifice location helps predict lateral thickness variations in extrusive units that are below the resolution of seismic data.

Volcanic edifices also provide a host of volcanological information that can be used for hazard assessment (e.g. Cronin and Neall 2001; Riedel et al. 2003; Houghton et al.

2006) and for determining the effects of eruptions on the environment (e.g. Thordarson et al. 1996; Brown et al. 2014). The architecture of an edifice (i.e. its geometry and component pyroclasts) record temporal and spatial variations in depositional mechanisms (e.g. Sohn 1996). For instance, pyroclasts record the efficiency of magma fragmentation and explosion frequency (Valentine and Gregg 2008) and can be used to determine edifice construction timescales (e.g. Brown et al. 2014). Pyroclasts also retain fluid-dynamic and rheological information that is specific to the vent-proximal environment (e.g. Sumner 1998; Sumner et al. 2005). Paleo-environmental conditions (e.g. abundant surface water) can also be inferred from edifice architecture, since distinctive edifices (e.g. tuff cones or scoria cones) form in different hydrological regimes (e.g. Wohletz and Sheridan 1983; Sheridan and Wohletz 1983).

Furthermore, volcanoes provide insights into the underlying geology and feeder system. Clasts from the underlying stratigraphy are excavated during edifice construction (e.g. Valentine and Groves 1996; Németh and White 2003; Carrasco-Núñez et al. 2007; Valentine 2012) and eruption style is affected by dyke host-rock lithology (e.g. Sohn 1996). Pressure conditions and magma flux variations in the conduit are also recorded (Riggs and Duffield 2008; Valentine and Cortés 2013), as is information on crystallization and fluid dynamic processes in the ascending magma (Genareau et al. 2010).

1.4 The problem: identifying volcanic edifices and constraining their architecture

1.4.1 Identifying volcanic edifices in remote datasets

Seismic and well data are the most commonly used remote datasets during hydrocarbon exploration. There are several factors which make volcanic edifices difficult to locate in these datasets. Firstly, seismic data in volcanic-affected basins is often of poor quality beneath the uppermost basalt horizon. This is because the high density, internal structure and lithological heterogeneity of volcanic rocks causes scattering, attenuation and absorption of seismic waves (the "sub basalt imaging problem"; Fig. 1.2; see Jerram and Robbe 2001; Maresh et al. 2006; Shaw et al. 2008; Davison et al. 2010). Furthermore, fragmental volcanic rocks (e.g. pyroclasts) have a lower velocity than the surrounding lavas (e.g. Planke and Eldholm 1994; Nelson et al. 2009; Wright 2013). This produces an impedance contrast and causes a further loss of seismic energy, making edifices difficult to distinguish against background "noise" (Maresh and White 2005; Maresh et al. 2006; Shaw et al. 2008; Wright 2013). Additionally, some volcanic edifices (e.g. spatter

ramparts) are unresolvable due to their height and basal diameter being below the vertical resolution and line spacing of the seismic survey (e.g. Magee et al. 2013). Even if edifices are within the vertical resolution of the data, edifices may become buried by lavas from the same eruption (e.g. Keszthelyi et al. 2004).

When edifices have been identified, poor imaging has concealed their internal architecture (e.g. Thomson 2005). Alternatively, their architecture appears similar to that of sedimentary edifices and they have been misidentified until being drilled (e.g. Davies et al. 2002; Grove 2013). The inaccuracies associated with converting Two-Way-Time to absolute height also makes it difficult to make accurate measurements of edifice morphology, thus making them difficult to distinguish from other types of edifice (see Chapter 2, Section 2.6.2). Since few volcanic edifices have been positively identified, the seismic facies which typify vent-proximal areas are poorly constrained, unlike those of lava flow fields (e.g. Planke et al. 2000; Wright 2013).

Edifice-building sequences (e.g. pyroclastic rocks) have also yet to be recognised from well data, including information gathered by wireline log, core, formation micro-imaging (FMI) and formation micro-scanner (FMS) tools. Edifice building sequences can be quickly reworked (e.g. Manville et al. 2009 and references there-in), making it difficult to ascertain whether encountered sequences are in-situ. Secondly, due to the fragmental nature of the rocks and rapid transition of basaltic glass to clays (Pettijohn et al. 1987) it is difficult to determine primary textural characteristics in these sequences (e.g. Cummings and Blevin 2003; Clark 2014). Therefore pyroclastic successions are not recognised, and fragmental volcanic rocks are commonly described as “volcaniclastic”, with little indication of their origin (Planke et al. 2000; Bell and Butcher 2002; Wright 2013).

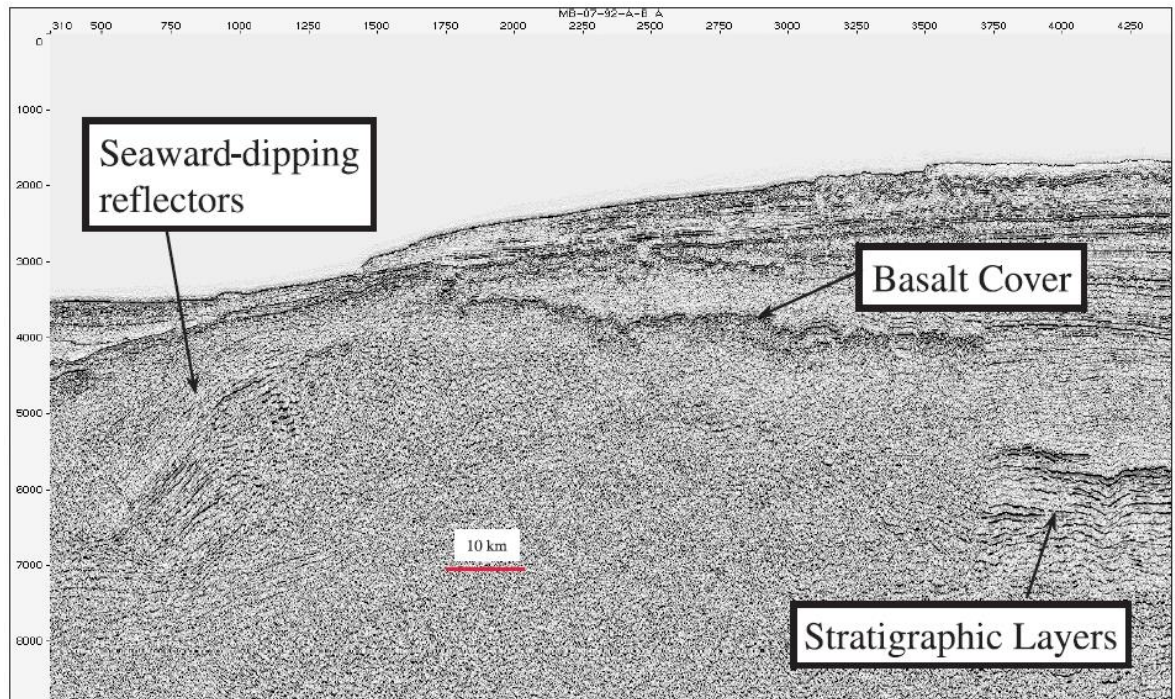


Figure 1.2. Seismic section from offshore Norway illustrating the sub-basalt imaging problem – notice that the stratigraphy is obscured beneath the basalt cover. Taken from Jerram (2002).

1.4.2 Characterising the architecture of volcanic edifices in the field

Monogenetic and small scale volcanic edifices have not traditionally been a research focus for volcanologists. Furthermore, there are a range of problems specific to these edifices that have made their internal architecture difficult to constrain. Although we can observe edifice construction (e.g. Moore and Ault 1965; Moore et al. 1966; Moore et al. 1980; Moore 1985; Wolfe et al. 1988), how the eruption processes are recorded is poorly known as the early products are buried by later products. Volcanic edifices also have a variable chance of preservation depending on background sedimentation rates (Manville et al. 2009). They may be eroded, such that the only record of their presence is the depocentre created by the vents themselves (Manville et al. 2009). Moreover, many edifices are degraded without exposure of their internal architecture (e.g. Wood 1980; Hooper and Sheridan 1998; Martin and Németh 2006).

In addition, edifices in flood basalt provinces are elusive; pyroclastic material may account for <0.001% of the volume of extruded material (Ross et al. 2005). Subsequent rifting and eruptions may occur along trends of earlier fissures, destroying evidence of the vent region (Hooper 2000; White et al. 2009). Our only examples of flood basalt edifices

come from the Columbia River Flood Basalt Province (e.g. Swanson et al. 1975; Reidel and Tolan 1992; Brown et al. 2014), which may not be typical of other flood basalt provinces (Bondre et al. 2004b).

There are also inherent difficulties in distinguishing between different types of volcanic edifices. For instance, several types produce pyroclastic density currents (PDCs), including tuff rings, tuff cones and rootless cones (e.g. Sohn and Chough 1989; Chough and Sohn 1990; Fagents et al. 2002; Sohn and Park 2005; Fagents and Thordarson 2007; Hamilton et al. 2010; White and Ross 2011). Since edifice architecture is determined by depositional method (e.g. Sohn 1996), these edifices share internal characteristics. Furthermore, since characterisation of an edifice is strongly based on their crater/basal diameter ratio (e.g. White and Ross 2011) eroded structures only providing internal exposure are difficult to identify. Identification becomes particularly problematic with edifices that are poorly described internally, e.g. spatter cones/ramparts, scoria cones and rootless cones. Correct identification is particularly important for rootless cones, since these structures are not dyke fed and can occur at significant distances away from the vent.

1.5 Aims

The aim of this thesis is to characterise the spatial and temporal development of monogenetic basaltic edifices using field, seismic and well data. Specifically, the thesis will:

- document the architecture, componentry and shallow level feeder system of basaltic fissure-derived edifices. This will help us to understand how edifice architecture varies as a result of variations in lava fountaining and associated clastogenic flow processes, as well as providing insights into the development of their feeder system. The outcomes of the study will aid recognition of fissure-derived edifices in field and well data sets, such as those affected by flood basalt volcanism (e.g. the FSB).
- document the architecture and componentry of rootless cones and their host lava flows. This will provide insights into the processes associated with their construction and help to distinguish between rootless cones and dyke-fed edifices. It will therefore allow accurate recognition of dyke-proximal settings in other volcanic provinces.
- use exceptionally high resolution 3D seismic data to analyse and characterise the architecture (e.g. seismic facies) and temporal development of submarine monogenetic basaltic edifices. This will allow us to distinguish between volcanic and similar non-

volcanic edifices (e.g. hydrothermal vents) in other seismic data sets, and provide insights into the 3D evolution of a submarine monogenetic volcanic field.

1.6 Thesis Outline

Chapter 1: An introduction to hydrocarbon exploration in volcanic-affected basins, the importance of volcanic edifices, problems associated with them and thesis aims.

Chapter 2: This chapter reviews: (1) the sub-aerial eruption and emplacement of basaltic lavas and edifices; (2) the architecture of the basaltic pyroclastic deposits as derived from field studies and from seismic datasets; (3) the criteria for distinguishing between volcanic and sedimentary edifices in seismic data.

Chapter 3: This chapter provides a detailed chronology of how volcanic edifices were constructed during a Holocene fissure eruption in NE Iceland. The internal architecture of edifices such as these is rarely exposed, and the chapter provides an unrivalled opportunity to link the deposits of low volume eruptions with those of high volume eruptions.

Chapter 4: This chapter uses field data from a newly-discovered rootless cone field in the Columbia River Flood Basalt Province to document and interpret the architecture and rootless cones. It also provides criteria to distinguish rootless cones and tephra from dyke-fed cones and tephra.

Chapter 5: This chapter uses 3D seismic data to document and interpret the architecture of submarine volcanic edifices offshore Australia. Currently, this chapter provides the only description of the development of a monogenetic volcanic field in seismic data.

Chapter 6: A discussion of the results of this study in the context of flood basalt emplacement and hydrocarbon exploration.

Chapter 7: A summary of the conclusions of the thesis.

Chapter 8: This chapter provides directions for future research.

1.7 References

- Bell B, Butcher H (2002) On the emplacement of sill complexes: evidence from the Faroe-Shetland Basin. Geological Society, London, Special Publications 197(1):307-329
- Bondre N, Duraiswami R, Dole G (2004a) Morphology and emplacement of flows from the Deccan Volcanic Province, India. *B Volcanol* 66(1):29-45
- Bondre N, Duraiswami R, Dole G (2004b) A brief comparison of lava flows from the Deccan Volcanic Province and the Columbia-Oregon Plateau Flood Basalts: Implications for models of flood basalt emplacement. *Journal of Earth System Science* 113(4):809-817
- Brown RJ, Blake S, Thordarson T, Self S (2014) Pyroclastic edifices record vigorous lava fountains during the emplacement of a flood basalt flow field, Roza Member, Columbia River Basalt Province, USA. *Geol Soc Am Bull* 126:875-891
- Bryan SE, Ernst RE (2008) Revised definition of large igneous provinces (LIPs). *Earth-Science Reviews* 86(1):175-202
- Bryan SE, Peate IU, Peate DW, Self S, Jerram DA, Mawby MR, Marsh JS, Miller JA (2010) The largest volcanic eruptions on Earth. *Earth-Science Reviews* 102(3-4):207-229
- Burns E, Williams C, Ingebritsen S, Voss C, Spane F, DeAngelo J (2014) Understanding heat and groundwater flow through continental flood basalt provinces: insights gained from alternative models of permeability/depth relationships for the Columbia Plateau, USA. *Geofluids*
- Carracedo JC, Rodriguez Badiola E, Soler V (1992) The 1730–1736 eruption of Lanzarote, Canary Islands: a long, high-magnitude basaltic fissure eruption. *J Volcanol Geoth Res* 53(1-4):239-250
- Carrasco-Núñez G, Ort MH, Romero C (2007) Evolution and hydrological conditions of a maar volcano (Atexcac crater, Eastern Mexico). *J Volcanol Geoth Res* 159(1):179-197
- Chough S, Sohn Y (1990) Depositional mechanics and sequences of base surges, Songaksan tuff ring, Cheju Island, Korea. *Sedimentology* 37(6):1115-1135
- Clark SJ (2014) Constraining diagenetic timings, processes and reservoir quality in igneous-affected basins. PhD Thesis, Durham University, Department of Earth Sciences.
- Coffin MF, Eldholm O (1992) Volcanism and continental break-up: a global compilation of large igneous provinces. Geological Society, London, Special Publications 68(1):17-30
- Coffin MF, Eldholm O (1994) Large igneous provinces: crustal structure, dimensions, and external consequences. *Reviews of Geophysics* 32(1):1-36
- Connor CB, Conway MF (2000) Basaltic volcanic fields. In: Sigurdsson H (ed) *Encyclopedia of Volcanoes*. Academic Press, San Diego, pp 331-343
- Courtillot V, Jaupart C, Manighetti I, Tapponnier P, Besse J (1999) On causal links between flood basalts and continental breakup. *Earth and Planetary Science Letters* 166(3):177-195
- Cronin SJ, Neall VE (2001) Holocene volcanic geology, volcanic hazard, and risk on Taveuni, Fiji. *New Zealand Journal of Geology and Geophysics* 44(3):417-437
- Cukur D, Horozal S, Kim DC, Lee GH, Han HC, Kang MH (2010) The distribution and characteristics of the igneous complexes in the northern East China Sea Shelf Basin and their implications for hydrocarbon potential. *Marine Geophysical Researches* 31(4):299-313
- Cummings AM, Blevin J (2003) Nature and distribution of igneous rocks. In: Blevin, J. (compiler), *Petroleum Geology of the Bass Basin - Interpretation Report, an Output of the Western Tasmanian Regional Minerals Program*. Geoscience Australia, Record 2003/19
- Davies R, Bell BR, Cartwright JA, Shoulders S (2002) Three-dimensional seismic imaging of Paleogene dike-fed submarine volcanoes from the northeast Atlantic margin. *Geology* 30(3):223-226
- Davison I, Stasiuk S, Nuttall P, Keane P (2010) Sub-basalt hydrocarbon prospectivity in the Rockall, Faroe–Shetland and Møre basins, NE Atlantic. Geological Society, London, Petroleum Geology Conference series 7:1025-1032
- Doyle MG (2001) Volcanic influences on hydrothermal and diagenetic alteration: evidence from Highway-Reward, Mount Windsor Subprovince, Australia. *Economic Geology* 96(5):1133-1148
- Fagents SA, Lanagan P, Greeley R (2002) Rootless cones on Mars: a consequence of lava-ground ice interaction. Geological Society, London, Special Publications 202(1):295-317

- Fagents SA, Thordarson T (2007) Rootless cones in Iceland and on Mars. In: Chapman M, Skilling IP (eds) *The Geology of Mars: Evidence from Earth-Based Analogues*. Cambridge University Press, pp 151–177
- Fedotov S, Chirkov A, Gusev N, Kovalev G, Slezin Y (1980) The large fissure eruption in the region of Plosky Tolbachik volcano in Kamchatka, 1975–1976. *B Volcanol* 43(1):47–60
- Genareau K, Valentine G, Moore G, Hervig R (2010) Mechanisms for transition in eruptive style at a monogenetic scoria cone revealed by microtextural analyses (Lathrop Wells volcano, Nevada, U.S.A.). *B Volcanol* 72(5):593–607
- Girard J-P, Deynoux M, Nahon D (1989) Diagenesis of the Upper Proterozoic siliciclastic sediments of the Taoudeni Basin (West Africa) and relation to diabase emplacement. *Journal of Sedimentary Research* 59(2)
- Grove C (2013) Submarine hydrothermal vent complexes in the Paleocene of the Faroe-Shetland Basin: Insights from three-dimensional seismic and petrographical data. *Geology* 41(1):71–74
- Grove C (2014) Direct and Indirect Effects of Flood Basalt Volcanism on Reservoir Quality Sandstone. PhD Thesis, Durham University, Department of Earth Sciences.
- Hamilton CW, Thordarson T, Fagents SA (2010) Explosive lava–water interactions I: architecture and emplacement chronology of volcanic rootless cone groups in the 1783–1784 Laki lava flow, Iceland. *B Volcanol* 72(4):449–467
- Holford S, Schofield N, MacDonald J, Duddy I, Green P (2012) Seismic analysis of igneous systems in sedimentary basins and their impacts on hydrocarbon prospectivity: examples from the Southern Australian margin. *Australian Petroleum Production and Exploration Association Journal* 52:229–252
- Holford S, Schofield N (in review) Three-dimensional seismic analysis for non-magmatic reactivation of buried volcanic complexes in sedimentary basins.
- Hooper DM, Sheridan MF (1998) Computer-simulation models of scoria cone degradation. *J Volcanol Geoth Res* 83(3):241–267
- Hooper PR (2000) Flood Basalt Provinces. In: Sigurdsson H (ed) *Encyclopedia of Volcanoes*.
- Houghton BF, Bonadonna C, Gregg CE, Johnston DM, Cousins WJ, Cole JW, Del Carlo P (2006) Proximal tephra hazards: Recent eruption studies applied to volcanic risk in the Auckland volcanic field, New Zealand. *J Volcanol Geoth Res* 155(1–2):138–149
- Jerram DA, Robbe O (2001) Building a 3-D model of a flood basalt: an example from the Etendeka, NW Namibia. *Visual Geosciences* 6(1):1–8
- Jerram DA (2002) Volcanology and facies architecture of flood basalts. *Geological Society of America Special Papers* 362:119–132
- Jerram DA, Stollhofen H (2002) Lava–sediment interaction in desert settings; are all peperite-like textures the result of magma–water interaction? *J Volcanol Geoth Res* 114(1–2):231–249
- Jerram DA, Widdowson M (2005) The anatomy of Continental Flood Basalt Provinces: geological constraints on the processes and products of flood volcanism. *Lithos* 79(3–4):385–405
- Karhunen R (1988) Eruption mechanism and rheomorphism during the basaltic fissure eruption in Biskupsfell, Kverkfjöll, North-central Iceland, Lic. Phil. thesis, University of Iceland, Department of Geology and Mineralogy.
- Kent RW, Thomson BA, Skelhorn RR, Kerr AC, Norry MJ, Walsh JN (1998) Emplacement of Hebridean Tertiary flood basalts: evidence from an inflated pahoehoe lava flow on Mull, Scotland. *J Geol Soc London* 155(4):599–607
- Keszthelyi L, Thordarson T, McEwen A, Haack H, Guilbaud MN, Self S, Rossi MJ (2004) Icelandic analogs to Martian flood lavas. *Geochemistry, Geophysics, Geosystems* 5(11)
- Magee C, Hunt-Stewart E, Jackson CAL (2013) Volcano growth mechanisms and the role of sub-volcanic intrusions: Insights from 2D seismic reflection data. *Earth and Planetary Science Letters* 373(0):41–53
- Manville V, Németh K, Kano K (2009) Source to sink: a review of three decades of progress in the understanding of volcanoclastic processes, deposits, and hazards. *Sedimentary Geology* 220(3):136–161
- Maresh J, White RS (2005) Seeing through a glass, darkly: strategies for imaging through basalt. *First Break* 23(5)
- Maresh J, White RS, Hobbs RW, Smallwood JR (2006) Seismic attenuation of Atlantic margin basalts: Observations and modeling. *Geophysics* 71(6):B211–B221

- Martin U, Németh K (2006) How Strombolian is a “Strombolian” scoria cone? Some irregularities in scoria cone architecture from the Transmexican Volcanic Belt, near Volcán Ceboruco, (Mexico) and Al Haruj (Libya). *J Volcanol Geoth Res* 155(1–2):104-118
- Mckinley JM, Worden RH, Ruffell AH (2001) Contact diagenesis: the effect of an intrusion on reservoir quality in the Triassic Sherwood Sandstone Group, Northern Ireland. *Journal of Sedimentary Research* 71(3):484-495
- Moore JG, Ault WU (1965) Historic littoral cones in Hawaii. *Pacific science* XIX(3-11)
- Moore JG, Nakamura K, Alcaraz A (1966) The 1965 Eruption of Taal Volcano. *Science* 151(3713):955-960
- Moore JG (1985) Structure and eruptive mechanisms at Surtsey Volcano, Iceland. *Geol Mag* 122(06):649-661
- Moore RB, Helz RT, Dzurisin D, Eaton GP, Koyanagi RY, Lipman PW, Lockwood JP, Puniwai GS (1980) The 1977 eruption of Kilauea volcano, Hawaii. *J Volcanol Geoth Res* 7(3):189-210
- Nelson CE, Jerram DA, Hobbs RW (2009) Flood basalt facies from borehole data: implications for prospectivity and volcanology in volcanic rifted margins. *Petroleum Geoscience* 15(4):313-324
- Németh K, White JDL (2003) Reconstructing eruption processes of a Miocene monogenetic volcanic field from vent remnants: Waipiata Volcanic Field, South Island, New Zealand. *J Volcanol Geoth Res* 124(1–2):1-21
- Passey SR, Bell BR (2007) Morphologies and emplacement mechanisms of the lava flows of the Faroe Islands Basalt Group, Faroe Islands, NE Atlantic Ocean. *B Volcanol* 70(2):139-156
- Pettijohn J, Potter P, Siever R (1987) Sand and sandstone. Published by Springer.
- Planke S, Eldholm O (1994) Seismic response and construction of seaward dipping wedges of flood basalts: Vøring volcanic margin. *Journal of Geophysical Research: Solid Earth* (1978–2012) 99(B5):9263-9278
- Planke S, Symonds PA, Alvestad E, Skogseid J (2000) Seismic volcanostratigraphy of large-volume basaltic extrusive complexes on rifted margins. *J. Geophys. Res.* 105(B8):19335-19351
- Rateau R, Schofield N, Smith M (2013) The potential role of igneous intrusions on hydrocarbon migration, West of Shetland. *Petroleum Geoscience* 19(3):259-272
- Reidel SP, Tolan TL (1992) Eruption and emplacement of flood basalt: An example from the large-volume Teepee Butte Member, Columbia River Basalt Group. *Geol Soc Am Bull* 104(12):1650-1671
- Riedel C, Ernst GGJ, Riley M (2003) Controls on the growth and geometry of pyroclastic constructs. *J Volcanol Geoth Res* 127(1–2):121-152
- Riggs NR, Duffield WA (2008) Record of complex scoria cone eruptive activity at Red Mountain, Arizona, USA, and implications for monogenetic mafic volcanoes. *J Volcanol Geoth Res* 178(4):763-776
- Rohrman M (2007) Prospectivity of volcanic basins: Trap delineation and acreage de-risking. *AAPG bulletin* 91(6):915-939
- Ross P-S, Ukstins Peate I, McClintock M, Xu Y, Skilling I, White J, Houghton B (2005) Mafic volcanoclastic deposits in flood basalt provinces: a review. *J Volcanol Geoth Res* 145(3):281-314
- Schofield N, Jolley DW (2013) Development of intra-basaltic lava-field drainage systems within the Faroe–Shetland Basin. *Petroleum Geoscience* 19(3):273-288
- Shaw F, Worthington M, White R, Andersen M, Petersen U (2008) Seismic attenuation in Faroe Islands basalts. *Geophysical Prospecting* 56(1):5-20
- Sheridan MF, Wohletz KH (1983) Hydrovolcanism: Basic considerations and review. *J Volcanol Geoth Res* 17(1–4):1-29
- Sheth H (1999) Flood basalts and large igneous provinces from deep mantle plumes: fact, fiction, and fallacy. *Tectonophysics* 311(1):1-29
- Sohn YK, Chough SK (1989) Depositional processes of the Suwolbong tuff ring, Cheju Island (Korea). *Sedimentology* 36(5):837-855
- Sohn YK (1996) Hydrovolcanic processes forming basaltic tuff rings and cones on Cheju Island, Korea. *Geol Soc Am Bull* 108(10):1199-1211
- Sohn YK, Park KH (2005) Composite tuff ring/cone complexes in Jeju Island, Korea: possible consequences of substrate collapse and vent migration. *J Volcanol Geoth Res* 141(1–2):157-175
- Sumner JM (1998) Formation of clastogenic lava flows during fissure eruption and scoria cone collapse: the 1986 eruption of Izu-Oshima Volcano, eastern Japan. *B Volcanol* 60(3):195-212

- Sumner JM, Blake S, Matela RJ, Wolff JA (2005) Spatter. *J Volcanol Geoth Res* 142(1-2):49-65
- Swanson DA, Wright TL, Helz RT (1975) Linear vent systems and estimated rates of magma production and eruption for the Yakima Basalt on the Columbia Plateau. *American Journal of Science* 275(8):877-905
- Thomson K (2005) Extrusive and intrusive magmatism in the North Rockall Trough. Geological Society, London, Petroleum Geology Conference series 6:1621-1630
- Thordarson T, Self S (1993) The Laki (Skaftár Fires) and Grímsvötn eruptions in 1783–1785. *B Volcanol* 55(4):233-263
- Thordarson T, Self S, Oskarsson N, Hulsebosch T (1996) Sulfur, chlorine, and fluorine degassing and atmospheric loading by the 1783–1784 AD Laki (Skaftár Fires) eruption in Iceland. *B Volcanol* 58(2-3):205-225
- Thordarson T, Self S (1998) The Roza Member, Columbia River Basalt Group: A gigantic pahoehoe lava flow field formed by endogenous processes? *J. Geophys. Res.* 103(B11):27411-27445
- Thordarson T, Rampino M, Keszthelyi LP, Self S (2009) Effects of megascale eruptions on Earth and Mars. *Geological Society of America Special Papers* 453:37-53
- Valentine G, Cortés J (2013) Time and space variations in magmatic and phreatomagmatic eruptive processes at Easy Chair (Lunar Crater Volcanic Field, Nevada, USA). *B Volcanol* 75(9):1-13
- Valentine GA, Groves KR (1996) Entrainment of Country Rock during Basaltic Eruptions of the Lucero Volcanic Field, New Mexico. *The Journal of Geology* 104(1):71-90
- Valentine GA, Gregg TKP (2008) Continental basaltic volcanoes — Processes and problems. *J Volcanol Geoth Res* 177(4):857-873
- Valentine GA (2012) Shallow plumbing systems for small-volume basaltic volcanoes, 2: Evidence from crustal xenoliths at scoria cones and maars. *J Volcanol Geoth Res* 223–224(0):47-63
- Walker GPL (1993) Basaltic-volcano systems. Geological Society, London, Special Publications 76(1):3-38
- Walker GPL (2000) Basaltic volcanoes and volcanic systems. In: Sigurdsson H (ed) *Encyclopedia of volcanoes*. Academic Press, San Diego, pp 283-289
- White J, Bryan S, Ross P, Self S, Thordarson T (2009) Physical volcanology of continental large igneous provinces: update and review. *Studies in Volcanology: The Legacy of George Walker*. Special Publications of IAVCEI 2:291-321
- White JDL, Ross PS (2011) Maar-diatreme volcanoes: A review. *J Volcanol Geoth Res* 201(1–4):1-29
- Wignall P (2001) Large igneous provinces and mass extinctions. *Earth-Science Reviews* 53(1):1-33
- Wohletz KH, Sheridan MF (1983) Hydrovolcanic explosions; II, Evolution of basaltic tuff rings and tuff cones. *American Journal of Science* 283(5):385-413
- Wolfe WE, Neal AC, Banks GN, Toni DJ (1988) The Puu Oo Eruption of Kilauea Volcano, Hawaii: Episodes 1 Through 20, January 3, 1983, Through June 8, 1984. U.S Geological Survey Professional Paper 1463
- Wood CA (1980) Morphometric evolution of cinder cones. *J Volcanol Geoth Res* 7(3–4):387-413
- Wright K (2013) Seismic Stratigraphy and Geomorphology of Palaeocene Volcanic Rocks, Faroe-Shetland Basin. PhD Thesis, Durham University, Department of Earth Sciences.

Chapter 2: Background Information

2.1 Introduction

This chapter first provides an outline of the Faroe-Shetland Basin (FSB) and the North Atlantic Igneous Province (NAIP) within which it is situated, since exploration within the FSB is the motivation for this research. I then review our understanding of basaltic volcanism, with a focus on monogenetic volcanism. This focus is driven by the occurrence of monogenetic eruptions in all volcanic regions, including those such as the FSB affected by flood basalt volcanism (e.g. Walker 1993; Brown et al. 2009). I also focus on eruptions driven by magmatic volatiles, since these eruptions have traditionally received less attention in the literature, despite their common occurrence. I begin with a discussion of the eruption of basaltic magma; focusing initially on how basaltic magma is transported to the surface in dykes. I then describe the physical processes governing the possible styles of eruption. Following this I summarise the literature describing lava fountains and related pyroclast accumulation processes.

In the proceeding section, I summarise the literature for basaltic lavas, since lavas are a significant component of volcanic-affected basins. This section is divided to describe the key terms of lava flows and flow fields, how lava is emplaced and the different types of lava that are found. I also detail the internal features of pāhoehoe lavas. Following this, I describe the numerous types of volcanic edifices produced during basaltic volcanism.

The chapter then describes the difficulties associated with recognising the aforementioned lavas and volcanoes in volcanic-affected hydrocarbon basins. I also provide a summary of non-volcanic edifices in seismic data, since there are superficial similarities between these features and volcanoes which can make them difficult to distinguish.

2.2 The North Atlantic Igneous Province

The NAIP encompasses Western Greenland, the Faroe Islands and the British Tertiary Igneous Province (BTIP; see Fig. 1.1, Chapter 1). The minimum areal extent of the province is $1.3 \times 10^6 \text{ km}^2$ (Eldholm and Grue 1994; Coffin and Eldholm 1994). The province was constructed as a result of seafloor spreading in the Late Paleocene – Early Eocene. The onset of volcanism is also explained by plume (Naylor et al. 1997) and non-plume hypotheses (Hansen et al. 2009). The province is characterised by predominantly subaerial lava flows, intrusions and volcanic centres. The earliest volcanism is recorded at

63 Ma (Naylor et al. 1997). Initial volcanic activity was characterised by interactions with water forming hyaloclastites, construction of shield volcanoes, emplacement of ponded lava flows. Minor acidic volcanism occurred at this time (Jerram and Widdowson 2005). The ensuing main volcanic phase was characterised by the emplacement of laterally extensive flood basalt plateaus (Jerram and Widdowson 2005). Later eruptions were dominated by more silicic magmas due to melting of continental crust or sediments (Ross et al. 2005; Jerram and Widdowson 2005; Bryan and Ernst 2008). Volcanism ceased once seafloor spreading had become established, and crustal subsidence dominated from the Paleocene onwards (Skogseid et al. 2000; Ceramicola et al. 2005; Praeg et al. 2005). The presence of numerous volcanic disconformities within the sequence suggests that there was significant lateral and temporal variation in volcanic style and eruption rate (Jerram and Widdowson 2005).

2.2.1 The Faroe Shetland Basin

The FSB is located between the Shetland and Faroe Islands (Fig. 2.1). The basin is a 260 km wide, 460 km long series of sub-rift basins that formed as a result of compression and rifting. Compression was initiated in the Early Palaeozoic by NE trending Caledonian Orogeny thrust belts (McKerrow et al. 2000; Ritchie et al. 2011). Subsequent rifting in the Permo-Triassic resulted in the formation of asymmetric half-graben basins in a semi-arid environment, and by the early Jurassic marine conditions had developed (Moy and Imber 2009 and references there-in). Elsewhere in NW Europe there is evidence for late Jurassic rifting (Doré et al. 1999), but the absence of north-south trending rifts in the FSB suggests this did not occur here (Moy and Imber 2009). Subsequent Cretaceous rifting led to the formation of NW-SE trending sub-basins (Roberts et al. 1999; Soper and Woodcock 2003; Ritchie et al. 2011). These sub-basins are separated along several transfer zones by structural highs associated with changes in crustal structure (Dean et al. 1999; Moy and Imber 2009; Wright 2013; Fletcher et al. 2013; Clark 2014).

The FSB is dominated by interbedded igneous and sedimentary rocks of Cretaceous and Palaeocene age. Most sediments were sourced from the Scotland-Shetland platform towards the east (Ritchie and Hitchen 1996; Ritchie et al. 1999; Sørensen 2003; Wright 2013), although their distribution and provenance was partially controlled by the structural lineaments and lava flow field morphology (Jolley and Morton 2007; Ellis et al. 2009; Moy and Imber 2009). The Colsay Member is the main target hydrocarbon reservoir (Schofield and Jolley 2013) whilst source rocks within the basin are dominantly the

Kimmeridgian mudstones (Holmes et al. 1999). Hiatuses during the main phase of volcanic activity are represented by the Sneiss and Prestfjall Formations, which are composed of volcanoclastic and siliciclastic rocks of fluvial and lacustrine association (Passey and Bell 2007).

The flood basalts of the FSB cover an area of 40 000 km² and act as seals to fluids in parts of the FSB (Naylor et al. 1997). The lavas were emplaced 57 Ma ago and are thought to have been erupted over 2.6 Ma (Passey and Jolley 2008). They form a 6.6 km thick succession, divided into the Beinissvörð (BF), Malinstindur (MF) and Enni (EF) Formations. These formations are underlain at the base by the Lopra Formation, a sequence of volcanoclastic rocks and sills (Ellis et al. 2002).

The BF is dominated by thick, laterally extensive aphyric sheet lobes that reach 3300 m in thickness (Passey and Bell 2007). These flows record the onset of flood basalt volcanism (Passey and Bell 2007; Wright 2013). The MF is composed of compound, subaerial lavas of olivine phyric, aphyric and plagioclase-phyric basalts (Passey and Bell 2007). The Enni Formation is composed of interbedded simple and compound flows (Passey and Bell 2007). The BF and EF are inferred to have been emplaced from fissures due to their sheet morphology (Passey and Bell 2007). The source fissures for the EF lavas may be located offshore (Schofield and Jolley 2013). In contrast, the compound flows of the EF are inferred to have been emplaced from low shields (Passey and Bell 2007 and references there-in). Conflicting evidence from seismic data and lava flow morphology suggests that the MF were sourced from fissures and/or shield volcanoes (Passey and Bell 2007; Schofield and Jolley 2013). The source fissure for the BF lavas is thought to be represented by a 1 km long NW-SE trending row of tuff-agglomerate deposits on the Faroe Islands (Larsen et al. 1999). Eruption of the lavas resulted in the formation of the Faroe-Shetland Escarpment. This escarpment is a curved structure across the basin, interpreted as a lava-fed delta system composed of steep, prograding foresets of hyaloclastite (Wright et al. 2012; Wright 2013). The escarpments' progradational structure suggests retreat of the shoreline as volcanism overwhelms the submarine basin.

Intrusive complexes are composed of dolerite sills and dykes which intrude preferentially into upper Cretaceous shales and the lower part of the Palaeocene, and which extend laterally beyond the flood basalt cover (Rateau et al. 2013). These complexes were intruded between 53 and 55 Ma (Ritchie and Hitchen 1996; Schofield and Jolley 2013).

Partially-eroded igneous centres are also recognised from seismic reflection data, gravity and magnetic surveys (Gatliff et al. 1984; Jolley and Bell 2002). These include the

Erlend complex and Brendans dome (Gatliff et al. 1984; Ritchie and Hitchen 1996). Whilst these structures provide seismic evidence of lava extrusion (Gatliff et al. 1984), most of the centres are identified solely by geophysical methods (e.g. the Westray volcanic centre, see Ritchie and Hitchen 1996). Therefore their link with the overlying extrusive units is uncertain. Fissures are recognised from seismic data in the Flett Basin (see Section 2.6.2.1.1), although their relationship to the surrounding lava flows is uncertain (Thomson 2007).

In summary, the source vents for the flood basalts that dominate the FSB are likely to be large complexes (such as Brendans Dome) and dyke-fed fissures, such as those identified onshore and offshore (e.g. Larsen et al. 1999; Thomson 2007; Schofield and Jolley 2013). However, these fissure vents are poorly described, and the architecture of the edifices along them is poorly constrained in both seismic and well data. The relationship (if any) between the fissures, their abundance and central complexes is also unknown. Given the conflicting evidence for the source of the MF lavas, the reliability of lava flow morphology (i.e. tabular or compound) as an indicator of source type is unknown.

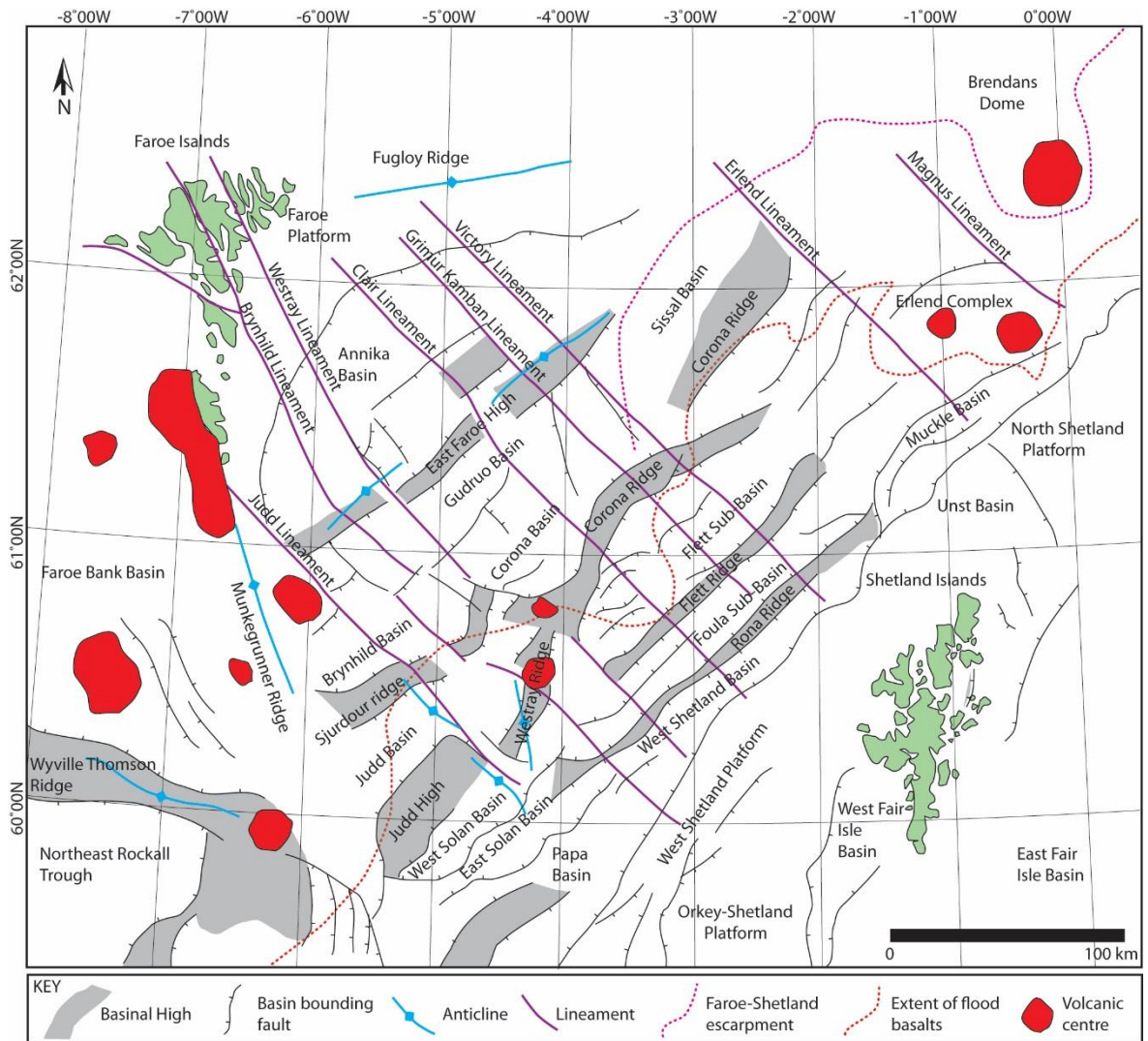


Figure 2.1. Location, structure and volcanic features of the Faroe-Shetland Basin. Modified from Stoker et al. (1993), Ritchie et al. (1996, 1999), Sørensen (2003), Ellis et al (2009), Moy and Imber (2009) and Wright (2013).

2.3 The eruption of basaltic magma

The products of basaltic eruptions are intimately linked to the eruption styles that produced them. Therefore, we need to understand the physical processes that govern these eruption styles. Furthermore, since the movement of magma in the shallow subsurface drives all basaltic eruptions, it is important to understand their feeder systems. This section first outlines the feeder dykes for magmatic, volatile-driven monogenetic basaltic eruptions. I then outline the range of basaltic eruption styles common at monogenetic volcanic centres. There is a particular focus on eruptions driven purely by magmatic volatiles (“dry” eruptions; see Chapter 1). I then outline pyroclast accumulation processes

(e.g. welding) and lava fountains, common during dry eruptions. These processes play an important part in governing the architecture of volcanic edifices during Hawaiian and Strombolian-style eruptions.

2.3.1 Feeder dykes for monogenetic eruptions

Feeder dykes bring magma to the surface, whilst non-feeder dykes do not (Geshi et al. 2010). Feeder dykes link to the paleo-surface and often have a flaring geometry (Keating et al. 2008; Geshi et al. 2010; Geshi and Oikawa 2014). Non-feeder dykes are observed to terminate 15–45 m beneath the surface (Geshi et al. 2010). In reality, it is unknown if many dykes are feeders or not, given that their uppermost portion is rarely observed.

The geometry of feeder dykes partially determines the style of eruption and hence the architecture of the deposits (see section 2.5). Eruption style is altered through a combination of shallow degassing and groundmass crystallisation in the feeder (hence increasing fragmentation, see section 2.3.2.1 and Valentine and Gregg 2008) and/or changes in volumetric flux (see section 2.3.2.1). At depth these dykes are decimetres to metres wide (Valentine and Krogh 2006; Valentine et al. 2006; Valentine and Keating 2007; Valentine 2012). The duration and type of discharge from the fissure is influenced by country rock lithology and irregularities in the fissure geometry (Wylie et al. 1999). The length of the dyke also affects eruption style, since longer dykes allow greater gas segregation, causing unstable variations in flow regime (Pioli et al. 2008). With time, fissure eruptions localise to form conduits due to thermal instabilities and convective processes within the magma (Bruce and Huppert 1989; Genareau et al. 2010; Valentine 2012), and due to wall rock widening (Valentine and Groves 1996; Keating et al. 2008; Valentine 2012). Localisation has been observed in historical eruptions (e.g. Richter 1970; Sumner 1998). This localisation increases the pressure and velocity of rising magma (Valentine and Groves 1996), resulting in increased volumetric flux (Wadge 1981).

Although there are numerous studies of the conduits for phreatomagmatic eruptions (Lorenz 1986; e.g. Németh et al. 2001), there are much fewer for studies of the shallow conduits of “dry” basaltic eruptions. This is because the dykes are commonly eroded to such a depth that it is impossible to determine their link (if any) to the paleosurface (e.g. Geiki 1897; Walker 1995). Alternatively, the erupted products bury the dykes (e.g. Doubik and Hill 1999). In these cases, indirect measurements (e.g. xenolith abundances in the pyroclastic stratigraphy) are used to infer shallow sub-surface conduit processes. Studies that use indirect measurements have concluded that feeder dykes flare upwards, most

prominently within the upper 50–200 m of stratigraphy (Valentine and Groves 1996; Doubik and Hill 1999; Valentine 2012).

Direct observations of feeder dykes in the shallow sub-surface (e.g. Keating et al. 2008; Geshi et al. 2010; Galindo and Gudmundsson 2012; Friese et al. 2013; Geshi and Oikawa 2014) support the conclusions of Valentine and Groves (1996); Doubik and Hill (1999) and Valentine (2012), showing that feeder dykes widen in the upper 200 m of stratigraphy. In addition to dyke material, the flared region may be filled with scoria, variably welded spatter, and basaltic and host rock breccias (Keating et al. 2008; Lefebvre et al. 2012; Valentine 2012). However, dyke widening is greater than predicted by numerical models by a factor of 10 at <50 m depth. Host rock heterogeneities and dyke splaying account for the greater widening. Furthermore, outcrops represent a final snapshot of conduit morphology and not a single, steady emplacement event as predicted by models (Keating et al. 2008).

Conduit widening processes are summarised by Keating et al. (2008) and Valentine and Groves (1996) and include: (1) thermal erosion resulting in host rock volume loss – particularly at greater depths where lithostatic pressure is too great for mechanical erosion to occur. (Bruce and Huppert 1989; Keating et al. 2008); (2) mechanical erosion – increasing with decreasing confining pressure and partly dependent on regional and local host rock heterogeneities (Delaney and Pollard 1981; Keating et al. 2008); (3) erosion from particle collisions (Macedonio et al. 1994); (4) conduit collapse due to variations in magmatic pressure as a result of conduit processes e.g. variations in magma pressure, shock/rarefaction waves (Wilson and Head 1981; Macedonio et al. 1994); (5) hydromagmatic processes involving the interaction of magma with groundwater or saturated sediments (Delaney and Pollard 1981; Lorenz 1986; White 1991); (6) magma viscosity variations induced by cooling of magma at dyke margins, leading to flow localization (Wylie et al. 1999); (7) inclusion of wall rock blocks where offshoot dykes re-join the master (Keating et al. 2008); (8) pore pressure build-up (Delaney and Pollard 1981).

Geshi and Oikawa (2014) concluded that feeder dyke morphology is related to eruptive style. Coherent dykes are inferred to represent effusive end-members, whilst dykes that fragment at depths of 20–150 m are inferred to represent highly explosive end members. Moderately explosive feeders have a morphology transitional between the two and the magma fragments at depths of <20 m. Feeder dykes can develop an irregular morphology as they intrude into overlying edifices (Hintz and Valentine 2012; Friese et al.

2013). Furthermore, dyke morphology and orientation is variably affected by regional stress orientation. Dykes intruded into relay structures between rifts change orientation relative to the regional stress, developing an arcuate shape over their length (Friese et al. 2013). In contrast, some dykes are unaffected by regional stress orientation (Hintz and Valentine 2012). Feeder dykes also trigger slip on pre-existing faults (Gudmundsson et al. 2008; Galindo and Gudmundsson 2012) and are accommodated by a combination of elastic and inelastic deformation of host rock (Valentine and Krogh 2006). Studies have also shown that magma frozen in the dyke may become more vesicular in shallow regions (Hintz and Valentine 2012; Galindo and Gudmundsson 2012). The vesicles are attributed to magmatic pulses caused by pressure fluctuations in the magma column (Hintz and Valentine 2012; Galindo and Gudmundsson 2012); inferred to be a common process in dyke emplacement (Hintz and Valentine 2012). However, this is not common to all examples (Lefebvre et al. 2012; Friese et al. 2013).

Despite a number of studies describing feeder dykes in the shallow sub-surface, whether feeder dyke geometry is diagnostic of all eruption styles is uncertain. For instance, although Geshi and Oikawa (2014) describe effusive feeder dykes, the morphology of dykes for Hawaiian or Strombolian style eruptions is unreported. Valentine and Gregg (2008) also outline problems related to the dyke-conduit transition; including how to predict the rate and location of the transition and whether the flared shape of conduits is a general feature across volcanic fields.

2.3.2 Eruption styles

Monogenetic basaltic volcanism is typified by a range of eruption styles. These styles are evidenced at historic eruptions (e.g. Krauskopf 1948; Thorarinsson 1966; Moore et al. 1966; Richter 1970; Thordarson and Self 1993) or have been inferred from deposit characteristics (e.g. Houghton and Schmincke 1989; Valentine and Gregg 2008; Carracedo Sánchez et al. 2012; Brown et al. 2014). Eruption styles are generally classified according to the degree of fragmentation (i.e. pyroclast size) and dispersal of the deposits (see Walker 1973). The broadest classification scheme is determined by the presence of magma–water interaction. Dry eruptions include weak ash emissions, Hawaiian, Strombolian and Violent Strombolian eruptions. Wet eruptions include Surtseyan and Taalian styles. Many studies document transitions between styles (e.g. Ross 1986; Houghton and Schmincke 1989; Valentine et al. 2005; Genareau et al. 2010; Németh et al. 2011; Otterloo et al. 2013).

2.3.2.1 Physical processes governing eruption style

In eruptions driven by magmatic volatiles, eruption style is determined by volumetric flux and pyroclast size. The effect of flux on eruption style is discussed in depth by Jaupart and Vergnolle (1988); Jaupart and Vergnolle (1989); Parfitt and Wilson (1995); Vergnolle and Mangan (2000) and Parfitt (2004). These authors have proposed two models. The Rise Speed Dependant (RSD) model suggests homogeneous, single fluid-phase flow of magma and gas within the conduit. Eruption style is governed by the speed at which the magma rises relative to the bubbles within it. When the magma rises quickly relative to the bubbles, the magma and bubbles are erupted together and behave as a single fluid phase. This results in a Hawaiian eruption. As magma rise speed (i.e. mass flux) decreases, bubbles may coalesce within the magma column. Bubble coalescence results in the formation of large gas slugs, producing Strombolian eruptions. This model is compatible with features observed during Hawaiian eruptions (Parfitt 2004).

In contrast, the Collapsing Foam (CF) model suggests that eruptions are the result of two-phase flow of magma and gas (Vergnolle and Jaupart 1986; Jaupart and Vergnolle 1988; Jaupart and Vergnolle 1989; Parfitt 2004). In this model, Hawaiian eruptions result from annular flow, whilst Strombolian eruptions result from slug flow. These varying flow regimes are the result of instantaneous foam collapse (for Hawaiian eruptions) and partial foam collapse (for Strombolian eruptions) deep in the magma storage system. The degree of collapse is related to the viscosity of the liquid, and thus Strombolian eruptions are more common in more viscous magmas. However, the CF model cannot explain many of the features observed during the 1983–1986 Pu’u ‘O’o eruption (see Parfitt 2004).

Pyroclast size determines the amount of heat transferred to the eruption column. Greater heat transfer results in higher columns, capable of dispersing tephra more widely. Clasts >64 mm are inefficient at transferring heat to the gas phase and prevent the formation of a buoyant eruption column (Woods and Bursik 1991). These clasts are typical of Strombolian and Hawaiian eruptions. Current estimates suggest that 50% of the erupted clasts must be >64 mm to prevent clast-gas heat transfer, although this fraction is poorly constrained (Valentine and Gregg 2008). Clast size can be decreased by increasing magma viscosity via crystallisation or rapid water quenching (e.g. Wohletz 1983; Genareau et al. 2010).

2.3.2.2 Hydromagmatic eruptions

Eruption styles resulting from magma-water interaction include Surtseyan (e.g. Thorarinsson 1966; Wohletz and Sheridan 1983; White and Houghton 2000) and Taalian (e.g. Moore et al. 1966; Kokelaar 1986). The water in these eruptions may be encountered in the subsurface (e.g. in aquifers; see Sohn 1996) or above ground (e.g. Thorarinsson 1966; Kokelaar and Durant 1983; Moore 1985). Surtseyan eruptions occur at submarine and emergent volcanoes. They produce pyroclastic density currents, tephra jets and eruption columns that reach several kilometres height (Kokelaar 1986; White and Houghton 2000). The deposits are characterised by vesiculated tuffs with abundant accretionary lapilli and lithic clasts (White and Houghton 2000). Surtseyan eruptions form steep-sided tuff cones (Sohn and Chough 1992; Sohn 1996; Cole et al. 2001). Taalian eruptions may initiate on land (Moore et al. 1966; Kokelaar 1986), although similar diatreme-forming eruptions occur in submarine settings (Lefebvre and Kurszlaukis 2008; Pittari et al. 2008; Suiting and Schmincke 2009). These eruptions produce dilute pyroclastic density currents (Kokelaar 1986), and generate eruption columns that reach heights of 15–20 km (White and Houghton 2000). Deposits from these eruptions are dominated by non-juvenile material of ash–block size. The eruptions produce craters at the site of eruption and may also form small cones and diatremes.

2.3.2.3 Magmatic volatile-driven eruptions

These eruption styles include Hawaiian, Strombolian, Violent Strombolian and weak ash emission (see Vergnolle and Mangan 2000; Parfitt 2004; Valentine and Gregg 2008). The deposits of eruptions can be classified according to their grain size, sorting, welding intensity and bedding. Since weak ash emissions do not build proximal edifices due to their low volume flux and negligible gas thrust they are not discussed (see Patrick et al. 2007; Valentine and Gregg 2008).

Hawaiian eruptions are typified by sustained fountains commonly <500 m in height that are composed of clots of lava (Vergnolle and Mangan 2000). Clasts are poorly coupled in momentum and thermal energy with the erupting gas. Thus Hawaiian eruptions have eruption columns <2 km in height (Valentine and Gregg 2008). Given the large clast size and relatively high mass flux, proximal deposits are often densely to partially welded (Valentine and Gregg 2008). However, pulsing in the fountain can result in beds of moderate or weak welding (Head and Wilson 1989; Valentine and Gregg 2008). Proximal deposits also include massive to inversely graded beds of partially welded coarse lapilli

and bombs in beds that are lenticular to continuous in geometry (Valentine and Gregg 2008). Cooler clasts from the outer part of the fountain are often stripped by the wind and fallout several kilometres downwind (Parfitt 1998).

Strombolian eruptions are characterised by intermittent, low fountains caused by the bursting of gas pockets rising through a slow moving magma column (Parfitt 2004; Valentine and Gregg 2008). These bursts produce lapilli and bombs that build a scoria cone through repeated episodes of grain avalanching (McGetchin et al. 1974; Chouet et al. 1974). In proximal regions Strombolian eruptions produce inversely graded to massive beds of coarse lapilli, bombs and blocks (Valentine and Gregg 2008). The beds are usually lenticular with local zones of dense welding close to the vent (Valentine and Gregg 2008). The deposits have a restricted dispersal past the base of the cone.

Violent Strombolian eruptions are characterised by sustained eruption columns <10 km in height (Arrighi et al. 2001; Valentine and Gregg 2008). These eruptions are typified by multiple eruption column events (Valentine and Gregg 2008). Their proximal deposits include massive and graded beds with internal stratification. These beds are composed of coarse ash and lapilli sized juvenile clasts with rare blocks and bombs. The beds are mainly planar, with local lenticular zones and cross bedded ash-rich horizons. Defining features of the deposits of these eruptions are the absence of welding (since clasts cool within the tall eruption column) and fall deposits that mantle underlying units with limited components of grain avalanching (Valentine and Gregg 2008).

2.3.2.3.1 Fissure eruptions

Basaltic fissures are found in all tectonic environments and are particularly common in extensional settings (e.g. Iceland). They are also found in association with central volcanoes (Walker 1995). Many fissure eruptions are Hawaiian in style (e.g. Swanson et al. 1979; Wolfe et al. 1988; Thordarson and Self 1993). However, fissures may also exhibit sub-Plinian behaviour (e.g. Walker et al. 1984; Thordarson and Self 1993; Sumner 1998; Sable et al. 2006; Brown et al. 2014). They produce a spectrum of pyroclastic edifices (see Section 2.5) and lavas (see Section 2.4).

Historic eruptions are characterised by low, linear fountains in their initial stages (e.g. Thorarinsson et al. 1973; Swanson et al. 1979; Wolfe et al. 1988). Early pyroclastic constructs and deposits are commonly rafted away from the vent (Parcheta et al. 2012), or become buried by subsequent deposits (e.g. Wolfe et al. 1988). Brief phreatomagmatic

episodes may occur throughout the eruption (Thordarson and Self 1993; Valentine and Cortés 2013). The fountain quickly localises to numerous point sources due to thermal instabilities along the fissure (Bruce and Huppert 1989; Keating et al. 2008). Localisation may result in an increase in fountains reaching 100–500 m in height (e.g. Heliker and Mattox 2003; Stovall et al. 2011; Parcheta et al. 2012). They may also become more sustained (e.g. Sumner 1998; Valentine et al. 2005) or intermittent with time (e.g. Thordarson and Self 1993; Németh et al. 2011). The final stages of eruptions may be characterised by rapid surges in eruption rate and abrupt cessation of fountaining (e.g. Stovall et al. 2011), or prolonged effusion events (Vergnolle and Mangan 2000).

Fissures are the source of some or all flood basalts in the Columbia River Flood Basalt Province (CRFBP), NAIP and Deccan Volcanic Province (DVP). Lava flows in the CRFBP can be linked petrologically to linear dyke swarms (e.g. Swanson et al. 1975). Rows of pyroclastic edifices occur along the strike of these dykes (Swanson et al. 1975; Reidel and Tolan 1992; Brown et al. 2014). The Hebridean lavas of northwest Scotland are flat lying, suggesting they were erupted over a large area (Walker 1995). Dykes associated with these lavas are widely scattered, contradictory to a point source (Walker 1995). An absence of pyroclastic deposits is also thought to be evidence of fissure fed flood basalts in eastern Iceland (Walker 1958; Gibson et al. 1966). Linear dyke swarms in the DVP are suggestive of a fissure source (Sheth 2006).

Whether lava flow morphology can be used accurately to infer the source (i.e. central volcano or fissure) is uncertain; both compound and simple flows are known to originate from fissures (Sheth 2006). Furthermore, as fissures are often found in close association with central volcanoes (Hjartardóttir et al. 2012; Óskarsson and Riishuus 2013) it is uncertain in the NAIP where fissure-fed lavas end and lavas erupted from central volcanoes begin (Walker 1995). Whether the dykes exposed in the NAIP represent feeder-dykes is uncertain; it is often impossible to determine the link between a dyke and erupted products (see Section 4.2.1).

2.3.3 Pyroclast accumulation and lava fountains

Welding, agglutination and coalescence are common processes during lava fountaining due to interactions between molten pyroclasts (see Cas and Wright 1987; Branney and Kokelaar 1992; Wolff and Sumner 2000; Sumner et al. 2005). These processes depend on clast accumulation rate and local temperature and are ultimately determined by the lava fountain structure. Welding is a compactional process and describes

the sticking together of clasts in a hot deposit due to overburden pressure. Numerical modelling has shown that welding can occur up to several kilometres from the vent given the right combination of exit velocity, ejection angle, and clast size, density and shape (Capaccioni and Cuccoli 2005). Carey et al. (2008) state that welding may be a “regional” process (i.e. present over tens of metres) or a “local” process, where discrete welding halos are created around larger clasts. However, the importance of regional versus local welding in monogenetic eruptions is not recorded. Agglutination describes the flattening of clasts as they impact on an accumulation surface (Sumner et al. 2005). Agglutination is promoted by the splashing of pyroclasts commonly ≥ 10 cm diameter, falling at terminal speed and with viscosities $< 10^5$ Pa s (Sumner et al. 2005). These conditions are easily met by clasts in the inner part of the lava fountain. However, the effects of shear and compaction on deposit texture have not been investigated. Coalescence describes the complete agglutination of fluidal clasts, forming a homogeneous liquid in which clast outlines are obliterated (Sumner et al. 2005). It is by rapid coalescence that clastogenic lavas are formed.

The lava fountain structure governs the architecture of pyroclastic deposits and clastogenic lavas. Fountain structure is primarily determined by magma gas content and volume flux (Fig. 2.2; Head and Wilson 1989). Gas content determines the height and collimation (i.e. spread from vertical) of the fountain. Non-collimated fountains with high volume fluxes (e.g. many Hawaiian eruptions) produce large pyroclasts that do not cool rapidly (e.g. spatter bombs). Most fall back into the vent and agglutinate and/or coalesce. Conversely, widely spread or high fountains produce abundant rapidly cooled clasts that are less likely to weld and agglutinate (e.g. scoria lapilli). Volume flux primarily controls clast size, which in turn controls local clast temperature. Fountain structure is also affected by local wind variations, as wind can strip clasts from the outer, cooler part of the fountain.

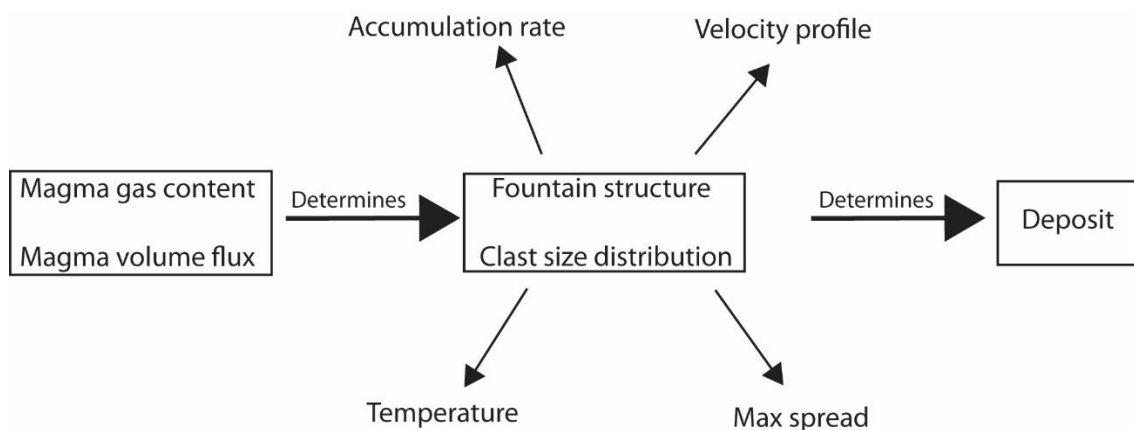


Figure 2.2 (overleaf). Factors controlling lava fountain structure. Modified from Head and Wilson (1989).

2.4. Basaltic lavas

Lava flows are ubiquitously encountered in hydrocarbon basins affected by basaltic volcanism (e.g. Gatliff et al. 1984; Maresh et al. 2006; Jerram et al. 2009; Davison et al. 2010; Holford et al. 2012). Lava flow fields can cover areas up to $3 \times 10^5 \text{ km}^2$ (Hooper 2000) and reach thicknesses of 2 km (Bondre et al. 2004b). They account for >99% of the erupted products in flood basalt provinces (Ross et al. 2005).

2.4.1 Definition of terms

The smallest individual package of a lava flow is a lava lobe (Self et al. 1998). Pāhoehoe lobes are initially 20–50 cm thick, 20–300 cm wide and 0.5–5 m long (Fig. 2.3; Self et al. 1998). The lobes can coalesce forming large sheets with steep monoclinial margins and distinctive flat tops up to thousands of metres wide (Hon et al. 1994). Sheet flows form on slopes $<2^\circ$ (Hon et al. 1994). Numerous lava lobes are the constituent parts of a lava flow, the product of a single outpouring of lava (Self et al. 1998). Long-lived eruptions may produce a number of lava flows constructing a lava flow field (Self et al. 1998). Thus a lava flow field is the largest descriptive unit of a single or numerous eruptions. Lava flows may also be described as either compound or simple flows. The terms were first used by Walker (1971) to differentiate between numerous flows of the same size (compound flows) and large sheet flows (simple flows). Jerram (2002) used similar descriptive terms for tabular classic (i.e. simple) and compound braided facies (i.e. compound) lava flows in flood basalt provinces (Fig. 2.4). Effusion rate is defined as the rate at which lava is erupted from a dyke (Harris et al. 2007). Effusion rate controls surface morphology, heat loss (and thus crystallisation) and pressure conditions within an inflating lava flow (Harris et al. 2007). Flow rate is defined as the volumetric discharge at the vent and is intimately linked to subsurface magma transport system (Rowland and Walker 1990).

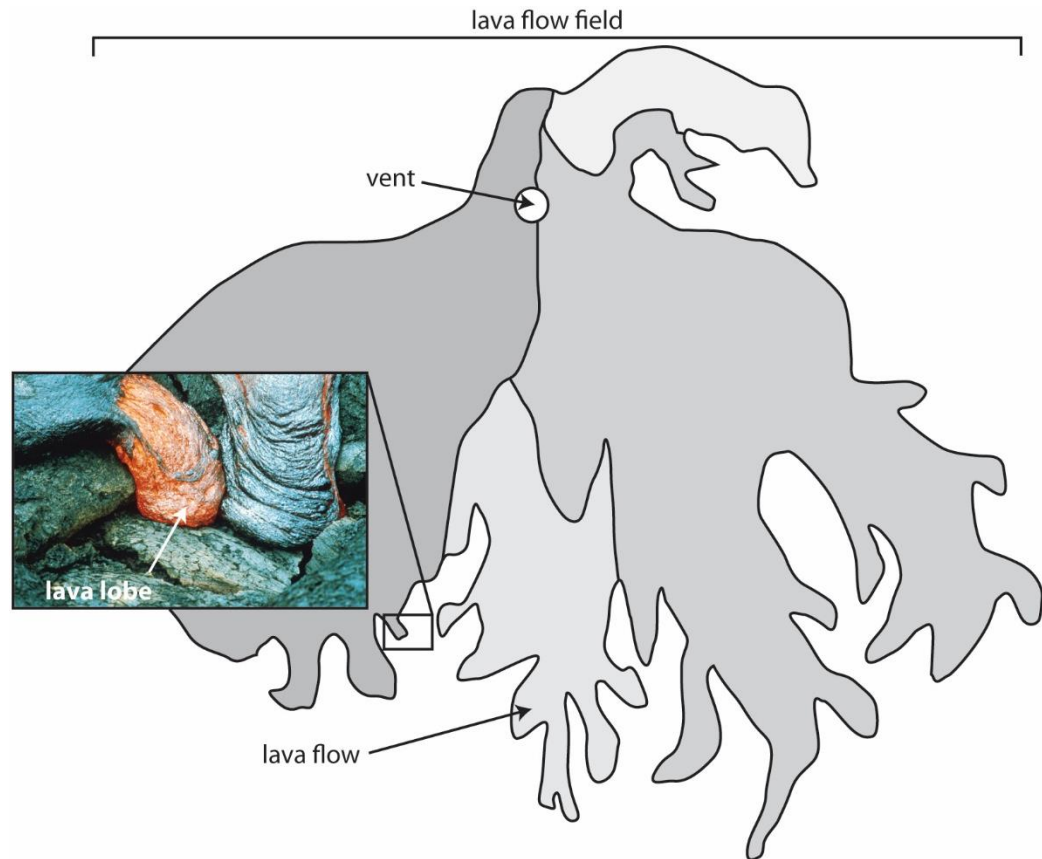


Figure 2.3. Schematic diagram illustrating the difference between lava flows, lobes and flow fields. The lava lobe shown is 300 cm wide. Individual lava flows are shaded. The lava flow field ranges in size from tens to hundreds of kilometres. Photograph from Swanson (1974). Diagram modified from Self et al. (1998).

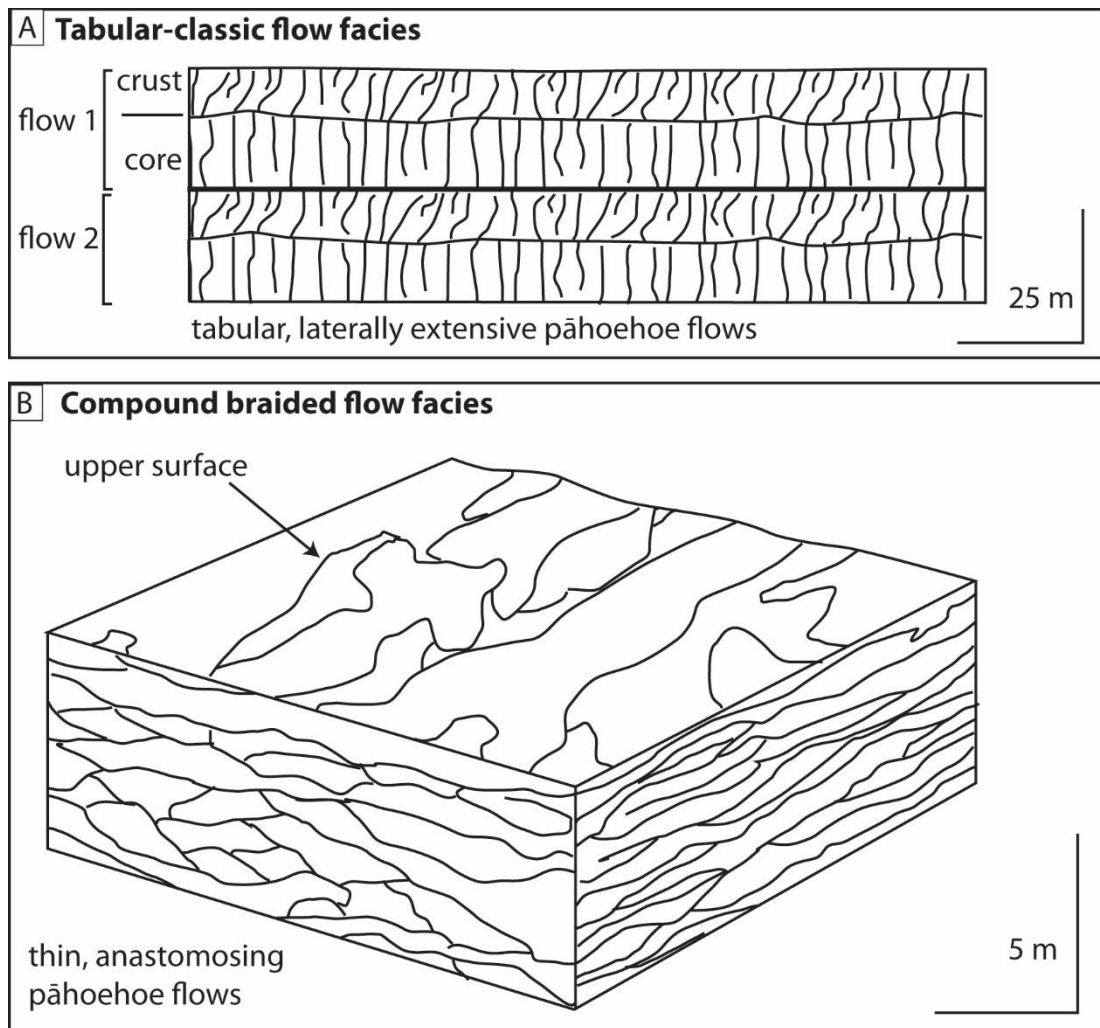


Figure 2.4. Tabular classic (A) and Compound braided flow facies (B) found within flood basalt provinces. Modified from Jerram (2002).

2.4.2 Emplacement

Two basaltic lava types are recognised: ‘ā‘ā and pāhoehoe (Macdonald 1953; Self et al. 1998). ‘Ā‘ā lavas (Fig. 2.5) are emplaced during eruptions with effusion rates $>5\text{--}10\text{ m}^3\text{ s}^{-1}$. They have clinkery basal and upper breccias that grade in to massive cores with irregular vesicles (Macdonald 1953). Near to the vent the flows move in a fashion similar to a caterpillar track (Rowland and Walker 1990). ‘Ā‘ā tends to travel within open channels 0.1–2.5 km wide (Rowland and Walker 1990). The flows grow exogenously, i.e. without inflating (see section below). During flow the lava core is continually overturned, promoting heat loss and rapid groundmass crystallisation (Booth and Self 1973; Crisp and Baloga 1994; Harris and Rowland 2001). Rapid crystallisation is critical for ‘ā‘ā lavas to form (Cashman et al. 1999; Soule and Cashman 2005).

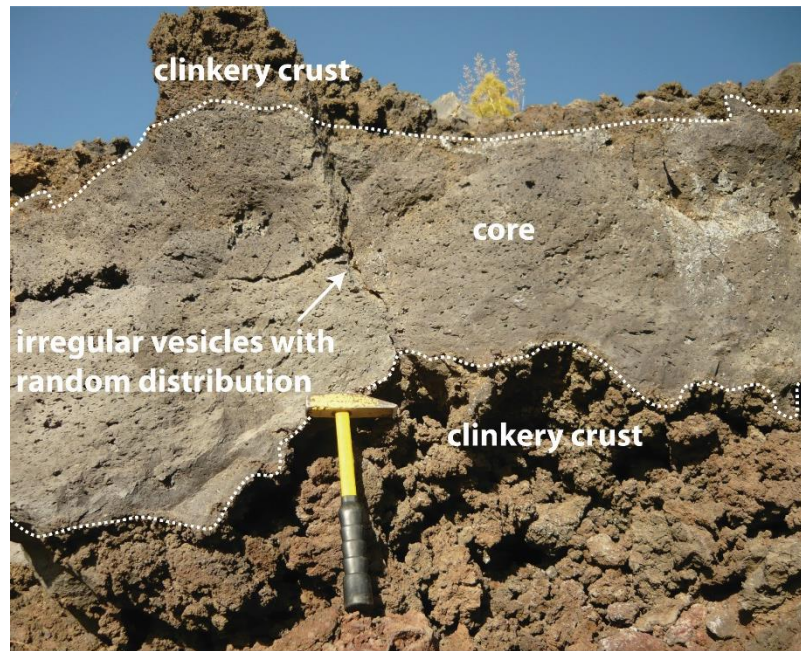


Figure 2.5. Cross section of an 'a'ā lava. The flow has a massive core with irregular vesicles and an upper and lower crust composed of clinker.

In contrast, pāhoehoe lavas have smooth, billowy and ropey upper surfaces that act to insulate the flow as it moves (Hon et al. 1994; Keszthelyi and Denlinger 1996; Keszthelyi and Self 1998). Pāhoehoe is emplaced during low effusion rates of $<5\text{--}10\text{ m}^3\text{ s}^{-1}$ (Rowland and Walker 1990). Flows typically move very slowly (Self et al. 1998) although rapid advancement is also documented (Solana et al. 2004). Pāhoehoe advances by budding and inflation and can be emplaced by tube and channel systems (e.g. Pinkerton and Wilson 1994; Dragoni et al. 1995; Calvari and Pinkerton 1998; Calvari and Pinkerton 1999; Cashman et al. 2006; Valerio et al. 2008). Pāhoehoe can also be produced by pyroclast coalescence and effusion (e.g. Cas and Wright 1987; Head and Wilson 1989; Wolff and Sumner 2000; Harris et al. 2007).

Lavas may transition from pāhoehoe to 'a'ā during flow. The transition between pāhoehoe and 'a'ā is dependent on an increase in viscosity and/or shear strain (Fig. 2.6; Peterson and Tilling 1980). Increases in viscosity are promoted by rapid cooling of the lava during flow (e.g. by channelisation on steep slopes, promoting turnover of the flow core; see Gregg and Fink 2000). Increased slope angle also increases strain rate within flows (Hon et al. 2003). Viscosity also changes as the lava degasses during flow and fountaining episodes. Degassing promotes crystallisation (Lipman et al. 1985), forming vesicles which affect the rate of heat loss from the lava flow surface (Keszthelyi 1994). In addition, the

lava eruption temperature affects the time crystallisation occurs, thus affecting viscosity. For a review of the transition, see Cashman et al. (1999).

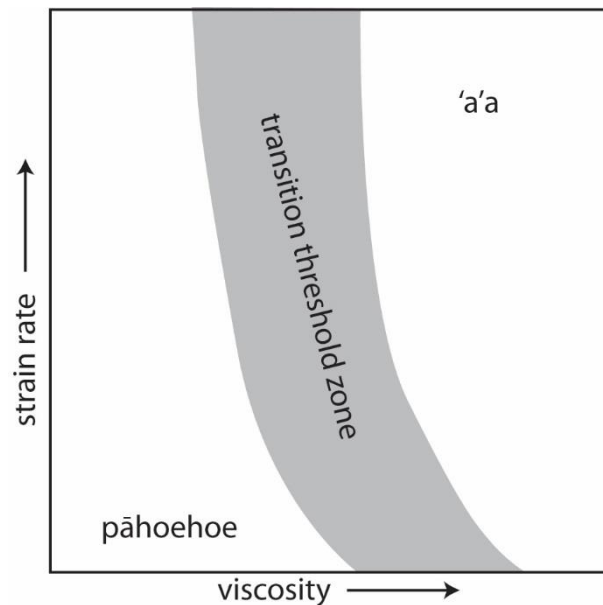


Figure 2.6. Schematic diagram illustrating how pāhoehoe lava transitions to 'a'a as a function of strain rate and viscosity. Modified from Peterson and Tilling (1980).

2.4.2.1 Inflation of pāhoehoe lavas

Inflation is the injection of lava beneath a cooled, solidified crust, causing thickening of the lava flow. As the lava flow thickens, new crustal material is accreted to the base of the upper crust and the flow propagates by budding of new lobes. Internally the flow develops a characteristic tripartite structure. The pioneering work of Hon et al. (1994) allowed quantitative determination of the time required to emplace an inflated pāhoehoe flow using the equation:

$$t = 164.8C^2$$

where t = time in hours

and C = crustal thickness in metres

Externally the flow field may develop tumuli and squeeze-outs. Recognising inflation in contemporary Hawaiian flows revolutionised understanding of flood basalt emplacement (e.g. Self et al. 1998; Thordarson and Self 1998). However, whether inflation

occurs via a series of lava pulses as opposed to by sustained lava input is debated (Anderson et al. 1999).

2.4.3 Types of pāhoehoe lavas

Pāhoehoe lavas are the most common type of basaltic lavas on Earth (Self et al. 1998). They are found in subaerial and submarine settings and dominate in flood basalt provinces (e.g. Walker 1971; Self et al. 1998; Thordarson and Self 1998; Jerram 2002; Bondre et al. 2004a; Bondre et al. 2004b; Waichel et al. 2006; Passey and Bell 2007; Duraiswami et al. 2008). Pāhoehoe lava types include: P-type (e.g. Wilmoth and Walker 1993; Self et al. 1998); S-type (e.g. Walker 1989); blue glassy (e.g. Self et al. 1998; Oze and Winter 2005); silvery (e.g. Self et al. 1998); shelly (e.g. Swanson 1973); spiny/toothpaste (e.g. Rowland and Walker 1987); slabby (e.g. Guilbaud et al. 2005); rubbly (e.g. Duraiswami et al. 2008); entrail (e.g. Kilburn 2000) and clastogenic (e.g. Cas and Wright 1987). These distinctions are based on surface texture/colour and internal characteristics (Figs. 2.7 and 2.8).

P-type pāhoehoe has pipe vesicles at the base of the lava flow (Wilmoth and Walker 1993; Self et al. 1998). These vesicles indicate emplacement on slopes $<4^\circ$ (Kent et al. 1998; Walker et al. 1999; Passey and Bell 2007). However, their formation mechanism is debated (Philpotts and Lewis 1987). These flows decrease in vesicularity toward their core. P-type lava flows are inflated (Self et al. 1998; Thordarson and Self 1998). S-type or spongy pāhoehoe has the opposite vesicle structure to P-type; with vesicles increasing in size and abundance towards the core of the flow. These flows are common in medial and distal areas (Walker 1989). The abundance or significance of S-type flows is otherwise unknown.

The surface colour of silvery pāhoehoe is the result of the trapping of a thin layer of air under a <1 mm thick glass layer (Self et al. 1998). S-type pāhoehoe commonly has a silvery colour, although silvery pāhoehoe may also have pipe vesicles (Self et al. 1998). In contrast, blue glassy pāhoehoe owes its surface colour to its longer residence time within the lava supply network, lower temperature than silvery pāhoehoe (Self et al. 1998) and the concentration of iron and magnesium at the surface (Oze and Winter 2005). Their colour may also result from gases being forced back into solution due to increased pressure during inflation (Hon et al. 1994). This lava indicates inflation occurred for at least two weeks prior to emplacement of the blue glassy flow (Self et al. 1998).

Shelly pāhoehoe can be divided into two types: sheet flood and amoeboid (Swanson 1973). However, inter gradation between types is common. Local relief at the source vent

and emplacement rate is thought to control morphology, with the sheet flood variety occurring where relief is <1 m and during faster emplacement (Swanson 1973). Both types are considered reliable indicators of proximity to the source vent; shelly pāhoehoe evolves rapidly into other lava types and has been used as an indicator of proximity to source in ancient successions (e.g. Swanson 1973; Reidel and Tolan 1992; Brown et al. 2014). (e.g. Swanson et al. 1975; Reidel and Tolan 1992; Self et al. 1998; Guilbaud et al. 2005). However, the maximum distance this lava is emplaced from the vent is unknown. Limiting factors in the lavas advance are described by Swanson (1973) as slopes of $>5^\circ$ and withdrawal of the lava feeding column. Shelly pāhoehoe also forms during lava channel overflows (e.g. Stevenson et al. 2012).

Spiny pāhoehoe is transitional between pāhoehoe and 'a'ā (see section 2.4.2). Its surface is characterised by longitudinal grooves and ridges, parallel to the direction of flow, with spines 1–5 long and 1 cm wide. It typically appears dull due to the abundance of microlites (Rowland and Walker 1987).

Slabby pāhoehoe is relatively rare, recognised only in the Laki flow field and Deccan Volcanic Province (Duraishwami et al. 2003; Guilbaud et al. 2005). It forms due to periods of differential inflation, with high flux rate periods leading to the disruption of the upper crust (Guilbaud et al. 2005). It provides evidence of incipient transformation of pāhoehoe lava to 'a'ā (Duraishwami et al. 2003). If disruption is cyclical, rubbly pāhoehoe may be formed (Duraishwami et al. 2008). Rubbly pāhoehoe is characterised by brecciated flow tops composed of varying sizes of disrupted, highly vesicular pāhoehoe crust (Bondre et al. 2004a). Flows have gently undulating tachylitic flow bases (Duraishwami et al. 2008).

Entrail pāhoehoe is an informal term used to describe the commonly small, compound flows whose lobes resemble intestines (Kilburn 2000). No studies define specific emplacement mechanisms. However, studies of compound flows in the Deccan Volcanic Province suggest they are produced during low effusion rate episodes (Walker 1971).

Lava flows of coalesced pyroclasts are known as clastogenic flows (Cas and Wright 1987). They may have pāhoehoe or 'a'ā type crusts (e.g. Thordarson and Self 1998; Waythomas et al. 2014). This lava is fountain-fed; produced from the agglutination and coalescence of pyroclasts. Fountain-fed lavas may be rootless, lacking a lithological link to the source vent (Cas and Wright 1987). Clastogenic pāhoehoe is exceptionally common although many lava flows retain little evidence of their pyroclastic origin (Thordarson and Self 1998). The importance of inflation during emplacement is unknown. Internally the flows are composed of agglutinated – coalesced agglutinate (e.g. Sumner 1998) and

contain numerous irregular vesicle patches that represent relict pyroclasts known as “ghost” clasts (e.g. Sumner 1998; Brown et al. 2014). The significance of these textures is interpreted in relevance to the accumulation rate of the constituent pyroclasts (Sumner et al. 2005). The effects of shear, compaction and inflation are not described. Furthermore, no studies document lateral and vertical changes in the lavas internal texture. Recent work by Sumner et al. (2005) showed that clastogenic lavas may also result from the collapse of an edifice; thought to be a common process during the construction of basaltic edifices. Clastogenic lavas are also found as ponds within vents (Carracedo Sánchez et al. 2012).

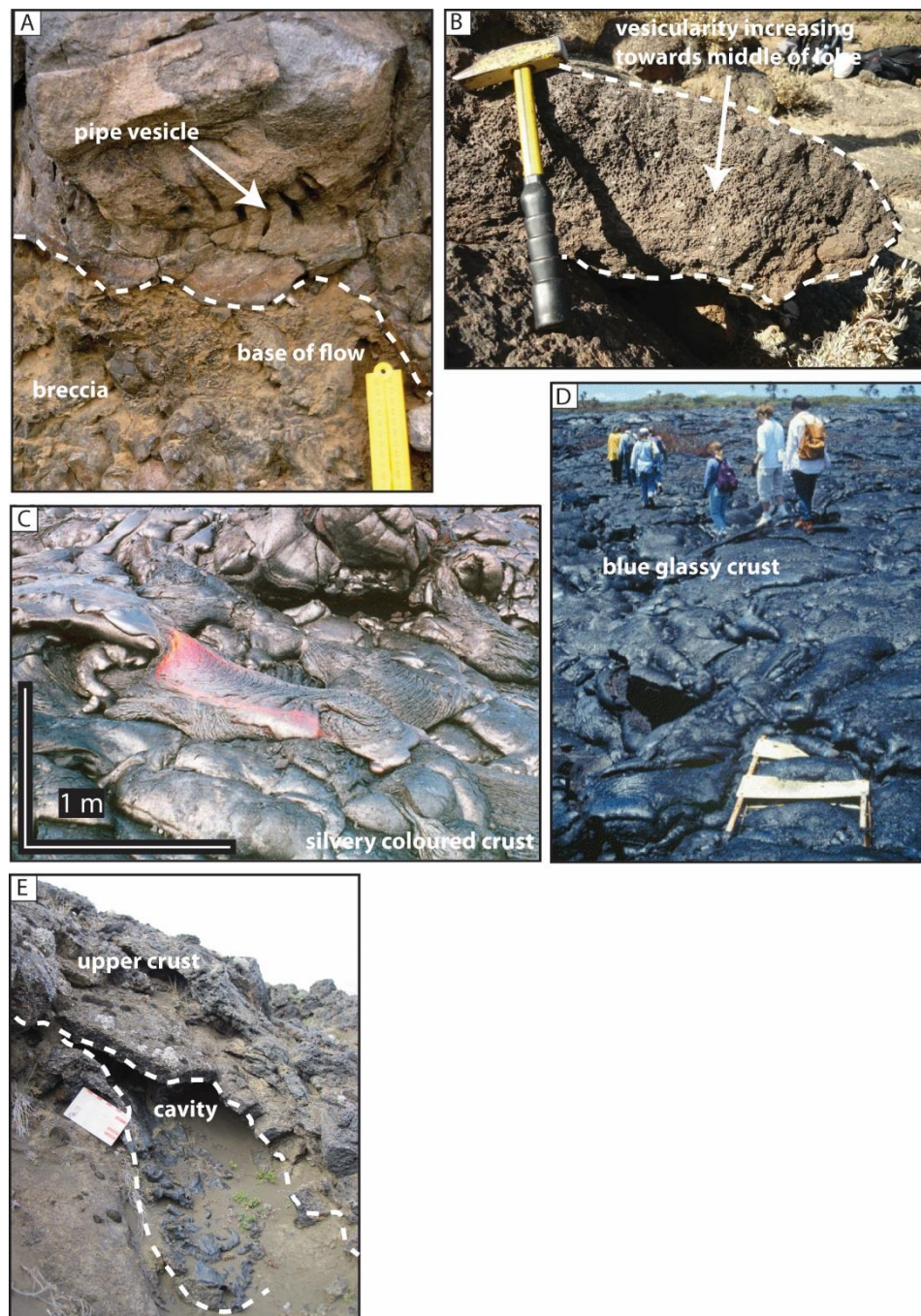


Figure 2.7. (overleaf) Photographs showing (A) P-type, (B) S-type, (C) silvery (D) blue glassy and (E) shelly pāhoehoe. Photograph C is from Leverington (2002) and D is from Wilch (2011). The ruler in A is 10 cm long and the scale card in E is 10 cm long.

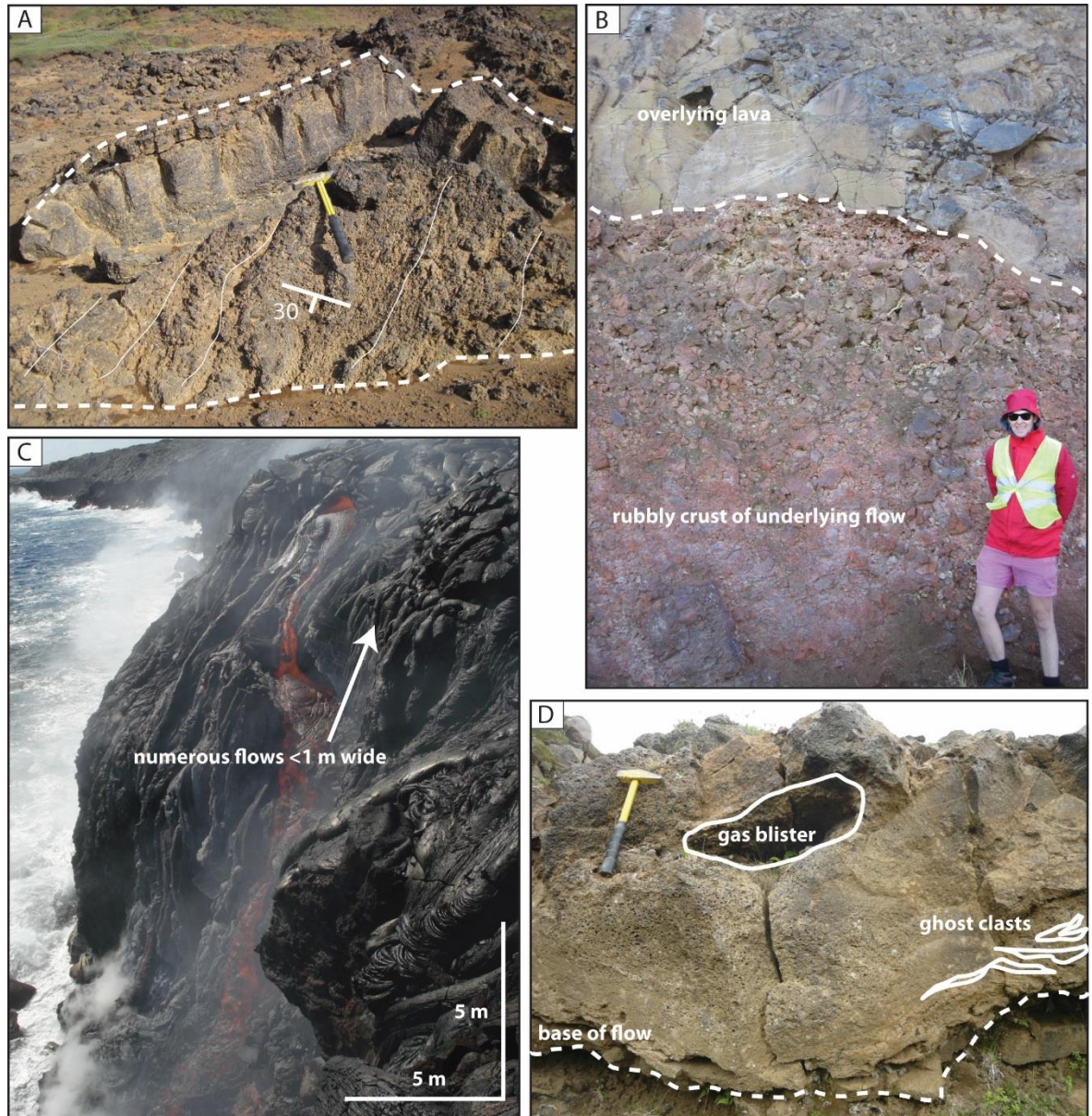


Figure 2.8. Photographs showing spiny (A), rubbly (B), entrail (C) and clastogenic (D) pāhoehoe. Photograph C from Pendred (2011).

2.4.4 Physical features of lava flow fields

Lava flow fields contain a range of large scale features that can be used to determine emplacement conditions (e.g. inflation). Features include tumuli, tubes, channels, squeeze-outs, rafted deposits and lava rise pits. Tumuli form during inflation and are roughly

circular or elongate mounds with axial or star-like clefts in their crust (Walker 1991). They are often found above tubes (Walker 1991). Tubes and channels represent arterial delivery systems to the distal regions of the flow field. Tubes and channels form within both *ʻā* and pāhoehoe lavas at varying effusion rates (e.g. Hon et al. 1994; Calvari and Pinkerton 1998; Calvari and Pinkerton 1999; Solana et al. 2004). Processes leading to their formation are described by Dragoni et al. (1995); Cashman et al. (2006) and Valerio et al. (2008). Squeeze-outs are found where injection of lava beneath the crust is extruded from beneath the solidified crust. They are common in distal regions of the flow field (Sumner 1998). Rafted deposits are fragments of pyroclasts or other lava flows that are carried down flow by the lava (Sumner 1998; Valentine and Gregg 2008; Riggs and Duffield 2008). The deposits may be carried entirely upon the top of the lava flow, or may begin to sink into the flow, depending on the rheology of the lava and deposit (Valentine and Gregg 2008). Lava rise pits result from topography inversion, and are depressions (originally topographic highs) between tumuli or lava rises. When a lava flow propagates into a large body of standing water, hyaloclastite and lava deltas form (see references within Wright 2013; Watton 2013). If a lava flow propagates into a marginal lacustrine or marshy environment, rootless eruptions may occur (e.g. Fagents et al. 2002; Fagents and Thordarson 2007; Hamilton et al. 2010a; Hamilton et al. 2010b).

2.4.4.1 Rootless eruptions

Rootless eruptions occur as a result of explosive interaction between saturated sediments and actively inflating pāhoehoe lava flows. These eruptions build cones on top of the lava flow and excavate a vent in the host lava flow. Similar rootless edifices (known as littoral cones) occur when lava flows enter the sea. Rootless cones vary in size from 2–40 m high and 5–450 m in basal diameter. They resemble small scoria cones, tuff cones or steep-sided spatter cones (Fagents and Thordarson 2007). They are composed of inversely graded beds of lapilli and bombs from fragmented molten lava core, clasts from the lava flow crust and sediment from beneath the lava flow (Hamilton et al. 2010b). Cones may exhibit complex stratigraphic relationships (Fagents and Thordarson 2007; Hamilton et al. 2010b) and occur in clusters that cover areas of up to 150 km² (Hamilton et al. 2010b). However, the stratigraphy, depositional sequence and componentry of these cones are poorly described. Furthermore, how the vents within the host lava flows are created, maintained and subsequently recognised in the field is not described.

2.4.5 Internal features of lava flows

2.4.5.1 Crustal structure

P-type pāhoehoe is comprised of an upper crust, a core and a basal crust (Self et al. 1998). This tripartite structure is defined by variations in vesicularity and indicates that the lava inflated (Fig. 2.9) (Self et al. 1998). The vesicular upper crust comprises 40–60% of the lobe thickness and its groundmass is hypohyaline – hypocrySTALLINE. It may contain prismatic or irregular joints. The crust often has horizontal vesicular zones (VZs) that are centimetres to decimetres thick. Bubbles within the zones increase in size with depth before increasing again at their base. They form due to variations in magma flux and/or pressure during inflation. The core is non-vesicular and holocrystalline. It contains vesicle sheets (VSs) and vesicle cylinders (VCs). Vesicle sheets are 1–5 cm thick and form due to the buoyant uprising of differentiated residuum from the core, which spread on contact with the solidified crust. Vesicle cylinders are similar to vesicle sheets and are formed by the diapiric rise of bubble-rich, low density residuum (Goff 1996). The basal crust can be almost as vesicular as the upper crust, but is only 20–100 mm thick regardless of flow thickness (Self et al. 1998). Its groundmass is hypohyaline – hypocrySTALLINE. The basal crust is sparsely jointed. The vesicularity, crustal structure of other lavas (e.g. shelly and clastogenic pāhoehoe) and the implications for their emplacement mechanisms remains un-investigated.

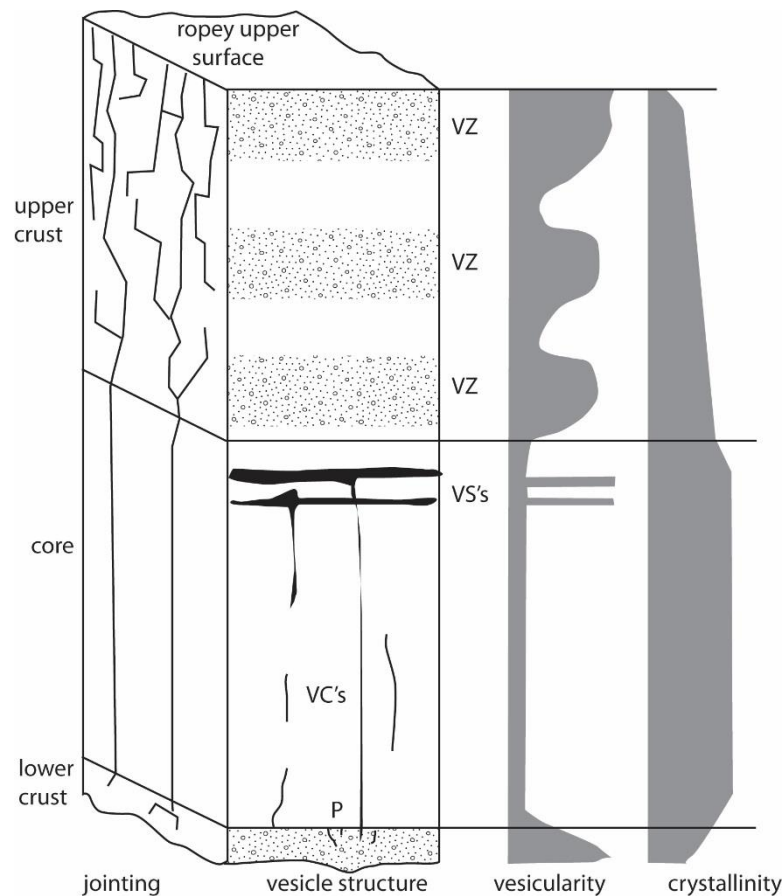


Figure 2.9. Schematic cross section through P-type pāhoehoe. The lobe has a tripartite structure defined by variations in vesicularity, crystallinity and jointing. The basal crust is 20–100 mm thick regardless of lobe thickness and is hypohyaline – hypocrySTALLINE. Cooling joints are sparse. The core of the flow is non-vesicular and holocrystalline. Columnar jointing may penetrate the core. Vesicle cylinders (VCs) and vesicle sheets (VSs) are found. The upper crust comprises 40–60% of the lobe thickness. It is vesicular and hypohyaline – hypocrySTALLINE. It may contain prismatic or irregular joints and numerous horizontal vesicle zones (VZs). Modified from Self et al. (1998).

2.4.5.2 Cooling joints

Both pāhoehoe and a’ā lava flows develop thermal contraction joints as they cool. These joints grow towards the interior of the flow as the crust thickens (Degraff et al. 1989). Many lava flows (eg. in Hawaii) have thin, crudely columnar tops, whilst larger flows (e.g. those within the Columbia River) have spectacular columnar jointing (Fig. 2.10). This jointed zone is defined as the colonnade (Tomkeieff 1940) and occurs in the core of lava flows (Thordarson and Self 1998). James (1920) considered that joint morphology is dependent on viscosity, temperature, rate and regularity of cooling and

homogeneity of the lava. Recent studies of cooling joints have shown that their radius is proportional to the cooling rate of the lava (Ryan and Sammis 1978; Goehring et al. 2006; Goehring and Morris 2008). Welded pyroclastic units can also develop columnar cooling joints (Brown et al. 2014).

The entablature (Fig. 2.10) is found in the upper crust of flows (e.g. Thordarson and Self 1998) and is produced by percolation of extreme rainfall ($>>250$ cm/yr) or flooding by fluvial systems (Long and Wood 1986). Similar pseudopillow fracture systems, formed by lava interaction with an aqueous coolant, indicate both brittle and ductile fracture mechanisms (Forbes et al. 2012). In all cases, percolating water uses master joints as a pathway for penetration into the lava flow (Forbes et al. 2014). Some lava flows have a tiered structure (Fig. 2.10) due to intermittent flooding events and dry periods (Long and Wood 1986).

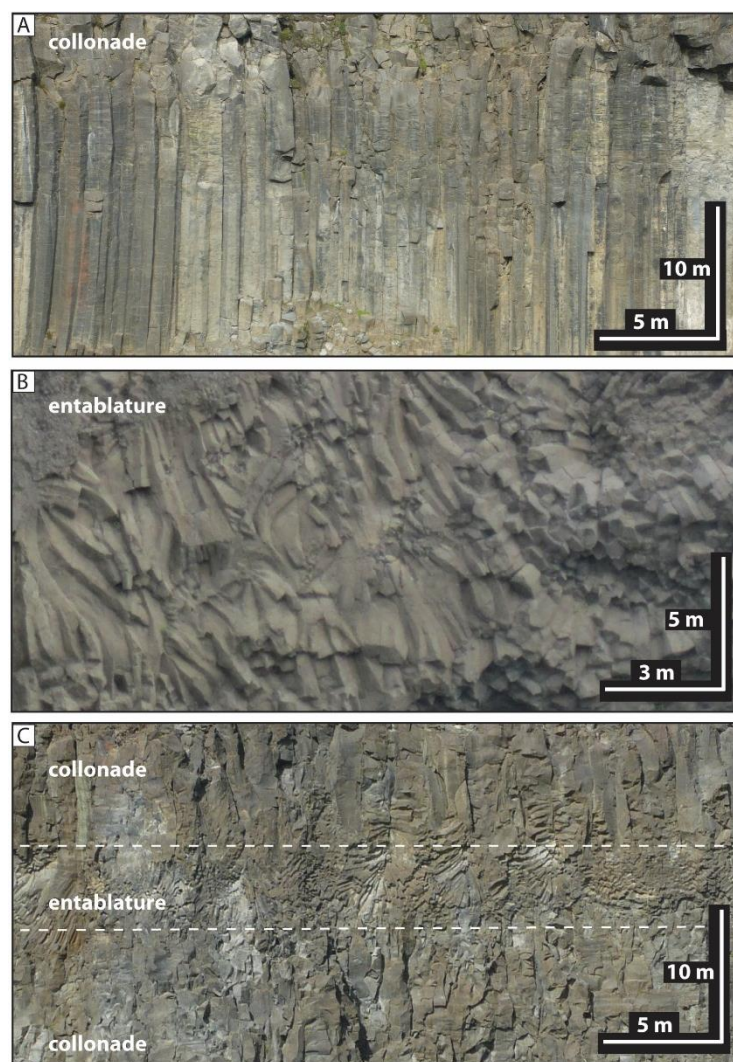


Figure 2.10. Jointing styles in lavas. (A) The colonnade of a lava flow with regular,

columnar jointing. These joints form due to thermal contraction during cooling. (B) The entablature of a lava flow with characteristic wavy-shaped joints. These joints form due to percolation of water through the cooling lava. (C) A tiered lava flow, displaying both an entablature and colonnade. This style of jointing develops due to intermittent flooding and dry periods.

2.5 Volcanic edifices

This section describes volcanic edifices in field datasets. A focus is given to monogenetic volcanic edifices formed during magmatic eruptions (e.g. scoria and spatter cones and spatter ramparts) since these edifices are found on fissures feeding flood basalt provinces and many other basaltic flow fields (e.g. Swanson et al. 1975; Reidel and Tolan 1992; Thordarson and Self 1993; Sumner 1998; Valentine et al. 2005; Riggs and Duffield 2008; Németh et al. 2011). Thus, edifices formed during magmatic volatile driven eruptions are candidates for volcanic edifices in hydrocarbon basins (e.g. the FSB).

These edifices may be monogenetic (i.e. erupt only once; Walker 2000) or polygenetic (i.e. erupt several times), which I describe in turn. I then provide a summary of seamounts, whose origin (i.e. mono or polygenetic) is often unknown.

2.5.1 Monogenetic volcanoes

Monogenetic edifices are 0.25–2.5 km in diameter and <30–450 m in height (Wood 1980; White and Ross 2011). They are common along fissures and may form linear chains along structural features (e.g. faults) or have scattered distributions (Walker 1993; Connor and Conway 2000). They are composed of lava flows and pyroclasts, depending on surface/ground water abundance, lava fountain structure, the underlying substrate and magma rheology/rise speed (Wohletz and Sheridan 1983; Jaupart and Vergnolle 1988; Head and Wilson 1989; Sohn 1996; e.g. Valentine and Gregg 2008). Edifices formed during magmatic eruptions include spatter cones, spatter ramparts, scoria cones, shield volcanoes and agglutinate cones. Edifices formed during magma-water interaction include tuff cones, tuff rings and maars. The amount of water involved in producing phreatomagmatic edifices is poorly constrained (see conflicting hypotheses in Vespermann and Schmincke 2000; White and Ross 2011). These edifices may intersect and merge in a complex fashion (e.g. Thordarson and Self 1993) and may form hybrid edifices (e.g. Verwoerd and Chevalier, 1987). Thus, edifices are part of a continuous spectrum of types.

Monogenetic edifices have a distinctive morphology (Tables 2.1 and 2.2; Vespermann and Schmincke 2000; White and Ross 2011). Field data suggests that the eruptions are fed by sills intruded to depths as shallow as 250 m (Németh and Martin 2007), whilst seismic data from historic eruptions show sills at depths of ~1.5 km feeding eruptions (Chadwick et al. 2006). These sills then feed dykes, which link to diatremes beneath maars and tuff rings. The exact methods by which edifices link to feeder systems in the shallow subsurface have been difficult to constrain (see section 2.3.1).

Vent type	Basal D (km)	Crater/plateau D (km)	Vertical scale of edifice (km)	Calculated height/basal diameter ratio	Volume (km ³)	Height/rim ratio	Flank dip (°)	Example
Spatter cone	<0.10	No data	0.10–0.30	No data	No data	No data	Steep, can approach vertical	Kapoho phase of Kilauea, Hawaii
Scoria cone	0.25–2.50	0.10–1.00	0.04–0.45	0.18	0.0001–1	0.45	25–38	Heimaey, Iceland
Shield-like volcano	1.0–12.00	0.10–1.80	0.05 –0.50	No data	0.4–11	No data	0–10	Rangitoto Island, New Zealand
Agglutinate cone	0.2–0.4		0.01–0.16	No data	0.0001–0.01	No data	15–19	Roza cones, Columbia River
Tuff cone	0.50–5	<0.1 –1	0.05–0.30	0.06	0.0001–1	0.5–0.2	10–30	Udo tuff cone, Korea
Tuff ring	1.60	0.20–3.00	<0.05	0.03	0.0001–1	0.13–0.15	1–20	Songaksan, Korea
Maar	1.4	0.2–3	<0.03	0.02	No data	0.13–0.15	1–20	Ukinrek West, Alaska
Polygenetic cone	No data	No data	0.35–2.25	No data	0.50–75	No data	Variable; 21–34 for simple cones	Mt. Teide, Tenerife
Seamount	0.70–2.30	No data	0.09–0.39	0.04–0.24	0.24–0.39	No data	<20–30	MOK seamount, East Pacific Rise
Table 2.1. Summary of volcanic edifice morphology. Data from Waters and Fisher (1971); Wood (1980); Head et al. (1981); Wilson and Head (1981); Thors and Jakousson (1982); Wohletz and Sheridan (1983); Gatliff et al. (1984); Ross (1986); Rossi (1996); Vespermann and Schmincke (2000); White and Ross (2011); Grosse et al. (2009); Mitchell et al. (2012) and (Brown et al., 2014).								

Vent type	Plumbing system	External morphology	Formation environment	Components
Spatter cone/ramparts	Dyke fed	Roughly circular in plan view (cones); linear, paired or singular features (ramparts), pipe like or fissure conduit remains open to several tens of feet below crater	Sub aerial, no magma-water interaction	Spatter and agglutinate
Scoria cone	Dyke fed	Small, truncated, cone shaped volcanic hills with bowl shaped craters	Sub aerial, no magma-water interaction	Ash, scoria, spatter and lava
Shield-like volcano	Dyke fed	Roughly circular in plan view, crater floors generally above land surface	Sub aerial	Basaltic lava flows; basaltic dredge samples from other similar structures
Agglutinate cone	Dyke fed	Roughly circular in plan view, crater floors above land surface	Sub aerial	Agglutinated spatter and scoria
Tuff cone	Dyke fed	Roughly circular in plan view crater floors generally above land surface	Subaerial, emergent submarine	Pyroclastic and crystalline basaltic rocks
Tuff ring	Underlain by shallow diatreme	Roughly circular in plan view with broad crater that may extend below surface	Sub aerial	Ash, scoria, spatter
Maar	Underlain by deep diatreme	Roughly circular in plan view with broad crater cutting 10–500 m into pre-eruption surface and low rim.	Requires enough water to allow explosive fragmentation, with hydrostatic pressure <30 bars.	Ash, abundant country rock
Polygenetic cone	Dyke fed	Very variable, from simple cones to massifs	Sub aerial and submarine	Pyroclasts and lava; variable in chemistry and texture
Seamount	Dyke fed	Broadly cone shaped, becoming flatter in shallower water, or flat where lava overflows from pond	Submarine, 200–400 m*	Lava, hyaloclastite, volcanoclastics
Table 2.2. Summary of volcanic edifice architecture (*water depth to summit). Data from Macdonald (1972); Wohletz (1983); Lorenz (1986); Rossi (1996); Riedel et al. (2003); Grosse et al. (2009); White and Ross (2011); Mitchell et al. (2012); Magee et al. (2013) and Brown et al. (2014).				

2.5.1.1 Spatter cones and ramparts

Spatter cones and ramparts are steep-sided edifices. Spatter cones range from 10–40 m high and 5–15 m in diameter (Green and Short 1971; Opheim and Gudmundsson 1989; Thordarson and Self 1993; Rymer et al. 1998; Heliker et al. 1998). They are dominantly composed of large, deformed and strongly welded spatter bombs (Riedel et al. 2003; Cimarelli et al. 2013). Variations in their morphology (e.g. crater – cone width) are not well documented. Spatter cones constructed along the Laki fissure are inferred to have been constructed during phases of dominantly effusive activity (Thordarson and Self 1993).

Spatter ramparts consist of variably welded scoria, spatter, rheomorphic spatter and lava (Alparone et al. 2003; Branca et al. 2009; Parcheta et al. 2012). Despite their abundance in many terrestrial volcanic environments and on Mars (e.g. Moore et al. 1980; Cattermole 1986; McNutt et al. 1991; Thordarson and Self 1993; Wilson et al. 1995; Dickson 1997; Alparone et al. 2003; Branca et al. 2009; Mourão et al. 2010; Parcheta et al. 2012), they have received very little attention in the literature. Ramparts form symmetrically or asymmetrically distributed, paired or single features. These are commonly elongated parallel to the strike of the fissure and set-back ≤ 30 m (Parcheta et al. 2012). Each rampart is ≤ 5 m in height, 12–24 m in width and 3–6 m in length (Moore et al. 1980; Dickson 1997; Parcheta et al. 2012). They may form at the site of maximum effusion from the fissure (e.g. Swanson et al. 1979).

A variety of clastogenic flow processes have been observed during their construction. McNutt et al. (1991) observed the partial collapse of an unstable, asymmetric rampart on steep slopes. Heslop et al. (1989) and Andronico et al. (2014) observed lava flows issuing from their base. Ramparts constructed during the 1977 eruption of Kilauea were eroded by lava drainback, suggesting that their outer surfaces remained molten (Moore et al. 1980). However, they also develop a brittle crust whilst they internally remaining molten (Heslop et al. 1989). Descriptions of the agglutinated deposits common in these edifices are found from literature describing scoria cones, lava ponds and cones in flood basalt provinces (e.g. Holm 1987; Sumner 1998; Valentine and Keating 2007; Riggs and Duffield 2008; Carracedo Sánchez et al. 2012; Brown et al. 2014).

2.5.1.2 Scoria cones

Scoria cones (Fig. 2.11) are truncated, cone-shaped volcanic hills with bowl-shaped craters (Macdonald 1972). They are commonly 0.25–5 km in basal diameter and ≤ 0.45 km

in height (Vespermann and Schmincke 2000). Their slopes dip 25–38° and their crater is above the land surface (White and Ross 2011). Scoria cones range in volume from 10^5 – 10^9 m³ and their crater is small in comparison to their basal diameter. Constituent fall deposits are lapilli–bomb size. Lithic clasts are rare. Examples include the Lathrop wells and Rothenberg scoria cones (see Houghton and Schmincke 1989; Valentine et al. 2005; Valentine et al. 2007; Genareau et al. 2010). They are commonly constructed by lava fountains <400 m in height (Head and Wilson 1989).

Wood (1980) and McGetchin et al. (1974) suggested that cone growth occurred via ballistic ejection of pyroclasts and outwards migration of the cone rim. As cone volume increased, a talus slope forms (McGetchin et al. 1974). The lava fountain also affects cone lithofacies architecture (Head and Wilson 1989). Riedel et al. (2003) demonstrated that cone growth dominantly occurred via deposition of lapilli from an eruption jet column.

Breaching and rafting of the cone by lava flows is a relatively common process (e.g. Valentine et al. 2005; Riggs and Duffield 2008; Valentine and Gregg 2008; Németh et al. 2011). Some breached cones may be partially or wholly rebuilt, leading to internal discontinuities within the edifice (e.g. Riggs and Duffield 2008). Lava flow effusion may be initiated by shallow degassing (e.g. Valentine and Keating 2007; Genareau et al. 2010), clastogenic flow (Sumner 1998), variations in magma flux and feeder dyke processes (Valentine and Gregg 2008). Lava may be effused from boccas at the base of cones (Sánchez et al. 2014) or occur as overspills from lakes in the crater (Carracedo Sánchez et al. 2012).

Scoria cone morphology and internal lithofacies architecture is dependent on variations in pyroclast accumulation rate; magma properties; breaching of the cone by lava flows; phreatomagmatic events and variations in conduit geometry. Variations in pyroclast accumulation rate (see section 2.3.3) can result from changes to fountain structure, inclination (e.g. pyroclast ejection angle, wind speed and direction) and intensity, and can result in variations in welding intensity (Wolfe et al. 1988; Head and Wilson 1989; Vespermann and Schmincke 2000). Variations in magma properties include the magma ascent rate, composition and gas content/flux. These may all result in variations in eruption style (see section 2.3.2).

Some cones are built on pre-existing tuff cones e.g. the Rothenburg scoria cone (Houghton and Schmincke 1989). Fluctuations in ground/surface water supply and magma flux can result in episodic phreatomagmatic events (e.g. Németh et al. 2001; Valentine and Cortés 2013). Variations in conduit geometry include widening (see section 2.3.1) and

constriction, which both affect eruption style (e.g. Keating et al. 2008). Constrictions are caused by lava withdrawal, causing partial collapse and blockage of the conduit neck (e.g. Wolfe et al. 1988).

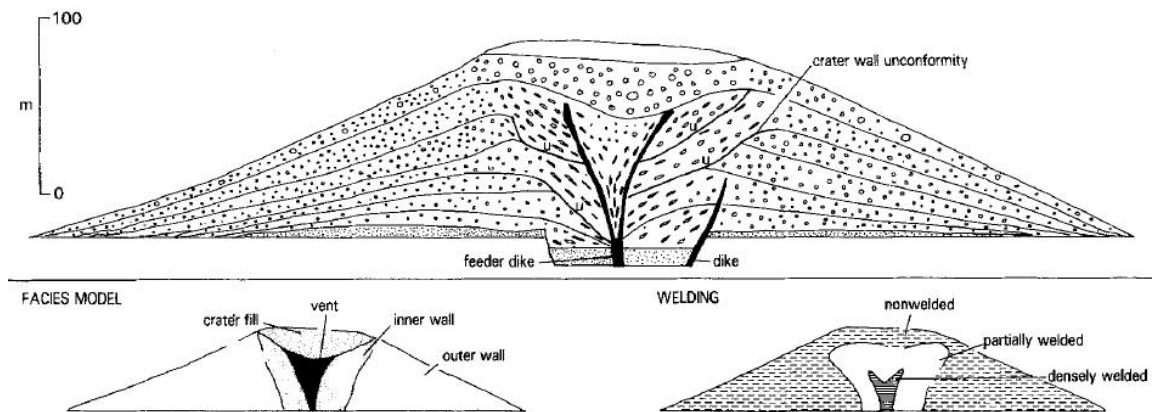


Figure 2.11. Schematic cross section of the Rothenburg scoria cone. Taken from Houghton and Schmincke (1989).

2.5.1.3 Shield volcanoes

Monogenetic shield volcanoes (Fig. 2.12) have basal diameters of 1–12 km and heights of 50–550 m (Rossi 1996). They are dominantly composed of lava flows that build a characteristic summit cone and an extensive lava apron. The cones are flat-topped or slightly convex to concave and convex-concave in cross-section and roughly symmetrical in plan view, with flanks that dip 0–10° (Rossi 1996). Their morphology is dependent on the changes in lava delivery (e.g. tube fed, overspill or rootless) and therefore effusion rate and eruption duration (Rossi 1996). There are few dissected examples of these edifices and the variations in morphology and construction mechanisms are unknown.

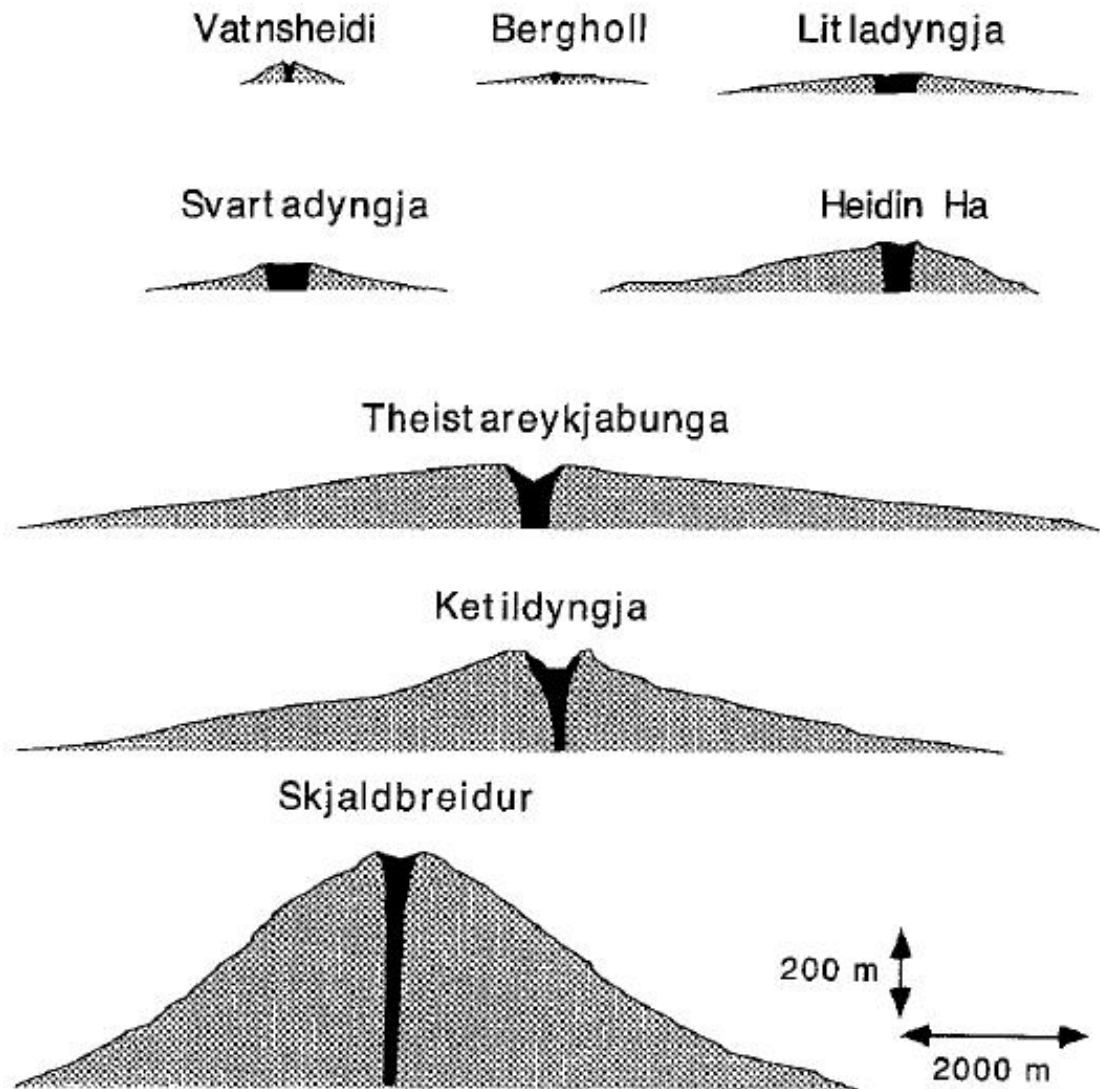


Figure 2.12. Profiles of shield volcanoes in Iceland. The dark column represents the feeder dyke. Taken from Rossi (1996).

2.5.1.4 Agglutinate cones

Agglutinate cones (Fig. 2.13) occur along the Roza fissure in the Columbia River Flood Basalt Province (Brown et al. 2014). The cones have basal diameters of 0.2–0.4 km and are 15–160 m in height. They are dominantly composed of agglutinate and scoria. The mean dip of the cone flanks is 15–19°. Edifices along the fissure are spaced ~1 km apart. The cones are inferred to have been constructed beneath a lava fountain 1 km in height (Brown et al. 2014).

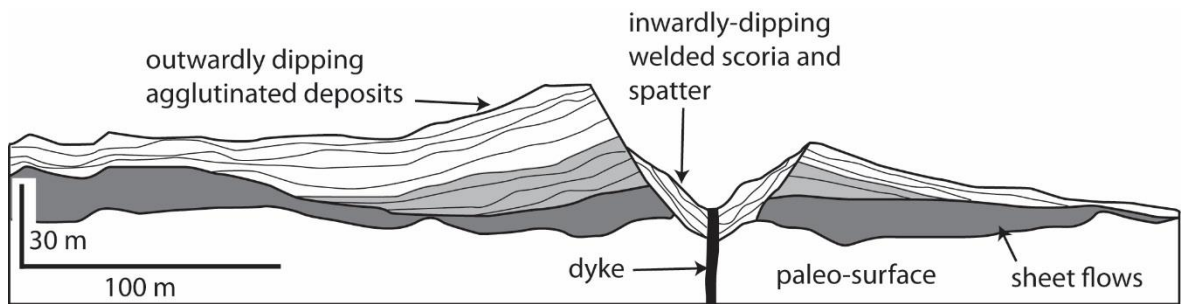


Figure 2.13. Schematic cross section of an agglutinate cone. Modified from Brown et al. (2014).

2.5.1.5 Tuff cones

Tuff cones (Fig. 2.14) are 0.25–5 km in basal diameter and ≤ 0.3 km in height (White and Ross 2011). They are formed during phreatomagmatic eruptions. Their slopes dip 10–30° and their crater floor is above the land surface (Vespermann and Schmincke 2000). The volume of tuff cones ranges from 10^5 – 10^9 m³ and the crater diameter is of medium size in comparison to the basal diameter of the cone (White and Ross 2011). Constituent pyroclasts are deposited by either fall or flow and are dominantly ash–lapilli sized (White and Ross 2011). Tuff cones are composed largely of juvenile clasts with subordinate amounts of accidental lithic clasts (Vespermann and Schmincke 2000). Re-deposition of pyroclasts may occur on steep slopes, resulting in lenticular, massive or chaotic bedded lapilli tuffs (Vespermann and Schmincke 2000). Examples of tuff cones include the Udo tuff cone in Korea and Surtsey, offshore Iceland (Thorarinsson 1966; Sohn and Chough 1993).

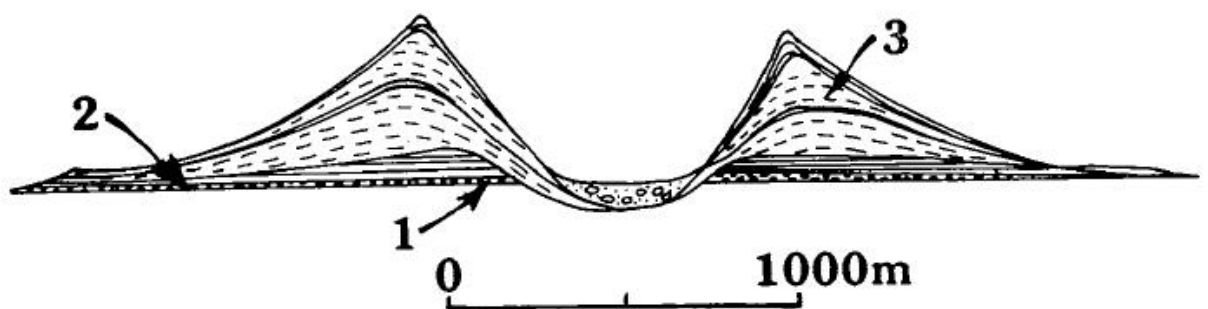


Figure 2.14. Schematic cross section of a tuff cone. (1) Explosion breccia, (2) thinly bedded deposits (3) thickly bedded, massive deposits. Adapted from Wohletz and Sheridan (1983).

2.5.1.6 Tuff rings

Tuff rings (Fig. 2.15) are constructional landforms formed during phreatomagmatic eruptions. They are commonly 0.25–5 km in basal diameter and up to 0.6 km in height. Their slopes dip sub-horizontally to 20° and their craters may extend below the land surface. Their volume ranges from 10^5 – 10^9 m³ (White and Ross 2011). Tuff rings have a large crater in comparison to their basal diameter. Component pyroclasts are deposited dominantly by flow and fall, and constituent pyroclasts are ash–lapilli size (White and Ross 2011). In comparison to tuff cones, flow is the dominant depositional method. They are dominantly composed of juvenile clasts; lithic clasts vary in abundance. Examples include the Suwolbong and Songaksan tuff rings in Korea (Sohn and Chough 1989; Chough and Sohn 1990).

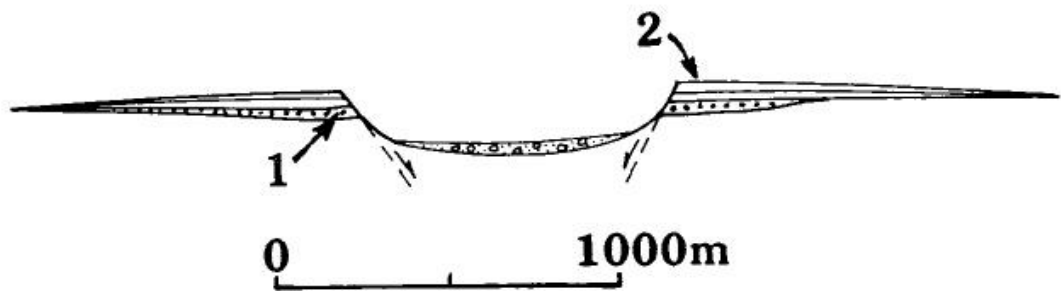


Figure 2.15. Schematic cross section of a tuff ring. (1) Explosion breccia, (2) thinly bedded deposits. Adapted from Wohletz and Sheridan (1983).

2.5.1.7 Maars

Maars (Fig. 2.16) are depressions in the land surface with a low rim of ejecta. Beds within the ejecta rim dip sub-horizontally to 20° and their craters vary from 0.2–3 km in diameter (Head et al. 1981). Individual maars may also overlap; within flood basalt provinces these complexes can be >30 km² in size (e.g. McClintock and White, 2006). Their volume range is unknown. Maars have a large crater in comparison to their basal diameter. Component pyroclasts are deposited dominantly by flow and fall, and constituent pyroclasts are ash–lapilli size (White and Ross 2011). They are composed of juvenile clasts and a high abundance of lithic clasts (White and Ross 2011). Examples include the crater formed during the 1965 eruption of Taal (Moore et al. 1966; White and Ross 2011). In comparison to tuff rings, maar-forming eruptions are triggered at greater depths beneath the surface. Maars are underlain by deep diatremes – a downwards-tapering structure cut

into the substrate (White and Ross 2011). They may reach up to 2500 m in depth and grade downwards into dykes (Vespermann and Schmincke 2000). They form via a combination of phreatomagmatic fragmentation and wall rock collapse (Vespermann and Schmincke 2000). See Lorenz (1975); White (1991); White and Ross (2011); Ross et al. (2013) and Graettinger et al. (2014) for in-depth discussions on their formation.

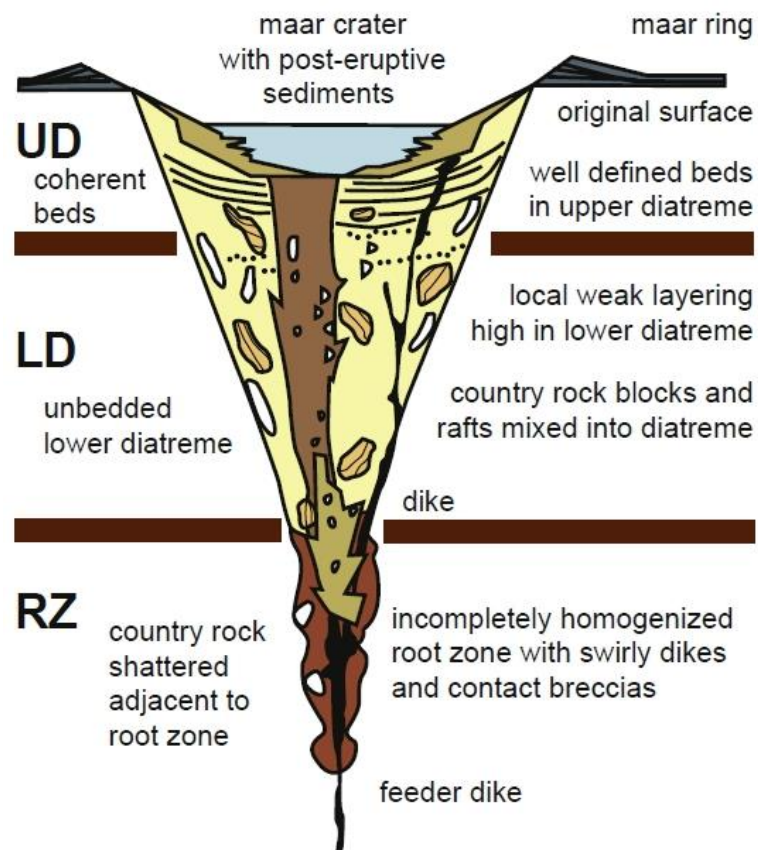


Figure 2.16. Schematic cross section of a maar and underlying diatreme. UD=Upper diatreme; LD=Lower Diatreme, RZ=root zone. Taken from White and Ross (2011).

2.5.2 Polygenetic volcanoes

Polygenetic or composite cones are constructed by numerous eruptions punctuated by periods of dormancy (e.g. Davidson and De Silva 2000). These long lived edifices are composed of a variety of extrusive volcanic rocks (including lavas and pyroclastic rocks of basaltic to dacitic and rhyolitic composition). They are found on convergent and divergent plate margins, as well as at mantle hotspots. These volcanoes may evolve from cones to overlapping massif structures (Grosse et al. 2009) and form linear chains 100's of kilometres in length (e.g. in the Andes). They are rarely >3000 m in height and have volumes of $\leq 200 \text{ km}^3$ (Davidson and De Silva 2000). Parasitic monogenetic volcanoes

form on the flanks of polygenetic edifices. When large scale evacuation of the magma chamber occurs, calderas form (e.g. Branney and Kokelaar 1994). Polygenetic volcanoes may evolve from submarine to sub aerial features, e.g. Mauna Loa, Hawaii. Brendan's Dome and the Darwin, Rockall and Erlend volcanic complexes and are reported as polygenetic centres within the FSB (Gatliff et al. 1984; Ritchie et al. 1997), although the emplacement mechanisms of these centres is not well documented .

2.5.2.1 Seamounts

Seamount is a term given to discrete elevations on the seafloor. They may be volcanic or non-volcanic. Non volcanic seamounts are restricted to forearc systems and are composed of horsts and diapirs of altered serpentinite (Schmidt and Schmincke 2000). Volcanic seamounts (Fig. 2.17) can be monogenetic or polygenetic structures (e.g. Hirano et al. 2008; McKee et al. 2010). These structures are common in all tectonic settings and there are estimated to be over 100,000 seamounts worldwide (Wessel et al. 2010). Due to their remoteness, they are commonly studied using a combination of sonar and seismic data (e.g. Thors and Jakousson 1982; Clague et al. 2000; Das et al. 2007; Mitchell et al. 2012). Bathymetric data and more rarely drill core data indicate that they are predominantly composed of hyaloclastite, pillow lavas and pelagic ooze (Schmidt and Schmincke 2000). Eruptions can build small (<200 m height) conical pillow volcanoes (Batiza and White 2000). In addition, their vents may also be composed of lithic breccias and scoria (Schmidt and Schmincke 2000; Mitchell et al. 2012). Vents formed in shallow waters (≤ 200 m summit depth) produce flat topped tephra cones (Mitchell et al. 2012). This 200 m cut-off from is a result of forced spreading of the eruption column at the air/water interface (Mitchell et al. 2012). Flat-topped seamounts are also formed as a result of continual overflow from long-lived lava ponds (Clague et al. 2000).

Large seamounts reach >100 km in basal diameter (e.g. Hawaii) and submerged structures are 0.05–8 km in height (Wessel et al. 2010). Seamounts align along faults, providing information on the local and regional stress field (Das et al. 2007; Paulsen and Wilson 2010). Different morphological types have been identified including shallow sloped, shield, inverted soup bowl, domed and flat topped types (Simkin 1972; Clague et al. 2000; Das et al. 2007; Mitchell et al. 2012). Some seamounts have pit craters and calderas, evidencing explosive activity (Schmidt and Schmincke 2000). Factors influencing their morphology include water depth (Clague et al. 2000; Mitchell et al. 2012), magma transport route (Mitchell et al. 2012), the effusion rate, eruption duration

and steadiness, the slope on which the edifice forms (Clague et al. 2000), the composition of the magma, conduit geometry, local and regional tectonics setting and the thermo-physical properties of the underlying lithosphere (Das et al. 2007).

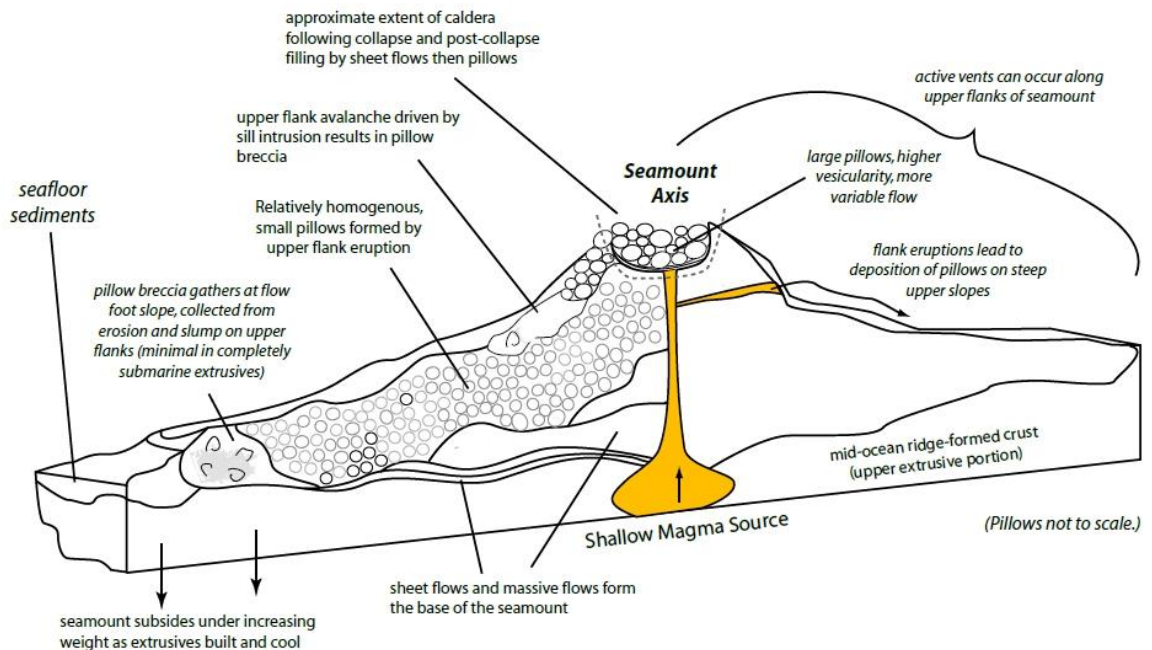


Figure 2.17. Schematic cross section of a polygenetic seamount. The seamount is ≥ 5 km in diameter and several hundred metres in height. Modified from Schnur (2007).

2.6 The identification and importance of volcanic features in hydrocarbon basins

2.6.1 Lavas

Lavas are important components in volcanic-affected hydrocarbon basins. They can decrease the porosity and permeability of underlying reservoir rocks, (Jerram and Stollhofen 2002; Grove 2014). Furthermore, they determine the architecture of overlying sedimentary systems (Schofield and Jolley 2013). The dense cores of lavas also act as seals (e.g. Schutter 2003; Rohrman 2007), whilst their vesicular crusts and cooling joints act as reservoirs and pathways for hydrocarbons (e.g. Burns et al. 2012; Burns et al. 2014). Drilling through lava sequences can also cause significant loss of drilling fluids and mud (e.g. Millett 2015). Lavas also provide indications of relative crustal movement (e.g. Seaward Dipping Reflectors; see Planke and Eldholm 1994) and help locate break-up axes in rift settings. Lavas also provide a range of challenges during seismic imaging (see below).

2.6.1.1 Basaltic lavas in seismic data

Lavas are responsible for the scattering and attenuation of seismic waves (Ogilvie et al. 2001; Jerram 2002; Maresh and White 2005; Maresh et al. 2006; Shaw et al. 2008; Nelson et al. 2009a; Wright 2013). In regions with significant basalt cover, this scattering creates what is known as “the sub-basalt imaging problem”, whereby large sections of stratigraphy underlying the basalt is so poorly imaged that no structure can be determined (e.g. Jerram 2002; White et al. 2003). In addition to the loss of imaging quality, volcanic rocks can also cause distortion of seismic data and result in the formation of multiples, which are repetitions of a seismic wave as it reverberates between the top of the volcanics and the sea bed and within a volcanic body itself (Fliedner and White 2001; Nelson et al. 2009a; Wright 2013). Distorted seismic data appears as pull-ups or push-downs that cause the reflection edifice to appear closer or further from the surface respectively. These are caused by seismic waves entering a low velocity structure that is overlain by high velocity lithologies (pull-up), or vice versa in the case of push-downs (Sheriff and Geldart 1995; Wright 2013).

Planke et al. (2000) and Wright (2013) have distinguished regional scale volcanic features (e.g. lava deltas) in seismic datasets, but as yet seismic facies typical of the vent-proximal regions have not been identified. In addition, the diversity of lavas outlined in section 2.4 has not been distinguished in seismic data. Furthermore, none of the common features of lava flow fields are recognised; features such as squeeze-outs that are potentially useful vent-proximity indicators are below the resolution of seismic data. However, compound and simple flows have been distinguished from seismic data in the FSB (Jerram et al. 2009) and can be diagnostic of vent proximity (Nelson et al. 2009b).

2.6.1.2 Basaltic lavas in well data

FMI and its precursor the Formation micro-scanner (FMS) are tools commonly used to collect well data. FMS can distinguish pillow lavas (Brewer et al. 1999). FMI data can recognise the vesicular flow tops characteristic of pāhoehoe lavas (Watton et al. 2014). ‘A‘ā lavas remain uncharacterised in well log, although it is hypothesised that their rubbly crusts could be recognised in FMI data (Watton et al. 2014). However, these breccias may be difficult to distinguish from coarse-grained pyroclastic deposits, identified in FMI as angular volcanic breccias (Watton et al. 2014). FMI can recognise cooling joints and their

orientation (Watton et al. 2014). This may help locate the vents of rootless cones that are surrounded by cooling joints atypical of the rest of the flow field (see Chapter 3).

Subaerial basalt and submarine basalts can be distinguished by their magnetic susceptibility and natural remnant magnetization (NRM) profiles (Delius et al. 2003). Tabular classic (P-type) lava flows and compound flows are recognised by their velocity and density characteristics (Nelson et al. 2009b). Flow type can be then used to constrain the 3D architecture of a basaltic province and provide better control on intra-basalt seismic imaging (Nelson et al. 2009b). Velocity variations within lava flows are also recognised by Planke and Cambray (1998) and record variations in total porosity, pore geometry and alteration. These variations can be used to determine lava flow structure (e.g. the presence of vesicular crusts) in volcanic-affected basins.

2.6.2 Volcanic edifices

Pyroclastic edifices are important features of volcanic-affected hydrocarbon basins (see Chapter 1). Their seismic characteristics and well data signature is outlined below.

2.6.2.1 Volcanic edifices in seismic data

A range of volcanic edifices have been imaged in seismic data (e.g. Gatliff et al. 1984; Faustmann 1995; Bell and Butcher 2002; Planke et al. 2005). However, our understanding of volcanic edifices in seismic data is incomplete and the diversity of volcanoes observed in the field (e.g. tuff rings, scoria cones, flat topped seamounts) has not been recognised in seismic datasets yet. In addition, numerous polygenetic structures are recognised but lack rigorous classification and distinction from monogenetic structures. The seismic characteristics of these edifices are outlined below (see also Table 2.3 and Fig. 2.18).

2.6.2.1.1 Monogenetic volcanoes

Surtsey is the only contemporary volcanic edifice for which seismic data is available (Thors and Jakousson 1982). However, this study is largely focused on the stratigraphy of the surrounding areas and gives sparse detail of the internal structure of the volcano itself. Spatter cones/ramparts, tuff rings and rootless cones are not currently recognised in seismic data. Ancient examples of tuff cones, scoria cones and maars include the study of Faustmann (1995) off the coast of Australia in the Bass Basin. Again, the internal structure of the edifices is not described in detail. Further studies in the South North Sea by Wall et

al. (2010) identified numerous elongate and circular craters that overly dykes and interpreted them to be maars. These structures are 200–2500 m wide and no details are given on the internal structure or the seismic facies of the vents. The craters are inferred to result from phreatomagmatic interaction in a water column 50–100 m deep. Fissures are recognised in the FSB (Thomson 2007) as a ridge-like feature, linked to underlying sills and dykes. The architecture of the edifices overlying the fissure is not described, and the products of the eruption are unknown. Volcanic edifices are also identified by Cukur et al. (2010) and Zhao et al. (2014) in 2D and 3D seismic data, although the genesis of the features is unclear. These edifices have high amplitude tops, and chaotic inner parts with variable amplitude.

Currently the most detailed description of volcanoes in seismic data is from monogenetic shield edifices in the Ceduna sub-basin offshore Australia (Magee et al. 2013). These cones have slightly rounded or flat tops, and concave/convex slope profiles. They range from ~2–19 km in basal diameter, with summit heights 0.02–1 km high. Three principal seismic facies were identified within the vents. Their lowermost parts were composed of high amplitude, early lava flows, overlain by continuous reflectors of varying amplitude. Their seismic velocities varied from 2365–6739 m s⁻¹. Some vents showed a plug-like chaotic internal region. The large size of these vents in comparison with other monogenetic vents (e.g. Walker 1993) is not discussed. They also have a wider range of morphologies (e.g. relationship between summit height and basal diameter) than other shield volcanoes (e.g. Rossi 1996). These vents were found within a sequence of limestone, implying a shallow marine environment – not the subaerial environment in which true monogenetic shield volcanoes form (e.g. Rossi 1996; Walker 2000).

2.6.2.1.2 Polygenetic volcanoes

Several polygenetic volcanoes have been described from seismic data. The Kora field, offshore New Zealand, has been subject to intense investigation owing to the presence of hydrocarbons within the structure (e.g. Bergman et al. 1991). However, there is little description of its internal architecture. Hübscher et al. (2015) describe the evolution of the Kolumbo polygenetic volcano in the southern Aegean Sea. Kolumbo is 1 km in height and 11 km in basal diameter. Explosive underwater eruptions of rhyolitic magma produced volcanoclastic units, forming several overlapping cones. The volcano has a combination of chaotic and weak internal reflections, with prograding reflectors in the edifice flanks. Studies in the North Atlantic have identified volcanic edifices thought to be polygenetic

shield volcanoes that are 2–4 km wide in basal diameter (Gatliff et al. 1984; Thomson 2005) and 400 m high (Gatliff et al. 1984). Internally, they have reflectors that dip radially outwards at $\leq 20^\circ$. The relationship of edifices to underlying sills is unknown, although the Erlend complex, NAIP, overlies a 14 km-wide pluton at 4 km depth (Gatliff et al. 1984). The edifice described by Thomson (2005) is underlain by a 2 km wide ring dyke or fault and has lava flows emanating from its summit and flanks.

2.6.2.1.3 Seamounts

Seismic data reveals that seamounts have high amplitude reflectors that dip outwards at $< 15^\circ$ and an onion ring geometry in plan view (Bell and Butcher 2002; Davies et al. 2002). Their internal reflectors downlap onto the underlying sediments (Thors and Jakousson 1982; Bell and Butcher 2002; Davies et al. 2002). They are found < 1200 m above sill tips (Bell and Butcher 2002; Davies et al. 2002) whilst those observed along active regions suggest that magma chambers are > 1400 m beneath the seafloor (Kent et al. 2003). However, the “hyaloclastite” edifice described by Davies et al. (2002) has been re-interpreted as a sedimentary hydrothermal edifice since drill core recovered from the edifice was composed of quartz, siltstone and dolerite sands, some of which preserve sedimentary laminations (Grove 2013).

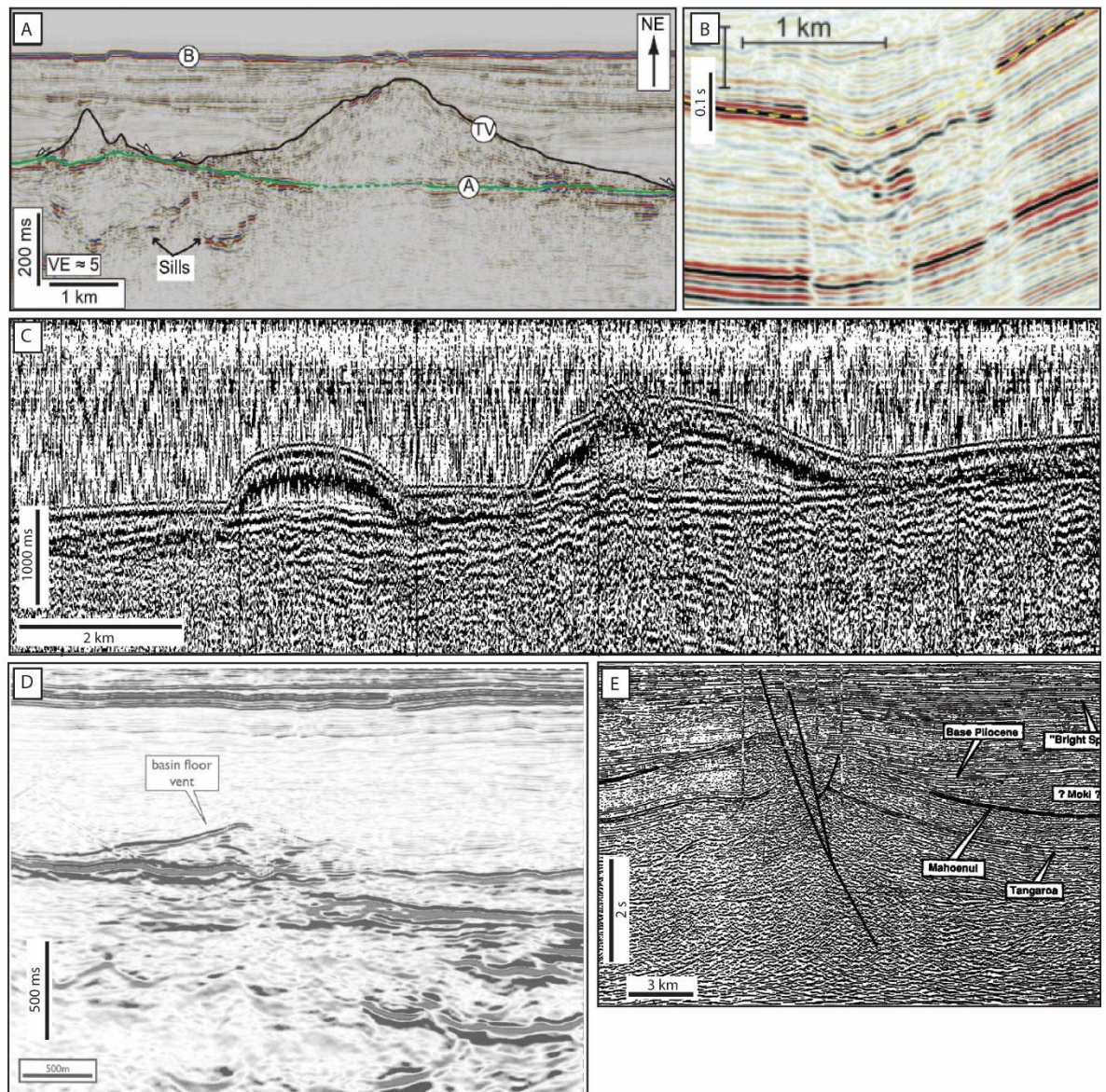


Figure 2.18. A comparison of the volcanoes currently recognised in seismic data. (A) Shield volcano, taken from Magee et al. (2013). (B) Maar crater, described by Wall et al. (2010). (C) Seismic line from Jólnir (left) and Stóra-Hraun (right) in the vicinity of Surtsey. Modified from Thors and Jakousson (1982). (D) Seamount in the Faroe-Shetland Basin, modified from Bell and Butcher (2002). (E) Kora andesitic stratovolcano, offshore New Zealand, modified from Bergman et al. (1991).

Edifice type	Basal relationship	Internal structure	Faulting	Relative Amplitude	Overlying stratigraphic relationship	Example in seismic data
Shield-like volcano	May cause pull-up, sometimes masked by basalt	Radially outwards dipping intra-basalt reflectors, dip approaching $\leq 12-20^\circ$	No data	No data	No data	North of Shetland and Ceduna Sub-Basin
Tuff cone	Concordant	Prograding flanks, chaotic central region, occasionally with a plug	No data	Not described	Unknown	Surtsey
Maar	Crater and diatreme truncate surrounding sediment	Filled with low amplitude sediments	Not described	Not described	Concordant	Southern North Sea
Polygenetic cone	Not described	Outwardly dipping prograding reflectors; some regions poorly imaged	Associated with normal faults	Not described	Onlapped	Kora, New Zealand
Seamount	Concordant	Onion ring in plan view, outward dipping reflectors in cross section	Unknown	Not detailed	Not detailed	NE Atlantic Margin

Table 2.3. Summary of the seismic characteristics of volcanic edifices in seismic section. Data from Thors and Jakousson (1982); Bergman et al. (1991); Bell and Butcher (2002); Thomson (2005); Wall et al. (2010) and Magee et al. (2013).

2.6.2.2 Volcanic edifices in well data

Basaltic volcanoclastic and pyroclastic rocks are poorly classified in well data. Their high resistivities and high FeO values are diagnostic of a basaltic component (Delius et al. 1998). Pyroclasts can be identified in FMI as angular volcanic breccias, but may appear similar to the rubbly tops of 'a'ā lavas (Watton et al. 2014). Cooling joints can be recognised from FMI (Watton et al. 2014); these are found in welded pyroclastic units (e.g. Brown et al. 2014). However, successions typical of volcanic edifices have yet to be characterised in well data.

2.7 Non-volcanic edifices found in hydrocarbon basins

In addition to the volcanic edifices found in hydrocarbon basins, there are also a range of non-volcanic edifices that have similar seismic characteristics. These edifices include mud volcanoes and hydrothermal vents. Their morphology and seismic characteristics are summarised below (see also Tables 2.4 and 2.5).

Vent type	Mean Basal D (km)	Crater/plateau D (km)	Vertical scale of edifice (km)	Calculated height/basal diameter ratio	Volume (km ³)	Height/rim ratio
Mud volcano	2–10	0.5–2	0.1–5	0.05–0.5	≤ 25	No data
Hydrothermal vent	0.40–11	≤ 11	0.03–0.45	0.12	Mean of 0.38	No data
	Plumbing system	External morphology	Formation environment	Lithology	Flank dip (°)	
Mud volcano	<10 m diameter feeder conduit contained within downward tapering conduit system, overly diapirs at depth	Circular, lenticular to biconic with flat, convex and concave tops	Sub aerial and sub marine	Argillaceous muds, pebbly muds with silt – sand sized matrix, occasionally brecciated blocks	>5	
Hydrothermal vent	Overly sill tips, with diatreme – like vertical feeder of fluidised sediment	Pit craters, dome and eye shaped	Sub aerial and sub marine	Mudstones, shales, sandstones, country rock boulders and zeolite cements, sediment/magma mixtures	2–13	

Table 2.4. Summary of the morphology of sedimentary edifices. Data from Kopf et al. (1998); Yusifov and Rabinowitz (2004); Davies and Stewart (2005); Planke et al. (2005); MØller Hansen (2006); Svensen et al. (2006); Svensen et al. (2007); Huuse et al. (2010); Grove (2013).

Edifice type	Basal relationship	Internal structure	Faulting	Relative Amplitude	Overlying stratigraphic relationship	Example in seismic data
Mud volcano	Down warped, concordant	Poorly imaged central chimney; outward dipping internal reflectors, central caldera, onion ring in plan view	Concentric, defining caldera, may overly faults linking to mud source	Varying across top surface, lows indicating mud flows	Onlapping, divergent	South Caspian Sea
Hydrothermal vent	Down warped, flat lying, truncated	Chaotic, downlapping, onion ring in plan view	Overly deep seated fault terminations	High amplitude top reflector	Onlapping, divergent and concordant	NE Atlantic Margin

Table 2.5. Summary of the seismic characteristics of sediment type vents in seismic section. Data from Kopf et al. (1998); Davies and Stewart (2005) Stewart and Davies (2006); Evans et al. (2007) and Roberts (2011).

2.7.1 Mud volcanoes

Mud volcanoes (Fig. 2.19) extrude fine-grained sediment and water onto the Earth's surface. They are found in marine and sub-aerial environments and have a spatial and genetic relationship to oil and gas fields (Kopf et al. 1998; Planke et al. 2003; Yusifov and Rabinowitz 2004; Davies and Stewart 2005; Roberts et al. 2011). They are common in extensional and collisional tectonic regimes and form due to overpressure at depth (Kopf et al. 1998; Kopf 2002). Many are found in regions that also contain numerous volcanic edifices (e.g. Lusi in Java and Dashgil in Azerbaijan; see Hovland et al. 1997; Roberts et al. 2011).

Each mud volcano is composed of a central edifice with numerous individual vents. The central edifice may be lenticular to circular or biconic in shape, occasionally with flat tops (Kopf 2002). The mudflows which construct the edifice are composed of poor- to well-sorted, mud- to sand-grade material containing pebbles and gravels. The sediment erupted is a mixture of muds, fluids and gases of varying proportions (Kopf et al. 1998; Deville et al. 2003; Evans et al. 2007; Roberts et al. 2011). These sediments are derived from the elutriation, stoping and brecciation of buried sediments sourced from deep clastic reservoirs up to 10 km beneath the edifice (e.g. Kopf et al. 1998; Graue 2000; Huuse et al.

2010). The edifice is constructed during successive eruptions that may build numerous cones on top of each other (Davies and Stewart 2005; Evans et al. 2007). Meanwhile slumping of unstable vent walls can degrade the edifice.

Originally, mud volcanoes were thought to have been fed by deep mud reservoirs and shale diapirs exploiting fault systems (Graue 2000; Planke et al. 2003). However, recent studies suggest that they are underlain by a root zone that feeds fluids, mud and gases along faults (Davies and Stewart 2005; Roberts et al. 2011). This root zone is considered to be composed of numerous fluidisation pipes and an underlying downward tapering cone of faulted country rock that focuses on buried aquifers (Davies and Stewart 2005). Other studies suggest that they are linked to thrust-cored anticlines at depth (Huuse et al. 2010).

Mud volcanoes reach up to 10 km in basal diameter and may be 10's of metres to 5 km in height. Their craters and calderas can be 0.5–2 km wide and 0.5 km deep (Graue 2000; Davies and Stewart 2005; Evans et al. 2007). They commonly align along faults and the hinges of anticlines with individual vents on the volcano changing orientation and elongation with time as they exploit localized faults and regional structures (Planke et al. 2003; Roberts et al. 2011). Individual vents are 0.01–360 m in diameter (Roberts et al. 2011).

When viewed in cross section in seismic data sets, mud volcanoes look extremely chaotic, with high amplitude tops and central chimney structures that allow gas (and fluid?) escape (Graue 2000; Evans et al. 2007). Low amplitude anomalies on the vent flanks form lobate and linear features that may represent mud flows (Evans et al. 2007). Internally mud volcanoes exhibit outwardly down-lapping reflectors giving them an onion-ring structure, and inward dipping reflectors in their central area (Fig. 2.20; Kopf et al. 1998).

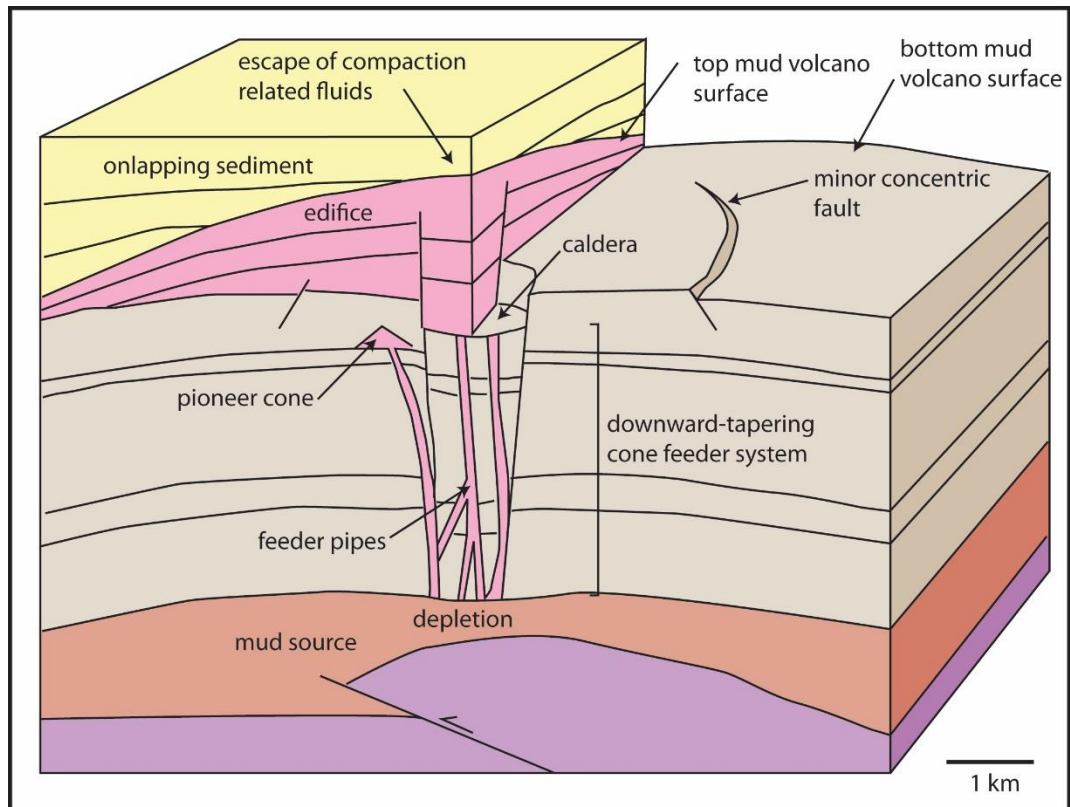


Figure 2.19. Schematic cross section of a mud volcano. The vertical scale varies from hundreds to thousands of metres. Modified from Evans et al. (2007).

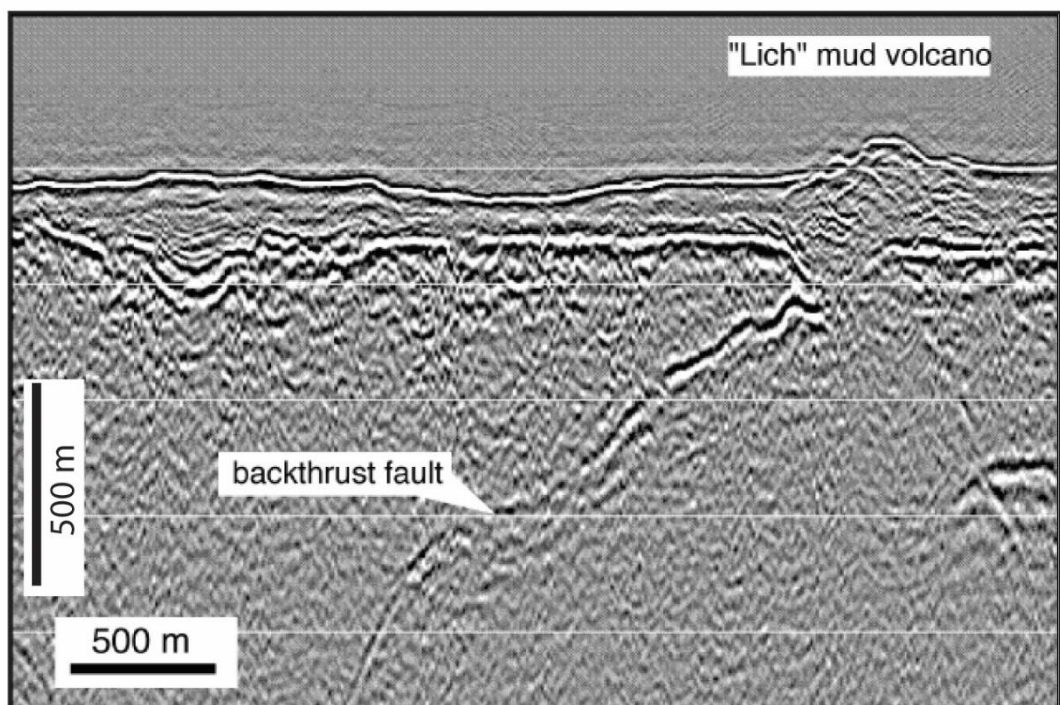


Figure 2.20. Seismic cross section of Lich mud volcano. Modified from Kopf (2002).

2.7.2 Hydrothermal vents

Hydrothermal vents (Fig. 2.21) are common in marine and fluvial environments. They are eye, crater or dome shaped in cross-section (Jamtveit et al. 2004; Svensen et al. 2006; Svensen et al. 2007; Grove 2013). Many hydrothermal vents occur within basins affected by igneous activity (e.g. the Karoo and Faroe Shetland Basin; see Svensen et al. 2006; Grove 2013). They form due to explosive brecciation of host strata and extrusion of fluidised sediment (Jamtveit et al. 2004; Grove 2013). The vents commonly overlie sills (Jamtveit et al. 2004). Thus, it is considered that sill emplacement leads to the boiling of pore fluids in the host rock. This boiling creates overpressure in the host rock due to vapour expansion and results in fluidisation (Jamtveit et al. 2004). Numerical models indicate that discharge occurs shortly after sill emplacement and is thought to occur whilst the magma in the sill is molten (Jamtveit et al. 2004). Fluid discharge continues until the steam is exhausted (Jamtveit et al. 2004).

Individual cones range in height from 30–450 m and are 0.4–11 km in basal diameter, displaying central craters up to 5 km wide (Svensen et al. 2006). The largest vents are underlain by the deepest intrusions (Planke et al. 2005). Vents form above the edges of sill tips (Planke et al. 2005) and may overlap to form linear chains (Grove 2013) similar to monogenetic volcanic edifices aligned along an igneous dyke. Their abundance varies from 1/40 km² to 1/130 km² (Svensen et al. 2006) and they are often found above the termination of deep seated faults. The vents are most common above sills that are layer-parallel rough (i.e. discontinuous with varying inclinations), planar transgressive and slightly saucer-shaped (Planke et al. 2005).

Hydrothermal vents are dominantly composed of loosely consolidated sediment and porous sedimentary rock (Jamtveit et al. 2004; Huuse et al. 2010). Fine to medium grained quartz sand is common since it is easily fluidised (Huuse et al. 2010) although laminated and bedded sandstone, mudstones, shale and country rock boulders are also found in vent structures (Svensen et al. 2006; Svensen et al. 2007; Grove 2013). Component lithologies are sourced from both the horizons in which sills were emplaced and the overlying stratigraphy (Svensen et al. 2003; Svensen et al. 2007). Drill core from breccia pipes beneath hydrothermal vents reveal that these vents can be composed of sediments that contain appreciable quantities of fragmented magma (i.e. peperite), which forms during the intrusion of the sill (Svensen et al. 2007).

In seismic datasets hydrothermal vents exhibit high amplitude tops (Davies et al. 2002; Grove 2013) and onion ring structures in plan view (Fig. 2.22; see Davies et al. 2002),

similar to mud volcanoes. They may have flat-lying, downwarped, truncated or concordant basal reflectors, and the overburden will commonly onlap, diverge or be concordant with the vent structure (Planke et al. 2005). Internally the vents may be chaotic or have progradational, downlapping reflectors (Planke et al. 2005). The vents also disturb underlying reflections (Planke et al. 2005).

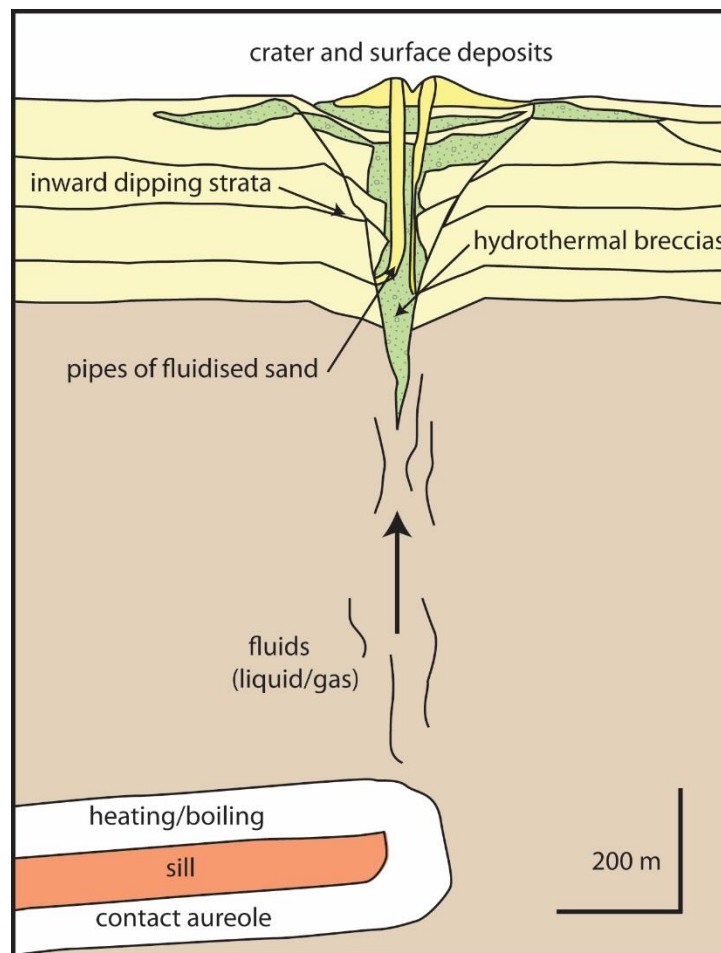


Figure 2.21. Schematic cross section of a hydrothermal vent. Vent formation is linked to the heating of pore fluids adjacent to the sill. Modified from Jamtveit et al. (2004).

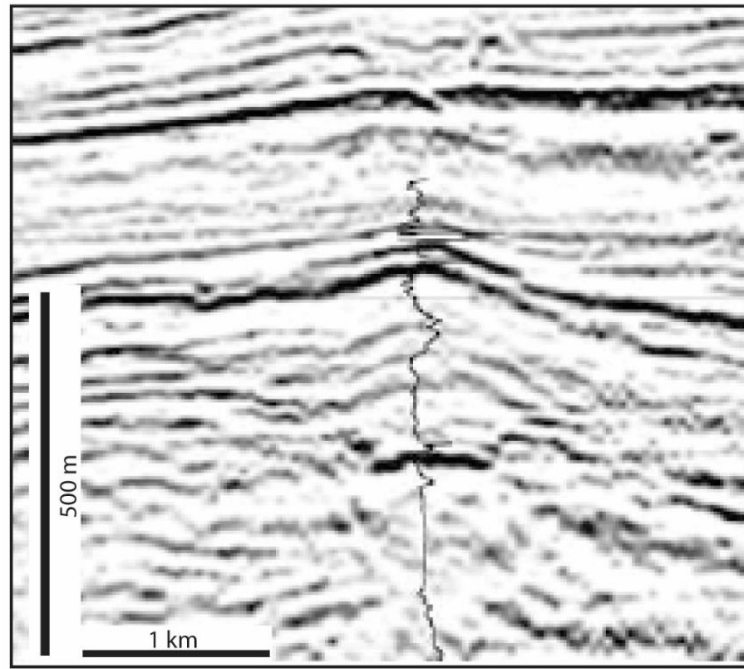


Figure 2.22. Seismic cross section of an eye-type hydrothermal vent. Modified from Svensen et al. (2003).

2.7.3 Comparison between types of sedimentary edifices

Mud volcanoes and hydrothermal vents can be distinguished based on field characteristics and by the inferred method that drove sediment effusion. Sediment effusion in both types is driven by pressure differences between the pore fluid pressure within a sub-surface permeable sedimentary layer and a lower pressurised layer (usually) nearer the surface (Huuse et al. 2010). In the case of hydrothermal vents, the increase in pressure is driven by vapour expansion caused by heating during igneous intrusion (Jamtveit et al. 2004). In mud volcanoes, fluid flow is driven by overpressure in the water phase (Huuse et al. 2010).

An initial assessment of hydrothermal vents and mud volcanoes would suggest that the two are easily distinguished by the larger size of mud volcanoes, their structural characteristics (e.g. calderas and exploitation of underlying faults) and the lithology of the effused sediment. However, the relationship of hydrothermal vents to structural features and the presence of calderas are as-yet unreported (e.g. Svensen et al. 2006). Also, an inherent flaw using field observations to distinguish between the two vent types is the inability to observe magmatic sills underlying mud volcanoes, which are thought to be a key feature in the formation of hydrothermal vents (Jamtveit et al. 2004; Svensen et al. 2006). Furthermore, there is currently no classification scheme that defines each vent type

based on its component lithologies. Both types may effuse sand and silt-sized rock fragments (Kopf et al. 1998; Huuse et al. 2010; Grove 2013).

Distinguishing between different edifices in seismic data is problematic since they have similar seismic responses (e.g. outward dipping internal layering, vertical chimneys of disturbed reflections, chaotic internal zones and high amplitude reflectors; see Graue 2000; Planke et al. 2005; Evans et al. 2007). The vents can be morphologically similar due to constructional processes (sediment effusion) and compactional processes at the seafloor governing morphology in both edifice types (Planke et al. 2005). Given these similarities, eye-shaped hydrothermal vents in seismic data from the Vøring Basin have also been interpreted as mud volcanoes (Jamtveit et al. 2004).

2.8 Summary

This chapter has provided a summary of the controls, styles and deposit of basaltic volcanism. In addition I have outlined the volcanic components of basaltic volcanism-affected basins. These components include feeder dykes, lavas and volcanic edifices. I have also outlined the difficulties in trying to identify volcanic edifices in volcanic-affected hydrocarbon basins. Recognising and distinguishing these edifices from hydrothermal vents remains a significant challenge in regions of hydrocarbon exploration.

2.9 References

- Alparone S, Andronico D, Lodato L, Sgroi T (2003) Relationship between tremor and volcanic activity during the Southeast Crater eruption on Mount Etna in early 2000. *Journal of Geophysical Research: Solid Earth* (1978–2012) 108(B5)
- Anderson SW, Stofan ER, Smrekar SE, Guest JE, Wood B (1999) Pulsed inflation of pahoehoe lava flows: implications for flood basalt emplacement. *Earth and Planetary Science Letters* 168(1-2):7-18
- Andronico D, Scollo S, Cristaldi A, Lo Castro M (2014) Representivity of incompletely sampled fall deposits in estimating eruption source parameters: a test using the 12–13 January 2011 lava fountain deposit from Mt. Etna volcano, Italy. *B Volcanol* 76(10):1-14
- Arrighi S, Principe C, Rosi M (2001) Violent strombolian and subplinian eruptions at Vesuvius during post-1631 activity. *B Volcanol* 63(2-3):126-150
- Batiza R, White JDL (2000) Submarine lavas and hyaloclastite. In: Sigurdsson H (ed) *Encyclopedia of volcanoes*. Academic Press, San Diego, pp 361-381
- Bell B, Butcher H (2002) On the emplacement of sill complexes: evidence from the Faroe-Shetland Basin. *Geological Society, London, Special Publications* 197(1):307-329
- Bergman SC, Talbot JP, Thompson PR (1991) The Kora Miocene submarine andesite stratovolcano hydrocarbon reservoir, Northern Taranaki Basin, New Zealand. In: *New Zealand Oil Exploration Conference Proceedings Ministry of Economic Development, New Zealand*, pp 178 - 206
- Bondre N, Duraiswami R, Dole G (2004a) Morphology and emplacement of flows from the Deccan Volcanic Province, India. *B Volcanol* 66(1):29-45

- Bondre N, Duraiswami R, Dole G (2004b) A brief comparison of lava flows from the Deccan Volcanic Province and the Columbia-Oregon Plateau Flood Basalts: Implications for models of flood basalt emplacement. *Journal of Earth System Science* 113(4):809-817
- Booth B, Self S (1973) Rheological Features of the 1971 Mount Etna Lavas. *Philosophical Transactions of the Royal Society of London. Series A, Mathematical and Physical Sciences* 274(1238):99-106
- Branca S, Del Carlo P, Lo Castro MD, De Beni E, Wijbrans J (2009) The occurrence of Mt Barca flank eruption in the evolution of the NW periphery of Etna volcano (Italy). *B Volcanol* 71(1):79-94
- Branney MJ, Kokelaar P (1992) A Reappraisal of Ignimbrite Emplacement - Progressive Aggradation and Changes from Particulate to Nonparticulate Flow during Emplacement of High-Grade Ignimbrite. *B Volcanol* 54(6):504-520
- Branney MJ, Kokelaar P (1994) Volcanotectonic faulting, soft-state deformation, and rheomorphism of tuffs during development of a piecemeal caldera, English Lake District. *Geol Soc Am Bull* 106(4):507-530
- Brewer TS, Harvey PK, Haggas S, Pezard PA, Goldberg D (1999) The role of borehole images in constraining the structure of the ocean crust: case histories from the Ocean Drilling Program. In: Lovell MA, Williamson G, Harvey PK (eds) *Borehole Imaging: Case Histories*. Geological Society, Special Publications, London, p 283-294
- Brown D, Holohan E, Bell B (2009) Sedimentary and volcano-tectonic processes in the British Paleocene Igneous Province: a review. *Geol Mag* 146(3):326-352
- Brown RJ, Blake S, Thordarson T, Self S (2014) Pyroclastic edifices record vigorous lava fountains during the emplacement of a flood basalt flow field, Roza Member, Columbia River Basalt Province, USA. *Geol Soc Am Bull* 126:875-891
- Bruce PM, Huppert HE (1989) Thermal control of basaltic fissure eruptions. *Nature* 342(6250):665-667
- Bryan SE, Ernst RE (2008) Revised definition of large igneous provinces (LIPs). *Earth-Science Reviews* 86(1):175-202
- Burns E, Williams C, Ingebritsen S, Voss C, Spane F, DeAngelo J (2014) Understanding heat and groundwater flow through continental flood basalt provinces: insights gained from alternative models of permeability/depth relationships for the Columbia Plateau, USA. *Geofluids*
- Burns ER, Snyder DT, Haynes JV, Waibel MS (2012) Groundwater Status and Trends for the Columbia Plateau Regional Aquifer System, Washington, Oregon, and Idaho.
- Calvari S, Pinkerton H (1998) Formation of lava tubes and extensive flow field during the 1991-1993 eruption of Mount Etna. *J. Geophys. Res.* 103(B11):27291-27301
- Calvari S, Pinkerton H (1999) Lava tube morphology on Etna and evidence for lava flow emplacement mechanisms. *J Volcanol Geoth Res* 90(3-4):263-280
- Capaccioni B, Cuccoli F (2005) Spatter and welded air fall deposits generated by fire-fountaining eruptions: Cooling of pyroclasts during transport and deposition. *J Volcanol Geoth Res* 145(3-4):263-280
- Carey R, Houghton B, Thordarson T (2008) Contrasting styles of welding observed in the proximal Askja 1875 eruption deposits II: Local welding. *J Volcanol Geoth Res* 171(1):20-44
- Carracedo Sánchez M, Sarrionandia F, Arostegui J, Eguiluz L, Gil Ibarguchi JI (2012) The transition of spatter to lava-like body in lava fountain deposits: features and examples from the Cabezo Segura volcano (Calatrava, Spain). *J Volcanol Geoth Res* 227-228(0):1-14
- Cas RAF, Wright JV (1987) *Volcanic Successions, Modern and Ancient: a Geological Approach to Processes, Products and Successions*. Allen and Unwin, London
- Cashman K, Kerr R, Griffiths R (2006) A laboratory model of surface crust formation and disruption on lava flows through non-uniform channels. *B Volcanol* 68(7):753-770
- Cashman KV, Thornber C, Kauahikaua JP (1999) Cooling and crystallization of lava in open channels, and the transition of Pāhoehoe Lava to 'A'ā. *B Volcanol* 61(5):306-323
- Cattermole P (1986) Linear volcanic features at Alba Patera, Mars-Probable spatter ridges. *Journal of Geophysical Research: Solid Earth* (1978-2012) 91(B13):E159-E165
- Ceramicola S, Stoker M, Praeg D, Shannon P, De Santis L, Hoult R, Hjelstuen B, Laberg S, Mathiesen A (2005) Anomalous Cenozoic subsidence along the 'passive' continental margin from Ireland to mid-Norway. *Marine and petroleum geology* 22(9):1045-1067

- Chadwick WW, Geist DJ, Jónsson S, Poland M, Johnson DJ, Meertens CM (2006) A volcano bursting at the seams: inflation, faulting, and eruption at Sierra Negra Volcano, Galápagos. *Geology* 34(12):1025-1028
- Chouet B, Hamisevicz N, McGetchin TR (1974) Photoballistics of Volcanic Jet Activity at Stromboli, Italy. *J. Geophys. Res.* 79(32):4961-4976
- Chough S, Sohn Y (1990) Depositional mechanics and sequences of base surges, Songaksan tuff ring, Cheju Island, Korea. *Sedimentology* 37(6):1115-1135
- Cimarelli C, Di Traglia F, de Rita D, Torrente DG (2013) Space–time evolution of monogenetic volcanism in the mafic Garrotxa Volcanic Field (NE Iberian Peninsula). *B Volcanol* 75(11):1-18
- Clague DA, Moore JG, Reynolds JR (2000) Formation of submarine flat-topped volcanic cones in Hawai'i. *B Volcanol* 62(3):214-233
- Clark SJ (2014) Constraining diagenetic timings, processes and reservoir quality in igneous-affected basins. PhD Thesis, Durham University, Department of Earth Sciences.
- Coffin MF, Eldholm O (1994) Large igneous provinces: crustal structure, dimensions, and external consequences. *Reviews of Geophysics* 32(1):1-36
- Cole P, Guest J, Duncan A, Pacheco J-M (2001) Capelinhos 1957–1958, Faial, Azores: deposits formed by an emergent surtseyan eruption. *B Volcanol* 63(2-3):204-220
- Connor CB, Conway MF (2000) Basaltic volcanic fields. In: Sigurdsson H (ed) *Encyclopedia of Volcanoes*. Academic Press, San Diego, pp 331-343
- Crisp J, Baloga S (1994) Influence of crystallization and entrainment of cooler material on the emplacement of basaltic aa lava flows. *J. Geophys. Res.* 99(B6):11819-11831
- Cukur D, Horozal S, Kim DC, Lee GH, Han HC, Kang MH (2010) The distribution and characteristics of the igneous complexes in the northern East China Sea Shelf Basin and their implications for hydrocarbon potential. *Marine Geophysical Researches* 31(4):299-313
- Das P, Iyer SD, Kodagali VN (2007) Morphological characteristics and emplacement mechanism of the seamounts in the Central Indian Ocean Basin. *Tectonophysics* 443(1–2):1-18
- Davidson J, De Silva S (2000) Composite volcanoes. p 679
- Davies R, Bell BR, Cartwright JA, Shoulders S (2002) Three-dimensional seismic imaging of Paleogene dike-fed submarine volcanoes from the northeast Atlantic margin. *Geology* 30(3):223-226
- Davies RJ, Stewart SA (2005) Emplacement of giant mud volcanoes in the South Caspian Basin: 3D seismic reflection imaging of their root zones. *J Geol Soc London* 162(1):1-4
- Davison I, Stasiuk S, Nuttall P, Keane P (2010) Sub-basalt hydrocarbon prospectivity in the Rockall, Faroe–Shetland and Møre basins, NE Atlantic. *Geological Society, London, Petroleum Geology Conference series* 7:1025-1032
- Dean K, McLachlan K, Chambers A (1999) Rifting and the development of the Faeroe-Shetland Basin. In: *Geological Society, London, Petroleum Geology Conference series*. Geological Society of London, pp 533-544
- Degraff JM, Long PE, Aydin A (1989) Use of joint-growth directions and rock textures to infer thermal regimes during solidification of basaltic lava flows. *J Volcanol Geoth Res* 38(3-4):309-324
- Delaney PT, Pollard DD (1981) Deformation of host rocks and flow of magma during growth of minette dikes and breccia-bearing intrusions near Ship Rock, New Mexico. *US Geol Surv Prof Pap* 1202
- Delius H, Bücker C, Wohlenberg J (1998) Determination and characterization of volcanoclastic sediments by wireline logs: Sites 953, 955, and 956, Canary Islands. *Proceedings of the Ocean Drilling, Scientific Results* 157:29-37
- Delius H, Brewer T, Harvey P (2003) Evidence for textural and alteration changes in basaltic lava flows using variations in rock magnetic properties (ODP Leg 183). *Tectonophysics* 371(1):111-140
- Deville E, Battani A, Griboulard R, Guerlais S, Herbin JP, Houzay JP, Muller C, Prinzhofer A (2003) The origin and processes of mud volcanism: new insights from Trinidad. *Geological Society, London, Special Publications* 216(1):475-490
- Dickson LD (1997) Volcanology and geochemistry of pliocene and quaternary basalts on Citadel Mountain, Lunar Crater Volcanic field, Pancake Range, Nevada.
- Doré AG, Lundin ER, Jensen LN, Birkeland Ø, Eliassen PE, Fichler C (1999). Principal tectonic events in the evolution of the northwest European Atlantic margin. In *Geological Society, London, Petroleum Geology Conference series* 5:41-61 Geological Society of London.

- Doubik P, Hill BE (1999) Magmatic and hydromagmatic conduit development during the 1975 Tolbachik Eruption, Kamchatka, with implications for hazards assessment at Yucca Mountain, NV. *J Volcanol Geoth Res* 91(1):43-64
- Dragoni M, Piombo A, Tallarico A (1995) A model for the formation of lava tubes by roofing over a channel. *J. Geophys. Res.* 100(B5):8435-8447
- Duraiswami RA, Dole G, Bondre N (2003) Slabby pahoehoe from the western Deccan Volcanic Province: evidence for incipient pahoehoe-aa transitions. *J Volcanol Geoth Res* 121(3-4):195-217
- Duraiswami RA, Bondre NR, Managave S (2008) Morphology of rubbly pahoehoe (simple) flows from the Deccan Volcanic Province: Implications for style of emplacement. *J Volcanol Geoth Res* 177(4):822-836
- Eldholm O, Grue K (1994) North Atlantic volcanic margins: dimensions and production rates. *Journal of Geophysical Research: Solid Earth* (1978–2012) 99(B2):2955-2968
- Ellis D, Bell BR, Jolley DW, O’Callaghan M (2002) The stratigraphy, environment of eruption and age of the Faroes Lava Group, NE Atlantic Ocean. Geological Society, London, Special Publications 197(1):253-269
- Ellis D, Passey S, Jolley D, Bell B (2009) Transfer zones: The application of new geological information from the Faroe Islands applied to the offshore exploration of intra basalt and sub-basalt strata. In: Faroe Islands Exploration Conference: Proceedings of the 2nd Conference. *Annales Societatis Scientiarum Færoensis*, Tórshavn. pp 205-226
- Evans RJ, Davies RJ, Stewart SA (2007) Internal structure and eruptive history of a kilometre-scale mud volcano system, South Caspian Sea. *Basin Research* 19(1):153-163
- Fagents SA, Lanagan P, Greeley R (2002) Rootless cones on Mars: a consequence of lava-ground ice interaction. Geological Society, London, Special Publications 202(1):295-317
- Fagents SA, Thordarson T (2007) Rootless cones in Iceland and on Mars. In: Chapman M, Skilling IP (eds) *The Geology of Mars: Evidence from Earth-Based Analogues*. Cambridge University Press, pp 151–177
- Faustmann C (1995) The seismic expression of volcanism in the Bass Basin referring to western Victorian analogues.
- Fletcher R, Kuszniir N, Roberts A, Hunsdale R (2013) The formation of a failed continental breakup basin: The Cenozoic development of the Faroe-Shetland Basin. *Basin Research* 25(5):532-553
- Fliedner MM, White RS (2001) Sub-basalt imaging in the Faeroe-Shetland Basin with large-offset data. *First Break* 19(5)
- Forbes, AES, Blake S, Mc Garvie, DW, Tuffen H (2012) Pseudopillow fracture systems in lavas: insights into cooling mechanisms and environments from lava flow fractures *J Volcanol Geoth Res* 245 (2012): 68-80.
- Forbes AES, Blake S, Tuffen H (2014) Entablature: fracture types and mechanisms. *B Volcanol* 76(5):1-13
- Friese N, Bense FA, Tanner DC, Gústafsson LE, Siegesmund S (2013) From feeder dykes to scoria cones: the tectonically controlled plumbing system of the Rauðhólar volcanic chain, Northern Volcanic Zone, Iceland. *B Volcanol* 75(6):1-19
- Galindo I, Gudmundsson A (2012) Basaltic feeder dykes in rift zones: geometry, emplacement, and effusion rates. *Natural Hazards and Earth System Sciences* 12(12):3683-3700
- Gatliff RW, Hitchen K, Ritchie JD, Smythe DK (1984) Internal structure of the Erlend Tertiary volcanic complex, north of Shetland, revealed by seismic reflection. *J Geol Soc London* 141(3):555-562
- Geiki A (1897) *The Ancient Volcanoes of Great Britain*. Macmillan, London
- Genareau K, Valentine G, Moore G, Hervig R (2010) Mechanisms for transition in eruptive style at a monogenetic scoria cone revealed by microtextural analyses (Lathrop Wells volcano, Nevada, U.S.A.). *B Volcanol* 72(5):593-607
- Geshi N, Kusumoto S, Gudmundsson A (2010) Geometric difference between non-feeder and feeder dikes. *Geology* 38(3):195-198
- Geshi N, Oikawa T (2014) The spectrum of basaltic feeder systems from effusive lava eruption to explosive eruption at Miyakejima volcano, Japan. *B Volcanol* 76(3):1-14
- Gibson IL, Kinsman D, Sugurdsson H, Walker G (1966) *Geology of the Faskrudsfjörður area, eastern Iceland*.

- Goehring L, Morris SW, Lin Z (2006) Experimental investigation of the scaling of columnar joints. *Physical Review E* 74(3):036115
- Goehring L, Morris SW (2008) Scaling of columnar joints in basalt. *J. Geophys. Res.* 113(B10):B10203
- Goff F (1996) Vesicle cylinders in vapor-differentiated basalt flows. *J Volcanol Geoth Res* 71(2–4):167-185
- Graettinger A, Valentine G, Sonder I, Ross PS, White J, Taddeucci J (2014) Maar-diatreme geometry and deposits: Subsurface blast experiments with variable explosion depth. *Geochemistry, Geophysics, Geosystems* 15(3):740-764
- Graue K (2000) Mud volcanoes in deepwater Nigeria. *Marine and Petroleum Geology* 17(8):959-974
- Green J, Short NM (1971) *Volcanic landforms and surface features: A photographic atlas and glossary*. Springer-Verlag
- Gregg TKP, Fink JH (2000) A laboratory investigation into the effects of slope on lava flow morphology. *J Volcanol Geoth Res* 96(3-4):145-159
- Grosse P, van Wyk de Vries B, Petrinovic IA, Euillades PA, Alvarado GE (2009) Morphometry and evolution of arc volcanoes. *Geology* 37(7):651-654
- Grove C (2013) Submarine hydrothermal vent complexes in the Paleocene of the Faroe-Shetland Basin: Insights from three-dimensional seismic and petrographical data. *Geology* 41(1):71-74
- Grove C (2014) Direct and Indirect Effects of Flood Basalt Volcanism on Reservoir Quality Sandstone. PhD Thesis, Durham University, Department of Earth Sciences.
- Gudmundsson A, Friese N, Galindo I, Philipp SL (2008) Dike-induced reverse faulting in a graben. *Geology* 36(2):123-126
- Guilbaud M-N, Self S, Thordarson T, Blake S (2005) Morphology, surface structures, and emplacement of lavas produced by Laki, A.D. 1783–1784. *Geological Society of America Special Papers* 396:81-102
- Hamilton CW, Fagents SA, Thordarson T (2010a) Explosive lava–water interactions II: self-organization processes among volcanic rootless eruption sites in the 1783–1784 Laki lava flow, Iceland. *B Volcanol* 72(4):469-485
- Hamilton CW, Thordarson T, Fagents SA (2010b) Explosive lava–water interactions I: architecture and emplacement chronology of volcanic rootless cone groups in the 1783–1784 Laki lava flow, Iceland. *B Volcanol* 72(4):449-467
- Hansen J, Jerram D, McCaffrey K, Passey S (2009) The onset of the North Atlantic Igneous Province in a rifting perspective. *Geol Mag* 146(03):309-325
- Harris A, Rowland SR (2001) FLOWGO: a kinematic thermo-rheological model for lava flowing in a channel. *B Volcanol* 63(1):20-44
- Harris AJ, Dehn J, Calvari S (2007) Lava effusion rate definition and measurement: a review. *B Volcanol* 70(1):1-22
- Head JW, Bryan W, Greeley R, Guest J, Shultz P, Sparks R, Walker G, Whitford-Stark J, Wood C, Carr M (1981) Distribution and morphology of basalt deposits on planets. *Basaltic Volcanism on the Terrestrial Planets*:702-887
- Head JW, Wilson L (1989) Basaltic pyroclastic eruptions: Influence of gas-release patterns and volume fluxes on fountain structure, and the formation of cinder cones, spatter cones, rootless flows, lava ponds and lava flows. *J Volcanol Geoth Res* 37(3–4):261-271
- Heliker C, Mangan M, Mattox T, Kauahikaua J, Helz R (1998) The character of long-term eruptions: inferences from episodes 50–53 of the Pu'u'Ō'ō-Kūpaianaha eruption of Kīlauea Volcano. *B Volcanol* 59(6):381-393
- Heliker C, Mattox T (2003) The first two decades of the Pu'u 'O'o-Kupaianaha eruption: chronology and selected bibliography. *US Geol Surv Prof Pap* 1676:1-28
- Heslop S, Wilson L, Pinkerton H, Head J, III (1989) Dynamics of a confined lava flow on Kilauea volcano, Hawaii. *B Volcanol* 51(6):415-432
- Hintz AR, Valentine GA (2012) Complex plumbing of monogenetic scoria cones: New insights from the Lunar Crater Volcanic Field (Nevada, USA). *J Volcanol Geoth Res*
- Hirano N, Koppers AAP, Takahashi A, Fujiwara T, Nakanishi M (2008) Seamounts, knolls and petit-spot monogenetic volcanoes on the subducting Pacific Plate. *Basin Research* 20(4):543-553

- Hjartardóttir ÁR, Einarsson P, Bramham E, Wright TJ (2012) The Krafla fissure swarm, Iceland, and its formation by rifting events. *B Volcanol* 74(9):2139-2153
- Holford S, Schofield N, MacDonald J, Duddy I, Green P (2012) Seismic analysis of igneous systems in sedimentary basins and their impacts on hydrocarbon prospectivity: examples from the Southern Australian margin. *Australian Petroleum Production and Exploration Association Journal* 52:229-252
- Holm RF (1987) Significance of agglutinate mounds on lava flows associated with monogenetic cones: An example at Sunset Crater, northern Arizona. *Geol Soc Am Bull* 99(3):319-324
- Holmes A, Griffith C, Scotchman I (1999) The Jurassic petroleum system of the West of Britain Atlantic margin—an integration of tectonics, geochemistry and basin modelling. In: Geological Society, London, Petroleum Geology Conference series. Geological Society of London, pp 1351-1365
- Hon K, Kauahikaua J, Delinger R, Mackay K (1994) Emplacement and inflation of pahoehoe sheet flows: Observations and measurements of active lava flows on Kilauea Volcano, Hawaii. *Geol Soc Am Bull* 106(3):351-370
- Hon K, Gansecki C, Kauahikaua JP (2003) The transition from 'a'ā to pāhoehoe crust on flows emplaced during the Pu'u 'O'ō-Kūpaianaha eruption. *US Geol Surv Prof Pap* 1676: 89–103
- Hooper PR (2000) Flood Basalt Provinces. In: Sigurdsson H (ed) *Encyclopedia of Volcanoes*.
- Houghton BF, Schmincke HU (1989) Rothenberg scoria cone, East Eifel: a complex Strombolian and phreatomagmatic volcano. *B Volcanol* 52(1):28-48
- Hovland M, Hill A, Stokes D (1997) The structure and geomorphology of the Dashgil mud volcano, Azerbaijan. *Geomorphology* 21(1):1-15
- Hübscher C, Ruhnau M, Nomikou P (2015) Volcano-tectonic evolution of the polygenetic Kolumbo submarine volcano/Santorini (Aegean Sea). *J Volcanol Geoth Res* 291:101-111
- Huuse M, Jackson CAL, Van Rensbergen P, Davies RJ, Flemings PB, Dixon RJ (2010) Subsurface sediment remobilization and fluid flow in sedimentary basins: an overview. *Basin Research* 22(4):342-360
- James AVG (1920) Factors Producing Columnar Structure in Lavas and Its Occurrence near Melbourne, Australia. *The Journal of Geology* 28(5):458-469
- Jamtveit B, Svensen H, Podladchikov YY, Planke S (2004) Hydrothermal vent complexes associated with sill intrusions in sedimentary basins. *Physical geology of high-level magmatic systems* 234:233-241
- Jaupart C, Vergnolle S (1988) Laboratory models of Hawaiian and Strombolian eruptions. *Nature* 331(6151):58-60
- Jaupart C, Vergnolle S (1989) The generation and collapse of a foam layer at the roof of a basaltic magma chamber. *Journal of Fluid Mechanics* 203:347-380
- Jerram DA (2002) Volcanology and facies architecture of flood basalts. *Geological Society of America Special Papers* 362:119-132
- Jerram DA, Stollhofen H (2002) Lava–sediment interaction in desert settings; are all peperite-like textures the result of magma–water interaction? *J Volcanol Geoth Res* 114(1–2):231-249
- Jerram DA, Widdowson M (2005) The anatomy of Continental Flood Basalt Provinces: geological constraints on the processes and products of flood volcanism. *Lithos* 79(3-4):385-405
- Jerram DA, Single RT, Hobbs RW, Nelson CE (2009) Understanding the offshore flood basalt sequence using onshore volcanic facies analogues: an example from the Faroe–Shetland basin. *Geol Mag* 146(03):353
- Jolley DW, Bell BR (2002) Genesis and age of the Erlend Volcano, NE Atlantic Margin. Geological Society, London, Special Publications 197(1):95-109
- Jolley DW, Morton AC (2007) Understanding basin sedimentary provenance: evidence from allied phytogeographic and heavy mineral analysis of the Palaeocene of the NE Atlantic. *J Geol Soc London* 164(3):553-563
- Keating G, Valentine G, Krier D, Perry F (2008) Shallow plumbing systems for small-volume basaltic volcanoes. *B Volcanol* 70(5):563-582
- Kent G, Harding A, Babcock J, Orcutt J, Detrick R, Canales J, Van Ark E, Carbotte S, Diebold J, Nedimovic M (2003) A new view of 3-D magma chamber structure beneath axial seamount and coaxial segment: Preliminary results from the 2002 Multichannel Seismic Survey of the Juan de Fuca Ridge. In: AGU Fall Meeting Abstracts. p 0755

- Kent RW, Thomson BA, Skelhorn RR, Kerr AC, Norry MJ, Walsh JN (1998) Emplacement of Hebridean Tertiary flood basalts: evidence from an inflated pahoehoe lava flow on Mull, Scotland. *J Geol Soc London* 155(4):599-607
- Keszthelyi L (1994) Calculated effect of vesicles on the thermal properties of cooling basaltic lava flows. *J Volcanol Geoth Res* 63(3):257-266
- Keszthelyi L, Denlinger R (1996) The initial cooling of pahoehoe flow lobes. *B Volcanol* 58(1):5-18
- Keszthelyi L, Self S (1998) Some physical requirements for the emplacement of long basaltic lava flows. *J. Geophys. Res.* 103(B11):27447-27464
- Kilburn CRJ (2000) Lava flows and flow fields. In: Sigurdsson H (ed) *Encyclopedia of Volcanoes*. Academic Press, San Diego, pp 291-305
- Kokelaar BP, Durant GP (1983) The submarine eruption and erosion of Surtla (Surtsey), Iceland. *J Volcanol Geoth Res* 19(3-4):239-246
- Kokelaar P (1986) Magma-water interactions in subaqueous and emergent basaltic. *B Volcanol* 48(5):275-289
- Kopf A, Robertson AHF, Clennell MB, Flecker R (1998) Mechanisms of mud extrusion on the Mediterranean Ridge Accretionary Complex. *Geo-Marine Letters* 18(2):97-114
- Kopf AJ (2002) Significance of mud volcanism. *Reviews of Geophysics* 40(2):1005
- Krauskopf KB (1948) Mechanism of eruption at Paricutin Volcano, Mexico *Geol Soc Am Bull* 59(8):711-732
- Larsen LM, Waagstein R, Pedersen AK, Storey M (1999) Trans-Atlantic correlation of the Palaeogene volcanic successions in the Faeroe Islands and East Greenland. *J Geol Soc London* 156(6):1081-1095
- Lefebvre N, Kurszlaukis S (2008) Contrasting eruption styles of the 147 Kimberlite, Fort à la Corne, Saskatchewan, Canada. *J Volcanol Geoth Res* 174(1):171-185
- Lefebvre NS, White JDL, Kjarsgaard BA (2012) Spatter-dike reveals subterranean magma diversions: Consequences for small multivert basaltic eruptions. *Geology* 40(5):423-426
- Leverington D (2002) New pahoehoe toes on the flanks of Kilauea. Texas Tech University, Department of Geosciences photographic collection.
- Lipman PW, Banks NG, Rhodes JM (1985) Degassing-induced crystallization of basaltic magma and effects on lava rheology.
- Long PE, Wood BJ (1986) Structures, textures, and cooling histories of Columbia River basalt flows. *Geol Soc Am Bull* 97(9):1144-1155
- Lorenz V (1975) Formation of phreatomagmatic maar-diatreme volcanoes and its relevance to kimberlite diatremes. *Physics and Chemistry of the Earth* 9:17-27
- Lorenz V (1986) On the growth of maars and diatremes and its relevance to the formation of tuff rings. *B Volcanol* 48(5):265-274
- Macdonald GA (1953) Pahoehoe, aa, and block lava. *American Journal of Science* 251(3):169-191
- Macdonald GA (1972) *Volcanoes*. Prentice-Hall, Englewood Cliffs, N.J.
- Macedonio G, Dobran F, Neri A (1994) Erosion processes in volcanic conduits and application to the AD 79 eruption of Vesuvius. *Earth and Planetary Science Letters* 121(1-2):137-152
- Magee C, Hunt-Stewart E, Jackson CAL (2013) Volcano growth mechanisms and the role of sub-volcanic intrusions: Insights from 2D seismic reflection data. *Earth and Planetary Science Letters* 373(0):41-53
- Maresh J, White RS (2005) Seeing through a glass, darkly: strategies for imaging through basalt. *First Break* 23(5)
- Maresh J, White RS, Hobbs RW, Smallwood JR (2006) Seismic attenuation of Atlantic margin basalts: Observations and modeling. *Geophysics* 71(6):B211-B221
- McClintock M, White JD (2006) Large phreatomagmatic vent complex at Coombs Hills, Antarctica: wet, explosive initiation of flood basalt volcanism in the Ferrar-Karoo LIP. *B Volcanol* 68(3), 215-239.
- McGetchin TR, Settle M, Chouet BA (1974) Cinder Cone Growth Modeled After Northeast Crater, Mount Etna, Sicily. *J. Geophys. Res.* 79(23):3257-3272
- McKee C, Harpp K, Geist D, Mittelstaedt E, Fornari D, Soule S (2010) Morphology, Size, and Spatial Distribution of Seamounts in the Northern Galápagos. In: *AGU Fall Meeting Abstracts*. p 2255

- McKerrow W, Mac Niocaill C, Dewey J (2000) The Caledonian orogeny redefined. *J Geol Soc London* 157(6):1149-1154
- McNutt SR, Miller TP, Taber JJ (1991) Geological and seismological evidence of increased explosivity during the 1986 eruptions of Pavlof volcano, Alaska. *B Volcanol* 53(2):86-98
- Millett J (2015) Offshore drilling through basaltic sequences: geological heterogeneity and its implications for drilling complications, VMSG, Norwich
- Mitchell N, Stretch R, Oppenheimer C, Kay D, Beier C (2012) Cone morphologies associated with shallow marine eruptions: east Pico Island, Azores. *B Volcanol* 74(10):2289-2301
- Møller Hansen D (2006) The morphology of intrusion-related vent structures and their implications for constraining the timing of intrusive events along the NE Atlantic margin. *J Geol Soc London* 163(5):789-800
- Moore JG, Nakamura K, Alcaraz A (1966) The 1965 Eruption of Taal Volcano. *Science* 151(3713):955-960
- Moore JG (1985) Structure and eruptive mechanisms at Surtsey Volcano, Iceland. *Geol Mag* 122(06):649-661
- Moore RB, Helz RT, Dzurisin D, Eaton GP, Koyanagi RY, Lipman PW, Lockwood JP, Puniwai GS (1980) The 1977 eruption of Kilauea volcano, Hawaii. *J Volcanol Geoth Res* 7(3):189-210
- Mourão C, Mata J, Doucelance R, Madeira J, Silveira ABd, Silva LC, Moreira M (2010) Quaternary extrusive calciocarbonatite volcanism on Brava Island (Cape Verde): A nephelinite-carbonatite immiscibility product. *Journal of African Earth Sciences* 56(2–3):59-74
- Moy D, Imber J (2009) A critical analysis of the structure and tectonic significance of rift-oblique lineaments ('transfer zones') in the Mesozoic–Cenozoic succession of the Faroe–Shetland Basin, NE Atlantic margin. *J Geol Soc London* 166(5):831-844
- Naylor PH, Bell BR, Jolley DW, Durnall P, Fredsted R (1997) Palaeogene magmatism in the Faeroe–Shetland Basin: influences on uplift history and sedimentation. 545-558
- Nelson CE, Jerram DA, Single RT, Hobbs RW (2009a) Understanding the facies architecture of flood basalts and volcanic rifted margins and its effect on geophysical properties, Faroe Islands Exploration Conference: Proceedings of the 2nd Conference,
- Nelson CE, Jerram DA, Hobbs RW (2009b) Flood basalt facies from borehole data: implications for prospectivity and volcanology in volcanic rifted margins. *Petroleum Geoscience* 15(4):313-324
- Németh K, Martin U, Harangi S (2001) Miocene phreatomagmatic volcanism at Tihany (Pannonian Basin, Hungary). *J Volcanol Geoth Res* 111(1–4):111-135
- Németh K, Martin U (2007) Shallow sill and dyke complex in western Hungary as a possible feeding system of phreatomagmatic volcanoes in “soft-rock” environment. *J Volcanol Geoth Res* 159(1–3):138-152
- Németh K, Risso C, Nullo F, Kereszturi G (2011) The role of collapsing and cone rafting on eruption style changes and final cone morphology: Los Morados scoria cone, Mendoza, Argentina. *Central European Journal of Geosciences* 3(2):102-118
- Ogilvie JS, Crompton R, Hardy NM (2001) Characterization of volcanic units using detailed velocity analysis in the Atlantic Margin, West of Shetlands, United Kingdom. *The Leading Edge* 20(1):34-50
- Opheim JA, Gudmundsson A (1989) Formation and geometry of fractures, and related volcanism, of the Krafla fissure swarm, northeast Iceland. *Geol Soc Am Bull* 101(12):1608-1622
- Óskarsson BV, Riishuus MS (2013) The mode of emplacement of Neogene flood basalts in Eastern Iceland: Facies architecture and structure of the Hólmar and Grjóta olivine basalt groups. *J Volcanol Geoth Res* 267(0):92-118
- Otterloo J, Cas RF, Sheard M (2013) Eruption processes and deposit characteristics at the monogenetic Mt. Gambier Volcanic Complex, SE Australia: implications for alternating magmatic and phreatomagmatic activity. *B Volcanol* 75(8):1-21
- Oze C, Winter JD (2005) The occurrence, vesiculation, and solidification of dense blue glassy pahoehoe. *J Volcanol Geoth Res* 142(3–4):285-301
- Parcheta C, Houghton B, Swanson D (2012) Hawaiian fissure fountains 1: decoding deposits—episode 1 of the 1969–1974 Mauna Ulu eruption. *B Volcanol* 74(7):1729-1743
- Parfitt EA, Wilson L (1995) Explosive volcanic eruptions—IX. The transition between Hawaiian-style lava fountaining and Strombolian explosive activity. *Geophysical Journal International* 121(1):226-232

- Parfitt EA (1998) A study of clast size distribution, ash deposition and fragmentation in a Hawaiian-style volcanic eruption. *J Volcanol Geoth Res* 84(3):197-208
- Parfitt EA (2004) A discussion of the mechanisms of explosive basaltic eruptions. *J Volcanol Geoth Res* 134(1-2):77-107
- Passey SR, Bell BR (2007) Morphologies and emplacement mechanisms of the lava flows of the Faroe Islands Basalt Group, Faroe Islands, NE Atlantic Ocean. *B Volcanol* 70(2):139-156
- Passey SR, Jolley DW (2008) A revised lithostratigraphic nomenclature for the Palaeogene Faroe Islands Basalt group, NE Atlantic Ocean. *Earth and Environmental Science Transactions of the Royal Society of Edinburgh* 99(3-4):127-158
- Patrick MR, Harris AJ, Ripepe M, Dehn J, Rothery DA, Calvari S (2007) Strombolian explosive styles and source conditions: insights from thermal (FLIR) video. *B Volcanol* 69(7):769-784
- Paulsen TS, Wilson TJ (2010) New criteria for systematic mapping and reliability assessment of monogenetic volcanic vent alignments and elongate volcanic vents for crustal stress analyses. *Tectonophysics* 482(1-4):16-28
- Pendred V (2011) Entrail pahoehoe, Hawaii. Personal photographic collection.
- Peterson DW, Tilling RI (1980) Transition of basaltic lava from pahoehoe to aa, Kilauea Volcano, Hawaii: Field observations and key factors. *J Volcanol Geoth Res* 7(3-4):271-293
- Philpotts AR, Lewis CL (1987) Pipe vesicles—An alternate model for their origin. *Geology* 15(10):971-974
- Pinkerton H, Wilson L (1994) Factors controlling the lengths of channel-fed lava flows. *B Volcanol* 56(2):108-120
- Pioli L, Erlund E, Johnson E, Cashman K, Wallace P, Rosi M, Delgado Granados H (2008) Explosive dynamics of violent Strombolian eruptions: The eruption of Parícutin Volcano 1943–1952 (Mexico). *Earth and Planetary Science Letters* 271(1-4):359-368
- Pittari A, Cas R, Lefebvre N, Robey J, Kurszlaukis S, Webb K (2008) Eruption processes and facies architecture of the Orion Central kimberlite volcanic complex, Fort à la Corne, Saskatchewan; kimberlite mass flow deposits in a sedimentary basin. *J Volcanol Geoth Res* 174(1):152-170
- Planke S, Eldholm O (1994) Seismic response and construction of seaward dipping wedges of flood basalts: Vøring volcanic margin. *Journal of Geophysical Research: Solid Earth* (1978–2012) 99(B5):9263-9278
- Planke S, Cambray H (1998) Seismic properties of flood basalts from hole 917A downhole data, southeast Greenland volcanic margin. *Proceedings of the Ocean Drilling Program, Scientific Results* 152
- Planke S, Symonds PA, Alvestad E, Skogseid J (2000) Seismic volcanostratigraphy of large-volume basaltic extrusive complexes on rifted margins. *J. Geophys. Res.* 105(B8):19335-19351
- Planke S, Svensen H, Hovland M, Banks D, Jamtveit B (2003) Mud and fluid migration in active mud volcanoes in Azerbaijan. *Geo-Marine Letters* 23(3-4):258-268
- Planke S, Rasmussen T, Rey SS, Myklebust R (2005) Seismic characteristics and distribution of volcanic intrusions and hydrothermal vent complexes in the Vøring and Møre basins. *Geological Society, London, Petroleum Geology Conference series* 6:833-844
- Praeg D, Stoker M, Shannon P, Ceramicola S, Hjelstuen B, Laberg J, Mathiesen A (2005) Episodic Cenozoic tectonism and the development of the NW European 'passive' continental margin. *Marine and Petroleum Geology* 22(9):1007-1030
- Rateau R, Schofield N, Smith M (2013) The potential role of igneous intrusions on hydrocarbon migration, West of Shetland. *Petroleum Geoscience* 19(3):259-272
- Reidel SP, Tolan TL (1992) Eruption and emplacement of flood basalt: An example from the large-volume Teepee Butte Member, Columbia River Basalt Group. *Geol Soc Am Bull* 104(12):1650-1671
- Richter DH (1970) Chronological narrative of the 1959-60 eruption of Kilauea Volcano, Hawaii: A detailed and pictorial account of an eruptive sequence consisting of a summit eruption, a flank eruption, and a summit collapse. US Government Printing Office
- Riedel C, Ernst GGJ, Riley M (2003) Controls on the growth and geometry of pyroclastic constructs. *J Volcanol Geoth Res* 127(1-2):121-152

- Riggs NR, Duffield WA (2008) Record of complex scoria cone eruptive activity at Red Mountain, Arizona, USA, and implications for monogenetic mafic volcanoes. *J Volcanol Geoth Res* 178(4):763-776
- Ritchie J, Hitchen K (1996) Early Paleogene offshore igneous activity to the northwest of the UK and its relationship to the North Atlantic Igneous Province. Geological Society, London, Special Publications 101(1):63-78
- Ritchie J, Gatliff R, Richards P (1999) Early Tertiary magmatism in the offshore NW UK margin and surrounds. In: Geological Society, London, Petroleum Geology Conference series. Geological Society of London, pp 573-584
- Ritchie J, Ziska H, Johnson H, Evans D (2011) Geology of the Faroe-Shetland Basin and adjacent areas. Nottingham, UK, British geological Survey, pp317.
- Ritchie JD, Gatliff RW, Richards PC (1997) Early Tertiary magmatism in the offshore NW UK margin and surrounds. 573-584
- Roberts D, Thompson M, Mitchener B, Hossack J, Carmichael S, Bjørnseth H-M (1999) Palaeozoic to Tertiary rift and basin dynamics: mid-Norway to the Bay of Biscay—a new context for hydrocarbon prospectivity in the deep water frontier. In: Geological Society, London, Petroleum Geology Conference series. Geological Society of London, pp 7-40
- Roberts KS (2011) Mud volcano systems: structure, evolution and processes. PhD thesis, Durham University, Department of Earth Sciences.
- Roberts KS, Davies RJ, Stewart SA, Tingay M (2011) Structural controls on mud volcano vent distributions: examples from Azerbaijan and Lusi, east Java. *J Geol Soc London* 168(4):1013-1030
- Rohrman M (2007) Prospectivity of volcanic basins: Trap delineation and acreage de-risking. *AAPG bulletin* 91(6):915-939
- Ross GM (1986) Eruptive style and construction of shallow marine mafic tuff cones in the Narakay Volcanic Complex (Proterozoic, Hornby Bay Group, Northwest Territories, Canada). *J Volcanol Geoth Res* 27(3-4):265-297
- Ross P-S, Ukstins Peate I, McClintock M, Xu Y, Skilling I, White J, Houghton B (2005) Mafic volcanoclastic deposits in flood basalt provinces: a review. *J Volcanol Geoth Res* 145(3):281-314
- Ross P-S, White J, Valentine G, Taddeucci J, Sonder I, Andrews R (2013) Experimental birth of a maar–diatreme volcano. *J Volcanol Geoth Res* 260:1-12
- Rossi M (1996) Morphology and mechanism of eruption of postglacial shield volcanoes in Iceland. *B Volcanol* 57(7):530-540
- Rowland SK, Walker GPL (1987) Toothpaste lava: Characteristics and origin of a lava structural type transitional between pahoehoe and aa. *B Volcanol* 49(4):631-641
- Rowland SK, Walker GPL (1990) Pahoehoe and aa in Hawaii: volumetric flow rate controls the lava structure. *B Volcanol* 52(8):615-628
- Ryan MP, Sammis CG (1978) Cyclic fracture mechanisms in cooling basalt. *Geol Soc Am Bull* 89(9):1295-1308
- Rymer H, de Vries BvW, Stix J, Williams-Jones G (1998) Pit crater structure and processes governing persistent activity at Masaya Volcano, Nicaragua. *B Volcanol* 59(5):345-355
- Sable J, Houghton B, Wilson C, Carey R (2006) Complex proximal sedimentation from Plinian plumes: the example of Tarawera 1886. *B Volcanol* 69(1):89-103
- Sánchez MC, Sarrionandia F, Ibarguchi JIG (2014) Post-depositional intrusion and extrusion through a scoria and spatter cone of fountain-fed nephelinite lavas (Las Herrerías volcano, Calatrava, Spain). *B Volcanol* 76(9):1-17
- Schmidt R, Schmincke HU (2000) Seamounts and island building. In: Sigurdsson H (ed) *Encyclopedia of Volcanoes*. Academic Press, San Diego, pp 383-402
- Schnur SR (2007) An Analysis of the Morphology and Physical Properties of Pillow Lavas of the Nicasio Reservoir Terrace, Marin County, California: Implications for Seamount Formation and Structure. Masters dissertation, Carleton College, Minnesota.
- Schofield N, Jolley DW (2013) Development of intra-basaltic lava-field drainage systems within the Faroe–Shetland Basin. *Petroleum Geoscience* 19(3):273-288
- Schutter SR (2003) Occurrences of hydrocarbons in and around igneous rocks. Geological Society, London, Special Publications 214(1):35-68
- Self S, Keszthelyi L, Thordarson T (1998) The importance of pahoehoe. *Annu. Rev. Earth Planet. Sci.* 26:81-110

- Shaw F, Worthington M, White R, Andersen M, Petersen U (2008) Seismic attenuation in Faroe Islands basalts. *Geophysical Prospecting* 56(1):5-20
- Sheriff RE, Geldart L (1995) *Exploration seismology*. Cambridge University Press
- Sheth H (2006) The emplacement of pahoehoe lavas on Kilauea and in the Deccan Traps. *Journal of earth system science* 115(6):615-629
- Simkin T (1972) Origin of some flat-topped volcanoes and guyots. *Geol. Soc. Am. Mem* 132:183-193
- Skogseid J, Planke S, Faleide JJ, Pedersen T, Eldholm O, Neverdal F (2000) NE Atlantic continental rifting and volcanic margin formation. *Geological Society, London, Special Publications* 167(1):295-326
- Sohn YK, Chough SK (1989) Depositional processes of the Suwolbong tuff ring, Cheju Island (Korea). *Sedimentology* 36(5):837-855
- Sohn YK, Chough SK (1992) The Ilchulbong tuff cone, Cheju Island, South Korea. *Sedimentology* 39(4):523-544
- Sohn YK, Chough SK (1993) The Udo tuff cone, Cheju Island, South Korea: transformation of pyroclastic fall into debris fall and grain flow on a steep volcanic cone slope. *Sedimentology* 40(4):769-786
- Sohn YK (1996) Hydrovolcanic processes forming basaltic tuff rings and cones on Cheju Island, Korea. *Geol Soc Am Bull* 108(10):1199-1211
- Solana MC, Kilburn CRJ, Rodriguez Badiola E, Aparicio A (2004) Fast emplacement of extensive pahoehoe flow-fields: the case of the 1736 flows from Montaña de las Nueces, Lanzarote. *J Volcanol Geoth Res* 132(2-3):189-207
- Soper N, Woodcock N (2003) The lost Lower Old Red Sandstone of England and Wales: a record of post-Iapetan flexure or Early Devonian transtension? *Geol Mag* 140(06):627-647
- Sørensen AB (2003) Cenozoic basin development and stratigraphy of the Faroes area. *Petroleum Geoscience* 9(3):189-207
- Soule SA, Cashman KV (2005) Shear rate dependence of the pāhoehoe-to-‘a‘ā transition: Analog experiments. *Geology* 33(5):361-364
- Stevenson J, Mitchell N, Cassidy M, Pinkerton H (2012) Widespread inflation and drainage of a pāhoehoe flow field: the Nesjahraun, Þingvellir, Iceland. *B Volcanol*:1-17
- Stewart SA, Davies RJ (2006) Structure and emplacement of mud volcano systems in the South Caspian Basin. *AAPG Bulletin* 90(5):771-786
- Stoker M, Hitchen K, Graham C (1993) The geology of the Hebrides and West Shetland shelves, and adjacent deep-water areas. The Stationery Office/Tso
- Stovall W, Houghton B, Gonnermann H, Fagents S, Swanson D (2011) Eruption dynamics of Hawaiian-style fountains: the case study of episode 1 of the Kīlauea Iki 1959 eruption. *B Volcanol* 73(5):511-529
- Suiting I, Schmincke H-U (2009) Internal vs. external forcing in shallow marine diatreme formation: A case study from the Iblean Mountains (SE-Sicily, Central Mediterranean). *J Volcanol Geoth Res* 186(3):361-378
- Sumner JM (1998) Formation of clastogenic lava flows during fissure eruption and scoria cone collapse: the 1986 eruption of Izu-Oshima Volcano, eastern Japan. *B Volcanol* 60(3):195-212
- Sumner JM, Blake S, Matela RJ, Wolff JA (2005) Spatter. *J Volcanol Geoth Res* 142(1-2):49-65
- Svensen H, Planke S, Jamtveit B, Pedersen T (2003) Seep carbonate formation controlled by hydrothermal vent complexes: a case study from the Vøring Basin, the Norwegian Sea. *Geo-Marine Letters* 23(3-4):351-358
- Svensen H, Jamtveit B, Planke S, Chevallier L (2006) Structure and evolution of hydrothermal vent complexes in the Karoo Basin, South Africa. *J Geol Soc London* 163(4):671-682
- Svensen H, Planke S, Chevallier L, Malthe-Sørenssen A, Corfu F, Jamtveit B (2007) Hydrothermal venting of greenhouse gases triggering Early Jurassic global warming. *Earth and Planetary Science Letters* 256(3-4):554-566
- Swanson D (1974) USGS Photographic Library.
- Swanson D, Duffield WA, Jackson DB, Peterson DW (1979) Chronological narrative of the 1969 - 1971 Mauna Ulu eruption of Kilauea volcano, Hawaii. U.S Geological Survey Professional Paper 1065:55

- Swanson DA (1973) Pahoehoe Flows from the 1969–1971 Mauna Ulu Eruption, Kilauea Volcano, Hawaii. *Geol Soc Am Bull* 84(2):615-626
- Swanson DA, Wright TL, Helz RT (1975) Linear vent systems and estimated rates of magma production and eruption for the Yakima Basalt on the Columbia Plateau. *American Journal of Science* 275(8):877-905
- Thomson K (2005) Extrusive and intrusive magmatism in the North Rockall Trough. Geological Society, London, Petroleum Geology Conference series 6:1621-1630
- Thomson K (2007) Determining magma flow in sills, dykes and laccoliths and their implications for sill emplacement mechanisms. *B Volcanol* 70(2):183-201
- Thorarinsson S (1966) The Surtsey eruption course of events and the development of the new island. In: Museum of Natural History, Reykjavik, Iceland
- Thorarinsson S, Steinthorsson S, Einarsson T, Kristmannsdottir H, Oskarsson N (1973) The eruption on Heimaey, Iceland. *Nature* 241:372-375
- Thordarson T, Self S (1993) The Laki (Skaftár Fires) and Grímsvötn eruptions in 1783–1785. *B Volcanol* 55(4):233-263
- Thordarson T, Self S (1998) The Roza Member, Columbia River Basalt Group: A gigantic pahoehoe lava flow field formed by endogenous processes? *J. Geophys. Res.* 103(B11):27411-27445
- Thors K, Jakousson SP (1982) Two seismic reflection profiles from the vicinity of Surtsey, Iceland. *Surtsey research progress report* 9:149
- Tomkeieff S (1940) The basalt lavas of the Giant's Causeway district of Northern Ireland. *B Volcanol* 6(1):89-143
- Valentine G, Cortés J (2013) Time and space variations in magmatic and phreatomagmatic eruptive processes at Easy Chair (Lunar Crater Volcanic Field, Nevada, USA). *B Volcanol* 75(9):1-13
- Valentine GA, Groves KR (1996) Entrainment of Country Rock during Basaltic Eruptions of the Lucero Volcanic Field, New Mexico. *The Journal of Geology* 104(1):71-90
- Valentine GA, Krier D, Perry FV, Heiken G (2005) Scoria cone construction mechanisms, Lathrop Wells volcano, southern Nevada, USA. *Geology* 33(8):629-632
- Valentine GA, Krogh KEC (2006) Emplacement of shallow dikes and sills beneath a small basaltic volcanic center – The role of pre-existing structure (Paiute Ridge, southern Nevada, USA). *Earth and Planetary Science Letters* 246(3–4):217-230
- Valentine GA, Perry FV, Krier D, Keating GN, Kelley RE, Cogbill AH (2006) Small-volume basaltic volcanoes: Eruptive products and processes, and post-eruptive geomorphic evolution in Crater Flat (Pleistocene), southern Nevada. *Geol Soc Am Bull* 118(11-12):1313-1330
- Valentine GA, Keating GN (2007) Eruptive styles and inferences about plumbing systems at Hidden Cone and Little Black Peak scoria cone volcanoes (Nevada, USA). *B Volcanol* 70(1):105-113
- Valentine GA, Krier DJ, Perry FV, Heiken G (2007) Eruptive and geomorphic processes at the Lathrop Wells scoria cone volcano. *J Volcanol Geoth Res* 161(1-2):57-80
- Valentine GA, Gregg TKP (2008) Continental basaltic volcanoes — Processes and problems. *J Volcanol Geoth Res* 177(4):857-873
- Valentine GA (2012) Shallow plumbing systems for small-volume basaltic volcanoes, 2: Evidence from crustal xenoliths at scoria cones and maars. *J Volcanol Geoth Res* 223–224(0):47-63
- Valerio A, Tallarico A, Dragoni M (2008) Mechanisms of formation of lava tubes. *J. Geophys. Res.* 113(B8):B08209
- Vergnolle S, Jaupart C (1986) Separated two-phase flow and basaltic eruptions. *J. Geophys. Res.* 91(B12):12842-12860
- Vergnolle S, Mangan MT (2000) Hawaiian and Strombolian Eruptions. In: Sigurdsson H (ed) *Encyclopedia of Volcanoes*. Academic press, San Diego, pp 447-461
- Verwoerd WJ, Chevallier L (1987) Contrasting types of surtseyan tuff cones on Marion and Prince Edward islands, southwest Indian Ocean. *Bull Volcanol* 49(1), 399-413.
- Vespermann D, Schmincke H-U (2000) Scoria cones and tuff rings. In: Sigurdsson H (ed) *Encyclopedia of Volcanoes*. Academic Press, San Diego. Academic Press, San Diego, pp 683-694
- Wadge G (1981) The variation of magma discharge during basaltic eruptions. *J Volcanol Geoth Res* 11(2–4):139-168

- Waichel B, de Lima E, Lubachesky R, Sommer C (2006) Pahoehoe flows from the central Paraná Continental Flood Basalts. *B Volcanol* 68(7):599-610
- Walker G (1971) Compound and simple lava flows and flood basalts. *B Volcanol* 35(3):579-590
- Walker G (1973) Explosive volcanic eruptions — a new classification scheme. *Geologische Rundschau* 62(2):431-446
- Walker G (1991) Structure, and origin by injection of lava under surface crust, of tumuli, “lava rises”, “lava-rise pits”, and “lava-inflation clefts” in Hawaii. *B Volcanol* 53(7):546-558
- Walker GPL (1958) Geology of the Rydarfjörður area, eastern Iceland. *Quarterly Journal of the Geological Society* 114(1-4):367-391
- Walker GPL, Self S, Wilson L (1984) Tarawera 1886, New Zealand — A basaltic plinian fissure eruption. *J Volcanol Geoth Res* 21(1-2):61-78
- Walker GPL (1989) Spongy pahoehoe in Hawaii: A study of vesicle-distribution patterns in basalt and their significance. *B Volcanol* 51(3):199-209
- Walker GPL (1993) Basaltic-volcano systems. Geological Society, London, Special Publications 76(1):3-38
- Walker GPL (1995) Flood basalts versus central volcanoes and the British Tertiary volcanic Province. Geological Society, London, Memoirs 16(1):195-202
- Walker GPL, Cañón-Tapia E, Herrero-Bervera E (1999) Origin of vesicle layering and double imbrication by endogenous growth in the Birkett basalt flow (Columbia river plateau). *J Volcanol Geoth Res* 88(1-2):15-28
- Walker GPL (2000) Basaltic volcanoes and volcanic systems. In: Sigurdsson H (ed) *Encyclopedia of volcanoes*. Academic Press, San Diego, pp 283-289
- Wall M, Cartwright J, Davies R, McGrandle A (2010) 3D seismic imaging of a Tertiary Dyke Swarm in the Southern North Sea, UK. *Basin Research* 22(2):181-194
- Watton TJ (2013) A multidisciplinary assessment of hyaloclastite deposits in petroleum systems using field studies, drill core, borehole image and wire-line log datasets.
- Watton TJ, Cannon S, Brown RJ, Jerram DA, Waichel BL (2014) Using formation micro-imaging, wireline logs and onshore analogues to distinguish volcanic lithofacies in boreholes: examples from Palaeogene successions in the Faroe–Shetland Basin, NE Atlantic. Geological Society, London, Special Publications 397
- Waythomas CF, Haney MM, Fee D, Schneider DJ, Wech A (2014) The 2013 eruption of Pavlof Volcano, Alaska: a spatter eruption at an ice-and snow-clad volcano. *B Volcanol* 76(10):1-12
- Wessel P, Sandwell DT, Kim S-S (2010) The global seamount census. *Oceanography* 23(1):24
- White JDL (1991) Maar-diatreme phreatomagmatism at Hopi Buttes, Navajo Nation (Arizona), USA. *B Volcanol* 53(4):239-258
- White JDL, Houghton B (2000) Surtseyan and related phreatomagmatic eruptions. In: Sigurdsson H (ed) *Encyclopedia of volcanoes*. Academic Press, San Diego, pp 495-511
- White JDL, Ross PS (2011) Maar-diatreme volcanoes: A review. *J Volcanol Geoth Res* 201(1-4):1-29
- White RS, Smallwood JR, Fliedner MM, Boslaugh B, Maresh J, Fruehn J (2003) Imaging and regional distribution of basalt flows in the Faeroe-Shetland Basin. *Geophysical Prospecting* 51(3):215-231
- Wilch T (2011) Glassy pahoehoe. In: Albion College Geology
- Wilmoth RA, Walker GPL (1993) P-type and S-type pahoehoe: a study of vesicle distribution patterns in Hawaiian lava flows. *J Volcanol Geoth Res* 55(1-2):129-142
- Wilson L, Head JW, III (1981) Ascent and Eruption of Basaltic Magma on the Earth and Moon. *J. Geophys. Res.* 86(B4):2971-3001
- Wilson L, Parfitt E, Head J (1995) Explosive volcanic eruptions—VIII. The role of magma recycling in controlling the behaviour of Hawaiian-style lava fountains. *Geophysical Journal International* 121(1):215-225
- Wohletz KH, Sheridan MF (1983) Hydrovolcanic explosions; II, Evolution of basaltic tuff rings and tuff cones. *American Journal of Science* 283(5):385-413
- Wohletz KH (1983) Mechanisms of hydrovolcanic pyroclast formation: Grain-size, scanning electron microscopy, and experimental studies. *J Volcanol Geoth Res* 17(1-4):31-63

- Wolfe WE, Neal AC, Banks GN, Toni DJ (1988) The Puu Oo Eruption of Kilauea Volcano, Hawaii: Episodes 1 Through 20, January 3, 1983, Through June 8, 1984. U.S Geological Survey Professional Paper 1463
- Wolff J, Sumner J (2000) Lava fountains and their products. In: Sigurdsson H (ed) Encyclopedia of volcanoes. Academic Press, San Diego, pp 321-329
- Wood CA (1980) Morphometric evolution of cinder cones. *J Volcanol Geoth Res* 7(3–4):387-413
- Woods AW, Bursik MI (1991) Particle fallout, thermal disequilibrium and volcanic plumes. *B Volcanol* 53(7):559-570
- Wright K (2013) Seismic Stratigraphy and Geomorphology of Palaeocene Volcanic Rocks, Faroe-Shetland Basin. PhD Thesis, Durham University, Department of Earth Sciences.
- Wright KA, Davies RJ, Jerram DA, Morris J, Fletcher R (2012) Application of seismic and sequence stratigraphic concepts to a lava-fed delta system in the Faroe-Shetland Basin, UK and Faroes. *Basin Research* 24(1):91-106
- Wylie JJ, Helfrich KR, Dade B, Lister JR, Salzig JF (1999) Flow localization in fissure eruptions. *B Volcanol* 60(6):432-440
- Yusifov M, Rabinowitz PD (2004) Classification of mud volcanoes in the South Caspian Basin, offshore Azerbaijan. *Marine and Petroleum Geology* 21(8):965-975
- Zhao F, Wu S, Sun Q, Huuse M, Li W, Wang Z (2014) Submarine volcanic mounds in the Pearl River Mouth Basin, northern South China Sea. *Mar Geol* 355(0):162-172

Chapter 3: The Evolution of the 6–8 kyr R-K Basaltic Fissure Eruption, Northeast Iceland

3.1 Introduction

Basaltic fissure eruptions occur in many tectonic settings (e.g. Fedotov et al. 1980; Karhunen 1988; Wolfe et al. 1988; Carracedo et al. 1992; Thordarson and Self 1993; Parcheta et al. 2012). They are common throughout the geologic record and in historic times (e.g. Carracedo et al. 1992; Thordarson and Self 1993; Thordarson et al. 2001; Gudmundsson et al. 2010; Németh and Cronin 2011; Wendel 2014). Whilst eruptions are usually low explosivity Hawaiian-type events, large-volume fissure eruptions can have significant environmental and climatic effects. Ash fall can cause crop failure (e.g. Thordarson and Self 1993), whilst sulphurous gases associated with vigorous eruption columns penetrate the lower stratosphere and impact the climate (e.g. Thordarson and Self 1993; Thordarson et al. 2001). Fissure eruptions have also produced some of the largest basaltic lava flows in historical times (Thordarson and Self 1993) and produce the lava flow fields that are the “building blocks” of flood basalt provinces (Swanson et al. 1975; Walker 1995; Reidel 1998; Bondre et al. 2004a; Brown et al. 2014).

The feeder dykes for fissures initiate eruptions from linear vents. With time, magma flow along a dyke localises to numerous point sources (e.g. Bruce and Huppert 1989), around which pyroclastic edifices are built. The type and geometry of the edifice produced during dry eruptions (i.e. without magma-water interaction) is largely controlled by the dynamics of the lava fountain. Lava fountains are the most common subaerial eruption mechanism on Earth (Sumner et al. 2005) and also occur on other planetary bodies (e.g. Io; see Keszthelyi et al. 2001). The spread angle of lava fountains is controlled by magma gas content and volume flux (Head and Wilson 1989). Hawaiian-style lava fountains are frequently 500 m in height (Wolff and Sumner 2000) although the height and intensity of the fountain often varies during an eruption (e.g. Wolfe et al. 1988; Thordarson and Self 1993; Parcheta et al. 2012; Valentine and Cortés 2013). The fountains produce a range of welded, non-welded and coalesced deposits depending on factors such as fountain collimation (i.e. spread from vertical) and wind profile (Head and Wilson 1989). These deposits vary in character with distance from the fissure, with welded and agglutinated deposits dominant in proximal regions (e.g. Head and Wilson 1989).

Despite their common occurrence, volumetric importance in the rock record and environmental and climatic impacts, the temporal evolution of fissure eruptions has

received little attention. Although there are observations of historic eruptions (e.g. Steingrímsson and Ólafsson 1783; Steingrímsson 1788; Swanson et al. 1979; Fedotov et al. 1980; Aramaki et al. 1986; Wolfe et al. 1988; Sumner 1998; Gudmundsson et al. 2010; Wendel 2014), few studies have access to the entire eruptive stratigraphy. The products of most fissure eruptions only allow examination of the most recent, last erupted surface deposits (e.g. the Laki fissure; see Thordarson and Self 1993), as earlier deposits are buried. The deposits of older, highly eroded sequences of basaltic fissure eruptions with good cross sectional exposure commonly cannot be correlated laterally (e.g. Tertiary fissure-fed lavas; see Kent et al. 1998). Thus there is a poor understanding of how the deposits from fissure eruptions transition laterally into a lava flow field, and how the eruptive sequence varies with time.

The aim of this study is to provide insights into the spatial and temporal variability of a Holocene basaltic fissure eruption. Erosional dissection has exposed the feeder dyke and a near-complete record of the vent-proximal erupted products. Geologic mapping and stratigraphic analysis are used to understand the construction of a scoria-agglutinate cone, scoria and spatter ramparts, sheet-like fall deposits and rootless cones. Documentation of these edifices can be used to identify vent-proximal locations in other settings, and link observed eruptive processes with deposits.

3.2 Geological setting

Iceland is located above a spreading plate boundary and a mantle plume (Thordarson and Larsen 2007). Active faulting and volcanism is confined to a 15–50 km wide axial zone that crosses Iceland from southwest to the north (Thordarson and Larsen 2007). The axial zone is the loci of active spreading and plate growth and is typified by tholeiitic magmatism (Thordarson and Larsen 2007). One of the core features of the axial zone is the Northern Volcanic Zone (NVZ; Thordarson and Larsen 2007). This zone forms the most northerly emergent part of the Mid-Atlantic ridge and is composed of numerous individual volcanic systems (Friese et al. 2013). It is linked to the offshore Mid-Atlantic ridge by the northwest-southeast striking Tjörnes Fracture Zone (TFV; Fig. 3.1; Gudmundsson 2007; Thordarson and Larsen 2007).

The 6–8 kyr Rauduborgir-Kvensödul (R-K) fissure is located in the NVZ (Figs. 3.1 and 3.2). Here, the Kraeduborgir, Rauðhólar and R-K fissures form an en-echelon, 150 km long fissure complex. This is part of either the Fremri-Namur or Askja volcanic system, extending from Melrakkasletta in the northeast to Utbruni in the southwest (Tentler and

Temperley 2007). There is no postglacial active central volcano associated with the fissure, but the presence of a magma chamber is indicated by the presence minor acidic volcanic rocks in a geothermally active zone (Tentler and Temperley 2007).

The R-K fissure strikes 025°, changing to 015° where it enters the Sveinar graben (Fig. 3.2); thus it is thought that the graben captured the fissure (Thorarinsson 1959). The fissure is marked by a 75 km-long row of pyroclastic edifices including scoria cones, spatter cones, half cones and hybrids there-of. This “mixed cone row” is typical of both large and small volume Icelandic eruptions (Thordarson and Larsen 2007).

Aphyric olivine tholeiite lavas associated with the fissure merge northwards with lavas from the 9 kyr Rauðhólar eruption (Thorarinsson 1959; Waite 2009; Friese et al. 2013). The aphyric R-K lavas are easily distinguished from the underlying columnar-jointed plagioclase porphyritic lavas, erupted 70 kyr BP (Slater et al. 1998). The study area consists of a 3 km² sections of the fissure (Figs. 3.3 and 3.4) along which 35 pyroclastic edifices are identified (Fig. 3.5).

The fissure is dissected by the Jökulsá canyon. This canyon exploits a fault that strikes sub-parallel to the TFZ (Figs. 3.1 and 3.4; see Gudmundsson 2007) and is thought to have partly existed before the Holocene (Kirkbride et al. 2006). The canyon has since hosted 16 glacial outbursts between 2–9 kyr BP (Alho et al. 2005; Kirkbride et al. 2006; Waite 2009). The largest of these were between 2–7 kyr BP, and just after deglaciation at 8–9 kyr BP (Alho et al. 2005; Kirkbride et al. 2006; Waite 2009). West of the river, the fissure is confined within the 30 km long, 0.5–1 km wide Sveinar graben that developed prior-to and during the R-K eruption (Thorarinsson 1959).

Previous work on the R-K fissure indicates that the dyke on the eastern Jökulsá a Fjöllum canyon wall led to reverse faulting along a pre-existing normal fault (Gudmundsson et al. 2008). Friese et al. (2013) briefly examined this dyke, stating that its flaring morphology was consistent with other nearby dykes in the shallow subsurface.

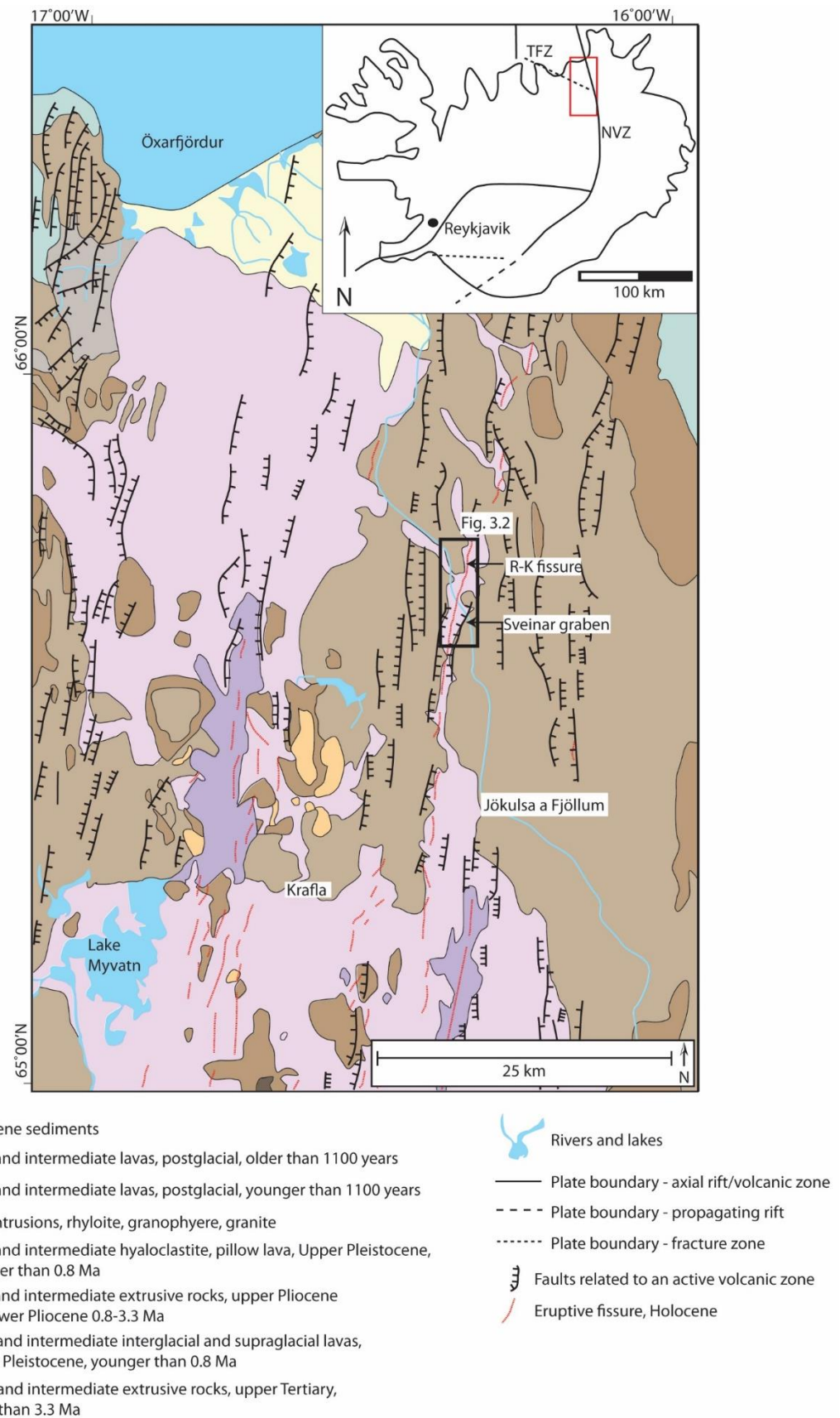


Figure 3.1. Location of the Sveinar graben in the Holocene rift zone of Northern Iceland. Inset map shows the location of the study area outlined in red and the Tjörnes Fracture Zone (TFZ). Adapted from Gudmundsson et al. (2008).

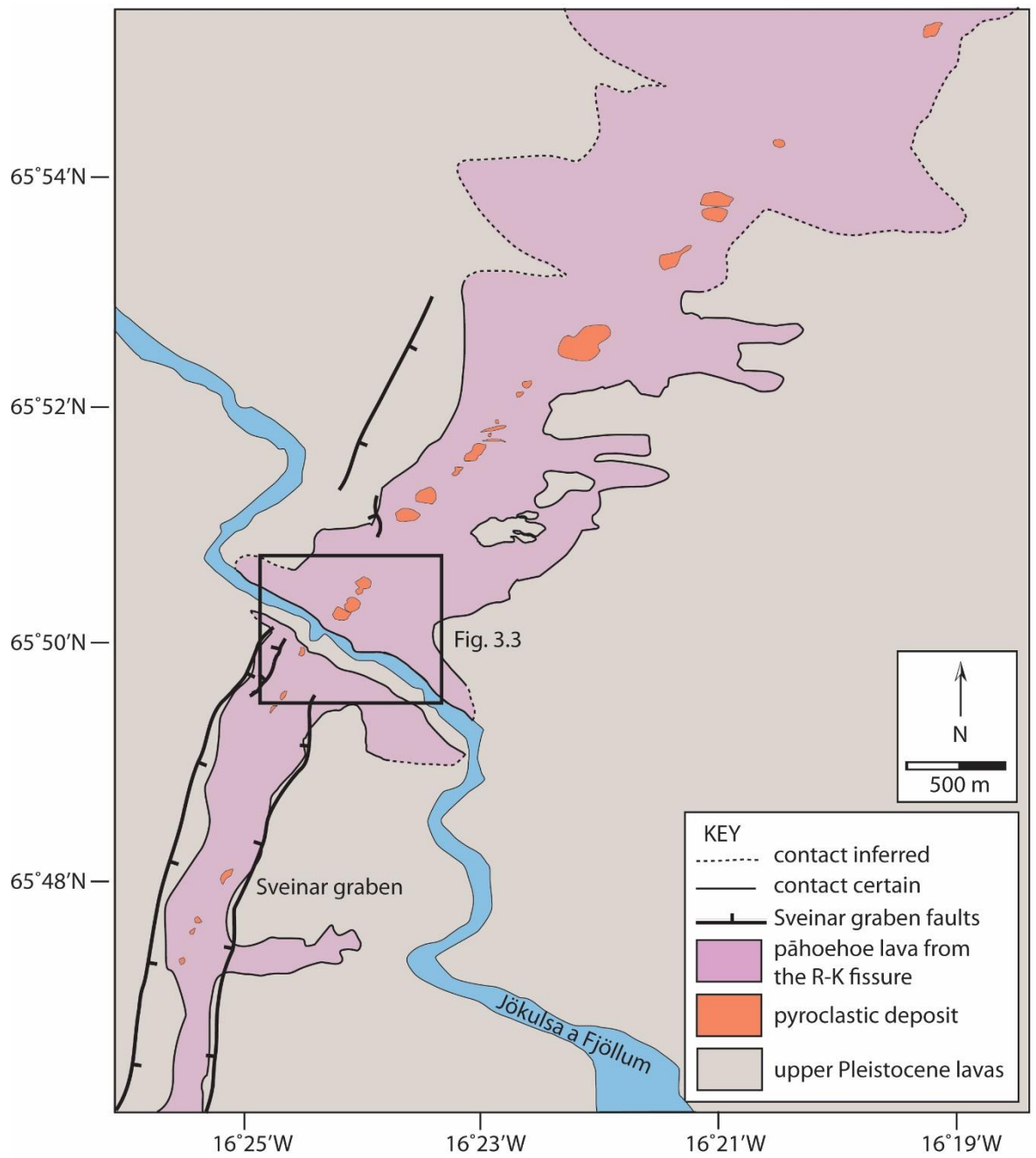


Figure 3.2. Regional geology map of the Rauduborgir-Kvensödul fissure. See Fig. 3.1 for location. Lavas produced during the eruption pond in the Sveinar graben towards the south.

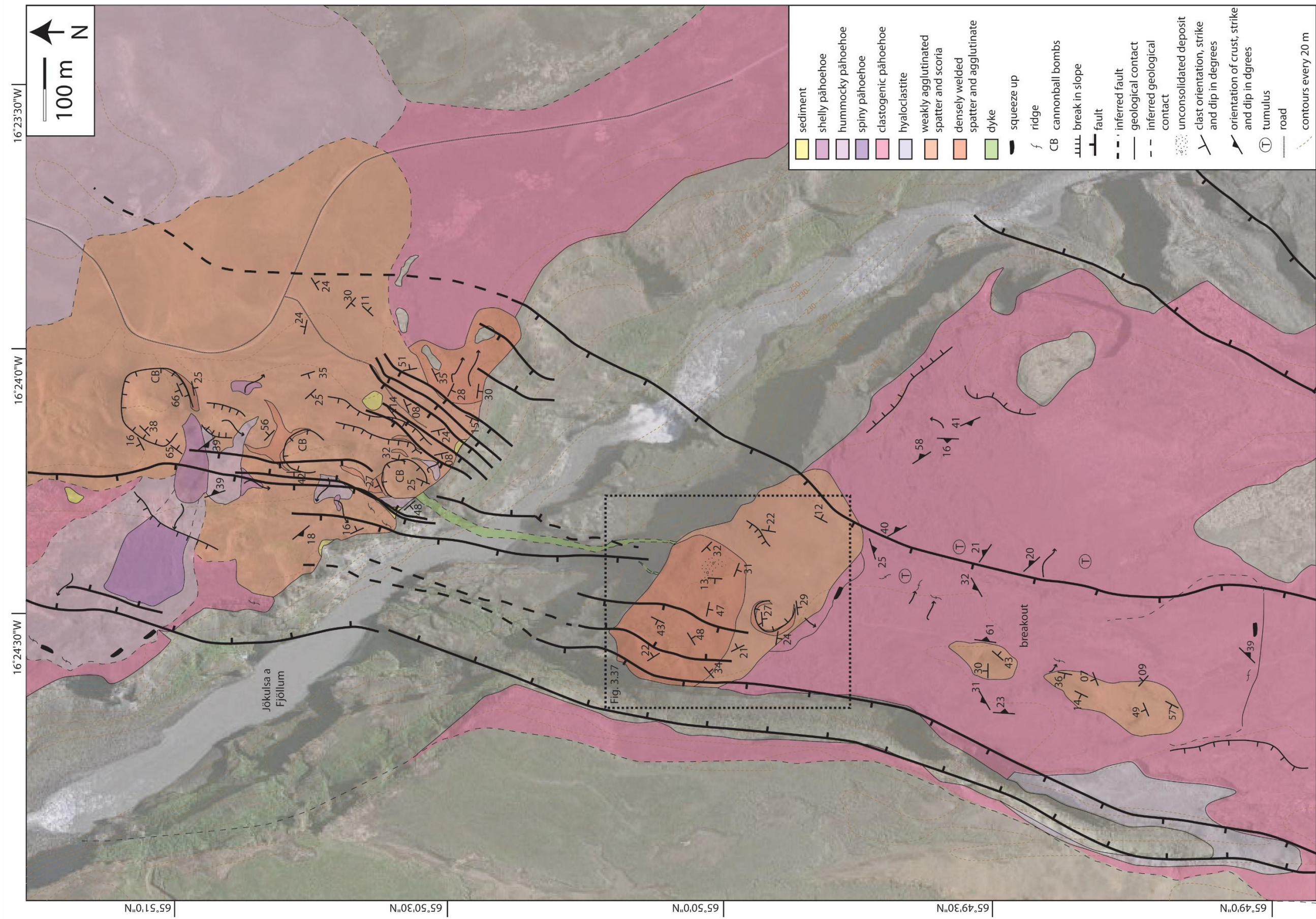


Figure 3.3 Geological map of the study area. See Fig. 3.2 for location.

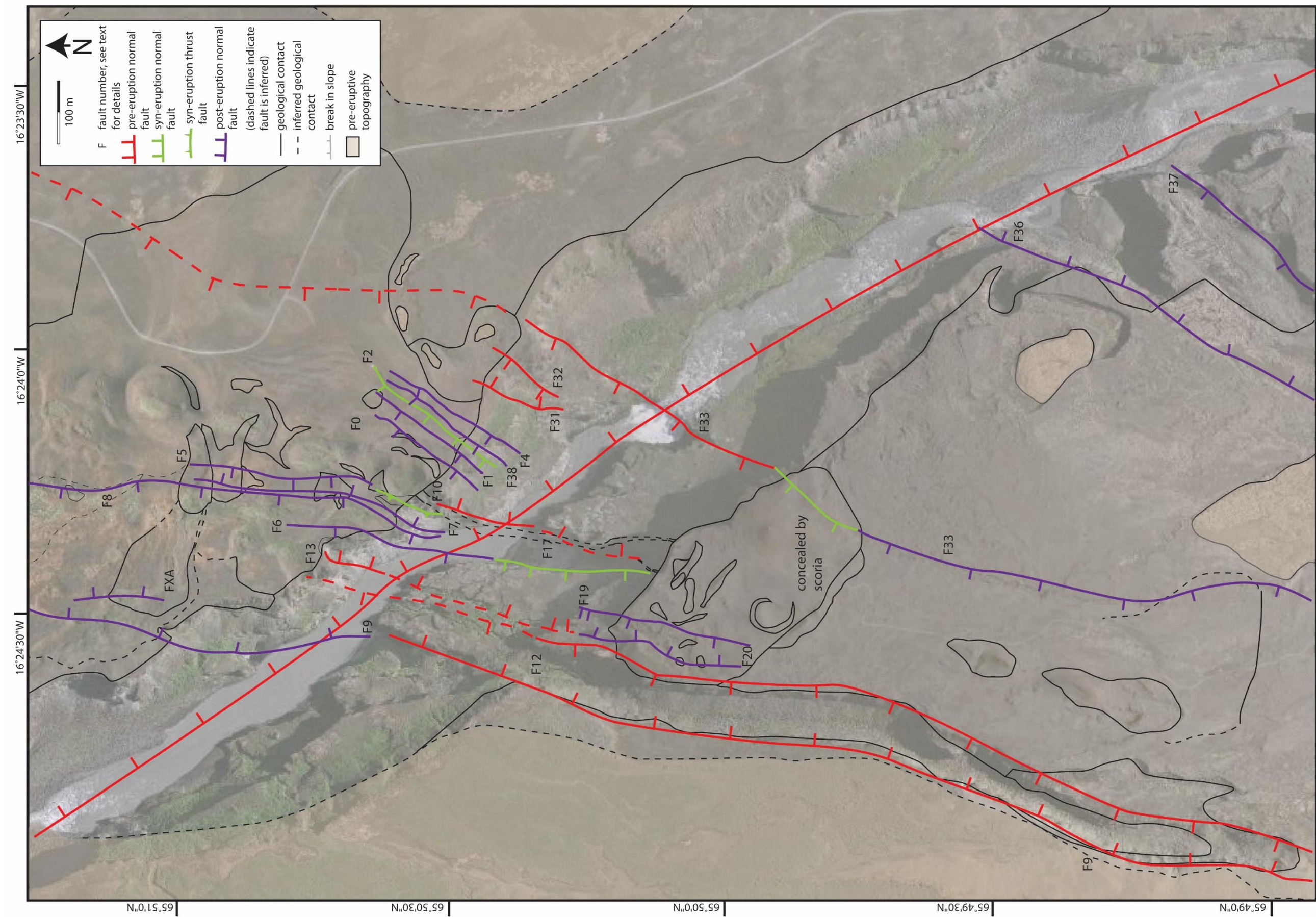


Fig. 3.4. Map of faults in the study area. The faults are coloured to indicate formation prior to, during, or post eruption. Black outline indicates the limit of the R-K stratigraphy. See text for details. See Fig. 3.2 for location.

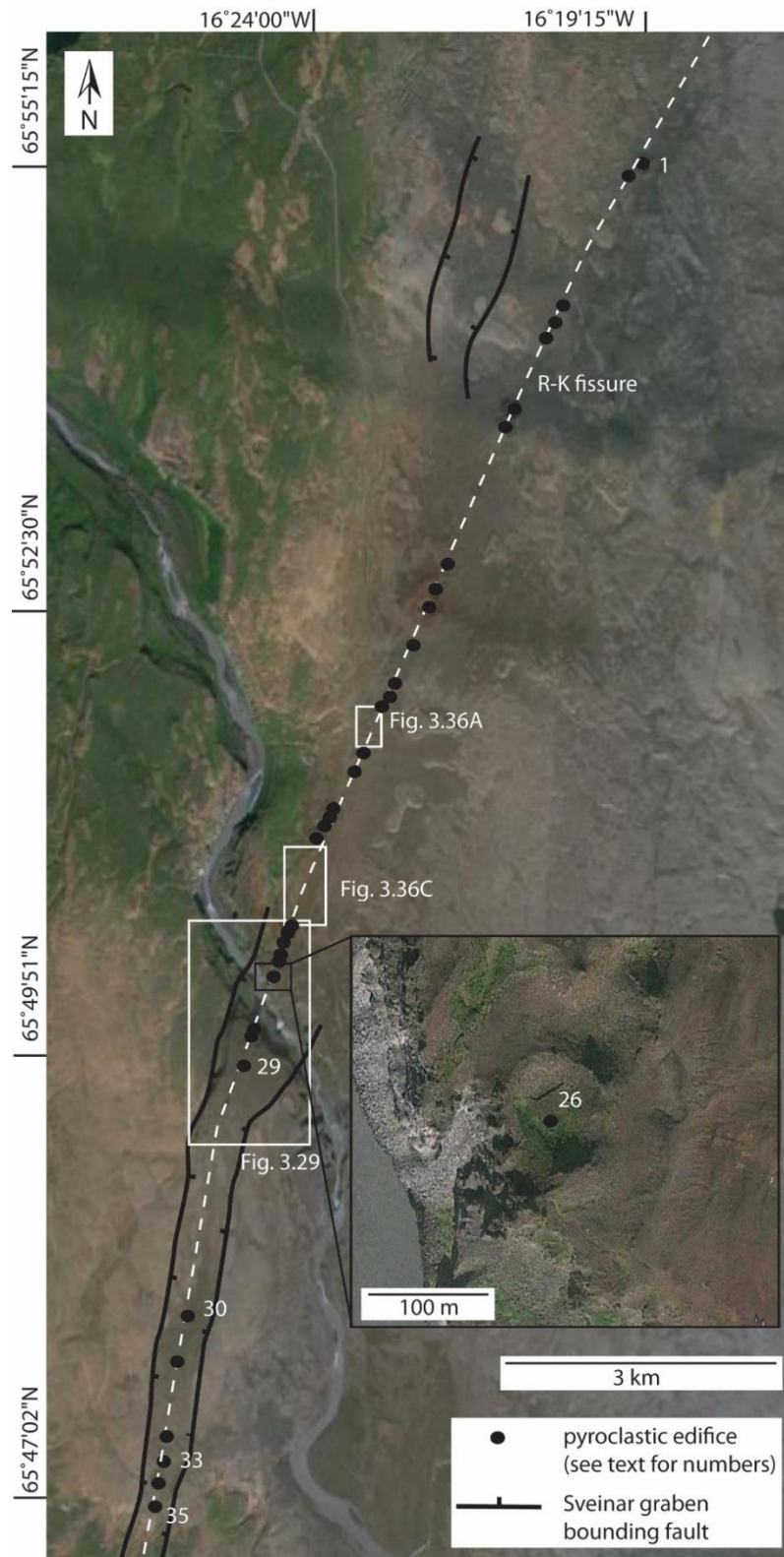


Figure 3.5. Google Earth image showing the change in strike of the R-K fissure as it is captured by the Sveinar graben. Pyroclastic edifices are shown; not all edifices are numbered for clarity. Note the large (3.5 km) gap between edifices 29 and 30, perhaps resulting from post-eruption erosion. Edifice 35 is located at the end of this section of the fissure.

3.3 Methods

The R-K pyroclastic deposits and lavas have been mapped at a 1:5000 scale. Geospatial data were recorded using a handheld global positioning system (GPS) with an accuracy of ± 5 m. Aerial photographs (extracted from Google Earth) were used to map small-scale features and were ground-truthed in the field. Much of the stratigraphy exposed on the canyon wall is inaccessible and has been mapped using photographs. Vertical sections that were measured in the field were then used to calibrate and analyse the photographs via image analysis (software ImageJ, <http://imagej.nih.gov/ij/>). Using this method, the expected errors are <5%. Exposures that allow detailed examination were logged on a centimetre scale to facilitate the identification of lithofacies and establish correlations across the study area.

Representative samples were used to calculate the density of pyroclasts using the method of Houghton and Wilson (1989). Most pyroclastic deposits are at least incipiently welded and sieving was unsuitable for determining the grain size distributions. Instead, the mean largest clast size was calculated by measuring the ten largest clasts per m². The lithic clast contents of the deposits were calculated using the method outlined by Valentine and Groves (1996). Since there is little exposure of the pyroclastic deposits away from the Jökulsá a Fjöllum canyon, isopleth and isopach maps were not constructed. The R-K volcanic sequence is described using the terminology as defined in Table 3.1.

Term	Definition
<i>Petrographic texture (after Thordarson and Self 1998 and references there-in)</i>	
Holocrystalline	(90–100% crystalline)
Hypocrystalline	(50–90% crystalline)
Hypohyaline	(10 – 50% crystalline)
Holohyaline	(0 – 10% crystalline)
<i>Vesicularity (after Houghton and Wilson 1989)</i>	
Non-vesicular	0 – 5 %
Incipiently vesicular	5 – 20 %
Poorly vesicular	20 – 40 %
Moderately vesicular	40 – 60 %
Highly vesicular	60 – 80 %
Extremely vesicular	>80 %
<i>Agglutination textures (after Sumner 1998; Wolff and Sumner 2000)</i>	
Agglutinate	Moderate flattening, complete clast outlines preserved
Deformed agglutinate	Extreme flattening, clast outlines retained
Highly deformed agglutinate	<50% of individual clast outlines preserved, deformation into swirling shapes
Coalesced	Patchy vesiculation, no unequivocal clast outlines
Agglutinated	Clasts that have become adjoined on deposition
Welded	Agglutinated pyroclastic deposits in which clasts are flattened and have partially or totally lost their outlines
<i>Pyroclastic textures (after Sumner et al. 2005)</i>	
Spatter	An accumulation of originally hot, fluid pyroclasts which agglutinate on landing
<i>Lava flow field architecture (after Self et al. 1998)</i>	
Lava lobe	The smallest individual package of a lava flow
Lava flow	The product of a single outpouring of lava
Lava flow field	The largest descriptive unit of a single or numerous lava flows

Table 3.1. Terminology and definitions.

3.4 Pyroclastic lithofacies

A variety of pyroclastic lithofacies are exposed along the R-K fissure. They are composed of numerous clasts (Fig. 3.6) and range from clast-supported, non-welded scoria lapilli (ScL) to clast-supported, densely welded spatter bombs (dwSp; Figs. 3.7 and 3.8). All juvenile material is composed of aphyric hypocrySTALLine to hypohyaline primitive olivine tholeiitic basalt (Jökulsárgljúfur Information Centre; Friese et al. 2013). The lithofacies vary in their componentry, crystallinity, vesicularity, texture and clast aspect ratio. Density histograms for selected pyroclastic deposits indicate that density increases with welding intensity and there is a positive correlation between the clast aspect ratio and density (Fig. 3.9). Primary features within the lithofacies are well preserved. A summary of lithofacies descriptions and interpretations are given in Table 3.2 and 3.3. Detailed stratigraphic logs reveal significant complexity to the architecture of the lithofacies (Figs. 3.10 and 3.11) and are used to infer depositional processes and the dynamics of the lava fountain along the fissure.

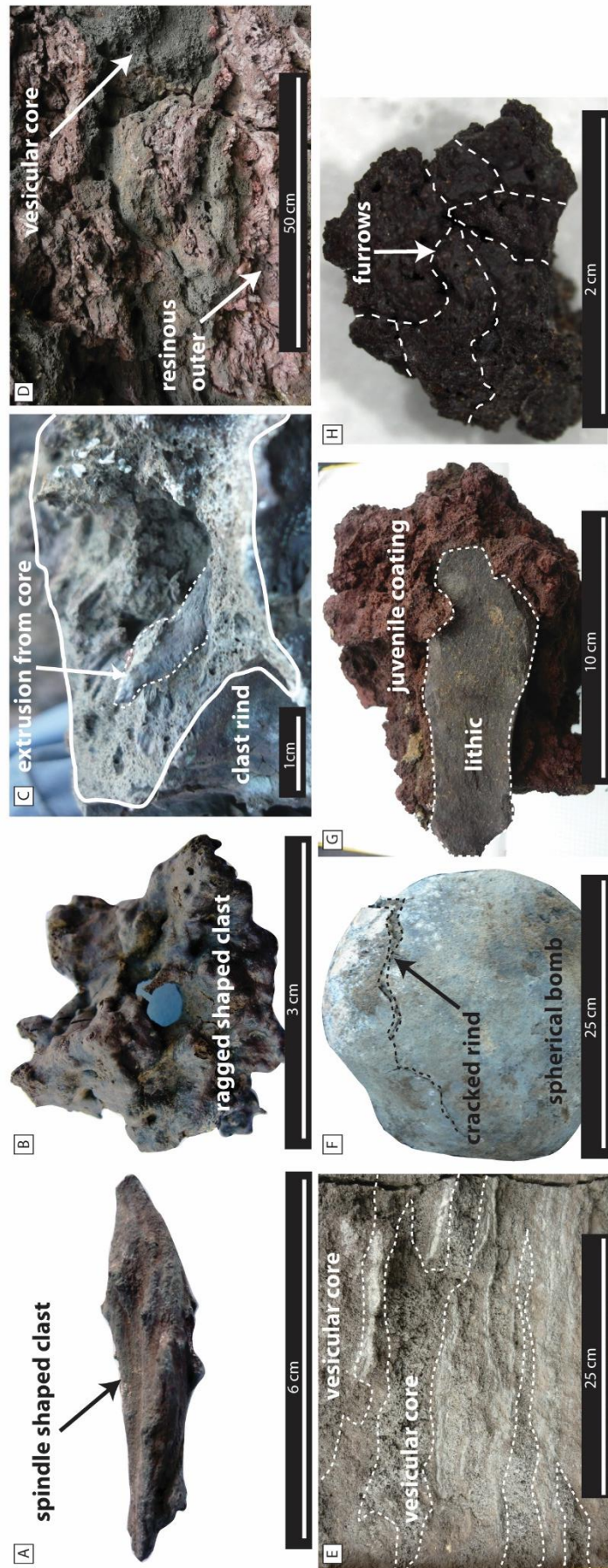


Figure 3.6. Pyroclast types identified in the study area. (A) Spindle-shaped and (B) ragged clast, typical of Hawaiian and Strombolian activity. (C) Clast with a brittle rind (outlined) extruding melt from its interiors (arrowed). (D) Fluid clasts that agglutinate, produced from the inner part of the lava fountain or a low fountain. (E) Fluid clasts that coalesce, produced from the inner lava fountain or a low fountain. (F) Cored bombs produced by the recycling of clasts within an edifice. They have a core of cognate lithic clasts and a 10 mm thick coating of lava. (G) An armoured clast with an accidental or cognate lithic core and a partial coating of lava. (H) Scoria lapilli produced from a rootless lava fountain. Notice the furrows in the crust, similar to those in breadcrust bombs.

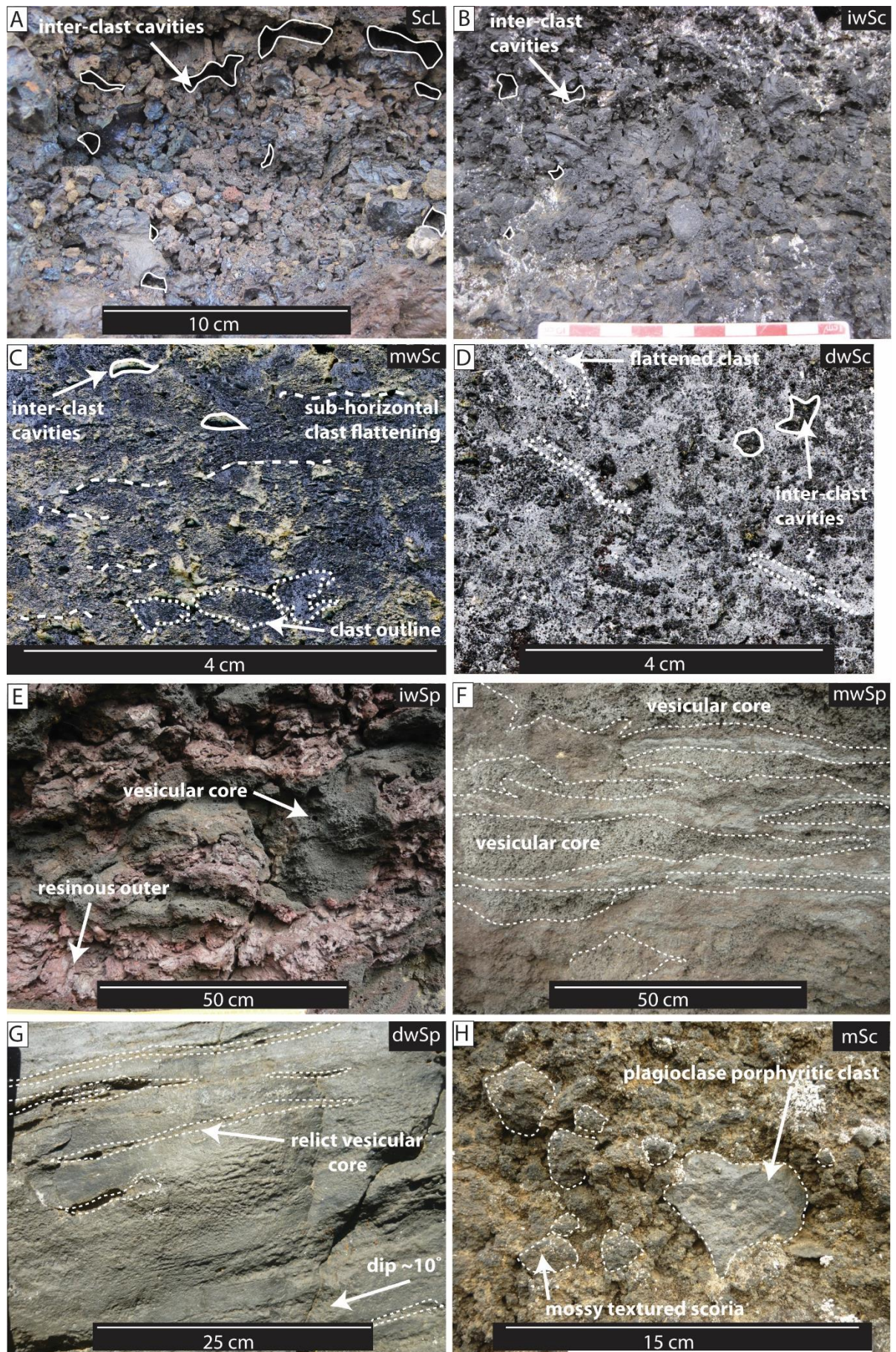


Figure 3.7 (overleaf). Pyroclastic lithofacies observed in the study area. (A) Non-welded scoria lapilli. Inter-clast cavities are visible (outlined). Note the absence of clast flattening. (UTM 557085/7264940). (B) Incipiently welded scoria. Inter-clast cavities are visible (outlined) and clasts are sintered at contacts. Minor clast flattening is observed. (UTM 557442/7264902). (C) Moderately welded scoria. Clast outlines are visible (dashed outline) and some inter-clast cavities (circled) remains. Sub-horizontal clast flattening is parallel to the dashed lines. (UTM 557356/7265748). (D) Densely welded scoria. Flattened clasts (dashed outline) are visible. Small (<1 cm diameter) inter-clast cavities remain. (UTM 563879/7301531). (E) Incipiently welded spatter. Resinous clast rinds are visible (arrowed). (UTM 557433/7264891). (F) Moderately welded spatter. Vesicular cores of clasts remain (dashed outline) and define the bedding. (UTM 557442/7264902). (G) Densely welded spatter. Thin relict vesicular cores (dashed outline) are visible between densely welded zones. The ghost clasts dip ~10°. (UTM 557356/7265748). (H) Massive scoria lapilli and bombs. The clasts are incipiently welded. Armoured clasts with an accidental lithic clast core are common in these deposits. (UTM: 557790/7264865).

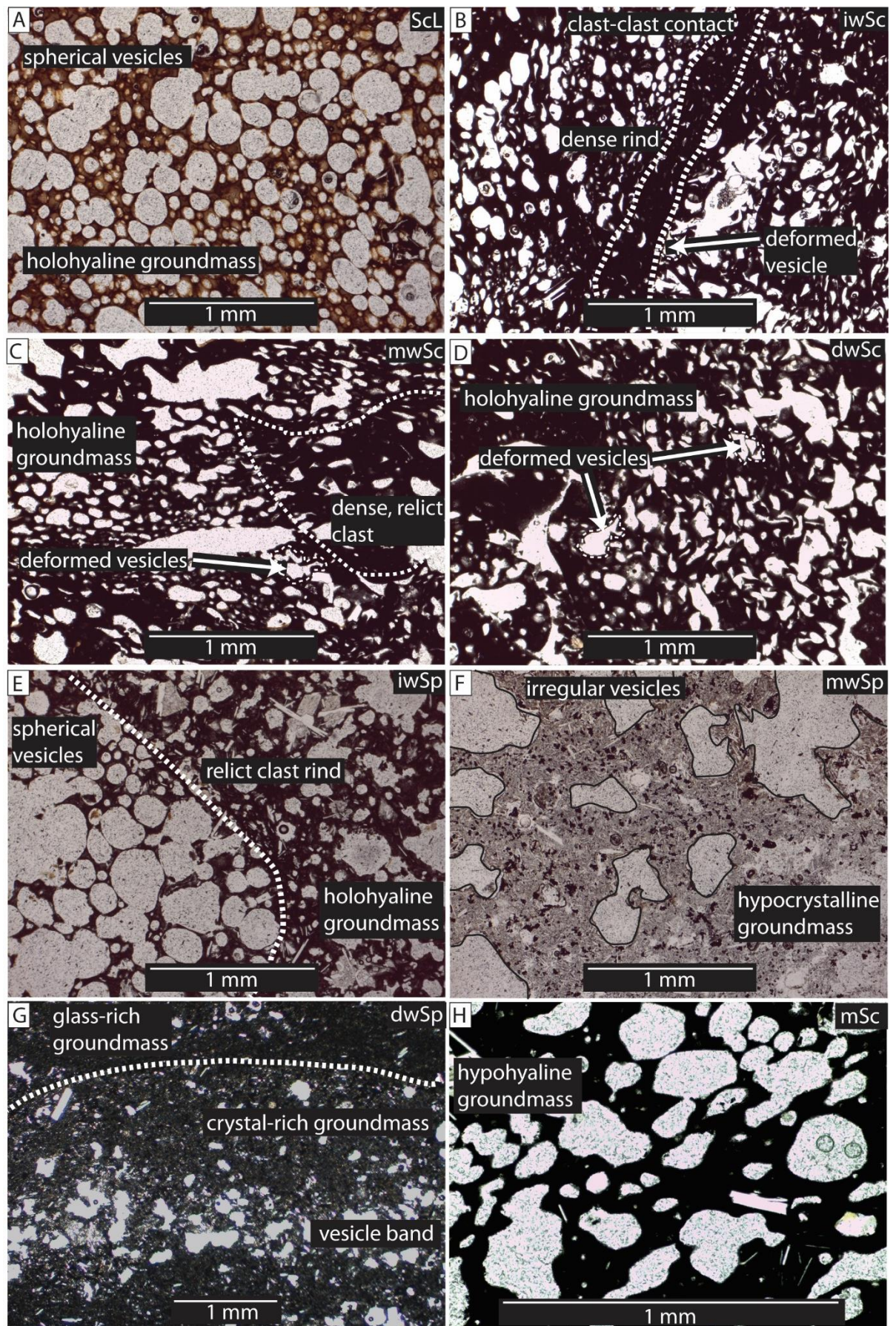


Figure 3.8 (overleaf). Thin section images of pyroclastic lithofacies (plane polarised light). (A) Non-welded scoria lapilli. Note the sphericity of the vesicles compared to the other lithofacies. (B) Incipiently welded scoria. The dashed line indicates an inferred contact between welded clasts. (C) Moderately welded scoria. Domains of less vesicular scoria (dashed outline) are inferred to represent welded clasts. (D) Densely welded scoria. The lithofacies appears texturally similar to clast-supported moderately welded scoria lapilli and bombs (mwSc). (E) Incipiently welded spatter. The dashed line indicates a clast rind folded into the clast core. (F) Moderately welded spatter. Note the increasing crystal content relative to (D) and (E). (G) Densely welded spatter. Note the laminated appearance of the groundmass. The crystal-rich groundmass contains a band of vesicles and is interpreted as the relict core of a spatter bomb. (H) Massive scoria lapilli and bombs. Note the thick bubble septae relative to A and B.

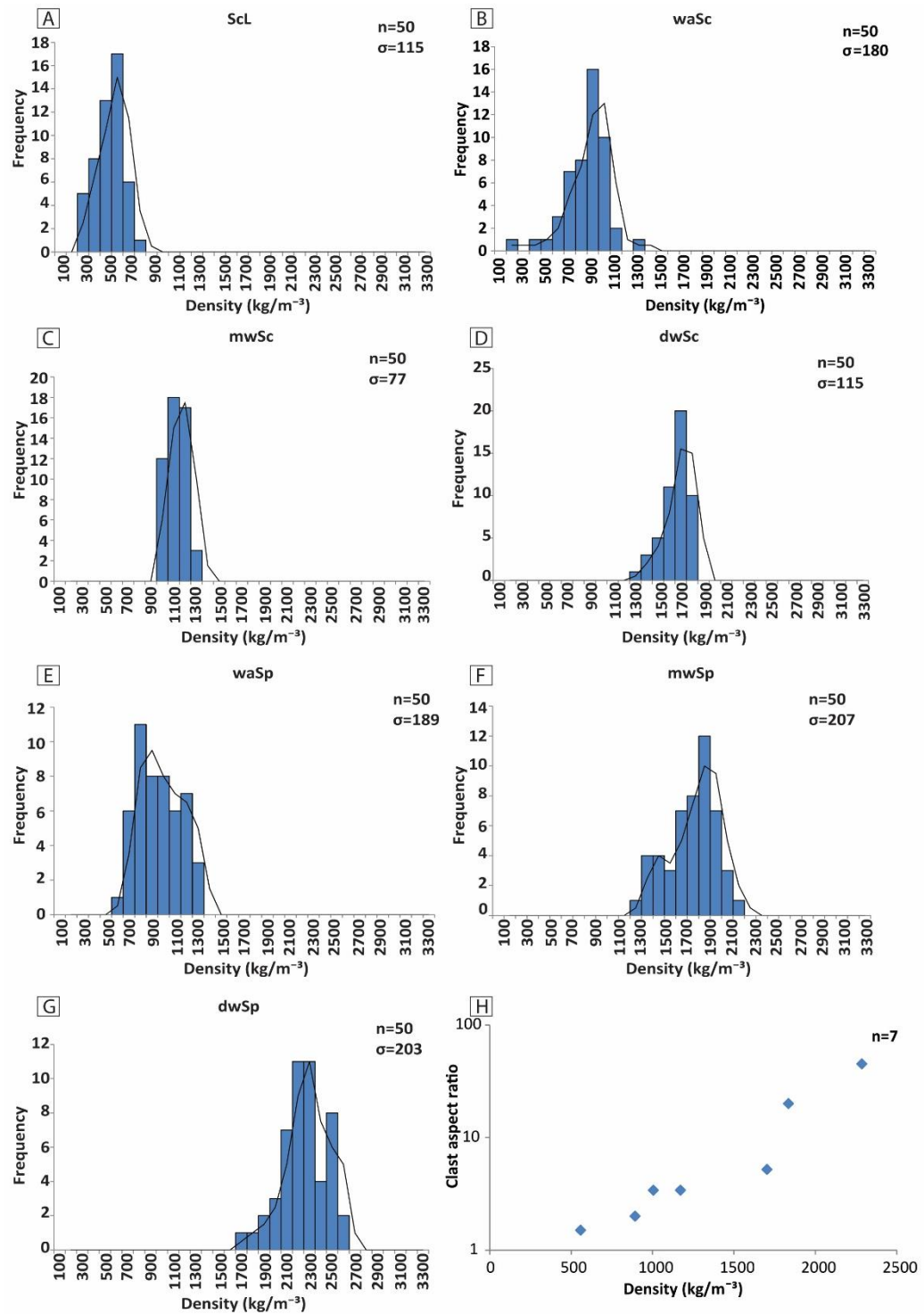


Figure 3.9. Density histograms for the pyroclastic lithofacies. (A) Scoria lapilli. (B) Incipiently welded scoria. (C) Moderately welded scoria. (D) Densely welded scoria. (E) Incipiently welded spatter. (F) Moderately welded spatter. (G) Densely welded spatter. (H) Graph showing that clast aspect ratio increases with density for the pyroclastic lithofacies (each point represents the mean of 50; see Table. 3.2).

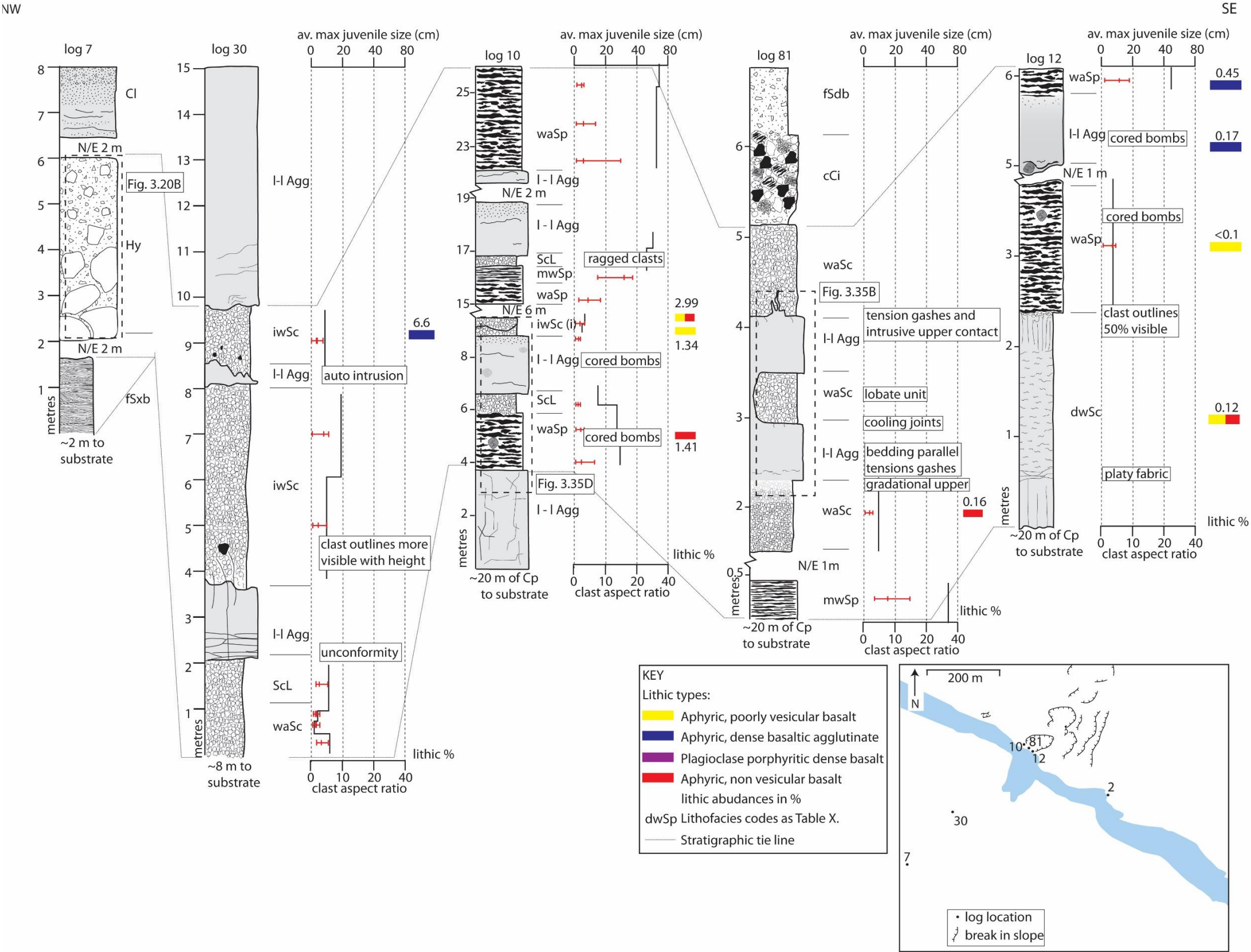


Figure 3.10. Stratigraphic logs showing variations in grain size (black line) and clast aspect ratio (red line); each the average of 10 measurements. Abbreviations for lithofacies are given in Table 3.2. Note the restriction of the lithic clasts to within the crater.

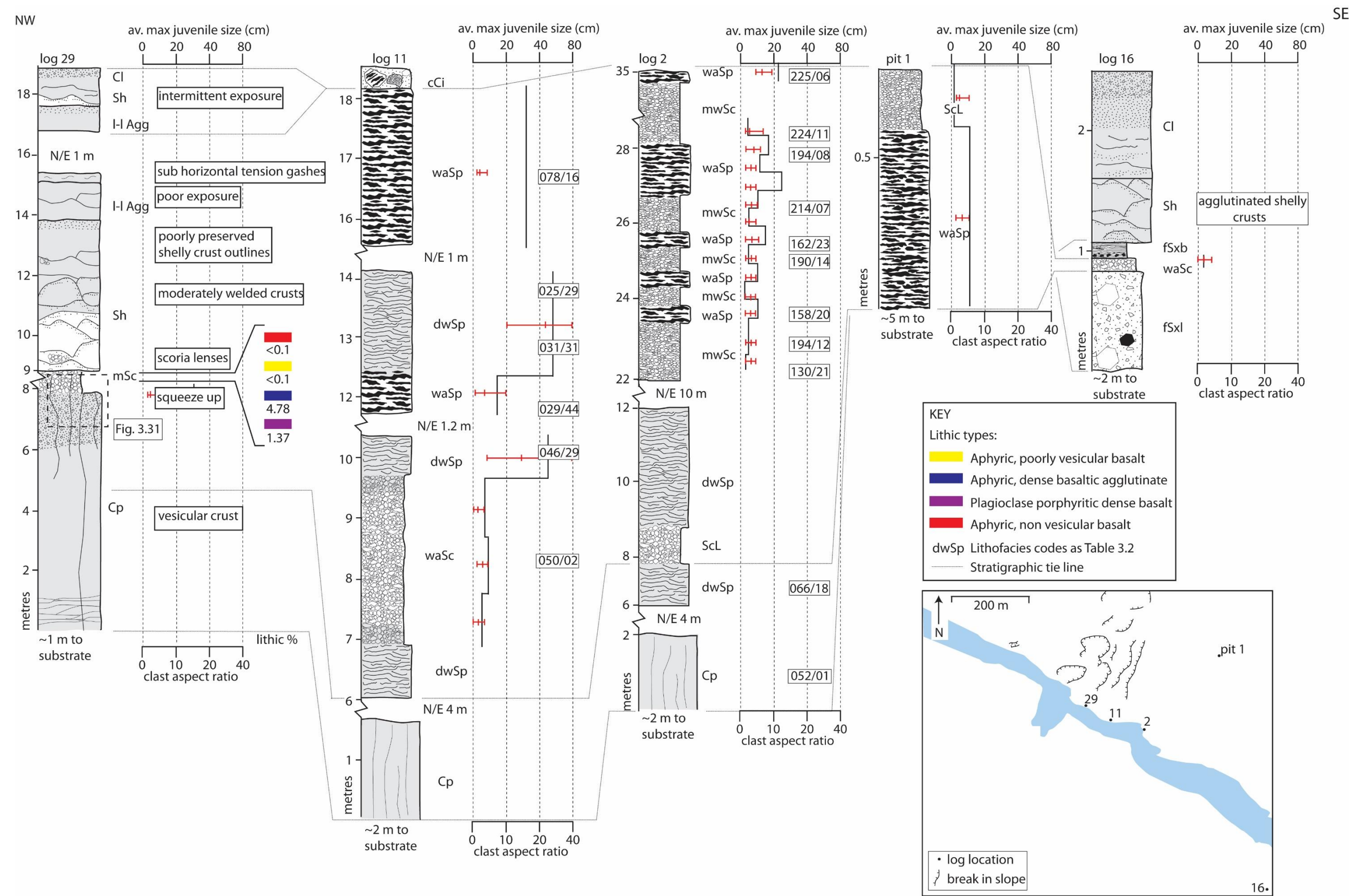


Figure 3.11. Stratigraphic logs showing variations in grain size (black line) and clast aspect ratio (red line); each the average of 10 measurements. Abbreviations for lithofacies are given in Table 3.2.

Lithofacies	Description	Componentry	Occurrence	Structure	Interpretation
ScL	Non-welded scoria lapilli	Spindle shaped or ragged scoria lapilli	The crater of edifice 26; the scoria rampart (location 280); surrounding the spatter ramparts	Unconsolidated deposit or clast-supported; moderately well sorted; bedding defined by stratigraphic contacts and minor clast size fluctuations	Fall deposit from a lava fountain; Hawaiian or Strombolian activity
waSc (i)	Weakly agglutinated scoria lapilli; inversely graded sub facies (i)	Agglutinated spindle-shaped scoria lapilli and bombs; armoured clasts with cognate-clast cores	The crater of edifice 26; scoria ramparts (locations 280) beneath lava flows in medial and distal locations	Clast-supported; moderately well sorted; bedding defined by stratigraphic contacts and clast flattening	Fall deposit from the outer part or a high (>100 m) lava fountain; agglutination promoted by burst cores of clasts and rapid accumulation. Sub facies (i): results from grain flow avalanches
mwSc	Moderately welded scoria lapilli	Spindle bombs with burst rinds; scoria lapilli/bombs that agglutinate	The scoria rampart at location 280	Clast-supported; moderately well sorted; bedding defined by stratigraphic contacts, minor clast size variation and clast flattening	Fall deposit from the inner part of a lava fountain or a high (>100 m) lava fountain
dwSc	Densely welded scoria lapilli	Agglutinated scoria lapilli and bombs	The crater of edifice 26	Clast-supported; moderately well sorted; bedding defined by stratigraphic contacts and clast flattening; often with cooling joints	Fall deposit from the inner part of a lava fountain or a high (>100 m) lava fountain; cooling joints formed as a result of rapid accumulation
waSp	Weakly agglutinated spatter	Agglutinated cowpat and ribbon-shaped spatter bombs; armoured clasts and cored bombs with cognate-clast cores	The crater of edifice 26; the scoria rampart at location 280	Clast-supported; well sorted; bedding defined by stratigraphic contacts and clast flattening	Fall deposit from the inner part of a lava fountain or a low fountain
mwSp	Moderately welded spatter	Agglutinated cowpat and ribbon-shaped spatter bombs	The crater of edifice 26; the scoria rampart at location 280	Clast-supported; well sorted; bedding defined by stratigraphic contacts and clast flattening	As waSp; rapid accumulation promotes agglutination
dwSp	Densely welded spatter	Agglutinated and coalesced spatter bombs	The scoria rampart at location 280	Clast-supported; well sorted; bedding defined by stratigraphic contacts and clast flattening	As waSp; rapid accumulation rate promotes coalescence of clasts
mSc	Massive scoria lapilli and bombs	Cauliflower-textured scoria lapilli and bombs; armoured clasts with accidental and cognate-clast cores	The vents of rootless cones	Clast-supported; moderately well sorted; massive; gradational contacts with underlying Cp	Fall deposit from a rootless lava fountain
vSpb	Volcaniclastic sandstone with planar bedding	Yellow/beige sand-grade matrix, blocks and cobbles of unknown provenance	Base of the R-K volcanic sequence along the strike of the dyke	Forms planar beds 100 mm thick	Fluvial sandstone or palagonitised tuff

Table 3.2. Summary descriptions of pyroclastic lithofacies.

Lithofacies	Crystallinity (%)	Clast aspect ratio	Density Mean (kg m ⁻³)	Density range (kg m ⁻³)	Vesicularity mean (%)	Vesicularity range (%)	Vesicle diameter (mm)	Av. Max clast size (mm)	Lithofacies thickness range (mm)	Maximum dispersal distance from fissure (m)
ScL	2	1	572	344–827	80	72–88	<0.1–1.5	35	100–1750	464
waSc (i)	5	2	889	290–1332	70	55–90	<0.1–2.4	55	50–3800	1247
mwSc	6	3	1172	1037–1349	60	57–82	<0.1–2.6	48	75–1500	500
dwSc	8	5	1703	1332–1891	43	36–55	<0.1–1.5	23	80–380	500
waSp	48	3	1005	623–1466	66	51–79	<0.1–2.5	244	170–8000	420
mwSp	77	20	1835	1374–2218	38	26.0–38.8	<0.1–3.3	823	340–2400	210
dwSp	86	45	2286	1705–2633	23	12–43	<0.1–0.9	>1000	470–1620	205
mSc	13	1.4	-	-	-	-	<0.001–2.04	80	250–4000	130
Table 3.3. Summary table of the texture, distribution and petrography of the pyroclastic lithofacies										

3.4.1 Lithofacies Descriptions

Lithofacies ScL – Clast-supported non-welded scoria lapilli

This lithofacies is composed of either spindle-shaped or ragged scoria lapilli (Fig. 3.6) that are often fragmented into angular fracture-bound clasts. Clasts are red, purple or black in colour. Their groundmass is holohyaline. Their brittle external rinds are <0.5 mm thick and glassy with hairline fractures. Clasts have a mean vesicularity of 80 %, ranging from 72–88% (see Appendix 1). The vesicles are <0.1–1.5 mm diameter and bubble septae are <0.5 mm thick (see Appendix 1).

The lithofacies is clast-supported and moderately well sorted. The constituent lapilli are non-welded and are easily dislodged by hand. Lithofacies density ranges from 344–827 kg m⁻³ (mean 572 kg m⁻³; Table 3.3). No clast flattening is observed (mean aspect ratio 1:1) and bedding is defined by distinct contacts with overlying lithofacies and minor clast size fluctuations between fine and coarse lapilli. The lithofacies occurs in units 100–1750 mm thick (see Appendix 1). Unconsolidated clast-supported non-welded scoria lapilli (ScL) surround the spatter ramparts west of the river (Fig. 3.3). The lithofacies occurs in the upper 20 m of the crater of cone 26 (log 10; Fig. 3.10) and ~400 m southeast from the fissure (pit 1; Fig. 3.11). It commonly over/underlies clast-supported weakly agglutinated scoria lapilli and bombs (waSc) and clast-supported incipiently welded spatter bombs (waSp) within edifice 26 and adjacent deposits.

Interpretation:

This lithofacies is interpreted as a fall deposit from a lava fountain (Head and Wilson 1989; Sumner et al. 2005). The spindle- and ragged-shaped clasts are typical of Strombolian and Hawaiian activity (Valentine and Gregg 2008). The absence of welding indicates that clasts were cool and brittle on deposition and they are inferred to have accumulated at a low rate from the upper and outer part of a lava fountain (e.g. Walker and Croasdale 1971; Head and Wilson 1989; Sumner et al. 2005). This fountain may have been intermittent, since intermittence promotes low-rate accumulation.

The association of this lithofacies with clast-supported weakly agglutinated scoria lapilli and bombs (waSc) and clast-supported weakly agglutinated spatter bombs (waSp; pit 1; Fig. 3.10) suggests that deposition from different parts of the fountain occurred in rapid succession due to rapidly changing fountain conditions (see section 3.4).

Lithofacies waSc(i) – Clast-supported weakly agglutinated scoria lapilli and bombs with inversely graded (i) sub facies

This lithofacies is composed of agglutinated spindle-shaped scoria lapilli (as described for clast-supported non-welded scoria lapilli; ScL), spindle bombs with fractured rinds and armoured clasts (<7 vol. %). The spindle bombs are red or black and have a holohyaline groundmass (see Appendix 1). Their brittle external rinds are <0.5 mm thick, resinous and often fractured, exposing a ~66% vesicular core that has extruded melt (Fig. 3.6). Clasts range from 55–90% vesicular (mean 70%) and vesicles are <0.1–2.4 mm diameter (see Appendix 1). Their septa are <0.5 mm thick and vesicles commonly have a flattened, eye-like shape. The armoured clasts are lapilli to bomb sized and have a core of cognate incipiently welded scoria lapilli or cognate dense agglutinate/lava. Their angular shape is formed by a singular coating of vesicular juvenile lava that partly encapsulates the core. These clasts are confined to the upper 15 m of the crater of cone 26.

The lapilli and bombs in this lithofacies are clast-supported and moderately well sorted. The scoria lapilli and bombs are incipiently welded, and some exhibit moderate amount clast flattening (mean aspect ratio 1:2). Lithofacies density ranges from 290–1332 kg m⁻³ (mean 889 kg m⁻³; Table 3.3). Bedding is defined by small variations in mean clast size and by the welding fabric. The lithofacies occurs in units 50–3800 mm thick and may have gradational or distinct contacts with over/underlying lithofacies (e.g. log 11; Fig. 3.11). This lithofacies occurs up to 1.2 km from the fissure (e.g. log 16; Fig. 3.10) and at the top of the R-K volcanic sequence (e.g. log 81; Fig. 3.10). It is also found beneath the oldest lavas west of the river (log 16; Fig. 3.11). The inversely graded sub facies (i) occurs within the crater of edifice 26 on moderate slopes (~10°). The lithofacies is commonly associated with clast-supported non-welded scoria lapilli (ScL) and spatter-dominated lithofacies (e.g. clast-supported incipiently welded spatter bombs; waSp; see Fig. 3.11).

Interpretation:

This lithofacies is interpreted as a fall deposit from the outer part of a lava fountain during Strombolian or Hawaiian-style activity. The spindle bombs are inferred to have fallen from the outer part of a lava fountain (e.g. Sumner et al. 2005). The cores of the burst bombs remained molten after deposition due to their large size. Impact-induced leakage of melt from the clasts resulted in the partial agglutination of adjacent and subjacent clasts (e.g. Sumner et al. 2005).

The armoured clasts indicate the ballistic ejection of lithic clasts during a single fountaining event. The bombs show no evidence of ductile deformation or impactation (e.g. a cowpat shape), thus are inferred to have cooled in-flight. They were formed in a fountain which was sufficiently spread to allow in-flight clast cooling. The cognate clast cores of the armoured clasts indicate removal of clasts from the vent region by collapse or remobilisation of pyroclasts into the vent.

Inversely graded scoria beds are typical of Hawaiian and Strombolian deposits (Valentine and Gregg 2008). Grading is inferred to result from grain flow avalanches (e.g. McGetchin et al. 1974); subsequent agglutination may have been promoted by the bursting of large bombs with molten cores. The abundance of the lithofacies across the study area indicates that it was produced from multiple sources along the fissure.

Lithofacies mwSc – Clast-supported moderately welded scoria lapilli and bombs

This lithofacies is composed of clast-supported and moderately well sorted spindle bombs with burst rinds (as described for clast-supported weakly agglutinated scoria lapilli and bombs; waSc) and agglutinated scoria lapilli/bombs. Agglutinated clasts are elongate (Fig. 3.6), with resinous purple/red rinds <0.5 mm thick. Clasts have a holohyaline groundmass and have a mean vesicularity of 60%, ranging from 57–82% (see Appendix 1). Vesicles are <0.1–2.6 mm in diameter and have a flattened eye-like shape. Their septae are <0.5 mm thick. Some clasts have folded rinds inside their cores.

The clasts are clast-supported and moderately well sorted. Lithofacies density ranges from 1037–1349 kg m⁻³ (mean 1172 kg m⁻³; Table 3.3). Moderate welding is indicated by clast mean aspect ratios of 1:3 and an associated loss of deposit pore space. The lithofacies forms planar beds 75–1500 mm thick (see Appendix 1), defined by stratigraphic contacts, clast flattening and clast size variation. The lithofacies is restricted to within 500 m of the fissure toward the southeast. It occurs ≤250 m from the fissure (e.g. log 2; Fig. 3.11) and has gradational contacts with overlying clast-supported incipiently welded spatter bombs (waSp).

Interpretation:

Agglutinated clasts are inferred to have been sourced from the inner part of a lava fountain during Hawaiian or Strombolian activity (e.g. Head and Wilson 1989; Sumner et al. 2005). The presence of internal rinds indicate recycling of clasts within the fountain (e.g. Sumner et al. 2005). Clast flattening indicates rapid accumulation of molten clasts.

Internal grain size variations may result from a variety of factors, as described for clast-supported non-welded scoria lapilli (ScL).

Lithofacies dwSc – Clast-supported densely welded scoria

This lithofacies is composed of densely welded clast-supported and moderately well sorted agglutinated scoria lapilli and bombs. Agglutinated clasts have resinous purple/red rinds <0.5 mm thick. The groundmass of the clasts is holohyaline (see Appendix 1). Clasts have a mean vesicularity of 43%, ranging from 36–55% (see Appendix 1). Vesicles are <0.1–1.5 mm in diameter and have a flattened eye-like shape. Bubble wall septae are <0.5 mm thick.

Lithofacies density ranges from 1332–1891 kg m⁻³ (mean 1703 kg m⁻³; Table 3.3). A distinctive fabric formed by clast flattening is visible (mean clast aspect ratio 1:5), although clast outlines are sometimes unclear due to dense welding. Clast flattening and stratigraphic contacts define beds 80–380 mm thick. Beds often have cooling joints spaced ~50 mm that penetrate the entire deposit thickness. The lithofacies occurs within the crater of edifice 26 (log 12, Fig. 3.10) and up to 500 m southeast of the fissure. It has distinct contacts with clast-supported incipiently welded spatter bombs (waSp), lava-like agglutinate (l-l Agg) and clastogenic pāhoehoe (Cl) and occurs in the upper 15 m of stratigraphy.

Interpretation:

This lithofacies is formed by the rapid accumulation of clasts, as described for clast-supported moderately welded scoria lapilli and bombs (mwSc). High accumulation rates are indicated by the dense welding and the formation of cooling joints which indicate that the beds cooled as a single unit.

Lithofacies waSp – Clast-supported weakly agglutinated spatter bombs

This lithofacies is composed of clast-supported and well sorted cored bombs (<5 vol. %) and agglutinated cowpat and ribbon-shaped spatter bombs with purple/red resinous rinds that are <0.5 mm thick. The spatter bombs are commonly >300 mm in diameter and overlap, often obscuring clast margins. Their groundmass is hypohyaline (see Appendix 1). Clasts have a mean vesicularity of 66%, ranging from 51–79% (see Appendix 1). Vesicles are <0.01–2.5 mm in size. Bubble septae are <0.5 mm thick and vesicles have a flattened, eye-like shape. Cored bombs are also found.

The cored bombs are sub-spherical and are often fractured and broken into jigsaw-fit fragments. Their sub-spherical shape is given by a 10 mm thick rind of multiple ~3 mm thick coatings of incipiently vesicular lava. The core of the bomb consists of cognate incipiently welded scoria lapilli or cognate dense agglutinate/lava.

The density of the lithofacies ranges from 623–1461 kg m⁻³ (mean 1005 kg m⁻³; Table 3.3). Weak agglutination has resulted in the minor flattening of clasts (mean aspect ratio 1:3). Clast flattening and stratigraphic contacts define planar beds which are 170–8000 mm thick (see Appendix 1). The lithofacies occurs up to 400 m from the fissure toward the southeast, and ~200 m toward the northwest. The lithofacies is common in the uppermost parts of the stratigraphy and is associated with edifice building sequences (e.g. log 2; Fig. 3.11). It rapidly grades vertically into densely welded lithofacies (e.g. clast-supported densely welded spatter bombs; dwSp, log 11; Fig. 3.11), and has sharp contacts with densely-welded lithofacies (e.g. clast-supported densely welded scoria; dwSc, log 12; Fig. 3.11).

Interpretation:

Spatter bombs are commonly deposited via fallout from the inner parts of the lava fountain or from low fountains during Hawaiian or Strombolian activity (Wolfe et al. 1988; Head and Wilson 1989; Sumner et al. 2005). The accumulation rate of pyroclasts was sufficiently low to prevent significant welding and allowed clast outlines to be preserved (Head and Wilson 1989; Sumner et al. 2005).

Cored bombs are formed by the recycling of pyroclasts or wall rock during Hawaiian or Strombolian activity (e.g. White and Houghton 2006; Valentine and Gregg 2008). The cognate clast cores of the cored bombs indicate removal of clasts from the vent region by collapse or remobilisation of pyroclasts into the vent. Their spherical shape is attained by: ball milling within the crater of an edifice during intermittent explosions (e.g. McGetchin et al. 1974); rolling down the outer slopes of a cone (e.g. Francis 1973); the presence of large clasts near the centre of the bomb (Rosseel et al. 2006) or moulding by surface tension (e.g. Macdonald 1972; Fisher and Schmincke 1984). These processes are not mutually exclusive. The multiple rinds suggest that the clasts were recycled within the vent during numerous fountaining events. The abundance of fractured and fragmented clasts indicates that traction occurred after the clast had cooled.

Lithofacies mwSp – Clast-supported moderately welded spatter bombs

This lithofacies is composed of clast-supported and well sorted agglutinated cowpat and ribbon-shaped spatter bombs. Their groundmass is hypocrySTALLINE. Clasts are commonly >300 mm length (see Appendix 1); they are recognised by their relict vesicular cores. Their purple/red rinds are difficult to discern, where visible they are <0.5 mm thick and deformed. Clasts have a mean vesicularity of 38%, ranging from 26–38% (see Appendix 1). Vesicles are <0.1–3.3 mm in size. The vesicles are often isolated in the groundmass and have a flattened, eye-like shape.

Lithofacies density ranges from 1374–2218 kg m⁻³ (mean 1835 kg m⁻³; Table 3.3). The lithofacies is moderately welded and clasts have mean aspect ratios of 1:20. Clast flattening and stratigraphic fabrics define 340–2400 mm thick beds which are common in the uppermost parts of the R-K volcanic sequence (see Appendix 1). The lithofacies occurs within the upper 10 m of the R-K volcanic sequence and is associated with edifice building sequences (e.g. log 81; Fig. 3.10), rapidly grading into more/less densely welded deposits. Alternatively, the lithofacies may have distinct stratigraphic contacts (e.g. log 10; Fig. 3.10). It is located ≤210 m from the fissure toward the southeast and 195 m from the fissure toward the northwest.

Interpretation:

Spatter bombs are commonly deposited via fallout from the inner parts of the lava fountain or from low fountains during Hawaiian or Strombolian activity (Wolfe et al. 1988; Head and Wilson 1989; Sumner et al. 2005). Clast flattening indicates rapid accumulation of molten clasts and suggests increased accumulation rates relative to clast-supported incipiently welded spatter bombs (waSp).

Lithofacies dwSp – Clast-supported densely welded spatter bombs

This lithofacies is composed of clast-supported and well sorted agglutinated and coalesced spatter bombs. Clasts are often difficult to recognise; where discernible ghost clasts are commonly >300 mm length. The groundmass of this lithofacies is hypocrySTALLINE (see Appendix 1) and has a laminated appearance due to variations in groundmass crystallinity. The laminations are 0.5 mm thick and are sub-parallel. Vesicles occur within the more crystalline laminations and have an irregular shape. The lithofacies has a mean vesicularity of 23%, ranging from 12–43%. Vesicles are <0.1–0.9 mm in size (see Appendix 1).

The density of the lithofacies ranges from 1705–2633 kg m⁻³ (mean 2286 kg m⁻³; Table 3.3). Dense welding is recognised by intensely flattened clasts with mean aspect ratios of 1:45. Clast flattening and stratigraphic contacts define 470–1620 mm thick beds which are common throughout the R-K volcanic sequence (see Appendix 1). The lithofacies occurs in the upper 30 m of the R-K volcanic sequence and is associated with edifice building sequences (e.g. log 11; Fig. 3.11). The lithofacies rapidly grades into more/less densely welded deposits. Alternatively, it may have distinct contacts with other lithofacies (e.g. log 11; Fig. 3.11). It occurs in the crater of edifice 26 and up to 205 m southeast from the fissure. It also found west of the river, ~150 m from the fissure toward the southeast.

Interpretation:

This lithofacies is interpreted to have formed under similar conditions as clast-supported moderately welded spatter bombs (mwSp) but is inferred to have accumulated more rapidly. The laminated textured is inferred to result from intense welding. The crystal-rich laminations that contain vesicles are interpreted as the relict cores of spatter bombs. The crystal-poor laminations are interpreted as the relict chilled margins of flattened clasts.

Lithofacies vSpb – volcanoclastic sandstone with planar bedding

Outcrops of this lithofacies have only been observed with binoculars due its inaccessibility. It has an apparent yellow/beige sand-grade matrix and ~20 % blocks and cobbles. It forms planar beds ~100 mm thick that dip ~12° to the east (see Appendix 1). The lithofacies occurs towards the base of the R-K volcanic sequence and forms a lenticular deposit ~5 m thick and ~20 m in length. Its contacts with the adjacent and overlying lithofacies (clast-supported weakly agglutinated scoria lapilli and bombs; waSc) are defined by a distinct yellow/beige–brown colour change. Its basal contact is not exposed. It outcrops only on the west of the river along the strike of the fissure.

Interpretation:

I am unable to determine the genesis of the lithofacies from its geometry, contacts or componentry. It is probably a fluvial sandstone or a palagonitised tuff. If the lithofacies represents palagonitised tuff the blocks and cobbles are accidental clasts removed during explosive magma-interaction. Its occurrence only along the base of the R-K volcanic

sequence suggests protracted magma-water interaction during opening of the fissure. The deposits could be fall deposits or pyroclastic density current deposits (e.g. Wohletz and Sheridan 1983).

If the lithofacies represents a fluvial deposit the blocks and cobbles are clasts eroded from the underlying R-K volcanic sequence (see section 3.4). The distribution of the lithofacies at the base of the R-K volcanic sequence would be consistent with deposition in a river channel (e.g. Stow 2005).

Lithofacies mSc – Massive scoria lapilli and bombs

This lithofacies is composed of clast-supported and moderately well sorted scoria lapilli and bombs and armoured clasts (<5 vol. %). The scoria lapilli and bombs have a convoluted, cauliflower-like surface texture defined by furrows in the clast rind (Fig. 3.6). Clasts are often fragmented into angular shapes. Their groundmass is hypohyaline (see Appendix 1). Vesicles are <0.1–2.0 mm in diameter (see Appendix 1). Some clasts may have thick (≤ 10 mm) bubble septae. The armoured clasts are similar to those described for clast-supported weakly agglutinated scoria lapilli and bombs (waSc), but their lithic cores are composed variably of 1) aphyric, non-vesicular basaltic lava; 2) plagioclase porphyritic dense basalt; 3) aphyric, dense basaltic agglutinate; 4) plagioclase porphyritic, poorly vesicular basalt; 5) aphyric, poorly vesicular basalt.

Clasts are without flattening (clast aspect ratio 1:1; Table 3.3). The lithofacies forms a 1 cm thick margin on the columnar-jointed pāhoehoe with which it is always associated (see section 3.5). It was impossible to sample sufficient quantities of this lithofacies to calculate its density. The lithofacies has cooling joints spaced ~20 mm apart that penetrate into the underlying columnar-jointed pāhoehoe (Cp; Fig. 3.11). This lithofacies is only found 95 m southeast of the fissure (location 285; log 29, Fig. 3.11). It has gradational contacts with the columnar-jointed pāhoehoe (Cp) and is restricted to the lower 10 m of the R-K volcanic sequence.

Interpretation:

This lithofacies has many similar features to the proximal deposits of rootless eruptions, including a lapilli–bomb sized pyroclast population (e.g. Chapter 4; Hamilton et al. 2010); abundant lithic clasts (e.g. Chapter 4; Mattox and Mangan 1997) and an association with inflated lava flows (e.g. Chapter 4; Fagents et al. 2002; Fagents and Thordarson 2007; Hamilton et al. 2010). The component juvenile clasts differ from those

of other weakly agglutinated lithofacies (e.g. clast-supported weakly agglutinated scoria lapilli; waSc) since they have a cauliflower-like surface texture (Fig. 3.6). This surface texture suggests that cooling was partly water induced, similar to the bulbous and bread-crusted clasts described by Kokelaar (1986) and Mattox and Mangan (1997) respectively. The clasts also have thicker bubble walls than clast-supported weakly agglutinated scoria lapilli and bombs (waSc), suggesting that clasts are denser and underwent degassing prior to fragmentation (Fig. 3.9). The scoria clasts are thus interpreted to be a fall deposit from a rootless lava fountain (e.g. Mattox and Mangan 1997; Hamilton et al. 2010).

The rootless fountains formed during rootless explosions proximal to the fissure, suggesting that there was abundant surface water during the R-K eruption. (e.g. Jurado-Chichay et al. 1996; Mattox and Mangan 1997; Hamilton et al. 2010). The association of the massive scoria with the columnar-jointed pāhoehoe (Cp) indicates a genetic link between the two lithofacies; the columnar-jointed pāhoehoe (Cp) is inferred to be the host lava flow for rootless eruptions (see section 3.7.2).

The aphyric lithic cores of the armoured clasts are interpreted as clasts sourced from the crust of the host lava flow during rootless cone formation. The plagioclase porphyritic cores are interpreted as accidental clasts removed during rootless activity. The clasts are not thought to represent accidental clasts removed from the conduit region for two reasons. Firstly, the clasts are more than twice as abundant as those reported in other Hawaiian eruptions (e.g. Valentine and Groves 1996; Valentine 2012). Secondly, if the clasts represent clasts removed from the conduit, it is necessary to account for their occurrence in the rootless deposits. Perhaps the clasts had been removed from the conduit, deposited, and then erupted again from beneath the columnar-jointed pāhoehoe (Cp) during rootless activity. However, the clasts show no evidence of having been erupted twice (i.e. multiple coatings of lava).

3.4.2 Distribution of the pyroclastic lithofacies

Many of the pyroclastic lithofacies are asymmetrically distributed towards the east (e.g. clast-supported moderately welded scoria lapilli and bombs, mwSc; clast-supported weakly agglutinated scoria lapilli and bombs, waSc; clast-supported non-welded scoria lapilli, ScL). North westerly winds are dominant in Iceland today (Einarsson 1984) and were dominant in the mid-Holocene (e.g. Mauri et al. 2013 and references there-in). Therefore, the asymmetric distribution may result from the clasts stripping of the lava fountain by north-westerly winds. Alternatively, the asymmetry may suggest that the

fountain was inclined (e.g. Capaccioni and Cuccoli 2005). Some lava fountains are both inclined and affected by strong winds (e.g. Geist et al. 2008). The asymmetric distribution is not inferred to result from post-eruption fluvial erosion (see section 3.4.1). The observed R-K tephra thickness distribution (Fig. 3.12) is comparable to that of the 1959 Hawaiian-style Kilauea Iki eruption, which thinned to ≥ 150 cm at a distance of 1 km from the vent (Houghton et al. 2006). This eruption had a maximum fountain height of 570 m (Parfitt 1998). The restriction of clasts 1 m in size to within 600 m of the vent (Fig. 3.12) is similar to that of the Tavuyaga tephra, also the product of a Hawaiian-style eruption (Cronin and Neall 2001).

3.4.3 Temporal variations in pyroclast welding intensity, bedding and contacts

The aspect ratio of clasts and the bulk density of a lithofacies can be used to indicate welding intensity. Progressive increases in welding intensity can result from increases in the rate of accumulation of pyroclasts from a lava fountain. Increases in accumulation rates can result from increases in fountaining intensity, sustained fountaining or a more collimated fountain (i.e. less widely spread; see Head and Wilson 1989; Wolff and Sumner 2000; Sumner et al. 2005). Bedding (defined by minor clast size fluctuations) can also result from variations in the height and inclination of the fountain. In the R-K volcanic sequence, the gradational and distinct contacts with over/underlying lithofacies suggest both gradual and sudden changes in fountain conditions.

3.4.4 Variations in componentry

Cored bombs with cognate-clast cores are only found in the crater of edifice 26 in the lava-like agglutinate lithofacies (l-l Agg) and clast-supported weakly agglutinated spatter bombs lithofacies (waSp; e.g. log 10 and 12; Fig. 3.10). Cored bombs are absent from early pyroclastic deposits but become common in the upper ~15 m of the deposits of the R-K eruption sequence. These bombs indicate intermittent lava fountaining, perhaps triggered by decreasing magma flux in the later stages of the eruption (e.g. Swanson et al. 1979; Thordarson and Self 1993; Parfitt 2004) or bursting of gas bubbles in the conduit (e.g. Wolfe et al. 1988).

Armoured clasts with cognate cores in lithofacies massive scoria lapilli and bombs (mSc) account for <1–5 vol. % of the clast population (logs 29, Fig. 3.10). They are interpreted fragments of the host lava flow and indicate widening of rootless vents. Armoured clasts are also common (<1–7 vol. %) in lithofacies clast-supported weakly

agglutinated spatter bombs (waSp) and clast-supported weakly agglutinated scoria lapilli and bombs (waSc) towards the top of the R-K volcanic sequence. They are inferred to indicate the collapse of R-K pyroclasts back into the vent. Collapse processes and grain flow avalanches, common during many scoria cone eruptions, provide a mechanism for generating the cognate clasts (e.g. McGetchin et al. 1974; Heiken 1978; Valentine et al. 2005; Mattsson and Tripoli 2011; Alvarado et al. 2011).

Armoured clasts with accidental lithics as cores are restricted to the massive scoria lapilli and bombs (mSc) in the lower 10 m of the R-K volcanic sequence. This lithofacies is interpreted as rootless tephra (see section 3.4). The accidental clasts occur in low abundances (1–2 vol. %; log 29, Fig. 3.11). They are interpreted as clasts fragmented from the pre-R-K eruption lavas during rootless eruptions. Their restriction to the lowermost deposits of the R-K eruption sequence suggests that their deposition is dependent on rootless activity whilst surface water was abundant.

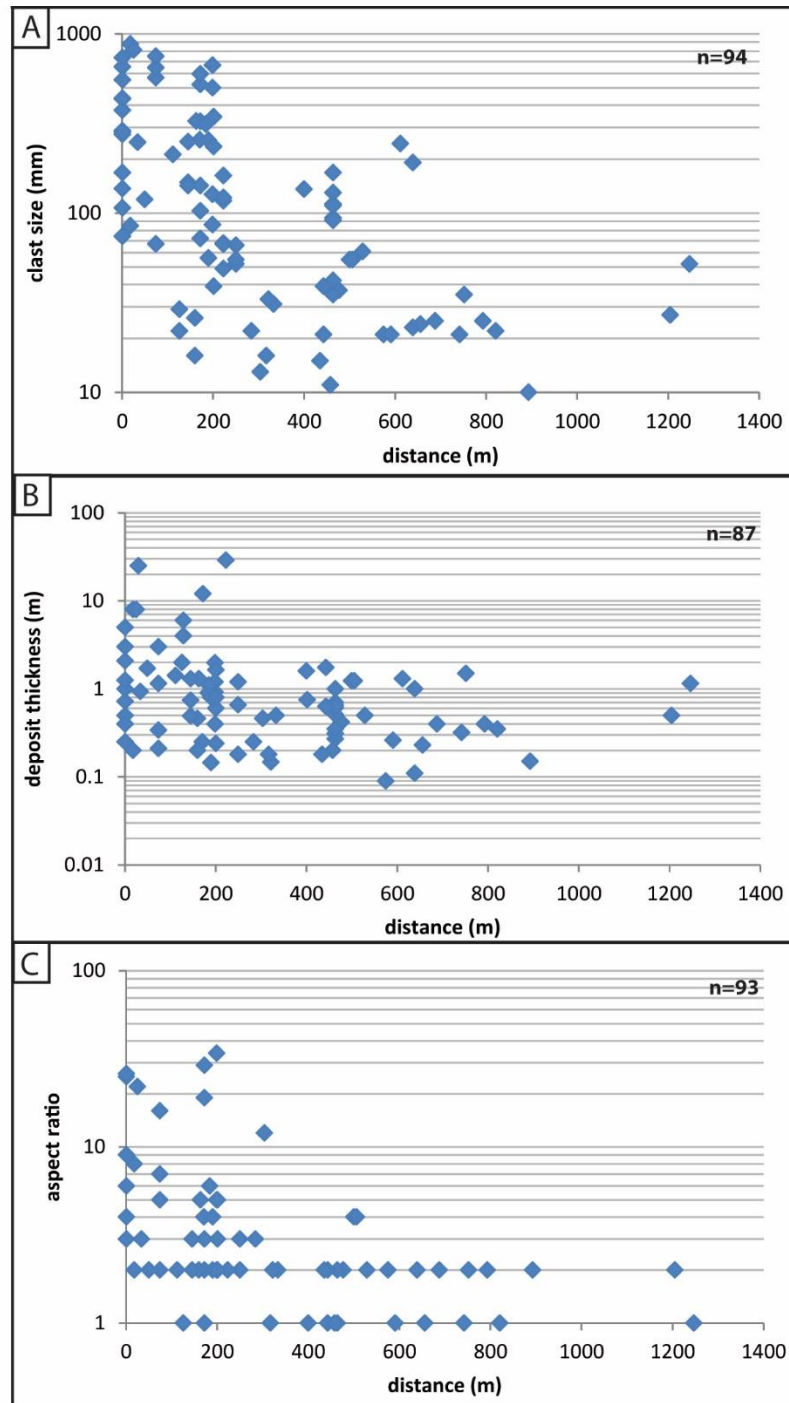


Figure 3.12. Dispersal and welding characteristics of the tephra and lavas. (A) Graph to show the relationship between distance from the fissure (m) and pyroclast size (mm). Pyroclasts decrease in size with distance. (B) Graph to show the relationship between distance from the fissure (m) and pyroclast lithofacies thickness (m). Deposits thin with distance. (C) Graph to show the relationship between distance from the fissure (m) and aspect ratio. Clast aspect ratio (i.e. welding intensity) decreases with distance. For descriptions of lithofacies see Tables 3.1 and 3.2.

3.5 Lava flow field architecture

A variety of lavas were emplaced during the R-K eruption (Figs. 3.13). The lavas are generally confined within the Sveinar graben. Assuming an average thickness of 15 m for the lavas, an average width of 750 m for the graben and a length of 75 km for the R-K fissure, I estimate that the R-K eruption produced $<1 \text{ km}^3$ of lava. This calculation ignores the contribution from pyroclasts, commonly considered a minor contribution during basaltic fissure eruptions (Thordarson and Self 1993). The lavas are differentiated by crust morphology, vesicle structure, internal texture and jointing. The groundmasses of the lavas also display differences in crystallinity and texture (Fig. 3.14). The density of lavas with an inferred pyroclastic origin is shown in Fig. 3.15. Their petrography is summarised in Table 3.4.

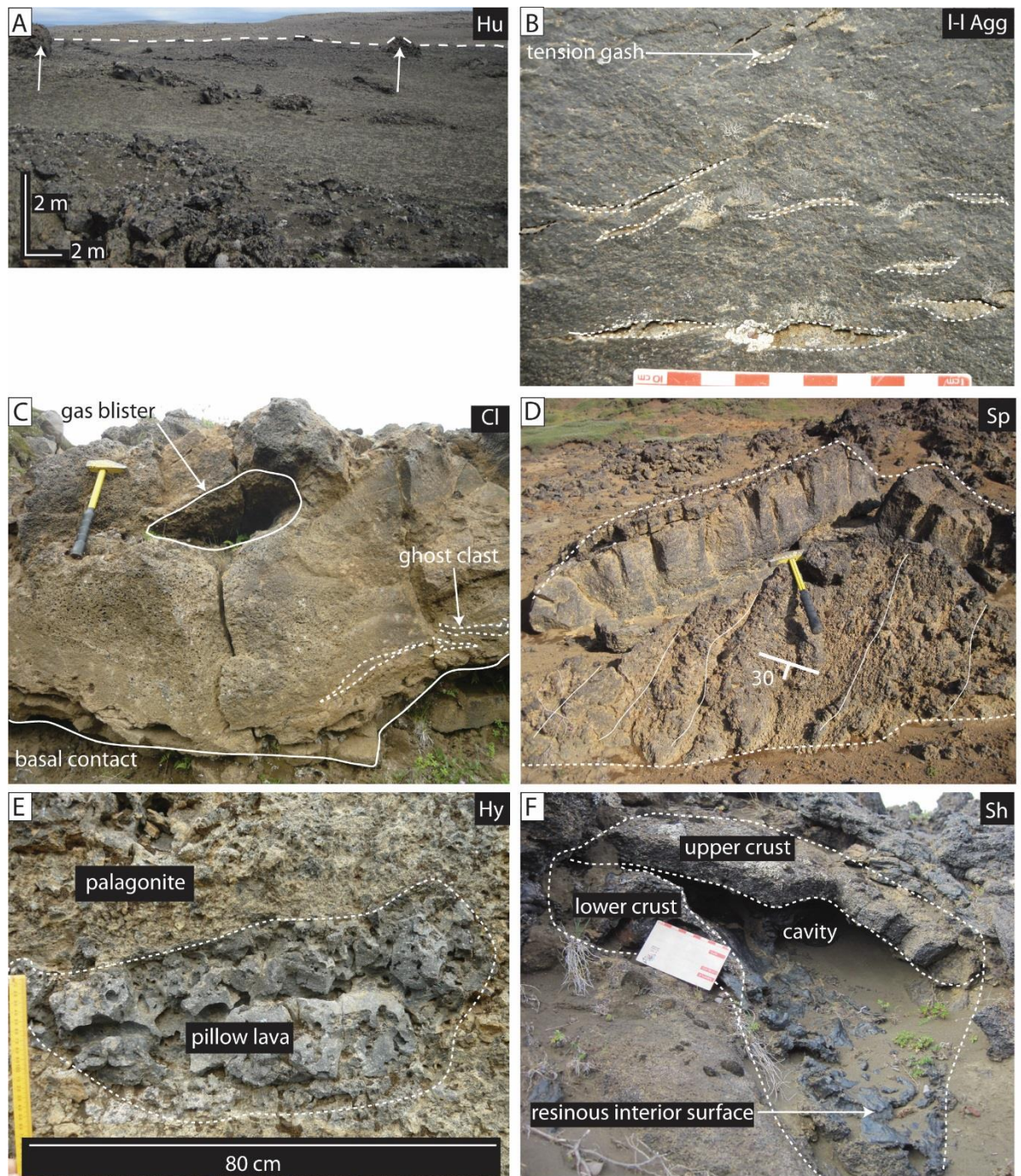


Figure 3.13. Lavas observed in the study area. (A) Hummocky lava (Hu) with little erosional dissection. Tumuli and squeeze outs (arrowed) create the hummocky topography. The contact with pre-existing topography is marked by the dashed line. (UTM 556219/7266138). (B) Lava-like agglutinate. Tension gashes (dashed outline) are sub-parallel to the basal contact (UTM 557447/7264902). (C) Clastogenic pāhoehoe (Cl). Gas blisters (outlined) are common. Ghost clasts are identified by intensely deformed non- and incipiently vesicular patches (dashed outline). (UTM 556985/7264113). (D) Crust of spiny pāhoehoe (dashed outline). The crust dips 30°

toward the viewer. Spines on the surface of the crust are oriented parallel to the solid white lines. Hammer for scale. (UTM 557457/7265092). (E) Hyaloclastite. The pillow lava (dashed outline) occurs in a matrix of palagonitised pillow fragments. (UTM 558272/7263904). (F) Shelly pāhoehoe. The crusts and internal cavity is visible. The resinous interior surface is thought to be caused by draining of lava from the lobe (UTM 557463/7264067).

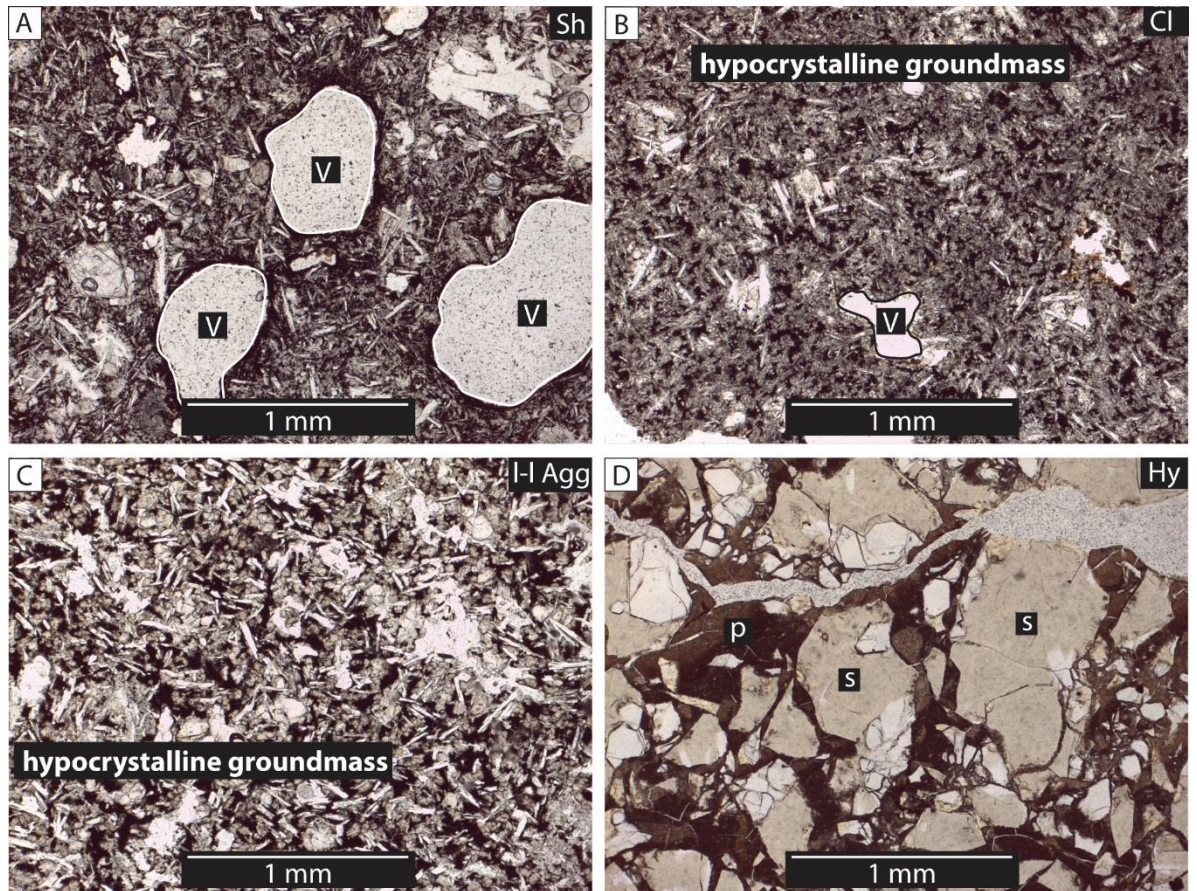


Figure 3.14. Thin section images of lavas (plane polarised light). (A) Shelly pāhoehoe. Note the large vesicles. (B) Clastogenic pāhoehoe. (C) Lava-like agglutinate. (D) Hyaloclastite. The thin section is taken from the palagonite matrix. Vesicles are labelled v; sideromelane fragments are labelled s and palagonite is labelled p.

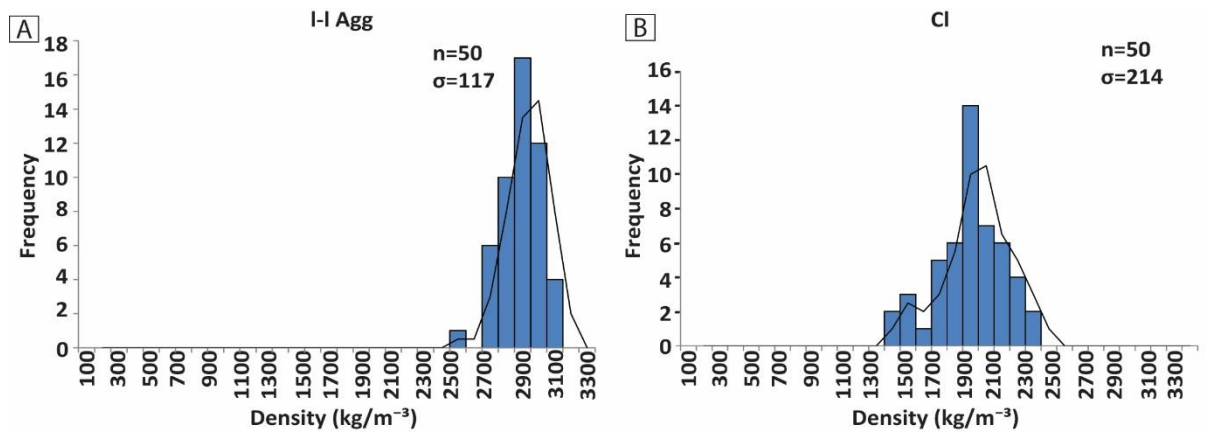


Figure 3.15. Density histograms for lava lithofacies with a pyroclastic origin. (A) Lava-like agglutinate. (B) Clastogenic lava.

Lava type	Crystallinity (%)	Density Mean (kg m ⁻³)	Density range (kg m ⁻³)	Vesicularity mean (%)	Vesicularity range (%)	Vesicle diameter (mm)	Lithofacies thickness range (mm)	Interpretation
Cp	-	-	-	30	-	-	1500–20000	Inflated pāhoehoe lava, sheet-like or hummocky flows
Cl	85	1943	1450–2322	35	22–51	-	510–3700	Produced by coalescence and subsequent flow of pyroclasts from the inner part of the lava fountain or a low fountain; lava possessed a yield strength on degassing; likely to contain a component of effused lava
Hu	-	-	-	-	-	-	-	Inflated pāhoehoe lava
I-I Agg	75	2747	2461–2964	8	1–17	<0.1–0.55	500–29000	Produced by coalescence and subsequent flow of pyroclasts from the inner part of the lava fountain or a low fountain
Sp	-	-	-	-	-	-	-	Down-flow transition of pāhoehoe caused by increase in substrate inclination
Hy	-	-	-	-	-	-	-	Formed by the entry of lava into bodies of surface water
Sh	34	-	-	-	-	-	255 – 1620	Gas rich lava effused from vents, also found as rafted debris and/or breakouts from parent clastogenic flows
Dyke*	86	-	-	-	-	-	-	Feeder dyke for the R-K eruption
Table 3.4. Summary table of lavas and dyke (* sample depth 80 m beneath paleo-surface)								

Cp – Columnar-jointed pāhoehoe

Columnar-jointed pāhoehoe outcrops on the Jökulsá canyon walls and many of the outcrops are inaccessible. Where accessible, the flows are characterised by a layered structure defined by vesicle abundance. The upper vesicular crust constitutes 25% of the flow thickness (Fig. 3.11) and is ~30 % vesicular (visual estimate). Megavesicles (Fig. 3.16) occur at the base of the crust (e.g. Thordarson and Self 1998). The dense core of the flows constitutes 75% of the flow thickness. The lower 10% of the core often has a sub-horizontal platy fabric, defined by fractures spaced 5–30 mm (Fig. 3.16). Vesicle cylinders are also found within the core (Fig. 3.16). The bases of the flows have not been observed. The flows are characterised by columnar joints that define a colonnade and an entablature. The joints are spaced 15–215 mm in the crust (mean 131 mm) and 250–450 mm in the cores (mean 352 mm). The basalt occurs on sub-horizontal slopes and has a morphology that varies from hummocky to sheet-like. The sheet-like units (Fig. 3.16) maintain a near-constant thickness across their length and have sub-parallel upper and lower contacts. The hummocky flows (Fig. 3.16) have an irregular shape and complex contacts between their cores and crusts.

The pāhoehoe flows vary from 1.5–20 m in thickness. They occur throughout the R-K volcanic sequence, though sheet-like units are dominant towards the base. The basalt often forms ≥ 50 % of the total stratigraphic thickness of the R-K eruption products. Spatially, the columnar-jointed pāhoehoe is generally confined within the Sveinar graben. The eastern Sveinar graben fault is poorly defined south of the river and occurs as segmented faults (F 31–33; Fig. 3.4). Fault 31 dips sub-vertically southeast whilst faults 32 and 33 dip sub-vertically northwest. The faults do not offset the R-K volcanic sequence but create thickness variations in the columnar-jointed pāhoehoe (Cp). West of the river fault 33 offsets the pre-eruptive topography by up to 20 m and the columnar-jointed pāhoehoe (Cp) pinches out against the footwall. There is 6 m of displacement of the columnar-jointed pāhoehoe (Cp) which has been emplaced on the graben footwall.

Northwest of the dyke the columnar-jointed pāhoehoe (Cp) has a distinct, sub-horizontal upper contact with the overlying clast-supported incipiently welded spatter bombs (waSp), clast-supported weakly agglutinated scoria lapilli and bombs (waSc) and hummocky pāhoehoe (Hu). The basalt contains lenses of clast-supported weakly agglutinated scoria lapilli and bombs (waSc) up to 10 m in diameter. At location 292 contacts are distinct with the overlying massive scoria lapilli and bombs (mSc).

Interpretation:

The vesicle-defined layered structure indicates that the columnar-jointed pāhoehoe inflated. Inflation requires emplacement on low angle slopes, a continued and sustained input of lava beneath a cooled crust and low effusion rates (e.g. Hon et al. 1994; Self et al. 1998). Many inflated lavas are also clastogenic in origin, but little evidence of their clastogenic origin is retained (Thordarson and Self 1993). The platy zone of the lavas records late stage horizontal shear along internal velocity boundaries in active lavas (Mackin 1961). The presence of entablature jointing suggests water-induced cooling (e.g. Long and Wood 1986; Forbes et al. 2012; Forbes et al. 2014), possibly caused by the lavas damming rivers. However, there are no foreset-bedded pillow breccias associated with the lavas (e.g. Huscroft et al. 2004) or lava channelization Hamblin (1994), commonly associated with lava dams.

The sheet-like flows are inferred to result from higher effusion rates and/or lower gradient slopes (Self et al. 1998). The hummocky flows indicate a moderate effusion rate/lava flux and/or increased substrate inclination. These factors resulted in differential inflation and the failure of numerous lobes to coalesce (Self et al. 1998; Guilbaud et al. 2005).

The stratigraphic thickness and abundance of the columnar-jointed pāhoehoe (Cp) suggests that inflation of pāhoehoe lobes was the dominant emplacement mechanism during the early stages of the R-K eruption. The pinching out of the columnar-jointed pāhoehoe (Cp) against the footwall of fault 33 suggests that the fault existed prior to the eruption. Thickness variations in the columnar-jointed pāhoehoe (Cp) overlying faults 31–33 suggest that either the faults developed during the eruption and the overlying lavas were viscous enough to have deformed in a ductile fashion, or that the faults pre-dated the eruption.

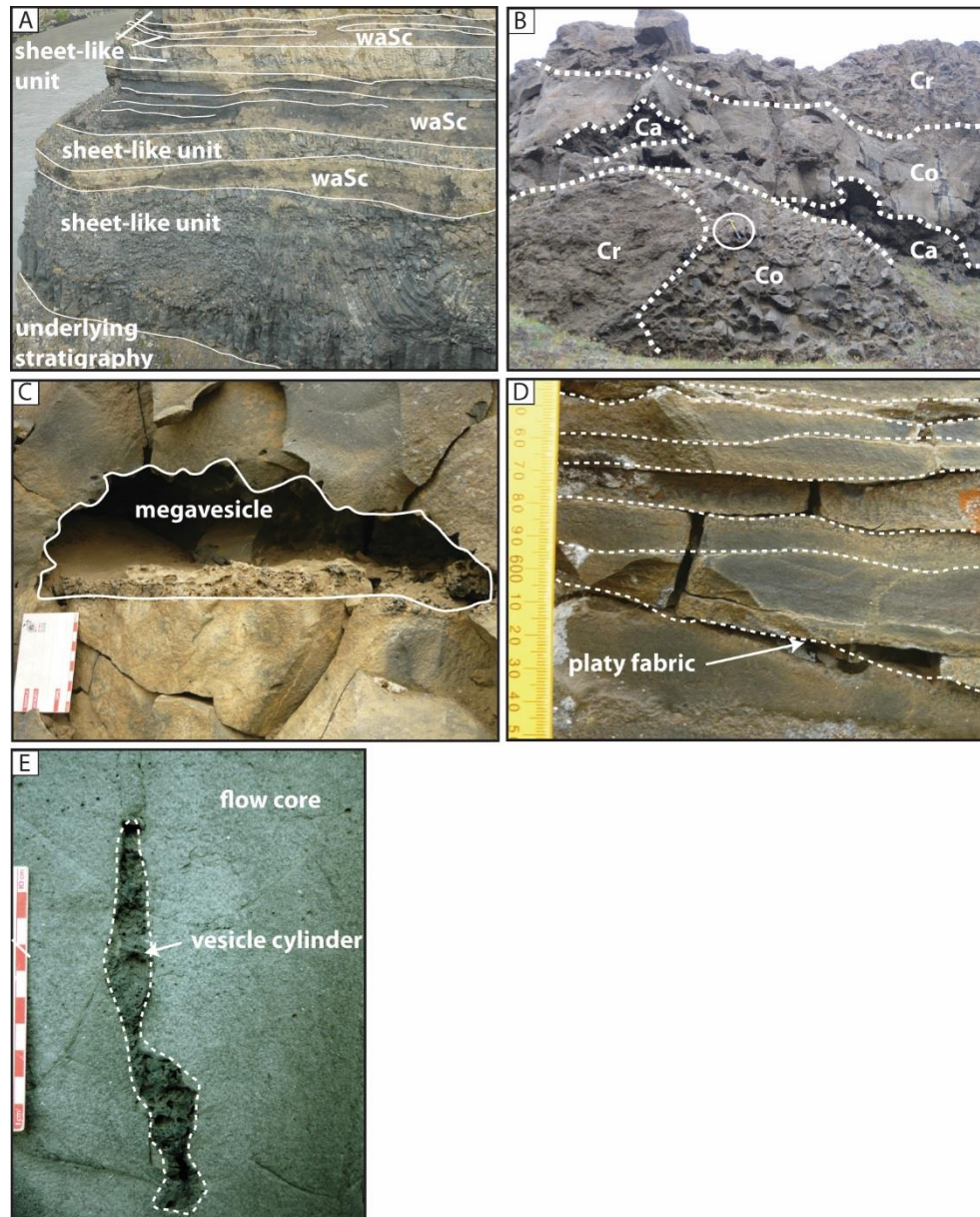


Figure 3.16. Features of the columnar-jointed pāhoehoe. (A) Alternating beds of sheet-like columnar-jointed pahoehoe (Cp) and clast-supported weakly agglutinated scoria lapilli and bombs (waSc) (UTM 557469/7264936). (B) Hummocky morphology flow (sensu Self et al. 1998); Cr: crust, Co: core, Ca: cavity. The hammer (circled) is 30 cm long. (UTM 557145/7265409). (C) Megavesicle in the flow core. Graticules on the scale card are 10 cm. (UTM 557772/7265756). (D) Platy fabric observed towards the base of the flow. The scale on the ruler is mm. (UTM 557772/7265756). (E) Vesicle cylinder in the core of a flow. Graticules on the scale card are 1 cm. (UTM 557544/72651054).

Cl – Clastogenic pāhoehoe

These lava flows have a ropey upper surface. Their groundmass is composed of hypocrySTALLINE, highly deformed and coalesced agglutinate with rare cored bomb ghost clasts (Fig. 3.17). They have a mean vesicularity of 35%, ranging from 22–51%. Vesicles are sub-horizontally aligned in bands ~10 cm thick or are randomly oriented. Vesicles are distributed throughout the flows. The density of the lava ranges from 1450–2322 kg m⁻³ (mean 1943 kg m⁻³). Ghost clasts occur throughout the entire thickness of the flow but are more common toward the base. They are 80–3700 mm in length with aspect ratios of 1:2–1:93. Gas blisters ~190 × 220 mm in size occur in many of the flows, often at or above the horizontal medial plane. The vesicularity of the lava increases towards the gas blisters forming an upper, spongy-type crust. This spongy crust lacks ghost clasts and is ~20 cm thick. Numerous shelly pāhoehoe crusts occur overlying the gas blisters and merge laterally with the clastogenic flows.

Many of the flows have columnar cooling joints spaced 230–1000 mm that penetrate downwards from the crust through 10–100% of the thickness of the flow. Lavas found within northwest/southwest oriented grabens display hackly jointing (Fig. 3.17). The hackly jointing is composed of two joint sets: master joints (spaced 8–108 cm) and sub-set joints (spaced 25–180 mm) that splay from the master joints.

Clastogenic lava occurs up to ~2 km from the vents. The lava flows thicken into topographic lows forming flows 51–370 cm in thickness. Between faults F9 and F12 (Fig. 3.4) the lava overlies hyaloclastite. The flows onlap onto the base of pyroclastic deposits (location 477; see section 3.7) and are dominant towards the South of the study area. The flow field is faulted by the F33 west of river (Fig. 3.4) but is unaffected by faulting east of the river. The clastogenic lava is overlain by hummocky lava in the north of the study area; in the south it is overlain by the spatter and scoria ramparts (Figs. 3.3 and 3.11).

Interpretation:

The clastogenic origin of the lava is evidenced by abundant ghost clasts sourced from the inner part of the lava fountain or from a low fountain that yielded a high proportion of spatter bombs (e.g. Wolfe et al. 1988; Head and Wilson 1989; Sumner et al. 2005). These lavas may also contain a component of effused lava, as observed in contemporary eruptions (Wolfe et al. 1988).

The pāhoehoe morphology indicates relatively low shear rates during emplacement. The sub-horizontal alignment of vesicles suggests late stage flow of lava causing

unidirectional simple shear (e.g. Walker 1989; Polacci et al. 1999). The medial gas blisters are a feature common to P-type, S-type and toothpaste pāhoehoe (Rowland and Walker 1987; Walker 1989; Wilmoth and Walker 1993) and indicate that the lavas possessed a yield strength on degassing (Walker 1989). This yield strength may result from the partial cooling and crystallisation of constituent pyroclasts during flight. Yield strength can also be acquired when lava vesicularity is >30% and forms a foam (Wilmoth and Walker 1993). The shelly pāhoehoe crusts that overlie the lavas may have been rafted from proximal regions. Alternatively, they may be breakouts or overspills from the parent clastogenic flow.

The absence of a tri-partite pāhoehoe structure within the flows suggests that they did not inflate and instead the clastogenic flow field grew exogenously. The hackly jointing suggests interaction between the cooling flows and surface water (Long and Wood 1986), likely related to flooding by rivers. These joints are similar to pseudopillow fracture systems (e.g. Forbes et al 2012), and may suggest that at some locations lava flows penetrated into bodies of open water.

In the north the lava was produced prior to the emplacement of hummocky lava. The clastogenic lava is the youngest lava in the south. The displacement of the lava by fault 33 indicates that slip occurred after the eruption.

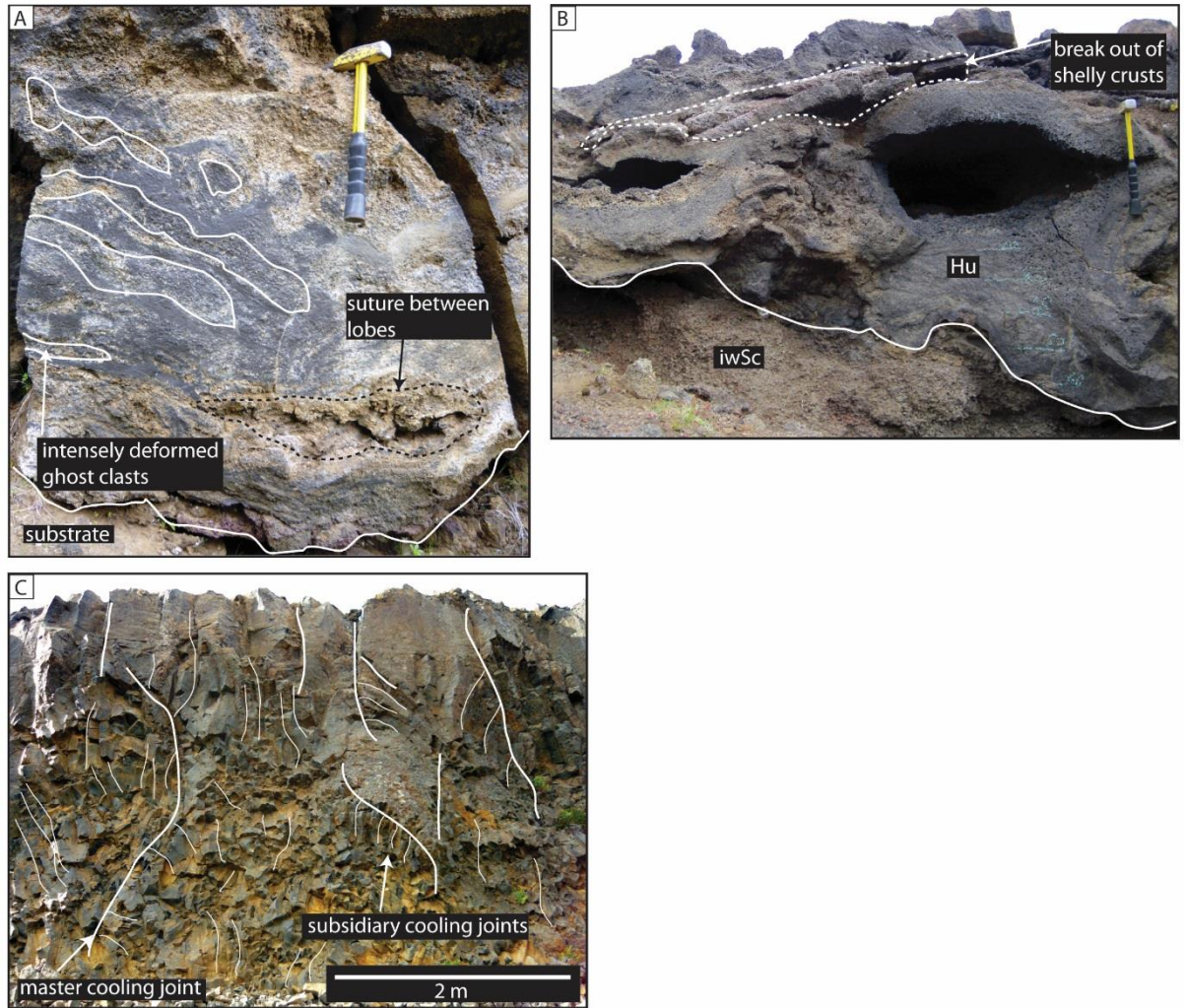


Figure 3.17. Features of the clastogenic lava. (A) Photograph showing the internal texture of the clastogenic flows, with highly deformed ghost clasts and a suture between lobes towards the base. Hammer for scale. (B) Clastogenic lava with a break out of shelly lava. The shelly lava has been subsequently covered by later clastogenic breakouts. Hammer for scale. (UTM 556985/7264113). (UTM 557465/7266307). (C) Clastogenic lava that has been flooded with water during cooling. The lava has a distinctive entablature comprised of two dominant sets of joints, in which the subsidiary set radiate from the master set. (UTM 556935/7263621).

Hu – Hummocky pāhoehoe

Hummocky pāhoehoe is recognised solely by surface textures and topography because there are no sections through the lava flow (Hu; Fig. 3.3). Numerous tumuli and squeeze-outs (Fig. 3.18) are observed throughout the flow field (Fig. 3.3). The tumuli range from 0.5–1 m in height and 1–2 m in diameter. They have a sub-circular shape in plan view. The squeeze-outs range from 1.5–2.5 m in height and are 1–4 m in diameter. They are sub-

circular to elongate in plan view and are composed of numerous ~10 cm thick crusts that dip radially outwards from their centre (Fig. 3.18). Sub-parallel ~3 mm deep grooves 1–3 mm wide occur on the outer surfaces of crusts, oriented parallel to the direction of dip.

Lava tubes 1 m in diameter occur east of the river and strike 280° (approximately perpendicular to the fissure). There is no evidence for overlying tumuli. The tubes have horizontal grooves along their internal surfaces and lava benches at 0.2 and 0.4 m height (Fig. 3.18). Channels occur west of the river (Fig. 3.18). They are <0.5 m in depth and ~4 m wide and their internal surfaces dip ~3°. The internal surfaces of the channels are marked by sub-vertical striations. The channels plunge 025° and 100° (Fig. 3.3).

Hummocky pāhoehoe outcrops over >0.25 km² to the north of the study area. It forms the uppermost unit of the R-K eruption sequence in medial and distal regions and overlies clastogenic lava (Cl, see above; Fig. 3.3). Within 600 m of the fissure, hummocky pāhoehoe is locally overlain by spiny pāhoehoe (Sp; see below) and shelly pāhoehoe (Sh; see below) and by clast-supported, incipiently–densely welded scoria and spatter bombs (waSc–dwSc; waSp–dwSp; Fig. 3.3). Outcrops in the northeast of the study area show that hummocky pāhoehoe passes downstream into spiny pāhoehoe where the slope increases; transitions in surface morphology have not been observed elsewhere.

Interpretation:

Tumuli indicate that the hummocky lava grew by inflation (e.g. Walker 1991) and the tubes indicate that the lava was fed by an arterial network on the east of the river. These arterial networks suggest that the lava was emplaced over slopes of >1–2° (e.g. Hon et al. 1994). The squeeze-outs indicate regions in a compressional regime (e.g. Sumner 1998) and are used to infer the margins of the flow. Scours on the flow crusts are inferred to have formed during extrusion of lava. The channels represent paleoflow networks in the flow field; their dip indicates the lava paleoflow direction (i.e. northeast and southeast; see Fig. 3.3). The vertical striations on the internal channel walls indicate draining of lava and sliding of solid crust during flow.

The hummocky pāhoehoe is inferred to have been sourced from vents in the north. It is the youngest R-K product in medial and distal regions. The down-flow transition from hummocky to spiny pāhoehoe suggests an increase in shear rate within the lava, caused by steeper slopes (e.g. Peterson and Tilling 1980).



Figure 3.18. Hummocky lava features. (A) A tumulus, with the upper crust partially eroded and the core exposed. Hammer for scale. (UTM 556481/7266232). (B) A lava channel on the surface of the flow field. The channel has resinous walls with vertical striations caused by the draining of lava within the channel. Direction of flow is inferred from the slope (toward viewer). The channel is ~3 m wide. (UTM 547155/7208827). (C) An elongate squeeze out at the margin of the flow field. The squeeze out is composed of numerous crusts that dip radially from the centre of the structure. Hammer for scale. (UTM 556215/7266339). (D) Photograph of the inside of a lava tube. Backpack for scale. (UTM 557462/7265995).

1-l Agg – Lava-like agglutinate

This lava is composed of dense to incipiently vesicular, highly deformed to coalesced hypocrySTALLINE agglutinate. Relict pyroclasts with vague outlines are present and account for ≤ 2 vol. % of the lava. These clasts are elongate (aspect ratios 1:8–1:40), 16–480 mm in

diameter and contain irregular vesicles <1 mm size. These clasts are occasionally overprinted by spherical vesicles 1–5 mm in diameter. The clasts are oriented parallel to the upper surface. Rectangular clasts are 70–200 mm in size and have spherical vesicles >1 mm size separated by ~1 mm thick septae (Fig. 3.19). They have no preferred orientation. 100–200 mm sized ghost clasts of non-vesicular, sub-spherical cored bombs are also found (Fig. 3.19). The agglutinate has mean vesicularity of 8% (range 1–17) and its mean density is 2747 kg m⁻³ (range 2461–2964 kg m⁻³).

The lava flows commonly exhibit ~100 mm long tension gashes that penetrate from their upper surface toward their centre (Fig. 3.19). Tension gashes also occur within the cores of lavas and are oriented sub-parallel to the upper and lower surfaces. The basal contacts of the agglutinate dip ≤5–60°. They form sheet-like flows with sub-parallel upper and lower contacts. They maintain a near-constant thickness across their length.

The lava-like agglutinate varies from 0.5–2.9 m in thickness. It is only found in the upper 15 m of the R-K volcanic sequence (in the crater of edifice 26) and within the spatter ramparts. Contacts with other units are complex: they may be gradational, distinct or locally intrusive into overlying pyroclastic units (e.g. clast-supported weakly agglutinated scoria lapilli and bombs; waSc), as observed within the crater of edifice 26 (log 81, Fig. 3.10).

Interpretation:

Ghost clasts indicate the agglutinate is clastogenic in origin. They are interpreted to have rapidly accumulated from the inner part of a lava fountain during high intensity fountaining, or from low fountains that yielded a high proportion of spatter bombs (e.g. Wolfe et al. 1988). The rectangular ghost clasts have a similar vesicularity and vesicle shape to pāhoehoe lava crust and are interpreted as fragments of entrained lava crust. Cored bombs are interpreted as for clast-supported weakly agglutinated spatter bombs (waSp).

The absence of a vesicular crust in the agglutinate flows suggests that they did not inflate and instead grew exogenously, most likely via the coalescence and subsequent flow of pyroclasts. Tension gashes are the result of shear within moving mass (e.g. Sumner 1998) and thus indicate late stage flow. The restriction of the agglutinate to within the edifices suggests that they formed only from the accumulation of clasts from the lower and inner parts of the fountain during the edifice-forming stages of the eruption.

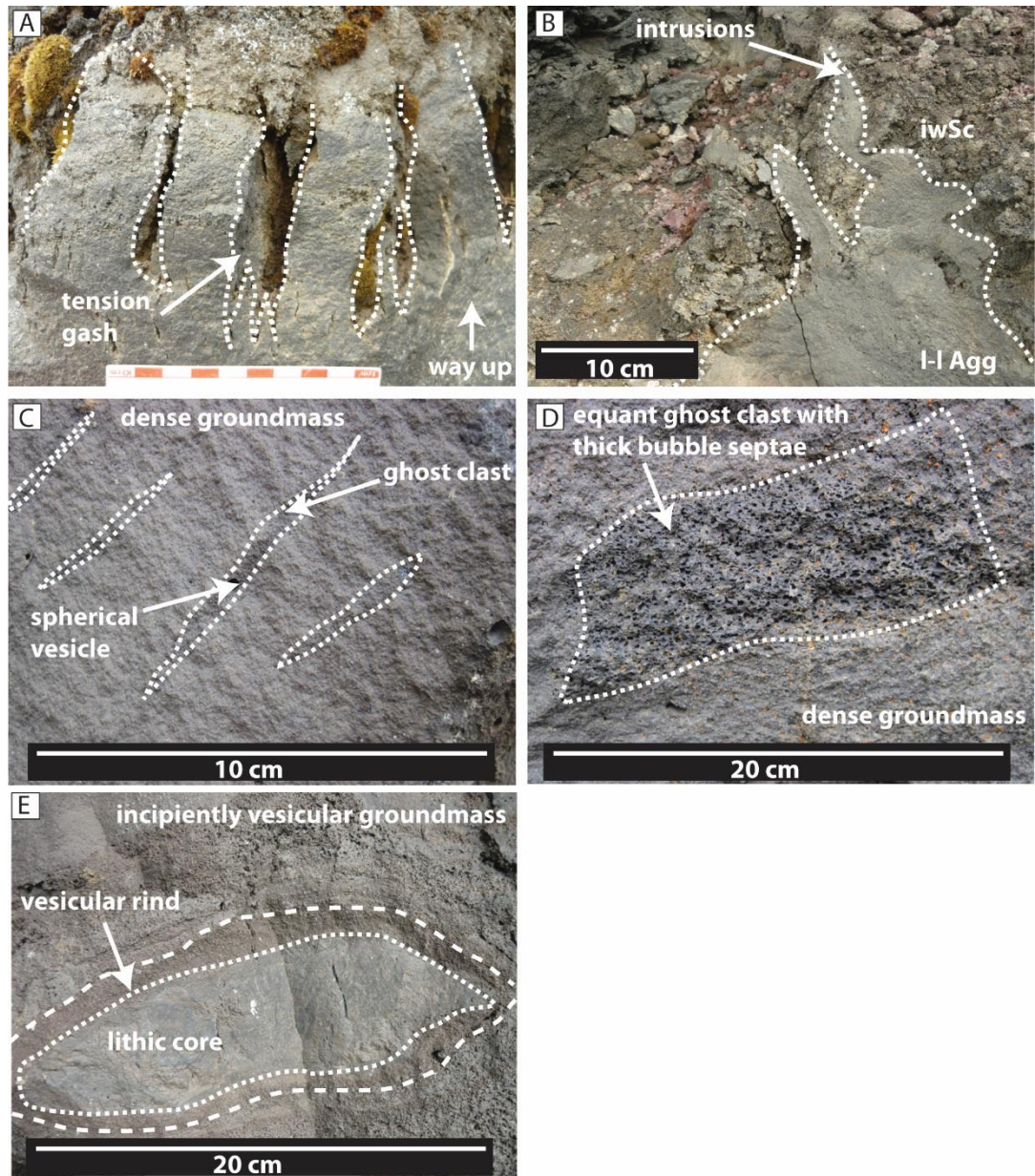


Figure 3.19. Features of the lava-like agglutinate (l-l Agg). (A) Tension gashes at the top of unit 5 in log 81. Graticules on the scale card are 1 cm, the arrow indicates up. (UTM 557442/7264902). (B) Intrusion of lava-like agglutinate (l-l Agg) into overlying clast-supported weakly agglutinated scoria lapilli and bombs (waSc). Dashed line indicates contact. (UTM 557442/7264902). (C) Ghost clasts (outlined) in lava-like agglutinate (l-l Agg), overprinted by a spherical vesicle (arrowed). These spherical vesicles suggest post depositional vesiculation of the lava. (UTM 557772/7265756). (D) Equant ghost clast (outlined) interpreted to represent a lava crust lithic. Compare this ghost clast with those in C and clast-supported moderately welded spatter bombs (mwSp; Fig. 3.7). (UTM 557772/7265756). (E) Cored bomb with a rind of vesicular juvenile magma. The core is composed of dense agglutinate. (UTM 557442/7264902).

Sp – Spiny pāhoehoe

Spiny pāhoehoe is recognised by its spinose surface that forms lineations parallel to the direction of effusion (Fig. 3.13). It occurs at the base of a slope near vent 22. Its up-flow morphology is unclear. The lava covers an area 0.05 km² in size. The lack of cross sectional exposure means that the internal features of the lava cannot be determined.

Interpretation:

Spiny pāhoehoe is transitional between pāhoehoe and a’ā lava types (Rowland and Walker 1987). The occurrence of the spiny pāhoehoe at the base of a break in slope suggests that the change in slope increased the shear rate within the lava (e.g. Peterson and Tilling 1980).

Hy – Hyaloclastite and pillow lavas

Hyaloclastite is composed of pillow lavas in a palagonitised matrix of pillow fragments. There is an upwards transition from coherent (pillow-dominated) to fragmental (palagonite-dominated) deposits (log 7, Figs. 3.10 and 3.20). The coherent units are 0.5–1 m thick and are composed of interlocking, sub-circular pillows that are 900 × 900 mm size. At their margins they have 2–4 cm thick chilled rinds which are often detached from the pillow (Fig. 3.20). Grading towards the core is a 5 cm wide zone characterised by 20 vol. % elongate vesicles that have their longest axis aligned parallel to the margin of the pillow. These vesicles are <1 cm in diameter. The cores of the pillows are characterised by large (~10 cm diameter) irregular vesicles that account for 10 vol. %. The fragmental deposits are 3.4–4 m thick and are composed of similar sized pillows with irregular shapes. These pillows are clast-supported in a lapilli–ash size palagonitised matrix of brittle quench fragments with pebble–block sized pillow fragments. The pillow fragments are commonly portions of the core or spalled rinds. The hyaloclastite deposits are 4.4–4.5 m thick. No structure (e.g. layering or dipping pillows) is observed. The hyaloclastite is overlain by clastogenic pāhoehoe (Cl) and underlain by fSxb (Figs. 3.11, 3.21 and 3.22). It occurs in the southern section of a graben that strikes 015° and is confined within faults F9 and F12 (Fig. 3.4).

Interpretation:

This lithofacies indicates interaction between pāhoehoe lava and bodies of surface water. Based on the thickness and extent of the hyaloclastite, the water body is inferred to

have been ≥ 4 m in depth and have extended laterally for ≥ 630 m. The pillow-dominated deposits are inferred to indicate the progressive penetration of small lobes of lava into water (the hP facies of Watton et al. 2013). The overlying fragmental deposits are interpreted as pillows engulfed by quenched debris during the passage of debris slurries from up-flow (the iP facies of Watton et al. 2013). Thus, the upwards transition from pillow-dominated to fragmental deposits is representative of a lava delta developing in a basin with steep banks (e.g. Watton et al. 2013). This delta may have temporarily dammed the water body (e.g. Hamblin 1992; Huscroft et al. 2004).

The overlying contact with the clastogenic pāhoehoe (CI) indicates that early lavas interacted with water forming hyaloclastite, whilst later lava flows did not. Whether the pillow lavas are lateral transitions of the clastogenic pāhoehoe (CI) or other lava flows produced during the eruption is unknown. The surface water supply was later cut-off (e.g. by lava damming of a river) or exhausted before emplacement of later lavas. Pillow lavas built up out of the water – essentially pushing the ‘shoreline’ backwards. The occurrence of the hyaloclastite within a graben suggests that the hyaloclastite is occupying a location that previously represented a river channel. The river channel existed prior to the eruption and occupied a graben formed by faults 9 and 12.



Figure 3.20. Features of the hyaloclastite. (A) Photograph showing the stratigraphic relationship of hyaloclastite and pillow lavas (Hy) with clastogenic pāhoehoe (Cl) and fSxb (UTM 557949/7263864). (B) Vertical section through the pillow-dominated and fragmental hyaloclastite. This section is also represented in log 7; Fig. 3.10 (UTM 557908/7263830). (C) Detail of a pillow lava. The chilled rinds have spalled or been abraded from the majority of the pillow. The aligned vesicles occur in a zone 5 cm wide. The core has large, irregular vesicles (UTM 558272/7263904).

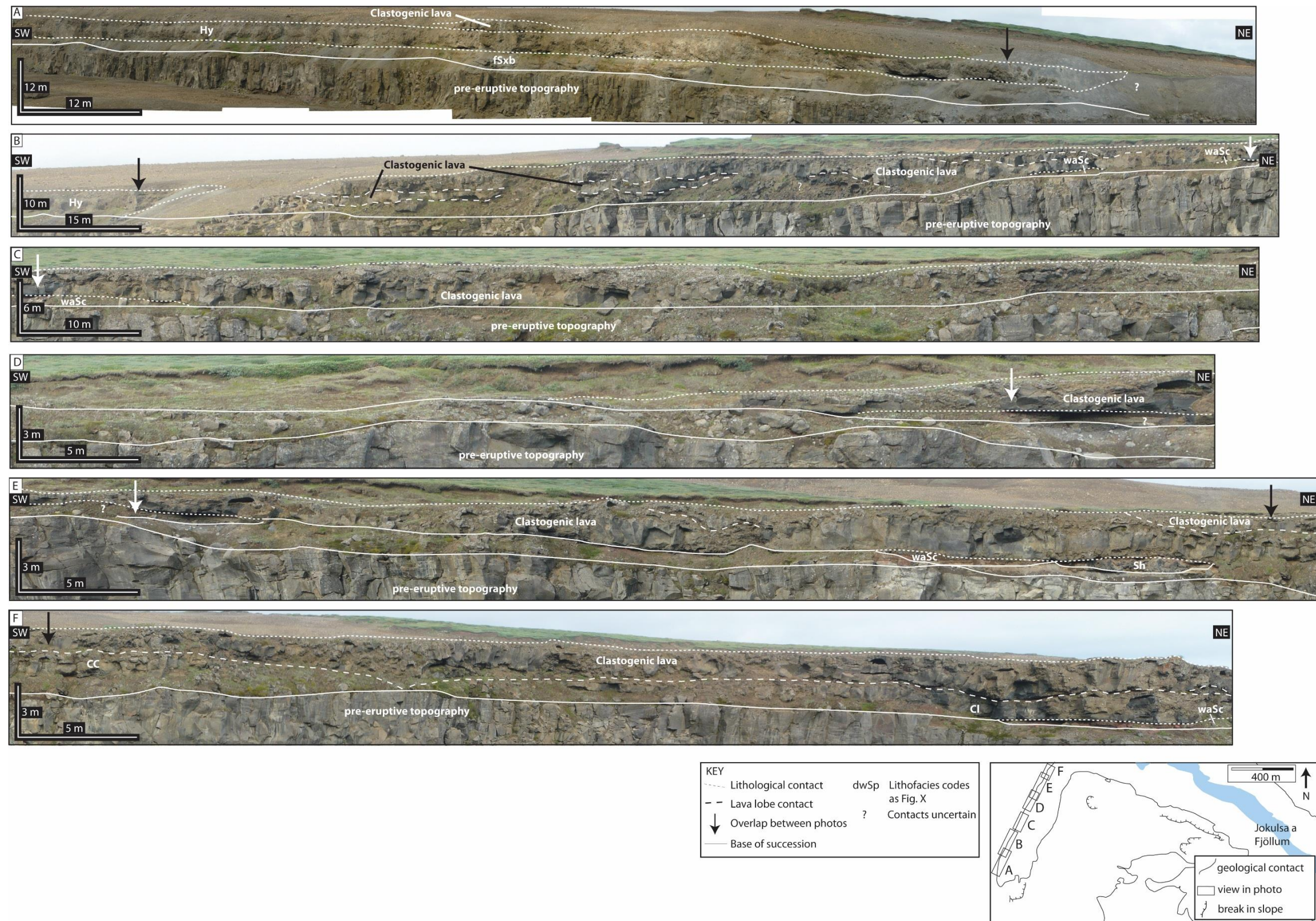


Figure 3.21. Panoramic photos of the western wall of the graben formed by faults F9 and F12. The photos show that the area is dominantly composed of clastogenic lavas underlain by lobate beds of clast-supported weakly agglutinated scoria lapilli and bombs (waSc) <0.5 m in thickness. 3 m wide flows of shelly pāhoehoe are also observed. Hyaloclastite thickens towards the southwest (Fig. 3.3) and is inferred to be underlain by fSxb, as observed on the east of the graben (Fig. 3.22). (A: UTM557585/7264214; B: UTM557595/7264181; C: UTM557601/7264125; D: UTM557616/7264059; E: UTM557649/726; F: UTM 557656/7263914).

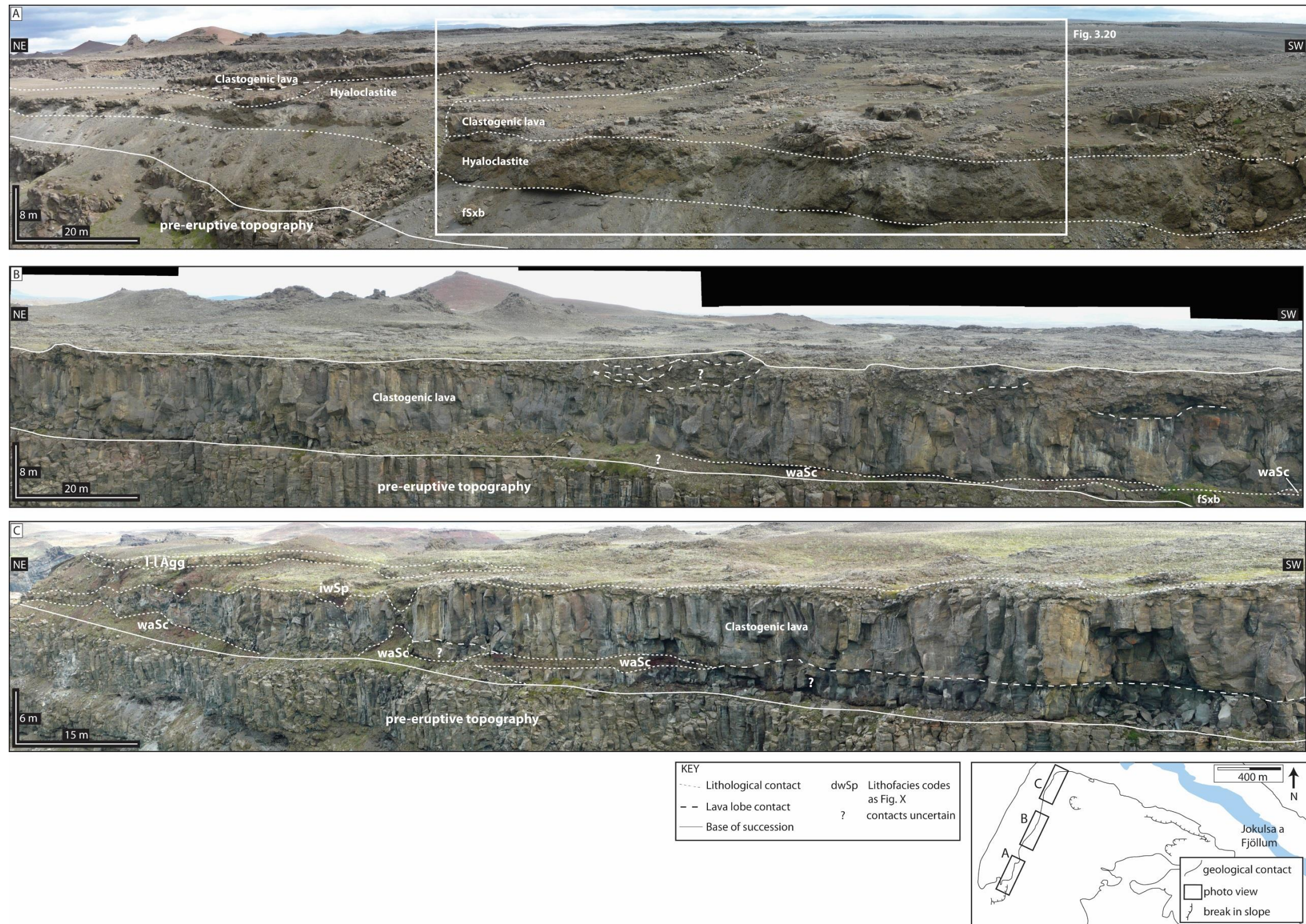


Figure 3.22. Panoramic photos of the eastern wall of the graben formed by faults F9 and F12. The photos show that the area is composed of clastogenic and hummocky lavas underlain by lobate beds of clast-supported weakly agglutinated scoria lapilli and bombs (waSc) <0.5 m in thickness. The contacts between the hummocky and clastogenic lavas are unclear. Numerous lobes 1–5 m thick are observed within the clastogenic lavas. Hyaloclastite thickens towards the southwest (Fig. 3.3) and is underlain by fSxb. Note the absence of Clast-supported weakly agglutinated scoria lapilli and bombs (waSc) at the base of the stratigraphy in (A), suggesting either that this section of the fissure was dominated by effusive activity, or that the pyroclasts coalesced to form lava which subsequently interacted with surface water (forming hyaloclastite). (A: UTM 557934/7263920; B: UTM 558083/7264079; C: UTM 557849/7264219).

Sh – Shelly pāhoehoe

Shelly pāhoehoe flows are composed of numerous 10–200 mm thick crusts that are often contorted. The groundmass is hypohyaline to hypocrystalline, and has an estimated vesicularity of 30 % (estimated with a grain size card). Crusts contain homogeneously distributed spherical and distorted vesicles. Flows often have large ($\sim 420 \times 60$ mm) gas cavities in their centres, with resinous surfaces forming the interior surfaces of the crusts. Shelly pāhoehoe occurs as breakouts from clastogenic pāhoehoe (Cl) lava flows and is also found within the openings of horseshoe-shaped scoria cones at the top of the R-K volcanic sequence (Fig. 3.23). The crusts occur in successions ranging from 255–1620 mm in thickness. The lava occurs as broad (>5000 mm wide) or as narrow (300 mm wide) lobes (Fig. 3.3). The flows cover an area 0.2 km^2 in size.

Interpretation:

Shelly pāhoehoe is a gas-rich lava (e.g. Swanson et al. 1975) and its occurrence as break-outs suggests that the parent flow clastogenic pāhoehoe (Cl) was also gas-rich. The resinous interior of the flow is inferred to be caused by lava draining from the flow, perhaps indicating a channel or tube system within the shelly pāhoehoe flows (e.g. Stevenson et al. 2012). Its occurrence at the opening of scoria cones suggests that the lava was effused from the vent late in the development of the fissure, although it may have accumulated from low (<100 m) lava fountains (e.g. Swanson et al. 1975).

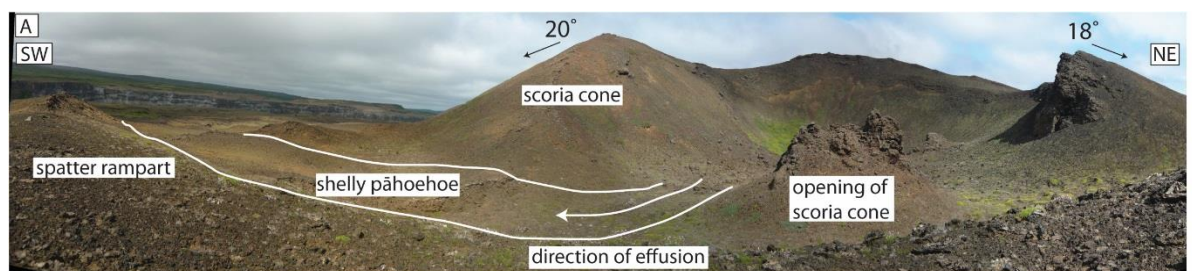


Figure 3.23. Photograph showing shelly pāhoehoe at the opening of a horseshoe-shaped scoria cone (UTM 557647/7265074).

3.6 Sedimentary lithofacies

The sedimentary lithofacies (Fig. 3.24; Table 3.5) are composed of basaltic sandstones and breccias consisting of basaltic pyroclasts and lava flow fragments. East of the river the sediments are confined to the top of the stratigraphy, whilst west of the sediments occur

both beneath and within the R-K volcanic sequence (Fig. 3.10 and 3.11). The sediment outcrops on both sides of the fissure.

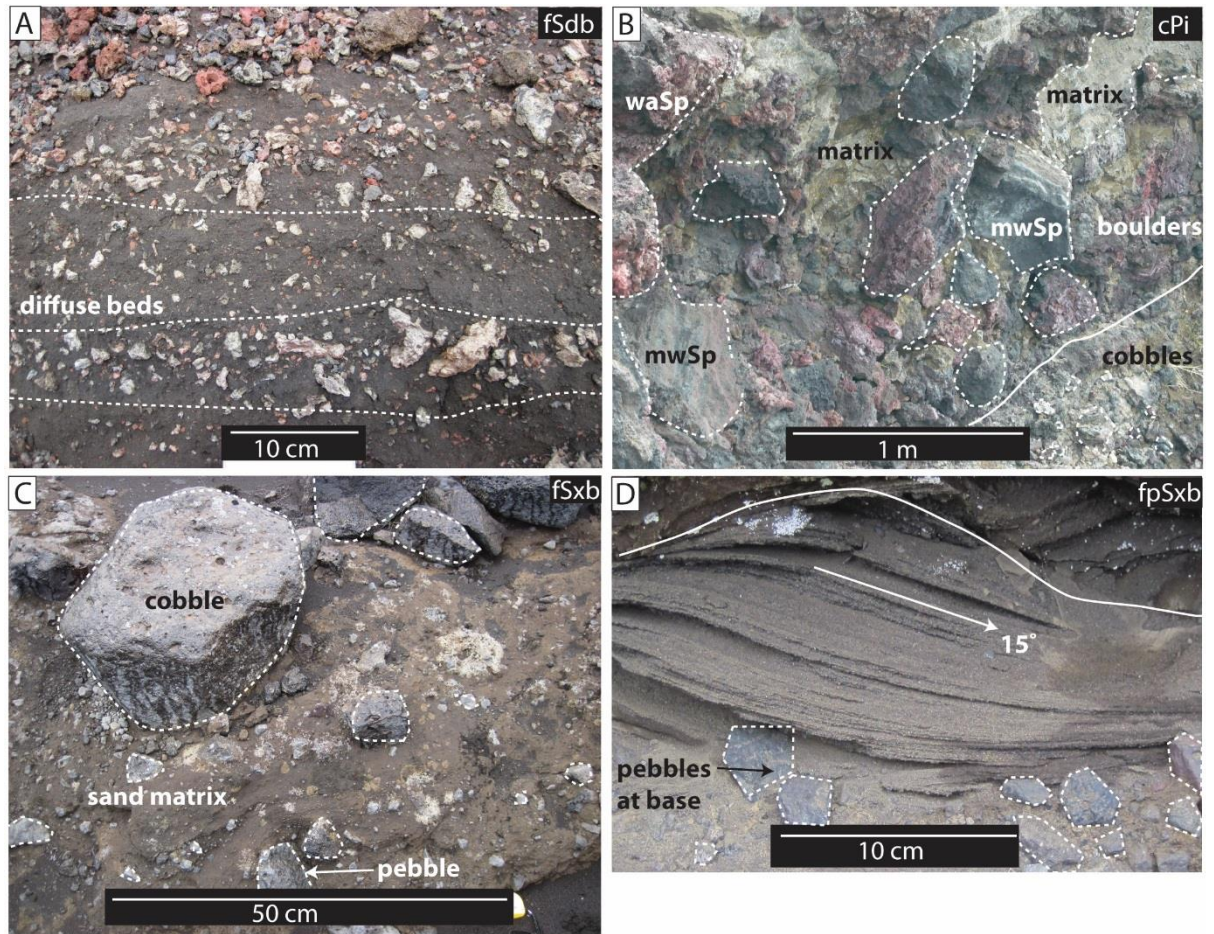


Figure 3.24. Sedimentary lithofacies observed in the study area. (A) Fine, diffusely bedded volcaniclastic pebbly sandstone (pebbles are outlined). See log 16 for stratigraphic position. (UTM 557437/7263977). (B) Inverse-graded cobble breccia. See log 16 for stratigraphic position. (UTM 557437/7263977). (C) Fine, cross bedded volcaniclastic sandstone with gravel, pebbles and cobbles. See log 81 for stratigraphic position. (UTM 557495/7265751). (D) Fine, hummocky cross-stratified pebbly sandstone. Sub-horizontal diffuse beds ~10 cm thick are marked by dashed lines. See log 81 for stratigraphic position. (UTM 557442/7264902). See Tables 3.5 for lithofacies descriptions.

Lithofacies	Description	Componentry	Structure	Occurrence
fSdb	Fine, diffusely bedded sandstone	Angular pebbles of R-K stratigraphy scoria and basaltic sands	Matrix supported; moderately well sorted; ~5 cm thick diffuse beds; units 0.75 m thick	Post eruption; uppermost deposits in the crater of edifice 26
cCi	Cobble conglomerate with inverse grading	Angular pebbles and boulders of R-K stratigraphy pyroclasts	Clast-supported; poorly sorted and inversely graded; units 0.2 – 1 m thick	Post eruption; uppermost deposit in the crater and flank of edifice 26
fSxl	Fine, cross laminated sandstone	Angular – sub-angular granules and cobbles; pyroclasts and dense basalt clasts sourced from R-K and pre-eruptive stratigraphy	Matrix supported; poorly sorted; laminations; units 0.8 – 1 m thick	Pre and post eruption; distal regions west of the river beneath the volcanic stratigraphy and within the flank of edifice 26
fSxb	Fine, trough cross bedded sandstone	Sub-angular granules; pyroclasts and dense basalt clasts sourced from R-K and pre-eruptive stratigraphy	Clast supported; moderately well sorted; 3 mm thick beds with foresets that dip 12°; pebbles of scoria at the base are normally graded; units 0.15 – 1.8 m thick	Pre- and syn-eruption; west of the river overlying iwSc and beneath Hy in distal regions
Table 3.5. Summary of sedimentary lithofacies. All lithofacies are interpreted as fluvial deposits, possibly related to glacial floods.				

Lithofacies fSdb – fine, diffusely bedded volcanoclastic pebbly sandstone

This matrix-supported and moderately well sorted sandstone is composed of fine basaltic sands (95–90 vol. %) of unknown provenance and angular, intraformational scoria pebbles (5–10 vol. %). Diffuse beds defined by variations in pebble abundance are ~5 cm thick and dip 15–20° to the S. The lithofacies occurs in units up to 0.75 m thick within the crater of edifice 26 (log 81, Fig. 3.10).

Lithofacies Cpi – inverse-graded cobble breccia

This breccia is composed of angular intraformational pebbles, cobbles and boulders of the R-K eruption (70 vol. %) and fine basaltic sands (30 vol. %) of unknown provenance. It is matrix-supported, poorly sorted and inversely graded. The beds are 0.2–1 m thick and occur in the crater and flank of edifice 26 (log 81, Fig. 3.10).

Lithofacies fSxb – fine, cross bedded volcanoclastic sandstone with gravel, pebbles and cobbles

This sandstone is matrix-supported and poorly sorted. It is composed of fine sand (80 vol. %) and angular and sub-angular granules, pebbles and cobbles (20 vol. %). These clasts are sourced from the underlying lithologies—either the R-K or pre-eruptive stratigraphy. It is trough cross-stratified with 3 mm thick foresets that dip 19° to the SW. It occurs in distal regions west of the river beneath the R-K volcanic sequence (log 16; location 462; Fig. 3.11) and ~200 m from the fissure (Fig. 3.3) in units 0.8–1 m thick.

Lithofacies fpSxb – fine, hummocky cross-stratified pebbly sandstone

This sandstone is composed of sub-angular granules and pebbles sourced from the underlying lithologies – either the R-K or pre-eruptive stratigraphy. The lithofacies is clast-supported and moderately well sorted. The lithofacies displays hummocky cross-stratification; foresets are 3 mm thick and dips 12° to the E. Scoria pebbles at the base of the unit are inversely graded. Units are 0.15–1.8 m thick and occur west of the river overlying clast-supported weakly agglutinated scoria lapilli and bombs (waSc) and beneath hyaloclastite and pillow lavas (Hy) in distal regions of the study area (logs 7 and 16; Fig. 3.11).

Interpretation:

The sediments exhibit features typical of those deposited in fluvial environments (e.g. sand–cobble grain size, moderate sorting, angular and rounded grains and trough cross-bedding; see Tucker 1995). Fluvial sedimentation is evidenced pre-, syn- and post-eruption, although the thickest deposits are pre- and post-eruption. In proximal regions post-eruption fluvial action has re-worked underlying pyroclastic units. In distal regions pre- and syn-eruptive fluvial action is evident, also re-working the underlying stratigraphy. Post-eruption fluvial action has incised channels in distal regions (e.g. between faults 36 and 37). The sedimentary lithofacies may be related to the glacial outbursts that occurred from 2–9 kyr BP (e.g. Alho et al. 2005; Kirkbride et al. 2006; Waitt 2009; Friese et al. 2013). The presence of the sediments both sides of the fissure suggests that the asymmetric distribution of pyroclastic deposits cannot be accounted for by erosion.

A high energy regime is indicated by the coarse grainsize and cross-bedding of lithofacies Cpi and fSxb (Tucker 1995). The inverse grading in the cobble breccia (Cpi) is common in the deposits of high concentration sediment-water mixtures and commonly occur in the lowest part of debris-flow deposits (Tucker 1995). These debris flows directly overlie the R-K volcanic sequence and record the onset of fluvial deposition. Hummocky cross-stratification suggests rapid aggradation from a uni-directional current (Dumas and Arnott 2006); consistent with high energy fluvial deposition. The presence of lithofacies fSxb within the volcanic R-K volcanic sequence indicates that fluvial deposition west of the river occurred during the eruption. The fluvial system may have flooded lava flows causing the formation of entablature-style jointing.

3.7 Architecture of the pyroclastic deposits

The Jökulsá a Fjöllum canyon exposes a near-complete record of the R-K volcanic sequence and its feeder dyke on both the eastern and western canyon wall (Fig. 3.25). Faults within this sequence occurred prior to, during and after the eruption (Figs 3.26, 3.27 and 3.28). Several pyroclastic constructs are recognised (Fig. 3.29), including rootless cones (location 285), scoria ramparts (locations 280, 477 and 302), a scoria-agglutinate cone (edifice 26, location 289), spatter ramparts (locations Y28, Y29) and sheet-like fall deposits (location 350). The characteristics of these constructs, their feeder dykes and conduit are discussed below (Table 3.6).

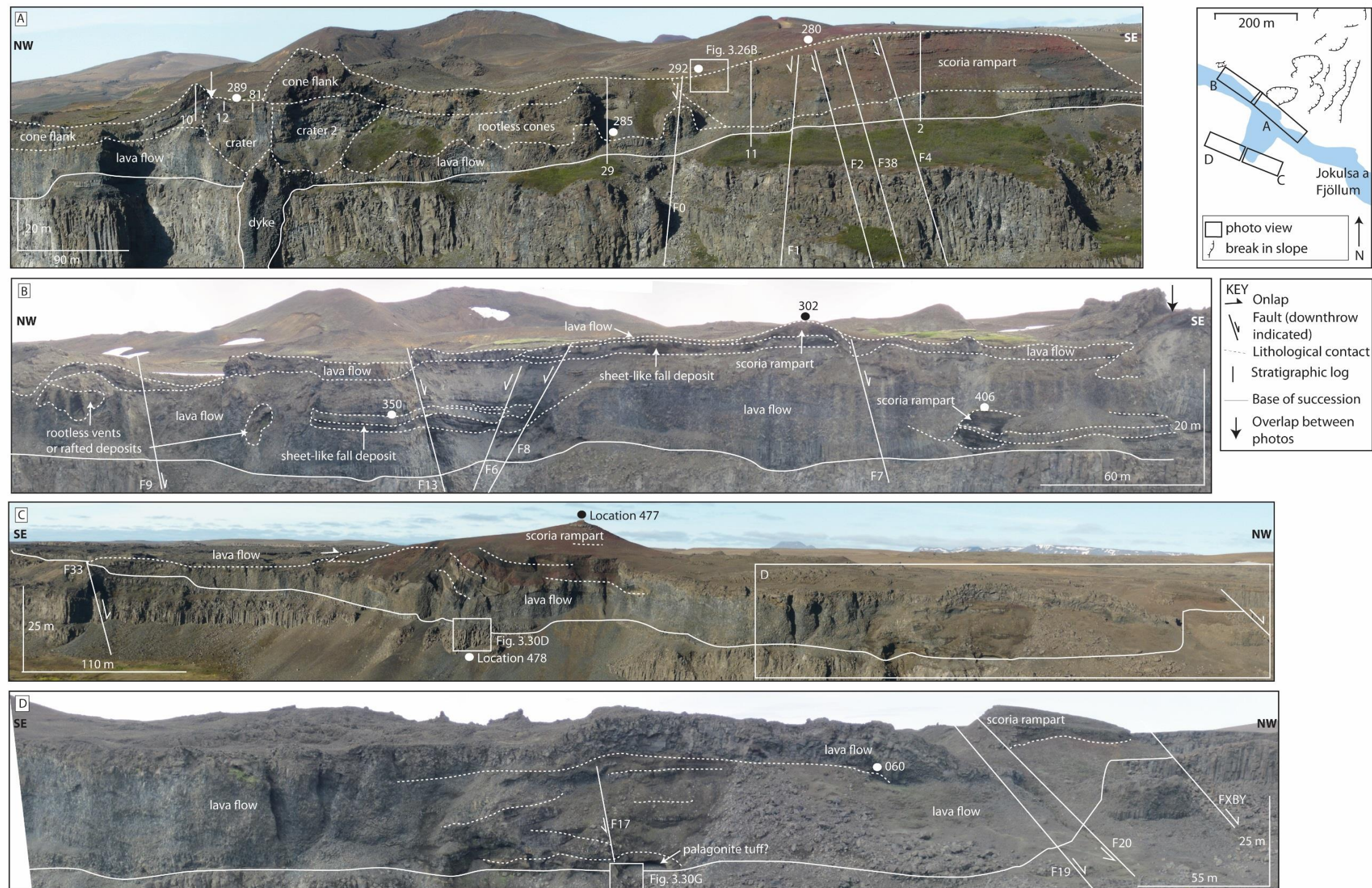


Figure 3.25. Photographs of the canyon walls. (A) Cross section of a scoria-agglutinate cone (location 289; edifice 26) and scoria rampart (location 280). Crater 2 of an overlapping edifice is also shown. (UTM 557542/7264269). (B) Photograph of the canyon wall north of image A. The R-K volcanic sequence is composed of sheet-like fall deposits, scoria ramparts and lava flows of columnar-jointed pāhoehoe (Cp) and clastogenic pāhoehoe (Cl). Numerous faults are visible with throws of ~1 m. The northwestern bounding fault of the Sveinar graben is ~20 m left of the image. (UTM 557617/7265642). (C) Photograph of the western canyon wall. A scoria rampart (Location 477) is observed and has anticlinal bedding at its base. Clastogenic lavas onlap the rampart towards the southeast. Contacts beneath the rampart within crystalline and clastic successions are gradational and beds may pinch-out laterally. The graben bounding fault (F33) is visible toward the southeast. The northwest graben fault is not visible from this location. (UTM 557356/7265748). (D) Photograph of the western canyon wall. The volcaniclastic sandstone with planar bedding (vSpb) is observed at the base of the R-K volcanic sequence. Faults are numbered according to Fig. 3.4. (UTM 557617/7265642).

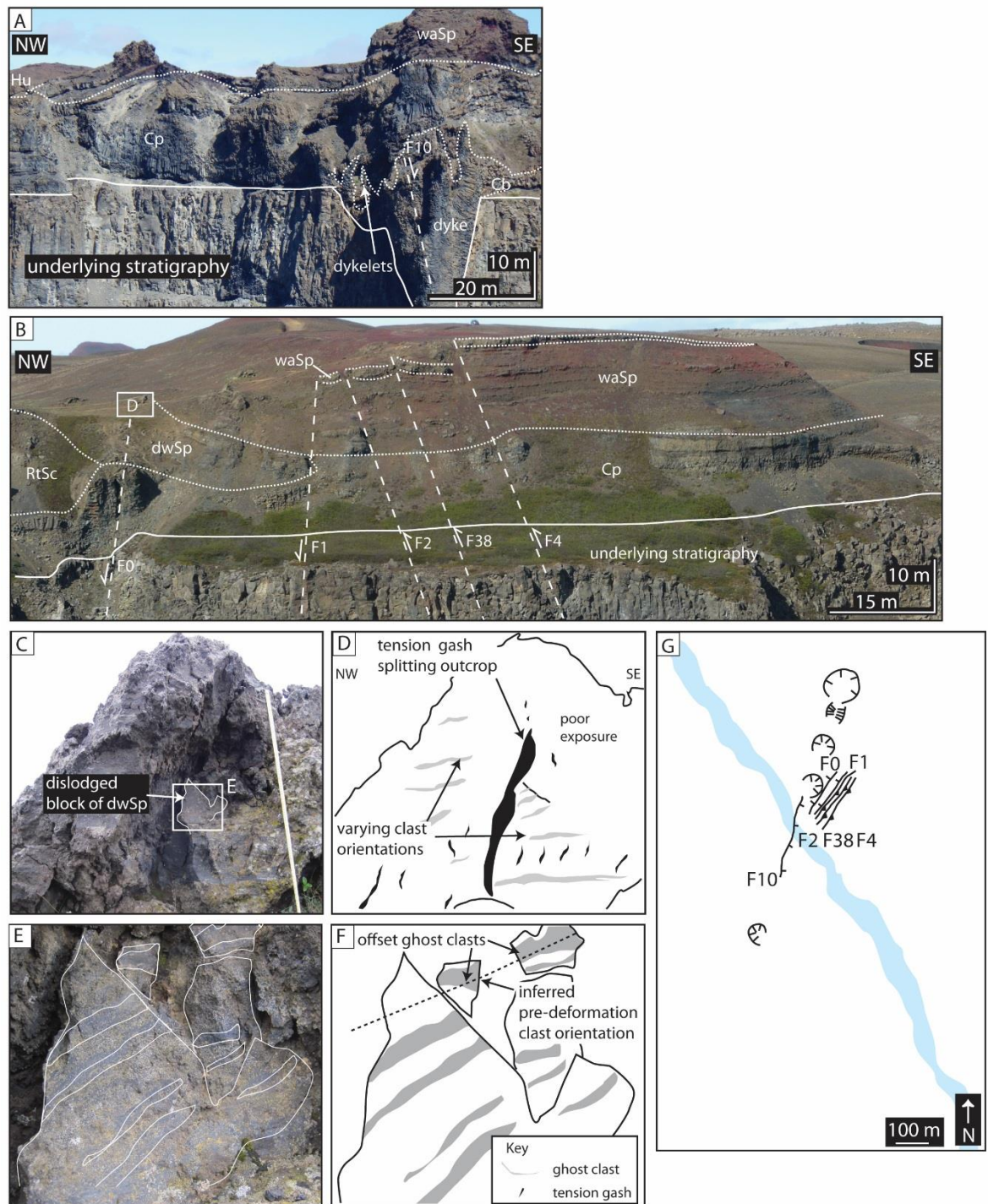


Figure 3.26. Location and orientation of faults associated with edifice 26 and the scoria rampart (location 280). Faults are labelled according to Fig. 3.4 and are indicated by the dashed line. Arrows indicate the direction of downthrown. The contact between the underlying stratigraphy and the R-K stratigraphy is indicated. (A) F10 is exploited by the R-K feeder dyke. Throw is observed to be ~3 m southeast. (UTM 557542/7264269). (B) Numerous faults in the scoria rampart (location 280). Note the throw in the upper pyroclastic units (stippled lines). (UTM 557465/7264189).

Images C–F show deformed blocks of clast-supported densely welded spatter bombs (dwSp) located at the top of normal faults (UTM 564033/7302375). Ghost clasts indicate the original depositional fabric, whilst tension gashes that intersect the bedding suggest ductile deformation in a viscous deposit. Movement was not along the depositional planes, nor confined to the margins of the clast-supported densely welded spatter bombs (dwSp). Ghost clasts are downthrown towards the west (indicated by the dashed line) and suggest extensional deformation. The ruler in C is 70 cm. The block in E is 20 mm wide. Similar features are observed in the clast-supported densely welded spatter bombs (dwSp) at the top of F2. Deformation is interpreted to be the result of syn-eruptive faulting. (G) Map showing location of the faults.

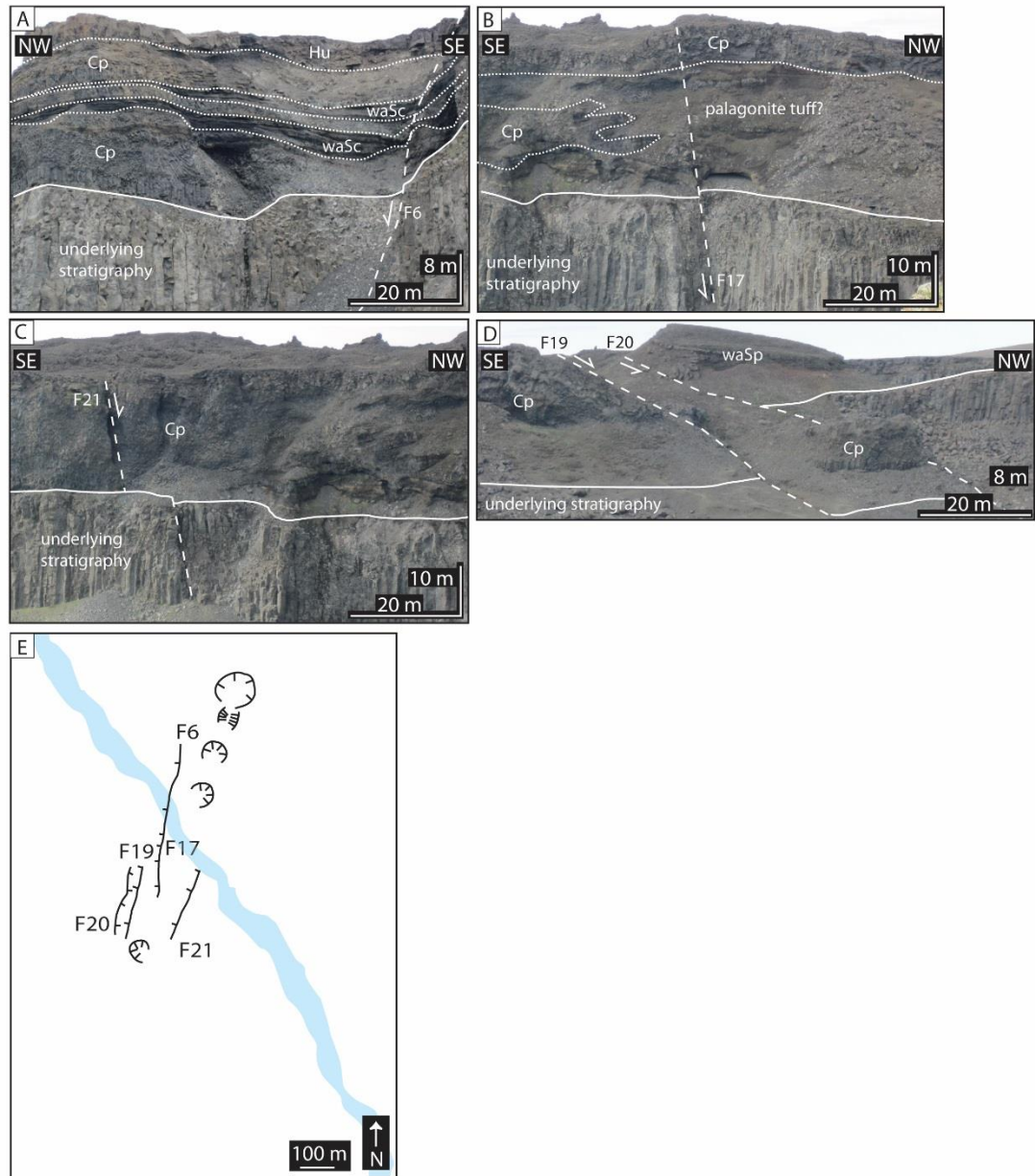


Figure 3.27 (overleaf). Location and orientation of selected faults (dashed lines). Faults are labelled according to Fig. 3.4. Arrows indicate direction of downthrown. The contact between the underlying stratigraphy and the R-K stratigraphy is indicated. (A) F6 forms the margin of an inlet and offsets the upper clastogenic pāhoehoe (Cp). (UTM 557601/7265530). (B) Syn-eruptive slip along F17 is inferred to have resulted in the ductile deformation of the upper agglutinated pyroclastic units resulting in a break in slope at the surface. (UTM 557772/7265756). (C) Fault 21 forms an inlet on the river and forms a gully. There is no topographic expression of the fault in the uppermost lavas. (UTM 557772/7265756). (D) Faults 19 and 20. Columnar-jointed pāhoehoe (Cp) occurs within the graben formed by these faults. (UTM 557601/7265530). (E) Map showing location of the faults.

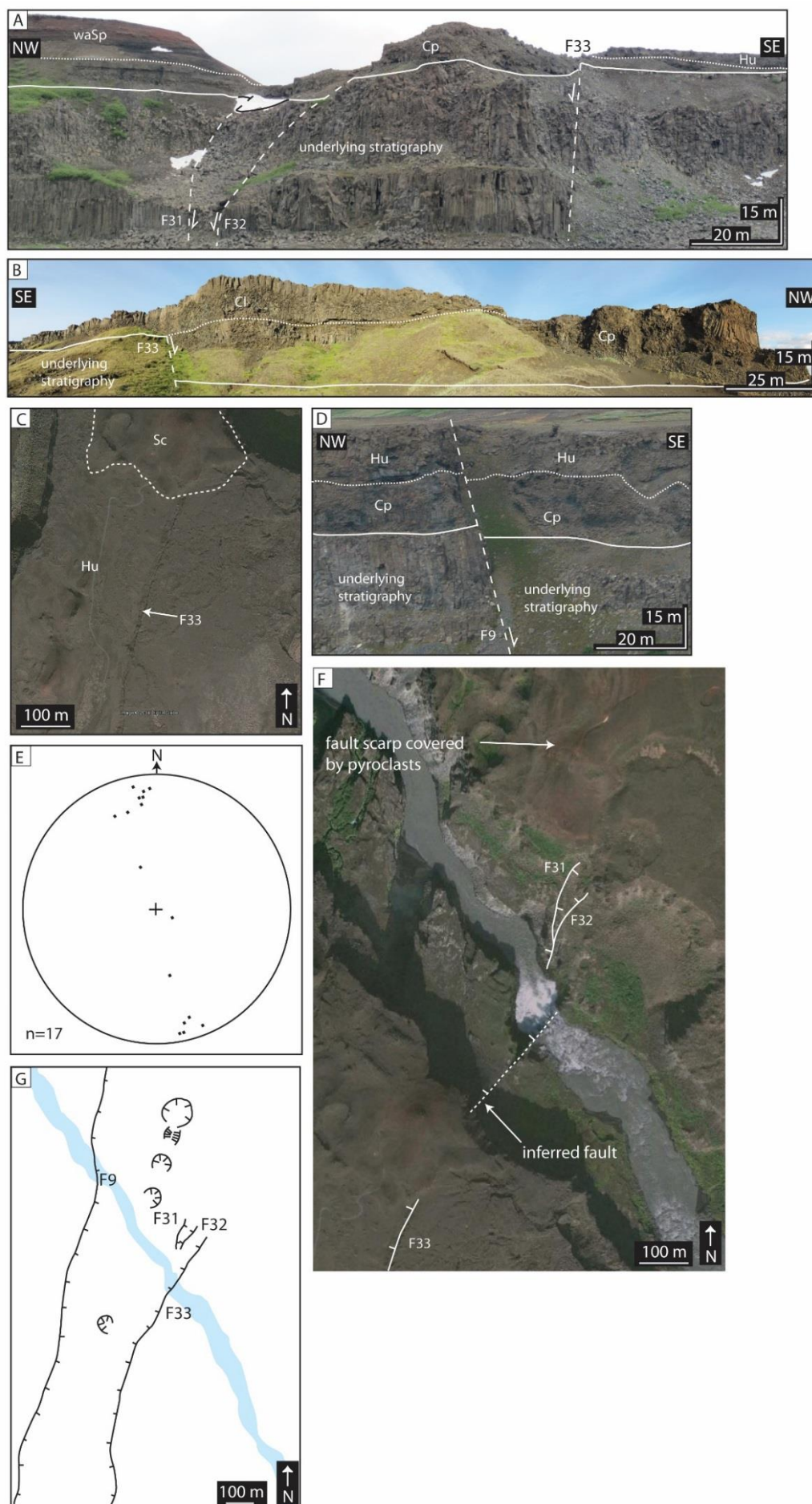
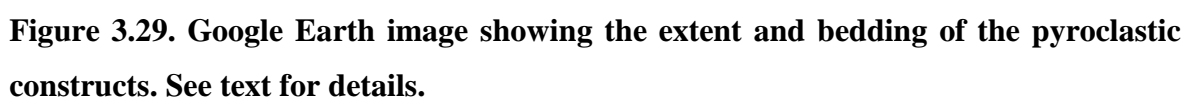


Figure 3.28 (overleaf). Location and orientation of the Sveinar graben bounding faults and stereonet data. Faults are labelled according to Fig. 3.4 and are indicated by the dashed line. Arrows indicate direction of downthrown. The contact between the underlying stratigraphy and the R-K stratigraphy is indicated. (A) Segmented graben bounding faults (F31–33) east of the river. (UTM 557432/7264244). (B) Graben bounding fault west of the river. The lava-like agglutinate (l-l Agg) terminates against the footwall of the graben. The contact between the lava-like agglutinate (l-l Agg) and clastogenic pāhoehoe (Cl) is shown as a stippled line. Note the absence of faulting in the hummocky pāhoehoe (Hu), indicating that the fault existed prior to the eruption. (UTM 563879/7301531). (C) Google Earth image showing F33 (arrowed) faulting the uppermost clastogenic lavas, indicating that the fault had several stages of growth. The fault is concealed further north by scoria (dashed outline). (D) F9 forming the margin of an inlet. The clastogenic pāhoehoe (Cp) is offset by the fault. (UTM 557617/7265642). (E) Pole to plane plot showing the orientation of faults XA, F0,1,4–6,9,13,17, 19–21, 31–33 and 38. (F) Google Earth image showing that F33 (the eastern Sveinar graben bounding fault) does not have a scarp east of the river. This suggests that either: the fault is segmented and slip did not occur on this section of the fault; and/or the eruption continued after faulting. (G) Map showing location of the faults.



Pyroclastic deposit	Characteristic lithofacies	Modal bedding (°)	Geometry	Basal diameter (m)	Thickness (m)	Distance from fissure (m)	Median grain size (cm)	Interpretation
Scoria-agglutinate cone	l-l Agg and waSp	28	Circular	228	34	0	22	intermittent fountaining from point source
Scoria rampart	mwSc and waSp	10	Linear	35–290*	4–40	130–150	10	intermittent fountaining from linear and possibly overlapping source(s)
Spatter rampart	l-l Agg	45	Linear	16–25*	<0.5–4.5	<50	-	sustained fountaining from linear and possibly overlapping source(s); clastogenic flow
Sheet-like fall deposit	waSc	11	Linear	-	≤1.1	<1300	2	medial/distal fall deposit
Rootless Cone	mSc	20	Circular	30	14	100	60	lava-water interaction
Table 3.6. Summary features of pyroclastic deposits. *shortest axis								

3.7.1 The R-K feeder dykes

On the east of the Jökulsá canyon edifice 26 is underlain by a conduit 80 m in height which flares upwards, widening from 4 m in diameter at its base to 28 m at its top (Fig. 3.30). The limited vertical exposure does not allow determination of the depth at which the conduit maintains an equal thickness. The northern conduit margin dips 53° while its southern margin dips 15° . Flaring is most pronounced in the upper 40 m of country rock, which is composed of plagioclase porphyritic basalt lava (Fig. 3.30). The conduit is composed of numerous coherent dykes of uniform hypocrySTALLINE, non-vesicular aphyric basalt (Fig. 3.30). The dykes exploit a normal fault (F10; Fig. 3.26) with a throw of ~ 3 m toward the southeast.

On the southern margin the dykes merge laterally with the columnar-jointed pāhoehoe (Cp; Fig. 3.25). On its northern margin the dykes have scallop-shaped contacts with the country rock and breaks up into 5 m thick, contorted dykes 5 m below the paleo-surface (Fig. 3.30). These dykes extend 10 m from the dyke, intruding into the overlying pyroclastic deposits. They thin with distance and have cooling joints across their entire width. The dykes dip $70\text{--}90^\circ$ to the southeast and northwest and fill scalloped shaped depressions within the country rock, merging laterally with the adjacent columnar-jointed pāhoehoe (Cp).

West of the river an 8 m-high section of dyke outcrops at the same elevation as the river (Fig. 3.30; Location 478). The dyke is aphyric and has columnar cooling joints spaced ~ 60 mm. Up to 200 mm from the dyke wall multiple chilled margins form sub-parallel laminations spaced ~ 25 mm apart. 10 m above the river, two ~ 1 m wide segments of dyke outcrop in the canyon walls. The eastern-most segment maintains a constant thickness and coherent texture and merges with the overlying columnar-jointed pāhoehoe (Cp; Fig. 3.30). The western-most segment terminates abruptly within the volcanoclastic sandstone with planar bedding (vS_{pb}) and maintains an equal thickness with height.

Interpretation:

Beneath edifice 26 the conduit is composed of numerous offshoot dykes, typical of monogenetic conduits (Keating et al. 2008). Dyke emplacement resulted in the activation of a pre-existing normal fault (F7; see Gudmundsson et al. 2008), consistent with the observations of Galindo and Gudmundsson (2012) for other feeder dykes. The feeder dykes were emplaced during numerous intrusive events, as evidenced by multiple chilled

margins and by intrusions into the columnar-jointed pāhoehoe (Cp; Fig. 3.30). The morphology of the dykes beneath edifice 26 and at location 478 are typical of effusive eruptions (Geshi and Oikawa 2014) since they merge with adjacent lava flows (columnar-jointed pāhoehoe, Cp) and are coherent beneath the surface. The abrupt termination of the more northerly dyke into the volcaniclastic sandstone with planar bedding (vSpb; Fig. 3.30) indicates that this dyke arrested before reaching the surface. However, it may have reached the surface elsewhere along its strike.

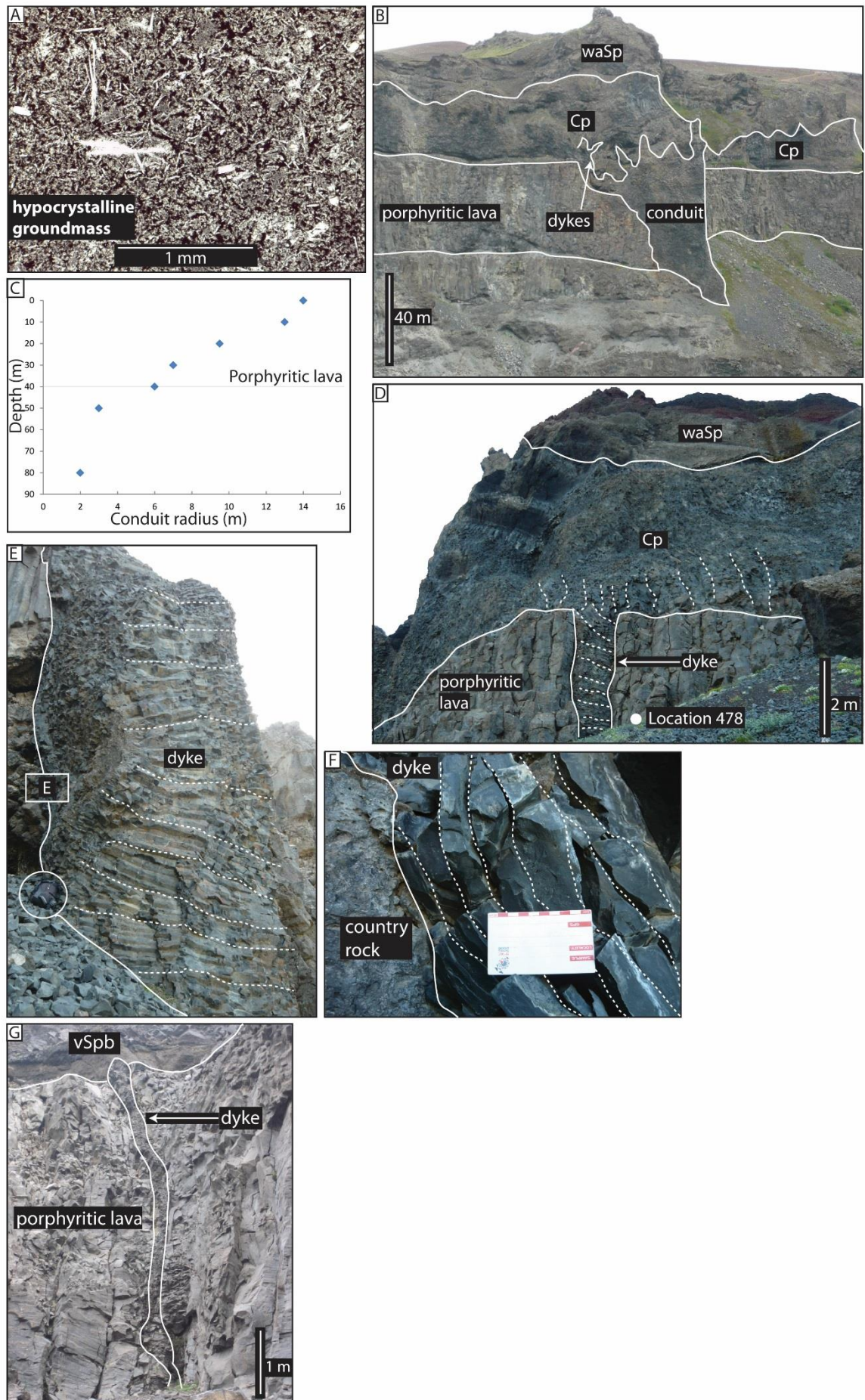


Figure 3.30 (overleaf). Architectural features of the dyke. (A) Thin section image of the dyke (plane polarised light). The sample is taken 30 cm from the country rock contact. (B) View toward the conduit from the west of the canyon. The underlying plagioclase porphyritic lava flows are the source of the lithic clasts in log 29 (Fig. 3.12). Note the scalloped contacts between the dyke and country rock and the numerous intrusions into the overlying pyroclasts. (UTM 557617/7265642). (C) Plot of depth from the top of the canyon vs. conduit radius. The flaring hinge is located at a depth of 40 m at the base of the porphyritic lavas. (D) An effusive dyke on the west of the canyon feeding overlying lava-like agglutinate (l-l Agg). Dashed lines indicate cooling joint orientations. See Fig. 3.25 for location. (UTM 557460/7264234). (E) A section of the dyke adjacent to the river on the west of the canyon. Dashed lines indicate cooling joint orientations. The solid line indicates the contact with the country rock. Bag (circled) is ~0.5 m. See Fig. 3.25 for location. (UTM 557510/7264268). (F) Multiple chilled margins at the dyke/country rock contact. The scale card is 10 cm long. Dashed lines indicate laminations spaced ~ 2 cm. See (D) for location. (UTM 557510/7264268). (G) Arrested dyke intruding into overlying pyroclastics west of the river. See Fig. 3.25 for location. Lithofacies codes are as Figs. 3.8 and 3.13. (UTM 557519/7264280).

3.7.2 Rootless cones

The columnar-jointed pāhoehoe (Cp) on the southeast of the dyke (location 285) has a hummocky, concave-up upper contact. The hummocks are up to 30 m in diameter. Cooling joints become more closely spaced (~10 mm) towards the upper contact, which is gradational with the overlying massive scoria lapilli and bombs (mSc; median grain size 2 cm). The columnar-jointed pāhoehoe is overlain by a 9.5 m-thick sequence of lava-like agglutinate (l-l Agg) and shelly pāhoehoe (Sh) that dips 20° radially outwards (modal value).

Interpretation:

The hummocky, concave-up upper contacts of the columnar-jointed pāhoehoe are interpreted as the vents of rootless cones. They are identical to the vents of rootless cones elsewhere in Iceland and the Columbia River (Fig. 3.31; see Chapter 4). Furthermore, rootless cones are common in the dyke-proximal regions of fissure eruptions (e.g. Thordarson and Self 1993; Hamilton et al. 2010). Since the size of the vent is proportional

to size of the overlying edifice (Fagents and Thordarson 2007; Hamilton et al. 2010), the cones are inferred to have been ≤ 30 m in diameter. The lava-like agglutinate (l-l Agg) and shelly pāhoehoe (Sh) that overly the vents and dip 30–40° radially outwards (Location 285; log 29) are interpreted as the products of rootless eruptions. However, the crater of the cone is inferred to have been flooded by later lavas and is not exposed (Fig. 3.29). Rootless cones are not observed elsewhere along the R-K fissure, suggesting that the studied section either represents a very localised rootless cone field in which surface/open water was particularly abundant, or that cones elsewhere along the fissure have been buried by later-erupted products (see also section 3.9.2).

An alternative suggestion is that the columnar-jointed pahoehoe (Cp) represents a feeder network for lava flows within dyke-fed pyroclastic deposits (e.g. Sánchez et al. 2014). However, this interpretation would provide no explanation for the cauliflower-like texture of the pyroclasts in the massive scoria lapilli and bombs (mSc; Fig. 3.7); the radial dip of the overlying lava-like agglutinate (l-l Agg) and shelly pāhoehoe (Sh) and the occurrence of armoured clasts with a plagioclase porphyritic-clast core.

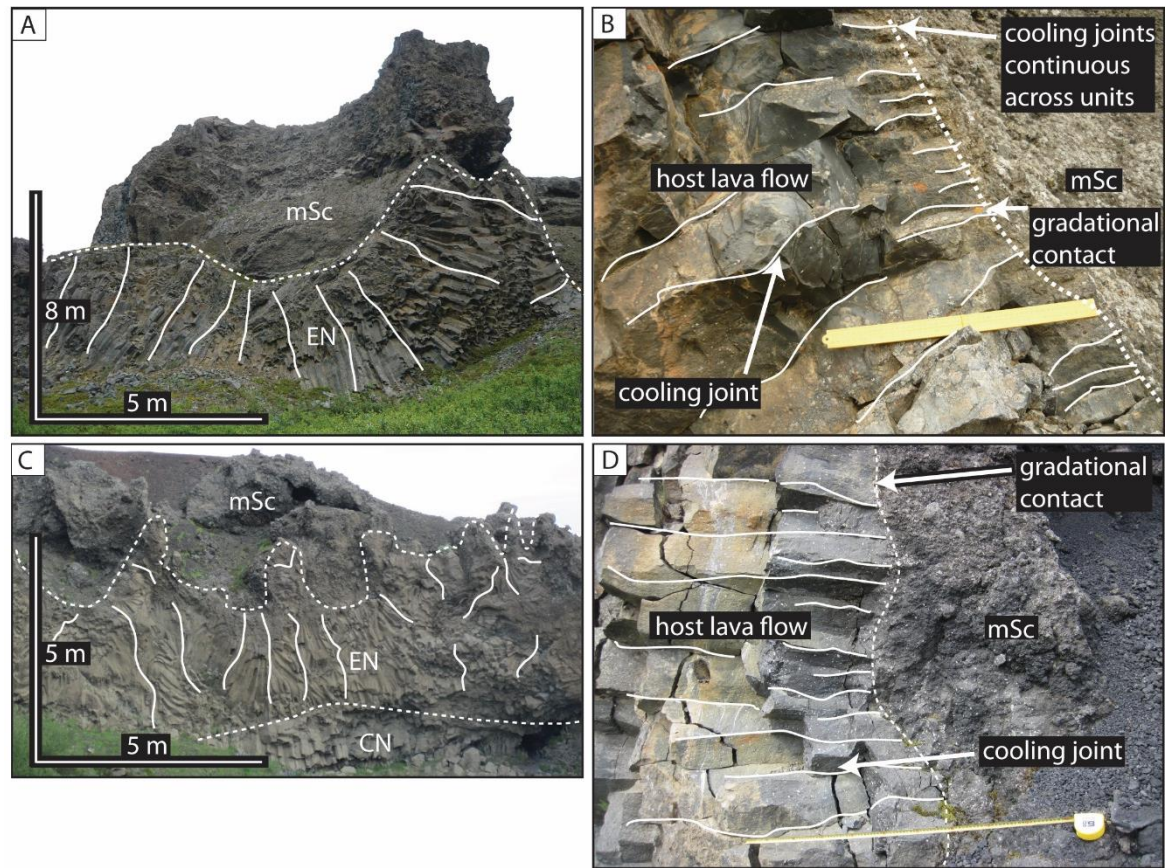


Figure 3.31. Comparison between rootless vents at Hjalparfoss (UTM 402187/7098548) and those along the R-K fissure (UTM 557772/7265756). Images A and C show the vents and the host lavas flows along the R-K fissure and at Hjalparfoss respectively, images B and D show the contact between the columnar jointed pāhoehoe (Cp) lava and massive scoria lapilli and bombs (mSc). Notice the colonnade (CN) and entablature (EN) of the lava flows with cooling joints that radiate from the hummocky, bowl-shaped upper contact. The ruler in B and D is 25 cm.

3.7.3 Scoria ramparts

Numerous small pyroclastic edifices are elongated parallel to the fissure (Fig. 3.29, locations 477, 280 and 077). These deposits have basal diameters of 35–290 m. Feeder dykes are not observed beneath the deposits (except location 477; see following discussion). They are composed of 4–40 m thick bedded sequences of clast-supported incipiently welded spatter bombs (waSp); clast-supported moderately welded scoria lapilli and bombs (mwSc); clast-supported densely welded spatter bombs (dwSp); clast-supported weakly agglutinated scoria lapilli and bombs (waSc) and scoria lapilli (ScL). The ramparts are characterised by low angle dips and are set-back 130–150 m from the fissure (Fig. 3.29). Their median grain size is 10 cm (see Table 3.6).

The ~20 m succession at Location 280 (Figs. 3.25 and 3.29) is represented on Logs 2 and 11 (Fig. 3.11). Log 11 shows that clast-supported densely welded spatter bombs (dwSp) unconformably overly the columnar-jointed pāhoehoe (Cp). The pyroclastic units dip 16–44° to the south and southeast. These beds are truncated on their northwestern margin by the present ground surface (Fig. 3.32). Numerous 10 m wide, sinuous channels occur in the surface of the deposit (Fig. 3.33). These channels are 1–5 m deep and strike 183°, covering an area of 38 m². Log 2 shows that clast-supported incipiently welded spatter bombs (waSp) and clast-supported moderately welded scoria lapilli and bombs (mwSc) unconformably overlie the clast-supported densely welded spatter bombs (dwSp) and columnar-jointed pāhoehoe (Cp). There is an absence of lithic clasts within both logs. Bedding within this succession dips northwest and southeast (see Fig. 3.29).

Faults 1, 2, 4, 38 and 63 occur in this deposit (see logs 2 and 11; Fig. 3.26). Blocks of deformed clast-supported densely welded spatter bombs (dwSp; Fig. 3.26) ~1 m³ in size occur at the tops of faults F 63 and F 1. These blocks contain ghost clasts that dip 11° to the southwest. The ghost clasts are intersected by 70 mm long tension gashes that dip 70° to the southwest. The tension gashes form numerous rotated blocks ~0.08 m³ in size and downthrow the ghost clasts by 2 cm. Other blocks of clast-supported densely welded spatter bombs (dwSp) show similar tension gashes and contain sheared vesicles and have irregular, deformed outer surfaces. Faults 1, 2, 38 and 4 generated a slip of ≤4 m toward the southeast in the upper units (clast-supported incipiently welded spatter bombs, waSp and clast-supported moderately welded scoria lapilli, mwSc; Fig. 3.27). No displacement is observed in the columnar-jointed pāhoehoe (Cp) at the base of the faults, but zones of hackly jointing are developed along the fault plane.

Another 20 m high dissected mound of scoria occurs west of the river. This mound is composed of clast-supported incipiently welded spatter bombs (waSp) that dip 30° northwest and northeast (Location 477; Figs. 3.25 and 3.29). The mound has an antiformal structure at depth, the dip of which shallows to 08° laterally and with height. It has gradational lateral and vertical contacts with the underlying and adjacent columnar-jointed pāhoehoe (Cp) and clast-supported incipiently welded spatter bombs (waSp). The bedding of the clast-supported incipiently welded spatter bombs (waSp) is truncated by the present ground surface. At its base the mound is composed of columnar-jointed pāhoehoe (Cp) which becomes less laterally extensive with height. Towards the southeast, the mound is onlapped by hummocky lavas (Hu).

Other elongate mounds occur further south along the fissure (Fig. 3.29; locations Y22–24). It is unclear whether these mounds are set back from the eastern or western margin of the fissure. Dissected mounds of scoria are also exposed on the eastern canyon wall. Location 302 is composed of clast-supported incipiently welded spatter bombs (waSp) and clast-supported weakly agglutinated scoria lapilli and bombs (waSc). It forms a ridge-like feature 70 m in length and 4.5 m high. Beneath this, another scoria mound occurs (Location 406; Fig. 3.25). This mound is inaccessible, but appears to be composed of columnar-jointed pāhoehoe (Cp) and clast-supported weakly agglutinated scoria lapilli and bombs (waSc) that dips 10° toward the southeast. It is 8 m high and 10 m in length and has a distinctive near-vertical northwest margin. It is overlain and underlain by the columnar-jointed pāhoehoe (Cp), with which it also has distinct lateral contacts.

Interpretation:

These pyroclastic sequences are interpreted as dissected scoria ramparts (the scoria "mounds" of Breed 1964). The ramparts are similar to the "scoria half cones" adjacent to the Laki fissure (Fig. 3.34) which are elongated parallel to the fissure, larger than the adjacent cones and set-back from the fissure. The linear shape of the ramparts in plan view suggests that they accumulated from a linear fountain or from overlapping fountains. The lava fountains were sufficiently collimated or tall to allow the formation of different clasts (e.g. spatter bombs and scoria lapilli). The dominance of juvenile clasts that show no evidence of recycling or ball milling (e.g. cored bombs) indicates that the ramparts formed prior to the adjacent pyroclastic cones. The massive beds defined by minor clast-size fluctuation and absence of rounded clasts suggest that the clasts were deposited in-situ without grain-flow avalanching, typical of Hawaiian activity (Valentine and Gregg 2008).

The abundant welding is also consistent with deposition during Hawaiian-style activity (Valentine and Gregg 2008). The size of the component clasts is typical of the deposits of Strombolian and Hawaiian-style eruptions (Valentine and Gregg 2008).

The pyroclastic sequence at Location 280 is inferred to be eroded, as indicated by the truncated beds and fluvial channels. This rampart may have been constructed as a result of the wind-stripping of pyroclasts from a lava fountain. The size difference between the ramparts at Locations 280 and 302 either side of the fissure (Fig. 3.25) is supportive of this interpretation. The abundance of clast-supported densely welded spatter bombs (dwSp; logs 11 and 2; Fig. 3.11) towards the base of the sequence suggests that deposition was dominated by clasts from the lower part of the fountain, or by a low fountain that contained a high proportion of spatter bombs. Towards the top of the scoria rampart, the abundance of clast-supported moderately welded scoria lapilli and bombs (mwSc) suggests that with time deposition was increasingly dominated by clasts from the outer and upper part of the fountain, or by a wider spread fountain which yielded higher proportion of these clasts. The changing dip directions at location 280 (log 2; Fig. 3.11) suggests that the source of pyroclastic material migrated from dominantly north to dominantly south with time. This may indicate either 1) a subtle change in dominant wind direction or 2) cessation of fountains towards the north.

Faulting is inferred to have altered the architecture of this rampart. Syn-eruptive slip along fault F9 resulted in the ductile extensional deformation of clast-supported densely welded spatter bombs (dwSp), indicated by the displacement of ghost clasts and tension gashes. Slip on faults 1, 2, 38 and 4 are inferred to have occurred post-eruption. Percolation of water down this fault may have initiated the hackly jointing along the fault planes.

The scoria rampart at location 477 has gradational contacts between clast-supported weakly agglutinated spatter bombs (waSp) and columnar-jointed pāhoehoe (Cp). These imply sustained accumulation, and lateral gradational changes result from either 1) pinching out of lenses of pyroclastic material 2) local zones of high or low accumulation rates. Since the other scoria ramparts (e.g. locations 280 and 302) are set-back from the fissure, not directly adjacent to it, this rampart is inferred to have been constructed by deposition from an adjacent section of the fissure, represented at locations Y27–Y32. Thus, the fissure was segmented, and the easterly section (feeding edifice 26; Fig. 3.3) closed prior to the westerly section. This westerly section feeds the southern part of the fissure. The rampart at location 406 is thought to have been deformed during lava flow

emplacement (e.g. Brown et al. in press). However, the exact method of deformation is unclear.

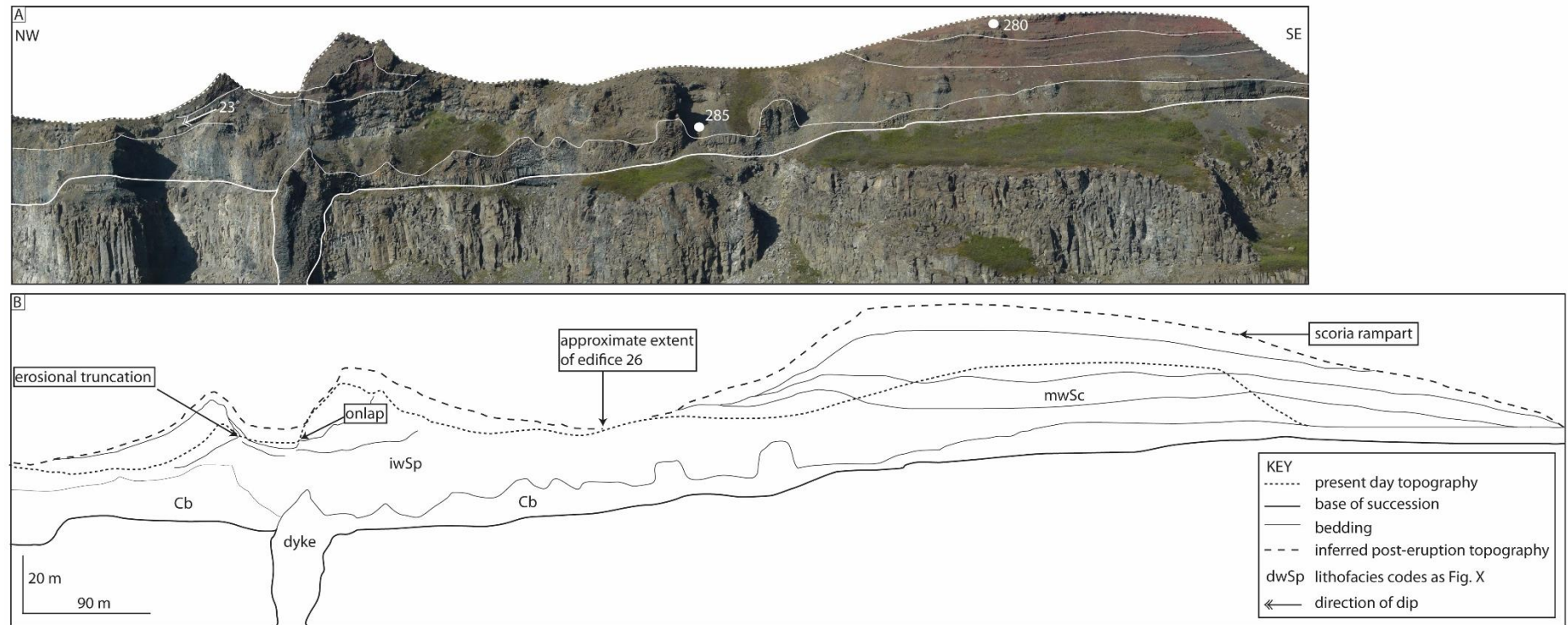


Figure 3.32. Photograph (A) and a reconstruction of the geometry of the pyroclastic constructs immediately after the eruption (B). Truncated beds are visible in the NW margin of the scoria rampart (location 280) and in the crater of cone 26. Field observations suggest ~10 m of stratigraphy is has been eroded from the cone and the rampart. (A: UTM 557542/7264269).



Figure 3.33. Google Earth image showing the inferred location of paleo-channels, contemporary channels and the outcrops of sedimentary lithofacies.

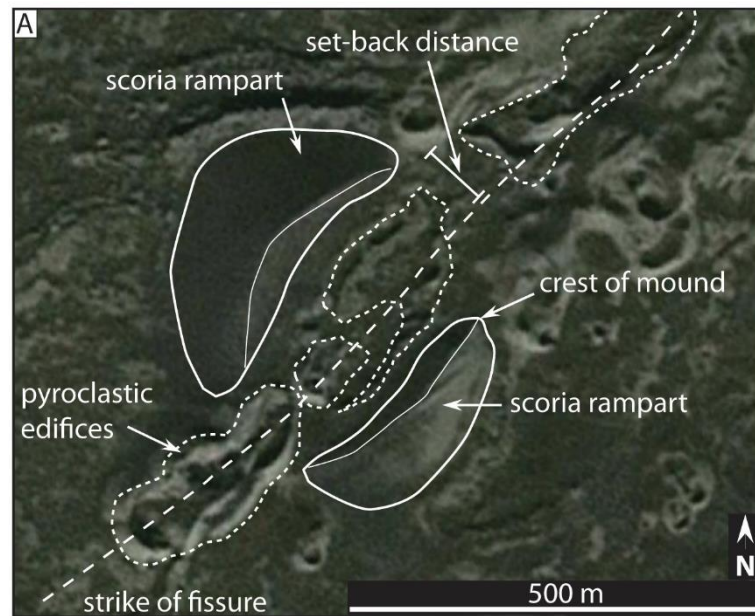


Figure 3.34. Scoria ramparts adjacent to the Laki fissure. (A) Google earth image showing that the ramparts are linear and crescent-shaped, elongated parallel to the fissure. They occur on the outer margin of the cones (UTM 361475/7159674).

3.7.4 Sheet-like fall deposits

Examples of these deposits occur on the eastern canyon wall (Location 350) and beneath the clastogenic lava, west of the river (log 16; location 462; Fig. 3.25). It is unknown whether the deposits on the eastern canyon wall are in-situ; they are found overlying a lava flow and may have been rafted (Sumner 1998; Brown et al. in press). The deposits west of the river (log 16, location 462, Fig. 3.25) overly the pre-eruption substrate, thus are in-situ. This deposit of clast-supported weakly agglutinated scoria lapilli and bombs (waSc) occurs ~500 m from the fissure, is <0.25 cm thick and has a mean grain size of 10 mm. Elsewhere on the southeast of the fissure, deposits ~1 m thick are recorded at ≤1300 m from the fissure (Fig. 3.12).

Interpretation:

The sheet-like fall deposits are interpreted as the medial deposits from a lava fountain. The welded nature of deposits is consistent with Hawaiian-style activity (Valentine and Gregg 2008). Tephra with similar dispersal characteristics is recorded by Aramaki et al. (1986) and Wolfe et al. (1988) during Hawaiian and Strombolian-style eruptions.

3.7.5 Scoria-agglutinate cone

Edifice 26 outcrops on the eastern canyon wall (Figs. 3.25, 3.26 and 3.29). This edifice was fed by the R-K feeder dyke (Figs. 3.3 and 3.26) and has a 90 m wide circular crater; the extent of which is marked by a 5–10 m high crater rim. Beds of lava-like agglutinate (l-l Agg) and clast-supported incipiently welded spatter bombs (waSp) on the northwest margin of the crater are truncated (Fig. 3.32) whilst on its southeast margin these beds onlap against the crater rim. The pyroclastic units are overlain by 2.25 m of sedimentary deposits (lithofacies fSdb and cCi; Fig. 3.32C).

The flanks of the edifice are dominated by spatter-rich lithofacies including lava-like agglutinate (l-l Agg), clast-supported, incipiently, moderately and densely welded spatter bombs (waSp, mwSp and dwSp); clast-supported weakly agglutinated scoria lapilli and bombs sometimes with inverse grading (waSc(i)); clast-supported non-welded scoria lapilli (ScL); and clast-supported densely welded scoria (dwSc). Component clasts range in size from 5–70 cm (median 22 cm). Beds dip inwardly towards the dyke at 12–60°, with units on the southeast of the crater dipping more steeply than those on the northwest. Outwardly dipping beds in the cone flank have a modal dip of 28° (Table 3.6).

The crater is underlain by columnar-jointed pāhoehoe (Cp; logs 10,81 and 12, Figs. 3.10, 3.25 and 3.35). A rosette structure (inferred to be composed of columnar-jointed pāhoehoe; Cp) 15 m in diameter occurs within the crater, with radial cooling joints spaced ~15 cm apart and cuboidal jointing in its core (Fig. 3.35). It occurs ~10 m below the present ground surface and is fed by the dyke. Cooling joints are sub-vertical on the rosettes' upper and lower surfaces but are poorly developed across the mid-section. Joints are longer and more widely spaced at the rosettes' base. At its margins the rosette bifurcates into numerous 1–5 m thick beds of columnar-jointed pāhoehoe (Cp) that dip ~20° to the SW.

The stratigraphic sequence within the crater is shown in logs 81 and 12 (Fig. 3.10). There are gradational and distinct contacts between the various pyroclastic lithofacies which include lava-like agglutinate (l-l Agg), clast-supported, incipiently and moderately welded spatter bombs (waSp and mwSp), clast-supported weakly agglutinated scoria lapilli and bombs (waSc) and clast-supported densely welded scoria (dwSc). Cored bombs and armoured clasts with aphyric lava and agglutinate cores are common within the upper 15 m of the R-K volcanic sequence. Lava-like agglutinate (l-l Agg) is also common and forms a bifurcating network of 0.5–2 m thick beds that intrude into the adjacent clast-supported incipiently welded scoria lapilli (waSc; log 81, Fig. 3.10). This creates 8 m wide and 1 m

thick lenses of clast-supported weakly agglutinated scoria lapilli and bombs (waSc) within the lava-like agglutinate (Fig. 3.32B). Tension gashes occur at the margins of the lava-like agglutinate (l-l Agg).

The southeast cone flank is dominated by clast-supported, incipiently welded spatter bombs (waSp). The northwest cone flank is composed of 27–50 cm thick variably welded, inversely graded and massive pyroclastic deposits and lava-like agglutinate (l-l Agg; logs 9 and 10; Figs. 3.11 and 3.35). Both the pyroclastic units and lava-like agglutinate (l-l Agg) contain cored bombs and aphyric basalt lithics. Beds of the lava-like agglutinate (l-l Agg) thicken with distance from the crater and merge laterally, dipping 13° west-northwest. Normally graded sequences of clast-supported incipiently welded spatter bombs (waSp) and clast-supported non-welded scoria lapilli (ScL) are also present (Fig. 3.35). These sequences contain ragged, Hawaiian-type scoria clasts that become abundant towards the top of the section. At distances of 20–100 m southeast from the dyke the cone flank is composed of columnar-jointed pāhoehoe (Cp) and clastogenic and shelly pāhoehoe (log 29, Fig. 3.11). Numerous outcrops of fine, cross bedded volcanoclastic sandstone with gravel, pebbles and cobbles (fSxb) occur in this area (Figs. 3.3 and 3.33).

Interpretation:

The present dimensions of edifice 26 are not thought to be representative of its original size. The sedimentary lithofacies (e.g. fSdb and cCi) and the truncated beds within the NW margin of the crater indicate that it has been eroded. Projecting the dip of the eroded crater beds upwards, an estimated ~10 m of stratigraphy has been removed. Extending the outward dipping units at 28° from this reconstructed height gives edifice dimensions of 34 m high and 228 m in basal diameter. These dimensions and the cone height–width relationship (0.15) is similar to that reported for scoria cones (e.g. Wood 1980). The circular crater suggests that the cone was formed beneath a point-sourced fountain rather than a fissure.

Evidence for grain flow avalanches (i.e., lithofacies waSc(i); log 10, Fig. 3.10) indicates that cone building occurred partly via talus slope formation (e.g. McGetchin et al. 1974). Steep bedding on the south-eastern crater rim indicates that material was accumulating more rapidly on this side of the cone. The coarse bombs, rapid variations in welding and thick, densely welded units are typical of Hawaiian-style activity (Valentine and Gregg 2008). The size of the component clasts is typical of the deposits of Strombolian and Hawaiian-style eruptions (Valentine and Gregg 2008).

Accumulation of pyroclasts (e.g. spatter and cowpat bombs; Fig. 3.10, logs 10, 12 and 81) occurred dominantly from the inner and lower part of the fountain, or from a fountain <100 m in height (similar to those observed by Wolfe et al. 1988). Steeply dipping intrusive contacts between the lava-like agglutinate (l-l Agg) and pyroclastic units (lithofacies log 81; Fig. 3.10) may represent a section through a network of lava sills and dykes that fed flows outside the cone (e.g. Sánchez et al. 2014). Normally graded sequences of clast-supported weakly agglutinated spatter bombs (waSp) and clast-supported non-welded scoria lapilli (ScL) towards the top of the crater could represent the weakening of fountaining intensity with time. The rosette structure (Fig. 3.35) is interpreted as the remnants of a lava lake in an adjacent edifice, which was subsequently eroded by the Jökulsá River. Outcrops of fSxb at the base of the cone flank indicate fluvial erosion in this region.

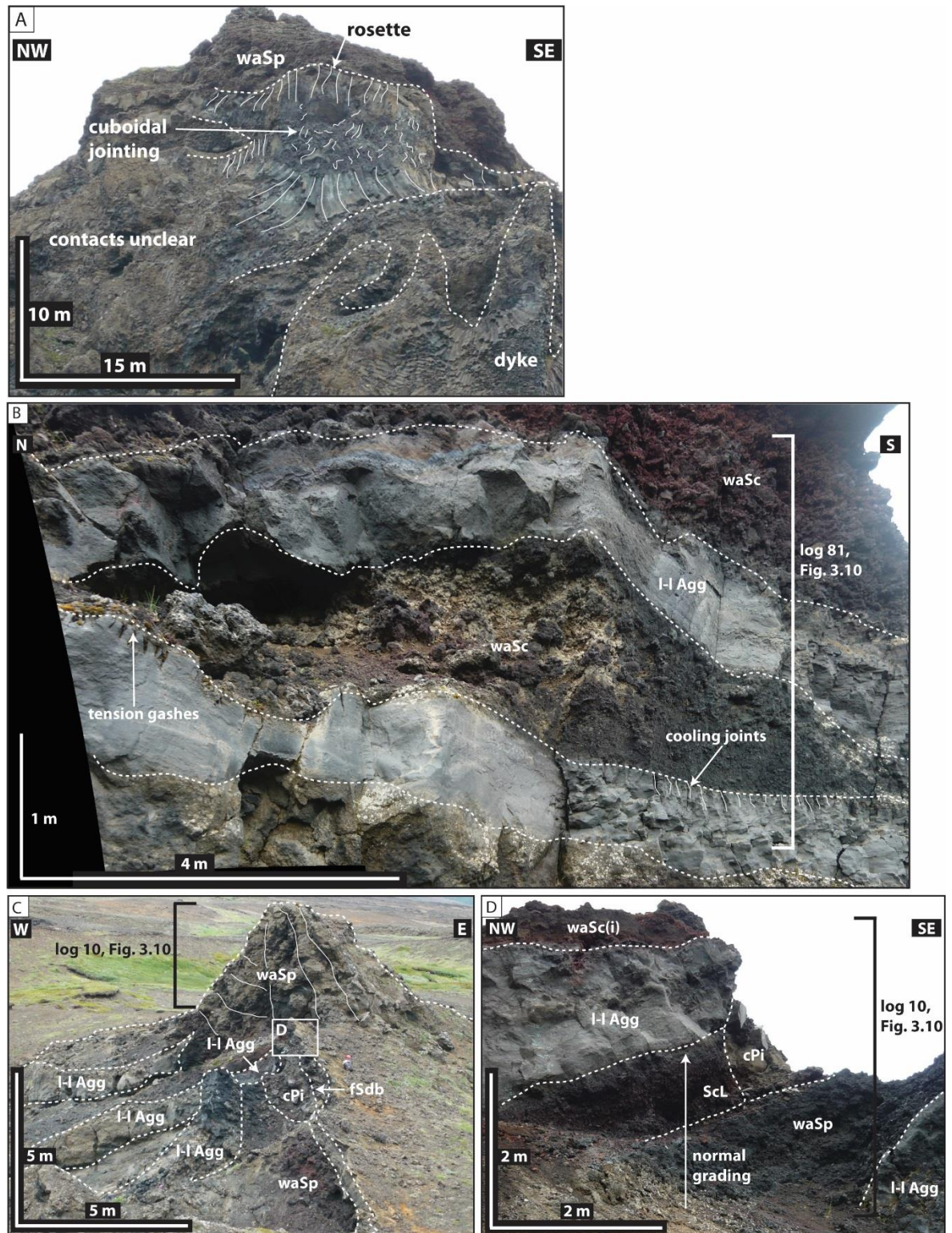


Figure 3.35. Photographs showing the architecture of edifice 26. (A) The rosette structure is located above the feeder dyke. The cooling joints at the top of the rosette are more closely spaced and shorter than those at the base, implying that the rosette cooled from the top downwards. (UTM 557498/7264870). (B) A lobate lense of clast-supported weakly agglutinated scoria lapilli and bombs (waSc) within the lava-like agglutinate (I-I Agg). The lava-like agglutinate (I-I Agg) has distinct contacts with the

clast-supported weakly agglutinated scoria lapilli and bombs (waSc) and is interpreted to be part of a lava sill/dyke network. (UTM 557447/7264902). (C) View of the northern crater rim showing the outwardly dipping units of lava-like agglutinate (l-l Agg) which merge further west. Inverse-graded cobble breccia (cPi) and fine, diffusely bedded volcanoclastic pebbly sandstone (fSdb) are visible inside the crater. (UTM 557438/7264880). (D) Photo of the outwardly dipping lithofacies on the crater rim. (UTM 557447/7264902).

3.7.6 The spatter ramparts

Spatter ramparts form 28–270 m long linear features along the fissure (Fig. 3.36). They are oriented both perpendicular and parallel to the strike of the fissure. They vary from <0.5–4.5 m in height and 16–25 m in width. Erosion exposes the internal architecture of a series of similar ridge-like features west of the river (Fig. 3.37). They are dominantly composed of lava-like agglutinate (l-l Agg) with minor components of clast-supported, incipiently, moderately and densely welded spatter bombs (waSp, mwSp and dwSp). Bedding in the ramparts has a modal dip of 45° (Table 3.6). They occur in a 100 m-wide zone centred above the strike of the fissure. Unconsolidated achneliths are common around the ramparts (Fig. 3.3).

The largest of these outcrops (Location Y29; Fig. 3.37) is 4.5 m high and 80 m in length. The southern face of the outcrop dips 40° to the south whilst its northern face dips up to 58° to the north and northwest. Both faces are composed of numerous discontinuous slabs of lava-like agglutinate (l-l Agg) and clast-supported weakly agglutinated spatter bombs (waSp). The agglutinate slabs are up to 4 m in length and 3 m in width and have a jigsaw-fit arrangement. At the apex of the rampart and where the dip changes from 08° to 55°, fractures 200 mm in width separate the slabs (Fig. 3.38). In some instances the slabs are missing, and lava-like agglutinate (l-l Agg) with a rubbly surface texture is exposed beneath. The slabs have resinous rinds 10 mm thick with ~3 mm deep scours on their external surfaces (Fig. 3.38). Some of these scours are overprinted by tension gashes oriented sub-perpendicular to the external surface dip direction. Many of these scours are oriented obliquely to the external surface dip direction (Fig. 3.38).

On the southern outcrop face, the texture of the crust on the uppermost agglutinate slab varies with height up the rampart. The upper 3 m of the slab has a scoured crust (Fig. 3.38), while the down-dip front (i.e. “snout”) of the slab has a rugose outer crust. This rugose crust is formed by ragged protrusions that vary in height and width from 10–40 mm

and 10–50 mm respectively. The protrusions are separated by tension gashes which form preferentially towards the snout of the agglutinate beds (Fig. 3.38). The tension gashes decrease in width with distance from the snout (Fig. 3.38).

Internally the slab has a vesicular upper and lower crust. Each of the crusts comprises ~30 % of the thickness of the slab. The crusts have homogeneously distributed <1–3 cm diameter vesicles that have a mean abundance of 15% (Fig. 3.39). The vesicles are irregular and elongate, with the direction of elongation sub-parallel to the crust surface. Underlying beds of spatter are discordant with the uppermost slab and give the rampart a “patchwork” internal character (Fig. 3.39). These beds dip 27–56° to the southwest and some have scoured upper surfaces similar to the outermost surface. Individual beds vary from 150–2500 mm thick and pinch out after ≤ 1 m. Relict pyroclasts are occasionally visible; where preserved they are ≤ 100 mm long and 10 mm thick, oriented parallel to the upper contact with the lava-like agglutinate (l-l Agg).

Location Y28 (Figs. 3.37 and 3.40) is another ridge-like outcrop that is 3 m high and 28 m in length. Its outer surface dips sub-vertically on the southern face and 47° on the northern face (Fig. 3.37). Internally the outcrop is composed of clast-supported weakly agglutinated spatter bombs (waSp) overlain by lava-like agglutinate (l-l Agg). The lowermost 240 mm of lava-like agglutinate (l-l Agg) is non vesicular and has 4 mm thick resinous laminations and tension gashes that dip 42° to the south. The lava-like agglutinate (l-l Agg) grades upwards into massive, incipiently vesicular lava-like agglutinate (l-l Agg). It is incipiently vesicular with a patchy, heterogeneous distribution of <1–10 mm diameter vesicles. 20 mm long ghost clasts that dip 20° to the SE are observed in the upper 400 mm. Tension gashes up to 170 mm in length intersect the 70 mm thick outer crust and fragment it into equant ~200 × 150 mm sized jigsaw-fit plates. Agglutinated, non-welded scoria lapilli cover <5% of the surface.

Interpretation:

The ridge-like features west of the river are interpreted as spatter rampart and cone-like features (e.g. Thordarson and Self 1993). They preserve delicate surface features (e.g. mm-scale scours and crustal protrusions; Fig. 3.38) indicating that there has been minimal erosion. It is possible that these ramparts represent the early aborted stages of scoria cone growth (e.g. Wolfe et al. 1988; Valentine and Cortés 2013). The ramparts are dominantly composed of lava-like agglutinate (l-l Agg) and provide no evidence of subsidence into the underlying columnar-jointed pāhoehoe (Cp) that would suggest rafting (e.g. squeeze-ups at

the margins of the rafted fragments; see Sumner 1998; Valentine et al. 2006). Their location within a 100 m-wide zone centred on the strike of the fissure (Fig. 3.37) suggests that they are in-situ and dyke-fed. There is no evidence to suggest that they formed above a lava tube, as required for hornito formation (Németh 2014).

Cross sectional exposure of the ramparts suggests that they accumulated rapidly from pyroclasts sourced from the inner part of the lava fountain, or from low fountains that yielded a high proportion of spatter bombs. Although the depositional processes are hard to discern due to the high degree of welding, a combination of post-depositional modification processes are observed. These processes include flow, scouring, brittle failure and gravitational spreading.

Numerous tension gashes in the agglutinate deposits indicate that they started to flow. Tension gashes become more abundant and widen towards the snout of agglutinate beds (e.g. Fig. 3.35) suggesting that that shear strain was concentrated here. Scours (location Y29) are inferred to result from the slip of solidified agglutinate sheets and/or pyroclastic deposits down the outer surface. Cross-sections through the rampart expose numerous scoured surfaces within the deposit, suggesting this process was repeated during rampart construction. The varying orientation of the scours suggests that material slid downwards as numerous separate sheets, as opposed to whole scale collapse of the external rampart face. The absence of lateral scours on the surfaces suggests that the scours were not caused by lava flow along the fissure (e.g. Parcheta et al. 2012). The tension gashes that overprint the scours suggest brittle deformation of the external surfaces of the rampart after material has scoured them. Location Y29 is inferred to have been constructed by the accumulation and coalescence of spatter bombs, which subsequently underwent clastogenic flow (Fig. 3.41). Brittle failure of the agglutinate is indicated by the angular external margins of the agglutinate slabs at location Y29 (Fig. 3.38). The brittle failure of the slab at the change in dip magnitude suggests failure was initiated by over-steepened depositional slopes.

Unstable agglutinate piles underwent gravitational spreading (Locality Y28, Fig. 3.42) as inferred from the tension gashes at the base of the deposit and those which fracture the crust into numerous jigsaw-fit plates. The non-vesicular base of the agglutinate may have acted as a slip plane during deformation (e.g. Sumner 1998). Spreading was induced by the steep dips maintained by the accumulating agglutinate pile. The outer crust and the ghost clasts have differing orientations, suggesting that the crust represents a cooling surface and not a depositional surface (e.g. bedding plane).

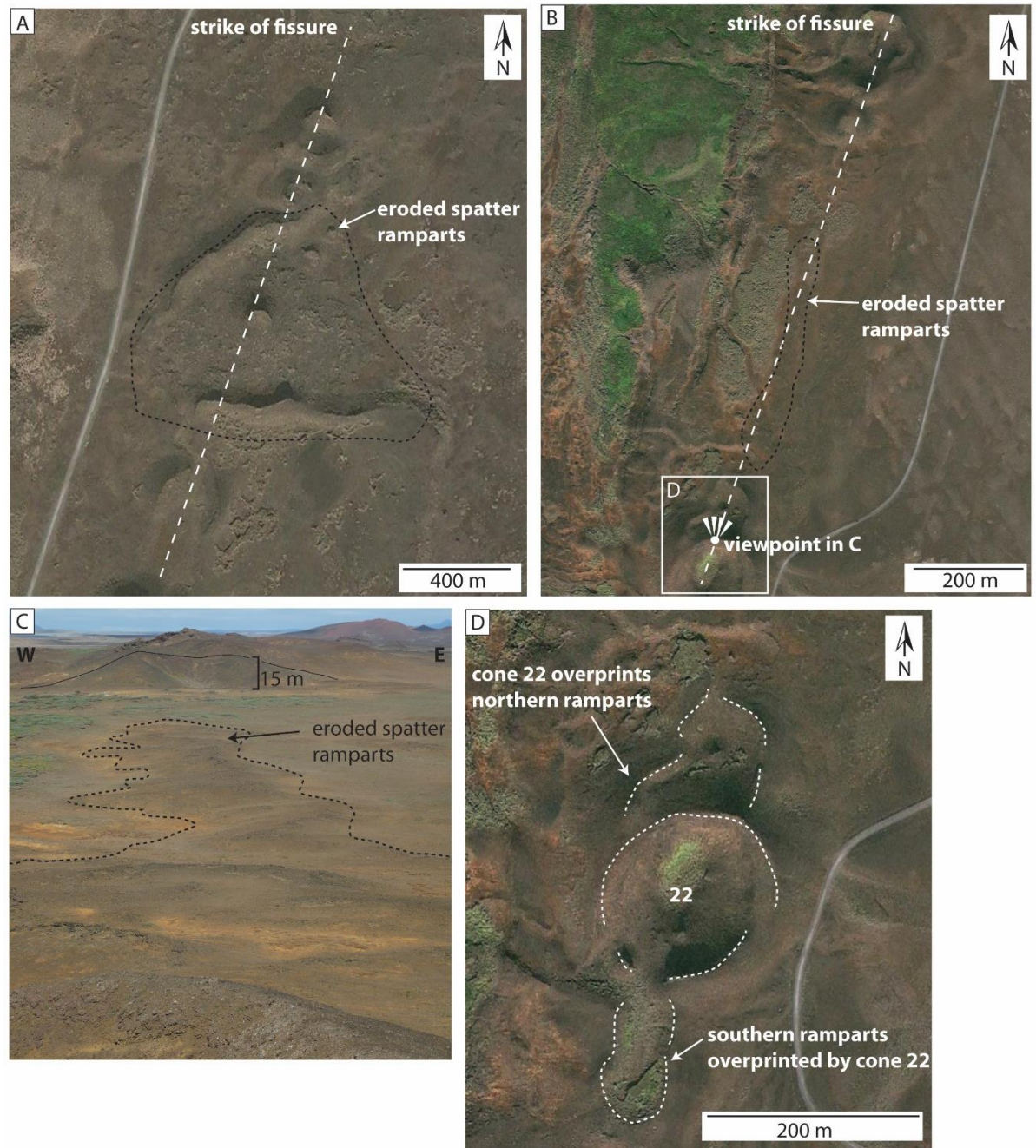


Figure 3.36. Orientation and onlap relationships of the spatter ramparts. (A) Google Earth image showing that some spatter ramparts are oriented perpendicular to the strike of the fissure. **(B)** Google Earth image of eroded spatter ramparts that are oriented parallel to the strike of the fissure. **(C)** Photograph of the spatter ramparts shown in B. **(D)** Google Earth image of scoria cone 22 overprinting adjacent spatter ramparts. The onlapping relationship of the edifices cannot be used to constrain the direction in which the fissure propagated. See Fig. 3.5 for location.

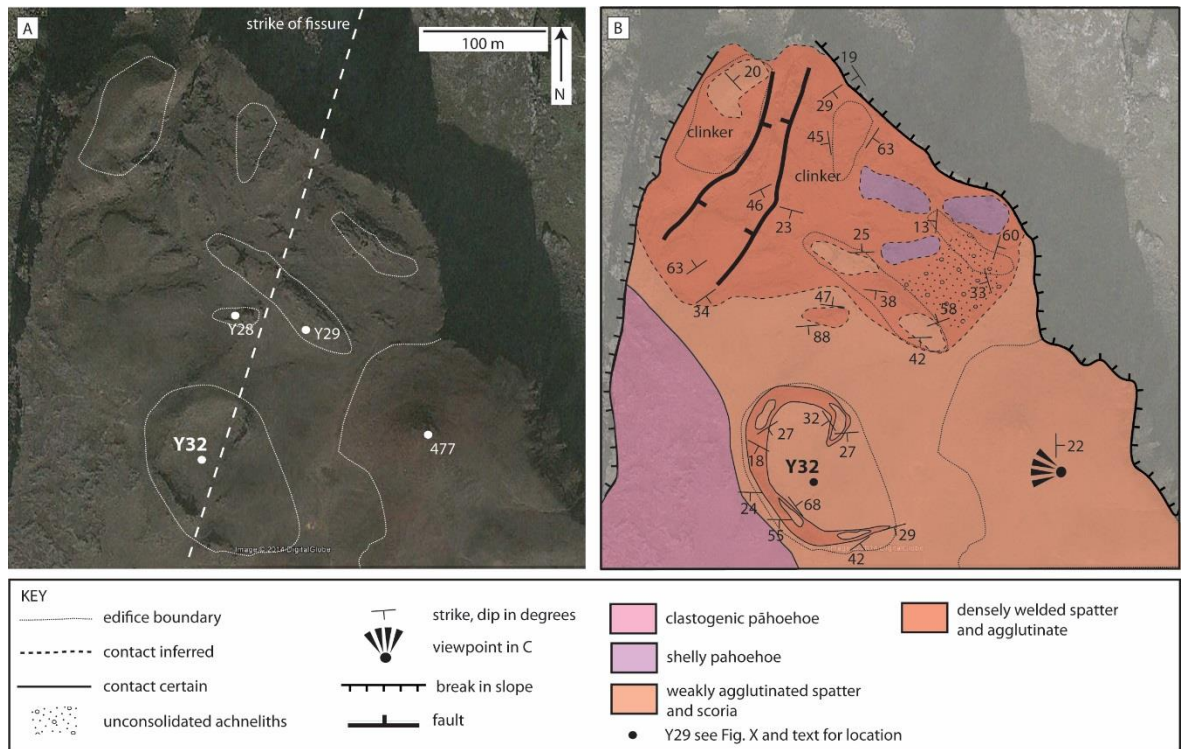


Figure 3.37. Google Earth image (A) and geological map (B) of the spatter ramparts west of the river. See Fig. 3.3 for location.

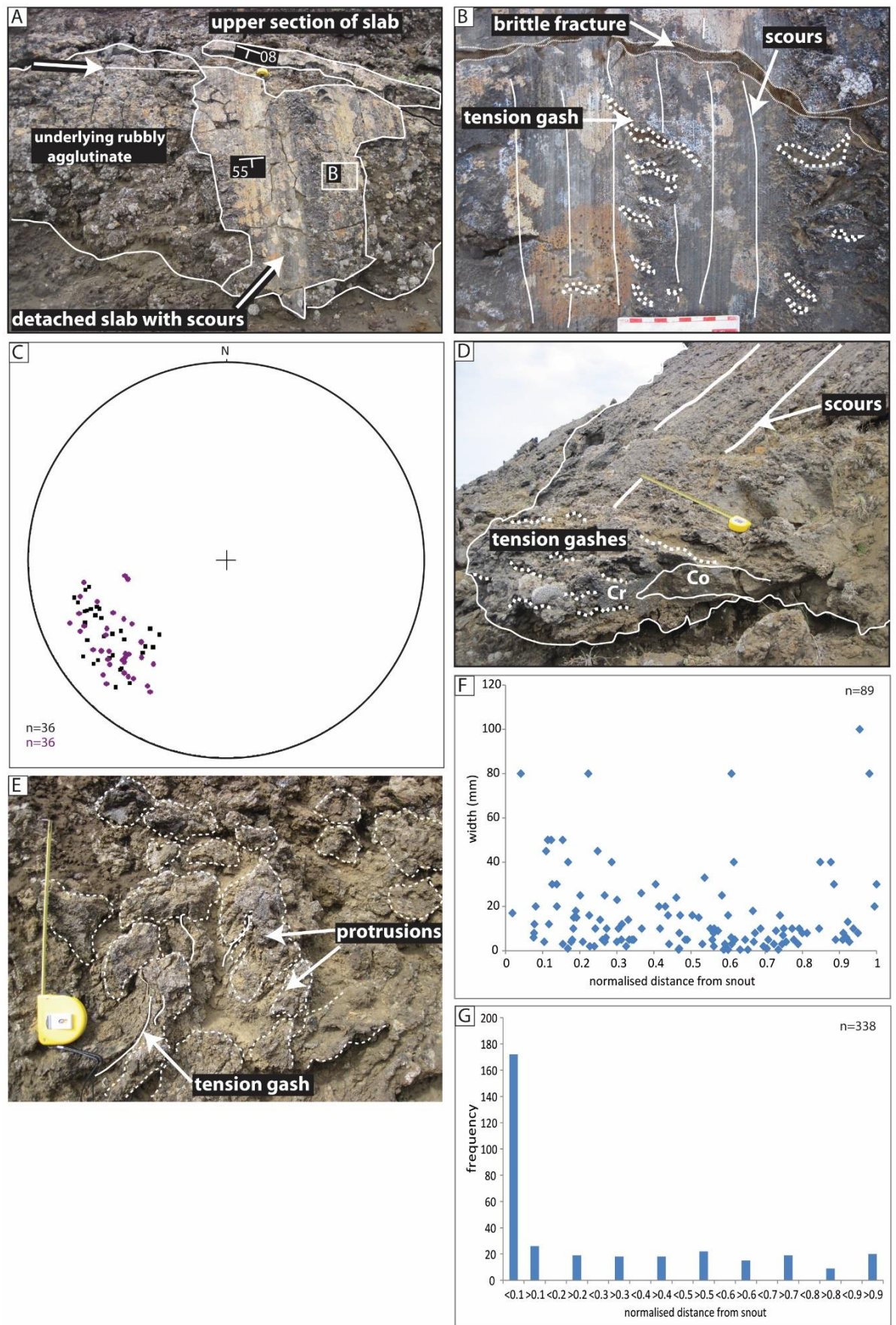


Figure 3.38 (overleaf). Features and measurements associated with location Y29. (A) Scoured agglutinate slab with adjacent sections missing, exposing underlying rubbly agglutinate. The slab has detached from the upper section (arrowed) where the dip of the outcrop changes. The tape measure (arrowed) is 1 m long. (UTM 564346/7301822). (B) Close up of the scours overprinted by tension gashes (outlined), indicating deformation of the agglutinate after the external surface was scoured. Graticules on the scale card are 1 cm. (UTM 564346/7301822). (C) Stereonet plot to show orientation of bedding (black) and scours (purple) on the southwest face of location Y29. The scour plunges are not parallel to the bedding dip direction suggesting that sliding from the outer face occurred in numerous directions with a component of lateral movement. (D) Cross sectional view of the snout of an agglutinate bed. The tension gashes (dashed lines) on the crust (Cr) are perpendicular to the scours (sub vertical striations) and give the snout a rugose texture. The core of the bed (Co) is also exposed (see Fig. 3.39 for details). The tape measure is 1 m long. (UTM 564346/7301822). (E) A rugose textured surface, showing irregular protrusions separated by tension gashes. The ruler is 10 cm long. (UTM 557584/72664247). (F) Graph showing that tension gashes are most abundant towards the snout of the agglutinate sheets, where 0 = the snout tip. (G) Graph showing that crenulation width tends to decrease with distance from the snout of agglutinate beds, where 0 = the snout tip. Graphs F and G suggest that strain is greatest towards the snout of the beds.

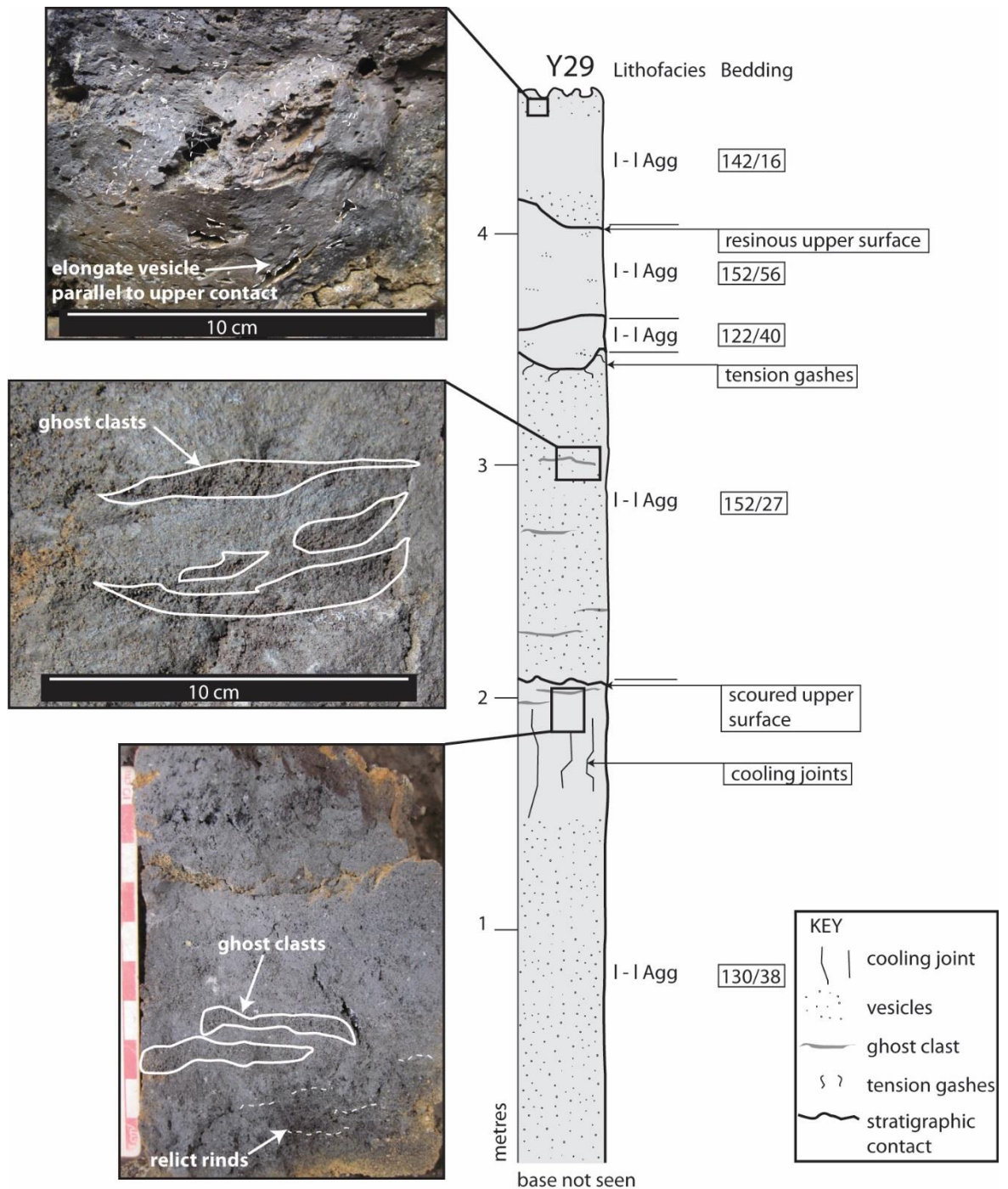


Figure 3.39. Stratigraphic log showing the internal componentry of location Y29. The outcrop is composed of numerous discordant slabs of agglutinate. The upper unit of agglutinate is shown in Fig. 3.38D. See Fig. 3.37 for the location.

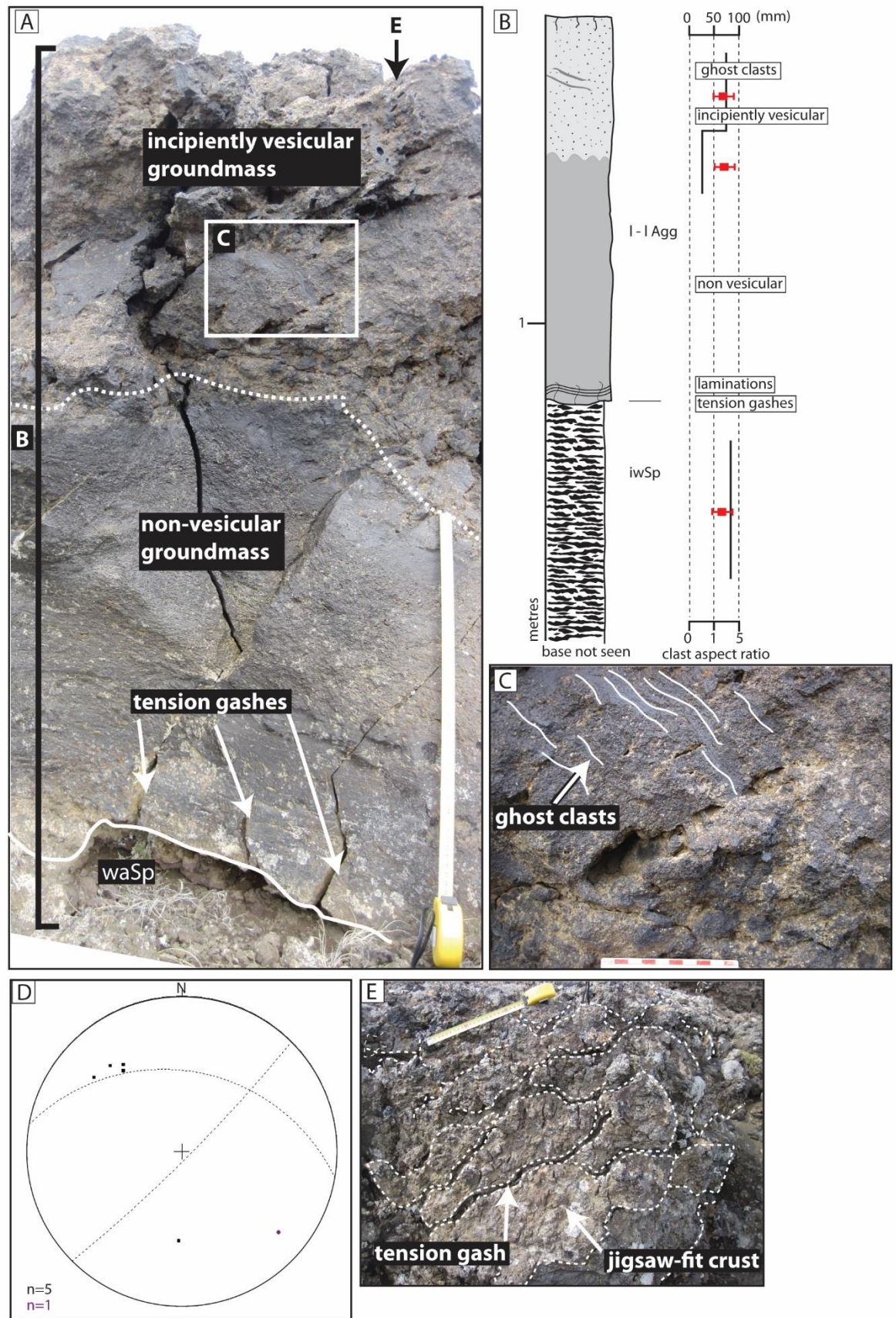


Figure 3.40. Photographs and measurements associated with location Y28. (UTM 564390/7301820). (A) Cross section of the agglutinate, with clast-supported incipiently

welded spatter bombs (waSp) beneath. The agglutinate becomes more vesicular with height and has a 70 mm thick platy crust. Tension gashes occur at the base (arrowed) and in the incipiently vesicular agglutinate in the upper 0.5 m. The tape measure is 50 cm long. (B) Log showing the internal stratigraphy of A. Clast aspect ratio is shown in red, juvenile clast size in black. (C) Details of the ghost clasts (solid lines). Graticules on the scale card are 1 cm. (D) Stereonet to show the orientation of the crust (great circles) tension gashes (black) and ghost clasts (purple). The tension gashes are approximately perpendicular to the outer crust. (E) Photo of the upper crust showing the jigsaw-fit plates. The tape measure is 25 cm long.

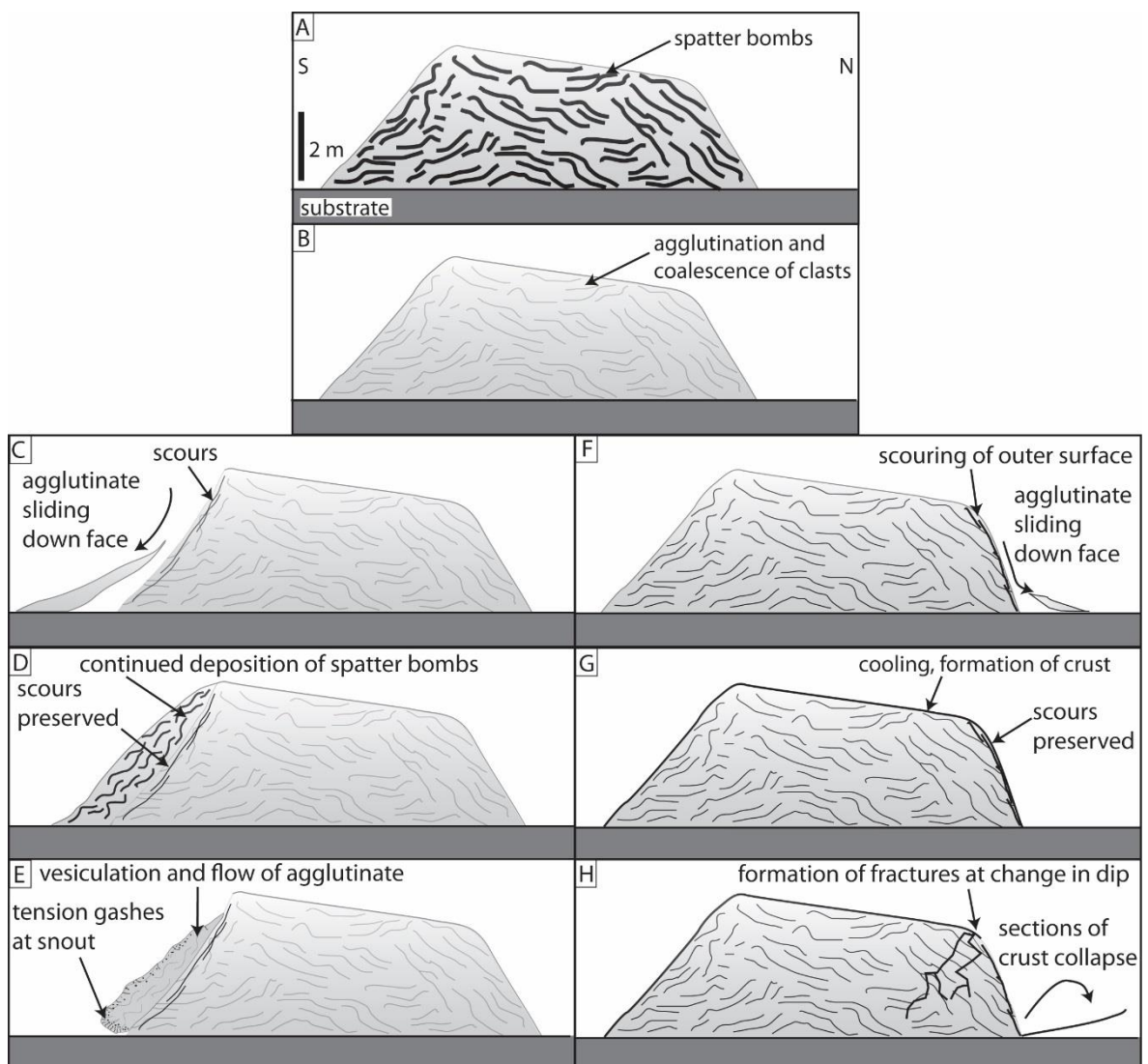


Figure 3.41. Schematic diagram to show the development of Location Y29. Images A and B show the accumulation and coalescence of constituent spatter bombs during Hawaiian-style activity. Images C–E show the evolution of the south face, whilst images F–H show the evolution of the north face of the rampart. (C) Agglutinate

slides down the rampart, scouring the underlying face. The material that causes the scouring is not observed. (D) Continued lava fountaining deposits spatter bombs atop the scoured surface. (E) The spatter bombs coalesce forming a slab of agglutinate, on which a crust develops. This crust is deformed by tension gashes (found dominantly towards the snout of the slab) during clastogenic flow. This slab has scours on its outer surface, suggesting repeating episodes of deposition and flow (not shown). The absence of material at the toe of the slab may suggest collapse of the slab in stages. (F) On the northern slope scouring occurs due to sliding of material down the outer rampart face. (G) The scours are preserved as the rampart cools and a brittle crust develops. (H) Fractures form at the change in dip amplitude and sections of the outer crust collapse due to gravitational instability.

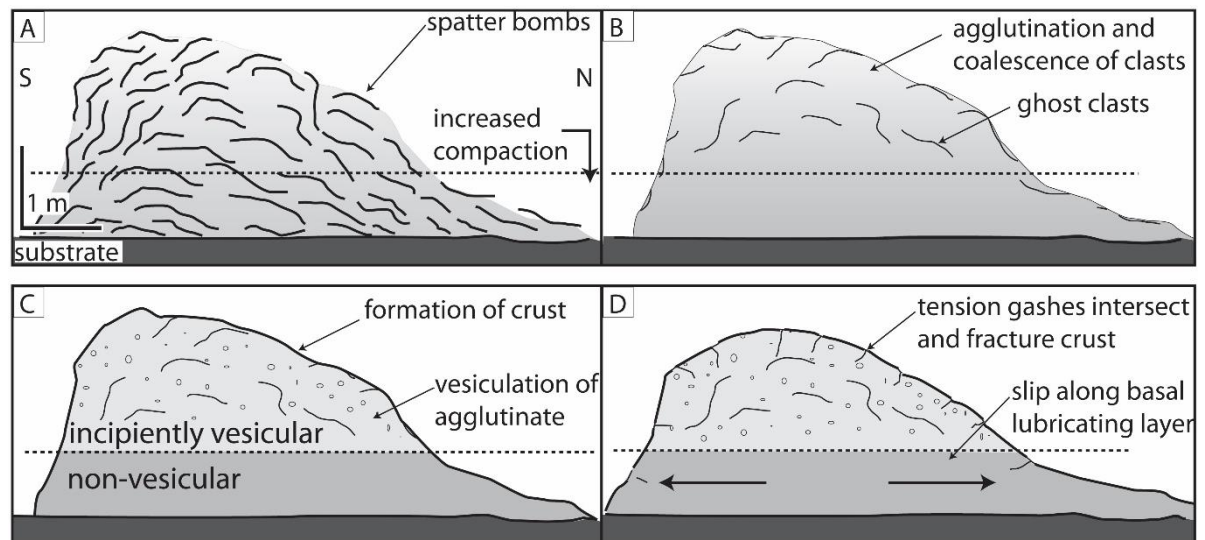


Figure 3.42. Interpretive picture to show the development of location Y28. (A) High rate accumulation of spatter bombs during lava fountaining. Welding intensity is greatest beneath the dashed line. (B) Agglutination and coalescence of pyroclasts. Ghost clasts remain in the upper part of the deposit. (C) Bubbles migrate upwards in the deposit and a crust forms. (D) Gravitational spreading is initiated along the basal lubricating layer. The crust is fractured into numerous plates. Note that stages A and B are contemporaneous: welding and coalescence occurring during deposition.

3.8 Evolution of the fissure

The R-K eruption was characterised by Hawaiian activity. The eruption chronology (Fig. 3.43) is described below.

Phase 0: Pre-eruption topography

The Sveinar graben and numerous other normal faults existed prior to the R-K eruption. The orientation of these faults was influenced by the regional northeast-southwest trending extensional tectonic regime and the TFZ (e.g. F9, F12, Figs. 3.4, 3.28 and 3.29). These faults controlled the location of surface water bodies.

Phase I: Initial eruption, effusion of lava flows and rootless cone explosions

The dyke fed numerous en-echelon fissure segments that propagated north-south. The fissure produced abundant flows of columnar-jointed pāhoehoe (Cp) which were largely confined to the southeast margin of the graben (F33). Interaction between inflating lava flows and surface water resulted in rootless explosions. Lava fountains were >100 m in height and constructed scoria ramparts (Location 406).

Phase II: Constriction of the fissure

Continued lava effusion deformed and buried early scoria ramparts. The fissure began to evolve to numerous point sources due to thermal instabilities along the fissure (e.g. Bruce and Huppert 1989; Thordarson and Self 1993; Keating et al. 2008; Brown et al. 2014). The decreasing abundance of columnar-jointed pāhoehoe (Cp) with time suggests that the magma flux decreased with time. Fountain heights may have increased due to narrowing of the conduit (e.g. Valentine and Cortés 2013). Scoria ramparts were constructed in proximal regions by fountains >100 m in height (location 280) and scoria fall deposits were dispersed ≥ 1 km from the fissure (location 462).

Phase III: Cone construction and flow of lava flows into water

Edifice 26 was constructed by fountains ≤ 100 m in height. Synchronous with the development of cone 26 was the development of an adjacent edifice, now eroded by the Jökulsá River. Further south, this section of the fissure began to close and an adjacent westerly section opened. Deposits from this lava fountain formed a scoria rampart (location 477). Clastogenic pāhoehoe (Cl) was also produced via a combination of effusion and pyroclast coalescence under fountains. Towards the south lavas entering bodies of

surface water (e.g. between F9 and F12) transformed into hyaloclastite and pillow lavas and filled these basins. Decreasing surface water abundance with time restricted hyaloclastite and pillow lavas to the base of the R-K volcanic sequence.

Phase IV: Spatter rampart formation and drowning of the topography

In the north of the study area, hummocky lava was emplaced. Further south, continued deposition from the westerly section of the fissure created spatter ramparts during Hawaiian-style activity. Clastogenic lava flooded the topography and was largely confined within the Sveinar graben. At the end of the eruption shelly lavas were effused from edifices (Fig. 3.3) during phases of low (<100 m) or absent fountains.

Phase V: Extensional faulting and fluvial erosion

Pyroclastic constructs were deformed by slip along faults 1, 2, 38 and 4. Post-eruption faulting associated with the Sveinar graben continued (faults 33 and 9). Flooding and percolation of water into cooling volcanic deposits resulted in the formation of hackly jointing (e.g. within the columnar-jointed pāhoehoe (Cp) in the scoria rampart; Fig. 3.25). Fluvial erosion, in part linked to glacial floods (e.g. Alho et al. 2005; Kirkbride et al. 2006; Waitt 2009) eroded the upper parts of the R-K volcanic sequence. Drainage channels became established along former pathways (e.g. between faults 9 and 12). Deepening of the Jökulsá a Fjöllum canyon exposed the feeder dyke, as observed today.

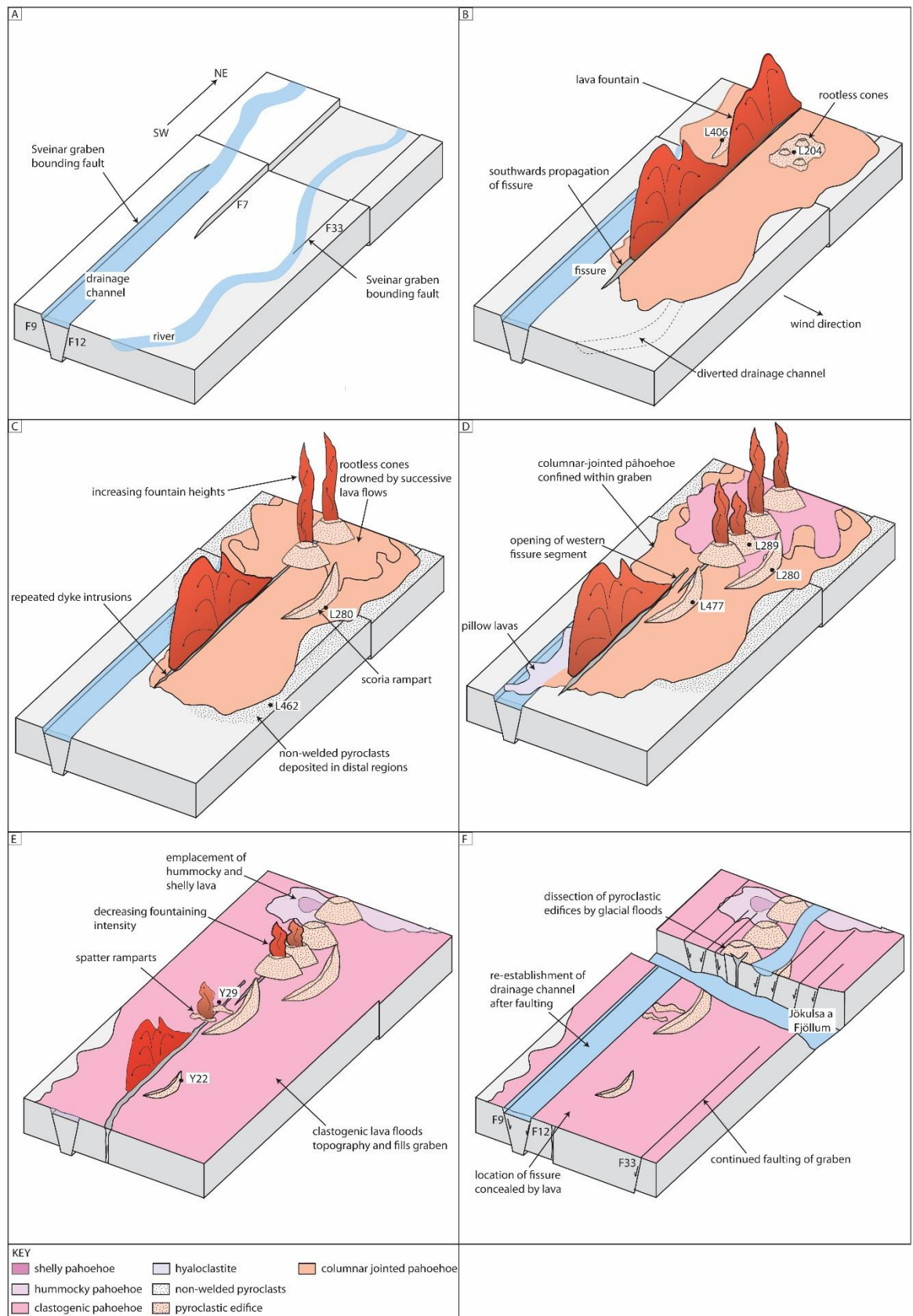


Figure 3.43 (overleaf). Schematic diagram to show the development of the R-K fissure. (A) Phase 0: The Sveinar graben pre-dates the fissure. Drainage patterns are controlled by pre-existing faults. (B) Phase I: The dyke fed numerous en-echelon fissure segments that propagated north-south. (C) Phase II: Lava flows buried scoria ramparts. The fissure began to evolve to numerous point sources due to thermal instabilities. (D) Phase III: Low fountains ≤ 100 m in height constructed edifice 26 (location 289). (E) Phase IV: In the north of the study area, hummocky lava was emplaced. (F) Phase V: Pyroclastic constructs were deformed by slip along faults. Post-eruption faulting associated with the Sveinar graben continued. Diagram not to scale.

3.9 Discussion

3.9.1 Feeder dyke and conduit morphology

The single set of cooling joints within the R-K feeder dyke is consistent with emplacement during a single injection (Sheth and Cañón-Tapia 2014). Widening of the conduit beneath the scoria-agglutinate cone dominantly occurs in the upper 50 m, as observed elsewhere (e.g. Keating et al. 2008; Geshi et al. 2010; Hintz and Valentine 2012). The conduit was enlarged by multiple intrusive events, and/or by dyke intrusion into the conduit when the eruption had ceased (e.g. Friese et al. 2013). Country rock lithics are absent from the dyke-fed R-K volcanic products, suggesting that dyke and conduit widening occurred without host rock removal. The evidence of syn-eruptive faulting throughout the R-K volcanic sequence suggests that graben development played an important role in accommodating dyke and conduit widening (e.g. Rubin 1992; Valentine and Krogh 2006), likely in tandem with free-surface effects (e.g. Galindo and Gudmundsson 2012).

I agree with the conclusions of Galindo and Gudmundsson (2012) and Geshi et al. (2010) that feeder dykes are segmented, sheet-shaped, widen towards the surface and trigger slip on existing faults (e.g. Gudmundsson et al. 2008). However, due to access, I am unable to observe if the dykes beneath edifice 26 contain cavities or vesicles in their uppermost sections (e.g. Galindo and Gudmundsson 2012). No vesicles or cavities were observed in the dyke at location 478; the significance of this (if any) is unknown.

3.9.2 Rootless eruption mechanisms

The rootless tephra deposits adjacent to the dyke (massive scoria lapilli and bombs; mSc; Figs. 3.11 and 3.31) have several features that are atypical of rootless tephra in other settings. The initiation of rootless explosions require a compressible, granular and water-saturated substrate; this substrate is commonly erupted along with the rootless tephra derived from the fragmentation of an inflating lava flow (Hamilton et al. 2010). No such substrate is observed within rootless tephra deposits. Although the lower contact of the columnar-jointed pāhoehoe (Cp) is not observed, there is <1 m between the base of the lava-like agglutinate and the underlying topography. This suggests that there is little or no sediment is present beneath the columnar-jointed pāhoehoe (Cp). Therefore, it is unlikely that rootless explosions occurred by penetration of lava into an unconsolidated substrate and another method is required. One hypothesis is that the influx of water post-dated the emplacement of the lava, but that explosive interaction occurred only after sufficient water had percolated beneath the inflating lava flow. Alternatively, a high water table in the underlying columnar-jointed plagioclase-porphyrific flows could have provided a reservoir of water. These mechanisms for rootless cone formation are as yet untested, but may provide insights into the diversity of lava-water mechanisms. These mechanisms have potential implications for hazard assessments and for the ability of rootless cones to form on other planetary bodies (Fagents et al. 2002; Fagents and Thordarson 2007).

Another hypothesis is that the features represent the vents of littoral-style cones, resulting from the penetration of lava flows into open water (e.g. Mattox and Mangan 1997). In this case, explosive interaction could have resulted from the collapse of a lava delta system (e.g. Mattox and Mangan 1997). I find no evidence of the delta system at this location; however this could have been removed during creation of the Jökulsá canyon.

3.9.3 Scoria ramparts

The R-K fissure is rare in exposing the internal architecture of scoria ramparts generated during basaltic fissure eruptions. The ramparts are inferred to have been produced by a fountain that was >100 m in height; fountains <100 m in height produce little tephra (Wolfe et al. 1988). The ramparts are composed of similar lithofacies to the cones (e.g. clast-supported incipiently welded spatter bombs, waSp; clast-supported moderately welded scoria lapilli and bombs, mwSc; clast-supported densely welded spatter bombs, dwSp; clast-supported weakly agglutinated scoria lapilli and bombs, waSc; and scoria lapilli, ScL). They are inferred to pre-date the formation of adjacent cones (e.g.

Thordarson and Self 1993). Scoria ramparts are observed elsewhere along the R-K fissure, suggesting that the section proximal to the Jökulsá canyon was not unique in terms of eruptional style.

Unlike scoria cones the ramparts lack lithic clasts, likely the result of poor thermal coupling of the lithic clasts with the lava fountain (see section 3.4). In ancient, heavily eroded examples, distinction between scoria ramparts and scoria cones is important because scoria ramparts are not always underlain by dykes (e.g. Location 280). Therefore, they do not necessarily provide insights into the subsurface geology. Furthermore, the ramparts form under different fountain conditions to cones. Misinterpreting eroded ramparts as cones may therefore lead to erroneous conclusions about eruption dynamics (e.g. fountain height).

3.9.4 Scoria-agglutinate cone

The componentry of edifice 26 is lithologically similar to that of spatter cones, which are commonly composed of large, deformed and strongly welded spatter bombs, deposited under fountains <100 m in height (Wolfe et al. 1988; Riedel et al. 2003; Cimarelli et al. 2013). However, edifice 26 is significantly larger spatter cones reported in the literature (10–40 m high and 5–15 m in diameter; see Green and Short 1971; Opheim and Gudmundsson 1989; Thordarson and Self 1993; Rymer et al. 1998; Heliker et al. 1998). The edifice is also smaller than the agglutinate cones described by Brown et al. (2014) and does not have the same characteristic low angle bedding. The edifice has a similar bedding dip, size and height:basal diameter relationship to that of a scoria cone (e.g. Wood 1980). However, scoria cones are typically composed of welded and non-welded beds of scoria lapilli (e.g. McGetchin et al. 1974; Houghton and Schmincke 1989; Valentine et al. 2006) with a median grain size of 1 cm (Riedel et al. 2003); unlike edifice 26.

Since the architecture of edifice 26 shares compositional similarities with spatter cones and is similar to a scoria cone in size, the term “scoria-agglutinate cone” is applied (e.g. Vespermann and Schmincke 2000). The edifice is thought to have formed under a fountain that favoured the high rate accumulation of spatter, likely <100 m in height (e.g. Wolfe et al. 1988). Based on an accumulation rate of >20 cm/min to produce the welded deposits (e.g. lava-like agglutinate and clast-supported moderately welded spatter bombs; see Sparks and Wright 1979; Thomas and Sparks 1992) the cone would have taken 3 hours to construct. Morphologically similar edifices that appear to be dominantly composed of

spatter-rich lithofacies are found elsewhere along the R-K fissure, suggesting that this section of the fissure was not unique in terms of eruption style.

3.9.5 Spatter ramparts

This is the first study to provide document the evolution of spatter ramparts. The Hawaiian-style volcanism that dominated during rampart construction is complementary to observations of historic eruptions (e.g. Parcheta et al. 2012). Spatter ramparts are commonly produced by fountains <100 m in height (Wolfe et al. 1988; Parcheta et al. 2012) and may develop to form spatter cones (e.g. Wolfe et al. 1988). Their preservation indicates that activity along this section of the fissure was not prolonged enough to allow a cone to develop. Activity ends along sections of the fissure when magma flow is focused elsewhere (Bruce and Huppert 1989; Keating et al. 2008), implying that this section of the fissure closed earlier than more southerly sections.

The ramparts have similarities with the spatter cones described by Thordarson and Self (1993), which are superimposed on adjacent scoria cones and half cones. These features commonly merge and intersect in a complex fashion. The ramparts are also comparable with those described by Dickson (1997); Moore et al. (1980) and Parcheta et al. (2012); all of which have heights of ≤ 5 m. However, unlike the ramparts described by Parcheta et al. (2012), some of the ramparts in this study are oriented perpendicular to the fissure. This may suggest the R-K ramparts are preserved at a stage of growth transitional between true ramparts and cones. The lengths of the features described in this study are considerably longer than those described elsewhere (e.g. Parcheta et al. 2012). The reason for this is speculative given the sparse data, but may relate to the length of the active fissure. Ramparts described by Parcheta et al. (2012) are located adjacent to the fissure, or set-back up to 30 m. The set-back of the ramparts in this study is difficult to determine as the location of the dyke is concealed: it is also impossible to determine which of the rampart faces is the inner face as described by Parcheta et al. (2012).

The post-depositional modification processes detailed in this study are broadly comparable to processes observed in contemporary eruptions. Location Y28 evidences the early stages of post-depositional flow at an asymmetric, over-steepened rampart (e.g., McNutt et al. (1991). However, the collapse observed by McNutt et al. (1991) occurred on steep slopes, unlike the shallow slopes on which the ramparts in this study were constructed. Partial collapse in this study is inferred to have been triggered by the

presence of a basal lubricating layer, similar to that described by Sumner (1998) during the collapse of the Izu-Oshima scoria cone.

The processes that resulted in the internal variability of the R-K ramparts are comparable with processes observed by Heslop et al. (1989) and Andronico et al. (2014), who describe lava flows issuing from spatter ramparts. We note the similarity with Location Y29 which exhibits lava-like agglutinate (l-l Agg) that seems to have flowed from the rampart. Furthermore, Heslop et al. (1989) suggest that ramparts can be composed of a molten core and brittle crust, similar to Y28 which had a jigsaw-fit, platy crust and molten interior.

Understanding the formation of spatter ramparts is important for helping us identify the locations of vents in the geological record. Understanding the methods by which they grow also has implications when modelling the growth of monogenetic constructs (Riedel et al. 2003). Furthermore, the post-depositional modification processes observed in this study has implications for our assessment of hazards associated with monogenetic edifices.

3.9.6 Comparison with flood basalt and high-volume (>1 km³) fissure eruptions

The R-K fissure is typical of fissure systems in Iceland; it is a mixed cone row composed of overlapping and merging scoria and spatter cones (e.g. Thordarson and Larsen 2007). High volume eruptions that produce >1km³ of lava (e.g. Laki in 1783–1785 and Eldgjá in 934), are also characterised by these mixed cone rows (Thordarson and Self 1993; Thordarson and Larsen 2007). The types of cones rows formed during flood basalt eruptions are poorly known. The best preserved example of a cone row in a flood basalt province (FBP) is the row of agglutinate cones along the Roza fissure in the Columbia River Flood Basalt Province (CRFBP). A number of features presumed to be shield volcanoes are also found discontinuously along the Roza fissure (Swanson et al. 1975). No other types of edifices are documented. Thus, the diversity of edifices that commonly typifies mixed cone rows (Thordarson and Larsen 2007) are not found from the Roza example. The assemblage of cones along the Roza fissure could be analogous to the rows of spatter-like cones found above the Threngslaborgir and Lúdentborgir fissures (Thordarson and Larsen 2007). Alternatively, the abundance of the agglutinate cones could reflect preservation bias. This preservation bias is a result of componentry of the cones; they are dominated by densely welded scoria and spatter (Brown et al. 2014). These lithofacies are less susceptible to erosion than more vesicular rocks (e.g. scoria, see Manville et al. 2009), therefore the cones stand a higher chance of preservation.

Furthermore, since rafting is dependent on the mass of the collapsing material and the yield strength of the underlying lava (Valentine and Gregg 2008), the agglutinate cones would have been less susceptible to syn-eruptive destruction and transport than edifices composed of vesicular pyroclasts (e.g. scoria cones).

The R-K edifices have many similarities with the edifices formed in flood basalt eruptions (Swanson et al. 1975; Reidel and Tolan 1992; Thordarson et al. 2001; Thordarson and Larsen 2007; Brown et al. 2014). These similarities include an abundance of clasts formed during Hawaiian-style lava fountaining (e.g. achneliths, cowpat bombs) that have similar vesicularities (Thordarson and Self 1993; Brown et al. 2014). In all examples there is an abundance of clastogenic and shelly pāhoehoe, as well as welded deposits. Furthermore, the R-K deposits indicate fluctuating fountaining intensity, as documented during the Laki and Roza eruptions (Thordarson and Self 1993; Brown et al. 2014). As in many examples, the R-K, Columbia River and Laki edifices are commonly asymmetric due to either wind (Reidel and Tolan 1992; Thordarson and Self 1993; Brown et al. 2014) or angled fountains (Brown et al. 2014). The R-K edifices are also found within a graben that developed during the eruption, as documented in Iceland and the CRFBP (Swanson et al. 1975; Thordarson and Self 1993). This is typical of many volcanic systems in which dyke intrusion causes faulting (Pollard et al. 1983; Rubin and Pollard 1988; Rubin 1992; Chadwick and Embley 1998).

The R-K feeder dyke is a single injection dyke, analogous to that for the 1783 Laki eruption (Sheth and Cañón-Tapia 2014 and references there-in). This is in contrast to the Joseph Creek dykes (Reidel and Tolan 1992) which have a similar appearance to the “multiple dykes” found in the Deccan Volcanic Province (Sheth and Cañón-Tapia 2014). These dykes indicate multiple intrusions during a single eruption (Sheth and Cañón-Tapia 2014). The different feeder systems for contemporary and flood basalt eruptions may explain the complex geochemical variation and magma storage problems that are not associated with large volume contemporary eruptions (Sheth and Cañón-Tapia 2014).

An important difference between the deposits of the R-K and high volume fissure eruptions is the character of the sheet-form fall deposits. The R-K eruption produced deposits ~1 m thick at ~1 km distance from the vents. These deposits are typical of Hawaiian eruptions (e.g. Aramaki et al. 1986; Houghton et al. 2006) in which lava fountains are commonly ~500 m high (Wolfe et al. 1988; Parfitt 1998; Vergnolle and Mangan 2000). In contrast, sheet-like fall deposits from the Laki, Roza and Eldgjá eruptions extend ≥ 1.7 km from the fissure and are >2 m thick, typical of Sub-Plinian and

violent Strombolian activity (Thordarson and Self 1993; Thordarson and Larsen 2007; White et al. 2009; Brown et al. 2014). This indicates that the studies section of the R-K fissure was not characterised by the high fountains that typified the Roza, Laki and Eldgjá eruptions. The absence of agglutinate cones, as found along the Roza fissure (Brown et al. 2014) further suggests that the R-K eruption was not characterised by $\gg 1$ km-high fountains.

The R-K volcanic sequence provides insights into the early stages of fissure eruptions that produce mixed cone rows. The deposits from these stages are not commonly observed along other fissures (e.g. Laki). The early stages of the R-K eruption were dominated by the production of lava flows. This is analogous to the high rate discharge of lava that occurred early in the Laki eruption and during the early stages of each eruption episode (Thordarson and Self 1993). The R-K lava flows then deformed and buried early pyroclastic deposits (e.g. Brown et al. in press). Thordarson and Self (1993) have been unable to recognise pyroclastic deposits buried in the proximal region of the Laki fissure. Some pyroclastic edifices formed during high volume fissure eruptions preserve evidence of unique fountaining conditions (Brown et al. 2014). Therefore similar edifices, perhaps preserved beneath the Laki lava flow field and within FBPs, may preserve evidence of fountaining conditions unique to high volume fissure eruptions.

The early R-K lava flows were also the hosts for rootless explosions in proximal regions; as evidenced by the dissected rootless conduits. These explosions may have occurred within the first few weeks of the eruption (as shown in Chapter 4). Rootless explosions are also observed in the Laki flow field, especially in the proximal region (Thordarson and Self 1993). The significance of these rootless eruptions in the proximal region is unknown. Rootless eruptions are thought to be controlled by lava and water availability (Chapter 4; Fagents and Thordarson 2007; Hamilton et al. 2010). Given that surface water was abundant across the Laki lava flow field, it is uncertain why these rootless explosions should be particularly common in the proximal region. This may be because the site of rootless interaction is thought to be partly controlled by substrate compressibility (Hamilton et al. 2010). In regions of high lithostatic load (i.e. thick sequences of lava, as found within the proximal region), the substrate would be more easily compressed. This would increase the likelihood of rootless interaction. However, the absence of a compressible substrate beneath the rootless conduit is noted in the R-K eruption. This suggests that factors such as local water percolation may be important in initiating rootless interactions (see section 3.9.2).

Development of the R-K lava flow field was followed by edifice construction. The R-K scoria-agglutinate cone, scoria ramparts and spatter ramparts have specific similarities with the edifices formed during the Laki eruption. Scoria half-cones are common features along the Laki fissure and in other low volume eruptions (Thordarson and Self 1993; Thordarson and Larsen 2007). The half-cones are elongated parallel to the fissure, are set-back from the fissure and are larger than the spatter cones superimposed on them. These features are similar to those of the scoria ramparts of the R-K eruption. The stratigraphy of the R-K rampart is also near identical to that preserved within the Laki scoria cones (Thordarson and Self 1993). The R-K scoria ramparts are composed of alternating layers of 0.5–1.5 m thick scoria overlain by 0.5–1 m thick spatter (log 2). Local spatter-rich successions in the R-K scoria ramparts (log 11) could suggest deposition from multiple sources along the fissure, or that log 11 represents part of an overlapping spatter cone that has been eroded (e.g. Thordarson and Self 1993). The similarity between the Laki scoria cones and half-cones and the R-K scoria ramparts suggest both were formed during Hawaiian activity that dominated towards the end of the eruption and each eruption episode (e.g. Thordarson and Self 1993).

The Laki scoria cones and half-cones are commonly overlain by spatter cones which intersect and merge in a complex fashion (Thordarson and Self 1993). These spatter cones are the most common feature along the Laki fissures (Thordarson and Self 1993) and are also formed during low volume fissure eruptions (Thordarson and Larsen 2007). These cones overly the fissure and are 10–40 m high (Thordarson and Self 1993). The cones increase in size towards the site of highest lava discharge (Thordarson and Self 1993). The Laki spatter cones form in the dying stages of the eruption (Thordarson and Self 1993). However, the internal features of these cones are not well described, and there are currently no studies describing the internal architecture and textures of these edifices. The R-K scoria-agglutinate cone and spatter ramparts have similar morphologic characteristics to the Laki spatter cones. Furthermore, the R-K scoria-agglutinate cone and spatter ramparts also post-date the scoria ramparts that are analogous to the Laki scoria half-cones. The R-K scoria-agglutinate cone suggests that the dying stages of the eruption are characterised by deposition from low and pulsating fountains, evidenced by the cored bombs and abundant spatter-dominated lithofacies. Since the R-K scoria agglutinate cone is not the largest cone along this section of the fissure, it suggests that the cone is not located on the site of highest discharge (e.g. Thordarson and Self 1993). The R-K scoria-agglutinate cone may also be representative of the Ice Harbor cones in the CRFBP, which are composed of

subaerial pāhoehoe flows and welded spatter (Swanson et al. 1975). This is speculative given the sparse data, but may suggest that the emplacement of the Ice Harbor member was similarly associated with the construction of scoria-agglutinate or spatter cones.

In summary, the R-K volcanic stratigraphy and edifices preserve many similarities with the products of high volume fissure eruptions. In particular, the R-K edifices are similar to those produced during the Laki eruption and evidence Hawaiian-style activity. The products of the Laki eruption and its dynamics are a useful analogue for the emplacement of flood basalts (Thordarson and Self 1998; Thordarson and Larsen 2007; White et al. 2009; Brown et al. 2014). The R-K edifices therefore serve as useful analogues for the edifices that may form during flood basalt eruptions. These edifices suggest that flood basalt eruptions could be associated with periods of Hawaiian-style activity (e.g. Reidel and Tolan 1992). This style of activity contrasts with that evidenced by the Roza agglutinate cones, suggesting significant temporal and spatial variation during flood basalt emplacement. Such variation is expected, given that FBP evidence a variety of emplacement styles (Jerram 2002; Bondre et al. 2004b) and that high volume Icelandic fissure eruptions produce a range of edifices and cone rows (Thordarson and Self 1993; Thordarson and Larsen 2007).

3.10 Summary

The low volume R-K fissure eruption produced a mixed cone row. This cone row contains a scoria-agglutinate cone, scoria and spatter ramparts and rootless cones, as well as sheet-like fall deposits. The architecture of these features and their feeder dyke has not been described before, and allows us to link processes observed in historic eruptions with preserved deposits. The scoria-agglutinate cone, scoria and spatter ramparts are analogous to those formed in high volume fissure eruptions and suggest that flood basalt eruptions may also be associated with periods of Hawaiian activity. This study also helps us to recognise fissure-derived edifices in other settings.

3.11 References

- Alho P, Russell AJ, Carrivick JL, Käyhkö J (2005) Reconstruction of the largest Holocene jökulhlaup within Jökulsá á Fjöllum, NE Iceland. *Quaternary Science Reviews* 24(22):2319-2334
- Alvarado GE, Pérez W, Vogel TA, Gröger H, Patiño L (2011) The Cerro Chopo basaltic cone (Costa Rica): An unusual completely reversed graded pyroclastic cone with abundant low vesiculated cannonball juvenile fragments. *J Volcanol Geoth Res* 201(1–4):163-177

- Andronico D, Scollo S, Cristaldi A, Lo Castro M (2014) Representivity of incompletely sampled fall deposits in estimating eruption source parameters: a test using the 12–13 January 2011 lava fountain deposit from Mt. Etna volcano, Italy. *B Volcanol* 76(10):1-14
- Aramaki S, Hayakawa Y, Fujii T, Nakamura K, Fukuoka T (1986) The October 1983 eruption of Miyakejima volcano. *J Volcanol Geoth Res* 29(1):203-229
- Bondre N, Duraiswami R, Dole G (2004a) Morphology and emplacement of flows from the Deccan Volcanic Province, India. *B Volcanol* 66(1):29-45
- Bondre N, Duraiswami R, Dole G (2004b) A brief comparison of lava flows from the Deccan Volcanic Province and the Columbia-Oregon Plateau Flood Basalts: Implications for models of flood basalt emplacement. *Journal of Earth System Science* 113(4):809-817
- Breed WJ (1964) Morphology and lineation of cinder cones in the San Francisco Volcanic Field. *Mus. North. Ariz. Bull* 40:65-71
- Brown RJ, Blake S, Thordarson T, Self S (2014) Pyroclastic edifices record vigorous lava fountains during the emplacement of a flood basalt flow field, Roza Member, Columbia River Basalt Province, USA. *Geol Soc Am Bull* 126:875-891
- Brown RJ, Thordarson T, Self S, Blake S (in press) Physical Disruption of Sheet-form Fall Deposits during Basaltic Eruptions.
- Bruce PM, Huppert HE (1989) Thermal control of basaltic fissure eruptions. *Nature* 342(6250):665-667
- Capaccioni B, Cuccoli F (2005) Spatter and welded air fall deposits generated by fire-fountaining eruptions: Cooling of pyroclasts during transport and deposition. *J Volcanol Geoth Res* 145(3–4):263-280
- Carracedo JC, Rodriguez Badiola E, Soler V (1992) The 1730–1736 eruption of Lanzarote, Canary Islands: a long, high-magnitude basaltic fissure eruption. *J Volcanol Geoth Res* 53(1–4):239-250
- Chadwick WW, Embley RW (1998) Graben formation associated with recent dike intrusions and volcanic eruptions on the mid-ocean ridge. *Journal of Geophysical Research: Solid Earth* 103(B5):9807-9825
- Cimarelli C, Di Traglia F, de Rita D, Torrente DG (2013) Space–time evolution of monogenetic volcanism in the mafic Garrotxa Volcanic Field (NE Iberian Peninsula). *B Volcanol* 75(11):1-18
- Cronin SJ, Neall VE (2001) Holocene volcanic geology, volcanic hazard, and risk on Taveuni, Fiji. *New Zealand Journal of Geology and Geophysics* 44(3):417-437
- Dickson LD (1997) Volcanology and geochemistry of pliocene and quaternary basalts on Citadel Mountain, Lunar Crater Volcanic field, Pancake Range, Nevada.
- Dumas S, Arnott RWC (2006) Origin of hummocky and swaley cross-stratification— The controlling influence of unidirectional current strength and aggradation rate. *Geology* 34(12):1073-1076
- Einarsson MA (1984) Climate of Iceland. In: Van Loon H (ed) *World Survey of Climatology: 15 : Climates of the Oceans*. Elsevier, Amsterdam, pp 673-697
- Fagents SA, Lanagan P, Greeley R (2002) Rootless cones on Mars: a consequence of lava-ground ice interaction. *Geological Society, London, Special Publications* 202(1):295-317
- Fagents SA, Thordarson T (2007) Rootless cones in Iceland and on Mars. In: Chapman M, Skilling IP (eds) *The Geology of Mars: Evidence from Earth-Based Analogues*. Cambridge University Press, pp 151–177
- Fedotov S, Chirkov A, Gusev N, Kovalev G, Slezin Y (1980) The large fissure eruption in the region of Plosky Tolbachik volcano in Kamchatka, 1975–1976. *B Volcanol* 43(1):47-60
- Fisher RV, Schmincke HU (1984) *Pyroclastic Rocks*. Springer, Berlin, Heidelberg, New York
- Forbes AES, Blake S, Mc Garvie DW, Tuffen H (2012) Pseudopillow fracture systems in lavas: insights into cooling mechanisms and environments from lava flow fractures *J Volcanol Geoth Res* 245 (2012): 68-80
- Forbes AES, Blake S, Tuffen H (2014) Entablature: fracture types and mechanisms. *B Volcanol* 76(5):1-13
- Francis PW (1973) Cannonball Bombs, A New Kind of Volcanic Bomb from the Pacaya Volcano, Guatemala. *Geol Soc Am Bull* 84(8):2791-2794
- Friese N, Bense FA, Tanner DC, Gústafsson LE, Siegesmund S (2013) From feeder dykes to scoria cones: the tectonically controlled plumbing system of the Rauðhólar volcanic chain, Northern Volcanic Zone, Iceland. *B Volcanol* 75(6):1-19

- Galindo I, Gudmundsson A (2012) Basaltic feeder dykes in rift zones: geometry, emplacement, and effusion rates. *Natural Hazards and Earth System Sciences* 12(12):3683-3700
- Geist DJ, Harpp KS, Naumann TR, Poland M, Chadwick WW, Hall M, Rader E (2008) The 2005 eruption of Sierra Negra volcano, Galápagos, Ecuador. *B Volcanol* 70(6):655-673
- Geshi N, Kusumoto S, Gudmundsson A (2010) Geometric difference between non-feeder and feeder dikes. *Geology* 38(3):195-198
- Geshi N, Oikawa T (2014) The spectrum of basaltic feeder systems from effusive lava eruption to explosive eruption at Miyakejima volcano, Japan. *B Volcanol* 76(3):1-14
- Green J, Short NM (1971) Volcanic landforms and surface features: A photographic atlas and glossary. Springer-Verlag
- Gudmundsson A (2007) Infrastructure and evolution of ocean-ridge discontinuities in Iceland. *Journal of Geodynamics* 43(1):6-29
- Gudmundsson A, Friese N, Galindo I, Philipp SL (2008) Dike-induced reverse faulting in a graben. *Geology* 36(2):123-126
- Gudmundsson MT, Pedersen R, Vogfjörð K, Thorbjarnardóttir B, Jakobsdóttir S, Roberts MJ (2010) Eruptions of Eyjafjallajökull Volcano, Iceland. *Eos, Transactions American Geophysical Union* 91(21):190-191
- Guilbaud M-N, Self S, Thordarson T, Blake S (2005) Morphology, surface structures, and emplacement of lavas produced by Laki, A.D. 1783–1784. *Geological Society of America Special Papers* 396:81-102
- Hamblin WK (1994) Late Cenozoic lava dams in the western Grand Canyon. *Geol Soc Am Mem* (183):1-142
- Hamilton CW, Thordarson T, Fagents SA (2010) Explosive lava–water interactions I: architecture and emplacement chronology of volcanic rootless cone groups in the 1783–1784 Laki lava flow, Iceland. *B Volcanol* 72(4):449-467
- Head JW, Wilson L (1989) Basaltic pyroclastic eruptions: Influence of gas-release patterns and volume fluxes on fountain structure, and the formation of cinder cones, spatter cones, rootless flows, lava ponds and lava flows. *J Volcanol Geoth Res* 37(3–4):261-271
- Heiken G (1978) Characteristics of tephra from cinder cone, Lassen volcanic National Park, California. *B Volcanol* 41(2):119-130
- Heliker C, Mangan M, Mattox T, Kauahikaua J, Helz R (1998) The character of long-term eruptions: inferences from episodes 50–53 of the Pu'u'Ō'ō-Kūpaianaha eruption of Kīlauea Volcano. *B Volcanol* 59(6):381-393
- Heslop S, Wilson L, Pinkerton H, Head J, III (1989) Dynamics of a confined lava flow on Kilauea volcano, Hawaii. *B Volcanol* 51(6):415-432
- Hintz AR, Valentine GA (2012) Complex plumbing of monogenetic scoria cones: New insights from the Lunar Crater Volcanic Field (Nevada, USA). *J Volcanol Geoth Res* 239–240:19-32
- Hon K, Kauahikaua J, Delinger R, Mackay K (1994) Emplacement and inflation of pahoehoe sheet flows: Observations and measurements of active lava flows on Kilauea Volcano, Hawaii. *Geol Soc Am Bull* 106(3):351-370
- Houghton BF, Schmincke HU (1989) Rothenberg scoria cone, East Eifel: a complex Strombolian and phreatomagmatic volcano. *B Volcanol* 52(1):28-48
- Houghton BF, Wilson CJN (1989) A vesicularity index for pyroclastic deposits. *B Volcanol* 51(6):451-462
- Houghton BF, Bonadonna C, Gregg CE, Johnston DM, Cousins WJ, Cole JW, Del Carlo P (2006) Proximal tephra hazards: Recent eruption studies applied to volcanic risk in the Auckland volcanic field, New Zealand. *J Volcanol Geoth Res* 155(1–2):138-149
- Huscroft CA, Ward BC, Barendregt RW, Jackson Jr, LE, Opdyke ND (2004) Pleistocene volcanic damming of Yukon River and the maximum age of the Reid Glaciation, west-central Yukon. *Canadian Journal of Earth Sciences* 41(2):151-164.
- Jerram DA (2002) Volcanology and facies architecture of flood basalts. *Geological Society of America Special Papers* 362:119-132
- Jurado-Chichay Z, Rowland S, Walker GL (1996) The formation of circular littoral cones from tube-fed pāhoehoe: Mauna Loa, Hawai'i. *B Volcanol* 57(7):471-482

- Karhunen R (1988) Eruption mechanism and rheomorphism during the basaltic fissure eruption in Biskupsfell, Kverkfjöll, North-central Iceland, Lic. Phil. thesis, University of Iceland, Department of Geology and Mineralogy.
- Keating G, Valentine G, Krier D, Perry F (2008) Shallow plumbing systems for small-volume basaltic volcanoes. *B Volcanol* 70(5):563-582
- Kent RW, Thomson BA, Skelhorn RR, Kerr AC, Norry MJ, Walsh JN (1998) Emplacement of Hebridean Tertiary flood basalts: evidence from an inflated pahoehoe lava flow on Mull, Scotland. *J Geol Soc London* 155(4):599-607
- Keszthelyi L, McEwen A, Phillips C, Milazzo M, Geissler P, Turtle E, Radebaugh J, Williams D, Simonelli D, Breneman H (2001) Imaging of volcanic activity on Jupiter's moon Io by Galileo during the Galileo Europa Mission and the Galileo Millennium Mission. *Journal of Geophysical Research: Planets* (1991–2012) 106(E12):33025-33052
- Kirkbride MP, Dugmore AJ, Brazier V (2006) Radiocarbon dating of mid-Holocene megaflood deposits in the Jokulsa a Fjollum, north Iceland. *The Holocene* 16(4):605-609
- Kokelaar P (1986) Magma-water interactions in subaqueous and emergent basaltic. *B Volcanol* 48(5):275-289
- Long PE, Wood BJ (1986) Structures, textures, and cooling histories of Columbia River basalt flows. *Geol Soc Am Bull* 97(9):1144-1155
- Macdonald GA (1972) *Volcanoes*. Prentice-Hall, Englewood Cliffs, N.J.
- Mackin JH (1961) A stratigraphic section in the Yakima basalt and the Ellensburg Formation in south-central Washington. *Rep. Invest., Wash. Div. Mines Geol.*, 19:45
- Manville V, Németh K, Kano K (2009) Source to sink: a review of three decades of progress in the understanding of volcanoclastic processes, deposits, and hazards. *Sedimentary Geology* 220(3):136-161
- Mattox TN, Mangan MT (1997) Littoral hydrovolcanic explosions: a case study of lava–seawater interaction at Kilauea Volcano. *J Volcanol Geoth Res* 75(1–2):1-17
- Mattsson HB, Tripoli BA (2011) Depositional characteristics and volcanic landforms in the Lake Natron–Engaruka monogenetic field, northern Tanzania. *J Volcanol Geoth Res* 203(1–2):23-34
- Mauri A, Davis B, Collins P, Kaplan J (2013) The influence of atmospheric circulation on the mid-Holocene climate of Europe: a data-model comparison. *Climate of the Past Discussions* 9(5):5569-5592
- McGetchin TR, Settle M, Chouet BA (1974) Cinder Cone Growth Modeled After Northeast Crater, Mount Etna, Sicily. *J. Geophys. Res.* 79(23):3257-3272
- McNutt SR, Miller TP, Taber JJ (1991) Geological and seismological evidence of increased explosivity during the 1986 eruptions of Pavlof volcano, Alaska. *B Volcanol* 53(2):86-98
- Moore RB, Helz RT, Dzurisin D, Eaton GP, Koyanagi RY, Lipman PW, Lockwood JP, Puniwai GS (1980) The 1977 eruption of Kilauea volcano, Hawaii. *J Volcanol Geoth Res* 7(3):189-210
- Németh K, Cronin SJ (2011) Drivers of explosivity and elevated hazard in basaltic fissure eruptions: the 1913 eruption of Ambrym Volcano, Vanuatu (SW-Pacific). *J Volcanol Geoth Res* 201(1):194-209
- Németh K (2014) Rootless Cone/Vent. In: *Encyclopedia of Planetary Landforms*. Springer New York, pp 1-7
- Opheim JA, Gudmundsson A (1989) Formation and geometry of fractures, and related volcanism, of the Krafla fissure swarm, northeast Iceland. *Geol Soc Am Bull* 101(12):1608-1622
- Parcheta C, Houghton B, Swanson D (2012) Hawaiian fissure fountains 1: decoding deposits—episode 1 of the 1969–1974 Mauna Ulu eruption. *B Volcanol* 74(7):1729-1743
- Parfitt EA (1998) A study of clast size distribution, ash deposition and fragmentation in a Hawaiian-style volcanic eruption. *J Volcanol Geoth Res* 84(3):197-208
- Parfitt EA (2004) A discussion of the mechanisms of explosive basaltic eruptions. *J Volcanol Geoth Res* 134(1-2):77-107
- Peterson DW, Tilling RI (1980) Transition of basaltic lava from pahoehoe to aa, Kilauea Volcano, Hawaii: Field observations and key factors. *J Volcanol Geoth Res* 7(3-4):271-293
- Polacci M, Cashman KV, Kauahikaua JP (1999) Textural characterization of the pāhoehoe–‘a‘a transition in Hawaiian basalt. *B Volcanol* 60(8):595-609
- Pollard DD, Delaney PT, Duffield WA, Endo ET, Okamura AT (1983) Surface deformation in volcanic rift zones. *Tectonophysics* 94(1–4):541-584

- Reidel SP, Tolan TL (1992) Eruption and emplacement of flood basalt: An example from the large-volume Teepee Butte Member, Columbia River Basalt Group. *Geol Soc Am Bull* 104(12):1650-1671
- Reidel SP (1998) Emplacement of Columbia River flood basalt. *J. Geophys. Res.* 103(B11):27393-27410
- Riedel C, Ernst GGJ, Riley M (2003) Controls on the growth and geometry of pyroclastic constructs. *J Volcanol Geoth Res* 127(1–2):121-152
- Rosseel J-B, White JDL, Houghton BF (2006) Complex bombs of phreatomagmatic eruptions: Role of agglomeration and welding in vents of the 1886 Rotomahana eruption, Tarawera, New Zealand. *J. Geophys. Res.* 111(B12):B12205
- Rowland SK, Walker GPL (1987) Toothpaste lava: Characteristics and origin of a lava structural type transitional between pahoehoe and aa. *B Volcanol* 49(4):631-641
- Rubin AM, Pollard DD (1988) Dike-induced faulting in rift zones of Iceland and Afar. *Geology* 16(5):413-417
- Rubin AM (1992) Dike-induced faulting and graben subsidence in volcanic rift zones. *Journal of Geophysical Research: Solid Earth* 97(B2):1839-1858
- Rymer H, de Vries BvW, Stix J, Williams-Jones G (1998) Pit crater structure and processes governing persistent activity at Masaya Volcano, Nicaragua. *B Volcanol* 59(5):345-355
- Sánchez MC, Sarrionandia F, Ibarguchi JIG (2014) Post-depositional intrusion and extrusion through a scoria and spatter cone of fountain-fed nephelinite lavas (Las Herrerías volcano, Calatrava, Spain). *B Volcanol* 76(9):1-17
- Self S, Keszthelyi L, Thordarson T (1998) The importance of pahoehoe. *Annu. Rev. Earth Planet. Sci.* 26:81-110
- Sheth H, Cañón-Tapia E (2014) Are flood basalt eruptions monogenetic or polygenetic? *International Journal of Earth Sciences*:1-16
- Slater L, Jull M, McKenzie D, Gronvöld K (1998) Deglaciation effects on mantle melting under Iceland: results from the northern volcanic zone. *Earth and Planetary Science Letters* 164(1):151-164
- Sparks R, Wright J (1979) Welded air-fall tuffs. *Geological Society of America Special Papers* 180:155-166
- Steingrímsson J, Ólafsson S (1783) Einföld og sönn frásaga um jardeldshlaupid í Skaftafellssyslu árid 1783 (A simple, but true narrative of the eruption in Skaftafell county in the year 1783), . *Safn til Sögu Íslands IV*(Copenhagen, 1907-1915):58-69
- Steingrímsson J (1788) Fulkomid Skrif um Sídueld (A complete description of the Síða volcanic fire), . *Safn til Sögu Íslands IV* (Copenhagen 1907-1915):58-69
- Stevenson J, Mitchell N, Cassidy M, Pinkerton H (2012) Widespread inflation and drainage of a pāhoehoe flow field: the Nesjahraun, Þingvellir, Iceland. *B Volcanol*:1-17
- Stow DA (2005) *Sedimentary rocks in the field*, Manson Publishing Ltd. London, pp320.
- Sumner JM (1998) Formation of clastogenic lava flows during fissure eruption and scoria cone collapse: the 1986 eruption of Izu-Oshima Volcano, eastern Japan. *B Volcanol* 60(3):195-212
- Sumner JM, Blake S, Matela RJ, Wolff JA (2005) Spatter. *J Volcanol Geoth Res* 142(1-2):49-65
- Swanson D, Duffield WA, Jackson DB, Peterson DW (1979) Chronological narrative of the 1969 - 1971 Mauna Ulu eruption of Kilauea volcano, Hawaii. *U.S Geological Survey Professional Paper* 1065:55
- Swanson DA, Wright TL, Helz RT (1975) Linear vent systems and estimated rates of magma production and eruption for the Yakima Basalt on the Columbia Plateau. *American Journal of Science* 275(8):877-905
- Tentler T, Temperley S (2007) Magmatic fissures and their systems in Iceland: A tectonomagmatic model. *Tectonics* 26(5):TC5019
- Thomas R, Sparks R (1992) Cooling of tephra during fallout from eruption columns. *B Volcanol* 54(7):542-553
- Thorarinsson S (1959) Some Geological Problems Involved in the Hydroelectric Development of the Jokulsa a Fjöllum. Report to the State Electricity Authority, Reykjavik.:35
- Thordarson T, Self S (1993) The Laki (Skaftár Fires) and Grímsvötn eruptions in 1783–1785. *B Volcanol* 55(4):233-263

- Thordarson T, Self S (1998) The Roza Member, Columbia River Basalt Group: A gigantic pahoehoe lava flow field formed by endogenous processes? *J. Geophys. Res.* 103(B11):27411-27445
- Thordarson T, Miller D, Larsen G, Self S, Sigurdsson H (2001) New estimates of sulfur degassing and atmospheric mass-loading by the 934 AD Eldgjá eruption, Iceland. *J Volcanol Geoth Res* 108(1):33-54
- Thordarson T, Larsen G (2007) Volcanism in Iceland in historical time: Volcano types, eruption styles and eruptive history. *Journal of Geodynamics* 43(1):118-152
- Tucker M (1995) *Sedimentary rocks in the field*, Wiley, Chichester.
- Valentine G, Cortés J (2013) Time and space variations in magmatic and phreatomagmatic eruptive processes at Easy Chair (Lunar Crater Volcanic Field, Nevada, USA). *B Volcanol* 75(9):1-13
- Valentine GA, Groves KR (1996) Entrainment of Country Rock during Basaltic Eruptions of the Lucero Volcanic Field, New Mexico. *The Journal of Geology* 104(1):71-90
- Valentine GA, Krier D, Perry FV, Heiken G (2005) Scoria cone construction mechanisms, Lathrop Wells volcano, southern Nevada, USA. *Geology* 33(8):629-632
- Valentine GA, Krogh KEC (2006) Emplacement of shallow dikes and sills beneath a small basaltic volcanic center – The role of pre-existing structure (Paiute Ridge, southern Nevada, USA). *Earth and Planetary Science Letters* 246(3–4):217-230
- Valentine GA, Perry FV, Krier D, Keating GN, Kelley RE, Cogbill AH (2006) Small-volume basaltic volcanoes: Eruptive products and processes, and post-eruptive geomorphic evolution in Crater Flat (Pleistocene), southern Nevada. *Geol Soc Am Bull* 118(11-12):1313-1330
- Valentine GA, Gregg TKP (2008) Continental basaltic volcanoes — Processes and problems. *J Volcanol Geoth Res* 177(4):857-873
- Valentine GA (2012) Shallow plumbing systems for small-volume basaltic volcanoes, 2: Evidence from crustal xenoliths at scoria cones and maars. *J Volcanol Geoth Res* 223–224(0):47-63
- Vergnolle S, Mangan MT (2000) Hawaiian and Strombolian Eruptions. In: Sigurdsson H (ed) *Encyclopedia of Volcanoes*. Academic press, San Diego, pp 447-461
- Vespermann D, Schmincke H-U (2000) Scoria cones and tuff rings. In: Sigurdsson H (ed) *Encyclopedia of Volcanoes*. Academic Press, San Diego. Academic Press, San Diego, pp 683-694
- Waite R (2009) Great Holocene floods along Jökulsá á Fjöllum, north Iceland. *Flood and Megaflood Processes and Deposits: Recent and Ancient Examples*, International Association of Sedimentologists special publication 32:37-51
- Walker G, Croasdale R (1971) Characteristics of some basaltic pyroclastics. *B Volcanol* 35(2):303-317
- Walker GPL (1989) Spongy pahoehoe in Hawaii: A study of vesicle-distribution patterns in basalt and their significance. *B Volcanol* 51(3):199-209
- Walker GPL (1991) Structure, and origin by injection of lava under surface crust, of tumuli, “lava rises”, “lava-rise pits”, and “lava-inflation clefts” in Hawaii. *B Volcanol* 53(7):546-558
- Walker GPL (1995) Flood basalts versus central volcanoes and the British Tertiary volcanic Province. *Geological Society, London, Memoirs* 16(1):195-202
- Watton TJ, Jerram DA, Thordarson T, Davies RJ (2013) Three-dimensional lithofacies variations in hyaloclastite deposits. *J Volcanol Geoth Res* 250(0):19-33
- Wendel J (2014) Continuing Bardarbunga eruption fuels scientific research. *Eos, Transactions American Geophysical Union* 95(44):401-401
- White J, Bryan S, Ross P, Self S, Thordarson T (2009) Physical volcanology of continental large igneous provinces: update and review. *Studies in Volcanology: The Legacy of George Walker*. Special Publications of IAVCEI 2:291-321
- White JDL, Houghton BF (2006) Primary volcanoclastic rocks. *Geology* 34(8):677-680
- Wilmoth RA, Walker GPL (1993) P-type and S-type pahoehoe: a study of vesicle distribution patterns in Hawaiian lava flows. *J Volcanol Geoth Res* 55(1-2):129-142
- Wohletz KH, Sheridan MF (1983) Hydrovolcanic explosions; II, Evolution of basaltic tuff rings and tuff cones. *American Journal of Science* 283(5):385-413
- Wolfe WE, Neal AC, Banks GN, Toni DJ (1988) The Puu Oo Eruption of Kilauea Volcano, Hawaii: Episodes 1 Through 20, January 3, 1983, Through June 8, 1984. U.S Geological Survey Professional Paper 1463

- Wolff J, Sumner J (2000) Lava fountains and their products. In: Sigurdsson H (ed) Encyclopedia of volcanoes. Academic Press, San Diego, pp 321-329
- Wood CA (1980) Morphometric evolution of cinder cones. J Volcanol Geoth Res 7(3–4):387-413

Chapter 4: Rootless Cone Processes Informed from Dissected Vent and Tephra Deposits

4.1 Introduction

Explosive interaction between water-logged sediments (or volcanoclastic deposits) and molten lava can result in the formation of rootless cones, also known as ‘pseudocraters’ (Fig. 4.1; Thorarinsson 1953). Rootless cones are present within flow fields where the lava advanced over lacustrine, marsh and fluvial environments (Fagents and Thordarson 2007; Hamilton et al. 2010a; Hamilton et al. 2010b). Explosions are driven by the interaction of molten lava with a water-saturated, unconsolidated substrate. Explosions initiated by interaction of molten lava with substrate pore water eject clasts composed of lava crust, disrupted liquid lava and substrate-derived sediment onto a stationary surface of an active lava flow, thereby building a cone. Similar rootless edifices, known as littoral cones, form when lava flows interact with seawater in a littoral environment (Moore and Ault 1965; Fisher 1968; Jurado-Chichay et al. 1996; Mattox and Mangan 1997; Jaeger et al. 2007). Rootless cone-like structures have also been observed on the surface of Mars near the Martian equator (Lanagan et al. 2001; Bruno et al. 2004; Fagents and Thordarson 2007; Hamilton et al. 2010a) and have been used to infer the former presence of fluids in the Martian substrate.

Two models for rootless eruptions have been proposed; one assuming static heat transfer and the other inferring dynamic heat transfer. The static heat transfer model infers rapid emplacement of lava above a water-logged substrate. Water trapped beneath the lava flow is converted to steam producing eruptions that are analogous to phreatic explosions (Thorarinsson 1951, 1953).

In contrast, the dynamic heat transfer model of Fagents and Thordarson (2007) argues that the explosive interactions are driven by physical (dynamic) mixing of the lava and the water-logged substrate. The model is based on observations that sediment from the substrate is physically mixed into the rootless cone deposits and found between the core and the rim in armoured bombs. Furthermore, the cones feature multiple layers of tephra, which increase upwards in grain size from coarse ash/fine lapilli to bomb-size clasts (Fagents and Thordarson 2007; Hamilton et al. 2010a). The presence of layering implies sustained eruptions (estimated to have lasted for hours to days; Thordarson and Höskuldsson 2008), maintained by quasi-steady input of molten lava to the explosion site.

During rootless cone activity on pāhoehoe lavas, initial sedimentation occurs from explosions that produce pyroclastic density currents (PDCs) that deposit broad, sheet-like platform deposits around the vent (Hamilton et al. 2010a). Later tephra jets and lava fountains deposit lapilli- to bomb-sized scoria and spatter that build a cone (Thordarson et al. 1998; Fagents and Thordarson 2007; Hamilton et al. 2010a). The deposits of rootless activity are usually unconsolidated, except in proximal regions (Hamilton et al. 2010a). Rootless cones vary from 1–40 m in height and 2–450 m in basal diameter. The cones are crudely bedded, inversely graded, and may contain layers of rheomorphic spatter. The degree of explosivity is controlled by a variety of factors including the explosion site geometry, the dynamics of melt and coolant, the percentage of solids in the coolant matrix, magma rheology and vesicularity, the rate of lava influx, and the amount and availability of external water. Tephra deposits within rootless cone fields can cover areas of up to 150 km² and may exhibit complex stratigraphic relationships (Fagents and Thordarson 2007; Hamilton et al. 2010a and references therein).

Despite the abundance of rootless cones (e.g. Lanagan et al. 2001; Greeley and Fagents 2001; Fagents et al. 2002; Fagents and Thordarson 2007; Hamilton et al. 2010a; Hamilton et al. 2010b; Hamilton et al. 2010c; Hamilton et al. 2011; Keszthelyi and Jaeger 2014), there is little documentation of their constituent pyroclasts and the characteristics of their host lava flows (e.g. Melchior Larsen et al. 2006; Hamilton et al. 2010a; Hamilton et al. 2010b). Furthermore, rootless cones are superficially similar to small scoria cones and spatter cones, both in size and componentry (e.g. Fagents and Thordarson 2007). They may also have a linear spatial arrangement, similar to that of edifices along a dyke (e.g. Hamilton et al. 2010a). The limited knowledge of the internal stratigraphy of rootless cones coupled with their similarity to other volcanic edifices means that it can be difficult to distinguish rootless tephra from tephra generated during dyke-fed eruptions. This is particularly the case in flood basalt provinces, where pyroclastic successions are usually poorly preserved and poorly exposed during the main and dying phases of volcanism (e.g. Swanson et al. 1975; Reidel and Tolan 1992; Brown et al. 2014).

In this chapter, I document a newly discovered rootless cone field within the 8.5 Ma Ice Harbor pāhoehoe lava flow field in the Columbia River Flood Basalt Province (CRFBP), USA. Erosional dissection allows me to examine the tephra deposits and conduits of the rootless cones. I use these features to inform on the nature of the explosions that created the

rootless cones and to help define criteria that distinguish the deposits of rootless cones from those of dyke-fed eruptions.

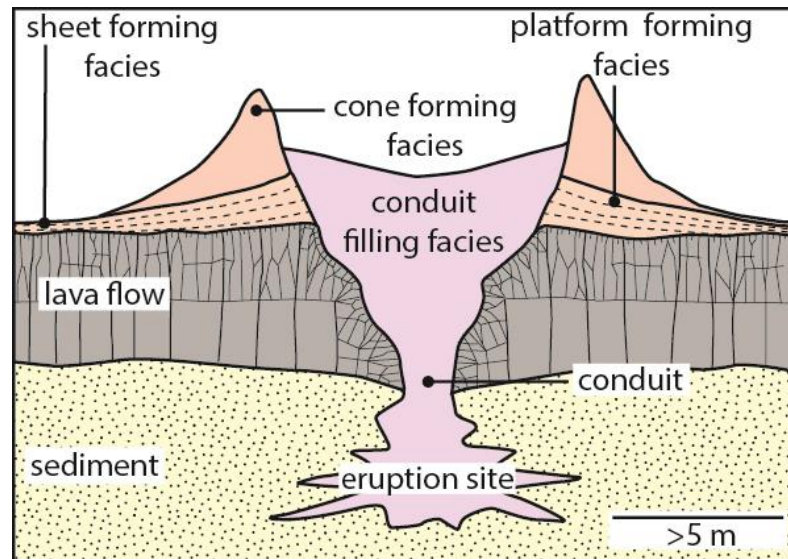


Figure 4.1. Generalised structure of a rootless cone. The cones form on active lava flows. The conduits in the host lava flow are irregular funnels that widen upwards. The upper parts of the conduits are filled with tephra. Cooling joints in the host lava flow radiate from the conduit. Cone forming deposits are composed of lapilli- to bomb-sized material that is often reversely graded and formed by fallout. Platform and sheet deposits are formed by fallout and deposition from pyroclastic density currents. Adapted from Hamilton et al. (2010a).

4.2 Geological setting of the Columbia River Basalt Province

Flood basalt volcanism in the NW USA initiated c. 17 m.y. ago in the Steens Mountain region, Oregon. Over the following ~11 m.y. the volume of erupted mafic magma exceeded >210 000 km³ across Oregon and Washington (now considered part of the CRFBP; Camp et al. 2003; Reidel et al. 2013). Eruptions were fed by ~300 km-long dyke swarms from crustal magma chambers under east-central Oregon/west-central Idaho (Wolff et al. 2008; Ramos et al. 2013). Pyroclastic rocks in the CRFBP are generally scarce, although exceptionally preserved examples of proximal tephra deposits (Swanson et al. 1975; Reidel and Tolan 1992; Brown et al. 2014), inferred rootless deposits (Thordarson and Self 1998) and drowned rootless cones (Keszthelyi and Jaeger 2014) are known.

The rootless cone deposits in this study occur in the 8.5 Ma Ice Harbor Member (Fig. 4.2), which is composed of three pāhoehoe lava flow fields that are the youngest products ascribed to the CRFBP (McKee et al. 1977; Swanson et al. 1979). The lavas have been divided into three chemically distinct types that were fed from a dyke system that was up to 90 km in length and on average <15 km in width (Swanson et al. 1975). The lava flow field has a minimum volume of 1.2 km³ (Swanson et al. 1975) and individual lava flows are typically <15 m thick. The pāhoehoe lavas are interbedded with the Ellensburg Formation sediments – diatomaceous muds, lacustrine sands and silts, volcanoclastic silt, conglomerates, and silicic volcanic ash probably sourced from eruptions of volcanoes in the NW USA. These sediments record deposition both within extensive lava-dammed lakes and by ephemeral and established rivers (Schminke 1967; Smith 1988; Tolan et al. 2002).

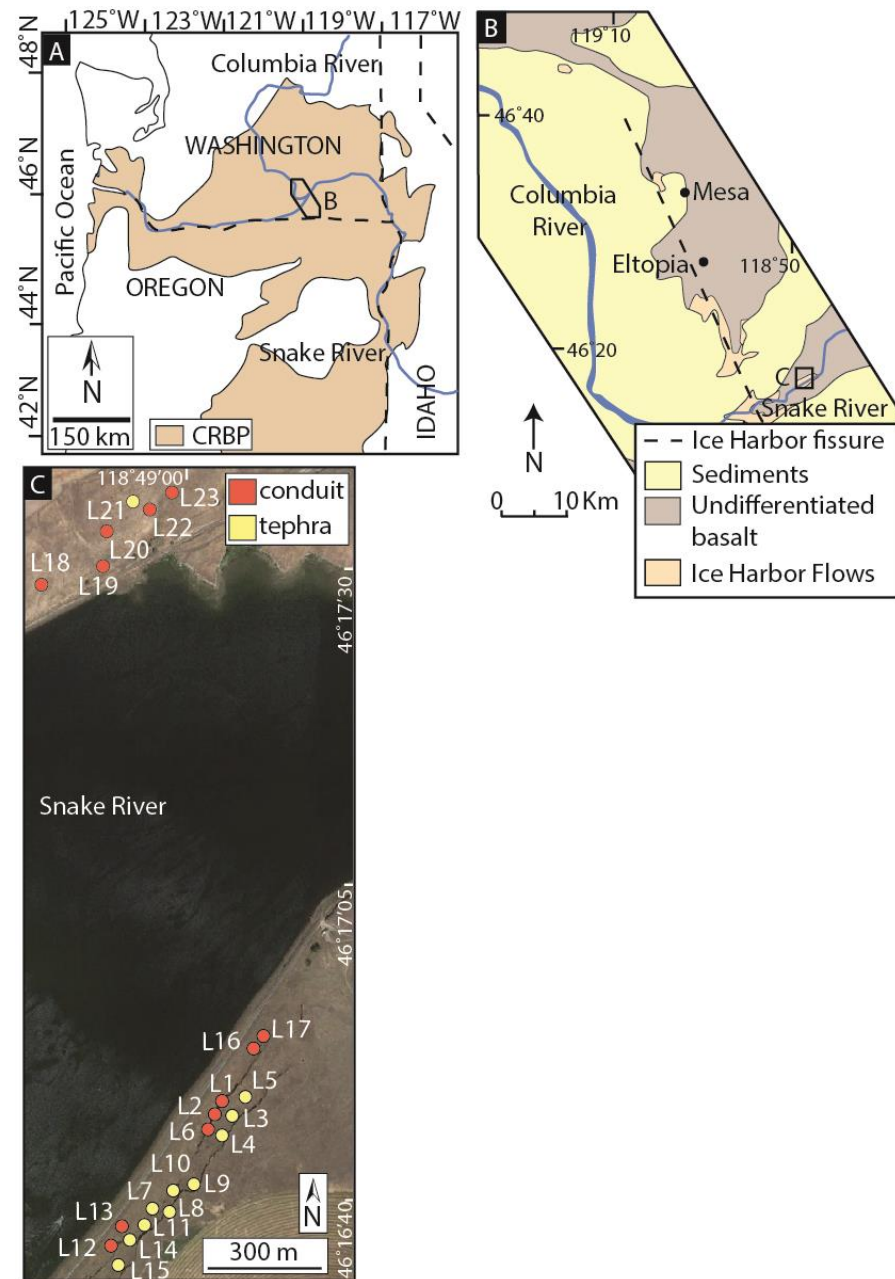


Figure 4.2. Location of the study area. (A) The CRFBP in the NW USA, adapted from Brown et al. (2014). (B) Map of the area showing the Ice Harbor fissure as described by Swanson et al. (1975) and the field area on the banks of the Snake River. (C) Sites of the tephra and conduit deposits described in this study.

4.3 Method

Field studies involved detailed sedimentary logging of tephra successions, lithofacies analysis, geological mapping and sampling. Locations were recorded using a handheld GPS

unit with an accuracy of ± 5 m. Petrographic characterisation was undertaken by optical microscopy on representative thin sections. Vesicle and clast dimensions and abundances were calculated using the image analysis software ImageJ (<http://imagej.nih.gov/ij/>) with representative samples and outcrop photographs. The crystal content of the cone deposits was calculated by point-counting representative samples. Clast densities were calculated on clasts >16 mm across using the method of Houghton and Wilson (1989). Grain size was determined by sieving.

4.4 Ice Harbor rootless cone field

The Ice Harbor rootless cone field is composed of: 1) the substrate over which the lava flows were emplaced (silicic volcanic ash); 2) the host pāhoehoe lava flows; 3) rootless cone conduits within the lava flows; 4) rootless cone- and platform-forming tephra deposits. The cone field is inferred to have occupied an area of ≥ 1 km², based on the distribution of the conduits and associated tephra. The cone field is overlain by later Ice Harbor lava flows.

4.4.1 Volcanic ash substrate

The pre-eruption substrate beneath the Ice Harbor flow field does not crop out in the study area, and the nature of the substrate has been inferred from analysis of material incorporated into the rootless cone tephra deposits. This material is composed of white, silicic, volcanic ash and forms 10–85 vol. % of all rootless cone tephra deposits (see Appendix 2). The volcanic ash is well-sorted ($1.2 \sigma\Phi$) and individual particles are platy, angular or cusped in shape and occasionally preserve vesicles (see Appendix 2). The volcanic ash has a median diameter of <0.25 mm. Smaller particles are blade shaped, whilst coarser particles have complex morphologies and exhibit bubble junctures.

Interpretation

The silicic volcanic ash is interpreted as a pyroclastic fall deposit within the Ellensburg Formation (Schminke 1967). The monolithologic character of the volcanic ash and the absence of organic matter or detrital sediment indicate that the volcanic ash had not been substantially reworked and that burial by the Ice Harbor lava may have occurred shortly after fallout. I infer that the volcanic ash fell out onto a flood plain or shallow lake; common features across the plateau-like CRFBP during the Miocene (e.g. Schminke 1967; Smith 1988;

Tolan et al. 2002). These environments are conducive to the formation of rootless cones (e.g. Thorarinsson 1951; Thorarinsson 1953; Fagents and Thordarson 2007; Hamilton et al. 2010a; Hamilton et al. 2010b).

4.4.2 Ice Harbor lava flows

The rootless cone field crops out along the banks of the Snake River (Fig. 4.2). The flow field is composed of pāhoehoe sheet lobes that reach 8 m thick and exhibit the tripartite structure typical of pāhoehoe sheet lobes in the CRFBP (e.g. Self et al. 1998; Thordarson and Self 1998). They have lower crusts that contain distorted pipe vesicles, massive, dense cores with columnar joints and vesicular upper crusts. The groundmass of the flows is composed of interstitial glass, and plagioclase and pyroxene microlites. Pyroxene and rare swallow-tail plagioclase phenocrysts and glomerocrysts 0.1–3 mm in diameter constitute 1–4 vol. % of the rock (see Appendix 2). Vesicles are partially filled with zeolite minerals. The Ice Harbor sheet lobes that contain the rootless cones have poorly vesicular cores and incipiently vesicular crusts (as defined by Houghton and Wilson 1989) that exhibit hackly, entablature-style joints spaced 11–21 cm apart (see Appendix 2).

Interpretation

I infer that inflation of the flows took several weeks, based on a lava upper crust thickness of ≥ 2 m and the relationship: $t = 164.8C^2$; where t = time in hours and C = crustal thickness in metres (see Hon et al. 1994). The presence of entablature-style jointing in the lava indicates that the flows were subjected to water enhanced cooling, implying emplacement in an environment where surface water was abundant (e.g. Long and Wood 1986). The swallow tail plagioclase microlites indicate that the lava cooled rapidly; this texture is also found in pillow lavas (e.g. Bryan 1972; Jafri and Charan 1992).

4.4.3 Rootless cone conduits

Cliffs along the Snake River reveal funnel-shaped, upward-flaring features in the Ice Harbor sheet lobes (Fig. 4.3). These features range from 1–4 m in diameter, are up to 4 m deep and have cross-sectional areas of 8–12 m². Their walls dip inwards $\sim 60^\circ$. All the funnels appear to terminate ≥ 0.5 m above the bases of the sheet lobes and sometimes form irregular, isolated cavities; these are likely 2D section effects (Fig. 4.3). Hackly cooling joints spaced

~16 cm apart radiate away from the funnel walls and extend up to ~4 m into the surrounding lava core (Fig. 4.3).

The inner surfaces of the funnels are coated with ropey-textured and bread-crust spatter that is ≤ 6 cm thick. The spatter has a hypohyaline groundmass texture, contains sheared vesicles and has multiple chilled rinds. The surface of the spatter has angular, hypocrySTALLINE and hypohyaline clasts of upper lava crust embedded in it. These clasts cover 10–30% of each funnel wall (see Appendix 2). There is a patchy, heterogeneous distribution of silicic volcanic ash across the surfaces; typically $< 5\%$. These funnels are often partially filled with tephra with a similar composition to the overlying cone deposits (massive spatter bombs, mSp; see below).

Twelve of these features have been recognised along a 450 m transect (Fig. 4.2); five on the north bank of the river and seven on the south. The features are spaced 3–206 m apart with tephra deposits exposed above them. Exposures spaced less than 5 m apart may represent irregular sections through the same feature.

Interpretation

I interpret these funnel-shaped features as remnants of rootless conduits because they have spatter, angular lapilli and patches of silicic ash plastered onto their inner wall which can only have occurred via explosive interactions. They are also filled with lapilli- to bomb-sized tephra. These features distinguish them from features described within rubbly pāhoehoe flows (e.g. Duraiswami et al. 2008; Keszthelyi et al. 2009). Sheared vesicles and rope-like textures on the conduit wall result from rheomorphic flow of spatter. The funnel shape of the conduits and their radiating cooling joints are similar to features seen in rootless cones in Iceland (e.g. Hamilton et al. 2010a).

Based on the abundance of conduits and the possibility that some locations represent irregular cross sections through the same conduit (e.g. L16/17; L1/2/6; L12/13) I suggest that the flow field hosted at least eight rootless cones. Since the size of the conduits is proportional to the size of the overlying cone (e.g. Hamilton et al. 2010a), the cones were likely to have been ≥ 5 m in basal diameter.

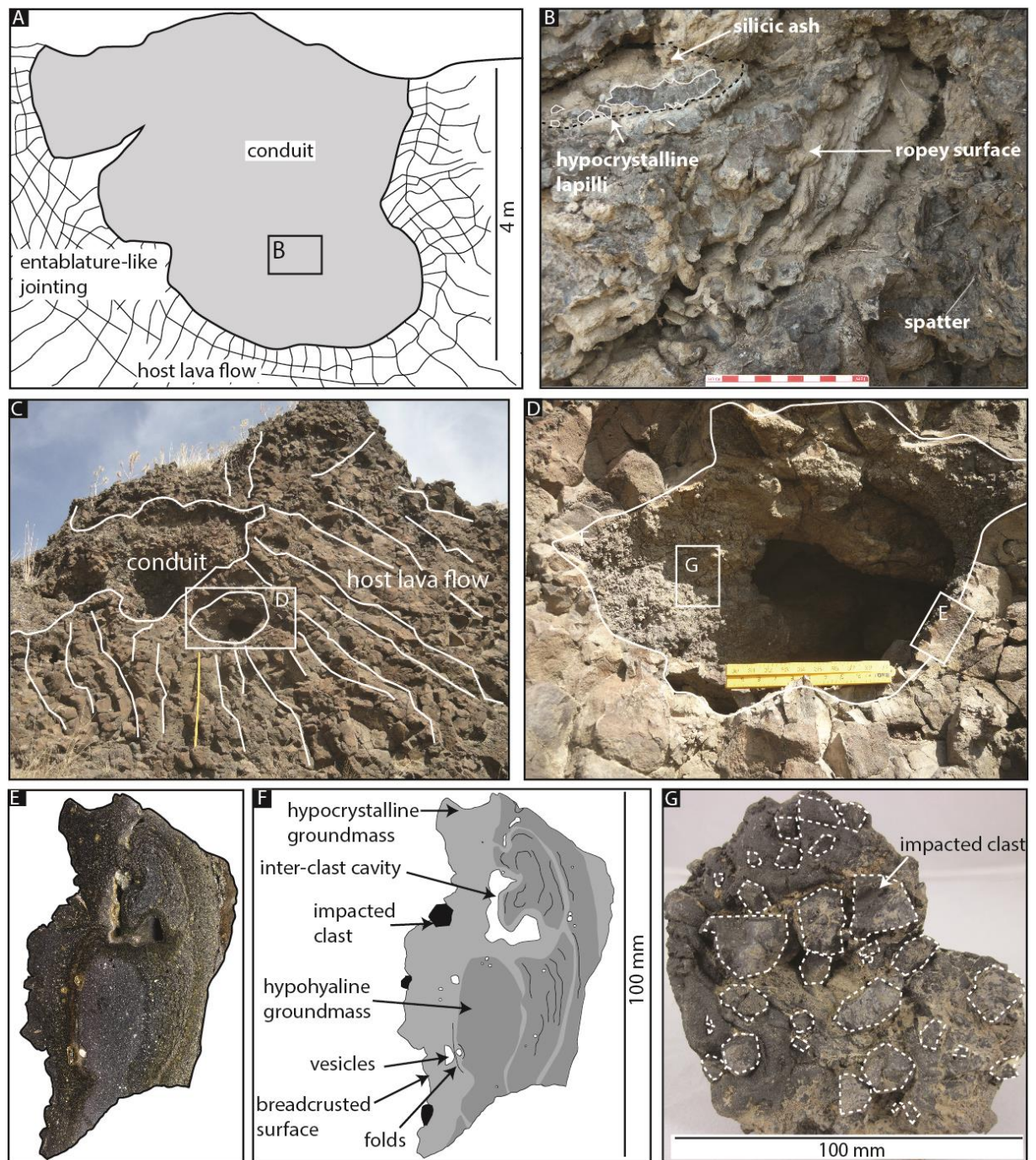


Figure 4.3. Field photographs and schematic diagrams showing the varying geometries of rootless conduits. (A) Field sketch showing the upper part of a funnel-shaped conduit at location 6 (UTM Nad83 zone 11T, 359 987 E/5 126 647 N). View to the southwest. (B) Field photograph of massive spatter (mSp) within the conduit in a, composed of spatter bombs, silicic volcanic ash and hypocrySTALLINE lapilli. (C) Irregular lower part of a conduit in the lava flow at location 22 (UTM Nad83 zone 11T, 359 724 E/5 128 162 N)

with cooling joints (white) radiating from the conduit/lava core contact (outlined). The ruler is 1 m. Inset D shows a close up of the conduit inner wall with embedded juvenile and lava crust lithic clasts. The ruler is 25 cm. Image E shows a cross section through the conduit wall, with hypohyaline lapilli embedded into the surface. (F) Interpretive sketch of E. (G) Plan view of a section of conduit wall, approximately 100 mm across, showing clasts that are inferred to have become embedded in the conduit wall during explosions (dashed outlines).

4.4.4 Rootless cone tephra deposits

Proximal rootless platform and cone-forming deposits are widely exposed over a 450 m-long transect along the south bank of the Snake River, and are intermittently exposed along the north bank of the river (Fig. 4.2). The tephra deposits are composed of juvenile pyroclasts (described below), silicic volcanic ash and fragmented lava crust.

4.4.4.1 Juvenile pyroclast types

The tephra deposits contain four different pyroclast types derived from the fragmentation and modification of the host lava flow (Fig. 4.4; Table 4.1). These juvenile clasts are (1) sideromelane ash and lapilli of both blocky and fluidal morphologies; (2) hypocrySTALLINE bombs (with both ventricular and globular morphologies) and angular lapilli; (3) armoured scoria bombs and lapilli; and (4) spatter bombs. All clasts have hypohyaline to hypocrySTALLINE groundmasses and are mineralogically similar to the host lava. The pyroclasts are incipiently to poorly vesicular, ranging between 15–36% vesicles, and are non to incipiently welded (see Appendix 2). The density of pyroclasts ranges from 1700–2300 kg m⁻³. The pyroclast types and their occurrence is summarised in Table 1.

Interpretation

The density of the Ice Harbor rootless tephra is significantly higher than that of non-welded basaltic pyroclasts produced during dyke-fed eruptions (typically 240–1440 kg m⁻³; see Chapter 3; Houghton and Wilson 1989; Parcheta et al. 2013). This suggests that the pyroclasts were sourced from lava that had already degassed at the source fissure and during transport to the rootless cone site. The ventricular and globular bombs are atypical of the deposits of fissure eruptions (e.g. Valentine and Gregg 2008); they are interpreted as water-

quenched globules of lava ejected from beneath the lava flow during explosive activity. These bombs were subsequently mechanically fragmented into angular lapilli upon eruption and deposition, enhanced by cooling contraction fractures. The spatter bombs are interpreted as proximal deposits from rootless lava fountains (e.g. as observed during the 1783–1785 Laki eruptions, see Thordarson et al. 1998) . Recycling by intermittent fountains appears necessary to form the armoured bombs. The blocky sideromelane clasts indicate cooling-contraction granulation and/or mechanical fragmentation. The fluidal, elongate sideromelane clasts indicate ductile disruption of molten lava and are common components of deposits from magmatic volatile driven eruptions (e.g. Walker and Croasdale 1971), MFCI (e.g. Zimanowski et al. 1997; Morrissey et al. 2000; Büttner et al. 2002) and peperite (see section 4.4.3; Skilling et al. 2002).

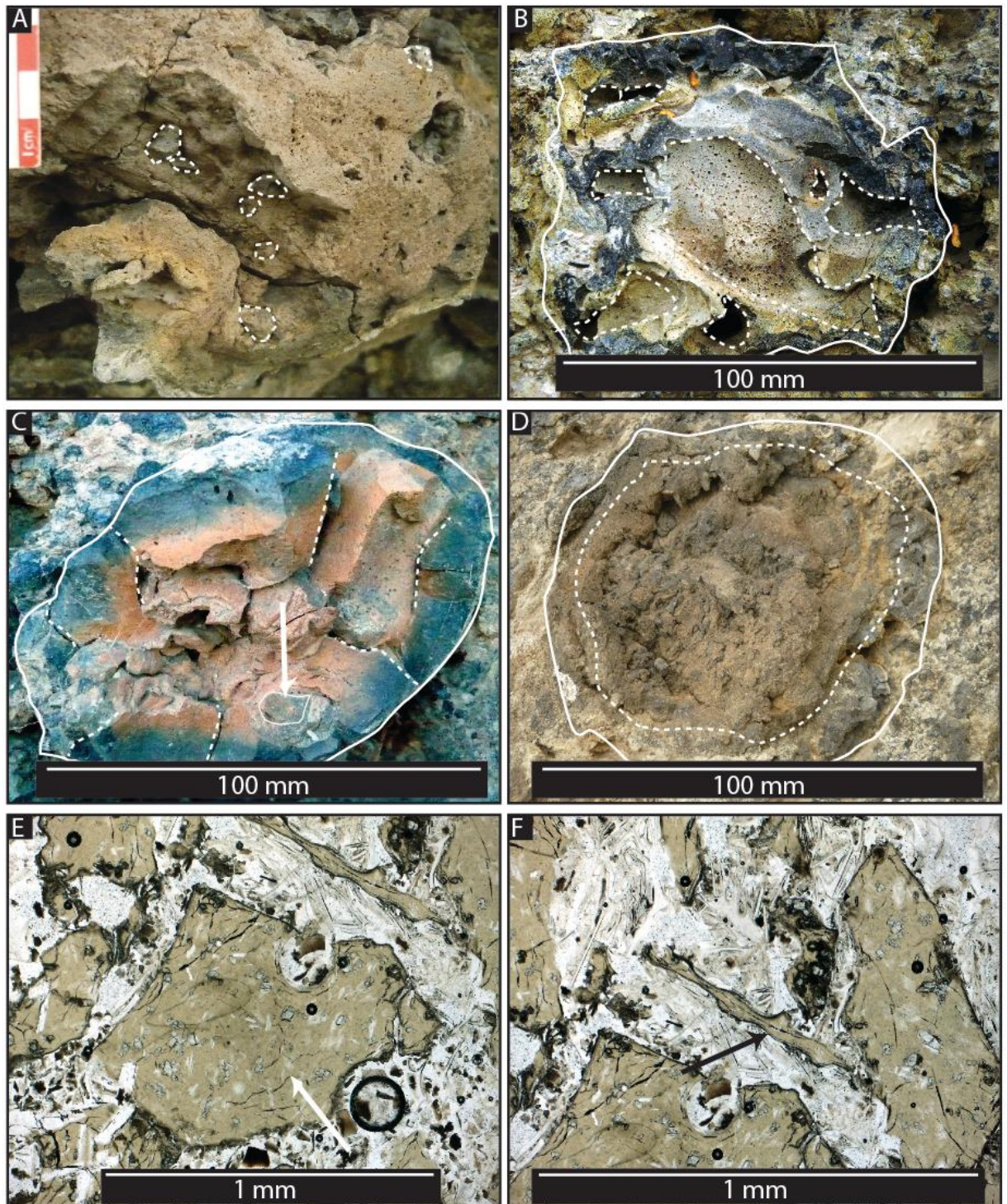


Figure 4.4. Clast types recognised in this study. (A) Folded spatter bomb with embedded lapilli (dashed outline). Graticules on the scale card are 1 cm (UTM Nad83 zone 11T, 359 942 E/5 126 519 N). (B) Ventricular clast (outlined). The clast has an amoeboid shape with a hypohyaline rind approx. 10 mm thick that grades inwards into the core. Vesicles up to 8 cm in diameter (dashed outline) have angular shapes and give clasts their

characteristic ventricular morphology (UTM Nad83 zone 11T, 359 942 E/5 126 519 N). (C) Globular bomb (outlined). The bombs have a sub-spherical shape and a black hypohyaline rind ~1 cm thick that becomes more orange in colour toward the core. Sub angular, dull black coloured basaltic lapilli (arrowed) are contained within the cores of the bombs. Cooling joints (dashed lines) penetrate from the clast margin up to 10 mm towards the core (UTM Nad83 zone 11T, 359 942 E/5 126 519 N). (D) Armoured bomb (solid outline) with 1 cm thick dense rind and vesicular core (dashed outline) (UTM Nad83 zone 11T, 360 015 E/5 126 664 N). (E) Sideromelane clast (arrowed) formed by fragmentation in a brittle state (arrowed). (F) Sideromelane clast (arrowed) formed by ductile disruption of molten lava.

Juvenile clast type	Description	Mean Density (kg m ⁻³)	Mean Vesicularity (%)	Mean Crystallinity (%)	Interpretation
Spatter bombs	Lithology: Forms irregular bombs with fluidal and ropey exteriors Structure: Clast supported (spBr); clast supported beds are parallel and dip 20°; flattening with distance from vent. Massive in lithofacies mspBr. Occurrence: Tephra deposits ((m)spBr); extends a maximum distance of ~70 m from source vent.	2200	19	31	Bombs indicate proximal fall deposition from a littoral-style lava fountain.
Hypocrystalline lapilli and ventricular or globular bombs	Lithology: Forming ventricular and globular shaped bombs frequently fragmented into blocky and equant clasts that occasionally preserve ropey textures on relict exterior surfaces; dominantly lapilli to bomb size; occasionally with radial fractures. Structure: Generally clast supported, occasionally matrix supported; forms cross stratified, massive and graded units (xsLA and m/nLA); also lenses and channels (lensLA). Occurrence: All tephra and conduit facies.	2300	15	44	Clasts represent quenched globules of lava, ejected from beneath/within the host lava flow during tephra jetting. Bombs were mechanically fragmented into angular shapes upon eruption and deposition, and due to cooling contraction granulation.
Cored scoria bombs and lapilli	Lithology: Black resinous rinds up to 10 mm thick and black scoriaceous cores; forming rounded bombs frequently fragmented into blocky and equant clasts; dominantly lapilli to bomb size. Structure: Clast-matrix supported; massive Occurrence: All tephra deposits.	1700	36	52	Produced by recycling of clasts in the conduit during intermittent and/or dry tephra jetting when surface water was less abundant.
Blocky or fluidal sideromelane ash and lapilli	Lithology: Clast shapes vary from blocky and equant to fluidal and elongate. Structure: Varying from matrix to clast supported; massive (spBr and xsLA), graded (m/nLA) and lenses and channels (lensLA). Occurrence: All tephra and conduit facies.	-	-	28	Blocky and equant clasts indicate cooling contraction granulation; fluidal, elongate shapes indicates free-air ductile fragmentation during MFCI. Bedding structures are interpreted to record deposition during the passage of density currents.
Table 4.1. Summary descriptions of pyroclast types.					

4.4.4.2 Pyroclastic lithofacies

The tephra deposits can be sub-divided into four lithofacies according to their componentry, grain size and depositional structures (Fig. 4.5; Table 4.2). In general the pyroclastic lithofacies appear moderately to very poorly sorted and are composed of juvenile clasts with <10–85 vol. % silicic volcanic ash (see Appendix 2). Lithofacies with the largest juvenile clasts tend to have the least silicic volcanic ash (Fig. 4.6). The lithofacies form proximal platform, cone or conduit-filling deposits. Sheet deposits are not found; these are commonly unconsolidated (Hamilton et al. 2010a). Contacts between the tephra deposits and underlying lavas are not exposed (Fig. 4.6).

Platform deposits include massive or normally graded lapilli-ash (m/nLAf), lenses of lapilli-ash (lensLA) and cross-stratified lapilli-ash (xsLA; Table 4.2; Fig. 4.5). These deposits are 1–5.5 m in thickness (Fig. 4.7) and are present beneath the parallel-bedded spatter (//bSp; Figs. 4.6 and 4.7). Pyroclasts within the deposits are dominantly of lapilli size. They are exposed over a ~600 m long transect. Bedding dips vary from 10–20°.

Cone deposits are composed of parallel-bedded spatter (//bSp; Table 4.2) that is 1–3 m thick (Fig. 4.6) and contains predominantly bomb-sized clasts. Deposits are exposed over a ~200 m long transect. The spatter varies from horizontally bedded to dipping up to 20°; whether this is towards or away from a conduit is unclear (Figs. 4.6 and 4.7).

The conduits are partially filled with massive spatter (mSp; Table 4.2) and are not observed in contact with overlying cone and/or platform deposits.

Interpretation

The Ice Harbor platform deposits are inferred to have been deposited from both PDCs and by fallout (e.g. Hamilton et al. 2010a). The occurrence of massive/normally graded lapilli-ash (m/nLAf), lenses of lapilli-ash (lensLA) and cross-stratified lapilli-ash (xsLA) beneath the spatter-rich deposits (e.g. //bSp) suggests that the platform was constructed prior to cone formation. Intermittent deposits of normally-graded lapilli ash (nLA) and cross-stratified lapilli-ash (xsLA; Fig. 4.6) overlying the spatter layers suggests that the cone field is composed of numerous overlapping cones formed in a sequence of rootless eruptions (e.g. Fagents and Thordarson 2007). The thickness and spatial distribution of the exposures suggest that the tephra platforms were ~5 m thick and were likely to be laterally extensive over 100's

of metres. Cone-forming and conduit-filling deposits of rootless cones commonly contain spatter-rich lithofacies (Hamilton et al. 2010a), as observed in this study. These coarse-grained deposits are produced as the explosivity of the eruptions decreases (Fagents and Thordarson 2007).

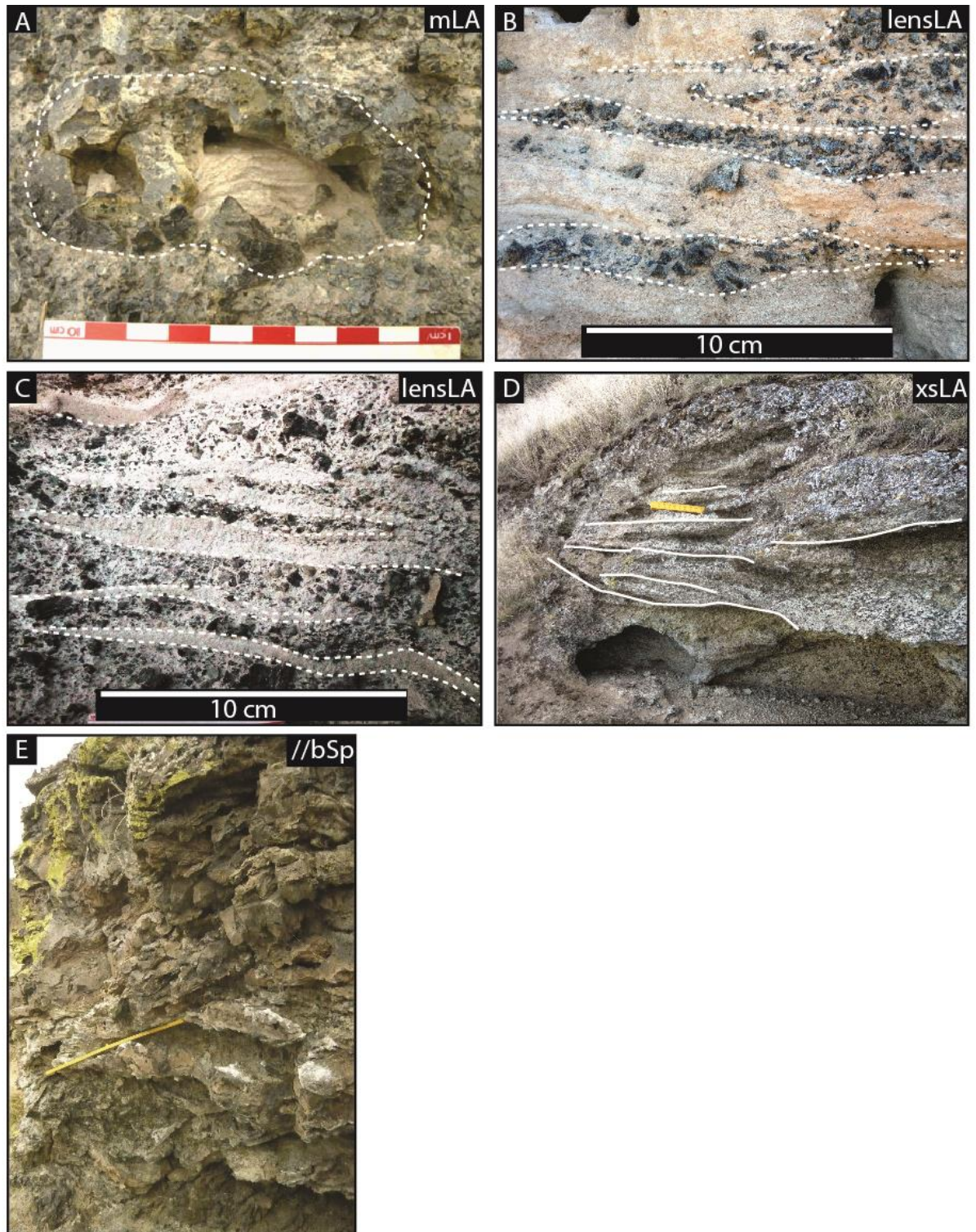


Figure 4.5 (overleaf). Lithofacies found in the study area. (A) mLA with ventricular bomb (outlined) enclosing laminated silicic volcanic ash. Graticules on the scale card are 1 cm (UTM Nad83 zone 11T, 359 881 E/5 126 506 N) (B) lensLA with hypocrySTALLINE lapilli-rich lenses. Dashed white outlines indicate lenses (UTM Nad83 zone 11T, 359 868 E/5 126 485 N) (C) lensLA with silicic ash-rich lenses. White outlines indicate lenses (UTM Nad83 zone 11T, 359 868 E/5 126 485 N) (D) xsLA, white outlines indicate beds. The ruler is 25 cm long (UTM Nad83 zone 11T, 359 868 E/5 126 485 N) (E) //bSp, showing bedded spatter bombs. The ruler is 50 cm (UTM Nad 83 zone 11T, 359 942 E/5 126 519 N).

Lithofacies	Components	Description	Av. max clast size (mm)	% silicic ash	Interpretation
LA Sub facies: n (normal graded), m (massive) f (fabric)	Hypocrystalline lapilli and bombs, sideromelane ash, silicic volcanic ash, clasts of lava crust	Very poorly sorted, hypocrystalline lapilli with rare ash sized fragments; clast supported in silicic ash.	128	20–75	Platform forming deposit. The general lack of evidence for traction sedimentation in the juvenile clasts suggest proximal fall deposition, localised fabrics suggest a minor amount of lateral transport. The coarse nature of some deposits results from the ballistic emplacement of bombs.
lensLA	Hypocrystalline lapilli, sideromelane ash, silicic volcanic ash, clasts of lava crust	Lenses and channels of moderately well sorted, sideromelane and hypocrystalline lapilli; clast supported in silicic volcanic ash; and lenses and channels of substrate within sideromelane and hypocrystalline lapilli dominated rock. Irregular lower contact.	60	25–85	Platform forming deposit. Indicates deposition from dilute PDC. Erosion and transportation of material occurred in locally confined channels. Irregular lower contacts may suggest local erosion of underlying units.
xsLA	Hypocrystalline lapilli and bombs, sideromelane ash, silicic volcanic ash, clasts of lava crust	Cross stratified, moderately sorted sideromelane and hypocrystalline lapilli; clast supported in silicic volcanic ash; beds approximately 5 cm thick.	70	20–55	Platform forming deposit. Crude cross-bedding formed during deposition from PDC's, currents were locally erosive.
//bSp Sub facies: m (massive)	Spatter bombs, hypocrystalline lapilli, silicic volcanic ash, clasts of lava crust	Parallel-bedded spatter bombs with embedded angular hypocrystalline lapilli and silicic volcanic ash. Sub facies is massive.	>1000	<10	Cone forming deposit; sub facies (mSp) conduit fill deposit. Bomb beds indicate proximal fall deposition from rootless lava fountains. Large grain size indicates decreasing explosivity when water availability was decreasing towards the end of the eruptions.

Table 4.2 Summary descriptions of cone-forming and conduit deposits.

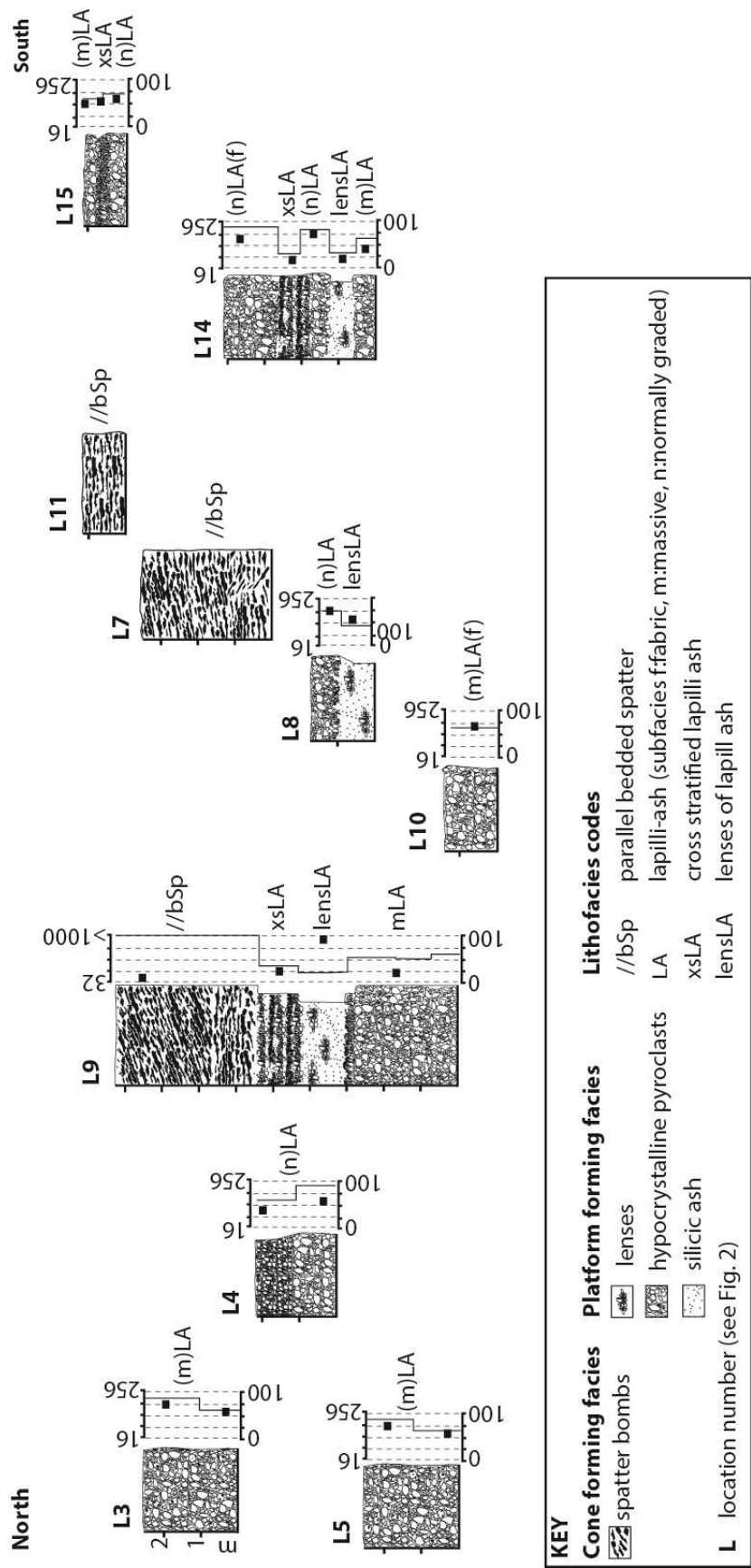


Figure 4.6. Lithofacies logs of tephra deposits south of the Snake River. Clast size is shown on the top axis with divisions at 32, 64, 128 and 256 mm (Location 9 uses 32, 64, 128, 256 and >1000 mm divisions). Silicic volcanic ash abundance (black squares; %) is shown across the bottom axis in 25% gradations. Logs are shown at relative altitudes. For locations of the sections see Fig. 4.2.

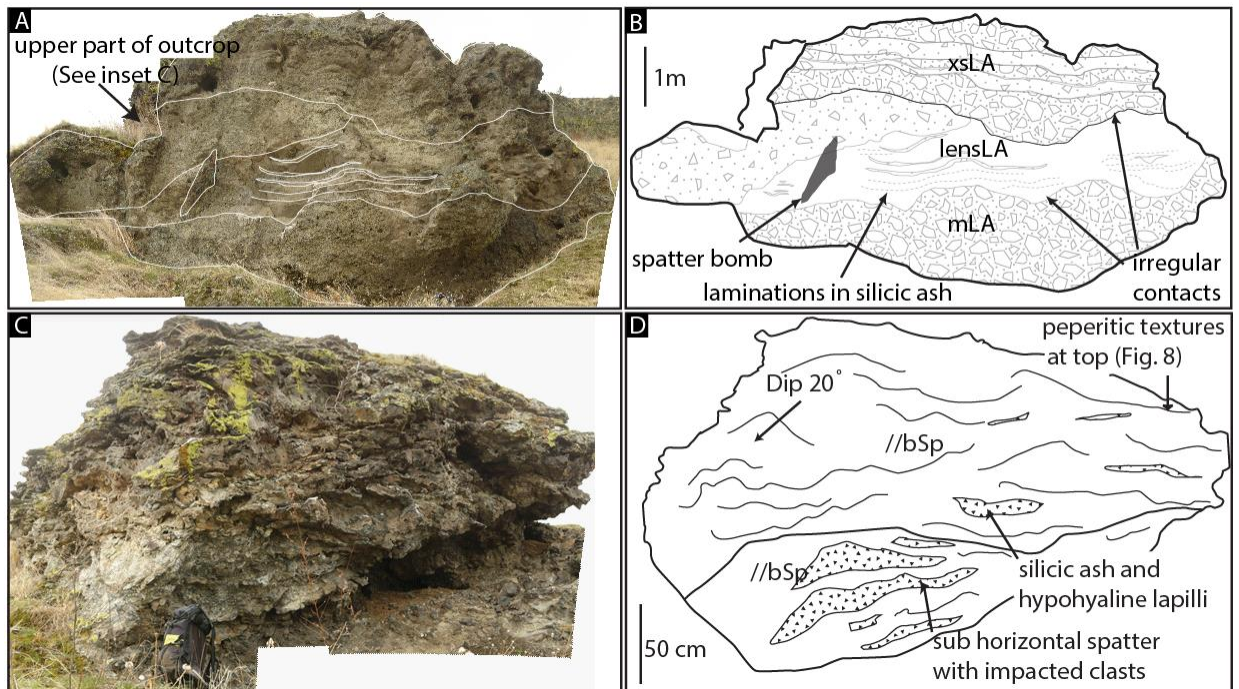


Figure 4.7. Photographs and interpretive pictures of Location 9 (UTM Nad 83 zone 11T, 359 942 E/5 126 519 N). a, b Outcrop of platform-forming admixed tephra and silicic volcanic ash. c,d Outcrop of cone-forming tephra composed of lithofacies //bSp.

4.4.4.3 Lava-silicic volcanic ash interaction textures in tephra deposits

A variety of peperite-like textures are observed in the tephra deposits (Fig. 4.8). Fluidal textures include spatter bombs that inter-finger with the silicic volcanic ash and associated globular and elongate spatter lapilli and ash found intimately mixed with the silicic volcanic ash. Within 2 cm of the spatter, the silicic volcanic ash is often thermally altered, becoming dark in colour and fused (e.g. Schminke 1967). Where fused, the silicic volcanic ash contains vesicles ≤ 2 mm in diameter. Vesicles in the spatter also contain silicic ash. Blocky textures include jigsaw-fit bombs; these clasts have hairline fractures filled with silicic volcanic ash. Other bombs have rinds that are partially separated from their core, encapsulating a 2 mm-thick domain of silicic volcanic ash between rind and core. These domains contain mm-scale globules of lava.

Interpretation

Peperite-like textures indicate interaction between hot juvenile clasts and unconsolidated sediment (e.g. Skilling et al. 2002). Vesicles in the fused silicic volcanic ash indicate that gas was generated during interaction (e.g. Kokelaar 1982; Skilling et al. 2002; Squire and McPhie 2002). Silicic ash-filled vesicles in the spatter indicate that the sediment was mobilised during interaction (e.g. Goto and McPhie 1996 and references there-in; Skilling et al. 2002). The fluidal and blocky textures indicate variations in mechanical stress, movement of lava, lava-silicic ash density contrasts and variations in lava viscosity and clast size (e.g. Skilling et al. 2002; Squire and McPhie 2002). These textures may represent a failed phreatomagmatic fragmentation process formed beneath the lava flow (e.g. Busby-Spera and White 1987; Hooten and Ort 2002). The bombs with encapsulated silicic volcanic ash are interpreted as intrusions of lava into the underlying substrate. Lava globules in the silicic volcanic ash domain indicate that the cores of these bombs were molten during intrusion.

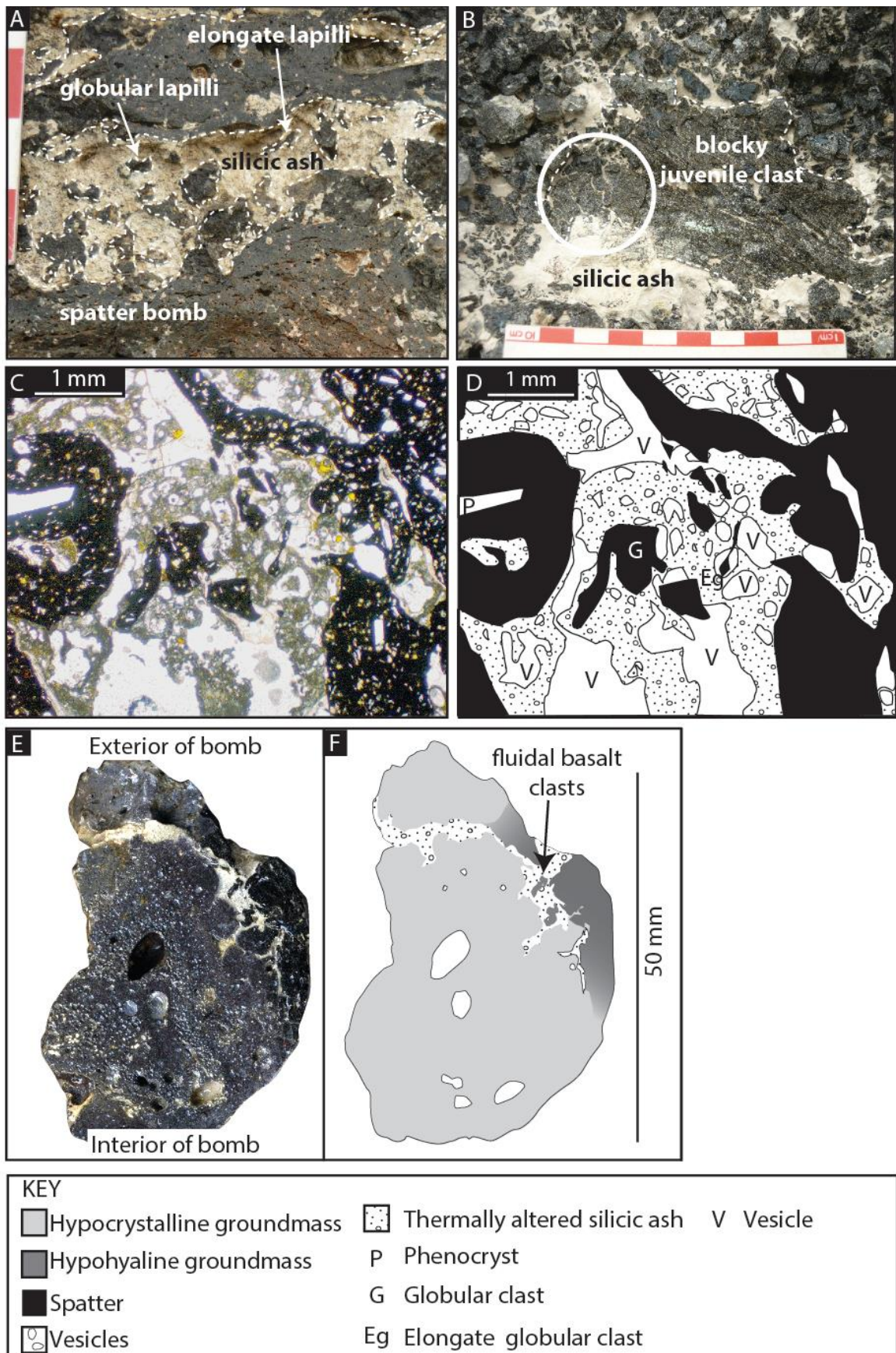


Figure 4.8 (overleaf). Peperite-like textures produced by the interaction of juvenile clasts and silicic volcanic ash. (A) Fluidal peperite with elongate and globular clasts in lithofacies //bSp (UTM Nad 83 zone 11T, 359 942 E/5 126 519 N). (B) Blocky peperite with jigsaw-fit fractures (circled). Graticules are 1 cm (UTM Nad 83 zone 11T, 360 014 E/5 126 649 N). Thin section C and interpretive sketch D shows section of mingled spatter and silicic volcanic ash. The spatter clasts exhibit elongate and globular morphologies. The silicic ash is thermally altered and contains vesicles. Vesicles within the spatter clasts enclose silicic volcanic ash. Section of a ventricular bomb E and interpretive sketch F are also shown. The hypohyaline rind is spalling from the core and has encapsulated a domain of silicic volcanic ash. Fluidal basalt clasts are found within the silicic ash domain (arrowed) indicating that the core of the bomb was molten when the sediment was encapsulated.

4.5 Emplacement of the Ice Harbor rootless cones

We infer that the Ice Harbor lava flows traversed a lacustrine or floodplain environment (Fig. 4.9). The ground was mantled by a layer of silicic volcanic ash fall derived from a major explosive eruption. As the lava flows inflated they developed brittle basal crusts (Hon et al. 1994). These crusts were weakened by the development of cooling fractures (Thordarson and Self 1998) which created a zone of weakness along the base of the flows. Cracking and subsequent failure of the crust would have been facilitated by heterogeneous subsidence of the flows during inflation (e.g. Fagents and Thordarson 2007; Hamilton et al. 2010a). Failure of the basal crust allowed extrusion of lava, analogous to the axial cleft of a tumulus (e.g. Walker 1991; Rossi and Gudmundsson 1996; Hamilton et al. 2010a).

Extrusion of lava through the basal crust resulted in the intimate mixing of molten lava with the water-saturated silicic volcanic ash. This mixing of the lava and sediment is evidenced by the peperite-like textures and abundance of silicic volcanic ash (i.e. substrate) in the tephra deposits. Lava-substrate mixing was followed by explosions. These explosions fragmented the lower lava crust and burst through the molten lava core creating transient conduits. The preservation of conduits requires the cooling and solidification of the conduit walls over time to prevent pressure-driven collapse of the walls between explosions. The presence of spatter lining the walls of the conduits indicates that they were stabilised from both material ejected during the explosions, as well as from the chilling of the molten lava

core. Explosive activity deposited the massive/normally graded lapilli-ash (lithofacies m/nLA (f)) on top of the lava flow. Some of the pyroclastic material formed PDCs (depositing lithofacies lensLA and xsLA; Table 4.2). These processes constructed the tephra platforms.

Spatter-rich lithofacies (e.g. //bSp and mSp; Table 4.2) were produced during rootless lava fountaining and cap the rootless cone successions and fill some conduits. The coarse clast size of these lithofacies indicates decreasing explosivity as water availability declined. Explosions also embedded juvenile clasts and lava crust lithics into the hot and ductile conduit walls.

The presence of the cones on top of sheet lobes suggests that the cones developed repelled, non-aligned spatial distributions (e.g. Hamilton et al. 2010a; Hamilton et al. 2010b). The cones were likely to have formed in topographic lows where lava and water were most abundant, and in regions of enhanced substrate compressibility (Hamilton et al. 2010a; Hamilton et al. 2010b). Exposures do not allow determination of the symmetry of the cones (e.g. radial or elongate). Growth of the cones was terminated by the decreasing availability of ground water, or by water being prevented from gaining access to the explosion site. Continued cooling stabilised the conduit walls and over time cooling joints radiated out into the core (e.g. Fig. 4.9).

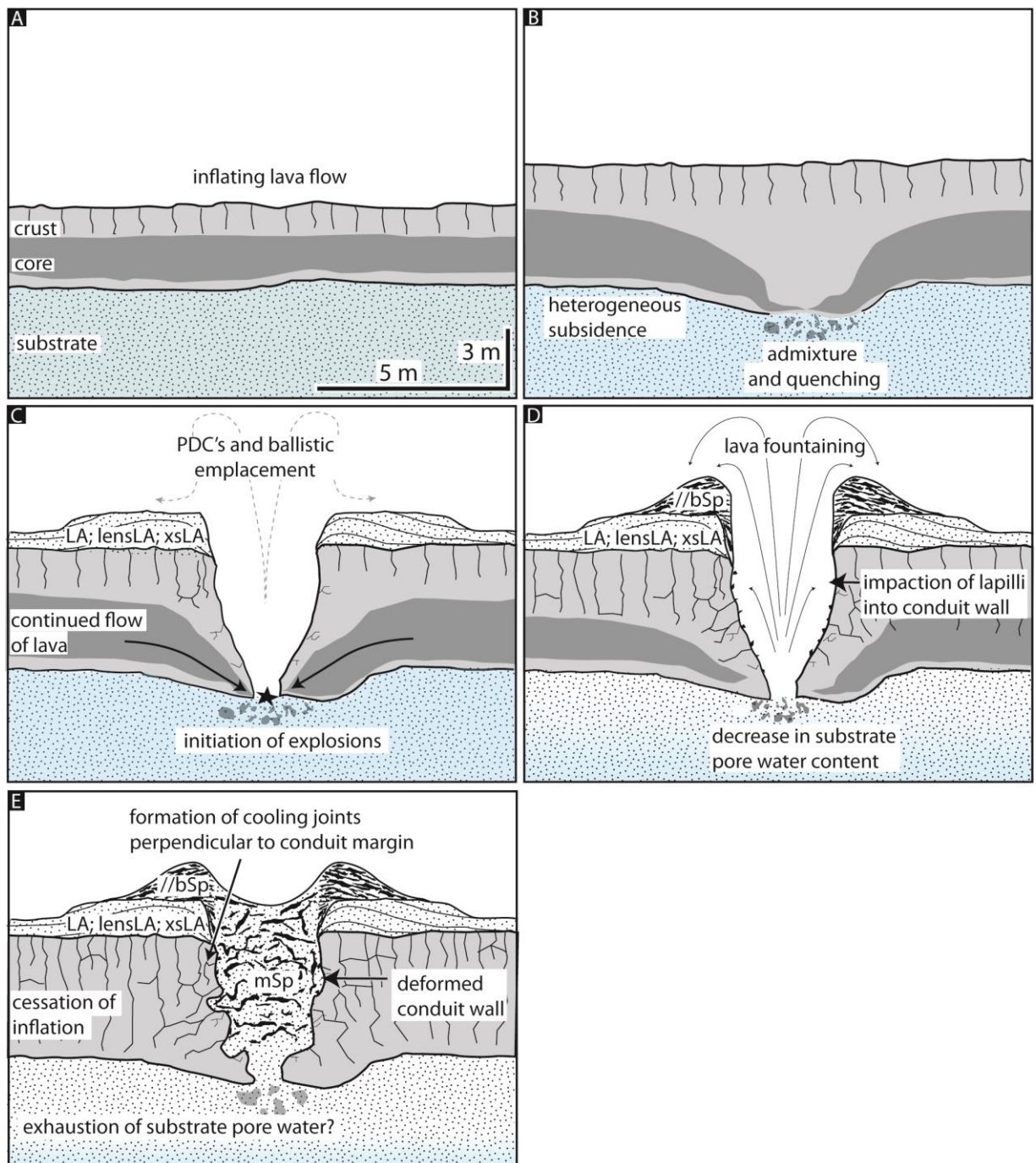


Figure 4.9. Inferred eruption chronology for the cones. (A) Lava flow traverses wet ground and subsides heterogeneously into the underlying silicic volcanic ash. (B) Initial mingling of lava with the silicic ash results in the formation of globular and ventricular juveniles and peperite-like textures. (C) Interaction between molten lava and water saturated silicic volcanic ash results in explosive brecciation of the host lava flow and fragmentation of the globular and ventricular juveniles into lapilli and ash sized clasts.

Episodic eruptions and dilute PDC's deposit poorly sorted juveniles and clasts sourced from the host lava flow, forming sheet and platform deposits (lithofacies m/nLA(f), lensLA, xsLA). Minor clast recycling may occur, producing armoured bombs. Substrate pore water is gradually depleted beneath the lava flow. (D) Decreasing water availability results in less efficient fragmentation and lava fountains are generated. These fountains produce lithofacies //bSp that builds a cone. Lapilli are also impacted into the cooling conduit walls. (E) With time water availability decreases and eruptions cease. The lava flow may continue to inflate and deform the conduit. Post-eruption cooling of the lava promotes the formation of cooling joints that radiate from the conduit.

4.6 Comparison with other rootless cones

The deposits in this study are comparable with the platform and cone-building deposits of rootless cones in Iceland (e.g. Table 4.3; Fig. 4.10), which show a similar pattern of sediment-rich PDC deposits overlain by coarse-grained fall deposits. These PDC and fall deposits are composed of scoria lapilli and bombs, spatter bombs and clastogenic lava, all intimately mixed with silt- to cobble-sized sediment. The coarse grainsize of the platform deposits in this study relative to others described in Iceland (Hamilton et al. 2010a) may result from the proximity of the Ice Harbor tephra platforms to the explosion source, or from less efficient magma-water interaction. Whilst the importance of sediment properties (e.g. grainsize distribution and thermal conductivity) in governing the explosivity of dyke-fed eruptions is recognised (e.g. Sohn 1996; White 1996; Auer et al. 2007; Ort and Carrasco-Nuñez 2009) the effect of sediment properties on rootless eruptions is as-yet unknown. Furthermore, the properties of the substrate would have evolved during the eruptions, due to mixing of basaltic pyroclasts and silicic volcanic ash beneath the lava flow.

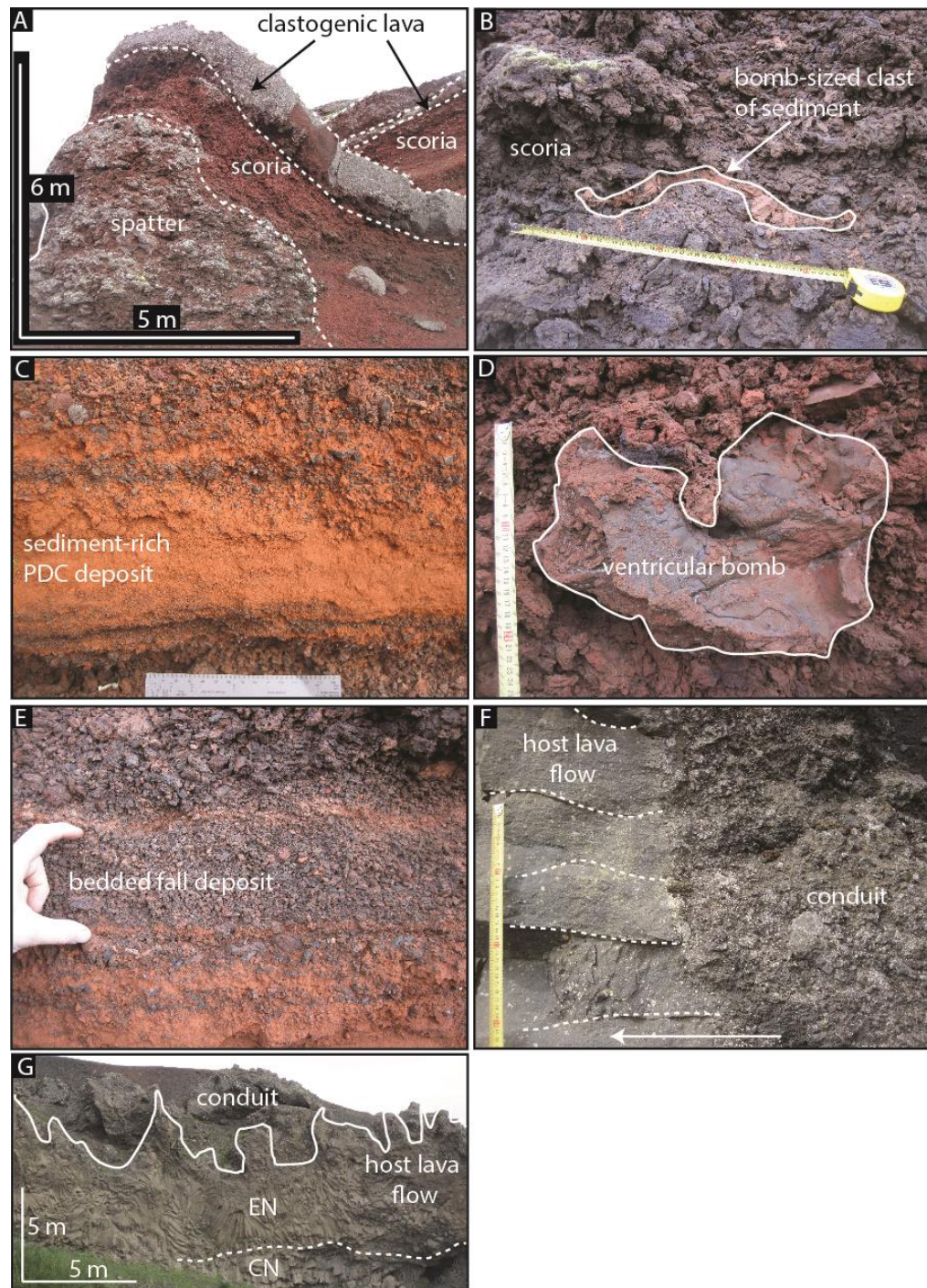


Figure 4.10. Photographs of Leitin and Búrfell rootless cones in southern Iceland (UTM Nad 83, zone 27, 500 000 E/7 097 014 N; 402 187 E/7 098 548 N respectively). (A) Overlapping cone stratigraphies composed of crudely bedded spatter and scoria bombs and lapilli and clastogenic lava. The sequence is ~6 m thick. (B) Bomb-sized clast of sediment (outlined) within a sequence of scoria and spatter. The ruler is 40 cm long. (C) Sediment-rich pyroclastic density current deposit at the base of the cone forming

stratigraphy. The reddish colour is given by the agglutinated sediment (inferred to be a lacustrine siltstone), not oxidation of the pyroclasts. The scale card is 120 mm long. (D) Bomb-sized, ventricular-type pyroclast (outlined) within the bedded spatter and scoria. The ruler is ~25 cm long. (E) Initial cone-forming fall deposit, composed of scoria lapilli. Beds often form inversely-graded couplets. The bed indicated is ~6 cm thick. Beds thickness and clast size increases up-section. (F) Cross section of the conduit wall, with lapilli sized pyroclasts agglutinated to the outer wall. Cooling joints (dashed lines) radiate from the contact and are perpendicular to the conduit contact. The arrow points towards the core of the lava flow. The ruler is 30 cm long. (G) A lava flow affected by rootless cone formation. The lava flow can be divided into a colonnade (CN) and an entablature (EN), and has an irregular upper contact that forms the rootless conduit. The lava is ~10 m thick.

Field Area	Cone height (m)	Cone basal diameter (m)	Structure	Juvenile Clast types	Environmental setting	Grading	Bedding	Deposition method	Substrate inclusions
Greenland	25	100– 200	Fines upwards into ash layers rich in shale, largest clasts proximal, central sediment filled chimney	Pillows and pillow fragments up to 0.5 m size at base of the unit, glass rich clasts with fluidal outlines and yellow brown sand sized volcanic at top	Subaqueous lacustrine	Normal	Bedding seen as clast alignment, flanks dip 20°	(No data)	Partly consolidated shale; 10–20 vol. %
Iceland	1–35	2– 450	Capped by spatter 1–2 m thick, inverse grading is common, occasionally with rheomorphic layers, form steep hornitos or broad cinder/tuff cones	Scoria and spatter, ash, lapilli and bombs	Lakes, marshes etc.	Inverse	<0.2 m thick beds of mud and ash, decimetre to metre thick beds of juveniles	PDC and fall	Common in lower sequences as beds, inclusions and coatings; no amounts given
Columbia River Ice Harbor lava flows	≥ 3	≥ 5	Sediment-rich tephra platforms at base, overlain by 1–3 m thick spatter sequences	Angular hypocrySTALLine ash and lapilli, armoured and spatter bombs	Flood plain or shallow lake	Inverse	Decimetre to metre thick beds of juveniles, rich in substrate	PDC and fall	Common in all except uppermost beds, admixed with juveniles; 20– 90 vol. %
Hawaii	10– 90	20– 100’s	Monomictic, variably welded and agglutinated, often form crescent shaped ridges at the shoreline	Scoria and spatter, ash, lapilli and cored bombs, Limu-o-Pele , lava crust lithics	Entry of lava into ocean	Normal and inverse	Massive to crudely bedded in proximal facies; poorly to moderately bedded in distal facies	Tephra jets, littoral lava fountains, lithic blasts, lava squeeze up and flow from cone, bubble bursts	(No data)

Table 4.3. Comparison of rootless and littoral cone structures using data from Simpson and McPhie (2001); Mattox and Mangan (1997); Moore and Ault (1965); Fisher (1968); Hamilton et al. (2010a); Melchior Larsen et al. (2006); Jurado-Chichay et al. (1996); and this study.

4.7 Conclusions

The Ice Harbor tephra deposits provide insights into the construction and componentry of a rootless cone field. Cross sections of conduits suggest that ≥ 8 cones were present in a cone field ≥ 1 km² in area. Cone- and platform-forming deposits are composed of admixed juvenile clasts, clasts from the host lava flow and silicic volcanic ash from an earlier, major explosive eruption in NW USA. Construction of the cone field occurred through a combination of deposition from PDCs and lava fountaining. Explosivity decreased with time as a result of decreasing water availability in the underlying silicic volcanic ash. This study demonstrates juvenile clast morphology and clast density are useful criteria for distinguishing between rootless tephra and tephra produced above an erupting dyke. Furthermore, the abundance of sediment (in this case, silicic volcanic ash) in the tephra can help distinguish rootless cones from superficially similar scoria cones.

4.8 References

- Auer A, Martin U, Nemeth, K (2007) The Fekete-hegy (Balaton Highland Hungary) “soft-substrate” and “hard-substrate” maar volcanoes in an aligned volcanic complex—Implications for vent geometry, subsurface stratigraphy and the palaeoenvironmental setting. *J Volcanol Geoth Res* 159(1), 225-245.
- Brown RJ, Blake S, Thordarson T, Self S (2014) Pyroclastic edifices record vigorous lava fountains during the emplacement of a flood basalt flow field, Roza Member, Columbia River Basalt Province, USA. *Geol Soc Am Bull* 126:875-891
- Bruno BC, Fagents S, Thordarson T, Baloga SM, Pilger E (2004) Clustering within rootless cone groups on Iceland and Mars: Effect of nonrandom processes. *Journal of geophysical research* 109(E7):1991-2012
- Bryan WB (1972) Morphology of quench crystals in submarine basalts. *Journal of Geophysical Research* 77(29):5812-5819
- Busby-Spera C, White JL (1987) Variation in peperite textures associated with differing host-sediment properties. *B Volcanol* 49(6):765-776
- Büttner R, Dellino P, La Volpe L, Lorenz V, Zimanowski B (2002) Thermohydraulic explosions in phreatomagmatic eruptions as evidenced by the comparison between pyroclasts and products from Molten Fuel Coolant Interaction experiments. *J. Geophys. Res.* 107(B11):2277
- Camp VE, Ross ME, Hanson WE (2003) Genesis of flood basalts and Basin and Range volcanic rocks from Steens Mountain to the Malheur River Gorge, Oregon. *Geol Soc Am Bull* 115(1):105-128
- Duraiswami RA, Bondre NR, Managave S (2008) Morphology of rubbly pahoehoe (simple) flows from the Deccan Volcanic Province: Implications for style of emplacement. *J Volcanol Geoth Res* 177(4):822-836
- Fagents SA, Lanagan P, Greeley R (2002) Rootless cones on Mars: a consequence of lava-ground ice interaction. *Geological Society, London, Special Publications* 202(1):295-317
- Fagents SA, Thordarson T (2007) Rootless cones in Iceland and on Mars. In: Chapman M, Skilling IP (eds) *The Geology of Mars: Evidence from Earth-Based Analogues*. Cambridge University Press, pp 151–177
- Fisher RV (1968) Puu Hou littoral cones, Hawaii. *Geologische Rundschau* 57(3):837-864

- Goto Y, McPhie J (1996) A Miocene basanite peperitic dyke at Stanley, northwestern Tasmania, Australia. *J Volcanol Geoth Res* 74(1):111-120
- Greeley R, Fagents SA (2001) Icelandic pseudocraters as analogs to some volcanic cones on Mars. *J. Geophys. Res.* 106(E9):20527-20546
- Hamilton CW, Thordarson T, Fagents SA (2010a) Explosive lava–water interactions I: architecture and emplacement chronology of volcanic rootless cone groups in the 1783–1784 Laki lava flow, Iceland. *B Volcanol* 72(4):449-467
- Hamilton CW, Fagents SA, Thordarson T (2010b) Explosive lava–water interactions II: self-organization processes among volcanic rootless eruption sites in the 1783–1784 Laki lava flow, Iceland. *B Volcanol* 72(4):469-485
- Hamilton CW, Fagents SA, Wilson L (2010c) Explosive lava-water interactions in Elysium Planitia, Mars: Geologic and thermodynamic constraints on the formation of the Tartarus Colles cone groups. *Journal of Geophysical Research: Planets* (1991–2012) 115(E9)
- Hamilton CW, Fagents SA, Thordarson T (2011) Lava–ground ice interactions in Elysium Planitia, Mars: Geomorphological and geospatial analysis of the Tartarus Colles cone groups. *Journal of Geophysical Research: Planets* (1991–2012) 116(E3)
- Hon K, Kauahikaua J, Delinger R, Mackay K (1994) Emplacement and inflation of pahoehoe sheet flows: Observations and measurements of active lava flows on Kilauea Volcano, Hawaii. *Geol Soc Am Bull* 106(3):351-370
- Hooten J, Ort M (2002) Peperite as a record of early-stage phreatomagmatic fragmentation processes: an example from the Hopi Buttes volcanic field, Navajo Nation, Arizona, USA. *J Volcanol Geoth Res* 114(1):95-106
- Houghton BF, Wilson CJN (1989) A vesicularity index for pyroclastic deposits. *B Volcanol* 51(6):451-462
- Jaeger WL, Keszthelyi LP, McEwen AS, Dundas CM, Russell PS (2007) Athabasca Valles, Mars: A Lava-Draped Channel System. *Science* 317(5845):1709-1711
- Jafri SH, Charan SN (1992) Quench textures in pillow basalt from the Andaman-Nicobar Islands, Bay of Bengal, India. *Proc. Indian Acad. Sci. (Earth Planet Sci.)* 101(1):99-107
- Jurado-Chichay Z, Rowland S, Walker GL (1996) The formation of circular littoral cones from tube-fed pāhoehoe: Mauna Loa, Hawai'i. *B Volcanol* 57(7):471-482
- Keszthelyi LP, Baker VR, Jaeger WL, Gaylord DR, Bjornstad BN, Greenbaum N, Self S, Thordarson T, Porat N, Zreda MG (2009) Floods of water and lava in the Columbia River Basin: Analogs for Mars. *Field Guides* 15:845-874
- Keszthelyi LP, Jaeger WL (2014) A field investigation of the basaltic ring structures of the Channeled Scabland and the relevance to Mars. *Geomorphology*
- Kokelaar BP (1982) Fluidization of wet sediments during the emplacement and cooling of various igneous bodies. *J Geol Soc London* 139(1):21-33
- Lanagan PD, McEwen AS, Keszthelyi LP, Thordarson T (2001) Rootless cones on Mars indicating the presence of shallow equatorial ground ice in recent times. *Geophysical Research Letters* 28(12):2365-2367
- Long PE, Wood BJ (1986) Structures, textures, and cooling histories of Columbia River basalt flows. *Geol Soc Am Bull* 97(9):1144-1155
- Mattox TN, Mangan MT (1997) Littoral hydrovolcanic explosions: a case study of lava–seawater interaction at Kilauea Volcano. *J Volcanol Geoth Res* 75(1–2):1-17
- McKee E, Swanson D, Wright T (1977) Duration and volume of Columbia River basalt volcanism, Washington, Oregon and Idaho. In: *Geol. Soc. Am. Abstr. Programs*. pp 463-464
- Melchior Larsen L, Ken Pedersen A, Krarup Pedersen G (2006) A subaqueous rootless cone field at Niuluut, Disko, Paleocene of West Greenland. *Lithos* 92(1-2):20-32
- Moore JG, Ault WU (1965) Historic littoral cones in Hawaii. *Pacific science* XIX(3-11)
- Morrissey M, Zimanowski B, Wohletz KH, Buettner R (2000) Phreatomagmatic fragmentation. In: Sigurdsson H (ed) *Encyclopedia of volcanoes*. Academic Press, San Diego, pp 431-445

- Ort MH, Carrasco-Núñez G (2009) Lateral vent migration during phreatomagmatic and magmatic eruptions at Tecuitlapa Maar, east-central Mexico. *J Volcanol Geoth Res* 181(1), 67-77.
- Parcheta CE, Houghton BF, Swanson DA (2013) Contrasting patterns of vesiculation in low, intermediate, and high Hawaiian fountains: A case study of the 1969 Mauna Ulu eruption. *J Volcanol Geoth Res* 255(0):79-89
- Ramos FC, Wolff JA, Starkel W, Eckberg A, Tollstrup DL, Scott S (2013) The changing nature of sources associated with Columbia River flood basalts: Evidence from strontium isotope ratio variations in plagioclase phenocrysts. *Geological Society of America Special Papers* 497:231-257
- Reidel SP, Tolan TL (1992) Eruption and emplacement of flood basalt: An example from the large-volume Teepee Butte Member, Columbia River Basalt Group. *Geol Soc Am Bull* 104(12):1650-1671
- Reidel SP, Camp VE, Tolan TL, Martin BS (2013) The Columbia River flood basalt province: stratigraphy, areal extent, volume, and physical volcanology. *Geological Society of America Special Papers* 497:1-43
- Rossi M, Gudmundsson A (1996) The morphology and formation of flow-lobe tumuli on Icelandic shield volcanoes. *J Volcanol Geoth Res* 72(3):291-308
- Schminke H-U (1967) Fused Tuff and Pépérites in South-Central Washington. *Geol Soc Am Bull* 78(3):319-330
- Self S, Keszthelyi L, Thordarson T (1998) The importance of pahoehoe. *Annu. Rev. Earth Planet. Sci.* 26:81-110
- Skilling IP, White JDL, McPhie J (2002) Peperite: a review of magma–sediment mingling. *J Volcanol Geoth Res* 114(1–2):1-17
- Smith GA (1988) Neogene synvolcanic and syntectonic sedimentation in central Washington. *Geol Soc Am Bull* 100(9):1479-1492
- Sohn YK (1996) Hydrovolcanic processes forming basaltic tuff rings and cones on Cheju Island, Korea. *Geol Soc Am Bull* 108(10):1199-1211
- Squire RJ, McPhie J (2002) Characteristics and origin of peperite involving coarse-grained host sediment. *J Volcanol Geoth Res* 114(1–2):45-61
- Swanson D, Wright TL, Hooper PR, Bentley RD (1979) Revisions in stratigraphic nomenclature of the Columbia River Basalt Group. *U.S Geological Survey Bulletin* 1457G:G1 - G59
- Swanson DA, Wright TL, Helz RT (1975) Linear vent systems and estimated rates of magma production and eruption for the Yakima Basalt on the Columbia Plateau. *American Journal of Science* 275(8):877-905
- Thorarinsson S (1951) Laxargljufur and Laxarhraun: a tephrochronological study. *Geograf Annal* 2:1–89
- Thorarinsson S (1953) The crater groups in Iceland. *B Volcanol* 14(1):3-44
- Thordarson T, Self S (1998) The Roza Member, Columbia River Basalt Group: A gigantic pahoehoe lava flow field formed by endogenous processes? *J. Geophys. Res.* 103(B11):27411-27445
- Thordarson T, Miller D, Larsen G (1998) New data on the Leidolfssfell cone group in South Iceland. *Jökull* 46:3-15
- Thordarson T, Höskuldsson Á (2008) Postglacial volcanism in Iceland. *Jökull* 58:197-228
- Tolan TL, Beeson MH, Lindsey KA (2002) The Effects of Volcanism and Tectonism on the Evolution of the Columbia River System. In: *A Field Guide to Selected Localities in the South-western Columbia River Plateau and Columbia River Gorge of Washington and Oregon State*. Northwest Geological Society,
- Valentine GA, Gregg TKP (2008) Continental basaltic volcanoes — Processes and problems. *J Volcanol Geoth Res* 177(4):857-873
- Walker G, Croasdale R (1971) Characteristics of some basaltic pyroclastics. *B Volcanol* 35(2):303-317
- Walker GPL (1991) Structure, and origin by injection of lava under surface crust, of tumuli, “lava rises”, “lava-rise pits”, and “lava-inflation clefts” in Hawaii. *B Volcanol* 53(7):546-558
- White JDL (1996) Impure coolants and interaction dynamics of phreatomagmatic eruptions. *J Volcanol Geoth Res* 74(3–4):155-170

- Wolff J, Ramos F, Hart G, Patterson J, Brandon A (2008) Columbia River flood basalts from a centralized crustal magmatic system. *Nature geoscience* 1(3):177-180
- Zimanowski B, Büttner R, Lorenz V (1997) Premixing of magma and water in MFCI experiments. *B Volcanol* 58(6):491-495

Chapter 5: The Construction of Submarine Volcanoes: Insights from 3D Seismic Data

5.1 Introduction

The use of three-dimensional (3D) seismic data within hydrocarbon basins has provided a unique opportunity to investigate the architecture of buried volcanoes (e.g. Gatliff et al. 1984; Ritchie and Hitchen 1996; Bell and Butcher 2002; Lee et al. 2006; Wall et al. 2010; Jackson 2012; Magee et al. 2013; Zhao et al. 2014). These edifices form in sub aerial and submarine environments (Chapter 2). Seismic data allows us to remotely interrogate these edifices externally and internally, without the requirement of erosional dissection. We are therefore able to examine the development of volcanoes (e.g. Magee et al. 2013), their magmatic plumbing system (e.g. Bell and Butcher 2002; Thomson 2007; Wall et al. 2010; Zhao et al. 2014) and their links to structural features within a basin (e.g. Zhao et al. 2014). These data also grant access to regions of the Earth inaccessible in the field (Thors and Jakousson 1982; Magee et al. 2013; Zhao et al. 2014). Previous studies using seismic data have identified shield volcanoes (Magee et al. 2013), diatremes (Wall et al. 2010) and seamounts (Bell and Butcher 2002; see Chapter 2). A range of volcanic edifices underlain by dykes are also recognised (e.g. Jackson 2012; Zhao et al. 2014), the genesis of which is unclear.

However, the location and structure of volcanoes can be concealed due to poor seismic imaging within and beneath layers of basaltic lava (e.g. Jerram 2002). Poor imaging is the result of the scattering and attenuation of seismic waves (see Chapter 2) and velocity contrasts between the edifice (composed of volcanoclastic rock and lavas) and the surrounding lava flows. As a result, few of the monogenetic edifices recognised in field data are also documented in seismic data. This is particularly true of edifices formed during submarine eruptions. Bathymetric data can be used to study the morphology of these features, but their internal architecture is not commonly exposed. Examples of dissected polygenetic submarine volcanoes exist (e.g. Schmidt and Schminke 2000), but these do not highlight the complexity of monogenetic eruptions commonly observed in subaerial examples (e.g. Valentine and Gregg 2008). Furthermore, observations of contemporary submarine eruptions are often limited to the emergent stages of activity (e.g. Thorarinsson 1966; Fiske et al. 1998; Baker et al. 2002; Németh et al. 2006), inhibiting our understanding of the early depositional mechanisms.

5.1.1 Aims

The aim of this study is to detail the seismic characteristics, morphology and plumbing system of submarine monogenetic volcanoes, offshore Australia. These edifices are free from overlying basalt lava cover and are also relatively young, making them ideal candidates to study. Through comparison with field analogues, I demonstrate that the volcanoes were constructed via a combination of explosive and effusive activity; evolving through initial maar-forming to later tuff cone-building stages. Transitions in eruptive style are thought to have been controlled by the site of magma fragmentation, intrinsic magma properties and decreasing hydrostatic pressure as the edifices grew towards the sea surface. This study can be used to understand the processes by which submarine edifices are constructed. Furthermore, it can help recognise volcanoes in other regions affected by basaltic volcanism, and differentiate them from similar hydrothermal vents. These hydrothermal vents are the result of phreatic eruptions (e.g. Jamtveit et al. 2004) and are dominantly composed of sediment (see Chapter 2). This study also has useful implications for understanding the feeder system underlying the edifices, and associated impacts on underlying hydrocarbon systems.

5.2 Geological setting

The southeastern Australian margin is associated with the Southern Rift System separating Australia from Antarctica. Opening of the rift was associated with onshore and offshore volcanism (Johnson 1989; Price et al. 2003; Sutherland 2003), much of which was monogenetic (Johnson 1989; Otterloo et al. 2013). The Bass Basin (Fig. 5.1) represents a failed intra-cratonic rift basin that formed along the margin (Blevin 2003). The basin consists of a series of Cretaceous northwest-southeast trending half-grabens (Cas et al. 1993) and contains a transgressive sequence of Cretaceous, Paleocene and Eocene siltstones, shales and sandstones, overlain by the Oligocene–Quaternary aged Torquay Group limestone. Numerous petroleum exploration wells have been drilled, targeting the late Cretaceous to early Miocene Eastern View Coal Measures (EVCN).

In addition to rift-related sediments, the basin also contains Cretaceous–Miocene aged lava flows, edifices and sills. Onshore Eocene–Miocene lava flows are tholeiitic to alkali basalts (e.g. Sutherland and Wellman 1986; Vogel and Keays 1997). The earliest evidence

of volcanism is Cretaceous volcanoclastic sandstones, although the source of these is unclear. Subsequent Mid-Cretaceous volcanism produced a series of edifices, flows and sills (Trigg et al. 2003; Cummings and Blevin 2003; Holford et al. 2007). Volcanism associated with syn- and post-rift activity peaked in the Paleocene and Oligocene-Miocene, (Cummings and Blevin 2003). This activity was widespread through the central and north-east Bass basin (Cummings and Blevin 2003) and emplaced lavas, sills, dykes and volcanoes (Faustmann 1995). These features are commonly associated with rift faults and structural accommodation zones (Trigg et al. 2003; Cummings and Blevin 2003).

The subject of this study is a series of Late Cretaceous lava flows and Miocene-aged sills and edifices, located within the EVCM and Torquay limestone sequence respectively. The edifices are overlapped by neritic claystones and are inferred to have been emplaced in water depths of 90–140 m, as indicated by biostratigraphic data (Geoscience Australia 2010; Holford and Schofield in review). Previous workers have suggested the edifices represent pyroclastic edifices, analogous to onshore volcanoes in the Otway Basin (Faustmann 1995; Holford et al. 2012). However, these studies have not provided a detailed assessment of the edifices' architecture, nor have they investigated the mechanisms by which they were constructed.

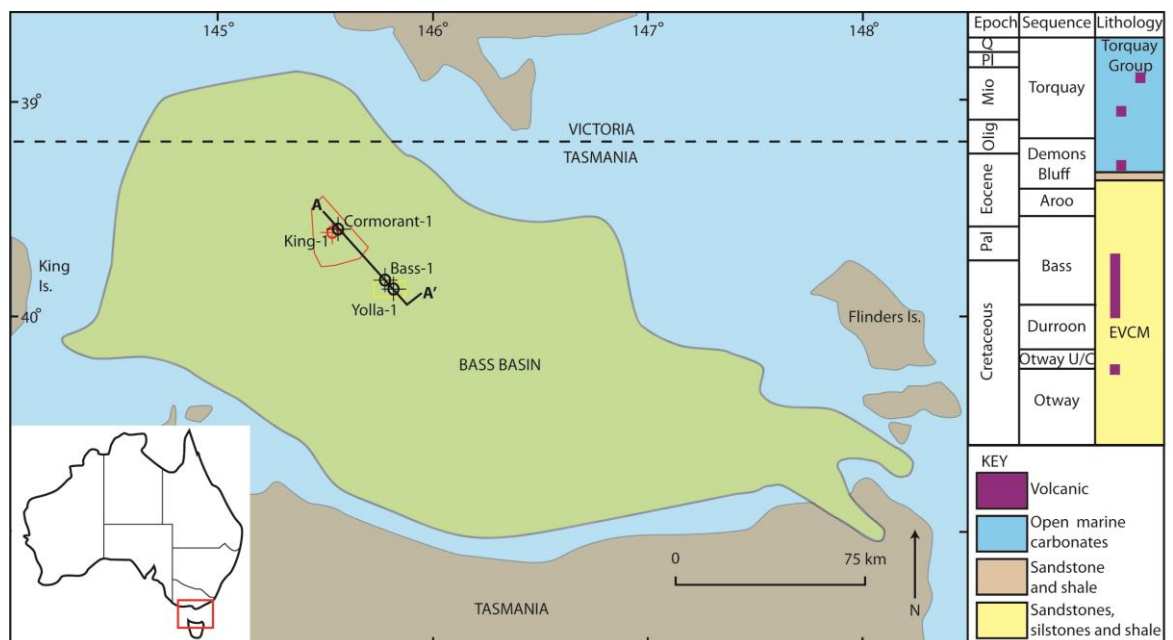


Figure 5.1. Location of the study area. The Bass Basin is shown in green, the red outline delimits the Labatt survey and the yellow delimits Yolla survey. Bass-1, King-1, Yolla-1 and Cormorant-1 wells are also shown. A 2D seismic line (A–A'; Fig. 5.2)

between the surveys is shown. A simplified stratigraphy of the Bass Basin is also shown. Modified from Boral Energy Resources Ltd. (1998).

5.3 Dataset and methodology

5.3.1 Seismic and well data

This study utilises 3D seismic data from the Yolla and Labatt surveys which were acquired in 1994 and 2008 respectively. The 525 km² Labatt survey has a bin size of 25 × 12.5 m (Tap Oil Ltd. 2008). The Yolla survey is smaller, covering 260 km² with a 12.5 × 25 m bin size (Boral Energy Resources Ltd. 1998). A 2D seismic line between these surveys shows the Bass-1, Yolla-1 and Cormorant-1 wells (section A–A', Figs. 5.1 and 5.2). The Bass-1 well was drilled to test the hydrocarbon potential of a Miocene “reef complex” at a depth of 790 m (Esso Exploration Australia Inc. 1965). This reef complex was proven to be a volcano, as the well intersected a 185 m thick sequence of volcanic rocks (Figs. 5.2 and 5.3). Core data recovered buff and light grey brown, finely grained and vesicular rocks with abundant zeolites (Esso Exploration Australia Inc. 1965). 80 m of gabbro was found deeper in the well at 2584 m, and 320 m of basalt was found at 3031 m (Figs. 5.2 and 5.3). These intervals were interpreted as intrusions and lava flows (Wheeler and Kjellgren 1986). The Yolla-1 well intersected volcanic rock at a depth of 1237 m (Figs. 5.2 and 5.3). This 68 m-thick sequence was interpreted to represent highly altered pyroclastics (Wheeler and Kjellgren 1986). Intrusions were also found in the Cormorant-1 well, which intersected 130 m of weathered volcanic rocks at a depth of 2470 m (Esso Exploration Australia Inc. 1970). All volcanic intervals produced decreases in Gamma Ray and increases in Sonic wireline data (Fig. 5.3). King-1 did not intersect any volcanic rock.

Petrophysical data from the Yolla-1 and Cormorant-1 wells has been used to constrain seismic events. The Miocene Top Volcanic (TV) and Base Volcanic (BV) were identified at 0.70 and 0.82 s Two-Way-Travel-Time (TWTT) in the Labatt data, and 1.01 and 1.15 s in the Yolla data respectively. The Oligocene (OH) and Eocene-aged Demons Bluff (DB) horizons were defined from the Yolla-1 well (Boral Energy Resources Ltd. 1998). The Lower Mid Miocene (LMM), Base Volcanic (BV) and Cretaceous Eastern View Coal

Measures (EVCN), Top Aroo (TR) and Base Aroo (BA) horizons were defined from the Cormorant-1 well (Tap Oil Ltd. 2010). High amplitude reflections in the Labatt survey were identified at depths of 1.5 s; these reflections represent lava flows and define the Cretaceous-aged Lower Volcanic (LV) horizon. The TV and BV horizons were picked in the Labatt (Figs. 5.4 and 5.5) and Yolla surveys (Figs. 5.6 and 5.7) to allow further investigation of the edifices.

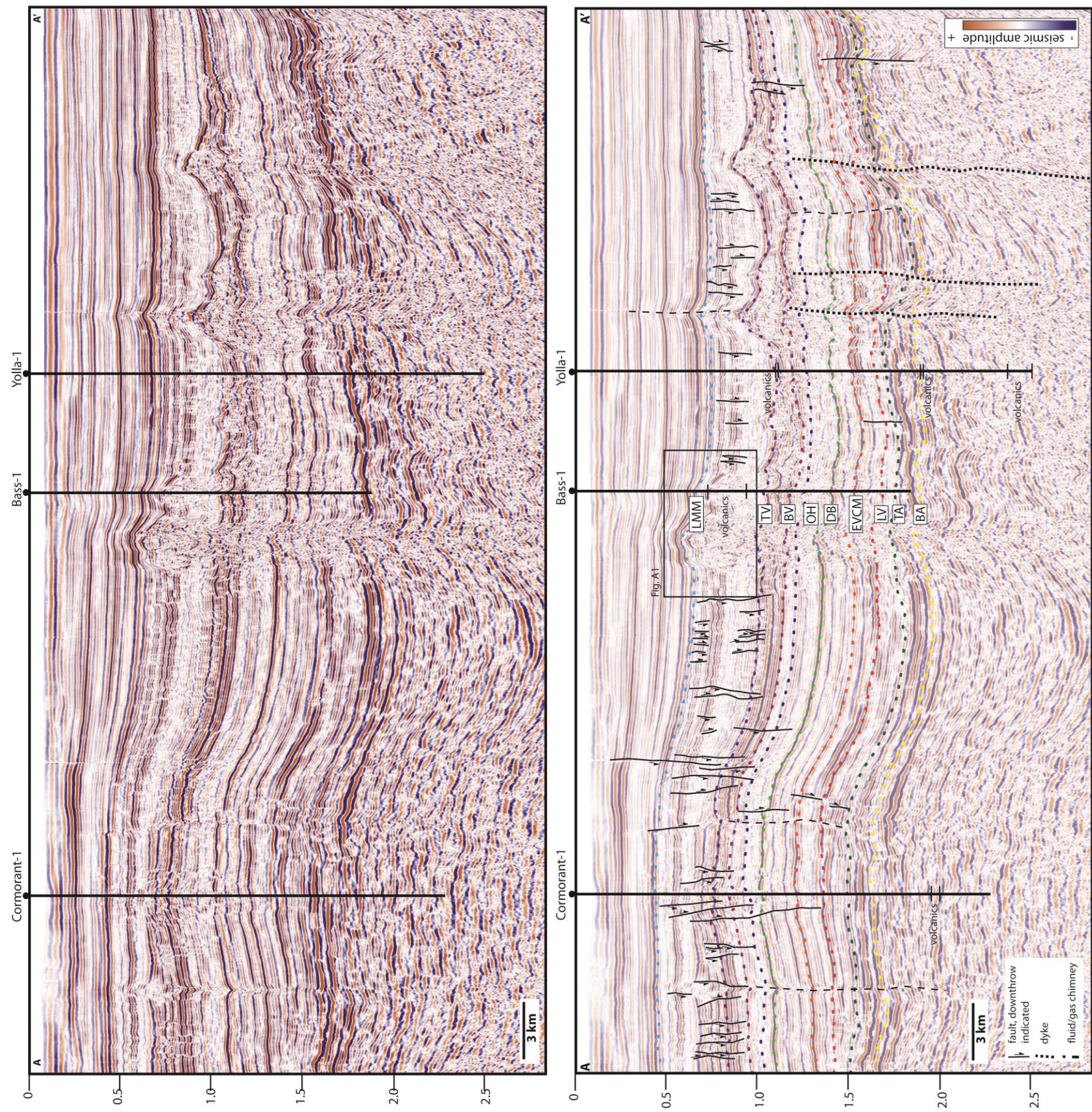


Figure 5.2. Seismic line A–A' and interpretation intersecting the Cormorant-1, Bass-1 and Yolla-1 wells. Correlated horizons are also shown.

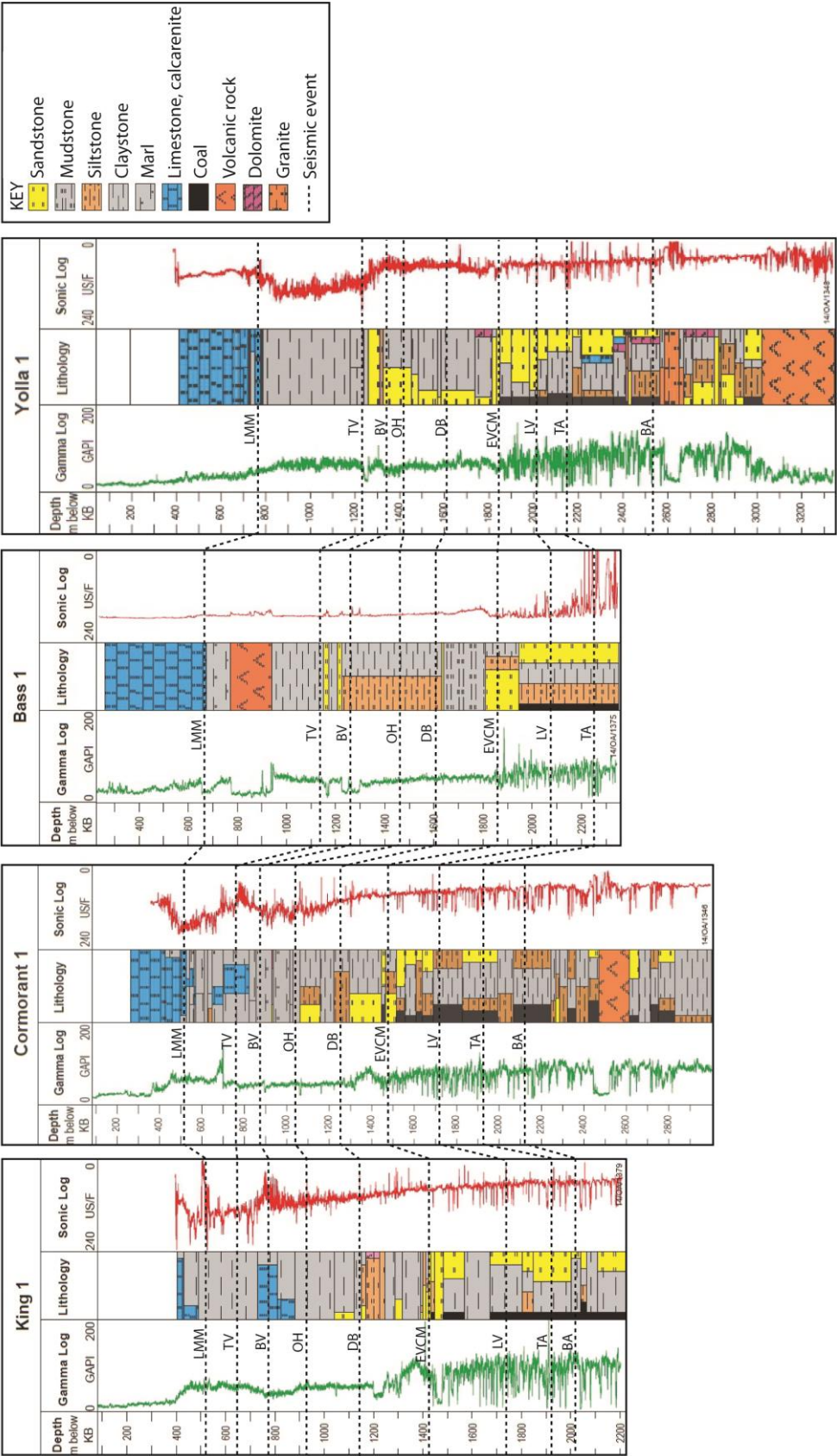


Figure 5.3. Well logs for King-1, Cormorant-1, Bass-1 and Yolla-1. Seismic horizons are also shown: LMM=Lower Mid Miocene, TV=Top Volcanic, BV=Base Volcanic, OH=Oligocene, Demons Bluff=DB, EVCM=Eastern View Coal Measures, LV=Lower Volcanic, TA=Top Aroo and BA=Base Aroo. Adapted from Trigg et al. (2003).

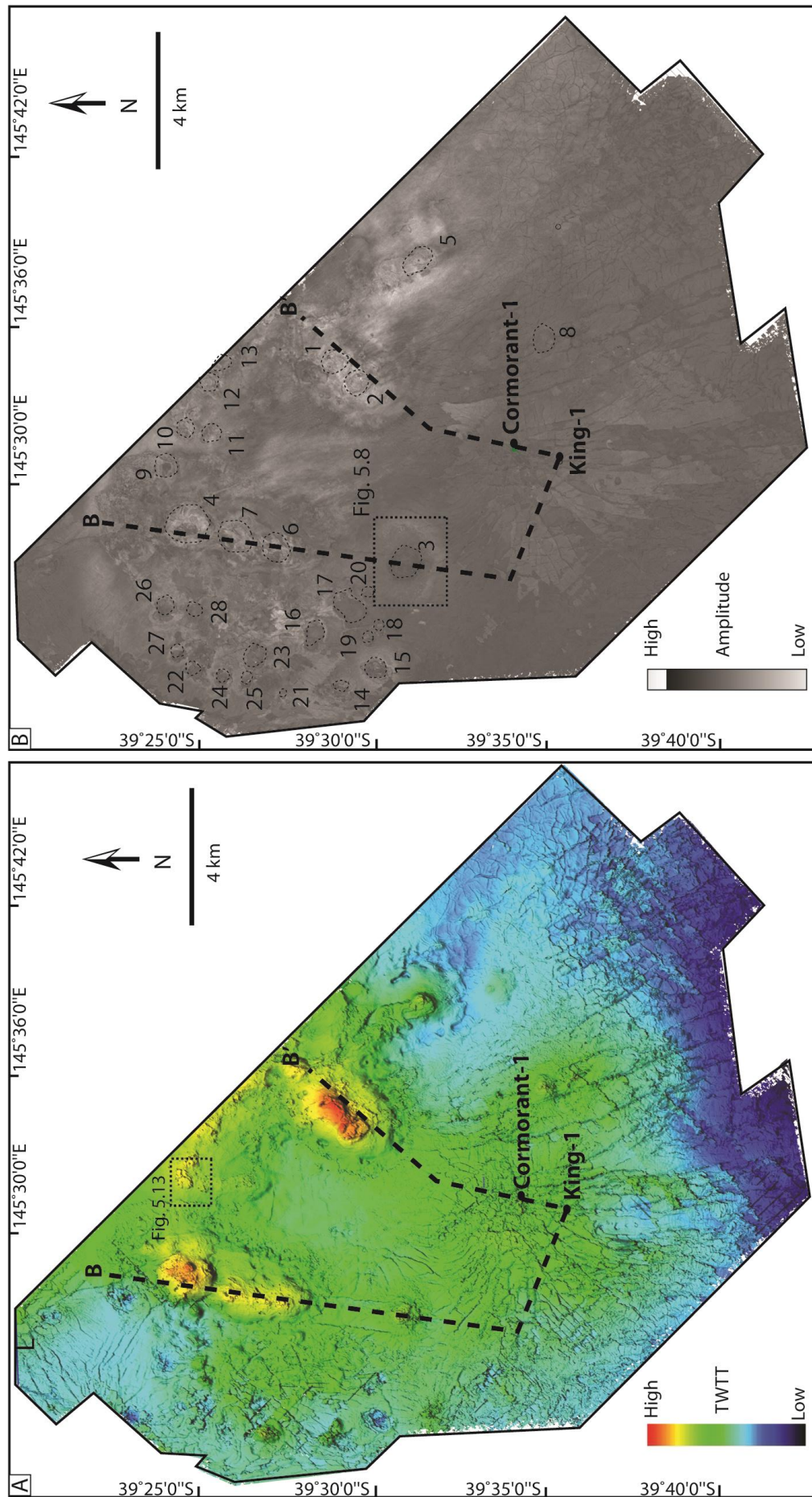


Figure 5.4. Time (A) and amplitude (B) maps of the TV horizon in the Labatt survey. The edifices (dashed outline) are numbered in B. See Fig. 5.5 for cross section.

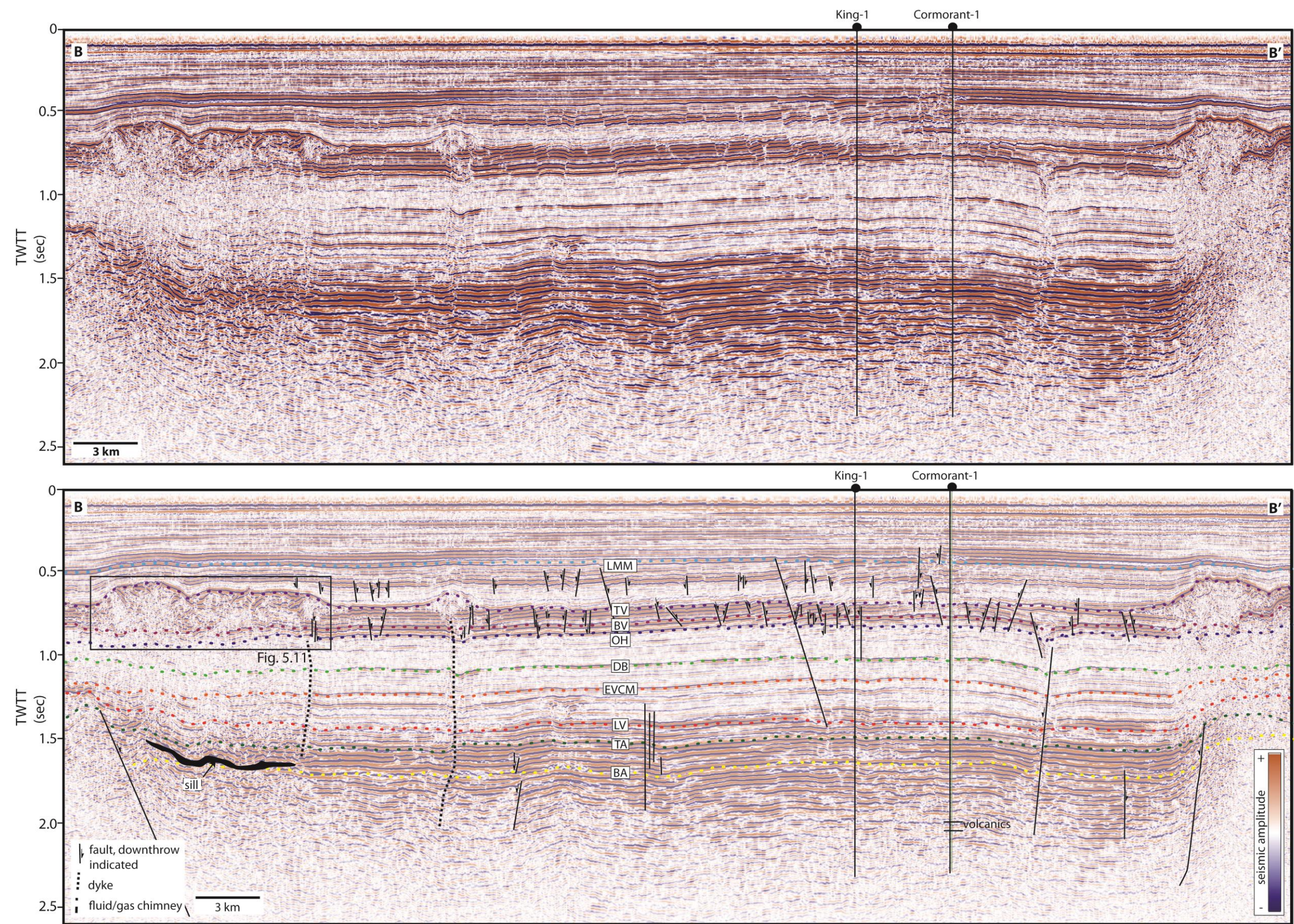


Figure 5.5. Seismic line B–B’ and interpretation in the Labatt survey. See Fig. 5.4 for location.

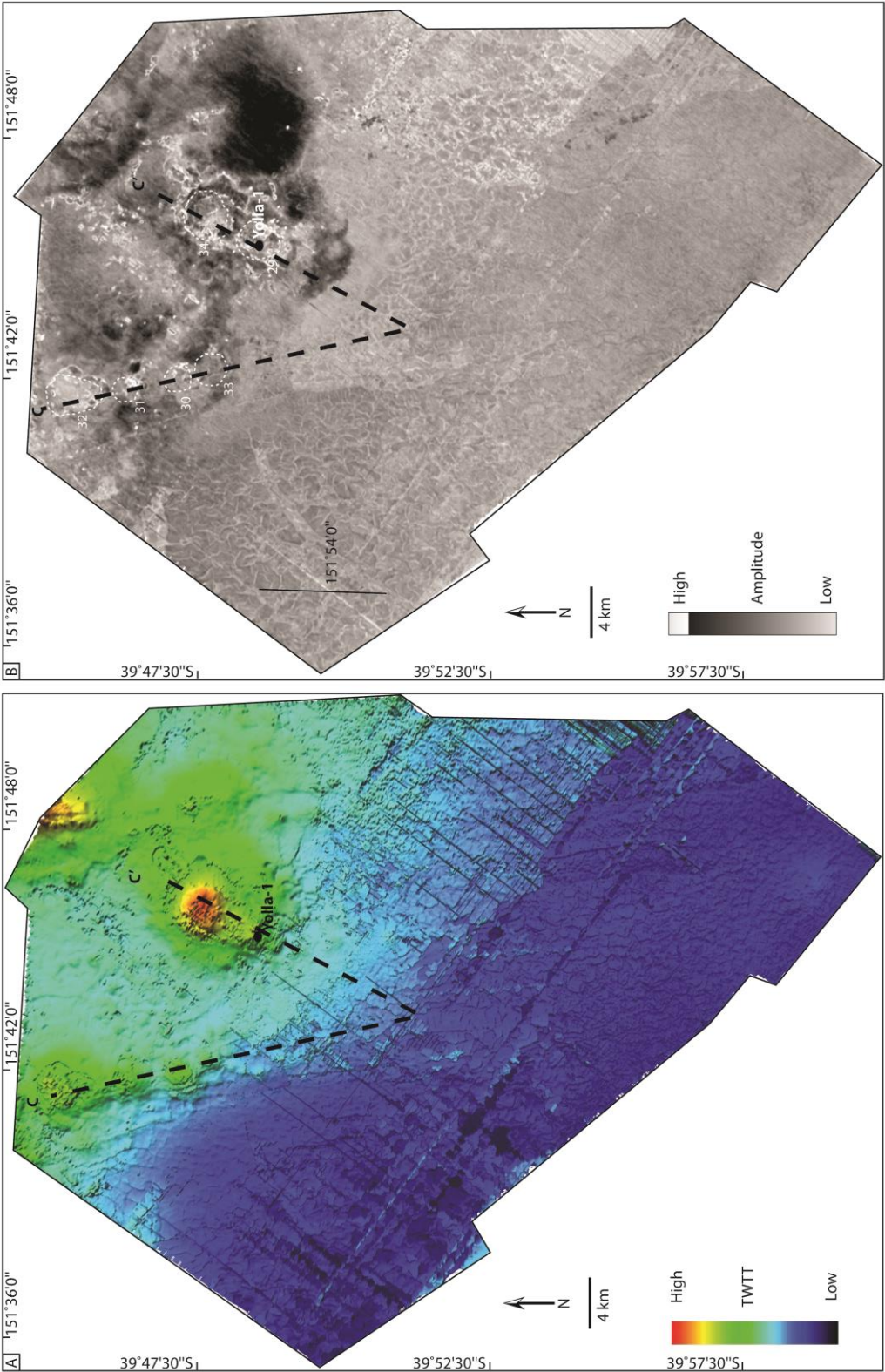


Figure 5.6. Time (A) and amplitude (B) maps of the TV horizon in the Yolla survey. The edifices (dashed outline) are numbered in B. See Fig. 5.7 for cross section.

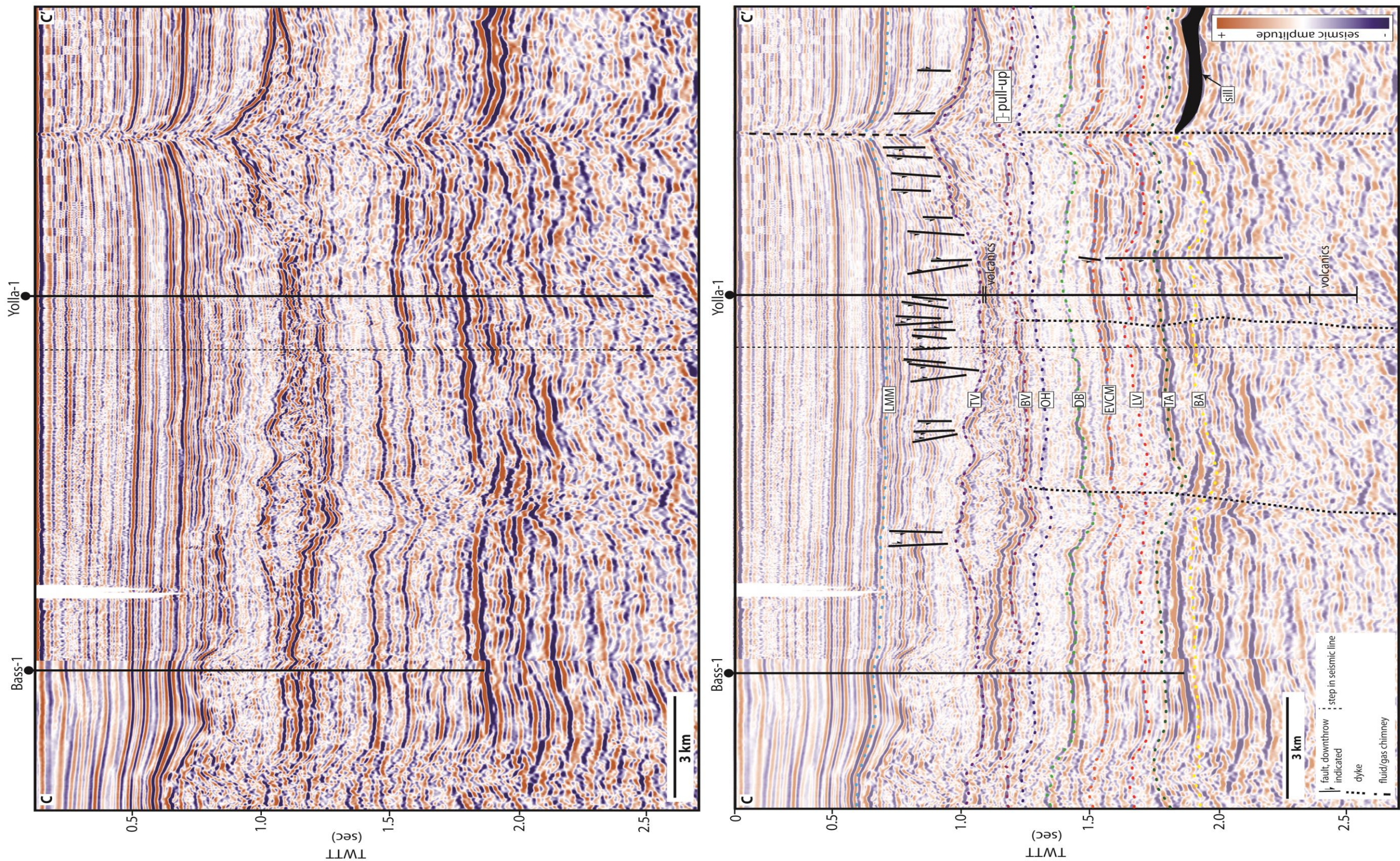


Figure 5.7. Seismic line C-C' and interpretation in the Yolla survey. See Fig. 5.6 for location.

5.3.2 Composition of the edifices

Time extractions of the TV surface define 34 edifices that are either cone-shaped topographic highs (positive TWTT anomalies) or pit craters (negative TWTT anomalies; Figs. 5.4 and 5.6). The Yolla-1 and Bass-1 wells indicate that the cone-shaped edifices are composed of volcanic rock. The edifices also have seismic characteristics typical of volcanic lithologies; they have high amplitude top reflections and reduce the quality of imaging beneath them (Figs. 5.4 and 5.6; see Planke et al. 2000; Jerram 2002; Bell and Butcher 2002; Wright et al. 2012; Schofield and Jolley 2013). Pull-ups beneath the edifices are typical of volcanic rocks within a sedimentary sequence (Jackson 2012; Magee et al. 2013). Many of the cone-shaped edifices and pit craters are underlain by sills, further suggesting a volcanic origin. Edifices beneath which the sills are not visible are inferred to be underlain by sills below the resolution of the data. These edifices were emplaced in a shallow marine environment, as indicated by the transgressive sequence within which the edifices are found, and by biostratigraphic data (see section 5.2).

5.3.3 Calculating edifice dimensions

Cone-shaped edifices are sub-circular to elongate in shape and often overlap in linear clusters. The pit craters are sub-circular in plan view. The diameters of the cone-shaped edifices were determined from amplitude maps and cross sections by the change in the seismic expression of the cone (Fig. 5.8), interpreted to represent a lateral transition from the cone to surrounding basin deposits. Variations in amplitude were used to measure the diameter of the pit craters.

The internal velocity of the edifices was calculated either from the thickness of pull ups beneath the edifice (see Magee et al. 2013) or from the Yolla-1 well data in cases where pull ups were absent. (Boral Energy Resources Ltd. 1998). Using this method, I calculate that the internal velocity of the edifices ranges between 2090–4025 m s⁻¹. This range is lower than that of lava flows (commonly 3300–6800 m s⁻¹; see Planke and Eldholm 1994; Berndt et al. 2000; Calvès et al. 2011; Magee et al. 2013), suggesting that the volcanic material is dominantly fragmental (e.g. pyroclasts and hyaloclastite), consistent with core descriptions. The velocities were used to calculate the heights of the edifices.

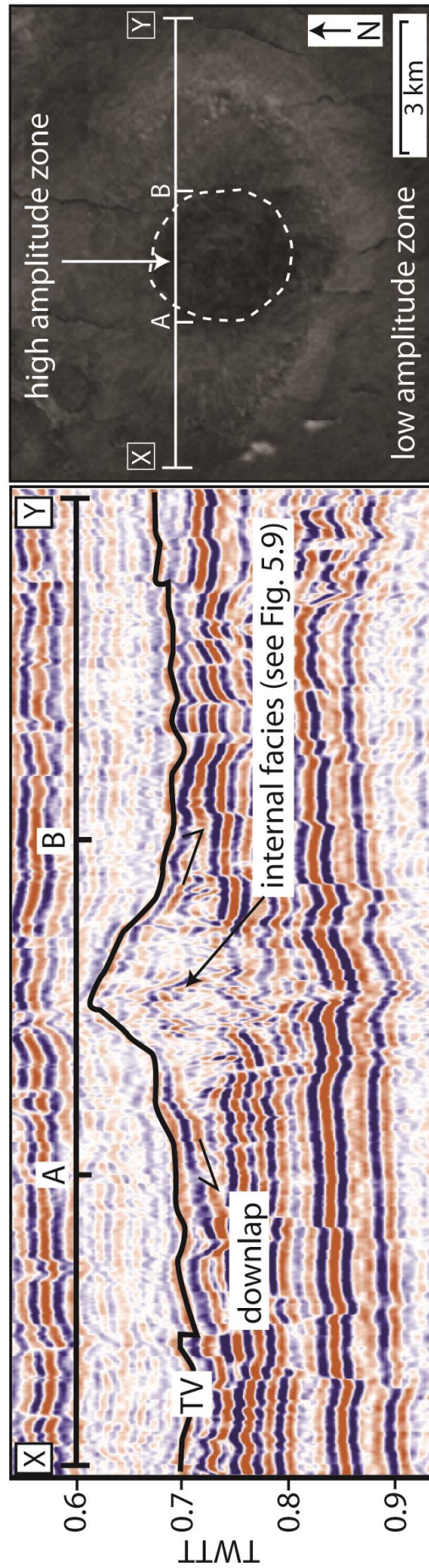


Figure 5.8. Seismic line X–Y showing that the basal diameter of the edifices (A–B) is calculated from the change in seismic facies and amplitude of the edifice. See Fig. 5.4 for location.

5.3.4 Seismic facies analysis

Four seismic facies have been recognised within the edifices based on the geometry, amplitude and continuity of the internal reflections (Table 5.1). Seismic facies indicate variation in the structure and composition of the volcanic succession (e.g. Planke et al. 2000; Calvès et al. 2011; Wright et al. 2012; Watton et al. 2013b). The reflections within the edifices lap out and are not truncated.

The hummocky facies (***Hu***) forms wedge-shaped bodies and only occurs within the flanks of cone-shaped edifices. The reflections are moderate to low amplitude and vary from semi-continuous to continuous. They grade outwards from the chaotic conduit zone of the edifices and prograde laterally, downlapping underlying facies. They are overlain by ***PHA*** facies (see below). ***Hu***-type facies are reported in other seismic datasets from volcanic margins, and represent fragmental igneous material (e.g. Planke et al. 2000; Thomson 2005; Jerram et al. 2009; Wright et al. 2012). I infer a similar origin for the ***Hu*** facies in this study, and suggest that the facies represents low velocity, fragmental igneous rocks such as hyaloclastite and/or pyroclasts; commonly produced during shallow submarine eruptions (e.g. Kokelaar 1986; Cas et al. 1989; Sohn 1995; White 2001; Suiting and Schmincke 2009; Watton et al. 2013b).

Planar, moderate amplitude facies (***PMA***) are composed of moderate amplitude, continuous and parallel reflections in a sub-horizontal or inclined orientation. They are found within all parts of the stratigraphy and commonly onlap the cone-shaped edifices. The facies has distinct contacts with overlying and underlying facies, but can inter-finger with ***Hu***. This facies is interpreted to represent non-volcanic lithologies, since they are found throughout the stratigraphy. However, within the edifices they may also represent volcanoclastic material with a lower velocity than coherent rocks, resulting in moderate amplitude reflections (e.g. Planke et al. 2000). The sub-parallel reflections represent sub-parallel interfaces between lithologies (e.g. Bacon et al. 2007) indicating that the component sediments are bedded.

The planar high amplitude facies (***PHA***) is composed of high amplitude, continuous reflections in a sub-horizontal or inclined orientation. They form the TV and BV horizon, as well as sills and the Late Cretaceous lava flows. The tops of cone-shaped edifices composed of this facies may appear segmented. This facies is typically thin and forms distinct contacts between over and underlying facies, although it can grade laterally into the ***PMA*** and ***Ch*** facies. They are overlain by ***PMA*** facies. Edifices with high amplitude, continuous reflections of ***PHA*** facies are interpreted as high velocity, dominantly coherent subaerial and/or submarine lava flows and hyaloclastite (e.g. Planke et al. 2000; Jerram et al. 2009;

Wright 2013). The sheet-like nature of the reflections suggests the flows form sub-planar units that maintain a near-constant thickness (e.g. Planke et al. 2000). Their sheet-like morphology may result from higher effusion rates relative to the hummocky facies (e.g. Gregg and Fink 1995; Self et al. 2000; Batiza and White 2000). **PHA** facies has a higher amplitude than **Hu** because **PHA** facies is overlain by **PMA**, whilst **Hu** is overlain by **PHA**. Therefore, the velocity contrast is greater for **PHA**. The presence of **PHA** or **PMA** facies on the tops of the edifices is interpreted to result from the variable grain size and vesicularity of hyaloclastite (e.g. Watton et al. 2013a; Watton et al. 2013b), both of which affect the velocity and hence seismic amplitude of the facies.

Chaotic facies (**Ch**) are low amplitude; discontinuous reflections found beneath and within cone-shaped edifices. The facies forms plug-like bodies and grades laterally into **Hu**. **Ch** facies represents the central region of the edifices that is poorly imaged. Poor imaging may result from the high impedance contrast of the uppermost **PHA** facies (e.g. Jerram 2002; Maresh et al. 2006). This central region may also contain numerous dykes intruded into the edifice (e.g. Moore 1985), creating high velocity contrasts between fragmental and coherent igneous material.

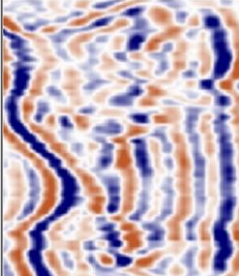
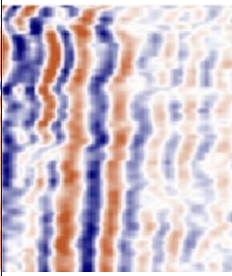
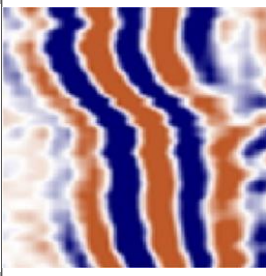
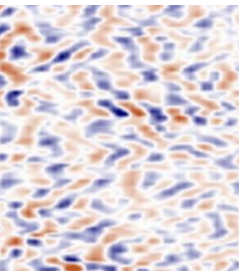
Seismic facies	Seismic reflections	Characteristics	Interpretation
Hummocky (Hu)		Moderate – low amplitude, semi-continuous – continuous reflectors. Form prograding, wedge-like bodies. Oriented sub-horizontally and may dip up to $\sim 18^\circ$. Found in the flanks of cratered and flat topped vents, also within isolated vents between the TV and BV horizons. Gradational into chaotic facies.	Low velocity, fragmental volcanic rock such as hyaloclastite and pyroclasts.
Planar, Moderate Amplitude (PMA)		Moderate – low amplitude, semi-continuous – continuous reflectors. Form sheet – like, sub-parallel units beneath the TV and BV, and occasionally forms the TV itself. Oriented sub-horizontally and may dip up to $\sim 11^\circ$. Found within isolated vents and pit craters.	Siliciclastic sediments and volcanoclastic sediments with a limited component of volcanic rock.
Planar, High Amplitude (PHA)		High amplitude, continuous reflectors with sheet-like geometries. May be segmented in the TV, and lap out and diverge. Found in cratered and flat topped vents; may form bowl-shaped reflectors that are offset at their tips and define the crater. Oriented sub-horizontally and may dip up to $\sim 18^\circ$. Commonly form the TV, BV and sills.	Dominantly coherent, sheet-like subaerial and/or submarine lava flows and associated hyaloclastite.
Chaotic (Ch)		Moderate – low amplitude, discontinuous reflectors that form plug-like bodies in vent conduits. Found beneath the TV and BV horizons within all vent types. Gradational into hummocky facies.	Poorly imaged conduit region of the edifices composed of coherent and fragmental volcanic rock.

Table 5.1. Summary characteristics and interpretation of seismic facies.

5.4 Edifice characteristics

5.4.1 Pit craters

Pit craters (n=15) are negative TWTT anomalies in the TV surface (Fig. 5.4). In cross section the pit craters are funnel-shaped, with conduits that truncate underlying **PHA** reflections. The conduits contain **PMA** reflections that onlap the conduit margin. Concentric, arcuate normal faults surround the conduit (Fig. 5.9A). The pit craters may be overlain by pointed edifices (Fig. 5.9B). The sub-circular craters of these vents range from 341–1166 m in diameter and the conduits extend 0.05–0.11 km into the subsurface (Table A3.1). Pit craters have a clustered distribution (Fig. 5.4) and are only found in the Labatt survey.

5.4.2 Cone-shaped edifices

The cone-shaped edifices can be categorised into 3 distinct types according to their profile and internal seismic characteristics: 1) cratered (n=5); 2) flat topped (n=7) and 3) pointed edifices (n=7; Fig. 5.9; Table 5.2). The flanks of these edifices dip outwards 5–18° (Table A3.1). All of the cone shaped edifices have flat lying, concordant basal surfaces. Cone-shaped edifices are also observed on the 2D seismic section between the Yolla and Labatt surveys (see Appendix C).

5.4.2.1 Pointed edifices

Pointed edifices (Fig. 5.9B) have a conical morphology and are identified by an upper unit of **PMA** or **PHA** facies that overlies internal **Ch** facies. These reflections grade laterally into **Hu** facies. The edifices are roughly symmetrical in plan view. Time slices beneath edifice 3 (Fig. 5.10) at 0.82 s TWT and 0.9 s TWT show concentric faulting and an upward flaring central conduit; identical to pits crater in cross-section (Fig. 5.9A). The pointed edifices also have a distinctive onion ring structure (Fig. 5.10). These edifices have a height/basal diameter ratio of 0.04–0.15 (heights 0.13–0.16 km, diameters 1.67–3.03 km; see Table A3.1). They have volumes of 0.4–1.1 km³. They are found in both surveys.

5.4.2.2 Flat-topped edifices

Flat-topped edifices (Fig. 5.9C) have a sub-horizontal, upper **PHA** facies gives the vents their characteristic flat top. Internally, **Hu** and **PMA** reflections emanate from a source within the BV and grade outwards from an internal plug-like **Ch** zone. Time slices of the edifices reveal an onion ring structure beneath the TV horizon. **PMA** reflections within the edifice onlap onto a central unconformity surface beneath the TV. These reflections become

fainter and more chaotic with depth. Imaging beneath the BV horizon is poor. These edifices have a height/basal diameter ratio of 0.06–0.16 (heights 0.12–0.52 km, diameters of 1.08–3.98 km; see Table 5.2). They range in volume from 1–1.4 km³. They are only found in the Labatt survey.

5.4.2.3 Cratered edifices

Cratered edifices (Fig. 5.9D) are characterised by an upper bowl shaped **PHA** reflector that defines a ~30 m deep crater in the centre of the edifice. Internally, their facies are similar to the flat-topped edifices. They have an onion ring structure and are often asymmetric with steeper slopes on their eastern flank. They have height/basal diameter ratios of 0.04–0.09, with heights of 0.20–0.31 km and diameters of 3.41–4.85 km (Table 5.2). They range in volume from 0.07–1.36 km³. Their craters are 380–950 m diameter. These edifices are found in both surveys.

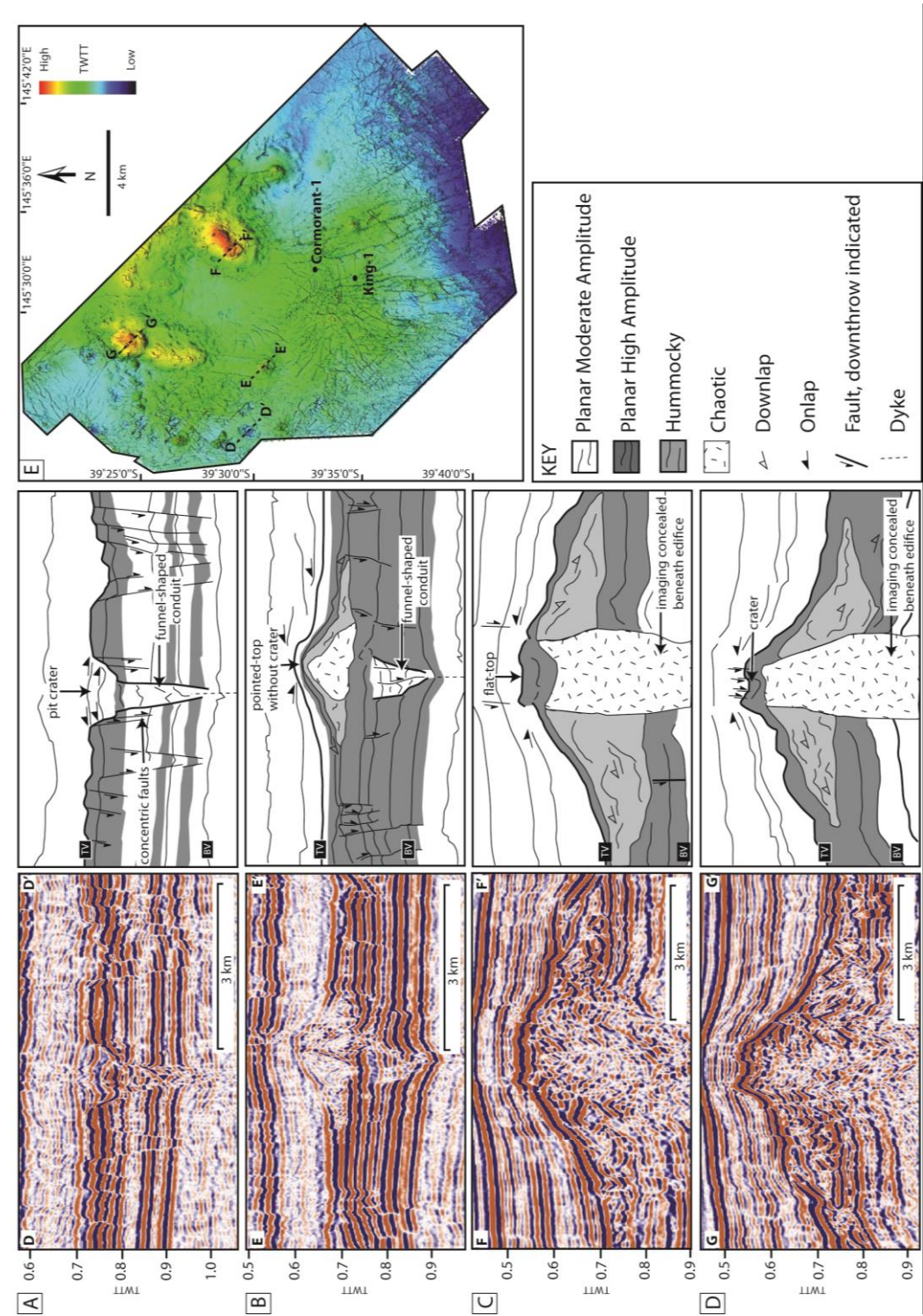


Figure 5.9. Seismic sections showing the seismic facies of the pit craters (A), pointed (B), flat-topped (C) and cratered (D) edifices. The location of the sections is shown in the time map of the Labatt survey (E).

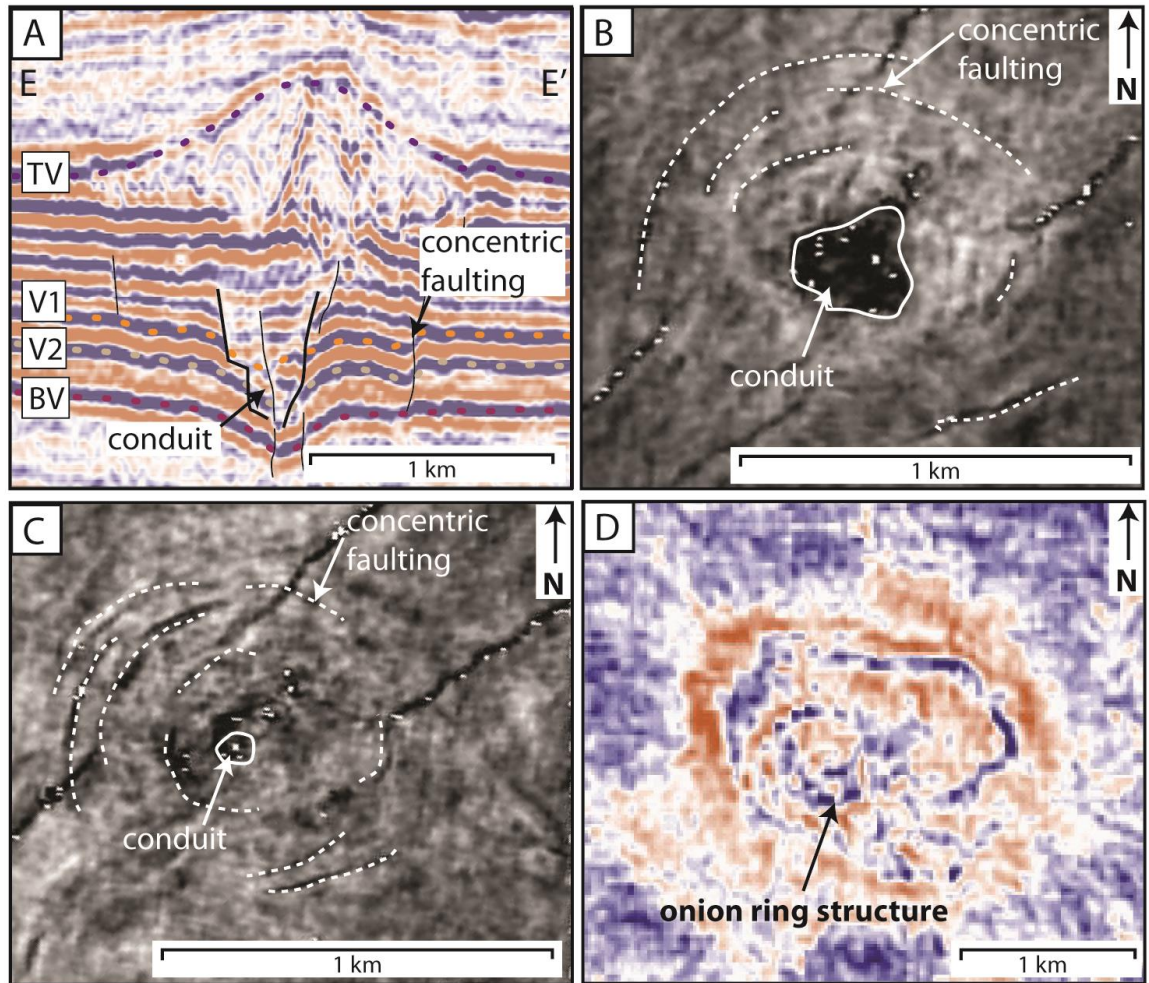


Figure 5.10. Features associated with the pointed edifices. Seismic line (A). Horizons V1 and V2 are shown in B and C respectively. See Fig. 5.9 for location. (B) Concentric faulting (dashed lines) in horizon V1 around the underlying conduit. (C) Concentric faulting (dashed lines) in horizon V2 around the underlying conduit. (D) Time slice at 0.63 s TWTT beneath the edifice showing an onion-ring structure.

5.4.3 Edifice distribution

The edifices occur in linear clusters, as isolated edifices, and in apparently randomly distributed clusters (Figs. 5.4 and 5.6). Linear and randomly distributed clusters overlap, whilst isolated edifices do not. Isolated edifices include structures 3, 5 and 8, which are pointed and flat topped in morphology (Fig. 5.4). Clustered edifices include all pit craters (14–28) and the flat topped edifices 10–13. Linear clusters include cratered, pointed and flat topped edifices that are spaced ~800–3000 m apart. The linear clusters of edifices may contain up to four individual edifices, which onlap in a northerly direction and decrease in volume towards the south (Fig. 5.11). The onlap relationship suggests the edifices young

north-south. Linear cluster 1 includes edifices 1 and 2, linear cluster 2 includes edifices 2, 7 and 6 and linear cluster 3 includes edifices 30–33.

There is a spatial relationship between the edifices, underlying sills and lava flows. Saucer-shaped and smooth layer-parallel sills (e.g. Planke et al. 2005) occur at depths of 495–1207 m beneath the BV. The lateral tips of these sills are linked to the centre of the overlying edifices (Fig. 5.12). In the north of the Labatt survey, lavas in the LV horizon were effused from a north-south trending linear source (Fig. 5.13). Spectral decomposition (using frequencies Red:17 Hz; Green: 24 Hz; Blue:60 Hz) clearly images these flows (Fig. 13). Edifices 4–7 in linear cluster 1 directly overly the lava flows (Fig. 5.4; Appendix C) and also have a north-south strike. No relationship is recognised between basement highs and the edifices.

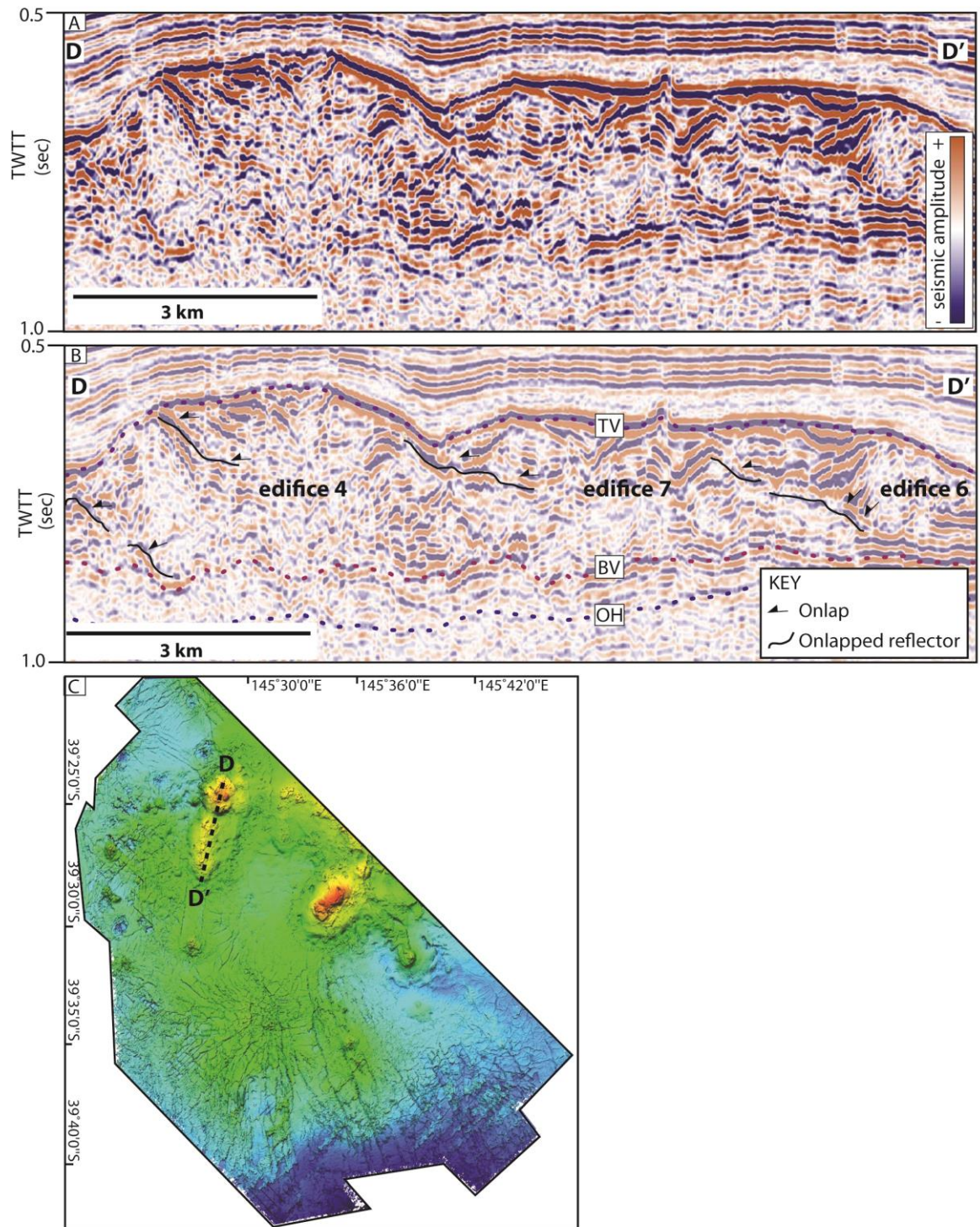


Figure 5.11. Seismic line (A) and interpretation (B) showing that the edifices in linear clusters young towards the south.

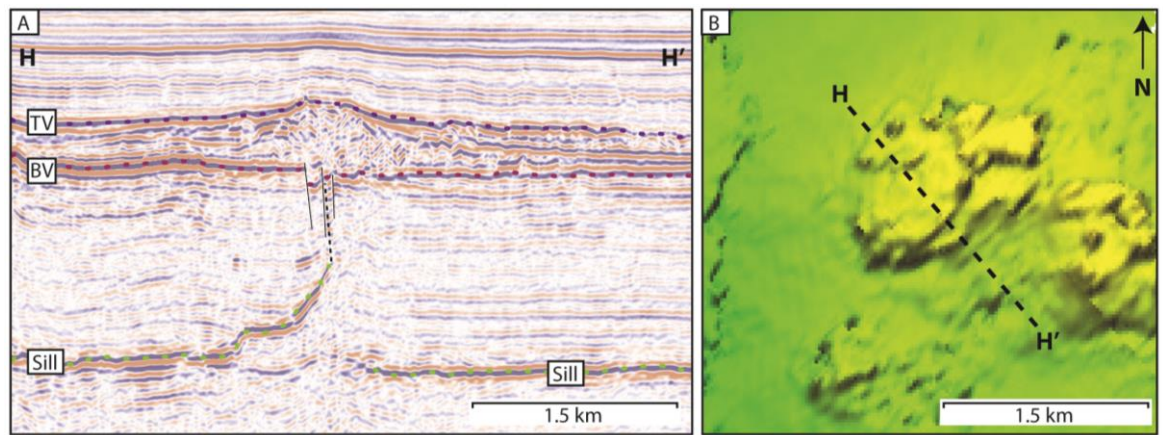


Figure 5.12. Seismic section (A) and time map (B) of a flat-topped edifice fed by a sill/dyke system. See Fig. 5.4 for location.

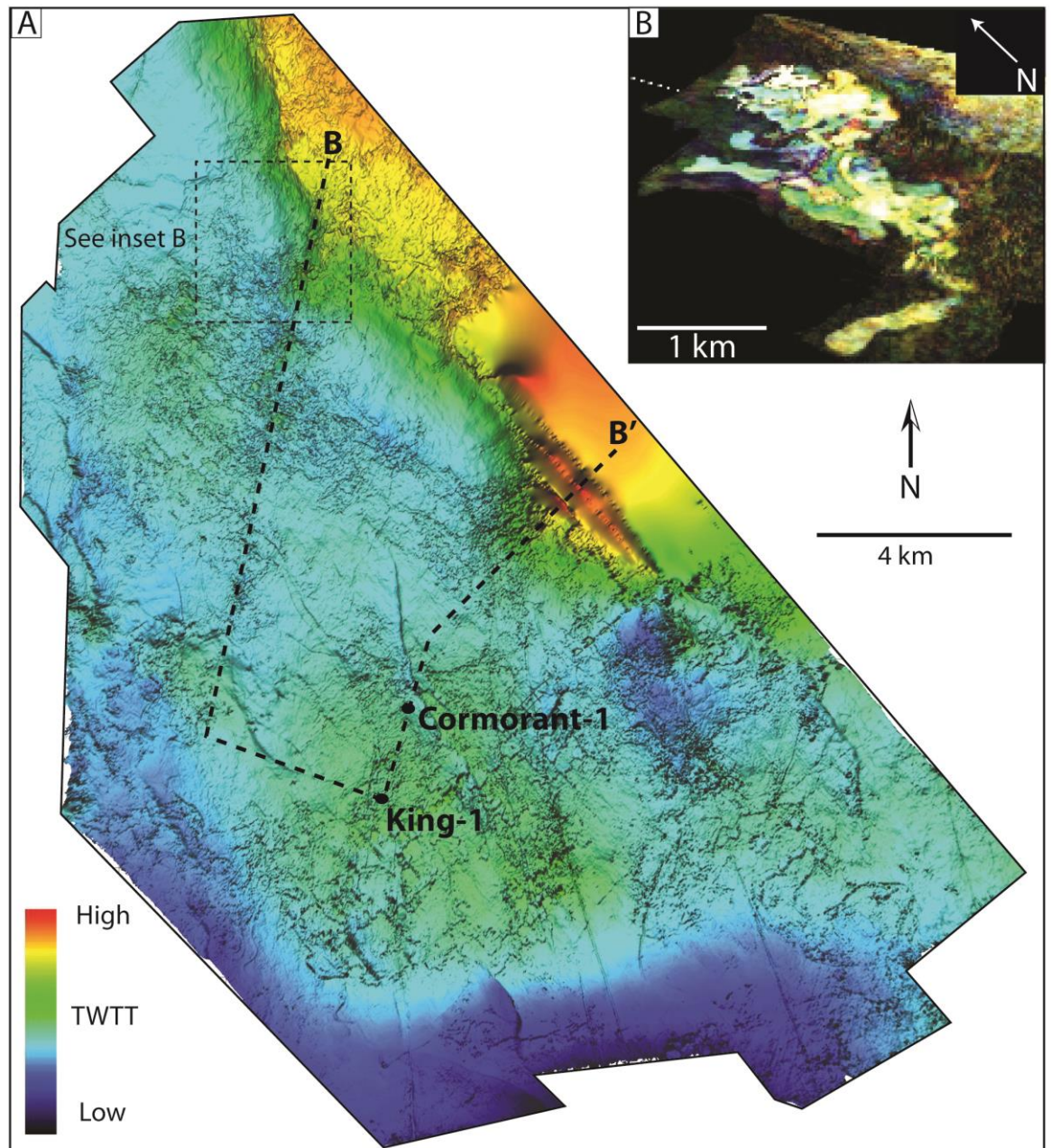


Figure 5.13. Amplitude map of the LV horizon. Inset B shows a RGB decomposition image of the lava flows.

5.5 Discussion

The edifices are interpreted as monogenetic volcanoes due to their low volumes (commonly $<1 \text{ km}^3$; Table 5.2); typical of these edifices (Walker 1993; Connor and Conway 2000; White and Ross 2011). The formation of the volcanoes is discussed below.

5.5.1 Physical volcanology of the edifices

The pit crater volcanoes are interpreted as maars; these are explosion craters in the country rock with diameters of 0.2–3 km (e.g. Urrutia-Fucugauchi and Uribe-Cifuentes 1999; Roger et al. 2000; Pirrung et al. 2003; Haller et al. 2006; Gençalioglu-Kuşcu et al. 2007; Kwon and Sohn 2008; White and Ross 2011; Ross et al. 2011; Suiting and Schmincke 2012). Maars also commonly overlap (White and McClintock 2001; Németh and White 2003; McClintock and White 2006; White and Ross 2011), as do the pit crater volcanoes in this study. The ejecta rings that surround maars are commonly <30 m in height (White and Ross 2011) and are not recognised; either they have been eroded or they are below the resolution of the data. Maar-forming eruptions result from magma-water interaction and subsurface magma fragmentation. This interaction produces Taalian-style eruptions (e.g. Kokelaar 1986; Vespermann and Schmincke 2000; White and Ross 2011).

The funnel-shaped conduits beneath the pit crater volcanoes are interpreted as diatremes (downward-tapering conduits), based on their similar morphology, dimensions and their relationship to the overlying maars (e.g. Lorenz 1975; White 1991; White and McClintock 2001; Lorenz and Kurszlauskis 2007; Kwon and Sohn 2008; Suiting and Schmincke 2010; White and Ross 2011; Suiting and Schmincke 2012). The funnel-shaped conduits observed in this study are surrounded by concentric and radial faults (Fig. 5.10), similar to diatremes described by Suiting and Schmincke (2009). Diatremes are filled by syn- and post-eruptive sediments (Lorenz 1986; White and Ross 2011). These sediments may be syn-eruptive debris flows or the products of eruption columns (e.g. Suiting and Schmincke 2009) and are bedded or massive (Francis 1970; White and Ross 2011). Bedded diatreme fill deposits indicate that the diatreme were open at the surface (White and Ross 2011). In the conduits beneath the pit crater volcanoes, these sediments are represented by the *PMA* reflections (see section 3.4). Underlying lower diatreme deposits are massive (White and Ross 2011); these are poorly imaged. The pit craters and their conduits are interpreted to have formed in a submarine environment, consistent with other studies (e.g. Lefebvre and Kurszlauskis 2008; Pittari et al. 2008; Suiting and Schmincke 2009; Kjarsgaard et al. 2009; Calvari and Tanner 2011; Suiting and Schmincke 2012; Elliott et al. 2015). Volcanoes similar to maars are known to effuse lavas later during their development (e.g. Brown et al. 2012).

The pointed edifices are interpreted as pillow volcanoes—a type of submarine volcano that forms during effusive activity. Pillow volcanoes are 100–400 m in height and lack a crater (Batiza and White 2000), as observed for the pointed edifices. Pillow volcanoes are commonly composed of hyaloclastite and pillow lavas (Skilling 1994; Smellie and Hole

1997; Batiza and White 2000), consistent with well data and the seismic facies in this study. The effusive, shallow water eruptions that typify these edifices are thought to be pre-cursors to tuff cone-building, Surtseyan activity (e.g. Moore 1985).

The flat-topped and cratered edifices are interpreted as tuff cones: the products of emergent submarine and ice-confined volcanism (e.g. Wohletz and Sheridan 1983; Moore 1985; Sohn 1996; Skilling 2009; White and Ross 2011). Tuff cones are also formed during high discharge fissure eruptions (Thordarson and Self 1993). Tuff cones are of a similar size and have craters of similar dimensions to the edifices in this study. Tuff cones are also composed of fragmental volcanic rock (e.g. tephra and hyaloclastite), consistent with well data and the seismic facies of the flat-topped and cratered edifices. Tuff cone-forming eruptions may effuse lava in the later stages (Thorarinsson 1966; Moore 1985) and the upper *PHA* facies that typifies the cratered and flat-topped edifices are interpreted as a carapace of lava flows and/or pillow lavas. The flat-tops of the edifices are interpreted as lava flows that ponded in the summit crater. The flat-topped and cratered edifices are larger than the pointed edifices, indicating that they formed from longer-lived eruptions or eruptions with higher effusion rates.

5.5.2 Temporal and spatial evolution of the Bass Basin volcanic field

The age relationships of the edifices provides insights into the transition from maar-forming to tuff cone-building activity (Fig. 5.14). The first stage of the eruption is recorded by the maar-diatreme complexes (represented by the pit crater volcanoes). Whether all maars within the field formed at the same time is uncertain; the age relationship between the clustered maars in the west of the basin and the cone-shaped edifices is unknown. However, a maar within the linear cluster is overlain by a pointed edifice (Fig. 5.9), indicating that in this instance the maar represents the edifice that formed earliest in the eruption. The superposition of the pointed edifice is interpreted to result from cone construction atop the maar during the same eruption (e.g. White 1991; Lefebvre and Kurszlaukis 2008). This records the transition from pit-crater-forming to effusive activity, as observed at other maar-like monogenetic volcanoes (e.g. Brown et al. 2012). The transition from maar-forming to pillow volcano-building activity indicates that magma ceased to fragment beneath the paleosurface. This may have resulted from decreased efficiency of magma-water interaction, caused by variations in magma flux and/or crystallinity and composition (e.g. Brown et al. 1994; Gutmann 2002; Nemeth et al. 2003; Houghton and Gonnermann 2008; Büchner and Tietz 2012; Graettinger et al. 2013; Valentine and Cortés 2013; Augustín-Flores et al. 2014).

Alternatively, water may have been prevented from gaining access to the vent (e.g. Calvari and Tanner 2011).

The pointed edifices are interpreted to represent the early stages of tuff cone growth. The subsequent onset of Surtseyan activity (building the cratered and flat-topped edifices) could have resulted from a variety of processes. These include: 1) collapse of the growing submarine edifice (e.g. Lonsdale and Batiza 1980; Fujibayashi and Sakai 2003; Wohletz 2003; Watton et al. 2013b) causing depressurisation of the feeder system (e.g. Fujibayashi and Sakai 2003; Riggs and Duffield 2008); 2) decreased hydrostatic pressure as the volcano grew towards the sea surface (e.g. Skilling 2009; Graettinger et al. 2013); 3) variations in magma flux (e.g. Brown et al. 1994; Gutmann 2002; Büchner and Tietz 2012; Valentine and Cortés 2013; Agustín-Flores et al. 2014); 4) variations in volatile content; 5) variations in magma crystallinity (Houghton and Gonnermann 2008; Graettinger et al. 2013) and; 6) variations in the composition of the magma (Nemeth et al. 2003).

In addition to the development of the Miocene edifices, I also highlight that the underlying Late Cretaceous LV lava flows in the Bass Basin are located along the same north-south trending source as the edifices 4, 7 and 6 (Fig. 5.4). These lava flows are located in an early transgressional part of the basin stratigraphy, possibly in subaerial conditions (Cummings and Blevin 2003). Given the absence of a central edifice (e.g. a shield volcano), the lavas are interpreted to have erupted from fissures (Thordarson and Self 1993; Brown et al. 2014). Subsequent Miocene eruptions occurred above this fissure, but were fed by a different dyke. This indicates that the dykes exploited the same pathways over tens of millions of years (e.g. Takada 1994; Connor and Conway 2000; Németh 2010). Dyke locations may reflect shallow crustal processes or deeper melt processes (Takada 1994; Connor and Conway 2000; Brown and Valentine 2013; Le Corvec et al. 2013). This spatial relationship also indicates that monogenetic eruptions can be spatially linked over millions of years, and could represent a novel style of polygenetic volcanism (Nemeth et al. 2003; Brenna et al. 2010; Németh 2010; Brenna et al. 2011; Moorhouse et al. 2015).

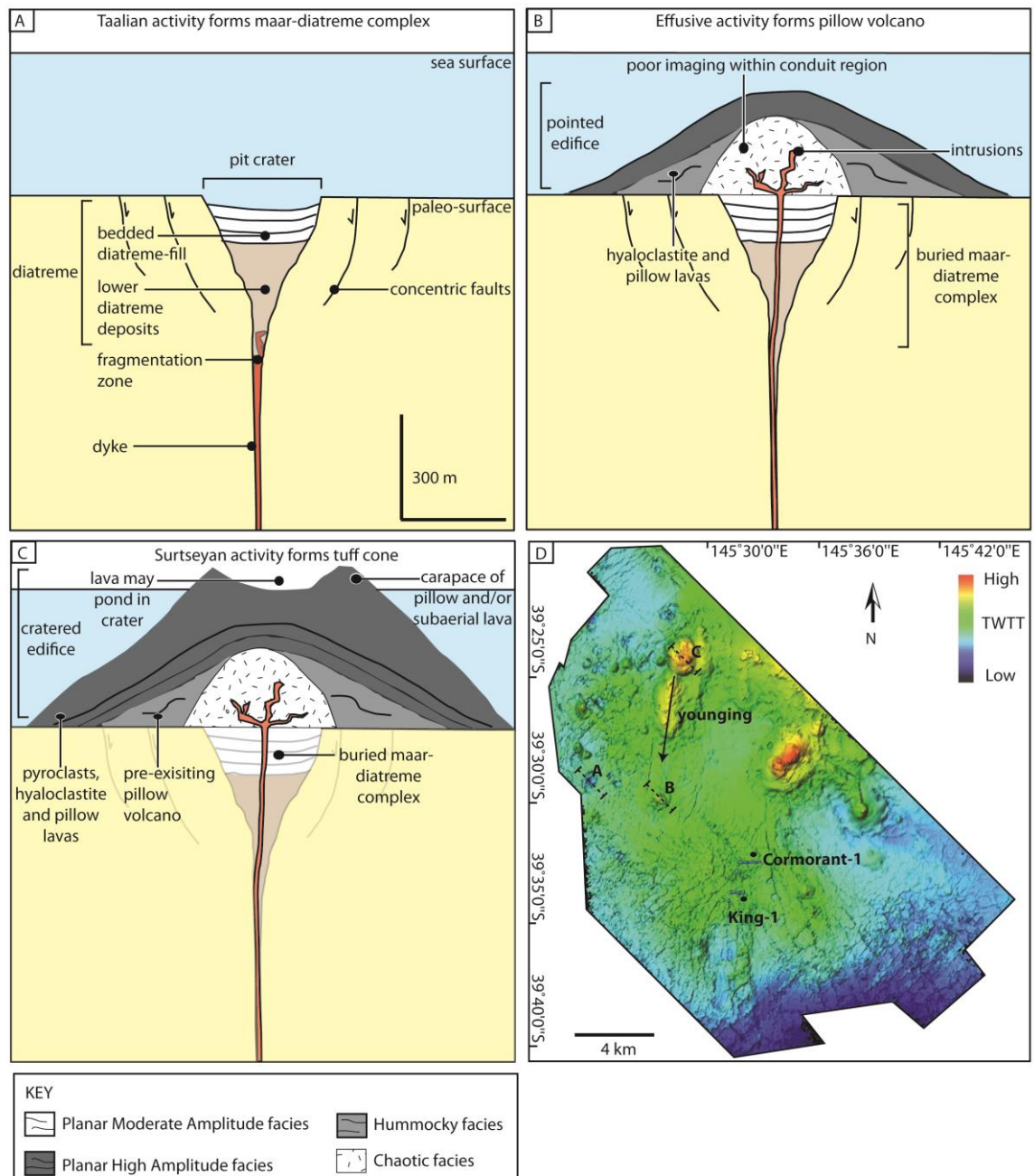


Figure 5.14. Schematic diagram to show the evolution of a submarine monogenetic volcano (A) Submarine maar-diatreme complexes form during Taalian-style activity. Syn- and post-eruptive sediments fill the craters. These are represented by the pit crater volcanoes. (B) Continued activity results in the submarine effusion of lavas, building pillow volcanoes. These are represented by the pointed edifices. (C) Tuff cones, represented by the flat-topped and cratered edifices, are formed during later Surtseyan activity. Ponding of lavas within the crater resulted in the formation of flat-topped volcanoes. These edifices may have been emergent. Image (D) shows the location of diagrams A–C.

5.5.3 Comparison with other volcanoes in seismic data

Volcanoes are reported in other seismic data sets in other tectonic settings worldwide (see Chapter 2). The pit craters in this study have a similar size, funnel-shaped geometry and facies to the maars described by Wall et al. (2010), in which the dyke is clearly imaged beneath the maar. This further supports a volcanic origin for the crater-type vents in this study. The facies and architecture of the edifices identified in this study are broadly similar to those of the submarine volcanoes and shield volcanoes described by Bell and Butcher (2002) and Magee et al. (2013). These edifices have onion ring structures in plan view, high amplitude tops and prograding reflections in their flanks. However, these features are not necessarily diagnostic of a volcanic origin. Zhao et al. (2014) describe “volcanic mounds” from the South China Sea, which have a similar size and depth relationship to sills to the edifices I describe. However, since detailed description of the edifices’ internal architecture is lacking, I am unable to provide further comparison.

There are a range of sedimentary edifices recognised in seismic data that can have similar morphologies, including mud volcanoes and hydrothermal vents. A volcanic origin for the edifices in this study is indicated by the presence of volcanic material in wells, and by the high velocities (2090–4025 m s⁻¹) of the volcanoes. Furthermore, unlike mud volcanoes, the volcanoes in this study have steep (>10°) slopes. The volcanoes also lack the inwardly dipping reflectors in their central area that are found within mud volcanoes (Kopf et al. 1998). The edifices I describe have chaotic and hummocky reflections that differentiate them from similar-sized hydrothermal edifices imaged by Grove (2013) that are composed of sediment. The Bass Basin edifices have superficially similar morphologies (i.e. a cone- or crater-like shape) and reflection characteristics (i.e. prograding internal reflections) to the hydrothermal vents documented by Planke et al. (2005). These vents have velocities of 1800 m s⁻¹ and are composed of diatomitic siltstone and carbonate (Svensen et al. 2003), unlike the edifices in this study. There are also several morphological features which distinguish the vents. Firstly, the eye-type hydrothermal vents described by Planke et al. (2005) have inwardly dipping reflections in their lower parts, unlike the cone-shaped edifices in this study. The dome-type vents described by Planke et al. (2005) also lack an underlying diatrema-like feature, as observed in this study. Instead, the dome-type vents are underlain by a cylindrical conduit zone (Planke et al. 2005). I also note the absence of sedimentary cones within the craters of the crater-type vents (e.g. Jamtveit et al. 2004). Furthermore, the hydrothermal vents described by Planke et al. (2005) are located above sills at ≥2000 m

depth. The edifices in this study are located above sills at 400–1200 m depth. Thus, the edifices in this study are fed by much shallower sills than the hydrothermal vents.

5.5.4 Implications for the identification of submarine volcanoes

This chapter provides insights into the growth of submarine edifices, volcanic fields and their plumbing systems. This information can be used to inform on plumbing systems and host rock interactions in other seismic data sets where imaging is concealed beneath edifices (e.g. Magee et al. 2013; Zhao et al. 2014).

The similarity between the edifices in this study and hydrothermal vents has important implications for structures not penetrated by wells (e.g. Lee et al. 2006; Rocchi et al. 2007; Inoue et al. 2008; Sun et al. 2014). Hydrothermal vents have been proposed as hydrocarbon plays (e.g. Grove 2013) and are underlain by sediment-filled breccia pipes (Svensen et al. 2006). They are thought to form during the early stages of volcanic continental rifting (e.g. Planke et al. 2005). In contrast, volcanoes represent sources of volcanic material that could potentially contaminate reservoir rocks. Furthermore, volcanoes are underlain by dykes that may compartmentalise underlying reservoirs or facilitate fluid flow (e.g. Rateau et al. 2013).

The data also suggests that the early stages of tuff cone growth may be characterised by pillow volcano construction. This highlights the usefulness of seismic data in helping constrain volcanic processes which may otherwise be inaccessible.

5.5.5 Edifice Preservation

The edifices are ≤ 550 m in height and were constructed in 90–140 m of water (Boral Energy Resources Ltd. 1998), suggesting that they were emergent. Emergent monogenetic edifices are rapidly eroded. For instance, a Surtla was eroded 10's of meters in decades leaving a plateau of pyroclastic material (e.g. Kokelaar and Durant 1983). However, the edifices in this study retain little evidence for erosion. Several factors are thought to have contributed to their preservation. Firstly, the seismic facies indicate the edifices had a protective carapace of hyaloclastite or lava (e.g. Kokelaar and Durant 1983; Andrews 2013). Secondly, the edifices are located in a basin, a site of sediment accumulation (Williamson et al. 1987). Furthermore, the results presented in this study suggest that water depth may have been deeper than inferred from biostratigraphic data, and/or that local areas of deep water existed.

5.5.6 Limitations of the study

Seismic interpretation is strongly dependent on the detection limit and resolution of the data. Detection and resolution are commonly on a scale of 10's of metres, thus seismic data represents a low resolution proxy for geologic interfaces (Sheriff and Geldart 1995). The resolution is affected by the depth of the interface, bed thickness, the impedance contrast across interfaces (i.e. lithology and the presence of fluids) and processing techniques (Sheriff and Geldart 1995). Processing techniques are capable of correcting seismic data to account for near-surface effects (e.g. irregular topography), improving the signal-noise ratio and correcting for offset between the recorded location of a seismic event and its location of the Earth's surface (Sheriff and Geldart 1995). However, since processing occurs before interpretation, and no processing reports were provided with the dataset, it is impossible to determine how the data may have appeared given different processing techniques and better resolution.

5.6 Conclusion

3D seismic and well data from the Bass Basin, offshore Australia, constrains the architecture and emplacement mechanisms of submarine volcanoes. The edifices evolved through a series of explosive and effusive stages, forming maar-diatreme complexes and volcanoclastic-dominated conical, flat-topped and cratered volcanoes. The pristine preservation of the edifices can be accounted for by a combination of a protective carapace on top of the edifices, sediment accumulation within the basin and basin subsidence concomitant with edifice growth. These volcanoes have different internal facies to morphologically-similar hydrothermal vents, and are located above shallow sills. These characteristics can be used to recognise similar volcanic features in other basins, and to distinguish these features from similar hydrothermal vents.

5.7 References

- Agustín-Flores J, Németh K, Cronin SJ, Lindsay JM, Kereszturi G, Brand BD, Smith IE (2014) Phreatomagmatic eruptions through unconsolidated coastal plain sequences, Maungataketake, Auckland Volcanic Field (New Zealand). *J Volcanol Geoth Res* 276:46-63
- Andrews B (2013) Eruptive and Depositional Mechanisms of an Eocene Shallow Submarine Volcano, Moeraki Peninsula, New Zealand. In: *Explosive Subaqueous Volcanism*. American Geophysical Union, pp 179-188
- Bacon M, Simm R, Redshaw T (2007) *3-D Seismic Interpretation*. Cambridge University Press
- Baker ET, Massoth GJ, de Ronde CEJ, Lupton JE, McInnes BIA (2002) Observations and sampling of an ongoing subsurface eruption of Kavachi volcano, Solomon Islands, May 2000. *Geology* 30(11):975-978

- Batiza R, White JDL (2000) Submarine lavas and hyaloclastite. In: Sigurdsson H (ed) *Encyclopedia of volcanoes*. Academic Press, San Diego, pp 361-381
- Bell B, Butcher H (2002) On the emplacement of sill complexes: evidence from the Faroe-Shetland Basin. *Geological Society, London, Special Publications* 197(1):307-329
- Berndt C, Skogly O, Planke S, Eldholm O, Mjelde R (2000) High-velocity breakup-related sills in the Vøring Basin, off Norway. *Journal of Geophysical Research: Solid Earth* (1978–2012) 105(B12):28443-28454
- Blevin J (2003) *Petroleum Geology of the Bass Basin - Interpretation Report*. In, Canberra Boral Energy Resources Ltd. (1998) Yolla 2 Well Proposal T/RL1. In: internal report.
- Brenna M, Cronin S, Smith IM, Sohn Y, Németh K (2010) Mechanisms driving polymagmatic activity at a monogenetic volcano, Udo, Jeju Island, South Korea. *Contributions to Mineralogy and Petrology* 160(6):931-950
- Brenna M, Cronin SJ, Németh K, Smith IEM, Sohn YK (2011) The influence of magma plumbing complexity on monogenetic eruptions, Jeju Island, Korea. *Terra Nova* 23(2):70-75
- Brenna M, Cronin SJ, Smith IE, Sohn YK, Maas R (2012) Spatio-temporal evolution of a dispersed magmatic system and its implications for volcano growth, Jeju Island Volcanic Field, Korea. *Lithos* 148:337-352
- Brenna M, Németh K, Cronin SJ, Sohn YK, Smith IE, Wijbrans J (2015) Co-located monogenetic eruptions~ 200 kyr apart driven by tapping vertically separated mantle source regions, Chagwido, Jeju Island, Republic of Korea. *B Volcanol* 77(5):1-17
- Brown RJ, Valentine GA (2013) Physical characteristics of kimberlite and basaltic intraplate volcanism and implications of a biased kimberlite record. *Geol Soc Am Bull* 125(7-8):1224-1238
- Brown RJ, Many S, Buisman I, Fontana G, Field M, Mac Niocaill C, Sparks RSJ, Stuart FM (2012) Eruption of kimberlite magmas: physical volcanology, geomorphology and age of the youngest kimberlitic volcanoes known on earth (the Upper Pleistocene/Holocene Igwisi Hills volcanoes, Tanzania) *B Volcanol* 74 (7) (2012): 1621-1643.
- Brown RJ, Blake S, Thordarson T, Self S (2014) Pyroclastic edifices record vigorous lava fountains during the emplacement of a flood basalt flow field, Roza Member, Columbia River Basalt Province, USA. *Geol Soc Am Bull* 126:875-891
- Brown S, Smith R, Cole J, Houghton B (1994) Compositional and textural characteristics of the strombolian and surtseyan K-Trig basalts, Taupo Volcanic Centre, New Zealand: Implications for eruption dynamics. *New Zealand Journal of Geology and Geophysics* 37(1):113-126
- Büchner J, Tietz O (2012) Reconstruction of the Landeskroner Scoria Cone in the Lusatian Volcanic Field, Eastern Germany—Long-term degradation of volcanic edifices and implications for landscape evolution. *Geomorphology* 151:175-187
- Calvari S, Tanner LH (2011) The Miocene Costa Giardini diatreme, Iblean Mountains, southern Italy: model for maar-diatreme formation on a submerged carbonate platform. *B Volcanol* 73(5):557-576
- Calvès G, Schwab AM, Huuse M, Clift PD, Gaina C, Jolley D, Tabrez AR, Inam A (2011) Seismic volcanostratigraphy of the western Indian rifted margin: The pre-Deccan igneous province. *Journal of Geophysical Research: Solid Earth* (1978–2012) 116(B1)
- Cas R, Landis C, Fordyce R (1989) A monogenetic, surtla-type, Surtseyan volcano from the Eocene-Oligocene Waiareka-Deborah volcanics, Otago, New Zealand: a model. *B Volcanol* 51(4):281-298
- Cas RAF, Simpson C, Sato H (1993) *Newer Volcanics Province - Processes and Products of Phreatomagmatic Activity*. IAVCEI Excursion Guide
- Connor CB, Conway MF (2000) Basaltic volcanic fields. In: Sigurdsson H (ed) *Encyclopedia of Volcanoes*. Academic Press, San Diego, pp 331-343
- Cummings AM, Blevin J (2003) Nature and distribution of igneous rocks. In: Blevin, J. (compiler), *Petroleum Geology of the Bass Basin - Interpretation Report*, an Output of the Western Tasmanian Regional Minerals Program. Geoscience Australia, Record 2003/19
- Elliott H, Gernon T, Roberts S, Hewson C (2015) Basaltic maar-diatreme volcanism in the Lower Carboniferous of the Limerick Basin (SW Ireland). *B Volcanol* 77(5):1-22
- Esso Exploration Australia Inc. (1965) *Esso Bass-1 Well Completion Report*. In, Esso Exploration Australia Inc. (1970) *Report - Cormorant 1*. In, Faustmann C (1995) *The seismic expression of volcanism in the Bass Basin referring to western Victorian analogues*.

- Fiske RS, Cashman KV, Shibata A, Watanabe K (1998) Tephra dispersal from Myojinsho, Japan, during its shallow submarine eruption of 1952–1953. *B Volcanol* 59(4):262-275
- Francis E (1970) Bedding in Scottish (Fifeshire) tuff-pipes and its relevance to maars and calderas. *Bull Volcanol* 34(3):697-712
- Fujibayashi N, Sakai U (2003) Vesiculation and eruption processes of submarine effusive and explosive rocks from the Middle Miocene Ogi Basalt, Sado Island, Japan. *Explosive Subaqueous Volcanism*:259-272
- Gatliff RW, Hitchen K, Ritchie JD, Smythe DK (1984) Internal structure of the Erlend Tertiary volcanic complex, north of Shetland, revealed by seismic reflection. *J Geol Soc London* 141(3):555-562
- Gençalioglu-Kuşcu G, Atilla C, Cas RA, Kuşcu İ (2007) Base surge deposits, eruption history, and depositional processes of a wet phreatomagmatic volcano in Central Anatolia (Cora Maar). *J Volcanol Geoth Res* 159(1):198-209
- Geoscience Australia (2010) Yolla Well Report - All Graphs. In: Australian Government, Graettinger AH, Skilling I, McGarvie D, Höskuldsson Á (2013) Subaqueous basaltic magmatic explosions trigger phreatomagmatism: A case study from Askja, Iceland. *J Volcanol Geoth Res* 264:17-35
- Gregg TK, Fink JH (1995) Quantification of submarine lava-flow morphology through analog experiments. *Geology* 23(1):73-76
- Grove C (2013) Submarine hydrothermal vent complexes in the Paleocene of the Faroe-Shetland Basin: Insights from three-dimensional seismic and petrographical data. *Geology* 41(1):71-74
- Gutmann JT (2002) Strombolian and effusive activity as precursors to phreatomagmatism: eruptive sequence at maars of the Pinacate volcanic field, Sonora, Mexico. *J Volcanol Geoth Res* 113(1):345-356
- Haller MJ, de Wall H, Martin U, Németh K (2006) Understanding the evolution of maar craters. Holford S, Schofield N, MacDonald J.D, Duddy I.R, P.F G (2007) Seismic Analysis of Igneous Systems in Sedimentary Basins and their Impacts on Hydrocarbon Prospectivity: Examples from the Southern Australian Margin.
- Holford S, Schofield N, MacDonald J, Duddy I, Green P (2012) Seismic analysis of igneous systems in sedimentary basins and their impacts on hydrocarbon prospectivity: examples from the Southern Australian margin. *Australian Petroleum Production and Exploration Association Journal* 52:229-252
- Holford S, Schofield N (in review) Three-dimensional seismic analysis for non-magmatic reactivation of buried volcanic complexes in sedimentary basins.
- Houghton B, Gonnermann H (2008) Basaltic explosive volcanism: constraints from deposits and models. *Chemie der Erde-Geochemistry* 68(2):117-140
- Inoue H, Coffin MF, Nakamura Y, Mochizuki K, Kroenke LW (2008) Intrabasement reflections of the Ontong Java Plateau: Implications for plateau construction. *Geochemistry, Geophysics, Geosystems* 9(4)
- Jackson CA-L (2012) Seismic reflection imaging and controls on the preservation of ancient sill-fed magmatic vents. *J Geol Soc London* 169(5):503-506
- Jamtveit B, Svensen H, Podladchikov YY, Planke S (2004) Hydrothermal vent complexes associated with sill intrusions in sedimentary basins. *Physical geology of high-level magmatic systems* 234:233-241
- Jerram DA (2002) Volcanology and facies architecture of flood basalts. *Geological Society of America Special Papers* 362:119-132
- Jerram DA, Single RT, Hobbs RW, Nelson CE (2009) Understanding the offshore flood basalt sequence using onshore volcanic facies analogues: an example from the Faroe–Shetland basin. *Geol Mag* 146(03):353
- Johnson RW (1989) Intraplate volcanism in eastern Australia and New Zealand. Cambridge University Press
- Kjarsgaard B, Harvey S, McClintock M, Zonneveld J, Du Plessis P, McNeil D, Heaman L (2009) Geology of the Orion South kimberlite, Fort à la Corne, Canada. *Lithos* 112:600-617
- Kokelaar BP, Durant GP (1983) The submarine eruption and erosion of Surtla (Surtsey), Iceland. *J Volcanol Geoth Res* 19(3–4):239-246

- Kokelaar P (1986) Magma-water interactions in subaqueous and emergent basaltic. *B Volcanol* 48(5):275-289
- Kopf A, Robertson AHF, Clennell MB, Flecker R (1998) Mechanisms of mud extrusion on the Mediterranean Ridge Accretionary Complex. *Geo-Marine Letters* 18(2):97-114
- Kwon CW, Sohn YK (2008) Tephra-filled volcanic neck (diatreme) of a mafic tuff ring at Maegok, Miocene Eoil Basin, SE Korea. *Geosciences Journal* 12(4):317-329
- Le Corvec N, Menand T, Lindsay J (2013) Interaction of ascending magma with pre-existing crustal fractures in monogenetic basaltic volcanism: an experimental approach. *Journal of Geophysical Research: Solid Earth* 118(3):968-984
- Lee GH, Kwon YI, Yoon CS, Kim HJ, Yoo HS (2006) Igneous complexes in the eastern Northern South Yellow Sea Basin and their implications for hydrocarbon systems. *Marine and Petroleum Geology* 23(6):631-645
- Lefebvre N, Kurszlaukis S (2008) Contrasting eruption styles of the 147 Kimberlite, Fort à la Corne, Saskatchewan, Canada. *J Volcanol Geoth Res* 174(1):171-185
- Lonsdale P, Batiza R (1980) Hyaloclastite and lava flows on young seamounts examined with a submersible. *Geol Soc Am Bull* 91(9):545-554
- Lorenz V (1975) Formation of phreatomagmatic maar-diatreme volcanoes and its relevance to kimberlite diatremes. *Physics and Chemistry of the Earth* 9:17-27
- Lorenz V (1986) On the growth of maars and diatremes and its relevance to the formation of tuff rings. *B Volcanol* 48(5):265-274
- Lorenz V, Kurszlaukis S (2007) Root zone processes in the phreatomagmatic pipe emplacement model and consequences for the evolution of maar-diatreme volcanoes. *J Volcanol Geoth Res* 159(1-3):4-32
- Magee C, Hunt-Stewart E, Jackson CAL (2013) Volcano growth mechanisms and the role of sub-volcanic intrusions: Insights from 2D seismic reflection data. *Earth and Planetary Science Letters* 373(0):41-53
- Maresh J, White RS, Hobbs RW, Smallwood JR (2006) Seismic attenuation of Atlantic margin basalts: Observations and modeling. *Geophysics* 71(6):B211-B221
- McClintock M, White J (2006) Large phreatomagmatic vent complex at Coombs Hills, Antarctica: Wet, explosive initiation of flood basalt volcanism in the Ferrar-Karoo LIP. *B Volcanol* 68(3):215-239
- Moore JG (1985) Structure and eruptive mechanisms at Surtsey Volcano, Iceland. *Geol Mag* 122(06):649-661
- Moorhouse B, White J, Scott J (2015) Cape Wanbrow: A stack of Surtseyan-style volcanoes built over millions of years in the Waiareka-Deborah volcanic field, New Zealand. *J Volcanol Geoth Res* 298:27-46
- Nemeth K, White JD, Reay A, Martin U (2003) Compositional variation during monogenetic volcano growth and its implications for magma supply to continental volcanic fields. *J Geol Soc London* 160(4):523-530
- Németh K, White JDL (2003) Reconstructing eruption processes of a Miocene monogenetic volcanic field from vent remnants: Waipiata Volcanic Field, South Island, New Zealand. *J Volcanol Geoth Res* 124(1-2):1-21
- Németh K, Cronin SJ, Charley DT, Harrison MJ, Garae E (2006) Exploding lakes in Vanuatu-"Surtseyan-style" eruptions witnessed on Ambae Island.
- Németh K (2010) Monogenetic volcanic fields: Origin, sedimentary record, and relationship with polygenetic volcanism. *Geological Society of America Special Papers* 470:43-66
- Otterloo J, Cas RF, Sheard M (2013) Eruption processes and deposit characteristics at the monogenetic Mt. Gambier Volcanic Complex, SE Australia: implications for alternating magmatic and phreatomagmatic activity. *B Volcanol* 75(8):1-21
- Pirrung M, Fischer C, Büchel G, Gaupp R, Lutz H, Neuffer FO (2003) Lithofacies succession of maar crater deposits in the Eifel area (Germany). *Terra Nova* 15(2):125-132
- Pittari A, Cas R, Lefebvre N, Robey J, Kurszlaukis S, Webb K (2008) Eruption processes and facies architecture of the Orion Central kimberlite volcanic complex, Fort à la Corne, Saskatchewan; kimberlite mass flow deposits in a sedimentary basin. *J Volcanol Geoth Res* 174(1):152-170

- Planke S, Eldholm O (1994) Seismic response and construction of seaward dipping wedges of flood basalts: Vøring volcanic margin. *Journal of Geophysical Research: Solid Earth* (1978–2012) 99(B5):9263–9278
- Planke S, Symonds PA, Alvestad E, Skogseid J (2000) Seismic volcanostratigraphy of large-volume basaltic extrusive complexes on rifted margins. *J. Geophys. Res.* 105(B8):19335–19351
- Planke S, Rasmussen T, Rey SS, Myklebust R (2005) Seismic characteristics and distribution of volcanic intrusions and hydrothermal vent complexes in the Vøring and Møre basins. Geological Society, London, Petroleum Geology Conference series 6:833–844
- Price R, Nicholls I, Gray C (2003) Cainozoic igneous activity: widespread volcanism resulting from long-term mantle instability and rifting.
- Rateau R, Schofield N, Smith M (2013) The potential role of igneous intrusions on hydrocarbon migration, West of Shetland. *Petroleum Geoscience* 19(3):259–272
- Riggs NR, Duffield WA (2008) Record of complex scoria cone eruptive activity at Red Mountain, Arizona, USA, and implications for monogenetic mafic volcanoes. *J Volcanol Geoth Res* 178(4):763–776
- Ritchie J, Hitchen K (1996) Early Paleogene offshore igneous activity to the northwest of the UK and its relationship to the North Atlantic Igneous Province. Geological Society, London, Special Publications 101(1):63–78
- Rocchi S, Mazzotti A, Marroni M, Pandolfi L, Costantini P, Giuseppe B, Biase Dd, Federici F, Lô PG (2007) Detection of Miocene saucer-shaped sills (offshore Senegal) via integrated interpretation of seismic, magnetic and gravity data. *Terra Nova* 19(4):232–239
- Roger S, Coulon C, Thouveny N, Féraud G, Van Velzen A, Fauquette S, Cocheme JJ, Prevot M, Verosub K (2000) $^{40}\text{Ar}/^{39}\text{Ar}$ dating of a tephra layer in the Pliocene Senèze maar lacustrine sequence (French Massif Central): constraint on the age of the Réunion–Matuyama transition and implications on paleoenvironmental archives. *Earth and Planetary Science Letters* 183(3):431–440
- Ross P-S, Delpit S, Haller MJ, Németh K, Corbella H (2011) Influence of the substrate on maar–diatreme volcanoes—an example of a mixed setting from the Pali Aike volcanic field, Argentina. *J Volcanol Geoth Res* 201(1):253–271
- Schmidt R, Schminke HU (2000) Seamounts and island building. In: Sigurdsson H (ed) *Encyclopedia of volcanoes*. Academic Press, San Diego, pp 361–381
- Schofield N, Jolley DW (2013) Development of intra-basaltic lava-field drainage systems within the Faroe–Shetland Basin. *Petroleum Geoscience* 19(3):273–288
- Self S, Keszthelyi LP, Thordarson T (2000) Discussion of: “Pulsed inflation of pahoehoe lava flows: implications for flood basalt emplacement”, by S.W. Anderson, E.R. Stofan, E.R. Smrekar, J.E. Guest and B. Wood [*Earth Planet. Sci. Lett.* 168 (1999) 7–18]. *Earth and Planetary Science Letters* 179(2):421–423
- Sheriff RE, Geldart L (1995) *Exploration seismology*. Cambridge University Press
- Skilling I (1994) Evolution of an englacial volcano: Brown Bluff, Antarctica. *B Volcanol* 56(6–7):573–591
- Skilling IP (2009) Subglacial to emergent basaltic volcanism at Hlöðufell, south-west Iceland: a history of ice-confinement *J Volcanol Geoth Res* 185(4): 276–289.
- Smellie J, Hole M (1997) Products and processes in Pliocene–Recent, subaqueous to emergent volcanism in the Antarctic Peninsula: examples of englacial Surtseyan volcano construction. *B Volcanol* 58(8):628–646
- Sohn Y (1995) Geology of Tok Island, Korea: eruptive and depositional processes of a shoaling to emergent island volcano. *B Volcanol* 56(8):660–674
- Sohn YK (1996) Hydrovolcanic processes forming basaltic tuff rings and cones on Cheju Island, Korea. *Geol Soc Am Bull* 108(10):1199–1211
- Suiting I, Schmincke H-U (2009) Internal vs. external forcing in shallow marine diatreme formation: A case study from the Iblean Mountains (SE-Sicily, Central Mediterranean). *J Volcanol Geoth Res* 186(3):361–378
- Suiting I, Schmincke H-U (2010) Iblean diatremes 2: shallow marine volcanism in the Central Mediterranean at the onset of the Messinian Salinity Crisis (Iblean Mountains, SE-Sicily)—a multidisciplinary approach. *International Journal of Earth Sciences* 99(8):1917–1940

- Suiting I, Schmincke H-U (2012) Iblean diatremes 3: volcanic processes on a Miocene carbonate platform (Iblean Mountains, SE-Sicily): a comparison of deep vs. shallow marine eruptive processes. *B Volcanol* 74(1):207-230
- Sun Q, Wu S, Cartwright J, Wang S, Lu Y, Chen D, Dong D (2014) Neogene igneous intrusions in the northern South China Sea: Evidence from high-resolution three dimensional seismic data. *Marine and Petroleum Geology* 54:83-95
- Sutherland F (2003) 'Boomerang' migratory intraplate Cenozoic volcanism, eastern Australian rift margins and the Indian-Pacific mantle boundary. *Geological Society of America Special Papers* 372:203-221
- Sutherland FL, Wellman P (1986) Potassium-argon ages of Tertiary volcanic rocks, Tasmania. *Papers and Proceedings of the Royal Society of Tasmania* 120
- Svensen H, Planke S, Jamtveit B, Pedersen T (2003) Seep carbonate formation controlled by hydrothermal vent complexes: a case study from the Vøring Basin, the Norwegian Sea. *Geo-Marine Letters* 23(3-4):351-358
- Svensen H, Jamtveit B, Planke S, Chevallier L (2006) Structure and evolution of hydrothermal vent complexes in the Karoo Basin, South Africa. *J Geol Soc London* 163(4):671-682
- Takada A (1994) The influence of regional stress and magmatic input on styles of monogenetic and polygenetic volcanism. *Journal of Geophysical Research: Solid Earth* (1978–2012) 99(B7):13563-13573
- Tap Oil Ltd. (2008) Labatt 3D Seismic Survey Acquisition Report. In: Internal report.
- Tap Oil Ltd. (2010) T/47P Bass Basin, Tasmania – 2007 Labatt 3D and 2008 Molson 2D Seismic Interpretation Report. In,
- Thomson K (2005) Volcanic features of the North Rockall Trough: application of visualisation techniques on 3D seismic reflection data. *B Volcanol* 67(2):116-128
- Thomson K (2007) Determining magma flow in sills, dykes and laccoliths and their implications for sill emplacement mechanisms. *B Volcanol* 70(2):183-201
- Thorarinsson S (1966) The Surtsey eruption course of events and the development of the new island. In: Museum of Natural History, Reykjavik, Iceland
- Thordarson T, Self S (1993) The Laki (Skaftár Fires) and Grímsvötn eruptions in 1783–1785. *B Volcanol* 55(4):233-263
- Thors K, Jakousson SP (1982) Two seismic reflection profiles from the vicinity of Surtsey, Iceland. *Surtsey research progress report* 9:149
- Trigg KR, Blevine JE, Boreham CJ (2003) An Audit of Petroleum Exploration Wells in the Bass Basin 1965 - 1999. *Geoscience Australia*
- Urrutia-Fucugauchi J, Uribe-Cifuentes RM (1999) Lower-crustal xenoliths from the Valle de Santiago maar field, Michoacan-Guanajuato volcanic field, central Mexico. *International Geology Review* 41(12):1067-1081
- Valentine GA, Gregg TKP (2008) Continental basaltic volcanoes — Processes and problems. *J Volcanol Geoth Res* 177(4):857-873
- Valentine GA, Cortés J (2013) Time and space variations in magmatic and phreatomagmatic eruptive processes at Easy Chair (Lunar Crater Volcanic Field, Nevada, USA). *B Volcanol* 75(9):1-13
- Vespermann D, Schmincke H-U (2000) Scoria cones and tuff rings. In: Sigurdsson H (ed) *Encyclopedia of Volcanoes*. Academic Press, San Diego. Academic Press, San Diego, pp 683-694
- Vogel DC, Keays RR (1997) The petrogenesis and platinum-group element geochemistry of the Newer Volcanic Province, Victoria, Australia. *Chemical Geology* 136(3):181-204
- Walker GPL (1993) Basaltic-volcano systems. *Geological Society, London, Special Publications* 76(1):3-38
- Wall M, Cartwright J, Davies R, McGrandale A (2010) 3D seismic imaging of a Tertiary Dyke Swarm in the Southern North Sea, UK. *Basin Research* 22(2):181-194
- Watton TJ, Wright KA, Jerram DA, Brown RJ (2013a) The Petrophysical and Petrographical Properties of Hyaloclastite Deposits: Implications for Petroleum Exploration. *AAPG Bulletin* (20,130,909)
- Watton TJ, Jerram DA, Thordarson T, Davies RJ (2013b) Three-dimensional lithofacies variations in hyaloclastite deposits. *J Volcanol Geoth Res* 250(0):19-33
- Wheeler BF, Kjellgren GM (1986) Yolla-1 final well report. In: Amoco Australian Petroleum Company,

- White JD (2001) Eruption and reshaping of Pahvant Butte volcano in Pleistocene Lake Bonneville. *Volcaniclastic Sedimentation in Lacustrine Settings*:(Special Publication 30 of the IAS) 54:61
- White JDL (1991) Maar-diatreme phreatomagmatism at Hopi Buttes, Navajo Nation (Arizona), USA. *B Volcanol* 53(4):239-258
- White JDL, McClintock MK (2001) Immense vent complex marks flood-basalt eruption in a wet, failed rift: Coombs Hills, Antarctica. *Geology* 29(10):935-938
- White JDL, Ross PS (2011) Maar-diatreme volcanoes: A review. *J Volcanol Geoth Res* 201(1–4):1-29
- Williamson P, Pigram C, Colwell J, Scherl A, Lockwood K, Branson J (1987) Review of stratigraphy, structure, and hydrocarbon potential of Bass Basin, Australia. *AAPG bulletin* 71(3):253-280
- Wohletz KH, Sheridan MF (1983) Hydrovolcanic explosions; II, Evolution of basaltic tuff rings and tuff cones. *American Journal of Science* 283(5):385-413
- Wohletz KH (2003) Water/magma interaction: physical considerations for the deep submarine environment. *Explosive subaqueous volcanism*:25-49
- Wright K (2013) Seismic Stratigraphy and Geomorphology of Palaeocene Volcanic Rocks, Faroe-Shetland Basin. PhD Thesis, Durham University, Department of Earth Sciences.
- Wright KA, Davies RJ, Jerram DA, Morris J, Fletcher R (2012) Application of seismic and sequence stratigraphic concepts to a lava-fed delta system in the Faroe-Shetland Basin, UK and Faroes. *Basin Research* 24(1):91-106
- Zhao F, Wu S, Sun Q, Huuse M, Li W, Wang Z (2014) Submarine volcanic mounds in the Pearl River Mouth Basin, northern South China Sea. *Mar Geol* 355(0):162-172

Chapter 6: Discussion

6.1 Introduction

Chapters 3, 4 and 5 describe the architecture of basaltic volcanic edifices. In this chapter, I assess the importance of each edifice for hydrocarbon systems. I also discuss how the fissure-derived and rootless edifices detailed in Chapters 3 and 4 can be recognised in hydrocarbon basins using core, cutting and FMI well data. Since this thesis did not determine the petrophysical properties of pyroclastic rocks in wireline data, this remains a topic worthy of future research (see Chapter 8). I also discuss the challenges associated with recognising the edifices described in Chapters 3 and 4 in seismic data.

6.2 Fissure eruption-derived volcanoes

Chapter 3 details the edifices formed during a low volume fissure eruption. These edifices are analogous to those formed during large-volume fissure eruptions and were formed during Hawaiian-style activity. This suggests that flood basalt emplacement may also be associated with a diversity of eruption styles. The edifices are underlain by dykes that widen towards the surface (e.g. Chapter 3; see also Keating et al. 2008; Geshi et al. 2010; Geshi and Oikawa 2014). Dykes are typified by abundant cooling joints which may form permeable pathways (Rateau et al. 2013). This permeability can subsequently be enhanced or decreased through tectonic fracturing, diagenesis, weathering and hydrothermal alteration (Rateau et al. 2013). Thus, the dykes and conduit could act as a hydrocarbon reservoir (e.g. Schutter 2003), fluid pathway or a barrier to fluid flow (e.g. Rateau et al. 2013). The planes of the graben bounding faults that undergo post-eruption displacement (e.g. Chapter 3) may also act as hydrocarbon migration pathways (e.g. Walker et al. 2013). Thus, the fissure-proximal region could be an important region for hydrocarbon migration. The fissure-proximal region could also act as a reservoir, since 4-way dip closure of sediments above the edifices can form a seal for underlying hydrocarbons (Schutter 2003).

There are not thought to be any effects on hydrocarbon source rock unique to the fissure-proximal region. Fissure-proximal regions are underlain by complex assemblages of sills and dykes (Thomson 2007) which have important effects on source rock maturation (Raymond and Murchison 1988; Bishop and Abbott 1995). However, sills and dykes are found throughout volcanic basins (Planke et al. 2005; Hansen and Cartwright 2006; Polteau et al. 2008; Goultly and Schofield 2008; Galerne et al. 2008; Galerne et al. 2011), and are not unique to the fissure-proximal region.

Features that can be used to recognise the fissure-proximal region from FMI data include variations in vesicle distribution and foliation textures. Vesicles are recognised in FMI by a distinct mottled appearance (Watton et al. 2014). Irregular vesicle patches are common in the core of clastogenic lavas (Chapter 3). These lavas are characteristic of the vent-proximal region in many basaltic settings (e.g. Chapter 3; see also Swanson et al. 1975; Sumner 1998; Thordarson and Self 1998; Carracedo Sánchez et al. 2012; Brown et al. 2014). Alternating vesicle-rich and vesicle-poor zones also indicate welding fabrics such as those found in clast supported densely welded spatter bombs (dwSp) and in the crusts of stacked shelly pāhoehoe lobes. Again, these facies are common in the vent-proximal region (e.g. Chapter 3; see also Swanson et al. 1975; Thordarson and Self 1998; Brown et al. 2014). Foliation textures (i.e. laminations) resulting from welding occur in clast supported densely welded spatter bombs (dwSp). Tension gashes in lava-like agglutinate (l-l Agg; logs 30 and 11, Figs. 10 and 11) also give this lithofacies a foliated appearance. Similar laminations are recognised in sequences <0.25 m thick in FMI logs (Watton et al. 2014) suggesting that vent-proximal sequences can be recognised by their laminated texture. However, it may be difficult to distinguish these features from other foliated textures not diagnostic of a fissure-proximal location, such as the platy zone found at the base of pāhoehoe lava flows (e.g. Thordarson and Self 1998). The petrographic textures documented in Chapter 3 have been reported from other studies of fissure-derived pyroclastic edifices (Thordarson and Self 1998; Brown et al. 2014), thus do not provide further insights into how dyke-fed edifices can be recognised from core and cutting data.

This thesis highlights that the fissure-derived edifices in Chapter 3 will be difficult to detect in seismic data. Seismic data commonly has a resolution of 10's of metres (Sheriff and Geldart 1995). Therefore, the edifices described will be difficult, if not impossible to detect, especially if they are located beneath the "Top Basalt" reflection (Jerram 2002; Roberts et al. 2005).

Furthermore, fissure-derived edifices may not be recognised because of their close association with grabens. Chapter 3 shows that the R-K fissure eruption occurred within the Sveinar graben. Grabens associated with fissure eruptions are thought to form as a result deflation of the underlying feeder system (Tentler and Temperley 2007) and/or intrusion of the feeder dyke (Pollard et al. 1983; Rubin and Pollard 1988; Rubin 1992; Chadwick and Embley 1998). Syn-eruptive graben formation results in the ponding of lavas (e.g. Chapter 3) and drowning of the edifices (e.g. Thordarson and Self 1993; Keszthelyi et al. 2004). These lavas would then mask the underlying reflections (Jerram

2002; Roberts et al. 2005), rendering the edifices unresolvable. Grabens are also likely to be favourable pathways for the re-establishment for drainage systems (e.g. Chapter 3; Ebinghaus et al. 2014) enhancing erosion and degradation of the edifices.

Erosion serves to decrease the likelihood of fissure-proximal locations being recognised from seismic data. Erosion of volcanic edifices is partly linked to the vesicularity and density of the constituent lithofacies, since vesicular clasts are more easily entrained in water than dense clasts (e.g. Manville 2009). Therefore, edifices composed of densely welded lithofacies (e.g. spatter ramparts and scoria-agglutinate cones) are likely to stand a higher chance of preservation than those composed of vesicular lithofacies (e.g. scoria ramparts and rootless cones). However, small edifices such as spatter ramparts are more likely to be buried by lava (e.g. Keszthelyi et al. 2004) and are thus more difficult to resolve from seismic data.

Erosion is also linked to climate, most notably rainfall and temperature (e.g. Wood 1980; Hooper and Sheridan 1998). The flood basalts of the NAIP were predominantly emplaced sub aerially (Brown et al. 2009) during the Paleocene-Eocene Thermal Maximum (Jolley and Widdowson 2005). This period was typified by a warm and wet climate, where fluvial channels were abundant (Brown et al. 2009). These conditions would have favoured rapid erosion of pyroclastic edifices (e.g. Wood 1980; Németh and Cronin 2007; Németh et al. 2009; Manville et al. 2009). This situation is in contrast to the eruptions in the Bass Basin (Chapter 4) which occurred beneath sea level, therefore favouring edifice preservation.

6.3 Rootless cones

Chapter 4 provides quantitative data on rootless juvenile clast morphology, density and lithofacies architecture that can be used to differentiate between dyke-fed and rootless edifices. Differentiating between rootless and dyke-fed edifices is important because dyke-fed edifices can be used to inform on magma plumbing systems (Valentine and Groves 1996; Valentine and Keating 2007; Valentine 2012), conduit conditions (Taddeucci et al. 2004; Genareau et al. 2010), environmental impacts (Thordarson et al. 1996; Thordarson et al. 2001; Brown et al. 2014) and magma flux (Di Traglia et al. 2009; Németh et al. 2011; Valentine and Cortés 2013) and fragmentation processes (Sumner et al. 2005; Valentine and Gregg 2008). If rootless edifices are incorrectly identified as dyke-fed edifices (or vice-versa) incorrect conclusions may be drawn about these processes and conditions. Furthermore, dyke-fed edifices can also be used to identify structural trends (e.g. Connor

and Conway 2000), in contrast to rootless edifices which indicate lava flow pathways (e.g. tubes; see Hamilton et al. 2010). I presume that rootless eruptions were common in the North Atlantic Igneous Province, since the lava flows were emplaced in an environment where ephemeral lakes, swamps and small fluvial channels were common (Brown et al. 2009). However, no rootless cones have been discovered to date.

Rootless vents (as described in Chapter 4) are important features for hydrocarbon migration. The vents occur in lava flow cores, which commonly act as seals in volcanic-affected basins (Schutter 2003; Rohrman 2007). They also create highly anisotropic flow regimes in basalt aquifers (Burns et al. 2014). Although the preservation potential of the void that characterises the vents is unknown, the vents and associated joints extend from the base to the top of a lava flow. This will increase the porosity and permeability of the core, particularly in the vertical plane, providing an efficient vertical migration pathway. The net result will be to decrease the effectiveness of the host lava flow as a seal (e.g. Rohrman 2007). The vents and joints may also provide zones of accelerated fluid loss whilst drilling through the basalt sequence (e.g. Millett 2015). Since rootless cone fields cover areas up to 150 km² (Hamilton et al. 2010), these considerations are important over a basin-wide scale.

My research highlights the importance of rootless cones as paleo-environmental indicators and sources of hydrocarbon reservoir and source rock contamination. Rootless cones form on clay–cobble sized substrates (e.g. Chapter 4; see also Fagents and Thordarson 2007; Hamilton et al. 2010). Sand-sized sediments could act as inter-basalt reservoirs (Schofield and Jolley 2013). These are difficult to detect in seismic data if their thickness is <50 m, or if sub-basalt imaging is sufficiently poor (e.g. Jerram 2002). Therefore rootless cones can be used to identify sediment packages unresolvable in seismic data. Although the effect of cone formation on the sediment is unknown, there is likely to be contamination of the sediment by igneous material during cone formation. Therefore rootless cone formation is detrimental to the quality of underlying reservoirs in a basin. Rootless cone formation is also detrimental to source rock quality. Source rocks are commonly formed in lacustrine environments, in which rootless cone are found (e.g. Chapter 4; see also Fagents and Thordarson 2007; Hamilton et al. 2010). Rootless cones also distribute pyroclastic material throughout the basin, and could contaminate overlying reservoir rocks (e.g. Clark 2014).

However, distinguishing rootless edifices from dyke-fed edifices in well core data would present a significant challenge. The rootless juvenile clasts that have morphologies

atypical of dyke-fed tephra (see Chapter 4) are unlikely to be recognised from core data; angular volcanic “breccias” are often highly fractured during drilling (Watton et al. 2014), thus hampering recognition of clast shape and size. Although the abundance of sediment in the rootless tephra documented in Chapter 4 proves a useful criterion for distinguishing dyke-fed from rootless tephra in field data sets, intimately mixed sediment and tephra is also characteristic of epiclastic successions (Fisher 1961; Fisher 1966; White and Houghton 2006; Clark 2014) and peperite (Skilling et al. 2002) which are found in many settings. Furthermore, diagenesis may alter the porosity and mineralogy of primary volcanoclastic rocks (Clark 2014), thus increasing the difficulty of distinguishing between epiclastic, dyke-fed and rootless pyroclastic successions.

FMI data is also of limited use in distinguishing dyke-fed from rootless tephra. The resolution of FMI is such it does not allow determination of lava fragmentation mechanism, welding or sedimentation processes (Watton et al. 2014). Therefore, it would be difficult to distinguish primary volcanoclastic rocks, dyke-fed and rootless tephra (e.g. Watton et al. 2014). Although the density of an FMI facies can be determined to 0.1 gm/cm^3 (Watton et al. 2014), welding and clast morphology cannot be accurately determined on a scale of $<25 \text{ cm}$ (Watton et al. 2014). Therefore, it would be difficult to determine if dense pyroclastic successions are welded (and potentially dyke-fed) or are composed of fragmented, degassed lava (as is the case for rootless tephra).

As described for dyke-fed edifices, the size of rootless edifices would hamper recognition of these edifices in seismic data. Furthermore, rootless cones have a low preservation potential due to the vesicular and unconsolidated nature of the component lithofacies (e.g. Chapter 4; see also Mattox and Mangan 1997; Melchior Larsen et al. 2006; Hamilton et al. 2010). This would further limit the chances of them being detected in seismic data.

6.4 Monogenetic edifices in seismic data

Chapter 5 provides insights into the seismic facies that characterise submarine volcanic edifices. These facies can be used to recognise volcanic edifices from other seismic data sets. These insights are especially useful in other volcanic-affected basins where the edifices have not been penetrated by wells. Chapter 5 also shows that the edifices directly overlie the site of previous lava extrusion (within the Lower Volcanic horizon, Chapter 5). This spatial relationship exists in other volcanic fields (e.g. Takada

1994; Connor and Conway 2000; Németh 2010) and may exist within FBP (e.g. the FSB; see also White et al. 2009).

Buried volcanic edifices also act as fluid pathways (Holford and Schofield, in review). The edifices described by Holford and Schofield (in review) have been identified in this thesis as tuff cones (Chapter 5); relatively common features along fissures (e.g. Thordarson and Larsen 2007; Zanon et al. 2009; Németh and Cronin 2011). This suggests tuff cones are likely to be important features for vertical fluid migration in other hydrocarbon basins also affected by fissure volcanism. Chapter 5 also shows that the feeder dyke for the Miocene edifices exploited the same vertical pathway as the dyke for the Lower Volcanic (LV) lava flows. Since dykes may act as conduits for fluid migration (Rateau et al. 2013), vertical fluid pathways are also likely to exist between edifices that formed over several millions of years (e.g. Takada 1994; Connor and Conway 2000; Németh 2010).

6.5 References

- Bishop A, Abbott G (1995) Vitrinite reflectance and molecular geochemistry of Jurassic sediments: the influence of heating by Tertiary dykes (northwest Scotland). *Organic Geochemistry* 22(1):165-177
- Brown D, Holohan E, Bell B (2009) Sedimentary and volcano-tectonic processes in the British Paleocene Igneous Province: a review. *Geol Mag* 146(3):326-352
- Brown RJ, Blake S, Thordarson T, Self S (2014) Pyroclastic edifices record vigorous lava fountains during the emplacement of a flood basalt flow field, Roza Member, Columbia River Basalt Province, USA. *Geol Soc Am Bull* 126:875-891
- Burns E, Williams C, Ingebritsen S, Voss C, Spane F, DeAngelo J (2014) Understanding heat and groundwater flow through continental flood basalt provinces: insights gained from alternative models of permeability/depth relationships for the Columbia Plateau, USA. *Geofluids*
- Carracedo Sánchez M, Sarrionandia F, Arostegui J, Eguiluz L, Gil Ibarguchi JI (2012) The transition of spatter to lava-like body in lava fountain deposits: features and examples from the Cabezo Segura volcano (Calatrava, Spain). *J Volcanol Geoth Res* 227–228(0):1-14
- Chadwick WW, Embley RW (1998) Graben formation associated with recent dike intrusions and volcanic eruptions on the mid-ocean ridge. *Journal of Geophysical Research: Solid Earth* 103(B5):9807-9825
- Clark SJ (2014) Constraining diagenetic timings, processes and reservoir quality in igneous-affected basins. PhD Thesis, Durham University, Department of Earth Sciences.
- Connor CB, Conway MF (2000) Basaltic volcanic fields. In: Sigurdsson H (ed) *Encyclopedia of Volcanoes*. Academic Press, San Diego, pp 331-343
- Di Traglia F, Cimorelli C, de Rita D, Gimeno Torrente D (2009) Changing eruptive styles in basaltic explosive volcanism: Examples from Croscat complex scoria cone, Garrotxa Volcanic Field (NE Iberian Peninsula). *J Volcanol Geoth Res* 180(2–4):89-109
- Ebinghaus A, Hartley AJ, Jolley DW, Hole M, Millett J (2014) Lava–Sediment Interaction and Drainage-System Development In A Large Igneous Province: Columbia River Flood Basalt Province, Washington State, USA. *Journal of Sedimentary Research* 84(11):1041-1063
- Fagents SA, Thordarson T (2007) Rootless cones in Iceland and on Mars. In: Chapman M, Skilling IP (eds) *The Geology of Mars: Evidence from Earth-Based Analogues*. Cambridge University Press, pp 151–177
- Fisher RV (1961) Proposed Classification of Volcaniclastic Sediments and Rocks. *Geol Soc Am Bull* 72(9):1409-1414

- Fisher RV (1966) Rocks composed of volcanic fragments and their classification. *Earth-Science Reviews* 1(4):287-298
- Galerne CY, Neumann E-R, Planke S (2008) Emplacement mechanisms of sill complexes: Information from the geochemical architecture of the Golden Valley Sill Complex, South Africa. *J Volcanol Geoth Res* 177(2):425-440
- Galerne CY, Galland O, Neumann E-R, Planke S (2011) 3D relationships between sills and their feeders: evidence from the Golden Valley Sill Complex (Karoo Basin) and experimental modelling. *J Volcanol Geoth Res* 202(3-4):189-199
- Genareau K, Valentine G, Moore G, Hervig R (2010) Mechanisms for transition in eruptive style at a monogenetic scoria cone revealed by microtextural analyses (Lathrop Wells volcano, Nevada, U.S.A.). *B Volcanol* 72(5):593-607
- Geshi N, Kusumoto S, Gudmundsson A (2010) Geometric difference between non-feeder and feeder dikes. *Geology* 38(3):195-198
- Geshi N, Oikawa T (2014) The spectrum of basaltic feeder systems from effusive lava eruption to explosive eruption at Miyakejima volcano, Japan. *B Volcanol* 76(3):1-14
- Goulty N, Schofield N (2008) Implications of simple flexure theory for the formation of saucer-shaped sills. *Journal of Structural Geology* 30(7):812-817
- Hamilton CW, Thordarson T, Fagents SA (2010) Explosive lava–water interactions I: architecture and emplacement chronology of volcanic rootless cone groups in the 1783–1784 Laki lava flow, Iceland. *B Volcanol* 72(4):449-467
- Hansen DM, Cartwright J (2006) Saucer-shaped sill with lobate morphology revealed by 3D seismic data: implications for resolving a shallow-level sill emplacement mechanism. *J Geol Soc London* 163(3):509-523
- Holford S, Schofield N (in review) Three-dimensional seismic analysis for non-magmatic reactivation of buried volcanic complexes in sedimentary basins.
- Hooper DM, Sheridan MF (1998) Computer-simulation models of scoria cone degradation. *J Volcanol Geoth Res* 83(3):241-267
- Jerram DA (2002) Volcanology and facies architecture of flood basalts. *Geological Society of America Special Papers* 362:119-132
- Jolley DW, Widdowson M (2005) Did Paleogene North Atlantic rift-related eruptions drive early Eocene climate cooling? *Lithos* 79(3-4):355-366
- Keating G, Valentine G, Krier D, Perry F (2008) Shallow plumbing systems for small-volume basaltic volcanoes. *B Volcanol* 70(5):563-582
- Keszthelyi L, Thordarson T, McEwen A, Haack H, Guilbaud MN, Self S, Rossi MJ (2004) Icelandic analogs to Martian flood lavas. *Geochemistry, Geophysics, Geosystems* 5(11)
- Manville V, Németh K, Kano K (2009) Source to sink: a review of three decades of progress in the understanding of volcanoclastic processes, deposits, and hazards. *Sedimentary Geology* 220(3):136-161
- Mattox TN, Mangan MT (1997) Littoral hydrovolcanic explosions: a case study of lava–seawater interaction at Kilauea Volcano. *J Volcanol Geoth Res* 75(1-2):1-17
- Melchior Larsen L, Ken Pedersen A, Krarup Pedersen G (2006) A subaqueous rootless cone field at Niuluut, Disko, Paleocene of West Greenland. *Lithos* 92(1-2):20-32
- Millett J (2015) Offshore drilling through basaltic sequences: geological heterogeneity and its implications for drilling complications, VMSG, Norwich
- Németh K, Cronin SJ (2007) Syn-and post-eruptive erosion, gully formation, and morphological evolution of a tephra ring in tropical climate erupted in 1913 in West Ambrym, Vanuatu. *Geomorphology* 86(1):115-130
- Németh K, Cronin SJ, Stewart RB, Charley D (2009) Intra- and extra-caldera volcanoclastic facies and geomorphic characteristics of a frequently active mafic island–arc volcano, Ambrym Island, Vanuatu. *Sedimentary Geology* 220(3-4):256-270
- Németh K (2010) Monogenetic volcanic fields: Origin, sedimentary record, and relationship with polygenetic volcanism. *Geological Society of America Special Papers* 470:43-66
- Németh K, Risso C, Nullo F, Kereszturi G (2011) The role of collapsing and cone rafting on eruption style changes and final cone morphology: Los Morados scoria cone, Mendoza, Argentina. *Central European Journal of Geosciences* 3(2):102-118

- Németh K, Cronin SJ (2011) Drivers of explosivity and elevated hazard in basaltic fissure eruptions: the 1913 eruption of Ambrym Volcano, Vanuatu (SW-Pacific). *J Volcanol Geoth Res* 201(1):194-209
- Planke S, Rasmussen T, Rey SS, Myklebust R (2005) Seismic characteristics and distribution of volcanic intrusions and hydrothermal vent complexes in the Vøring and Møre basins. Geological Society, London, Petroleum Geology Conference series 6:833-844
- Pollard DD, Delaney PT, Duffield WA, Endo ET, Okamura AT (1983) Surface deformation in volcanic rift zones. *Tectonophysics* 94(1-4):541-584
- Polteau S, Ferré E, Planke S, Neumann ER, Chevallier L (2008) How are saucer-shaped sills emplaced? Constraints from the Golden Valley Sill, South Africa. *Journal of Geophysical Research: Solid Earth* (1978–2012) 113(B12)
- Rateau R, Schofield N, Smith M (2013) The potential role of igneous intrusions on hydrocarbon migration, West of Shetland. *Petroleum Geoscience* 19(3):259-272
- Raymond AC, Murchison DG (1988) Development of organic maturation in the thermal aureoles of sills and its relation to sediment compaction. *Fuel* 67(12):1599-1608
- Roberts A, White R, Lunnon Z, Christie P, Spitzer R, iSIMM T (2005) Imaging magmatic rocks on the Faroes margin. In: *Petroleum Geology: North-West Europe and Global Perspectives—Proceedings of the 6th Petroleum Geology Conference*. pp 00-01
- Rohrman M (2007) Prospectivity of volcanic basins: Trap delineation and acreage de-risking. *AAPG bulletin* 91(6):915-939
- Rubin AM, Pollard DD (1988) Dike-induced faulting in rift zones of Iceland and Afar. *Geology* 16(5):413-417
- Rubin AM (1992) Dike-induced faulting and graben subsidence in volcanic rift zones. *Journal of Geophysical Research: Solid Earth* 97(B2):1839-1858
- Schofield N, Jolley DW (2013) Development of intra-basaltic lava-field drainage systems within the Faroe–Shetland Basin. *Petroleum Geoscience* 19(3):273-288
- Schutter SR (2003) Occurrences of hydrocarbons in and around igneous rocks. Geological Society, London, Special Publications 214(1):35-68
- Sheriff RE, Geldart L (1995) *Exploration seismology*. Cambridge University Press
- Skilling IP, White JDL, McPhie J (2002) Peperite: a review of magma–sediment mingling. *J Volcanol Geoth Res* 114(1-2):1-17
- Sumner JM (1998) Formation of clastogenic lava flows during fissure eruption and scoria cone collapse: the 1986 eruption of Izu-Oshima Volcano, eastern Japan. *B Volcanol* 60(3):195-212
- Sumner JM, Blake S, Matela RJ, Wolff JA (2005) Spatter. *J Volcanol Geoth Res* 142(1-2):49-65
- Swanson DA, Wright TL, Helz RT (1975) Linear vent systems and estimated rates of magma production and eruption for the Yakima Basalt on the Columbia Plateau. *American Journal of Science* 275(8):877-905
- Taddeucci J, Pompilio M, Scarlato P (2004) Conduit processes during the July–August 2001 explosive activity of Mt. Etna (Italy): inferences from glass chemistry and crystal size distribution of ash particles. *J Volcanol Geoth Res* 137(1-3):33-54
- Takada A (1994) The influence of regional stress and magmatic input on styles of monogenetic and polygenetic volcanism. *Journal of Geophysical Research: Solid Earth* (1978–2012) 99(B7):13563-13573
- Tentler T, Temperley S (2007) Magmatic fissures and their systems in Iceland: A tectonomagmatic model. *Tectonics* 26(5):TC5019
- Thomson K (2007) Determining magma flow in sills, dykes and laccoliths and their implications for sill emplacement mechanisms. *B Volcanol* 70(2):183-201
- Thordarson T, Self S (1993) The Laki (Skaftár Fires) and Grímsvötn eruptions in 1783–1785. *B Volcanol* 55(4):233-263
- Thordarson T, Self S, Oskarsson N, Hulsebosch T (1996) Sulfur, chlorine, and fluorine degassing and atmospheric loading by the 1783–1784 AD Laki (Skaftár Fires) eruption in Iceland. *B Volcanol* 58(2-3):205-225
- Thordarson T, Self S (1998) The Roza Member, Columbia River Basalt Group: A gigantic pahoehoe lava flow field formed by endogenous processes? *J. Geophys. Res.* 103(B11):27411-27445

- Thordarson T, Miller D, Larsen G, Self S, Sigurdsson H (2001) New estimates of sulfur degassing and atmospheric mass-loading by the 934 AD Eldgjá eruption, Iceland. *J Volcanol Geoth Res* 108(1):33-54
- Thordarson T, Larsen G (2007) Volcanism in Iceland in historical time: Volcano types, eruption styles and eruptive history. *Journal of Geodynamics* 43(1):118-152
- Valentine G, Cortés J (2013) Time and space variations in magmatic and phreatomagmatic eruptive processes at Easy Chair (Lunar Crater Volcanic Field, Nevada, USA). *B Volcanol* 75(9):1-13
- Valentine GA, Groves KR (1996) Entrainment of Country Rock during Basaltic Eruptions of the Lucero Volcanic Field, New Mexico. *The Journal of Geology* 104(1):71-90
- Valentine GA, Keating GN (2007) Eruptive styles and inferences about plumbing systems at Hidden Cone and Little Black Peak scoria cone volcanoes (Nevada, USA). *B Volcanol* 70(1):105-113
- Valentine GA, Gregg TKP (2008) Continental basaltic volcanoes — Processes and problems. *J Volcanol Geoth Res* 177(4):857-873
- Valentine GA (2012) Shallow plumbing systems for small-volume basaltic volcanoes, 2: Evidence from crustal xenoliths at scoria cones and maars. *J Volcanol Geoth Res* 223–224(0):47-63
- Walker RJ, Holdsworth RE, Armitage PJ, Faulkner DR (2013) Fault zone permeability structure evolution in basalts. *Geology* 41(1):59-62
- Watton TJ, Cannon S, Brown RJ, Jerram DA, Waichel BL (2014) Using formation micro-imaging, wireline logs and onshore analogues to distinguish volcanic lithofacies in boreholes: examples from Palaeogene successions in the Faroe–Shetland Basin, NE Atlantic. Geological Society, London, Special Publications 397
- White J, Bryan S, Ross P, Self S, Thordarson T (2009) Physical volcanology of continental large igneous provinces: update and review. *Studies in Volcanology: The Legacy of George Walker*. Special Publications of IAVCEI 2:291-321
- White JDL, Houghton BF (2006) Primary volcanoclastic rocks. *Geology* 34(8):677-680
- Wood CA (1980) Morphometric analysis of cinder cone degradation. *J Volcanol Geoth Res* 8(2):137-160
- Zanon V, Pacheco J, Pimentel A (2009) Growth and evolution of an emergent tuff cone: Considerations from structural geology, geomorphology and facies analysis of São Roque volcano, São Miguel (Azores). *J Volcanol Geoth Res* 180(2–4):277-291

Chapter 7: Summary

7.1 Summary and conclusions

Many flood basalt provinces host hydrocarbon reserves. These provinces are constructed as the result of multiple fissure eruptions. This thesis uses data from a dissected subaerial fissure and a submarine volcanic field to help recognise fissure-derived edifices in field, seismic and well data. These edifices are analogous to those produced high volume fissure eruptions. In addition, data from a newly-discovered rootless cone field is used to help distinguish these features from dyke-fed edifices. The edifices described have important implications for hydrocarbon basin development, architecture and fluid flow.

Chapter 3 details the internal architecture of a scoria-agglutinate cone, scoria and spatter ramparts, rootless cones and sheet-like fall deposits produced during a Holocene basaltic fissure eruption. These features formed as a result of variations in lava fountain intensity and lava-water interaction. They allow us to link processes observed in contemporary eruptions with preserved deposits, and inform on the early stages of the eruption which are commonly buried. The scoria-agglutinate cone, spatter ramparts and scoria ramparts have many similarities with edifices produced during high-volume eruptions, suggesting that flood basalt eruptions may also be associated with periods of Hawaiian-style activity. This supports the notion that flood basalt eruptions can be associated with a diversity of emplacement styles.

Chapter 4 provides insights into rootless eruption processes based on dissected tephra deposits and conduits. These eruptions result from explosive lava-water interaction beneath the host lava flow. I have also provided quantitative data on the rootless cone- and platform-building tephra successions, characterising the juvenile clasts and lava-sediment interaction textures that typify these deposits. My research has shown that rootless cones formed in the Columbia River Flood Basalt Province are analogous to rootless cones in Iceland. In both study areas, the explosivity decreases as surface water availability declines. This chapter also shows that juvenile clast morphology and clast density are useful criteria for distinguishing between rootless tephra and tephra generated above an erupting dyke.

Chapter 5 uses well data and exceptional quality 3D seismic data to detail the architecture of submarine basaltic edifices. These edifices are free from overlying basalt cover and are relatively young, making them ideal candidates to inform on the seismic facies and eruption processes that typify submarine monogenetic edifices. I identify three

types of edifice, including maar-diatreme complexes, pillow volcanoes and tuff cones. The edifices are shown to have evolved during a combination of effusive and explosive activity. The spatial relationship of the edifices with underlying lava flows suggests that monogenetic eruptions can be spatially linked over millions of years.

Chapter 8: Future Work

8.1 Directions for future work

Chapter 3 highlights the diversity of lavas and pyroclasts deposited in the fissure-proximal region. Better classifying the petrophysical properties of these deposits will enhance our understanding of the architecture of volcanic-affected basins. Lavas observed include shelly pāhoehoe, clastogenic pāhoehoe, lava-like agglutinate and spiny pāhoehoe. Currently, only hyaloclastite, compound and tabular flows are recognised in wireline data (Nelson et al. 2009). These facies are recognised by variations in P-wave velocity (V_p), a function of vesicularity (Nelson et al. 2009). Shelly pāhoehoe is characterised by vesicular crusts, likely giving them a low V_p response. The clastogenic lavas have variably vesicular cores and vesicular crusts, again likely giving them a low V_p response. Lava-like agglutinate is massive and incipiently vesicular, suggesting it would have a similar V_p response to the cores of tabular classic flows. Spiny pāhoehoe inflates (Guilbaud et al. 2005), thus has a similar internal structure to tabular classic flows. However, the flows described in Chapter 3 are often <10 m thick, suggesting they would be difficult to distinguish from similar-sized compound flows which have variable V_p responses (Nelson et al. 2009).

In order to recognise pyroclasts, it would be necessary to distinguish pyroclastic sequences from other primary volcanoclastic sequences such as hyaloclastite. Hyaloclastite can show spikes in Spectral Gamma Ray responses associated with foraminifera (Watton et al. 2014). Since these microfossils are deposited in a marine environment, they would be uncharacteristic of in-situ subaerial pyroclastic sequences. Hyaloclastite is also recognised by its uniform P-wave distribution (Nelson et al. 2009). However, hyaloclastite is highly variable in its density and componentry (Watton et al. 2013). Therefore, to distinguish pyroclastic sequences from hyaloclastite it would first be necessary to better classify the range of hyaloclastite facies.

Chapter 4 details the products of rootless eruptions. These can be initiated beneath ‘ā‘ā and pāhoehoe lava flows, as well beneath as the deposits of pyroclastic density currents (Moore and Ault 1965; Moyer and Swanson 1987; Fagents et al. 2002; Fagents and Thordarson 2007; Hamilton et al. 2010). Given that ‘ā‘ā lava flows and the deposits of density currents do not inflate, it is possible that rootless eruptions can result from both physical mixing and phreatic-type eruptions (e.g. Mastin 1995; Fagents and Thordarson 2007). However, the substrate beneath the site of rootless eruptions is not commonly exposed. Studies of the substrate may provide insights into the triggering mechanisms for

rootless explosions. It is likely that eruptions resulting from physical mixing preserve evidence of such processes beneath the lava flow, evidenced by peperite-like textures (e.g. Skilling et al. 2002; Hooten and Ort 2002). In contrast, those arising from phreatic-type eruptions may preserve “uncontaminated” sedimentary sequences, or volcanoclastic successions without evidence of molten lava-sediment mixing. Studies could also seek to identify other environmental settings in which rootless cones form (e.g. those without a compressible substrate, see Chapter 3). This would help understand the diversity of settings in which rootless eruptions occur, and better constrain the usefulness of rootless cones as indicators of underlying, water-saturated substrate.

Chapter 5 highlights the superficial similarity of volcanic and hydrothermal edifices in seismic data. Hydrothermal vents are dominated by sedimentary lithologies, but also contain volcanic rocks (e.g. Jamtveit et al. 2004). However, the source and fragmentation mechanism of this material is unknown. A better understanding of the genesis of the volcanic material would have implications for understanding the fragmentation and triggering mechanism for hydrothermal eruptions (e.g. phreatic or MFCI). This could have important implications for understanding the early stages of volcanic activity in rift basins (e.g. Planke et al. 2005).

8.2 References

- Fagents SA, Lanagan P, Greeley R (2002) Rootless cones on Mars: a consequence of lava-ground ice interaction. *Geological Society, London, Special Publications* 202(1):295-317
- Fagents SA, Thordarson T (2007) Rootless cones in Iceland and on Mars. In: Chapman M, Skilling IP (eds) *The Geology of Mars: Evidence from Earth-Based Analogues*. Cambridge University Press, pp 151–177
- Guilbaud M-N, Self S, Thordarson T, Blake S (2005) Morphology, surface structures, and emplacement of lavas produced by Laki, A.D. 1783–1784. *Geological Society of America Special Papers* 396:81-102
- Hamilton CW, Thordarson T, Fagents SA (2010) Explosive lava–water interactions I: architecture and emplacement chronology of volcanic rootless cone groups in the 1783–1784 Laki lava flow, Iceland. *B Volcanol* 72(4):449-467
- Hooten J, Ort M (2002) Peperite as a record of early-stage phreatomagmatic fragmentation processes: an example from the Hopi Buttes volcanic field, Navajo Nation, Arizona, USA. *J Volcanol Geoth Res* 114(1):95-106
- Jamtveit B, Svensen H, Podladchikov YY, Planke S (2004) Hydrothermal vent complexes associated with sill intrusions in sedimentary basins. *Physical geology of high-level magmatic systems* 234:233-241
- Mastin LG (1995) Thermodynamics of gas and steam-blast eruptions. *B Volcanol* 57(2):85-98
- Moore JG, Ault WU (1965) Historic littoral cones in Hawaii. *Pacific science* XIX(3-11)
- Moyer TC, Swanson DA (1987) Secondary hydroeruptions in pyroclastic-flow deposits: Examples from Mount St. Helens. *J Volcanol Geoth Res* 32(4):299-319
- Nelson CE, Jerram DA, Hobbs RW (2009) Flood basalt facies from borehole data: implications for prospectivity and volcanology in volcanic rifted margins. *Petroleum Geoscience* 15(4):313-324

Planke S, Rasmussen T, Rey SS, Myklebust R (2005) Seismic characteristics and distribution of volcanic intrusions and hydrothermal vent complexes in the Vøring and Møre basins. Geological Society, London, Petroleum Geology Conference series 6:833-844

Skilling IP, White JDL, McPhie J (2002) Peperite: a review of magma–sediment mingling. J Volcanol Geoth Res 114(1–2):1-17

Watton TJ, Jerram DA, Thordarson T, Davies RJ (2013) Three-dimensional lithofacies variations in hyaloclastite deposits. J Volcanol Geoth Res 250(0):19-33

Watton TJ, Cannon S, Brown RJ, Jerram DA, Waichel BL (2014) Using formation micro-imaging, wireline logs and onshore analogues to distinguish volcanic lithofacies in boreholes: examples from Palaeogene successions in the Faroe–Shetland Basin, NE Atlantic. Geological Society, London, Special Publications 397

Appendix 1: Support Material for Chapter 3

fault number	strike	dip	fault number	strike	dip	fault number	strike	dip	fault number	strike	dip
XA	010	75	13	031	78	31	195	42	9	014	80
F0	191	85	17	007	85	32	047	42	5	187	75
1	191	85	19	190	78	33	037	80	6	182	85
2	008	70	20	011	79	38	008	75	21	193	85
4	010	75									

Table A1.1. Orientations of faults.

waSc	glass	microlite	pyx	olv	lithic	total	matrix crystallinity %
count	734	20	17	1	28	800	4.922
%	91.7	2.5	2.1	0.1	3.5		
dwSp	glass	microlite	pyx	olv	glass		86.1
count	12	181	508	0	99	800	
%	1.5	22.6	63.5	0	12.3		
mwSp	microlite	pyx	glass	glass			
count	171	447	168	14		800	77.1
%	21.3	55.8	21	1.7			
waSp	glass	microlite	pyx	olv			
count	419	302	77	2		800	47.5
%	52.3	37.7	9.6	0.2			
ScL	glass	microlite	pyx	olv			
count	391	8	1	0		400	2.25
L-l Agg	97.75	2	0.25	0			
l-l Agg	glass	microlite	pyx	olv			
count	198	219	381	2		800	75.25
%	24.75	27.375	47.625	0.25			
dwSc	glass	microlite	pyx	olv			
count	735	46	19	0		800	
	91.8	5.7	2.3	0			8
mwSc	glass	microlite	pyx	olv	plag		
count	752	28	10	0	10	800	
	94	3.5	1.2	0	1.2		5.9
Cl	pyx	feld	glass	oxides			
count	474	206	117	3		800	
	59.2	25.7	14.6	0.3			84.9
dyke	feld	pyx	glass	olv			

count	140	546	111	3			
	17.5	68.2	13.8	0.3		800	86
mSc	feld	pyx	glass	olv			
count	96	8	696	0			
%	12	1	87	0		800	13
Table A1.2. Point count data for lithofacies.							

Total unit thickness (mm)	Platy zone spacing (mm)	mean spacing (mm)
12	13.45454545	7950
30		
14		
6		
7		
10		
12		
17		
14		
21		
5		
Table A1.3. Measurements of platy zone in columnar basalt, log 14, unit 4.		

Platy zone spacing (mm)	mean spacing (mm)	Total unit thickness (mm)
65	82.22222222	1700
55		
70		
75		
30		
90		
110		
60		
60		
190		
Table A1.4. Measurements of platy zone in columnar basalt, Log 30, unit 1.		

Platy zone spacing (mm)	Platy zone spacing (mm)	mean spacing (mm)	Total unit thickness (mm)
25	30	29.83333333	2300
34	29		
30	16		
35	69		
10	65		
45	12		
25	16		
20	46		
54	10		
22	42		
11	10		
45	14		
25	16		
34	30		
30			
45			
Table A1.5. Measurements of platy zone in columnar basalt, Log 12, unit 11.			

number	Wc air				Wc+s water			Ws water	Wc water	SG	DENSITY kg m ⁻³	density sorted	density mean of 90
	dry uncoated	coated	wet	ballast wet	clast wet	sheet dry weight	sheet %	sheet wet weight (g)	clast wet no sheet				
1	12.06	13.42	12.24	15.78	-3.54	1.36	10.13413	-0.358748137	-3.181251863	0.791274	791.2735849	623.2091691	1007.045387
2	21.77	23.06	8.12	15.78	-7.66	1.29	5.594102	-0.428508239	-7.231491761	0.750651	750.6510417	634.7634763	stdev
3	5.73	6.72	13.07	15.78	-2.71	0.99	14.73214	-0.399241071	-2.310758929	0.712619	712.6193001	685.3932584	192.7530006
4	13.45	14.52	18.95	15.78	3.17	1.07	7.369146	0.233601928	2.936398072	1.279295	1279.295154	712.6193001	
5	14.42	15.55	16.1	15.78	0.32	1.13	7.266881	0.023254019	0.296745981	1.021011	1021.011162	720	mean of 50
6	14.94	16.03	14.73	15.78	-1.05	1.09	6.79975	-0.07139738	-0.97860262	0.938525	938.5245902	729.8787211	1005.700428
7	8.78	9.59	14.27	15.78	-1.51	0.81	8.446298	-0.127539103	-1.382460897	0.863964	863.963964	750.6510417	stdev
8	6.98	7.67	15.16	15.78	-0.62	0.69	8.996089	-0.05577575	-0.56422425	0.925211	925.2110977	788.91258	189.3211468
9	4.57	5.05	14.67	15.78	-1.11	0.48	9.50495	-0.10550495	-1.00449505	0.819805	819.8051948	790.2511078	
10	13.66	14.48	19.55	15.78	3.77	0.82	5.662983	0.213494475	3.556505525	1.352007	1352.00747	791.2735849	mean of 30
11	9.7	10.86	15.11	15.78	-0.67	1.16	10.6814	-0.071565378	-0.598434622	0.941891	941.8907199	796.1165049	993.1854134
12	10.36	11.17	16.73	15.78	0.95	0.81	7.251567	0.068889884	0.881110116	1.092955	1092.95499	806.4516129	st dev
13	7.63	8.26	14.66	15.78	-1.12	0.63	7.627119	-0.085423729	-1.034576271	0.880597	880.5970149	807.0866142	214.3864122
14	8.26	8.82	12.35	15.78	-3.43	0.56	6.349206	-0.217777778	-3.212222222	0.72	720	811.5653041	
15	10.05	10.62	17.62	15.78	1.84	0.57	5.367232	0.098757062	1.741242938	1.209567	1209.567198	811.9001919	vesic
16	12.28	12.87	16.6	15.78	0.82	0.59	4.584305	0.037591298	0.782408702	1.06805	1068.049793	812.2119816	66.4766524
17	6.82	7.4	13.8	15.78	-1.98	0.58	7.837838	-0.155189189	-1.824810811	0.788913	788.91258	819.3717277	79.23333333
18	5.62	6.15	14.31	15.78	-1.47	0.53	8.617886	-0.126682927	-1.343317073	0.807087	807.0866142	819.8051948	51.13333333
19	15.84	16.47	19.55	15.78	3.77	0.63	3.825137	0.14420765	3.62579235	1.29685	1296.850394	821.0639441	
20	9.62	10.2	16.83	15.78	1.05	0.58	5.686275	0.059705882	0.990294118	1.114754	1114.754098	825.8212376	
21	11.29	12.15	14.95	15.78	-0.83	0.86	7.078189	-0.058748971	-0.771251029	0.936055	936.05547	839.348903	
22	8.37	8.72	14.63	15.78	-1.15	0.35	4.013761	-0.046158257	-1.103841743	0.883485	883.485309	841.7266187	
23	13.26	13.82	18.68	15.78	2.9	0.56	4.052098	0.117510854	2.782489146	1.265568	1265.567766	859.2132505	
24	17.61	18.21	20.53	15.78	4.75	0.6	3.294893	0.156507414	4.593492586	1.352897	1352.897474	861.0763454	
25	13.44	14.13	18.38	15.78	2.6	0.69	4.883227	0.126963907	2.473036093	1.225499	1225.498699	863.67713	
26	10.01	10.81	13.5	15.78	-2.28	0.8	7.400555	-0.168732655	-2.111267345	0.825821	825.8212376	863.963964	
27	5.11	5.77	12.46	15.78	-3.32	0.66	11.43847	-0.379757366	-2.940242634	0.634763	634.7634763	866.1242604	
28	15.01	15.71	13.41	15.78	-2.37	0.7	4.455761	-0.105601528	-2.264398472	0.868916	868.9159292	868.9159292	
29	15.29	15.78	19.31	15.78	3.53	0.49	3.105196	0.109613435	3.420386565	1.288163	1288.163265	871.4285714	
30	7.41	7.93	16.75	15.78	0.97	0.52	6.557377	0.063606557	0.906393443	1.139368	1139.367816	880.5970149	
31	10	10.7	12.94	15.78	-2.84	0.7	6.542056	-0.185794393	-2.654205607	0.790251	790.2511078	883.485309	
32	11.2	11.88	14.35	15.78	-1.43	0.68	5.723906	-0.081851852	-1.348148148	0.892562	892.5619835	892.5619835	
33	20.03	20.74	20.58	15.78	4.8	0.71	3.423337	0.164320154	4.635679846	1.301129	1301.129235	913.9344262	
34	16.95	17.59	15.79	15.78	0.01	0.64	3.638431	0.000363843	0.009636157	1.000569	1000.568828	914.3730887	
35	13.5	14.1	17.67	15.78	1.89	0.6	4.255319	0.080425532	1.809574468	1.154791	1154.791155	925.2110977	
36	22.79	23.41	18.72	15.78	2.94	0.62	2.648441	0.077864161	2.862135839	1.143625	1143.624817	935.483871	
37	10.25	10.98	14.16	15.78	-1.62	0.73	6.648452	-0.107704918	-1.512295082	0.871429	871.4285714	936.05547	
38	13.43	14.03	18.48	15.78	2.7	0.6	4.27655	0.115466857	2.584533143	1.238305	1238.305384	938.4449244	

39	13.43	14.05	16.92	15.78	1.14	0.62	4.412811	0.05030605	1.08969395	1.088304	1088.303641	938.5245902	
40	10.22	10.84	15.97	15.78	0.19	0.62	5.719557	0.010867159	0.179132841	1.01784	1017.840376	941.8907199	
41	4.02	4.46	15.36	15.78	-0.42	0.44	9.865471	-0.041434978	-0.378565022	0.913934	913.9344262	956.2101911	
42	5.46	5.98	15.22	15.78	-0.56	0.52	8.695652	-0.048695652	-0.511304348	0.914373	914.3730887	967.1574179	
43	6.42	6.82	16.25	15.78	0.47	0.4	5.865103	0.027565982	0.442434018	1.074016	1074.015748	980.5886036	
44	6.25	7.05	14.15	15.78	-1.63	0.8	11.34752	-0.184964539	-1.445035461	0.812212	812.2119816	984.9219171	
45	11.71	12.32	15.62	15.78	-0.16	0.61	4.951299	-0.007922078	-0.152077922	0.987179	987.1794872	987.1794872	
46	20.22	21.02	19.25	15.78	3.47	0.8	3.805899	0.1320647	3.3379353	1.197721	1197.720798	987.2611465	
47	7.09	9.63	14.26	15.78	-1.52	2.54	26.37591	-0.400913811	-1.119086189	0.863677	863.67713	1000.568828	
48	13.49	13.92	16.94	15.78	1.16	0.43	3.08908	0.035833333	1.124166667	1.090909	1090.909091	1017.840376	
49	11.18	11.8	17.49	15.78	1.71	0.62	5.254237	0.089847458	1.620152542	1.169475	1169.474727	1021.011162	
50	8.02	8.54	15.49	15.78	-0.29	0.52	6.088993	-0.01765808	-0.27234192	0.967157	967.1574179	1025.929127	
51	11.36	11.85	16.12	15.78	0.34	0.49	4.135021	0.014059072	0.325940928	1.02954	1029.539531	1027.681661	
52	9.38	9.75	16.14	15.78	0.36	0.37	3.794872	0.013661538	0.346338462	1.038339	1038.338658	1029.539531	
53	7.57	8.3	14.42	15.78	-1.36	0.73	8.795181	-0.119614458	-1.240385542	0.859213	859.2132505	1038.338658	
54	7.18	7.75	13.92	15.78	-1.86	0.57	7.354839	-0.1368	-1.7232	0.806452	806.4516129	1047.012733	
55	11.3	12.01	15.23	15.78	-0.55	0.71	5.91174	-0.032514571	-0.517485429	0.95621	956.2101911	1068.049793	
56	11.23	11.88	16.1	15.78	0.32	0.65	5.47138	0.017508418	0.302491582	1.027682	1027.681661	1074.015748	
57	17.03	17.63	19.09	15.78	3.31	0.6	3.40329	0.112648894	3.197351106	1.231145	1231.145251	1077.887198	
58	10.97	11.6	14.98	15.78	-0.8	0.63	5.431034	-0.043448276	-0.756551724	0.935484	935.483871	1081.166273	
59	13.98	14.83	19.6	15.78	3.82	0.85	5.731625	0.218948078	3.601051922	1.346957	1346.957312	1082.106894	
60	6.17	6.88	14.67	15.78	-1.11	0.71	10.31977	-0.114549419	-0.995450581	0.861076	861.0763454	1088.303641	
61	15.42	16.12	18.85	15.78	3.07	0.7	4.342432	0.133312655	2.936687345	1.235249	1235.249042	1090.909091	
62	13.3	13.97	16.84	15.78	1.06	0.67	4.795991	0.050837509	1.009162491	1.082107	1082.106894	1092.95499	
63	14.71	15.52	20.49	15.78	4.71	0.81	5.219072	0.245818299	4.464181701	1.435708	1435.707678	1103.673469	
64	13.42	14.22	17.42	15.78	1.64	0.8	5.625879	0.092264416	1.547735584	1.130366	1130.36566	1114.754098	
65	10.83	11.87	16.08	15.78	0.3	1.04	8.761584	0.026284751	0.273715249	1.025929	1025.929127	1130.36566	
66	12.79	13.72	16.81	15.78	1.03	0.93	6.778426	0.069817784	0.960182216	1.081166	1081.166273	1139.367816	
67	14.55	15.28	12.45	15.78	-3.33	0.73	4.777487	-0.159090314	-3.170909686	0.821064	821.0639441	1143.624817	
68	9.94	10.69	16.26	15.78	0.48	0.75	7.015903	0.033676333	0.446323667	1.047013	1047.012733	1154.791155	
69	12.78	13.52	17.05	15.78	1.27	0.74	5.473373	0.069511834	1.200488166	1.103673	1103.673469	1169.474727	
70	6.6	7.32	12.42	15.78	-3.36	0.72	9.836066	-0.330491803	-3.029508197	0.685393	685.3932584	1176.591376	
71	17.68	18.29	15.5	15.78	-0.28	0.61	3.335156	-0.009338436	-0.270661564	0.984922	984.9219171	1187.977099	
72	11.13	11.86	13.51	15.78	-2.27	0.73	6.155143	-0.139721754	-2.130278246	0.839349	839.348903	1197.720798	
73	8.05	8.7	10.52	15.78	-5.26	0.65	7.471264	-0.392988506	-4.867011494	0.623209	623.2091691	1209.567198	
74	8.6	9.39	13.71	15.78	-2.07	0.79	8.413206	-0.174153355	-1.895846645	0.819372	819.3717277	1213.496933	
75	5.86	6.62	13.33	15.78	-2.45	0.76	11.48036	-0.281268882	-2.168731118	0.729879	729.8787211	1225.498699	
76	10.63	11.46	17.5	15.78	1.72	0.83	7.242583	0.124572426	1.595427574	1.176591	1176.591376	1227.321238	
77	10.84	11.71	13.97	15.78	-1.81	0.87	7.429547	-0.134474808	-1.675525192	0.866124	866.1242604	1228.571429	
78	7.63	8.14	13.89	15.78	-1.89	0.51	6.265356	-0.118415233	-1.771584767	0.811565	811.5653041	1231.145251	
79	10.99	11.61	17.94	15.78	2.16	0.62	5.340224	0.115348837	2.044651163	1.228571	1228.571429	1235.249042	
80	8.51	9.36	14.02	15.78	-1.76	0.85	9.081197	-0.15982906	-1.60017094	0.841727	841.7266187	1238.305384	
81	9.12	9.84	13.26	15.78	-2.52	0.72	7.317073	-0.184390244	-2.335609756	0.796117	796.1165049	1265.567766	
82	18.88	19.78	19.26	15.78	3.48	0.9	4.550051	0.158341759	3.321658241	1.213497	1213.496933	1279.295154	
83	7.82	8.46	13.82	15.78	-1.96	0.64	7.565012	-0.148274232	-1.811725768	0.8119	811.9001919	1288.163265	

84	8.55	9.3	15.66	15.78	-0.12	0.75	8.064516	-0.009677419	-0.110322581	0.987261	987.2611465	1296.850394	
85	7.88	8.69	15.21	15.78	-0.57	0.81	9.321059	-0.053130035	-0.516869965	0.938445	938.4449244	1301.129235	
86	14.89	15.66	15.47	15.78	-0.31	0.77	4.916986	-0.015242656	-0.294757344	0.980589	980.5886036	1346.957312	
87	11.3	12.04	16.65	15.78	0.87	0.74	6.146179	0.053471761	0.816528239	1.077887	1077.887198	1352.00747	
88	20	20.89	22.43	15.78	6.65	0.89	4.260412	0.283317377	6.366682623	1.466994	1466.994382	1352.897474	
89	10.63	11.5	17.91	15.78	2.13	0.87	7.565217	0.16113913	1.96886087	1.227321	1227.321238	1435.707678	
90	11.94	12.45	17.75	15.78	1.97	0.51	4.096386	0.080698795	1.889301205	1.187977	1187.977099	1466.994382	
Table A1.6. Density measurements for waSp.													

number				Wc+s water			Ws water	Wc water	SG	DENSITY kg m^-3	density sorted	density range	density mean of 90
				clast wet	sheet dry weight	sheet %	sheet wet weight (g)	clast wet no sheet					
1	16.3	16.75	9.07	9.07	0.45	2.686567	0.243671642	8.826328358	2.18099	2180.989583	1374.331551	1374	1835.79601
2	12.86	13.2	6.15	6.15	0.34	2.575758	0.158409091	5.991590909	1.87234	1872.340426	1459.71564	2218	208.2805532
3	13.04	13.33	7.08	7.08	0.29	2.175544	0.154028507	6.925971493	2.1328	2132.8	1470.760234		
4	14.45	14.72	7.32	7.32	0.27	1.834239	0.134266304	7.185733696	1.989189	1989.189189	1473.537604		mean of 50
5	12.4	12.73	4.81	4.81	0.33	2.592302	0.124689709	4.685310291	1.607323	1607.323232	1492.783505		1835.79601
6	15.41	15.87	5.1	5.1	0.46	2.898551	0.147826087	4.952173913	1.473538	1473.537604	1548.75717		stdev
7	13.18	13.46	5.34	5.34	0.28	2.080238	0.111084695	5.228915305	1.657635	1657.635468	1551.214361		207.7034687
8	14.94	15.44	6.47	6.47	0.5	3.238342	0.209520725	6.260479275	1.721293	1721.2932	1581.294964		
9	29.49	30.02	13.8	13.8	0.53	1.76549	0.243637575	13.55636243	1.850801	1850.80148	1582.371459		mean of 30
10	21.24	21.85	10.76	10.76	0.61	2.791762	0.300393593	10.45960641	1.970243	1970.243463	1607.323232		1880.072076
11	10.93	11.22	4.89	4.89	0.29	2.58467	0.126390374	4.763609626	1.772512	1772.511848	1657.635468		st dev
12	27.18	27.7	13.75	13.75	0.52	1.877256	0.258122744	13.49187726	1.985663	1985.663082	1675.115207		207.7316072
13	14.37	14.63	7.16	7.16	0.26	1.77717	0.127245386	7.032754614	1.958501	1958.500669	1700.205339		
14	20.15	20.62	10.35	10.35	0.47	2.27934	0.235911736	10.11408826	2.00779	2007.789679	1709.849157		vesic
15	25.99	26.33	12.67	12.67	0.34	1.291303	0.163608052	12.50639195	1.927526	1927.525622	1721.2932		38.80679965
16	9.94	10.27	5.64	5.64	0.33	3.213242	0.181226874	5.458773126	2.218143	2218.142549	1738.317757		54.2
17	29.31	29.7	14.46	14.46	0.39	1.313131	0.189878788	14.27012121	1.948819	1948.818898	1772.511848		26.06666667
18	17.34	17.64	8.86	8.86	0.3	1.70068	0.150680272	8.709319728	2.009112	2009.111617	1773.672055		
19	6.88	7.24	2.39	2.39	0.36	4.972376	0.118839779	2.271160221	1.492784	1492.783505	1775.655022		
20	6.77	7.07	3.16	3.16	0.3	4.243281	0.134087694	3.025912306	1.808184	1808.184143	1801.438849		
21	14.73	14.92	7.22	7.22	0.19	1.273458	0.0919437	7.1280563	1.937662	1937.662338	1802.904564		
22	17.27	17.38	7.74	7.74	0.11	0.632911	0.048987342	7.691012658	1.802905	1802.904564	1808.184143		
23	14.55	15.08	5.55	5.55	0.53	3.514589	0.195059682	5.354940318	1.582371	1582.371459	1850.80148		
24	13.33	13.62	6.75	6.75	0.29	2.129222	0.143722467	6.606277533	1.982533	1982.532751	1870.198675		
25	19.06	19.33	10.41	10.41	0.27	1.396793	0.145406105	10.2645939	2.16704	2167.040359	1872.340426		
26	15.85	16.15	8.14	8.14	0.3	1.857585	0.15120743	7.98879257	2.01623	2016.229713	1874.055416		
27	9.79	10.06	3.22	3.22	0.27	2.683897	0.086421471	3.133578529	1.47076	1470.760234	1887.675507		
28	11.81	12.1	5.69	5.69	0.29	2.396694	0.136371901	5.553628099	1.887676	1887.675507	1924.348379		

29	7.15	7.44	3.47	3.47	0.29	3.897849	0.135255376	3.334744624	1.874055	1874.055416	1926.486486		
30	11.55	11.82	6.18	6.18	0.27	2.284264	0.141167513	6.038832487	2.095745	2095.744681	1927.525622		
31	17.42	17.82	8.57	8.57	0.4	2.244669	0.192368126	8.377631874	1.926486	1926.486486	1935.135135		
32	31.9	32.53	14.21	14.21	0.63	1.936674	0.275201353	13.93479865	1.775655	1775.655022	1937.662338		
33	13.66	13.95	7.08	7.08	0.29	2.078853	0.147182796	6.932817204	2.030568	2030.567686	1948.324022		
34	13.72	14.12	6.57	6.57	0.4	2.832861	0.18611898	6.38388102	1.870199	1870.198675	1948.818898		
35	15.08	15.36	6.7	6.7	0.28	1.822917	0.122135417	6.577864583	1.773672	1773.672055	1958.500669		
36	15.02	15.4	4.85	4.85	0.38	2.467532	0.119675325	4.730324675	1.459716	1459.71564	1970.243463		
37	24.56	25.04	11.14	11.14	0.48	1.916933	0.213546326	10.92645367	1.801439	1801.438849	1982.532751		
38	18.82	19.27	8	8	0.45	2.335236	0.186818889	7.813181111	1.709849	1709.849157	1985.663082		
39	14.38	14.69	5.22	5.22	0.31	2.110279	0.110156569	5.109843431	1.551214	1551.214361	1989.189189		
40	6.91	7.16	3.46	3.46	0.25	3.49162	0.120810056	3.339189944	1.935135	1935.135135	2007.789679		
41	13.71	13.95	6.79	6.79	0.24	1.72043	0.116817204	6.673182796	1.948324	1948.324022	2009.111617		
42	9.65	9.91	5	5	0.26	2.623613	0.131180626	4.868819374	2.01833	2018.329939	2016.229713		
43	9.35	9.61	4.91	4.91	0.26	2.705515	0.132840791	4.777159209	2.044681	2044.680851	2018.329939		
44	7.4	7.71	2.1	2.1	0.31	4.020752	0.084435798	2.015564202	1.374332	1374.331551	2030.567686		
45	10.71	10.99	4.04	4.04	0.28	2.547771	0.102929936	3.937070064	1.581295	1581.294964	2044.680851		
46	16.32	16.56	6.82	6.82	0.24	1.449275	0.09884058	6.72115942	1.700205	1700.205339	2095.744681		
47	7.19	7.44	3.16	3.16	0.25	3.360215	0.106182796	3.053817204	1.738318	1738.317757	2132.8		
48	7	7.27	2.93	2.93	0.27	3.713893	0.108817056	2.821182944	1.675115	1675.115207	2167.040359		
49	7.8	8.1	2.87	2.87	0.3	3.703704	0.106296296	2.763703704	1.548757	1548.75717	2180.989583		
50	29.83	30.27	14.54	14.54	0.44	1.453584	0.211351173	14.32864883	1.924348	1924.348379	2218.142549		
51	25.64	26.13	13.63	13.63	0.49	1.875239	0.255595101	13.3744049	2.0904	2090.4			
52	26.33	26.92	12.61	12.61	0.59	2.191679	0.276370728	12.33362927	1.881202	1881.201957			
53	20.99	21.33	10.72	10.72	0.34	1.593999	0.170876699	10.5491233	2.010368	2010.367578			
54	19.16	19.61	8.26	8.26	0.45	2.294748	0.18954615	8.07045385	1.727753	1727.753304			
55	16.07	16.45	7.24	7.24	0.38	2.31003	0.167246201	7.072753799	1.786102	1786.102063			
56	14.54	14.91	7.59	7.59	0.37	2.481556	0.188350101	7.401649899	2.036885	2036.885246			
57	22.12	22.52	11.01	11.01	0.4	1.776199	0.195559503	10.8144405	1.95656	1956.559513			
58	17.32	17.69	8.4	8.4	0.37	2.091577	0.175692482	8.224307518	1.904198	1904.198062			
59	14.2	14.52	5.86	5.86	0.32	2.203857	0.129146006	5.730853994	1.676674	1676.674365			
60	16.11	16.4	6.84	6.84	0.29	1.768293	0.12095122	6.71904878	1.715481	1715.481172			
61	17.39	17.75	8.18	8.18	0.36	2.028169	0.165904225	8.014095775	1.854754	1854.754441			
62	18.42	18.94	6.25	6.25	0.52	2.745512	0.171594509	6.078405491	1.492514	1492.51379			
63	13.45	13.75	6.31	6.31	0.3	2.181818	0.137672727	6.172327273	1.848118	1848.11828			
64	16.65	16.94	8.13	8.13	0.29	1.711924	0.139179457	7.990820543	1.922815	1922.814983			
65	15.46	15.8	8.48	8.48	0.34	2.151899	0.182481013	8.297518987	2.15847	2158.469945			
66	22.69	23.12	12.43	12.43	0.43	1.859862	0.231180796	12.1988192	2.162769	2162.768943			
67	20.16	20.63	8.71	8.71	0.47	2.278236	0.198434319	8.511565681	1.730705	1730.704698			
68	14.27	14.56	6.98	6.98	0.29	1.991758	0.139024725	6.840975275	1.920844	1920.844327			
69	19.42	19.73	9.63	9.63	0.31	1.571211	0.151307653	9.478692347	1.953465	1953.465347			
70	14.05	14.32	6.2	6.2	0.27	1.885475	0.116899441	6.083100559	1.763547	1763.546798			
71	11.82	12.11	5.79	5.79	0.29	2.394715	0.138654005	5.651345995	1.916139	1916.139241			
72	8.32	8.61	3.87	3.87	0.29	3.368177	0.130348432	3.739651568	1.816456	1816.455696			
73	17.63	17.89	9.42	9.42	0.26	1.453326	0.136903298	9.283096702	2.112161	2112.160567			

74	16.48	16.75	8.4	8.4	0.27	1.61194	0.135402985	8.264597015	2.005988	2005.988024			
75	9.18	9.46	3.95	3.95	0.28	2.959831	0.116913319	3.833086681	1.716878	1716.878403			
76	16.75	17.04	9.48	9.48	0.29	1.701878	0.161338028	9.318661972	2.253968	2253.968254			
77	15.41	15.71	8.34	8.34	0.3	1.909612	0.159261617	8.180738383	2.131615	2131.614654			
78	26.9	27.48	14.2	14.2	0.58	2.110626	0.299708879	13.90029112	2.069277	2069.277108			
79	20.39	20.73	9.56	9.56	0.34	1.640135	0.156796913	9.403203087	1.855864	1855.863921			
80	21.65	22.12	11.85	11.85	0.47	2.124774	0.251785714	11.59821429	2.153846	2153.846154			
81	34.4	34.85	8.57	8.57	0.45	1.291248	0.110659971	8.459340029	1.326104	1326.103501			
82	23.79	24.17	11.08	11.08	0.38	1.572197	0.174199421	10.90580058	1.846448	1846.44767			
83	14.06	14.38	5.19	5.19	0.32	2.225313	0.115493741	5.074506259	1.564744	1564.744287			
84	14.65	15.05	5.9	5.9	0.4	2.657807	0.156810631	5.743189369	1.644809	1644.808743			
85	25.02	25.48	13.1	13.1	0.46	1.805338	0.236499215	12.86350078	2.058158	2058.15832			
86	17.7	18.15	7.83	7.83	0.45	2.479339	0.194132231	7.635867769	1.758721	1758.72093			
87	17.43	17.85	7.13	7.13	0.42	2.352941	0.167764706	6.962235294	1.665112	1665.11194			
88	17.6	18.01	8.36	8.36	0.41	2.276513	0.190316491	8.169683509	1.866321	1866.321244			
89	25.6	26.03	12.96	12.96	0.43	1.65194	0.214091433	12.74590857	1.991584	1991.58378			
90	9.81	10.1	3.28	3.28	0.29	2.871287	0.094178218	3.185821782	1.480938	1480.938416			
Table A1.7. Density measurements for mwSp.													

number						Wc+s water			Ws water	Wc water	SG	DENSITY kg m^-3		density range	density mean of 90
				ballast dry	ballast wet	clast wet	sheet dry weight	sheet %	sheet wet weight (g)	clast wet no sheet					
1	27. 77	28.0 4	18.0 1			18.01	0.27	0.96291	0.173420114	17.83657989	2.79561 3	2795.613161	2461.02449 9	2461.02449 9	2680.640285
2	23. 66	23.9 5	15.6 8			15.68	0.29	1.21085 6	0.189862213	15.49013779	2.89601	2896.009674	2533.61344 5	2964	stdev
3	24. 14	24.4 4	15.9 1			15.91	0.3	1.22749 6	0.195294599	15.7147054	2.86518 2	2865.181712	2565.21739 1		118.0170483
4	19. 65	19.9	12.6 1			12.61	0.25	1.25628 1	0.158417085	12.45158291	2.72976 7	2729.766804	2566.55844 2		
5	24. 71	25.0 5	16.9 7			16.97	0.34	1.35728 5	0.230331337	16.73966866	3.10024 8		2590.72978 3		mean of 50
6	17. 72	17.9 5	11.6 3			11.63	0.23	1.28133 7	0.149019499	11.4809805	2.84019	2840.189873	2590.73842 3		2751.971105
7	14. 7	14.9 2	9.77			9.77	0.22	1.47453 1	0.144061662	9.625938338	2.89708 7	2897.087379	2597.96672 8		stdev
8	15. 69	16	10.2 7			10.27	0.31	1.9375	0.19898125	10.07101875	2.79232 1	2792.321117	2621.66962 7		117.3245864
9	13. 47	13.7 6	8.84			8.84	0.29	2.10755 8	0.18630814	8.65369186	2.79674 8	2796.747967	2626.24035 3		
10	14. 69	14.9 8	9.62			9.62	0.29	1.93591 5	0.18623498	9.43376502	2.79477 6	2794.776119	2626.30792 2		mean of 30
11	12. 9	13.2 2	8.71			8.71	0.32	2.42057 5	0.210832073	8.499167927	2.93126 4	2931.263858	2655.17241 4		2790.214219

12	11.89	12.18	8.13			8.13	0.29	2.380952	0.193571429	7.936428571	3.007407		2656.716418		stdev
13	13.54	13.06	8.43			8.43	-0.48	-3.67534	-0.309831547	8.739831547	2.820734	2820.734341	2664.605873		83.9472812
14	12.8	13.08	8.43			8.43	0.28	2.140673	0.180458716	8.249541284	2.812903	2812.903226	2666.015625		
15	17.7	17.99	11.67			11.67	0.29	1.612007	0.188121178	11.48187882	2.846519	2846.518987	2669.030733		vesic
16	9.98	10.26	6.59			6.59	0.28	2.729045	0.179844055	6.410155945	2.79564	2795.640327	2689.612015		10.64532383
17	9.99	10.26	6.58			6.58	0.27	2.631579	0.173157895	6.406842105	2.788043	2788.043478	2692.307692		17.96585004
18	13.31	13.62	8.63			8.63	0.31	2.276065	0.196424376	8.433575624	2.729459	2729.458918	2704.866562		1.2
19	8.81	9.1	5.72			5.72	0.29	3.186813	0.182285714	5.537714286	2.692308	2692.307692	2716.755319		
20	10.9	11.29	7.06			7.06	0.39	3.454384	0.243879539	6.816120461	2.669031	2669.030733	2723.642173		
21	20.13	20.43	12.91			12.91	0.3	1.468429	0.189574156	12.72042584	2.716755	2716.755319	2724.233983		
22	16.74	17.05	10.79			10.79	0.31	1.818182	0.196181818	10.59381818	2.723642	2723.642173	2729.198185		
23	17.74	18.04	11.43			11.43	0.3	1.662971	0.190077605	11.23992239	2.729198	2729.198185	2729.458918		
24	14.77	15.02	9.69			9.69	0.25	1.664447	0.161284953	9.528715047	2.818011	2818.011257	2729.766804		
25	22.4	22.7	14.52			14.52	0.3	1.321586	0.191894273	14.32810573	2.775061	2775.061125	2734.581498		
26	13.34	13.65	8.53			8.53	0.31	2.271062	0.193721612	8.336278388	2.666016	2666.015625	2765.847348		
27	18.43	18.59	12.32			12.32	0.16	0.860678	0.106035503	12.2139645	2.964912	2964.912281	2775.061125		
28	18.7	19.02	12.24			12.24	0.32	1.68244	0.205930599	12.0340694	2.80531	2805.309735	2786.68942		
29	25.89	26.27	16.13			16.13	0.38	1.446517	0.233323182	15.89667682	2.59073	2590.729783	2788.043478		
30	22.32	22.6	14.65			14.65	0.28	1.238938	0.181504425	14.46849558	2.842767	2842.767296	2792.321117		
31	16.05	16.33	10.47			10.47	0.28	1.714636	0.179522352	10.29047765	2.786689	2786.68942	2794.776119		
32	21.09	21.38	13.65			13.65	0.29	1.356408	0.185149673	13.46485033	2.765847	2765.847348	2795.613161		
33	20.94	21.25	13.8			13.8	0.31	1.458824	0.201317647	13.59868235	2.852349	2852.348993	2795.640327		
34	16.76	17.01	11.13			11.13	0.25	1.469724	0.163580247	10.96641975	2.892857	2892.857143	2796.747967		
35	15.18	15.46	10.24			10.24	0.28	1.811125	0.18545925	10.05454075	2.961686	2961.685824	2805.309735		
36	21.27	21.53	14.26			14.26	0.26	1.207617	0.172206224	14.08779378	2.961486	2961.485557	2812.903226		

37	16.91	17.24	10.77			10.77	0.33	1.914153	0.206154292	10.56384571	2.664606	2664.605873	2818.011257		
38	29.11	29.52	18.26			18.26	0.41	1.388889	0.253611111	18.00638889	2.62167	2621.669627	2820.734341		
39	27.66	28.11	17.29			17.29	0.45	1.600854	0.27678762	17.01321238	2.597967	2597.966728	2840.189873		
40	12.2	12.39	7.56			7.56	0.19	1.533495	0.115932203	7.444067797	2.565217	2565.217391	2842.767296		
41	10.78	11.05	6.56			6.56	0.27	2.443439	0.160289593	6.399710407	2.461024	2461.024499	2846.518987		
42	24.54	24.83	15.75			15.75	0.29	1.167942	0.183950866	15.56604913	2.734581	2734.581498	2852.348993		
43	17.31	17.57	10.88			10.88	0.26	1.479795	0.161001707	10.71899829	2.626308	2626.307922	2865.181712		
44	23.55	23.82	14.75			14.75	0.27	1.133501	0.167191436	14.58280856	2.62624	2626.240353	2892.857143		
45	13.96	14.24	8.88			8.88	0.28	1.966292	0.174606742	8.705393258	2.656716	2656.716418	2896.009674		
46	17.81	18.09	10.95			10.95	0.28	1.547816	0.169485904	10.7805141	2.533613	2533.613445	2897.087379		
47	19.28	19.56	12.38			12.38	0.28	1.431493	0.177218814	12.20278119	2.724234	2724.233983	2931.263858		
48	20.46	20.71	12.71			12.71	0.24	1.15942	0.147362319	12.56263768	2.590738	2590.738423	2961.485557		
49	21.18	21.49	13.5			13.5	0.31	1.442531	0.19474174	13.30525826	2.689612	2689.612015	2961.685824		
50	13.57	13.86	8.64			8.64	0.29	2.092352	0.180779221	8.459220779	2.655172	2655.172414	2964.912281		
51	15.5	15.81	9.65			9.65	0.31	1.960784	0.189215686	9.460784314	2.566558	2566.558442			
52	16.92	17.23	10.86			10.86	0.31	1.799187	0.195391759	10.66460824	2.704867	2704.866562			
53	12.11	12.37	7.87			7.87	0.26	2.101859	0.16541633	7.70458367	2.748889	2748.888889			
54	8.49	8.77	5.57			5.57	0.28	3.192702	0.177833523	5.392166477	2.740625	2740.625			
55	11.74	12.03	7.57			7.57	0.29	2.41064	0.182485453	7.387514547	2.697309	2697.309417			
56	15.41	15.72	9.6			9.6	0.31	1.97201	0.189312977	9.410687023	2.568627	2568.627451			
57	11.82	12.08	7.29			7.29	0.26	2.152318	0.156903974	7.133096026	2.521921	2521.920668			
58	22.1	22.36	13.89			13.89	0.26	1.162791	0.161511628	13.72848837	2.639906	2639.905549			
59	14.88	15.16	9.53			9.53	0.28	1.846966	0.176015831	9.353984169	2.692718	2692.717584			
60	22.73	23.25	14.45			14.45	0.52	2.236559	0.323182796	14.1268172	2.642045	2642.045455			
61	8.14	8.43	5.29			5.29	0.29	3.440095	0.18198102	5.10801898	2.684713	2684.713376			

62	21.95	22.23	13.75			13.75	0.28	1.259559	0.173189384	13.57681062	2.621462	2621.462264			
63	24.21	24.46	15.51			15.51	0.25	1.022077	0.158524121	15.35147588	2.732961	2732.960894			
64	27.5	27.88	17.4			17.4	0.38	1.362984	0.237159254	17.16284075	2.660305	2660.305344			
65	29.13	29.43	18.68			18.68	0.3	1.019368	0.190417941	18.48958206	2.737674	2737.674419			
66	33.04	33.37	21.14			21.14	0.33	0.988912	0.209056038	20.93094396	2.728536	2728.536386			
67	23.44	23.77	14.79			14.79	0.33	1.388305	0.205330248	14.58466975	2.646993	2646.993318			
68	21.02	21.31	13.24			13.24	0.29	1.360863	0.18017832	13.05982168	2.640644	2640.644362			
69	30.01	30.36	18.87			18.87	0.35	1.152833	0.217539526	18.65246047	2.642298	2642.29765			
70	31.69	32.06	19.91			19.91	0.37	1.154086	0.22977854	19.68022146	2.638683	2638.683128			
71	31.33	31.69	15.5			15.5	0.36	1.136005	0.176080783	15.32391922	1.957381	1957.381099			
72	23.12	23.43	14.72			14.72	0.31	1.32309	0.194758856	14.52524114	2.690011	2690.011481			
73	21.79	22.04	12.98			12.98	0.25	1.134301	0.147232305	12.8327677	2.432671	2432.671082			
74	20.34	20.7	12.1			12.1	0.36	1.73913	0.210434783	11.88956522	2.406977	2406.976744			
75	20.11	20.4	12.76			12.76	0.29	1.421569	0.181392157	12.57860784	2.670157	2670.157068			
76	26.08	26.35	16			16	0.27	1.024668	0.163946869	15.83605313	2.545894	2545.89372			
77	27.42	27.7	16.88			16.88	0.28	1.01083	0.170628159	16.70937184	2.560074	2560.073937			
78	15.76	16	9.49			9.49	0.24	1.5	0.14235	9.34765	2.457757	2457.757296			
79	12.17	12.42	7.61			7.61	0.25	2.012882	0.153180354	7.456819646	2.582121	2582.120582			
80	18.28	18.52	11.43			11.43	0.24	1.295896	0.14812095	11.28187905	2.61213	2612.12976			
81	16.04	16.34	9.95			9.95	0.3	1.835985	0.182680539	9.767319461	2.557121	2557.120501			
82	10.03	10.3	5.76			5.76	0.27	2.621359	0.150990291	5.609009709	2.268722	2268.722467			
83	12.79	13.07	7.64			7.64	0.28	2.142311	0.163672533	7.476327467	2.406998	2406.998158			
84	30.41	30.74	18.89			18.89	0.33	1.07352	0.202787899	18.6872121	2.594093	2594.092827			
85	35.82	36.08	22.39			22.39	0.26	0.720621	0.161347007	22.22865299	2.6355	2635.500365			
86	30.96	31.28	19.25			19.25	0.32	1.023018	0.196930946	19.05306905	2.600166	2600.166251			

87	24.92	25.28	15.71			15.71	0.36	1.424051	0.223718354	15.48628165	2.641588	2641.588297			
88	51.17	51.67	32.23			32.23	0.5	0.96768	0.311883104	31.9181169	2.657922	2657.921811			
89	32.51	32.95	20.44			20.44	0.44	1.335357	0.272946889	20.16705311	2.633893	2633.892886			
90	28.7	29.04	18.01			18.01	0.34	1.170799	0.210860882	17.79913912	2.63282	2632.819583			
Table A1.8. Density measurements for l-l Agg.															

number				Wc+s water			Ws water	Wc water	SG	DENSITY kg m^-3	density sorted	density range	density mean of 50
				clast wet	sheet dry weight	sheet %	sheet wet weight (g)	clast wet no sheet					
1	34.51	35.11	19.46	19.46	0.6	1.708915	0.332554828	19.12744517	2.24345	2243.450479	1705.270007	1705	2286.2697
2	21.09	21.36	13.25	13.25	0.27	1.264045	0.167485955	13.08251404	2.633785	2633.78545	1828.729282	2633	stdev
3	28.84	29.14	17.17	17.17	0.3	1.029513	0.17676733	16.99323267	2.434419	2434.419382	1905.30303		203.4711388
4	14.29	14.6	7.98	7.98	0.31	2.123288	0.169438356	7.810561644	2.205438	2205.438066	1936.144578		
5	11.76	12.05	6.67	6.67	0.29	2.406639	0.160522822	6.509477178	2.239777	2239.776952	2002.533784		vesic
6	17.88	18.18	10.99	10.99	0.3	1.650165	0.181353135	10.80864686	2.528512	2528.511822	2059.299191		23.79101
7	20.79	21.04	12.83	12.83	0.25	1.188213	0.152447719	12.67755228	2.562728	2562.72838	2085.477178		43.16666667
8	22.82	23.17	10.5	10.5	0.35	1.510574	0.158610272	10.34138973	1.828729	1828.729282	2110.009911		12.23333333
9	12.95	13.22	7.57	7.57	0.27	2.04236	0.154606657	7.415393343	2.339823	2339.823009	2117.256637		
10	31.85	32.16	18.59	18.59	0.31	0.96393	0.179194652	18.41080535	2.369934	2369.933677	2136.363636		
11	18.85	19.14	10.1	10.1	0.29	1.515152	0.153030303	9.946969697	2.117257	2117.256637	2155.868545		
12	24.67	24.95	15.11	15.11	0.28	1.122244	0.169571142	14.94042886	2.535569	2535.569106	2159.847245		
13	21.78	22.1	12.16	12.16	0.32	1.447964	0.176072398	11.9839276	2.22334	2223.34004	2169.522092		
14	17.91	18.18	10.97	10.97	0.27	1.485149	0.162920792	10.80707921	2.521498	2521.49792	2186.734694		
15	15.8	16.06	8.92	8.92	0.26	1.618929	0.144408468	8.775591532	2.2493	2249.29972	2203.052422		
16	22.77	23.09	13.23	13.23	0.32	1.385881	0.1833521	13.0466479	2.341785	2341.78499	2205.438066		
17	21.01	21.29	11.2	11.2	0.28	1.315171	0.147299202	11.0527008	2.11001	2110.009911	2223.34004		
18	32.81	33.2	18.13	18.13	0.39	1.174699	0.212972892	17.91702711	2.203052	2203.052422	2225.683408		
19	39.03	39.59	21.26	21.26	0.56	1.414499	0.300722405	20.9592776	2.159847	2159.847245	2235.9447		
20	42.37	42.86	23.26	23.26	0.49	1.143257	0.265921605	22.99407839	2.186735	2186.734694	2239.776952		
21	36.12	36.65	21.88	21.88	0.53	1.446112	0.316409277	21.56359072	2.481381	2481.381178	2240.619902		
22	45.44	45.92	24.62	24.62	0.48	1.045296	0.257351916	24.36264808	2.155869	2155.868545	2243.450479		
23	31.44	31.86	19.25	19.25	0.42	1.318267	0.253766478	18.99623352	2.526566	2526.566217	2249.29972		
24	25.68	26.21	10.84	10.84	0.53	2.022129	0.219198779	10.62080122	1.70527	1705.270007	2256.768559		
25	34.51	35.01	19.28	19.28	0.5	1.428163	0.2753499	19.0046501	2.225683	2225.683408	2275.316456		
26	41.7	42.11	24.05	24.05	0.41	0.97364	0.234160532	23.81583947	2.331672	2331.672204	2314.058957		
27	35.03	35.43	20.47	20.47	0.4	1.128987	0.231103585	20.23889642	2.368316	2368.315508	2318.623785		
28	47.94	48.49	28.78	28.78	0.55	1.134254	0.326438441	28.45356156	2.460173	2460.172501	2331.672204		
29	40.25	40.82	23.18	23.18	0.57	1.396374	0.323679569	22.85632043	2.314059	2314.058957	2339.823009		
30	40.53	41.05	23.63	23.63	0.52	1.266748	0.299332521	23.33066748	2.356487	2356.486797	2341.78499		
31	40.62	41.1	24.73	24.73	0.48	1.167883	0.288817518	24.44118248	2.51069	2510.690287	2356.486797		
32	25.38	25.84	14.39	14.39	0.46	1.780186	0.256168731	14.13383127	2.256769	2256.768559	2368.315508		

33	27.18	27.47	15.21	15.21	0.29	1.055697	0.160571533	15.04942847	2.24062	2240.619902	2369.863014		
34	27.09	27.36	16.06	16.06	0.27	0.986842	0.158486842	15.90151316	2.421239	2421.238938	2369.933677		
35	25.99	26.24	16.2	16.2	0.25	0.952744	0.154344512	16.04565549	2.613546	2613.545817	2371.342079		
36	30.45	31	17.63	17.63	0.55	1.774194	0.312790323	17.31720968	2.318624	2318.623785	2375.523013		
37	22.21	22.49	13	13	0.28	1.244998	0.161849711	12.83815029	2.369863	2369.863014	2421.238938		
38	22.47	22.71	13.15	13.15	0.24	1.056803	0.138969617	13.01103038	2.375523	2375.523013	2434.419382		
39	23.72	24.06	12.97	12.97	0.34	1.413134	0.183283458	12.78671654	2.169522	2169.522092	2460.172501		
40	23.23	23.5	13.59	13.59	0.27	1.148936	0.156140426	13.43385957	2.371342	2371.342079	2481.381178		
41	21.27	21.57	12.09	12.09	0.3	1.390821	0.168150209	11.92184979	2.275316	2275.316456	2510.690287		
42	29.25	24.53	14.87	14.87	-4.72	-19.2417	-2.861247452	17.73124745	2.539337	2539.337474	2521.49792		
43	19.38	19.68	11.9	11.9	0.3	1.52439	0.181402439	11.71859756	2.529563	2529.562982	2526.566217		
44	23.95	24.26	13.41	13.41	0.31	1.277824	0.171356142	13.23864386	2.235945	2235.9447	2528.511822		
45	24.7	25.13	13.08	13.08	0.43	1.711102	0.223812177	12.85618782	2.085477	2085.477178	2529.562982		
46	20.39	20.68	11	11	0.29	1.402321	0.154255319	10.84574468	2.136364	2136.363636	2535.569106		
47	14.96	15.28	7.86	7.86	0.32	2.094241	0.16460733	7.69539267	2.059299	2059.299191	2539.337474		
48	9.76	10.06	4.78	4.78	0.3	2.982107	0.142544732	4.637455268	1.905303	1905.30303	2562.72838		
49	23.42	23.71	11.87	11.87	0.29	1.223113	0.145183467	11.72481653	2.002534	2002.533784	2613.545817		
50	15.7	16.07	7.77	7.77	0.37	2.302427	0.178898569	7.591101431	1.936145	1936.144578	2633.78545		
Table A1.9. Density measurements for dwSp.													

number					Wc+s water			Ws water	Wc water	SG	DENSITY kg m^-3	density sorted	density range	density mean of 90
				ballast wet	clast wet	sheet dry weight	sheet %	sheet wet weight (g)	clast wet no sheet					
1	3.67	4.16	12.03	15.78	-3.75	0.49	11.77885	-0.441706731	-3.308293269	0.525917	525.9165613	344.1589918	344.1589918	558.4204358
2	4.03	4.32	14.17	15.78	-1.61	0.29	6.712963	-0.108078704	-1.501921296	0.728499	728.4991568	353.5911602	827	stdev
3	3.38	3.84	8.76	15.78	-7.02	0.46	11.97917	-0.8409375	-6.1790625	0.353591	353.5911602	371.1340206		115.1955497
4	6.84	7.34	11.96	15.78	-3.82	0.5	6.811989	-0.260217984	-3.559782016	0.657706	657.7060932	382.6754386		
5	3.03	3.49	10.15	15.78	-5.63	0.46	13.18052	-0.742063037	-4.887936963	0.382675	382.6754386	384.6908734		mean of 50
6	6.84	7.1	2.25	15.78	-13.53	0.26	3.661972	-0.495464789	-13.03453521	0.344159	344.1589918	404.2792793		572.2514541
7	3.23	3.63	12.35	15.78	-3.43	0.4	11.01928	-0.377961433	-3.052038567	0.514164	514.1643059	416.091954		stdev
8	5.51	5.92	8	15.78	-7.78	0.41	6.925676	-0.538817568	-7.241182432	0.432117	432.1167883	420.8074534		122.948321
9	2.88	3.32	11.68	15.78	-4.1	0.44	13.25301	-0.543373494	-3.556626506	0.447439	447.4393531	426.744186		vesic
10	6.51	7.01	13.01	15.78	-2.77	0.5	7.132668	-0.197574893	-2.572425107	0.716769	716.7689162	432.1167883		80.92495153
11	5.19	5.59	12.26	15.78	-3.52	0.4	7.155635	-0.251878354	-3.268121646	0.613611	613.611416	447.4393531		88.52803361
12	2.25	2.71	12.05	15.78	-3.73	0.46	16.97417	-0.633136531	-3.096863469	0.420807	420.8074534	455.6786704		72.43333333
13	3.19	3.59	10.49	15.78	-5.29	0.4	11.14206	-0.589415042	-4.700584958	0.404279	404.2792793	472.1407625		

14	4.27	4.78	12.89	15.78	-2.89	0.51	10.66946	-0.30834728	-2.58165272	0.623207	623.2073012	505.0505051		
15	4.69	5.08	11.46	15.78	-4.32	0.39	7.677165	-0.331653543	-3.988346457	0.540426	540.4255319	513.8568129		
16	4.85	5.29	12.55	15.78	-3.23	0.44	8.31758	-0.268657845	-2.961342155	0.620892	620.8920188	514.1643059		
17	1.42	1.81	13.24	15.78	-2.54	0.39	21.54696	-0.547292818	-1.992707182	0.416092	416.091954	525.9165613		
18	4.38	4.95	12.9	15.78	-2.88	0.57	11.51515	-0.331636364	-2.548363636	0.632184	632.183908	540.4255319		
19	7.25	7.79	11.8	15.78	-3.98	0.54	6.931964	-0.275892169	-3.704107831	0.661852	661.8521665	540.8805031		
20	6.77	7.28	11.8	15.78	-3.98	0.51	7.005495	-0.278818681	-3.701181319	0.646536	646.5364121	540.9153953		
21	4.66	5.22	12.93	15.78	-2.85	0.56	10.72797	-0.305747126	-2.544252874	0.64684	646.8401487	545.5519829		
22	1.74	2.16	12.12	15.78	-3.66	0.42	19.44444	-0.711666667	-2.948333333	0.371134	371.1340206	547.7792732		
23	4.63	5.09	11.54	15.78	-4.24	0.46	9.037328	-0.383182711	-3.856817289	0.545552	545.5519829	569.9570815		
24	3.86	4.45	11.57	15.78	-4.21	0.59	13.25843	-0.558179775	-3.651820225	0.513857	513.8568129	573.7298637		
25	3.16	3.67	10.85	15.78	-4.93	0.51	13.89646	-0.685095368	-4.244904632	0.426744	426.744186	583.0429733		
26	4.13	4.51	13.71	15.78	-2.07	0.38	8.425721	-0.174412417	-1.895587583	0.68541	685.4103343	587.0445344		
27	4.23	4.63	12.34	15.78	-3.44	0.4	8.639309	-0.297192225	-3.142807775	0.57373	573.7298637	600.3787879		
28	3.62	4.07	12.42	15.78	-3.36	0.45	11.05651	-0.371498771	-2.988501229	0.547779	547.7792732	600.9389671		
29	3.88	4.29	13.88	15.78	-1.9	0.41	9.55711	-0.181585082	-1.718414918	0.693053	693.0533118	613.611416		
30	4.59	5.05	12.98	15.78	-2.8	0.46	9.108911	-0.255049505	-2.544950495	0.643312	643.3121019	620.8920188		
31	3.92	4.3	12.13	15.78	-3.65	0.38	8.837209	-0.32255814	-3.32744186	0.540881	540.8805031	622.0930233		
32	5.27	5.76	13.46	15.78	-2.32	0.49	8.506944	-0.197361111	-2.122638889	0.712871	712.8712871	623.2073012		
33	4.29	4.83	10.38	15.78	-5.4	0.54	11.18012	-0.603726708	-4.796273292	0.472141	472.1407625	632.183908		
34	3.39	3.84	13.23	15.78	-2.55	0.45	11.71875	-0.298828125	-2.251171875	0.600939	600.9389671	632.3687031		
35	6.19	6.64	10.77	15.78	-5.01	0.45	6.777108	-0.339533133	-4.670466867	0.569957	569.9570815	636.7346939		
36	5.88	6.34	11.56	15.78	-4.22	0.46	7.255521	-0.306182965	-3.913817035	0.600379	600.3787879	643.3121019		
37	2.81	3.29	11.85	15.78	-3.93	0.48	14.58967	-0.57337386	-3.35662614	0.455679	455.6786704	646.5364121		
38	5.58	6.06	14.52	15.78	-1.26	0.48	7.920792	-0.09980198	-1.16019802	0.827869	827.8688525	646.8401487		
39	5.5	5.9	12.35	15.78	-3.43	0.4	6.779661	-0.232542373	-3.197457627	0.632369	632.3687031	648.9361702		
40	4.54	5.02	12.19	15.78	-3.59	0.48	9.561753	-0.343266932	-3.246733068	0.583043	583.0429733	657.7060932		
41	3.34	3.9	12.47	15.78	-3.31	0.56	14.35897	-0.475282051	-2.834717949	0.540915	540.9153953	661.8521665		
42	3.57	4	11.86	15.78	-3.92	0.43	10.75	-0.4214	-3.4986	0.505051	505.0505051	685.4103343		
43	4.03	4.45	14.5	15.78	-1.28	0.42	9.438202	-0.120808989	-1.159191011	0.776614	776.6143106	693.0533118		
44	3.84	4.27	13.47	15.78	-2.31	0.43	10.07026	-0.232622951	-2.077377049	0.648936	648.9361702	712.8712871		
45	3.85	4.28	13.18	15.78	-2.6	0.43	10.04673	-0.261214953	-2.338785047	0.622093	622.0930233	716.7689162		
46	4.21	4.68	13.11	15.78	-2.67	0.47	10.04274	-0.268141026	-2.401858974	0.636735	636.7346939	728.4991568		
47	3.4	3.92	9.51	15.78	-6.27	0.52	13.26531	-0.831734694	-5.438265306	0.384691	384.6908734	776.6143106		
48	6.17	6.69	13.98	15.78	-1.8	0.52	7.772795	-0.139910314	-1.660089686	0.787986	787.9858657	787.9858657		
49	1.19	1.45	14.76	15.78	-1.02	0.26	17.93103	-0.182896552	-0.837103448	0.587045	587.0445344	796.0444994		
50	5.97	6.44	14.13	15.78	-1.65	0.47	7.298137	-0.120419255	-1.529580745	0.796044	796.0444994	827.8688525		
51	5.19	5.77	10.85	15.78	-4.93	0.58	10.05199	-0.495563258	-4.434436742	0.539252	539.2523364			
52	3.25	3.63	13.07	15.78	-2.71	0.38	10.46832	-0.28369146	-2.42630854	0.572555	572.555205			
53	3.29	3.65	9.66	15.78	-6.12	0.36	9.863014	-0.603616438	-5.516383562	0.373593	373.5926305			
54	3.24	3.66	13.22	15.78	-2.56	0.42	11.47541	-0.293770492	-2.266229508	0.588424	588.4244373			
55	4.2	4.58	13.87	15.78	-1.91	0.38	8.296943	-0.158471616	-1.751528384	0.705701	705.7010786			
56	2.98	3.43	12.87	15.78	-2.91	0.45	13.11953	-0.381778426	-2.528221574	0.541009	541.0094637			
57	3.02	3.42	14.24	15.78	-1.54	0.4	11.69591	-0.180116959	-1.359883041	0.689516	689.516129			
58	2.3	2.83	12.22	15.78	-3.56	0.53	18.72792	-0.666713781	-2.893286219	0.442879	442.8794992			

59	5.46	6.02	13.08	15.78	-2.7	0.56	9.302326	-0.251162791	-2.448837209	0.690367	690.3669725			
60	4.97	5.43	12.43	15.78	-3.35	0.46	8.471455	-0.283793738	-3.066206262	0.618451	618.4510251			
61	4.18	4.67	12.97	15.78	-2.81	0.49	10.49251	-0.2948394	-2.5151606	0.624332	624.3315508			
62	3.31	3.69	14.19	15.78	-1.59	0.38	10.2981	-0.163739837	-1.426260163	0.698864	698.8636364			
63	4.45	4.86	12.44	15.78	-3.34	0.41	8.436214	-0.281769547	-3.058230453	0.592683	592.6829268			
64	3.3	3.73	11.92	15.78	-3.86	0.43	11.52815	-0.444986595	-3.415013405	0.491436	491.4361001			
65	5.17	5.62	10.67	15.78	-5.11	0.45	8.007117	-0.409163701	-4.700836299	0.523765	523.7651445			
66	2.97	3.27	12.98	15.78	-2.8	0.3	9.174312	-0.256880734	-2.543119266	0.538715	538.7149918			
67	3.48	3.86	12.76	15.78	-3.02	0.38	9.84456	-0.297305699	-2.722694301	0.561047	561.0465116			
68	3.3	3.69	11.32	15.78	-4.46	0.39	10.56911	-0.471382114	-3.988617886	0.452761	452.7607362			
69	3.39	3.69	13.47	15.78	-2.31	0.3	8.130081	-0.187804878	-2.122195122	0.615	615			
70	3.06	3.35	13.26	15.78	-2.52	0.29	8.656716	-0.218149254	-2.301850746	0.570698	570.6984668			
71	1.91	2.14	12.88	15.78	-2.9	0.23	10.74766	-0.311682243	-2.588317757	0.424603	424.6031746			
72	1.98	2.26	13.61	15.78	-2.17	0.28	12.38938	-0.268849558	-1.901150442	0.510158	510.1580135			
73	2.01	2.27	13.09	15.78	-2.69	0.26	11.45374	-0.308105727	-2.381894273	0.457661	457.6612903			
74	3.63	3.88	12.66	15.78	-3.12	0.25	6.443299	-0.201030928	-2.918969072	0.554286	554.2857143			
75	2.77	3.02	14	15.78	-1.78	0.25	8.278146	-0.147350993	-1.632649007	0.629167	629.1666667			
76	3.3	3.6	14.01	15.78	-1.77	0.3	8.333333	-0.1475	-1.6225	0.670391	670.3910615			
77	3.21	3.54	14.29	15.78	-1.49	0.33	9.322034	-0.138898305	-1.351101695	0.703777	703.777336			
78	1.69	1.95	13.6	15.78	-2.18	0.26	13.33333	-0.290666667	-1.889333333	0.472155	472.1549637			
79	3.17	3.47	13.81	15.78	-1.97	0.3	8.645533	-0.170317003	-1.799682997	0.637868	637.8676471			
80	1.18	1.45	12.23	15.78	-3.55	0.27	18.62069	-0.661034483	-2.888965517	0.29	290			
81	3.54	3.82	13.23	15.78	-2.55	0.28	7.329843	-0.186910995	-2.363089005	0.599686	599.6860283			
82	2.85	3.13	13.44	15.78	-2.34	0.28	8.945687	-0.209329073	-2.130670927	0.572212	572.2120658			
83	2.62	2.99	12.74	15.78	-3.04	0.37	12.37458	-0.376187291	-2.663812709	0.495854	495.854063			
84	1.93	2.29	12.8	15.78	-2.98	0.36	15.72052	-0.468471616	-2.511528384	0.434535	434.5351044			
85	3.36	3.83	11.38	15.78	-4.4	0.47	12.27154	-0.539947781	-3.860052219	0.465371	465.3705954			
86	1.39	1.66	11.82	15.78	-3.96	0.27	16.26506	-0.644096386	-3.315903614	0.295374	295.3736655			
87	4.26	4.56	9.72	15.78	-6.06	0.3	6.578947	-0.398684211	-5.661315789	0.429379	429.3785311			
88	3.07	3.48	12.39	15.78	-3.39	0.41	11.78161	-0.399396552	-2.990603448	0.50655	506.5502183			
89	3.99	4.3	12.36	15.78	-3.42	0.31	7.209302	-0.24655814	-3.17344186	0.556995	556.9948187			
90	2.23	2.48	13.38	15.78	-2.4	0.25	10.08065	-0.241935484	-2.158064516	0.508197	508.1967213			

Table A1.10. Density measurements for ScL.

number					Wc+s water			Ws water	Wc water	SG	DENSITY kg m^- 3	density sorted	density range	density mean of 90
				ballast wet	clast wet	sheet dry weight	sheet %	sheet wet weight (g)	clast wet no sheet					
1	6.71	6.98	12.9 7	15.78	-2.81	0.27	3.86819 5	-0.108696275	-2.701303725	0.71297 2	712.9724208	290.5355833	290.535583 3	#DIV/0!
2	6.58	6.84	15.7 5	15.78	-0.03	0.26	3.80117	-0.001140351	-0.028859649	0.99563 3	995.6331878	480.1297648	1332.68608 4	stdev
3	10.9 2	11.2 2	16.3 2	15.78	0.54	0.3	2.67379 7	0.014438503	0.525561497	1.05056 2	1050.561798	550.5415162		#DIV/0!

4	7.52	7.8	15.6 5	15.78	-0.13	0.28	3.58974 4	-0.004666667	-0.125333333	0.98360 7	983.6065574	638.5426654		
5	8.04	8.37	11.2 9	15.78	-4.49	0.33	3.94265 2	-0.17702509	-4.31297491	0.65085 5	650.8553655	650.8553655		mean of 50
6	3.72	3.96	6.11	15.78	-9.67	0.24	6.06060 6	-0.586060606	-9.083939394	0.29053 6	290.5355833	676.2402089		889.9081384
7	5.36	5.65	13.6 8	15.78	-2.1	0.29	5.13274 3	-0.107787611	-1.992212389	0.72903 2	729.0322581	712.9724208		stdev
8	4.89	5.18	13.3	15.78	-2.48	0.29	5.59845 6	-0.138841699	-2.341158301	0.67624	676.2402089	729.0268456		180.540113
9	8.45	8.77	15.5 8	15.78	-0.2	0.32	3.64880 3	-0.007297605	-0.192702395	0.97770 3	977.703456	729.0322581		vesic
10	8.12	8.69	12.5 5	15.78	-3.23	0.57	6.55926 4	-0.211864212	-3.018135788	0.72902 7	729.0268456	730.5475504		70.33639539
11	5.68	5.99	15.6	15.78	-0.18	0.31	5.17529 2	-0.009315526	-0.170684474	0.97082 7	970.8265802	748.1108312		90.31548056
12	4.03	4.34	15.3 6	15.78	-0.42	0.31	7.14285 7	-0.03	-0.39	0.91176 5	911.7647059	765.1057402		55.57713053
13	12.1 6	12.4 8	16.6	15.78	0.82	0.32	2.56410 3	0.021025641	0.798974359	1.07032 6	1070.325901	768.1623932		
14	10.6	10.9	15.0 2	15.78	-0.76	0.3	2.75229 4	-0.020917431	-0.739082569	0.93482	934.8198971	819.7226502		
15	8.76	9.15	8.31	15.78	-7.47	0.39	4.26229 5	-0.318393443	-7.151606557	0.55054 2	550.5415162	822.4299065		
16	8.58	9.1	15.1 4	15.78	-0.64	0.52	5.71428 6	-0.036571429	-0.603428571	0.93429 2	934.2915811	826.3555251		
17	6.01	6.27	16.3	15.78	0.52	0.26	4.14673	0.021562998	0.498437002	1.09043 5	1090.434783	843.75		
18	5.63	5.92	9.37	15.78	-6.41	0.29	4.89864 9	-0.314003378	-6.095996622	0.48013	480.1297648	864.1686183		
19	4.88	5.18	15.9 5	15.78	0.17	0.3	5.79150 6	0.00984556	0.16015444	1.03393 2	1033.932136	872.9472774		
20	5.23	5.49	15.8 6	15.78	0.08	0.26	4.73588 3	0.003788707	0.076211293	1.01478 7	1014.787431	878.5607196		
21	7.54	7.83	16.2 1	15.78	0.43	0.29	3.70370 4	0.015925926	0.414074074	1.05810 8	1058.108108	890.7103825		
22	5.92	6.18	15.8 3	15.78	0.05	0.26	4.20712	0.00210356	0.04789644	1.00815 7	1008.156607	900.2744739		
23	7.16	7.38	14.6 2	15.78	-1.16	0.22	2.98103	-0.034579946	-1.125420054	0.86416 9	864.1686183	911.7647059		
24	2.97	3.26	15.5 9	15.78	-0.19	0.29	8.89570 6	-0.01690184	-0.17309816	0.94492 8	944.9275362	925.1101322		
25	3.95	4.2	15.4 4	15.78	-0.34	0.25	5.95238 1	-0.020238095	-0.319761905	0.92511	925.1101322	928.1524927		
26	5.04	5.32	14.6 1	15.78	-1.17	0.28	5.26315 8	-0.061578947	-1.108421053	0.81972 3	819.7226502	934.2915811		
27	4.91	5.18	15.8 8	15.78	0.1	0.27	5.21235 5	0.005212355	0.094787645	1.01968 5	1019.685039	934.8198971		
28	5.89	6.16	14.4 5	15.78	-1.33	0.27	4.38311 7	-0.058295455	-1.271704545	0.82243	822.4299065	935.0282486		

29	4.8	5.07	13.9 1	15.78	-1.87	0.27	5.32544 4	-0.099585799	-1.770414201	0.73054 8	730.5475504	944.9275362		
30	6.42	6.66	12.0 1	15.78	-3.77	0.24	3.60360 4	-0.135855856	-3.634144144	0.63854 3	638.5426654	954.9668874		
31	6.09	6.33	15.2 9	15.78	-0.49	0.24	3.79146 9	-0.018578199	-0.471421801	0.92815 2	928.1524927	959.5170455		
32	2.77	2.97	14.7 8	15.78	-1	0.2	6.73400 7	-0.067340067	-0.932659933	0.74811 1	748.1108312	964.7546648		
33	12.9 4	13.5 1	16.8 1	15.78	1.03	0.57	4.21909 7	0.043456699	0.986543301	1.08253 2	1082.532051	970.8265802		
34	15.2 8	13.0 4	14.1 8	15.78	-1.6	-2.24	-17.1779	0.274846626	-1.874846626	0.89071	890.7103825	977.703456		
35	13.8 9	14.4 2	15.1	15.78	-0.68	0.53	3.67545 1	-0.024993065	-0.655006935	0.95496 7	954.9668874	983.6065574		
36	19.9 6	20.5 9	20.9 2	15.78	5.14	0.63	3.05973 8	0.15727052	4.98272948	1.33268 6	1332.686084	987.6847291		
37	9.54	10.1 3	12.6 7	15.78	-3.11	0.59	5.82428 4	-0.181135242	-2.928864758	0.76510 6	765.1057402	995.6331878		
38	13.5 3	13.9 6	15.2 7	15.78	-0.51	0.43	3.08022 9	-0.015709169	-0.494290831	0.96475 5	964.7546648	1007.371007		
39	11.5 5	12.0 3	15.6 3	15.78	-0.15	0.48	3.99002 5	-0.005985037	-0.144014963	0.98768 5	987.6847291	1008.156607		
40	9.3	9.84	14.6 9	15.78	-1.09	0.54	5.48780 5	-0.059817073	-1.030182927	0.90027 4	900.2744739	1014.787431		
41	11.4 6	12.0 4	13.2 5	15.78	-2.53	0.58	4.81727 6	-0.121877076	-2.408122924	0.82635 6	826.3555251	1019.685039		
42	12.4 1	13	17.2 5	15.78	1.47	0.59	4.53846 2	0.066715385	1.403284615	1.12749 3	1127.493495	1033.932136		
43	6.82	7.19	13.6 1	15.78	-2.17	0.37	5.14603 6	-0.111668985	-2.058331015	0.76816 2	768.1623932	1050.561798		
44	11.1 7	11.7 2	14.1 6	15.78	-1.62	0.55	4.69283 3	-0.076023891	-1.543976109	0.87856 1	878.5607196	1058.108108		
45	9.55	10.1	14.3 1	15.78	-1.47	0.55	5.44554 5	-0.080049505	-1.389950495	0.87294 7	872.9472774	1070.325901		
46	20.0 1	20.5 6	17.6 8	15.78	1.9	0.55	2.67509 7	0.050826848	1.849173152	1.10182 2	1101.822079	1082.532051		
47	12.9 6	13.5 1	15.2 1	15.78	-0.57	0.55	4.07105 8	-0.023205033	-0.546794967	0.95951 7	959.5170455	1090.434783		
48	11.7 4	12.3	15.8 7	15.78	0.09	0.56	4.55284 6	0.004097561	0.085902439	1.00737 1	1007.371007	1101.822079		
49	8.17	8.64	14.1 8	15.78	-1.6	0.47	5.43981 5	-0.087037037	-1.512962963	0.84375	843.75	1127.493495		
50	12.7 9	13.2 4	14.8 6	15.78	-0.92	0.45	3.39879 2	-0.031268882	-0.888731118	0.93502 8	935.0282486	1332.686084		
51	5.62	6.12	13.8 2	15.78	-1.96	0.5	8.16993 5	-0.160130719	-1.799869281	0.75742 6	757.4257426			
52	9.12	9.73	15.2 2	15.78	-0.56	0.61	6.26927	-0.035107914	-0.524892086	0.94557 8	945.5782313			
53	14.2 5	14.7 8	17.9 7	15.78	2.19	0.53	3.58592 7	0.0785318	2.1114682	1.17394 8	1173.947577			

54	16.2 2	16.8 3	13.1 8	15.78	-2.6	0.61	3.62448	-0.094236482	-2.505763518	0.86618 6	866.1863098			
55	7.99	8.48	15.5 4	15.78	-0.24	0.49	5.77830 2	-0.013867925	-0.226132075	0.97247 7	972.4770642			
56	6.98	7.29	15.5 8	15.78	-0.2	0.31	4.25240 1	-0.008504801	-0.191495199	0.97329 8	973.2977303			
57	10.7 5	11.1 2	14.8	15.78	-0.98	0.37	3.32733 8	-0.032607914	-0.947392086	0.91900 8	919.0082645			
58	4.23	4.5	16.0 4	15.78	0.26	0.27	6	0.0156	0.2444	1.06132 1	1061.320755			
59	3.37	3.67	14.4 4	15.78	-1.34	0.3	8.17438 7	-0.109536785	-1.230463215	0.73253 5	732.5349301			
60	3.28	3.55	15.1 9	15.78	-0.59	0.27	7.60563 4	-0.044873239	-0.545126761	0.85748 8	857.4879227			
61	2.2	2.52	15.3 5	15.78	-0.43	0.32	12.6984 1	-0.054603175	-0.375396825	0.85423 7	854.2372881			
Table A1.11. Density measurements for waSc.														

number				Wc+s water			Ws water	Wc water	SG	DENSITY kg m^-3	density sorted	density range	density mean of 900
				clast wet	sheet dry weight	sheet %	sheet wet weight (g)	clast wet no sheet					
1	10.52	11.07	1.98	1.98	0.55	4.968383	0.098373984	1.881626016	1.217822	1217.821782	1037.481259	1037.481259	#DIV/0!
2	7.58	8.05	1.2	1.2	0.47	5.838509	0.070062112	1.129937888	1.175182	1175.182482	1046.464646	1349	stdev
3	5.48	5.96	0.9	0.9	0.48	8.053691	0.072483221	0.827516779	1.177866	1177.865613	1049.309665		#DIV/0!
4	4.22	4.54	0.74	0.74	0.32	7.048458	0.05215859	0.68784141	1.194737	1194.736842	1058.252427		
5	6.18	6.53	0.74	0.74	0.35	5.359877	0.039663093	0.700336907	1.127807	1127.806563	1060.606061		mean of 50
6	8.6	9.09	1.33	1.33	0.49	5.390539	0.071694169	1.258305831	1.171392	1171.391753	1061.776062		1172.542647
7	8.53	9.08	1.8	1.8	0.55	6.057269	0.109030837	1.690969163	1.247253	1247.252747	1069.767442		stdev
8	9.26	9.76	1.4	1.4	0.5	5.122951	0.071721311	1.328278689	1.167464	1167.464115	1083.707025		77.73529688
9	4.79	5.18	0.23	0.23	0.39	7.528958	0.017316602	0.212683398	1.046465	1046.464646	1084.821429		
10	7.71	8.25	0.48	0.48	0.54	6.545455	0.031418182	0.448581818	1.061776	1061.776062	1089.84375		vesicularity
11	7.69	8.21	1.11	1.11	0.52	6.333739	0.070304507	1.039695493	1.156338	1156.338028	1094.736842		60.9152451
12	5.54	5.93	1	1	0.39	6.576728	0.065767285	0.934232715	1.20284	1202.839757	1099.885189		65.41729135
13	7.13	7.59	1.04	1.04	0.46	6.060606	0.063030303	0.976969697	1.158779	1158.778626	1101.5625		55.03333333
14	3.88	4.2	0.24	0.24	0.32	7.619048	0.018285714	0.221714286	1.060606	1060.606061	1117.194183		
15	15.96	16.53	3.85	3.85	0.57	3.448276	0.132758621	3.717241379	1.303628	1303.62776	1127.806563		
16	10.42	10.99	2	2	0.57	5.186533	0.103730664	1.896269336	1.222469	1222.46941	1128.808864		
17	4.16	4.45	0.77	0.77	0.29	6.516854	0.050179775	0.719820225	1.209239	1209.23913	1131.147541		
18	5.94	6.2	1.18	1.18	0.26	4.193548	0.049483871	1.130516129	1.23506	1235.059761	1153.939394		
19	3.87	4.16	0.36	0.36	0.29	6.971154	0.025096154	0.334903846	1.094737	1094.736842	1156.338028		
20	4.73	5.04	0.88	0.88	0.31	6.150794	0.054126984	0.825873016	1.211538	1211.538462	1158.778626		
21	12.56	13.06	1.37	1.37	0.5	3.828484	0.05245023	1.31754977	1.117194	1117.194183	1160.674157		
22	8.8	9.16	1.39	1.39	0.36	3.930131	0.054628821	1.335371179	1.178893	1178.893179	1167.464115		
23	6.79	7.05	1.47	1.47	0.26	3.687943	0.054212766	1.415787234	1.263441	1263.44086	1171.391753		
24	12.34	12.93	1.96	1.96	0.59	4.563032	0.089435422	1.870564578	1.178669	1178.669098	1175.182482		

25	15.22	15.73	2.74	2.74	0.51	3.242212	0.088836618	2.651163382	1.210931	1210.931486	1177.865613		
26	8.6	9.2	0.6	0.6	0.6	6.521739	0.039130435	0.560869565	1.069767	1069.767442	1177.94836		
27	13.47	13.95	1.15	1.15	0.48	3.44086	0.039569892	1.110430108	1.089844	1089.84375	1178.669098		
28	9.36	9.89	2.25	2.25	0.53	5.358948	0.12057634	2.12942366	1.294503	1294.502618	1178.893179		
29	6.66	7.05	0.65	0.65	0.39	5.531915	0.035957447	0.614042553	1.101563	1101.5625	1181.603774		
30	11.56	12.04	2.09	2.09	0.48	3.986711	0.083322259	2.006677741	1.21005	1210.050251	1194.736842		
31	6.63	6.95	1.8	1.8	0.32	4.604317	0.082877698	1.717122302	1.349515	1349.514563	1201.447527		
32	9.04	9.58	0.87	0.87	0.54	5.636743	0.049039666	0.820960334	1.099885	1099.885189	1202.839757		
33	4.68	4.83	0.56	0.56	0.15	3.10559	0.017391304	0.542608696	1.131148	1131.147541	1209.23913		
34	15.95	16.88	2.55	2.55	0.93	5.509479	0.140491706	2.409508294	1.177948	1177.94836	1210.050251		
35	6.62	6.92	0.25	0.25	0.3	4.33526	0.01083815	0.23916185	1.037481	1037.481259	1210.931486		
36	7.96	8.23	1.78	1.78	0.27	3.28068	0.058396112	1.721603888	1.275969	1275.968992	1211.538462		
37	6.13	6.44	1.13	1.13	0.31	4.813665	0.05439441	1.07560559	1.212806	1212.806026	1212.806026		
38	6.15	6.44	1.33	1.33	0.29	4.503106	0.059891304	1.270108696	1.260274	1260.273973	1217.821782		
39	9.66	9.96	1.67	1.67	0.3	3.012048	0.050301205	1.619698795	1.201448	1201.447527	1222.46941		
40	5.79	6.06	1.51	1.51	0.27	4.455446	0.067277228	1.442722772	1.331868	1331.868132	1235.059761		
41	9.16	9.46	1.91	1.91	0.3	3.171247	0.060570825	1.849429175	1.25298	1252.980132	1236.842105		
42	7.54	8.15	0.93	0.93	0.61	7.484663	0.069607362	0.860392638	1.128809	1128.808864	1247.252747		
43	6.29	6.58	1.26	1.26	0.29	4.407295	0.055531915	1.204468085	1.236842	1236.842105	1252.980132		
44	9.76	10.33	1.43	1.43	0.57	5.517909	0.078906099	1.351093901	1.160674	1160.674157	1260.273973		
45	6.71	7.25	0.56	0.56	0.54	7.448276	0.041710345	0.518289655	1.083707	1083.707025	1263.44086		
46	9.45	10.02	1.54	1.54	0.57	5.688623	0.08760479	1.45239521	1.181604	1181.603774	1275.968992		
47	9.02	9.52	1.27	1.27	0.5	5.252101	0.066701681	1.203298319	1.153939	1153.939394	1294.502618		
48	4.6	4.86	0.38	0.38	0.26	5.349794	0.020329218	0.359670782	1.084821	1084.821429	1303.62776		
49	4.06	4.36	0.24	0.24	0.3	6.880734	0.016513761	0.223486239	1.058252	1058.252427	1331.868132		
50	4.93	5.32	0.25	0.25	0.39	7.330827	0.018327068	0.231672932	1.04931	1049.309665	1349.514563		
Table A.1.12. Density measurements for mwSc.													

number				Wc+s water			Ws water	Wc water	SG	DENSITY kg m^-3	density sorted	density range	density mean of 90
				clast wet	sheet dry weight	sheet %	sheet wet weight (g)	clast wet no sheet					
1	13.24	13.3	7.31	7.31	0.06	0.451128	0.032977444	7.277022556	2.220367	2220.367279	1450	1450	#DIV/0!
2	13.28	13.76	4.7	4.7	0.48	3.488372	0.163953488	4.536046512	1.518764	1518.763797	1465.783664	2322	stdev
3	12.55	13.03	6.16	6.16	0.48	3.683807	0.226922487	5.933077513	1.896652	1896.652111	1518.763797		#DIV/0!
4	12.05	12.26	5.99	5.99	0.21	1.712887	0.102601958	5.887398042	1.955343	1955.342903	1527.777778		
5	13.52	13.79	6.32	6.32	0.27	1.957941	0.123741842	6.196258158	1.846051	1846.05087	1544.850498		mean of 50
6	5.13	5.43	2.19	2.19	0.3	5.524862	0.120994475	2.069005525	1.675926	1675.925926	1675.925926		1943.681403
7	13.7	14.3	7.29	7.29	0.6	4.195804	0.305874126	6.984125874	2.039943	2039.942939	1719.723183		stdev
8	17.67	17.88	10.12	10.12	0.21	1.174497	0.11885906	10.00114094	2.304124	2304.123711	1751.740139		214.4349911
9	7.15	7.55	3.24	3.24	0.4	5.298013	0.171655629	3.068344371	1.75174	1751.740139	1778.611632		
10	11.26	11.88	6.69	6.69	0.62	5.218855	0.349141414	6.340858586	2.289017	2289.017341	1785.854617		vesicularity
11	7.19	7.64	4.05	4.05	0.45	5.890052	0.23854712	3.81145288	2.128134	2128.133705	1786.786787		35.2106199
12	10.04	10.5	5.39	5.39	0.46	4.380952	0.236133333	5.153866667	2.054795	2054.794521	1816.129032		51.66666667

13	6.63	7.13	3.39	3.39	0.5	7.012623	0.23772791	3.15227209	1.906417	1906.417112	1836.689038		22.6
14	17.74	18.28	9.61	9.61	0.54	2.954048	0.283884026	9.326115974	2.10842	2108.419839	1846.05087		
15	11.24	11.55	3.99	3.99	0.31	2.683983	0.107090909	3.882909091	1.527778	1527.777778	1847.727273		
16	6.65	7.06	3.85	3.85	0.41	5.807365	0.223583569	3.626416431	2.199377	2199.376947	1874.58194		
17	9.49	9.9	5.28	5.28	0.41	4.141414	0.218666667	5.061333333	2.142857	2142.857143	1896.652111		
18	10.8	11.21	5.23	5.23	0.41	3.657449	0.191284567	5.038715433	1.874582	1874.58194	1906.417112		
19	7.77	8.28	4.24	4.24	0.51	6.15942	0.26115942	3.97884058	2.049505	2049.50495	1910.958904		
20	6.41	6.98	3.83	3.83	0.57	8.166189	0.312765043	3.517234957	2.215873	2215.873016	1914.691943		
21	7.52	8.13	3.73	3.73	0.61	7.503075	0.279864699	3.450135301	1.847727	1847.727273	1915.09434		
22	12.49	13	6.79	6.79	0.51	3.923077	0.266376923	6.523623077	2.093398	2093.397746	1924.205379		
23	4.32	4.65	1.64	1.64	0.33	7.096774	0.116387097	1.523612903	1.54485	1544.850498	1930.693069		
24	6.76	7.19	3.93	3.93	0.43	5.980529	0.235034771	3.694965229	2.205521	2205.521472	1950.596252		
25	8.38	9.09	4	4	0.71	7.810781	0.312431243	3.687568757	1.785855	1785.854617	1955.342903		
26	5.31	5.58	2.66	2.66	0.27	4.83871	0.128709677	2.531290323	1.910959	1910.958904	1955.357143		
27	11.11	11.42	5.61	5.61	0.31	2.714536	0.152285464	5.457714536	1.965577	1965.576592	1955.451348		
28	12.95	13.19	6.57	6.57	0.24	1.81956	0.11954511	6.45045489	1.992447	1992.44713	1965.576592		
29	5.88	6.01	2.97	2.97	0.13	2.163062	0.064242928	2.905757072	1.976974	1976.973684	1965.859031		
30	10.48	10.85	5.54	5.54	0.37	3.410138	0.188921659	5.351078341	2.043315	2043.314501	1976.973684		
31	13.99	14.4	7.2	7.2	0.41	2.847222	0.205	6.995	2	2000	1992.44713		
32	8.12	8.55	4.65	4.65	0.43	5.02924	0.233859649	4.416140351	2.192308	2192.307692	2000		
33	4.59	4.97	2.08	2.08	0.38	7.645875	0.159034205	1.920965795	1.719723	1719.723183	2039.942939		
34	7.53	7.78	4.43	4.43	0.25	3.213368	0.142352185	4.287647815	2.322388	2322.38806	2043.314501		
35	4.9	5.22	1.62	1.62	0.32	6.130268	0.099310345	1.520689655	1.45	1450	2049.50495		
36	9.05	9.48	4.15	4.15	0.43	4.535865	0.188238397	3.961761603	1.778612	1778.611632	2054.794521		
37	17.44	17.85	8.77	8.77	0.41	2.296919	0.201439776	8.568560224	1.965859	1965.859031	2079.608939		
38	13.69	14.21	6.79	6.79	0.52	3.659395	0.248472906	6.541527094	1.915094	1915.09434	2093.397746		
39	7.85	8.08	3.86	3.86	0.23	2.846535	0.109876238	3.750123762	1.914692	1914.691943	2108.419839		
40	11.06	11.45	5.58	5.58	0.39	3.406114	0.190061135	5.389938865	1.950596	1950.596252	2128.133705		
41	5.7	5.95	2.62	2.62	0.25	4.201681	0.110084034	2.509915966	1.786787	1786.786787	2142.857143		
42	5.32	5.63	2.53	2.53	0.31	5.506217	0.139307282	2.390692718	1.816129	1816.129032	2151.807229		
43	8.49	8.76	4.28	4.28	0.27	3.082192	0.131917808	4.148082192	1.955357	1955.357143	2192.307692		
44	16.16	16.68	8.15	8.15	0.52	3.117506	0.254076739	7.895923261	1.955451	1955.451348	2199.376947		
45	6.3	6.64	2.11	2.11	0.34	5.120482	0.108042169	2.001957831	1.465784	1465.783664	2205.521472		
46	14.46	14.89	7.73	7.73	0.43	2.887844	0.223230356	7.506769644	2.079609	2079.608939	2215.873016		
47	8.7	8.93	4.78	4.78	0.23	2.575588	0.123113102	4.656886898	2.151807	2151.807229	2220.367279		
48	7.91	8.21	3.74	3.74	0.3	3.65408	0.136662607	3.603337393	1.836689	1836.689038	2289.017341		
49	7.52	7.8	3.76	3.76	0.28	3.589744	0.134974359	3.625025641	1.930693	1930.693069	2304.123711		
50	7.59	7.87	3.78	3.78	0.28	3.557814	0.134485388	3.645514612	1.924205	1924.205379	2322.38806		

Table A1.13. Density measurements for Cl.

number				Wc+s water			Ws water	Wc water	SG	DENSITY kg m ⁻³	density sorted	density range	density mean of 900
				clast wet	sheet dry weight	sheet %	sheet wet weight (g)	clast wet no sheet					
1	9.56	10	4.51	4.51	0.44	4.4	0.19844	4.31156	1.821494	1821.493625	1332.512315	1332.512315	#DIV/0!
2	12.91	13.37	5.21	5.21	0.46	3.440539	0.179252057	5.030747943	1.63848	1638.480392	1410.282258	1891.156463	stdev
3	16.57	17.13	6.27	6.27	0.56	3.269119	0.20497373	6.06502627	1.577348	1577.348066	1476.712329		#DIV/0!
4	14.44	14.93	6.52	6.52	0.49	3.281983	0.213985265	6.306014735	1.775268	1775.267539	1499.51784		
5	19.45	20.02	8.74	8.74	0.57	2.847153	0.248841159	8.491158841	1.774823	1774.822695	1561.759729		mean of 50
6	19.75	20.29	8.87	8.87	0.54	2.66141	0.236067028	8.633932972	1.776708	1776.707531	1564.924115		1703.560426
7	11.17	11.71	5.09	5.09	0.54	4.611443	0.234722459	4.855277541	1.768882	1768.882175	1577.348066		stdev
8	19.92	20.51	9.2	9.2	0.59	2.876646	0.26465139	8.93534861	1.813439	1813.439434	1577.487765		119.2009012
9	10.2	10.62	4.86	4.86	0.42	3.954802	0.19220339	4.66779661	1.84375	1843.75	1587.352626		vesic
10	6.13	6.38	2.52	2.52	0.25	3.918495	0.098746082	2.421253918	1.65285	1652.849741	1610.508757		43.21465246
11	10.65	11.1	4.75	4.75	0.45	4.054054	0.192567568	4.557432432	1.748031	1748.031496	1612.423447		55.58292282
12	9.22	9.64	3.67	3.67	0.42	4.356846	0.159896266	3.510103734	1.61474	1614.740369	1614.740369		36.96145125
13	15.07	15.55	5.18	5.18	0.48	3.086817	0.159897106	5.020102894	1.499518	1499.51784	1635.018496		
14	17.86	18.43	7	7	0.57	3.092784	0.216494845	6.783505155	1.612423	1612.423447	1638.480392		
15	18.69	19.34	7.08	7.08	0.65	3.36091	0.23795243	6.84204757	1.577488	1577.487765	1652.849741		
16	18.24	18.71	8.01	8.01	0.47	2.512026	0.201213255	7.808786745	1.748598	1748.598131	1656.580938		
17	14.35	14.81	5.48	5.48	0.46	3.106009	0.170209318	5.309790682	1.587353	1587.352626	1665.384615		
18	13.64	13.99	4.07	4.07	0.35	2.501787	0.101822731	3.968177269	1.410282	1410.282258	1671.985816		
19	11.49	11.97	5.39	5.39	0.48	4.010025	0.216140351	5.173859649	1.819149	1819.148936	1691.566265		
20	10.97	11.38	5.34	5.34	0.41	3.602812	0.192390158	5.147609842	1.884106	1884.10596	1697.443182		
21	10.55	10.95	4.34	4.34	0.4	3.652968	0.158538813	4.181461187	1.656581	1656.580938	1704		
22	10.85	11.25	5.01	5.01	0.4	3.555556	0.178133333	4.831866667	1.802885	1802.884615	1706.970128		
23	12.12	12.57	5.85	5.85	0.45	3.579952	0.209427208	5.640572792	1.870536	1870.535714	1707.943925		
24	14.15	14.62	6.06	6.06	0.47	3.214774	0.194815321	5.865184679	1.707944	1707.943925	1714.457831		
25	10.77	11.26	4.88	4.88	0.49	4.351687	0.212362345	4.667637655	1.76489	1764.890282	1739.783153		
26	23.74	24.24	10.55	10.55	0.5	2.062706	0.217615512	10.33238449	1.770636	1770.6355	1742.362525		
27	17.38	17.87	8.13	8.13	0.49	2.742026	0.222926693	7.907073307	1.834702	1834.702259	1748.031496		
28	10.72	11.12	5.24	5.24	0.4	3.597122	0.188489209	5.051510791	1.891156	1891.156463	1748.598131		
29	15.71	16.15	6.97	6.97	0.44	2.724458	0.189894737	6.780105263	1.759259	1759.259259	1759.259259		
30	6.67	7.02	2.87	2.87	0.35	4.985755	0.143091168	2.726908832	1.691566	1691.566265	1760.830325		
31	16.65	17.11	7.29	7.29	0.46	2.688486	0.195990649	7.094009351	1.742363	1742.362525	1764.890282		
32	13.69	14.23	5.93	5.93	0.54	3.7948	0.225031623	5.704968377	1.714458	1714.457831	1766.326531		
33	19.04	19.51	8.43	8.43	0.47	2.409021	0.203080472	8.226919528	1.76083	1760.830325	1768.421053		
34	27.29	27.84	10.05	10.05	0.55	1.975575	0.198545259	9.851454741	1.564924	1564.924115	1768.882175		
35	11.3	11.76	5.11	5.11	0.46	3.911565	0.199880952	4.910119048	1.768421	1768.421053	1770.6355		
36	18.75	19.31	7.32	7.32	0.56	2.900052	0.212283791	7.107716209	1.610509	1610.508757	1774.822695		
37	8.83	9.23	3.32	3.32	0.4	4.333694	0.143878657	3.176121343	1.56176	1561.759729	1775.267539		
38	18.09	18.58	8.33	8.33	0.49	2.637244	0.219682454	8.110317546	1.812683	1812.682927	1775.376555		
39	12.83	13.26	5.15	5.15	0.43	3.242836	0.167006033	4.982993967	1.635018	1635.018496	1775.675676		
40	19.26	19.71	8.61	8.61	0.45	2.283105	0.196575342	8.413424658	1.775676	1775.675676	1776.707531		
41	11.56	12	4.97	4.97	0.44	3.666667	0.182233333	4.787766667	1.70697	1706.970128	1802.884615		
42	16.85	17.31	7.51	7.51	0.46	2.657423	0.199572501	7.310427499	1.766327	1766.326531	1812.682927		
43	11.49	11.95	4.91	4.91	0.46	3.849372	0.189004184	4.720995816	1.697443	1697.443182	1813.439434		

44	8.93	9.43	3.79	3.79	0.5	5.302227	0.200954401	3.589045599	1.671986	1671.985816	1819.148936		
45	21.07	21.56	6.96	6.96	0.49	2.272727	0.158181818	6.801818182	1.476712	1476.712329	1821.493625		
46	20.29	20.86	8.87	8.87	0.57	2.732502	0.242372963	8.627627037	1.739783	1739.783153	1834.702259		
47	26.55	27.11	11.84	11.84	0.56	2.065658	0.244573958	11.59542604	1.775377	1775.376555	1843.75		
48	12.57	12.99	5.19	5.19	0.42	3.233256	0.167806005	5.022193995	1.665385	1665.384615	1870.535714		
49	5.14	5.41	1.35	1.35	0.27	4.990758	0.067375231	1.282624769	1.332512	1332.512315	1884.10596		
50	3.98	4.26	1.76	1.76	0.28	6.57277	0.115680751	1.644319249	1.704	1704	1891.156463		
Table A1.14. Density measurements for dwSc.													

Edifice	log	dip (°)	dip (°)	dip (°)	dip (°)	dip (°)	dip (°)	dip (°)	dip (°)	dip (°)	dip (°)
cone 26	10	21	28	33	30	40	40	20			
	81	42	22	28	18						
	12	28	32	2							
	9	36	45	48	48	40	18				
	8	24	35	33	25	17	20	21	10	11	10
	8	16	16	16	6	8	18	14	13	42	72
	8	73	74	44	38	33	22	32	31	22	24
scoria rampart	L8	25	30	10	23						
	L13	39	29	41	50	41	37	41	44	39	35
	L13	43	31	26	29	19	16	32	21		
	L17	13	9	15							
	L20	34	29	18	24	32	39	30	35	32	34
	L20	43	55	30	28						
	L21	32	28	22	35	37	24	49	51	53	57
	L21	63	26	29	25	42	10	24	21	11	17
	L21	3	12	9	20	14	11	23	1	7	7
	L21	18	8	8	11	14	6	18	12	8	
	2	10	16	18	18	15	33	16	24	40	14
	2	14	40	44	41	43	42	5	26	24	25
	2	38	14	32	22	21	34				
	13	21	35	16	9	10	10	11	6	11	
spatter rampart		42	31	35	40	16	32	19	32	28	24
		24	24	22	26	31	48	47	37	22	22
		29	30	25	36	26	28	40	25	23	20
		14	28	23	16	31	28	22	18	64	62
		48	19	53	58	33	45	8	58	51	37
		46	31	12	46	38	71	39	46	46	38
		42	42	55	71	69	64	82	82	64	64
		38	58	46	40	60	37	28	28	85	45
		35	25	13	35	33	40	48	24	31	31
		67	38	33	45	44	45	53	45	62	60
		86	32	35	68	52	74	46	64	44	41

		72	70	74	72	71	65	77	81	81	69
		78	81	67	57	75	60	58	63	62	80
		65	66	59	65	66	68	68	48	70	71
		60	58	60	44	68	44	82	52		
	L3	40	51	10							
	L4	45	32	53	39	44					
	L5	29									
	L6	17	23	34	20	43	47				
	L9	27	40	56							
	L11	36	53	39	31	49	37	43	25	21	33
	L11	45	28	30	50	45					
sheet-like fall deposit		11	11	5	6	8	10	17	14	3	11
		19	28	28	28	9	16	6	27	11	6
		3									
rootless cone		33	20	28	35	70	78	46	38	48	38
		46	64	42	48	28	28	16	35	18	52
		27	20	41	39	14	41	39	43	32	39
		58	20	29	24	6	43	26	34		
Table A1.15. Bedding measurements for edifices.											

WP	log	unit	max clast size	unit thickness (mm)	distance from fissure (m)	facies	aspect ratio	thickness (m)
374	8	1	434	1000	1	waSp	9.3	1
374	8	2	653	250	1	dwsp	24.8	0.25
374	8	4	287	2080	1	waSp	3.6	2.08
374	8	5	137	500	1	waSp	3.1	0.5
374	8	6	107	1000	1	waSp	2.7	1
374		7	552.5	500	1	mwSp	26.2	0.5
374		9	374.444 4444	1250	1	waSp	6.4	1.25
375	10	5	275	3000	1	waSp	3.1	3
375	10	7	67.2	210	74	waSc	1.7	0.21
375	10	9	569	1150	74	waSp	6.8	1.15
375	10	10	648	340	74	mwsp	16	0.34
375	9	4	750	3000	74	waSp	4.85	3
NA	12	2	168		1	waSp	2.8	0
NA	12	3	283		1	waSp	3.2	0
NA	12	5	437		1	waSp	3.7	0
NA	81	1	737	400	1	mwsp	9	0.4
NA	81	3	74	720	1	waSc	2.5	0.72
298	28	1	877	8000	18	waSp	8.2	8
303	14	5	244	1300	612	waSp	2.9	1.3
480	21	1	66	180	250	waSc	2	0.18
480	21	3	52	1200	250	waSc	1.7	1.2
480	21	5	55	660	250	mwSc	3	0.66
406	13	1	86	400	199	waSc	1.7	0.4
406	13	2-4	127	1980	199	waSp	1.7	1.98
406	13	6	500	920	199	waSp	5.2	0.92
406	13	5	667	1200	199	mwsp	34.2	1.2
297	3	1	52	1150	1247	waSc	1.3	1.15
401	11	1-3	103		172	waSc	1.3	0
401	11	4	522		172	dwsp	18.7	0
401	11	5	142		172	waSp	3.2	0
401	11	6	597		172	dwsp	28.6	0
401	11	7	325		172	waSp	2	0
401	11	8	72		172	waSc	1.5	0
293	2	7-9	68		223	waSc	2	0
293	2	10	122		223	waSp	2.3	0
293	2	11	49		223	waSc	1.6	0
293	2	12	117		223	waSp	1.5	0
293	2	13	67		223	waSc	1.7	0
293	2	14	162		223	waSp	1.6	0
293	2	17	122		223	waSp		0
486	N	1	37	420	477	waSc	2.2	0.42

	A							
497	24	4	35	1500	752	waSc	1.7	1.5
508	26	3	25	400	688	NA	1.8	0.4
494	23	1	61	500	529	waSc	1.8	0.5
505	27	2	191	1000	639	waSc	1.6	1
505	27	3	23	110	639	dwSc	1.6	0.11
31	pit	1	112	510	464	waSp	1.3	0.51
31		2-3	35	270	464	scl	1.5	0.27
31	pit 2		94	610	464	scl	1.3	0.61
31	pit 3	1	130	310	464	waSp	1.3	0.31
31		2	42	350	464	scl	1.6	0.35
31	pit 4		110	700	464	waSp	1.8	0.7
31	pit 5		168	1000	464	waSp	1.2	1
31	pit 6		91	650	464	waSp	1.5	0.65
287	29	3	29		126	waSc	1.2	0
287		4	22	2000	126	waSc	1.4	2
41		1-3	136	1600	400	waSp	1.4	1.6
79			326	1300	163	waSp	5.1	1.3
81			256	250	171	waSp	3.8	0.25
84			314	900	184	waSp	5.7	0.9
297			27	500	1205	scl	1.8	0.5
141	31	2	31	500	333	waSc	1.5	0.5
145		1	56	145	190	waSc	1.7	0.145
145		2	254	800	190	waSp	3.5	0.8
147	32	1	33	147	322	mwSc	2.3	0.147
151	33	1	22	250	284	mwSc	3	0.25
158	34	1	55	1230	500	mwSc	3.5	1.23
483	22	2	39	630	443	waSc	1.8	0.63
483		4	21	1750	443	scl	1.4	1.75
158			55	1230	506	mwSc	3.5	1.23
147	32	2	13	460	304	dwSc	12.3	0.46
401	15	1	16	200	160	waSc	2	0.2
401	15	2-3	26	460	160	waSc	2	0.46
y48	16	2	21	90	575	waSc	1.6	0.09
y42	11	2-3	248	930	34	waSp	2.8	0.93
y26	6	1-3	212	1420	112	waSp	2.3	1.42
y28	3	2	85	200	18	waSp	2.1	0.2
77	8	2-3	148	1300	145	waSp	2.5	1.3
77		4	142	740	145	waSp	2.1	0.74
77		5	250	490	145	waSp	3.1	0.49
477	17	1	39	240	201	waSc	1.8	0.24

		2	345	600	201	waSp	4.5	0.6
		4	235	800	201	waSp	3.2	0.8
y57			11	200	458	scl	1.3	0.2
y58			21	260	591	scl	1.4	0.26
y59			21	320	742	scl	1.4	0.32
y60			10	150	893	scl	1.6	0.15
y61			22	350	821	scl	1.2	0.35
y62			25	400	793	scl	1.5	0.4
pr			119	1710	50	scl	1.8	1.71
477	17			1100	185	dwsp		1.1
y56			16	180	317	scl	1.4	0.18
Z22			24	230	656	scl	1.3	0.23
y40			15	180	435	waSc	1.7	0.18
y22			812	8000	25	waSp	21.5	8
y26	6	1-3	212	1420	112	waSp	4.7	1.42
point 1 (see AI)				25000	30			25
30				6000	129			6
12				5000	1			5
2				29000	223			29
11				12000	172			12
pit 1					402			0.75
29					129			4
477				1640	201			1.64
Table A1.16. Dispersal characteristics for the tephra.								

sheet	date	wp	unit	Strike (°)	Dip (°)	modular direction of dip (°)	height from base (mm)
114	24-Jun	401	1	358	48	88	300
				352	61	82	
				352	63	82	
			2	3	78	93	1600
				344	73	74	
				350	83	80	
				341	69	71	
			3	336	78	66	200
				342	80	72	
				25	75	115	
			4	3	75	93	220
				5	68	95	
				14	61	104	
				16	75	106	
			5	5	79	95	75
				10	69	100	
				6	72	96	
			6	6	81	96	180
				356	81	86	
				32	71	122	
			7	32	41	122	260
				21	45	111	
			8	16	52	106	170
13	23-Jun	y46	2	24	39	114	8470
			2	46	29	136	8470
			2	32	41	122	8470
			2	25	50	115	8470
			2	19	41	109	8470
			2	11	37	101	8470
			3	20	41	110	8790
			3	29	44	119	8790
			3	25	39	115	8790
			4	16	35	106	11190
			4	36	43	126	11190
			4	31	31	121	11190
			5	57	26	147	11400
			5	25	29	115	11400
			5	353	19	83	11400
			6	78	16	168	11610
			7	20	21	110	11610
			7	352	32	82	11610
			8	20	21	110	12150

			8	352	32	262	12150
11		401	2	284	17	194	
			2	256	13	166	
11		401	3	183	20	93	
			3	150	8	60	
			3	172	13	82	
			4	166	40	76	
			4	144	44	54	
			4	162	41	72	
			4	156	43	66	
2		293	4	59	10	329	
			4	74	16	344	
			4	66	18	336	
			4	64	18	334	
			7	80	40	350	
			7	28	14	298	
			7	29	14	299	
			9	104	33	14	
			9	90	16	0	
			11	66	6	336	
			11	60	7	330	
			13	32	2	302	
			17	130	21	220	
			17	226	11	316	
			17	180	17	270	
			18	195	3	285	
			18	194	12	284	
			18	230	9	320	
			19	158	20	248	
			21	190	14	280	
			21	208	11	298	
			23	162	23	252	
			23	212	1	302	
			24	214	7	304	
			25	222	7	312	
			26	196	18	286	
			27	194	8	284	
			27	195	8	285	
			29	224	11	314	
			29	310	14	40	
			30	225	6	315	
			32	172	18	262	
			32	178	12	268	
			32	218	8	308	

Table A1.17. Bedding measurements in scoria rampart.

log	unit	X axis (mm)	Y axis (mm)	aspect ratio
8	1	800	50	16
		740	150	4.933333333
		480	30	16
		470	30	15.66666667
		430	45	9.555555556
		360	50	7.2
		340	60	5.666666667
		305	35	8.714285714
		220	70	3.142857143
		200	30	6.666666667
			mean	9.354603175
	av max clast (mm)	434.5	55	
log	unit	X (mm)	Y (mm)	aspect ratio
8	2	1000	25	40
		800	20	40
		210	40	5.25
		600	20	30
		560	30	18.66666667
		750	50	15
				#DIV/0!
				#DIV/0!
				#DIV/0!
				#DIV/0!
			mean	24.81944444
	av max clast (mm)	653.3333	30.83333333	
log	unit	X (mm)	Y (mm)	aspect ratio
8	4	610	120	5.083333333
		180	150	1.2
		500	70	7.142857143
		185	70	2.642857143
		400	60	6.666666667
		130	70	1.857142857
		190	90	2.111111111
		220	60	3.666666667
		300	110	2.727272727
		160	45	3.555555556
			mean	3.66534632
	av max clast (mm)	287.5	84.5	
log	unit	X (mm)	Y (mm)	aspect ratio
8	5	190	60	3.166666667
		120	50	2.4
		250	30	8.333333333
		150	40	3.75
		170	50	3.4

		70	30	2.333333333
		100	90	1.111111111
		155	50	3.1
		65	35	1.857142857
		100	55	1.818181818
			mean	3.126976912
	av max clast (mm)	137	49	
log	unit	X (mm)	Y (mm)	aspect ratio
8	6	90	40	2.25
		65	40	1.625
		150	45	3.333333333
		80	40	2
		85	40	2.125
		90	30	3
		80	44	1.818181818
		130	35	3.714285714
		160	70	2.285714286
		140	25	5.6
			mean	2.775151515
	av max clast (mm)	107	40.9	
log	unit	X (mm)	Y (mm)	aspect ratio
8	7	450	25	18
		630	63	10
		750	95	7.894736842
		580	11	52.72727273
		870	10	87
		190	20	9.5
		500	70	7.142857143
		450	25	18
			mean	26.28310834
	av max clast (mm)	552.5	39.875	
log	unit	X (mm)	Y (mm)	aspect ratio
8	9	250	80	3.125
		220	160	1.375
		200	30	6.666666667
		270	100	2.7
		320	30	10.66666667
		550	170	3.235294118
		520	30	17.33333333
		640	100	6.4
		400	60	6.666666667
				#DIV/0!
			mean	6.463180828

	av max clast (mm)	374.4444	84.4444444	
log	unit	X (mm)	Y (mm)	aspect ratio
10	5	460	60	7.666666667
	m1	250	40	6.25
		250	200	1.25
		240	160	1.5
		140	100	1.4
		400	100	4
		340	70	4.857142857
		150	130	1.153846154
		220	105	2.095238095
		300	200	1.5
			mean	3.167289377
	av max clast (mm)	275	116.5	
log	unit	X (mm)	Y (mm)	aspect ratio
10	5	400	130	3.076923077
	m2	300	55	5.454545455
		500	80	6.25
		120	35	3.428571429
		100	55	1.818181818
		150	60	2.5
		70	60	1.166666667
		200	55	3.636363636
		155	70	2.214285714
		320	150	2.133333333
			mean	3.167887113
	av max clast (mm)	231.5	75	
log	unit	X (mm)	Y (mm)	aspect ratio
10	5	45	30	1.5
	m3	60	30	2
		70	55	1.272727273
		60	50	1.2
		50	50	1
		45	35	1.285714286
		50	30	1.666666667
		30	15	2
		100	20	5
		30	30	1
			mean	1.376406926
	av max clast (mm)	54	34.5	
log	unit	X (mm)	Y (mm)	aspect ratio
10	7	30	22	1.363636364
		15	10	1.5
		13	10	1.3

		15	9	1.666666667
		55	40	1.375
		30	18	1.666666667
		20	20	1
		290	60	4.833333333
		20	12	1.666666667
		20	14	1.428571429
			mean	1.780054113
	av max clast (mm)	50.8	21.5	
log	unit	X (mm)	Y (mm)	aspect ratio
10	8	95	25	3.8
		50	20	2.5
		55	22	2.5
		29	10	2.9
		140	24	5.833333333
		120	65	1.846153846
		79	25	3.16
		19	15	1.266666667
		25	20	1.25
		60	36	1.666666667
			mean	2.672282051
	av max clast (mm)	67.2	26.2	
log	unit	X (mm)	Y (mm)	aspect ratio
10	9	490	70	7
		640	110	5.818181818
		600	80	7.5
		950	100	9.5
		240	40	6
		90	30	3
		490	70	7
		640	110	5.818181818
		600	80	7.5
		950	100	9.5
			mean	6.863636364
	av max clast (mm)	569	79	
log	unit	X (mm)	Y (mm)	aspect ratio
10	10	1150	55	20.90909091
		800	30	26.66666667
		450	40	11.25
		1000	35	28.57142857
		280	50	5.6
		700	60	11.66666667
		160	20	8
			mean	16.09483612
	av max clast (mm)	648.5714	41.4285714	

log	unit	X (mm)	Y (mm)	aspect ratio
9	4	460	80	5.75
	m1	1000	250	4
		1000	80	12.5
		250	70	3.571428571
		700	200	3.5
		440	200	2.2
		1500	105	14.28571429
		210	110	1.909090909
		0	0	#DIV/0!
		0	0	#DIV/0!
			mean	5.964529221
	av max clast (mm)	695	136.875	
log	unit	X (mm)	Y (mm)	aspect ratio
9	4	600	80	7.5
	m2	750	85	8.823529412
		290	100	2.9
		500	90	5.555555556
		750	100	7.5
		660	110	6
		620	220	2.818181818
		800	170	4.705882353
				#DIV/0!
				#DIV/0!
			mean	5.725393642
	av max clast (mm)	621.25	119.375	
log	unit	X (mm)	Y (mm)	aspect ratio
9	4	500	95	5.263157895
	m3	1250	250	5
		500	250	2
				#DIV/0!
				#DIV/0!
				#DIV/0!
				#DIV/0!
				#DIV/0!
				#DIV/0!
				#DIV/0!
			mean	4.087719298
	av max clast (mm)	750	198.3333333	
log	unit	X (mm)	Y (mm)	aspect ratio
12	2	120	70	1.714285714
		300	70	4.285714286
		160	70	2.285714286
		190	65	2.923076923
		190	45	4.222222222

		200	70	2.857142857
		130	50	2.6
		160	50	3.2
		115	45	2.555555556
		120	70	1.714285714
			mean	2.835799756
	av max clast (mm)	168.5	60.5	
log	unit	X (mm)	Y (mm)	aspect ratio
12	3	140	90	1.555555556
		400	50	8
		190	120	1.583333333
		400	130	3.076923077
		190	100	1.9
		380	120	3.166666667
				#DIV/0!
				#DIV/0!
				#DIV/0!
				#DIV/0!
			mean	3.213746439
	av max clast (mm)	283.3333	101.666667	
log	unit	X (mm)	Y (mm)	aspect ratio
12	5	440	90	4.888888889
		670	180	3.722222222
		230	50	4.6
		120	90	1.333333333
		410	100	4.1
		550	130	4.230769231
		250	80	3.125
		700	140	5
		570	180	3.166666667
			mean	3.796320038
	av max clast (mm)	437.7778	115.555556	
log	unit	X (mm)	Y (mm)	aspect ratio
81	1	410	45	9.111111111
		500	100	5
		1300	100	13
				#DIV/0!
				#DIV/0!
				#DIV/0!
				#DIV/0!
				#DIV/0!
				#DIV/0!
				#DIV/0!
			mean	9.037037037

	av max clast (mm)	736.6667	81.6666667	
log	unit	X (mm)	Y (mm)	aspect ratio
81	3	55	35	1.571428571
		45	30	1.5
		150	50	3
		110	50	2.2
		80	25	3.2
		70	65	1.076923077
		50	10	5
		70	25	2.8
		50	20	2.5
		65	30	2.166666667
			mean	2.501501832
	av max clast (mm)	74.5	34	
log	unit	X (mm)	Y (mm)	aspect ratio
81	7	460	250	1.84
		370	100	3.7
		310	100	3.1
		170	90	1.888888889
		270	100	2.7
		135	50	2.7
		250	100	2.5
		100	20	5
		190	20	9.5
		135	40	3.375
			mean	3.630388889
	av max clast (mm)	239	87	
log	unit	X (mm)	Y (mm)	aspect ratio
28	1	910	200	4.55
	m3	430	90	4.777777778
		720	130	5.538461538
		1250	120	10.41666667
		910	70	13
		900	80	11.25
		1170	100	11.7
		1120	70	16
		750	140	5.357142857
		610	60	10.16666667
			mean	8.25548433
	av max clast (mm)	877	106	
log	unit	X (mm)	Y (mm)	aspect ratio
28	1	79	30	2.633333333
	m6	34	30	1.133333333
		29	20	1.45
		90	60	1.5

		49	22	2.227272727
		49	25	1.96
		55	25	2.2
		37	26	1.423076923
		130	80	1.625
		60	30	2
			mean	1.815201632
	av max clast (mm)	61.2	34.8	
log	unit	X (mm)	Y (mm)	aspect ratio
14	5	370	220	1.681818182
		970	90	10.77777778
		350	90	3.888888889
		40	30	1.333333333
		230	100	2.3
		40	30	1.333333333
		40	35	1.142857143
		85	43	1.976744186
		75	35	2.142857143
				#DIV/0!
			mean	2.953067776
	av max clast (mm)	244.4444	74.7777778	
log	unit	X (mm)	Y (mm)	aspect ratio
21	1	85	40	2.125
		46	39	1.179487179
		115	24	4.791666667
		59	49	1.204081633
		50	40	1.25
		90	35	2.571428571
		49	25	1.96
		56	30	1.866666667
		55	25	2.2
		55	35	1.571428571
			mean	2.071975929
	av max clast (mm)	66	34.2	
log	unit	X (mm)	Y (mm)	aspect ratio
21	3	54	40	1.35
		70	45	1.555555556
		50	36	1.388888889
		54	19	2.842105263
		36	20	1.8
		24	20	1.2
		62	45	1.377777778
		64	19	3.368421053
		50	51	0.980392157
		59	40	1.475

			mean	1.733814069
	av max clast (mm)	52.3	33.5	
log	unit	X (mm)	Y (mm)	aspect ratio
21	5	49	20	2.45
		71	10	7.1
		29	23	1.260869565
		40	24	1.666666667
		56	15	3.733333333
		57	12	4.75
		25	25	1
		44	24	1.833333333
		75	26	2.884615385
		34	10	3.4
			mean	3.007881828
	av max clast (mm)	48	18.9	
	sum avmax clast (mm)	55.43333		
log	unit	X (mm)	Y (mm)	aspect ratio
13	1	100	50	2
		85	70	1.214285714
		70	23	3.043478261
		93	70	1.328571429
		65	35	1.857142857
		70	45	1.555555556
		80	70	1.142857143
		55	40	1.375
		65	45	1.444444444
		185	70	2.642857143
			mean	1.760419255
	av max clast (mm)	86.8	51.8	
log	unit	X (mm)	Y (mm)	aspect ratio
13	2	75	35	2.142857143
		250	105	2.380952381
		70	64	1.09375
		90	55	1.636363636
		77	50	1.54
		75	65	1.153846154
		195	75	2.6
		130	75	1.733333333
		130	35	3.714285714
		70	40	1.75
			mean	1.974538836
	av max clast (mm)	116.2	59.9	
log	unit	X (mm)	Y (mm)	aspect ratio
13	3	150	50	3
		115	80	1.4375

		160	90	1.777777778
		100	80	1.25
		100	60	1.666666667
		105	65	1.615384615
		160	70	2.285714286
		120	95	1.263157895
		170	110	1.545454545
		92	70	1.314285714
			mean	1.71559415
	av max clast (mm)	127.2	77	
log	unit	X (mm)	Y (mm)	aspect ratio
13	4	105	90	1.166666667
		80	60	1.333333333
		135	70	1.928571429
		110	74	1.486486486
		50	46	1.086956522
		110	80	1.375
		120	80	1.5
		75	20	3.75
		160	105	1.523809524
		125	70	1.785714286
			mean	1.693653825
	av max clast (mm)	107	69.5	
log	unit	X (mm)	Y (mm)	aspect ratio
13	6	460	90	5.111111111
		400	80	5
		370	60	6.166666667
		590	100	5.9
		680	160	4.25
				#DIV/0!
				#DIV/0!
				#DIV/0!
				#DIV/0!
				#DIV/0!
			mean	5.285555556
	av max clast (mm)	500	98	
log	unit	X (mm)	Y (mm)	aspect ratio
13	5	900	20	45
		820	50	16.4
		650	20	32.5
		710	10	71
		570	10	57
		860	60	14.33333333
		160	50	3.2
				#DIV/0!

				#DIV/0!
				#DIV/0!
			mean	34.2047619
	av max clast (mm)	667.1429	31.4285714	
	sum av max clast (mm)	229.1918		
log	unit	X (mm)	Y (mm)	aspect ratio
3	1	78	50	1.56
		60	34	1.764705882
		79	69	1.144927536
		64	49	1.306122449
		39	26	1.5
		34	32	1.0625
		34	30	1.133333333
		44	33	1.333333333
		56	34	1.647058824
		41	39	1.051282051
			mean	1.350326341
	av max clast (mm)	52.9	39.6	
log	unit	X (mm)	Y (mm)	aspect ratio
11	3	60	50	1.2
	m1	95	55	1.727272727
		29	20	1.45
		100	65	1.538461538
		55	35	1.571428571
		45	35	1.285714286
		30	25	1.2
		45	40	1.125
		65	40	1.625
		65	59	1.101694915
			mean	1.382457204
	av max clast (mm)	58.9	42.4	
log	unit	X (mm)	Y (mm)	aspect ratio
11	3	90	50	1.8
	m2	60	69	0.869565217
		120	55	2.181818182
		65	53	1.226415094
		230	40	5.75
		80	35	2.285714286
		180	60	3
		60	25	2.4
		35	30	1.166666667
		110	40	2.75
			mean	2.343017945
	av max clast (mm)	103	45.7	
log	unit	X (mm)	Y (mm)	aspect ratio

11	3	70	65	1.076923077
	m3	100	74	1.351351351
		80	80	1
		54	40	1.35
		96	39	2.461538462
		66	30	2.2
		50	45	1.111111111
		64	55	1.163636364
		60	50	1.2
		82	53	1.547169811
			mean	1.446173018
	av max clast (mm)	72.2	53.1	
log	unit	X (mm)	Y (mm)	aspect ratio
11	4	600	15	40
		290	18	16.11111111
		500	35	14.28571429
		820	40	20.5
		480	25	19.2
		870	35	24.85714286
		150	50	3
		470	40	11.75
				#DIV/0!
				#DIV/0!
			mean	18.71299603
	av max clast (mm)	522.5	32.25	
log	unit	X (mm)	Y (mm)	aspect ratio
11	5	335	40	8.375
		135	60	2.25
		140	50	2.8
		155	60	2.583333333
		205	50	4.1
		140	50	2.8
		135	60	2.25
		40	20	2
		55	35	1.571428571
		80	20	4
			mean	3.27297619
	av max clast (mm)	142	44.5	
log	unit	X (mm)	Y (mm)	aspect ratio
11	6	500	40	12.5
		540	40	13.5
		800	10	80
		520	20	26
		360	20	18
		520	20	26

		860	30	28.66666667
		630	30	21
		650	20	32.5
				#DIV/0!
			mean	28.68518519
	av max clast (mm)	597.7778	25.5555556	
log	unit	X (mm)	Y (mm)	aspect ratio
11	7	415	170	2.441176471
		300	180	1.666666667
		250	200	1.25
		400	140	2.857142857
		430	320	1.34375
		280	110	2.545454545
		200	100	2
				#DIV/0!
				#DIV/0!
				#DIV/0!
			mean	2.014884363
	av max clast (mm)	325	174.285714	
log	unit	X (mm)	Y (mm)	aspect ratio
11	8	180	150	1.2
		95	70	1.357142857
		60	40	1.5
		55	30	1.833333333
		40	30	1.333333333
		40	25	1.6
		45	40	1.125
		85	40	2.125
		55	30	1.833333333
				#DIV/0!
			mean	1.545238095
	av max clast (mm)	72.77778	50.5555556	
log	unit	X (mm)	Y (mm)	aspect ratio
2	7	59	33	1.787878788
		75	32	2.34375
		59	39	1.512820513
		49	24	2.041666667
		79	20	3.95
		33	22	1.5
		45	19	2.368421053
		34	22	1.545454545
		75	10	7.5
		23	18	1.277777778
			mean	2.582776934
	av max clast (mm)	53.1	23.9	

log	unit	X (mm)	Y (mm)	aspect ratio
2	8	46	28	1.642857143
		60	45	1.333333333
		110	90	1.222222222
		75	50	1.5
		69	30	2.3
		65	45	1.444444444
		79	51	1.549019608
		53	52	1.019230769
		62	59	1.050847458
		64	29	2.206896552
			mean	1.526885153
	av max clast (mm)	68.3	47.9	
log	unit	X (mm)	Y (mm)	aspect ratio
2	9	70	28	2.5
		100	60	1.666666667
		45	36	1.25
		64	40	1.6
		45	25	1.8
		69	30	2.3
		54	24	2.25
		75	73	1.02739726
		84	39	2.153846154
				#DIV/0!
			mean	1.838656676
	av max clast (mm)	67.33333	39.4444444	
log	unit	X (mm)	Y (mm)	aspect ratio
2	10	119	80	1.4875
		250	50	5
		99	90	1.1
		120	69	1.739130435
		105	52	2.019230769
		135	40	3.375
		78	51	1.529411765
		99	34	2.911764706
		150	55	2.727272727
		69	50	1.38
			mean	2.32693104
	av max clast (mm)	122.4	57.1	
log	unit	X (mm)	Y (mm)	aspect ratio
2	11	44	15	2.933333333
		55	30	1.833333333
		31	29	1.068965517
		50	24	2.083333333
		59	40	1.475

		54	31	1.741935484
		50	49	1.020408163
		60	50	1.2
		49	36	1.361111111
		45	25	1.8
			mean	1.651742028
	av max clast (mm)	49.7	32.9	
log	unit	X (mm)	Y (mm)	aspect ratio
2	12	79	86	0.918604651
		110	55	2
		109	84	1.297619048
		125	75	1.666666667
		155	80	1.9375
		155	60	2.583333333
		130	90	1.444444444
		106	85	1.247058824
		130	70	1.857142857
		80	79	1.012658228
			mean	1.596502805
	av max clast (mm)	117.9	76.4	
log	unit	X (mm)	Y (mm)	aspect ratio
2	13	85	35	2.428571429
		71	70	1.014285714
		105	30	3.5
		60	35	1.714285714
		59	26	2.269230769
		45	30	1.5
		99	79	1.253164557
		39	20	1.95
		42	36	1.166666667
		65	60	1.083333333
			mean	1.787953818
	av max clast (mm)	67	42.1	
log	unit	X (mm)	Y (mm)	aspect ratio
2	14	200	183	1.092896175
		116	120	0.966666667
		199	188	1.058510638
		225	100	2.25
		110	60	1.833333333
		88	82	1.073170732
		288	120	2.4
		135	90	1.5
		78	50	1.56
		185	70	2.642857143
			mean	1.637743469

	av max clast (mm)	162.4	106.3	
log	unit	X (mm)	Y (mm)	aspect ratio
2	15	47	27	1.740740741
	m3	44	20	2.2
		59	29	2.034482759
		124	44	2.818181818
		53	44	1.204545455
		80	40	2
		100	79	1.265822785
		75	40	1.875
		86	51	1.68627451
		55	26	2.115384615
			mean	1.894043268
	av max clast (mm)	72.3	40	
log	unit	X (mm)	Y (mm)	aspect ratio
2	16	142	72	1.972222222
		70	65	1.076923077
		115	99	1.161616162
		86	36	2.388888889
		66	55	1.2
		140	50	2.8
		240	115	2.086956522
		130	60	2.166666667
		130	70	1.857142857
		102	56	1.821428571
			mean	1.853184497
	av max clast (mm)	122.1	67.8	
log	unit	X (mm)	Y (mm)	aspect ratio
2	17	424	119	3.56302521
	top m of entire section	189	70	2.7
		130	42	3.095238095
		99	88	1.125
		99	72	1.375
		260	65	4
		81	56	1.446428571
		177	140	1.264285714
		110	55	2
		150	55	2.727272727
			mean	2.329625032
	av max clast (mm)	171.9	76.2	
log	unit	X (mm)	Y (mm)	aspect ratio
2	17	350	80	4.375
	base	120	100	1.2
		120	40	3
		70	40	1.75

		90	28	3.214285714
		120	60	2
		140	40	3.5
		105	60	1.75
		130	60	2.166666667
		220	60	3.666666667
			mean	2.662261905
	av max clast (mm)	146.5	56.8	
log	unit	X (mm)	Y (mm)	aspect ratio
2	17	360	160	2.25
	m1	240	100	2.4
		180	120	1.5
		350	130	2.692307692
		300	160	1.875
		820	140	5.857142857
		360	120	3
		420	100	4.2
		980	90	10.88888889
		430	180	2.388888889
			mean	3.705222833
	av max clast (mm)	444	130	
log	unit	X (mm)	Y (mm)	aspect ratio
2	17	195	90	2.166666667
	m2	280	160	1.75
		550	100	5.5
		190	70	2.714285714
		3800	100	38
		385	150	2.566666667
		2650	50	53
				#DIV/0!
				#DIV/0!
				#DIV/0!
			mean	15.09965986
	av max clast (mm)	1150	102.857143	
log	unit	X (mm)	Y (mm)	aspect ratio
2	17	200	100	2
	m3	200	150	1.333333333
		370	90	4.111111111
		260	80	3.25
		620	190	3.263157895
		230	80	2.875
		220	180	1.222222222
		210	130	1.615384615
		280	90	3.111111111
		390	60	6.5

			mean	2.928132029
	av max clast (mm)	298	115	
log	unit	X (mm)	Y (mm)	aspect ratio
2	17	80	25	3.2
	4500-4100	105	30	3.5
		65	23	2.826086957
		140	40	3.5
		95	35	2.714285714
		70	40	1.75
		120	50	2.4
		65	40	1.625
		95	20	4.75
		120	50	2.4
			mean	2.866537267
	av max clast (mm)	95.5	35.3	
log	unit	X (mm)	Y (mm)	aspect ratio
2	17	330	120	2.75
	5000-4500	150	70	2.142857143
		140	65	2.153846154
		115	80	1.4375
		270	110	2.454545455
		125	60	2.083333333
		105	34	3.088235294
		115	40	2.875
		80	35	2.285714286
		170	60	2.833333333
			mean	2.4104365
	av max clast (mm)	160	67.4	
	sum av max red scoria clast (mm)	198.1431		
log	unit	X (mm)	Y (mm)	aspect ratio
16	2	26	22	1.181818182
		20	19	1.052631579
		24	21	1.142857143
		15	10	1.5
		20	16	1.25
		20	11	1.818181818
		18	17	1.058823529
		20	17	1.176470588
		22	17	1.294117647
				#DIV/0!
			mean	1.274988943
	av max clast (mm)	20.55556	16.6666667	
log	unit	X (mm)	Y (mm)	aspect ratio
17	1	20	9	2.222222222
		13	9	1.444444444

		14	10	1.4
		21	19	1.105263158
		17	12	1.416666667
		21	5	4.2
		25	12	2.083333333
		21	15	1.4
		21	9	2.333333333
				#DIV/0!
			mean	1.956140351
	av max clast (mm)	19.22222	11.11111111	
log	unit	X (mm)	Y (mm)	aspect ratio
19		40	20	2
		27	25	1.08
		29	30	0.966666667
		21	30	0.7
		16	75	0.213333333
		26	25	1.04
		35	10	3.5
		22	17	1.294117647
		9	7	1.285714286
		14	14	1
			mean	1.307983193
	av max clast (mm)	23.9	25.3	
log	unit	X (mm)	Y (mm)	aspect ratio
	1	25	19	1.315789474
pg94 bk3		34	10	3.4
		40	12	3.333333333
		26	10	2.6
		49	16	3.0625
		49	30	1.633333333
		40	20	2
		60	30	2
		25	20	1.25
		24	16	1.5
			mean	2.209495614
	av max clast (mm)	37.2	18.3	
log	unit	X (mm)	Y (mm)	aspect ratio
	2	300	20	15
log	unit	X (mm)	Y (mm)	aspect ratio
24	4	28	25	1.12
		32	17	1.882352941
		30	20	1.5
		30	25	1.2
		28	25	1.12
		64	35	1.828571429

		50	25	2
		32	10	3.2
		34	30	1.133333333
		28	12	2.333333333
			mean	1.731759104
	av max clast (mm)	35.6	22.4	
log	unit	X (mm)	Y (mm)	aspect ratio
26	3	25	15	1.666666667
		42	13	3.230769231
		39	15	2.6
		31	20	1.55
		17	9	1.888888889
		17	15	1.133333333
		32	13	2.461538462
		24	15	1.6
		11	7	1.571428571
		15	12	1.25
			mean	1.895262515
	av max clast (mm)	25.3	13.4	
log	unit	X (mm)	Y (mm)	aspect ratio
26	5	10	20	0.5
		35	21	1.666666667
		13	9	1.444444444
		16	10	1.6
		11	9	1.222222222
		34	10	3.4
		20	9	2.222222222
		13	10	1.3
		21	19	1.105263158
		17	15	1.133333333
			mean	1.559415205
	av max clast (mm)	19	13.2	
log	unit	X (mm)	Y (mm)	aspect ratio
23	1	43	35	1.228571429
		65	70	0.928571429
		100	40	2.5
		40	40	1
		75	30	2.5
		66	60	1.1
		74	30	2.466666667
		39	30	1.3
		49	12	4.083333333
		62	40	1.55
			mean	1.865714286
	av max clast (mm)	61.3	38.7	

log	unit	X (mm)	Y (mm)	aspect ratio
27	2	300	130	2.307692308
		100	70	1.428571429
		180	170	1.058823529
		190	160	1.1875
		130	90	1.444444444
		130	40	3.25
		70	55	1.272727273
		250	100	2.5
		160	150	1.066666667
		400	340	1.176470588
			mean	1.669289624
	av max clast (mm)	191	130.5	
log	unit	X (mm)	Y (mm)	aspect ratio
27	3	22	13	1.692307692
		22	15	1.466666667
		19	10	1.9
		21	13	1.615384615
		33	26	1.269230769
		26	15	1.733333333
				#DIV/0!
				#DIV/0!
				#DIV/0!
				#DIV/0!
			mean	1.612820513
	av max clast (mm)	23.83333	15.3333333	
log	unit	X (mm)	Y (mm)	aspect ratio
27	1	120	25	4.8
		86	26	3.307692308
		70	30	2.333333333
		90	22	4.090909091
		70	35	2
		65	45	1.444444444
		95	50	1.9
		110	70	1.571428571
		85	25	3.4
		70	45	1.555555556
			mean	2.64033633
	av max clast (mm)	86.1	37.3	
log	unit	X (mm)	Y (mm)	aspect ratio
wp204	1	20	10	2
		25	15	1.666666667
		35	11	3.181818182
		26	15	1.733333333
		25	19	1.315789474

		29	10	2.9
		15	15	1
		29	15	1.933333333
		40	15	2.666666667
		19	14	1.357142857
			mean	1.975475051
	av max clast (mm)	26.3	13.9	
log	unit	X (mm)	Y (mm)	aspect ratio
pit 1	1	96	73	1.315068493
		120	67	1.791044776
		139	110	1.263636364
		106	58	1.827586207
		115	99	1.161616162
		78	44	1.772727273
		139	115	1.208695652
		110	100	1.1
		129	113	1.14159292
		90	70	1.285714286
			mean	1.386768213
	av max clast (mm)	112.2	84.9	
log	unit	X (mm)	Y (mm)	aspect ratio
pit 1	2	39	20	1.95
		24	15	1.6
		19	11	1.727272727
		29	21	1.380952381
		37	31	1.193548387
		26	15	1.733333333
		33	24	1.375
		29	22	1.318181818
		41	32	1.28125
		36	30	1.2
			mean	1.475953865
	av max clast (mm)	31.3	22.1	
log	unit	X (mm)	Y (mm)	aspect ratio
pit 1	3	39	24	1.625
		24	10	2.4
		30	22	1.363636364
		36	32	1.125
		35	29	1.206896552
		28	20	1.4
		33	22	1.5
		34	23	1.47826087
		46	34	1.352941176
		45	23	1.956521739
			mean	1.54082567

	av max clast (mm)	35	23.9	
log	unit	X (mm)	Y (mm)	aspect ratio
pit 2		80	65	1.230769231
		110	85	1.294117647
		103	72	1.430555556
		100	70	1.428571429
		75	30	2.5
		144	120	1.2
		75	76	0.986842105
		70	70	1
		110	80	1.375
		77	67	1.149253731
			mean	1.35951097
	av max clast (mm)	94.4	73.5	
log	unit	X (mm)	Y (mm)	aspect ratio
pit 3	1	199	150	1.326666667
		100	95	1.052631579
		225	160	1.40625
		106	66	1.606060606
		85	66	1.287878788
		160	115	1.391304348
		103	80	1.2875
		115	90	1.277777778
		70	60	1.166666667
		145	70	2.071428571
			mean	1.3874165
	av max clast (mm)	130.8	95.2	
log	unit	X (mm)	Y (mm)	aspect ratio
pit 3	2	49	30	1.633333333
		46	20	2.3
		51	19	2.684210526
		36	29	1.24137931
		47	35	1.342857143
		39	27	1.444444444
		34	22	1.545454545
		46	27	1.703703704
		39	34	1.147058824
		40	25	1.6
			mean	1.664244183
	av max clast (mm)	42.7	26.8	
log	unit	X (mm)	Y (mm)	aspect ratio
pit 4		76	70	1.085714286
		140	85	1.647058824
		70	59	1.186440678
		90	90	1

		100	45	2.222222222
		90	65	1.384615385
		95	65	1.461538462
		140	25	5.6
		110	75	1.466666667
		190	110	1.727272727
			mean	1.878152925
	av max clast (mm)	110.1	68.9	
log	unit	X (mm)	Y (mm)	aspect ratio
pit 5		100	95	1.052631579
		100	74	1.351351351
		120	100	1.2
		245	150	1.633333333
		310	330	0.939393939
		240	200	1.2
		170	120	1.416666667
		130	120	1.083333333
		130	95	1.368421053
		135	120	1.125
			mean	1.237013126
	av max clast (mm)	168	140.4	
log	unit	X (mm)	Y (mm)	aspect ratio
pit 6		130	100	1.3
		120	71	1.690140845
		100	55	1.818181818
		160	140	1.142857143
		100	40	2.5
		65	55	1.181818182
		85	80	1.0625
		85	60	1.416666667
		65	45	1.444444444
		90	50	1.8
			mean	1.53566091
	av max clast (mm)	100	69.6	
	sum av max clast (mm)	91.61111		
log	unit	X (mm)	Y (mm)	aspect ratio
29	3	45	48	0.9375
		20	24	0.833333333
		24	37	0.648648649
		30	47	0.638297872
		28	16	1.75
		18	15	1.2
		43	30	1.433333333
		38	23	1.652173913
		25	11	2.272727273

		19	18	1.055555556
			mean	1.242156993
	av max clast (mm)	29	26.9	
log	unit	X (mm)	Y (mm)	aspect ratio
29	4	25	20	1.25
		15	9	1.666666667
		25	22	1.136363636
		20	15	1.333333333
		22	15	1.466666667
		20	16	1.25
		19	13	1.461538462
		20	10	2
		40	40	1
		21	14	1.5
			mean	1.406456876
	av max clast (mm)	22.7	17.4	
log	unit	X (mm)	Y (mm)	aspect ratio
wp041	1	130	125	1.04
		170	120	1.416666667
		80	75	1.066666667
		105	75	1.4
		126	95	1.326315789
		135	75	1.8
		180	110	1.636363636
		189	105	1.8
		105	80	1.3125
				#DIV/0!
			mean	1.422056973
	av max clast (mm)	135.5556	95.5555556	
log	unit	X (mm)	Y (mm)	aspect ratio
wp401	2	105	50	2.1
		140	90	1.555555556
		145	80	1.8125
		130	100	1.3
		185	130	1.423076923
		155	140	1.107142857
		110	85	1.294117647
		160	110	1.454545455
		125	90	1.388888889
		105	70	1.5
			mean	1.493582733
	av max clast (mm)	136	94.5	
log	unit	X (mm)	Y (mm)	aspect ratio
wp401	3	135	70	1.928571429
		140	90	1.555555556

		125	70	1.785714286
		140	65	2.153846154
		90	60	1.5
		55	38	1.447368421
		90	35	2.571428571
		150	70	2.142857143
		120	70	1.714285714
		100	60	1.666666667
			mean	1.846629394
	av max clast (mm)	114.5	62.8	
	sum av max clast (mm)	128.6852		
log	unit	X (mm)	Y (mm)	aspect ratio
30	2	250	200	1.25
		155	90	1.722222222
		230	110	2.090909091
		110	100	1.1
		270	140	1.928571429
		130	60	2.166666667
		200	155	1.290322581
		100	85	1.176470588
		150	110	1.363636364
		60	45	1.333333333
			mean	1.542213227
	av max clast (mm)	165.5	109.5	
log	unit	X (mm)	Y (mm)	aspect ratio
30	2	300	140	2.142857143
	m4	310	130	2.384615385
		150	110	1.363636364
		90	60	1.5
		80	50	1.6
		370	110	3.363636364
		125	50	2.5
		200	80	2.5
		200	100	2
		245	150	1.633333333
			mean	2.098807859
	av max clast (mm)	207	98	
log	unit	X (mm)	Y (mm)	aspect ratio
30	4	75	50	1.5
		80	65	1.230769231
		60	40	1.5
		100	95	1.052631579
		165	200	0.825
		110	40	2.75
		70	45	1.555555556

		100	65	1.538461538
		170	140	1.214285714
		70	35	2
			mean	1.516670362
	av max clast (mm)	100	77.5	
log	unit	X (mm)	Y (mm)	aspect ratio
wp079		170	40	4.25
		240	85	2.823529412
		370	30	12.33333333
		360	50	7.2
		390	120	3.25
		280	120	2.333333333
		290	60	4.833333333
		360	60	6
		440	120	3.666666667
		360	80	4.5
			mean	5.119019608
	av max clast (mm)	326	76.5	
log	unit	X (mm)	Y (mm)	aspect ratio
wp081		330	120	2.75
		190	85	2.235294118
		240	70	3.428571429
		280	60	4.666666667
		260	50	5.2
		290	60	4.833333333
				#DIV/0!
				#DIV/0!
				#DIV/0!
				#DIV/0!
			mean	3.852310924
	av max clast (mm)	265	74.1666667	
log	unit	X (mm)	Y (mm)	aspect ratio
wp084		280	70	4
		260	50	5.2
		410	70	5.857142857
		200	40	5
		260	70	3.714285714
		295	60	4.916666667
		450	50	9
		360	45	8
				#DIV/0!
				#DIV/0!
			mean	5.711011905
	av max clast (mm)	314.375	56.875	
log	unit	X (mm)	Y (mm)	aspect ratio

297 bk4pg77		26	15	1.733333333
		25	12	2.083333333
		23	12	1.916666667
		21	11	1.909090909
		42	35	1.2
		31	16	1.9375
		24	13	1.846153846
		22	12	1.833333333
		32	18	1.777777778
		26	13	2
			mean	1.82371892
	av max clast (mm)	27.2	15.7	
log	unit	X (mm)	Y (mm)	aspect ratio
31	2	45	20	2.25
		35	35	1
		35	30	1.166666667
		45	28	1.607142857
		19	19	1
		42	40	1.05
		25	15	1.666666667
		13	5	2.6
		30	16	1.875
		25	20	1.25
			mean	1.546547619
	av max clast (mm)	31.4	22.8	
log	unit	X (mm)	Y (mm)	aspect ratio
wp145	1	55	24	2.291666667
		70	50	1.4
		75	40	1.875
		47	30	1.566666667
		59	55	1.072727273
		70	30	2.333333333
		45	40	1.125
		59	30	1.966666667
		35	20	1.75
		50	25	2
			mean	1.738106061
	av max clast (mm)	56.5	34.4	
log	unit	X (mm)	Y (mm)	aspect ratio
wp145	2	340	100	3.4
		220	110	2
		500	130	3.846153846
		220	60	3.666666667
		240	50	4.8
		370	80	4.625

		120	70	1.714285714
		200	60	3.333333333
		140	30	4.666666667
		190	50	3.8
			mean	3.585210623
	av max clast (mm)	254	74	
	sum av max clast (mm)	155.25		
log	unit	X (mm)	Y (mm)	aspect ratio
32	1	25	15	1.666666667
		40	16	2.5
		16	5	3.2
		34	9	3.777777778
		20	10	2
		45	16	2.8125
		26	24	1.083333333
		50	13	3.846153846
		30	30	1
		50	36	1.388888889
			mean	2.327532051
	av max clast (mm)	33.6	17.4	
log	unit	X (mm)	Y (mm)	aspect ratio
33	1	22	19	1.157894737
		20	6	3.333333333
		20	15	1.333333333
		21	6	3.5
		23	5	4.6
		32	7	4.571428571
		16	5	3.2
		22	14	1.571428571
		26	5	5.2
		19	9	2.111111111
			mean	3.057852966
	av max clast (mm)	22.1	9.1	
log	unit	X (mm)	Y (mm)	aspect ratio
wp152		27	10	2.7
		12	15	0.8
		30	14	2.142857143
		20	12	1.666666667
		40	30	1.333333333
		15	12	1.25
		44	30	1.466666667
		32	11	2.909090909
		30	15	2
		25	15	1.666666667
			mean	1.793528139

	av max clast (mm)	27.5	16.4	
log	unit	X (mm)	Y (mm)	aspect ratio
34	1	64	15	4.266666667
		55	25	2.2
		50	20	2.5
		40	10	4
		65	30	2.166666667
		70	20	3.5
		46	6	7.666666667
		39	10	3.9
		30	10	3
		95	45	2.111111111
			mean	3.531111111
	av max clast (mm)	55.4	19.1	
log	unit	X (mm)	Y (mm)	aspect ratio
wp174		95	70	1.357142857
		99	55	1.8
		70	50	1.4
		120	90	1.333333333
		80	65	1.230769231
		140	60	2.333333333
		85	60	1.416666667
		270	100	2.7
		120	100	1.2
		75	50	1.5
			mean	1.627124542
	av max clast (mm)	115.4	70	
log	unit	X (mm)	Y (mm)	aspect ratio
22	1	2000	105	19.04761905
		2250	200	11.25
		1350	60	22.5
				#DIV/0!
				#DIV/0!
				#DIV/0!
				#DIV/0!
				#DIV/0!
				#DIV/0!
				#DIV/0!
			mean	17.59920635
	av max clast (mm)	1866.667	121.666667	
log	unit	X (mm)	Y (mm)	aspect ratio
22	2	44	15	2.933333333
		34	12	2.833333333
		20	15	1.333333333
		32	20	1.6

		35	10	3.5
		60	40	1.5
		60	50	1.2
		25	15	1.666666667
		35	35	1
		45	42	1.071428571
			mean	1.863809524
	av max clast (mm)	39	25.4	
log	unit	X (mm)	Y (mm)	aspect ratio
22	3	2000	55	36.36363636
		600	15	40
		500	100	5
		115	10	11.5
		350	5	70
		560	5	112
				#DIV/0!
				#DIV/0!
				#DIV/0!
				#DIV/0!
			mean	45.81060606
	av max clast (mm)	687.5	31.6666667	
log	unit	X (mm)	Y (mm)	aspect ratio
22	4	35	32	1.09375
		20	15	1.333333333
		30	10	3
		30	25	1.2
		25	10	2.5
		12	12	1
		10	12	0.833333333
		15	15	1
		12	10	1.2
				#DIV/0!
			mean	1.462268519
	av max clast (mm)	21	15.6666667	
	sum av max clast (mm)	653.5417		
log	unit	X (mm)	Y (mm)	aspect ratio
wp165		1000	80	12.5
		640	110	5.818181818
		550	100	5.5
		900	65	13.84615385
		500	120	4.166666667
				#DIV/0!
				#DIV/0!
				#DIV/0!
				#DIV/0!

				#DIV/0!
			mean	8.366200466
	av max clast (mm)	718	95	
log	unit	X (mm)	Y (mm)	aspect ratio
wp166		1030	120	8.583333333
		1110	160	6.9375
		750	60	12.5
				#DIV/0!
				#DIV/0!
				#DIV/0!
				#DIV/0!
				#DIV/0!
				#DIV/0!
				#DIV/0!
			mean	9.340277778
	av max clast (mm)	963.3333	113.333333	
log	unit	X (mm)	Y (mm)	aspect ratio
wp174		95	70	1.357142857
		99	55	1.8
		70	50	1.4
		120	90	1.333333333
		80	65	1.230769231
		140	60	2.333333333
		85	60	1.416666667
		270	100	2.7
		120	100	1.2
		75	50	1.5
			mean	1.627124542
	av max clast (mm)	115.4	70	
log	unit	X (mm)	Y (mm)	aspect ratio
wp158		64	15	4.266666667
		55	25	2.2
		50	20	2.5
		40	10	4
		65	30	2.166666667
		70	20	3.5
		46	6	7.666666667
		39	10	3.9
		30	10	3
		95	45	2.111111111
			mean	3.531111111
	av max clast (mm)	55.4	19.1	
29	M1	15	18	0.8
		70	59	1.1
		29	5	5.8

		31	13	2.3
		22	11	2
		25	12	2
		26	18	1.4
		39	7	5.5
		28	4	7
		17	13	1.3
	Av max clast (mm)	30.2	16	2.9
29	M6	25	25	1
		30	22	1.3
		49	35	1.4
		25	30	0.8
		30	20	1.5
		25	24	1
		25	23	1.9
		31	15	2
		15	13	1.1
	Av max clast (mm)	28	21	
			mean	1.3
29	M7	75	30	2.5
		50	23	2.1
		18	17	1
		31	20	1.5
		25	19	1.3
		37	23	1.6
		29	25	1.1
		25	16	1.5
		22	14	1.5
		19	18	1
	Av max clast (mm)	33	20	1.5
			mean	1.5
Table A1.18. Stratigraphic log measurements from 2012.				

date	wp	lo g	bk,p g	unit	clast type	x (mm)	y (mm)	unit thickness (mm)	aspect ratio
24- Jun	401	1 5	5, 144	1	sc	16	8	200	2
						28	8		3.5
						13	11		1.181818 182
						25	7		3.571428 571
						32	20		1.6
						8	7		1.142857 143
						11	7		1.571428

									571
						10	8		1.25
						10	7		1.428571 429
						14	4		3.5
					mean	16.7	8.7		2.074610 39
					agg	100	60		1.666666 667
						90	40		2.25
						110	40		2.75
						70	20		3.5
						60	40		1.5
					mean	86	40		2.333333 333
				2	sc	20	16	320	1.25
						16	8		2
						16	4		4
						22	16		1.375
						16	13		1.230769 231
						23	15		1.533333 333
						10	8		1.25
						22	15		1.466666 667
						16	9		1.777777 778
						13	4		3.25
					mean	17.4	10.8		1.913354 701
				3	sc	32	6	140	5.333333 333
						15	5		3
						32	10		3.2
						32	30		1.066666 667
						30	21		1.428571 429
						20	10		2
					mean	26.833 33	13.666 67		2.671428 571
				4	agg	80	20	250	4
						80	40		2
						60	50		1.2
						60	20		3
						130	54		2.407407 407

						70	50		1.4
					mean	80	39		2.334567 901
				6	agg	55	10		5.5
						60	16		3.75
						57	17		3.352941 176
						32	12		2.666666 667
						80	16		5
						50	30		1.666666 667
						59	8		7.375
						28	11		2.545454 545
						43	8		5.375
						39	20		1.95
					mean	50.3	14.8		3.918172 906
23- Jun	y46	1 3	5, 139	3	sc	21	16	320	1.3125
						28	15		1.866666 667
						22	8		2.75
						58	21		2.761904 762
						24	6		4
						60	10		6
						43	30		1.433333 333
						120	16		7.5
						64	33		1.939393 939
						28	24		1.166666 667
					mean	46.8	17.9		3.073046 537
				4, ml	sc	190	60	2400	3.166666 667
						105	50		2.1
						110	50		2.2
						80	30		2.666666 667
						150	40		3.75
						70	30		2.333333 333
						100	30		3.333333 333

						125	30		4.166666 667
						70	40		1.75
					mean	111.11 11	40		2.829629 63
				4, m2		100	30		3.333333 333
						75	60		1.25
						110	20		5.5
						150	55		2.727272 727
						110	40		2.75
						90	40		2.25
						110	35		3.142857 143
						70	20		3.5
						100	40		2.5
						80	30		2.666666 667
					mean	99.5	37		2.962012 987
				6, m1		63	16	5000	3.9375
						49	20		2.45
						100	20		5
						102	50		2.04
						69	20		3.45
						60	40		1.5
						36	28		1.285714 286
						63	24		2.625
						60	20		3
						54	16		3.375
					mean	65.6	25.4		2.866321 429
				m2		190	60		3.166666 667
						70	40		1.75
						130	40		3.25
						95	30		3.166666 667
						150	40		3.75
						90	50		1.8
						130	45		2.888888 889
						130	70		1.857142 857

						100	40		2.5
						80	40		2
					mean	116.5	45.5		2.612936 508
				1st bomb bed		160	60		2.666666 667
						120	60		2
						80	50		1.6
						210	50		4.2
						145	50		2.9
						230	40		5.75
					mean	157.5	51.666 67		3.186111 111
				m4		100	30		3.333333 333
						80	55		1.454545 455
						70	30		2.333333 333
						64	43		1.488372 093
						70	28		2.5
						64	40		1.6
						70	16		4.375
						190	40		4.75
						200	60		3.333333 333
						135	50		2.7
						130	40		3.25
					mean	106.63 64	39.272 73		2.778458 421
				upper 380		130	40		3.25
						160	60		2.666666 667
						160	70		2.285714 286
						170	80		2.125
						140	60		2.333333 333
						120	50		2.4
					mean	146.66 67	60		2.510119 048
				10		70	28	1500	2.5
						58	11		5.272727 273
						130	25		5.2
						90	8		11.25
						64	25		2.56

						74	32		2.3125
						58	16		3.625
						80	21		3.80952381
						73	16		4.5625
				mean		77.444	20.222		4.565805676
				8		28	20		1.4
						32	14		2.285714286
						80	30		2.666666667
						90	45		2
						60	23		2.608695652
						54	30		1.8
						50	10		5
				mean		56.285	24.571		2.537296658
01-Jul	y48	16	6,59	1	sediment	180	130	800	1.384615385
						110	80		1.375
						160	120		1.333333333
						180	80		2.25
						140	150		0.933333333
						800	670		1.194029851
				mean		261.66	205		1.41171865
				2	sc	16	10	90	1.6
						19	16		1.1875
						20	11		1.818181818
						16	20		0.8
						21	11		1.909090909
						23	16		1.4375
						24	20		1.2
						30	20		1.5
						30	8		3.75
						16	16		1
				mean		21.5	14.8		1.620227273
24-Jun	401	114	141	1	spatters	130	60	300	2.166666667
						190	45		4.222222

									222
						100	30		3.333333 333
						220	80		2.75
						190	70		2.714285 714
						200	80		2.5
						130	50		2.6
						320	80		4
				mean		185	61.875		3.035813 492
				2	mwew	430	40	1600	10.75
						600	70		8.571428 571
						400	10		40
						400	10		40
						680	45		15.11111 111
						270	40		6.75
						510	30		17
				mean		470	35		19.74036 281
				3	spatters	90	30	200	3
						160	15		10.66666 667
						200	80		2.5
						130	55		2.363636 364
						120	10		12
					mean	140	38		6.106060 606
				5	mwsc1	80	16	75	5
						58	8		7.25
						59	8		7.375
						64	30		2.133333 333
						32	16		2
						86	20		4.3
						64	24		2.666666 667
						51	20		2.55
						64	25		2.56
						50	10		5
					mean	60.8	17.7		4.0835
				6	scb	70	50	180	1.4
						70	70		1
						54	40		1.35

						130	32		4.0625
					mean	81	48		1.953125
				7	sp	300	120	260	2.5
						500	110		4.545454 545
					mean	400	115		3.522727 273
				8	mwsc1	20	16	170	1.25
						39	20		1.95
						20	16		1.25
						40	16		2.5
						50	8		6.25
						50	12		4.166666 667
					mean	36.5	14.666 67		2.894444 444
				9	sp	340	130	450	2.615384 615
				11	spatter s	140	30	1300	4.666666 667
						220	75		2.933333 333
						150	50		3
						210	70		3
						180	70		2.571428 571
						170	50		3.4
						155	35		4.428571 429
					mean	175	54.285 71		3.326923 077
17- Jun	y42	11 1	100	2	clots	130	55	270 - 500	2.363636 364
						170	90		1.888888 889
						80	60		1.333333 333
						230	80		2.875
						330	100		3.3
						100	80		1.25
						135	120		1.125
					mean	167.85 71	83.571 43		2.019408 369
				3	clots	100	70		1.428571 429
						420	40		10.5
						160	60		2.666666 667

						270	60		4.5
						270	70		3.857142857
						220	70		3.142857143
						300	70		4.285714286
					mean	248.5714	62.85714		3.477536075
11-Jun	y26	6	5,41	1	clots	65	20	360	3.25
						45	15		3
						160	120		1.333333333
						70	60		1.166666667
						170	80		2.125
						80	70		1.142857143
						150	80		1.875
						110	70		1.571428571
					mean	106.25	64.375		2.322753608
				3	clots	150	80	300-1060	1.875
						90	35		2.571428571
						90	90		1
						60	50		1.2
						900	30		30
						110	60		1.833333333
						90	30		3
					mean	212.8571	53.57143		4.724894408
					sp	60	40		1.5
						100	50		2
						115	30		3.833333333
						95	40		2.375
						95	60		1.583333333
						110	90		1.222222222
						80	50		1.6
						110	50		2.2
						90	60		1.5
						160	120		1.3333333

									333
						110	100		1.1
						60	35		1.714285 714
						110	90		1.222222 222
					mean	99.615 38	62.692 31		1.585039 683
11- Jun	y35	14	40	1		130	65	750	2
						80	40		2
						60	30		2
						120	70		1.714285 714
						75	50		1.5
						120	50		2.4
						45	40		1.125
						150	50		3
						55	30		1.833333 333
						65	30		2.166666 667
					mean	90	45.5		1.973928 571
10- Jun	y28	13	25	2	spatter s	55	30	200	1.833333 333
						70	20		3.5
						95	90		1.055555 556
						120	80		1.5
						115	30		3.833333 333
						55	50		1.1
					mean	85	50		2.179615 079
						20	10		2
						10	8		1.25
						5	3		1.666666 667
						20	8		2.5
						5	5		1
						12	10		1.2
						10	10		1
						20	15		1.333333 333
						20	17		1.176470 588
					mean	13.555	9.5555		1.530608

						56	56		567
				5	agg	20	20	210	1
						25	18		1.388888 889
						17	17		1
						55	18		3.055555 556
						24	20		1.2
						43	30		1.433333 333
						20	12		1.666666 667
						17	12		1.416666 667
						36	25		1.44
						10	5		2
					mean	26.7	17.7		1.560111 111
				6	agg	55	30	190	1.833333 333
						70	20		3.5
						100	50		2
						55	25		2.2
						110	80		1.375
						20	15		1.333333 333
						70	40		1.75
						45	20		2.25
						70	50		1.4
					mean	66.111 11	36.666 67		1.920177 778
12- Jun	77	8	59	2	spatter s	165	50	600	3.3
						180	50		3.6
						115	65		1.769230 769
						160	50		3.2
						130	60		2.166666 667
						80	40		2
						130	70		1.857142 857
						130	45		2.888888 889
						170	40		4.25
						90	40		2.25
					mean	135	51		2.728192 918

				3	spatters	90	90	700	1
						100	50		2
						310	110		2.818181818
						50	50		1
						135	130		1.038461538
						160	150		1.066666667
						125	60		2.083333333
						100	65		1.538461538
						160	55		2.909090909
						250	40		6.25
					mean	148	80		2.17041958
					sc	10	10		1
						15	14		1.071428571
						9	6		1.5
						8	8		1
						10	8		1.25
						14	10		1.4
						12	10		1.2
						14	10		1.4
						6	4		1.5
						6	3		2
					mean	10.4	8.3		1.332142857
				4a	sc	42	16	130	2.625
						22	8		2.75
						22	12		1.833333333
						16	11		1.454545455
						24	10		2.4
						20	16		1.25
						8	5		1.6
						11	6		1.833333333
						13	8		1.625
						22	16		1.375
					mean	20	10.8		1.874621212
				4	clots	90	85	740	1.058823

									529
						120	50		2.4
						90	70		1.285714 286
						270	80		3.375
					mean	142.5	71.25		1.767749 236
					sp	110	60		1.833333 333
						170	30		5.666666 667
						140	50		2.8
						105	35		3
						90	90		1
						120	60		2
					mean	122.5	54.166 67		2.512846 352
				5	spatters	360	110	490	3.272727 273
						210	100		2.1
						270	90		3
						370	90		4.111111 111
						180	60		3
						120	100		1.2
						200	70		2.857142 857
						400	90		4.444444 444
						240	70		3.428571 429
						150	40		3.75
						250	82		3.048780 488
					sc	42	16		2.625
						22	8		2.75
						22	12		1.833333 333
						16	11		1.454545 455
						24	10		2.4
						20	16		1.25
						8	5		1.6
						11	6		1.833333 333
						13	8		1.625
						22	16		1.375
					mean	20	10.8		1.874621

									212
11-Jun	y30	5	37	1	agg	200	140	600	1.428571429
						230	130		1.769230769
						280	250		1.12
						200	160		1.25
						200	130		1.538461538
						200	100		2
						230	160		1.4375
						100	75		1.333333333
					mean	205	143.125		1.484637134
09-Jul	location 477	17		1	sc	30	20	240	1.5
						30	18		1.666666667
						50	21		2.380952381
						53	11		4.818181818
						32	16		2
						32	30		1.066666667
						50	33		1.515151515
						35	30		1.166666667
						43	30		1.433333333
						40	35		1.142857143
					mean	39.5	24.4		1.869047619
				2	mwcw	320	70	600	4.571428571
						370	80		4.625
					mean	345	75		4.598214286
				4	mwcw	350	90	800	3.888888889
						230	75		3.066666667
						240	50		4.8
						200	60		3.333333333
						230	80		2.875

						200	70		2.857142 857
						200	90		2.222222 222
					mean	235.71 43	73.571 43		3.291893 424
23- Jun	285		5,13 5	1	llagg	90	2	1000	45
						110	2		55
						120	2		60
						140	2		70
						50	1		50
						90	2		45
						130	1		130
						100	1		100
						45	1		45
						190	2		95
						120	2		60
					mean	107.72 73	1.6363 64		68.63636 364
					llagg	64	1	1000	64
						80	1		80
						50	1		50
						40	1		40
						50	1		50
						23	1		23
						30	1		30
						40	1		40
						16	1		16
						20	1		20
									41.3
					mean	41.3	1	1000	
					llagg	30	1		30
						23	1		23
						30	3		10
						16	2		8
						80	2		40
						40	1		40
						30	2		15
						52	2		26
						34	1		34
						60	3		20
					mean	39.5	1.8		24.6
					llagg	100	4	5	25
						130	2		65
						160	2		80

						130	2		65
						18	15		1.2
					mean	107.6	5		47.24
					llagg	330	20	16	16.5
						150	10		15
						180	10		18
						160	30		5.333333 333
						270	15		18
						140	10		14
						100	30		3.333333 333
						80	20		4
						200	10		20
						160	24		6.666666 667
					mean	177	17.9		12.08333 333
					llagg	120	10	6	12
						480	220		2.181818 182
						240	25		9.6
						90	35		2.571428 571
						140	40		3.5
					mean	214	66		5.970649 351
17-Jul	y57		5,14 9		sc	15	8	100	1.875
						9	9		1
						10	8		1.25
						10	8		1.25
						13	10		1.3
						10	8		1.25
						10	8		1.25
						16	10		1.6
						9	6		1.5

						10	8		1.25
					mean	11.2	8.3		1.3525
17-Jul	y58		5,150		sc	29	24	>260	1.208333333
						21	14		1.5
						15	9		1.666666667
						23	12		1.916666667
						23	15		1.533333333
						19	11		1.727272727
						22	14		1.571428571
						26	18		1.444444444
						20	19		1.052631579
						20	19		1.052631579
					mean	21.8	15.5		1.46734089
17-Jul	y59		5,150		sc	12	8	320	1.5
						20	16		1.25
						32	15		2.133333333
						35	20		1.75
						22	15		1.466666667
						16	15		1.066666667
						22	16		1.375
						29	18		1.611111111
						10	10		1
						20	13		1.538461538
					mean	21.8	14.6		1.469123932
17-Jul	y60		5,152		sc	8	6	>150	1.333333333
						12	7		1.714285714
						10	7		1.428571429
						8	6		1.333333333

						10	7		1.428571 429
						12	10		1.2
						13	8		1.625
						10	8		1.25
						7	2		3.5
						16	10		1.6
					mean	10.6	7.1		1.641309 524
17- Jul	y61		5,15 2		sc	19	17	<350	1.117647 059
						19	16		1.1875
						29	20		1.45
						17	15		1.133333 333
						17	15		1.133333 333
						24	19		1.263157 895
						21	16		1.3125
						24	21		1.142857 143
						32	30		1.066666 667
						19	10		1.9
					mean	22.1	17.9		1.270699 543
17- Jul	y62		5,15 3		sc	24	21	<400	1.142857 143
						22	18		1.222222 222
						21	13		1.615384 615
						31	16		1.9375
						40	20		2
						31	29		1.068965 517
						30	16		1.875
						20	15		1.333333 333
						20	14		1.428571 429
						19	11		1.727272 727
					mean	25.8	17.3		1.535110 699
07- Jun	pr	11	5,3	1	sc	300	70	1710	4.285714 286
						60	50		1.2

						74	61		1.213114 754
						140	55		2.545454 545
						125	70		1.785714 286
						130	70		1.857142 857
						80	80		1
						111	40		2.775
						100	80		1.25
						70	65		1.076923 077
					mean	119	64.1		1.898906 381
17-Jul				A3		130	50	400	2.6
						80	35		2.285714 286
						135	40		3.375
						90	45		2
						100	50		2
						180	50		3.6
						135	75		1.8
						165	35		4.714285 714
						140	60		2.333333 333
						80	50		1.6
					mean	123.5	49		2.630833 333
17-Jul				a2		20	10	50	2
						14	10		1.4
						18	10		1.8
						22	16		1.375
						22	15		1.466666 667
						24	20		1.2
						26	20		1.3
						25	16		1.5625
						10	5		2
						10	7		1.428571 429
					mean	19.1	12.9	50	1.553273 81
17-Jul				a3		130	50		2.6

						80	35		2.285714 286
						135	40		3.375
						90	45		2
						100	50		2
						180	50		3.6
						135	75		1.8
						165	35		4.714285 714
						140	60		2.333333 333
						80	50		1.6
					mean	123.5	49		2.630833 333
29- Jun		2	6,31	17	sc	250	90	170	2.777777 778
						150	70		2.142857 143
						220	60		3.666666 667
						260	80		3.25
						190	40		4.75
						300	100		3
						250	50		5
						260	80		3.25
						260	90		2.888888 889
					mean	237.77 78	73.333 33		3.414021 164
29- Jun				18	sc	200	60	2300	3.333333 333
						270	60		4.5
						140	60		2.333333 333
						120	100		1.2
						80	30		2.666666 667
						40	25		1.6
						90	30		3
						70	25		2.8
									#DIV/0!
									#DIV/0!
					mean	126.25	48.75		2.679166 667
29- Jun				19	sc	200	50	300	4
						290	100		2.9

						110	35		3.142857 143
						100	50		2
						125	30		4.166666 667
						135	30		4.5
						210	40		5.25
						230	100		2.3
									#DIV/0!
									#DIV/0!
					mean	175	54.375		3.532440 476
29- Jun				20	sc	60	40	800	1.5
						70	35		2
						55	45		1.222222 222
						125	50		2.5
						100	30		3.333333 333
						70	25		2.8
						100	25		4
									#DIV/0!
									#DIV/0!
									#DIV/0!
					mean	82.857 14	35.714 29		2.479365 079
29- Jun				23		35	8	80	4.375
						21	8		2.625
						24	4		6
						22	4		5.5
						23	5		4.6
						20	4		5
						82	30		2.733333 333
						102	7		14.57142 857
						70	10		7
									#DIV/0!
					mean	44.333 33	8.8888 89		5.822751 323
29- Jun				24	sc	140	80	700	1.75
						200	40		5
						70	40		1.75
						70	20		3.5
						69	25		2.76

						75	40		1.875
						70	30		2.333333 333
						110	60		1.833333 333
									#DIV/0!
									#DIV/0!
					mean	100.5	41.875		2.600208 333
29- Jun				25	sc	270	160	410	1.6875
						270	55		4.909090 909
						240	100		2.4
						290	100		2.9
						180	120		1.5
						220	40		5.5
						210	50		4.2
						250	60		4.166666 667
									#DIV/0!
									#DIV/0!
					mean	241.25	85.625		3.407907 197
29- Jun				26	sc	320	60	2400	5.333333 333
						160	60		2.666666 667
						330	160		2.0625
						200	90		2.222222 222
						650	150		4.333333 333
						190	80		2.375
						220	80		2.75
						110	80		1.375
						200	70		2.857142 857
									#DIV/0!
					mean	264.44 44	92.222 22		2.886133 157
29- Jun				27	sc	45	14	240	3.214285 714
						40	19		2.105263 158
						53	10		5.3
						70	16		4.375
						39	21		1.857142

									857
						69	10		6.9
						130	20		6.5
						64	15		4.266666 667
						120	32		3.75
						80	16		5
					mean	71	17.3		4.326835 84
29- Jun				28	sc	180	100	500	1.8
						180	50		3.6
						300	100		3
						300	60		5
						180	50		3.6
						210	60		3.5
						330	45		7.333333 333
						135	50		2.7
						250	50		5
						230	90		2.555555 556
					mean	229.5	65.5		3.948148 148
29- Jun				29		85	25	150	3.4
						73	25		2.92
						70	8		8.75
						45	30		1.5
						43	20		2.15
						32	8		4
						74	18		4.111111 111
						50	32		1.5625
						48	11		4.363636 364
						70	15		4.666666 667
					mean	59	19.2		3.639694 164
29- Jun				30		300	110	220	2.727272 727
						300	75		4
						370	90		4.111111 111
						500	80		6.25
						510	70		7.285714 286

						550	140		3.928571 429
						640	160		4
									#DIV/0!
									#DIV/0!
									#DIV/0!
					mean	452.85 71	103.57 14		4.614667 079
29- Jun				31		80	40	110	2
						42	16		2.625
						30	15		2
						60	8		7.5
						69	21		3.285714 286
						27	4		6.75
						66	16		4.125
						50	10		5
						43	30		1.433333 333
						50	17		2.941176 471
					mean	51.7	17.7		3.857671 958
29- Jun				32		300	70	800	4.285714 286
						200	100		2
						160	45		3.555555 556
						480	120		4
						260	60		4.333333 333
						260	110		2.363636 364
						160	40		4
						205	90		2.277777 778
						220	110		2
						300	60		5
					mean	254.5	80.5		3.201779 702

Table A1.19. Stratigraphic log measurements from 2013.

Log	Unit	Type	Coating	X (mm)	Y (mm)	area (mm ²)	vol fraction
		1	n	50	43	2150	8.16E-09
10	7	1	n	65	32	2080	7.39E-09

		4	n	55	33	1815	4.91E-09
		4	n	60	30	1800	4.79E-09
		1	n	40	30	1200	1.42E-09
		1	n	20	22	440	7E-11
		1	n	25	15	375	4.33E-11
		1	n	30	11	330	2.95E-11
		1	n	25	13	325	2.82E-11
		1	n	20	15	300	2.22E-11
		1	n	20	15	300	2.22E-11
		1	n	25	11	275	1.71E-11
		1	n	20	12	240	1.14E-11
		1	n	15	16	240	1.14E-11
		1	n	23	10	230	1E-11
		1	n	14	15	210	7.61E-12
		1	n	12	15	180	4.79E-12
		2	n	17	10	170	4.04E-12
		1	n	15	11	165	3.69E-12
		4	n	12	12	144	2.45E-12
		2	n	10	9	90	5.99E-13
		1	n	15	5	75	3.47E-13
		1	n	15	5	75	3.47E-13
		1	n	10	6	60	1.77E-13
		1	n	10	6	60	1.77E-13
		1	n	6	5	30	2.22E-14
		1	n	5	4	20	6.57E-15
		1	n	4	3	12	1.42E-15
		1	n	4	3	12	1.42E-15
		1	n	4	2	8	4.21E-16
					sum area	13411	1.98E-06
					area %	1.3411	1.98E-18
							0
		1	n	54	100	5400	1.29E-07
		1	n	70	45	3150	2.57E-08
		1	n	55	30	1650	3.69E-09
	8	1	n	55	29	1595	3.33E-09
		1	n	60	22	1320	1.89E-09
		4	n	55	24	1320	1.89E-09
		1	n	55	20	1100	1.09E-09
		1	n	30	30	900	5.99E-10
		2	n	45	20	900	5.99E-10
		4	n	24	35	840	4.87E-10
		2	n	26	30	780	3.9E-10
		1	n	35	20	700	2.82E-10
		4	n	33	20	660	2.36E-10
		1	n	30	20	600	1.77E-10

		4	n	30	20	600	1.77E-10
		1	n	30	19	570	1.52E-10
		4	n	25	22	550	1.37E-10
		1	n	20	25	500	1.03E-10
		4	n	25	20	500	1.03E-10
		2	n	25	20	500	1.03E-10
		1	n	40	12	480	9.09E-11
		4	n	40	11	440	7E-11
		1	n	29	15	435	6.76E-11
		4	n	21	20	420	6.09E-11
		4	n	25	15	375	4.33E-11
		4	n	32	10	320	2.69E-11
		4	n	28	11	308	2.4E-11
		1	n	15	20	300	2.22E-11
		1	n	25	12	300	2.22E-11
		4	n	20	15	300	2.22E-11
		1	n	20	13	260	1.44E-11
		1	n	15	15	225	9.36E-12
		4	n	20	10	200	6.57E-12
		4	n	19	10	190	5.63E-12
		1	n	12	15	180	4.79E-12
		1	n	17	10	170	4.04E-12
		1	n	15	10	150	2.77E-12
		1	n	10	15	150	2.77E-12
		4	n	15	10	150	2.77E-12
		4	n	12	10	120	1.42E-12
		1	n	17	7	119	1.38E-12
		1	n	10	10	100	8.22E-13
		4	n	10	10	100	8.22E-13
		1	n	10	5	50	1.03E-13
					area (mm^2)	29977	2.21E-05
					area %	2.9977	2.21E-17
							0
12	3	2	n	135	80	10800	1.03E-06
		2	y	90	50	4500	7.49E-08
		1	y	80	50	4000	5.26E-08
					area sum	19300	5.91E-06
					area %	0.45	7.49E-20
	4	2	y	75	23	1725	4.22E-09
			n	80	80	6400	2.15E-07
					area sum	8125	4.41E-07
					area %	0.1725	4.22E-21
	2	1	n	21	30	630	2.05E-10
							0
							0

					area %	0.063	2.05E-22
	1	1	n	11	12	132	1.89E-12
		1	n	22	15	330	2.95E-11
		1	n	19	9	171	4.11E-12
		1	n	10	5	50	1.03E-13
		4	n	22	25	550	1.37E-10
					area sum	1233	1.54E-09
					area %	0.1233	1.54E-21
81	3	4	y	8	12	96	7.27E-13
		4	n	45	35	1575	3.21E-09
					area sum	1671	3.83E-09
					area %	0.1671	3.83E-21
	7	2	y	80	30	2400	1.14E-08
		2	n	50	45	2250	9.36E-09
		2	n	20	20	400	5.26E-11
					area sum	5050	1.06E-07
					area %	0.505	1.06E-19
						area (mm^2)	#VALUE!
8	6	4	n	90	80	7200	3.07E-07
		2	n	80	45	3600	3.83E-08
		2	n	50	35	1750	4.4E-09
					sum area	12550	1.62E-06
					area %	1.255	
						area (mm^2)	#VALUE!
		2	y	130	90	11700	1.32E-06
		4	y	120	90	10800	1.03E-06
	7	4	n	85	60	5100	1.09E-07
					sum area	27600	1.73E-05
					area %	2.76	1.73E-17
						area (mm^2)	#VALUE!
	9	4	n	95	95	9025	6.04E-07
		4	n	35	26	910	6.19E-10
		4	n	30	28	840	4.87E-10
					sum area	10775	1.03E-06
					area %	1.0775	1.03E-18
						area (mm^2)	#VALUE!
		4	y	75	55	4125	5.77E-08
		4	n	70	30	2100	7.61E-09
		1	n	40	35	1400	2.25E-09
		1	n	40	30	1200	1.42E-09
		4	n	45	25	1125	1.17E-09
		4	n	25	25	625	2.01E-10

		4	y	20	30	600	1.77E-10
		4	y	28	20	560	1.44E-10
10	5	4	n	21	26	546	1.34E-10
		1	n	30	15	450	7.49E-11
		4	n	20	19	380	4.51E-11
		4	n	20	15	300	2.22E-11
		4	n	20	12	240	1.14E-11
		4	n	23	10	230	1E-11
		4	n	18	10	180	4.79E-12
		4	n	8	9	72	3.07E-13
					sum area	14133	2.32E-06
					area %	1.4133	2.32E-18
1	m1	3	y	12	10	120	1.42E-12
		3	y	12	12	144	2.45E-12
		3	n	49	14	686	2.65E-10
		4	n	12	11	132	1.89E-12
		1	n	38	24	912	6.23E-10
		4	n	14	9	126	1.64E-12
		4	n	19	7	133	1.93E-12
		4	n	45	35	1575	3.21E-09
		4	n	32	31	992	8.02E-10
		3	y	110	85	9350	6.72E-07
		4	n	190	90	17100	4.11E-06
		4	n	19	17	323	2.77E-11
		4	n	45	25	1125	1.17E-09
		4	n	30	25	750	3.47E-10
		4	n	14	15	210	7.61E-12
		4	n	19	15	285	1.9E-11
		4	n	43	20	860	5.23E-10
		4	n	19	16	304	2.31E-11
		4	n	16	17	272	1.65E-11
		4	n	17	10	170	4.04E-12
		4	n	41	30	1230	1.53E-09
		4	n	12	17	204	6.97E-12
		3	n	22	18	396	5.1E-11
		3	n	32	10	320	2.69E-11
		3	n	19	17	323	2.77E-11
		3	n	35	28	980	7.73E-10
						39022	4.88E-05
					area %	3.9022	4.88E-17
	m2	4	n	610	240	146400	0.002578
		4	n	25	7	175	4.4E-12
		4	n	72	25	1800	4.79E-09
		4	n	60	25	1500	2.77E-09
		4	n	50	32	1600	3.36E-09

		3	n	17	13	221	8.87E-12
		4	n	17	10	170	4.04E-12
		4	n	32	5	160	3.36E-12
		4	n	18	10	180	4.79E-12
		4	n	24	18	432	6.62E-11
		4	n	8	8	64	2.15E-13
		2	n	30	29	870	5.41E-10
		4	n	85	45	3825	4.6E-08
		4	n	15	10	150	2.77E-12
		4	n	8	4	32	2.69E-14
		4	n	7	5	35	3.52E-14
		4	n	60	30	1800	4.79E-09
						159414	0.003328
					area %	15.9414	3.33E-15
	m4	4	n	170	110	18700	5.37E-06
		4	n	34	20	680	2.58E-10
		4	n	29	29	841	4.89E-10
		4	n	55	35	1925	5.86E-09
		4	n	19	10	190	5.63E-12
		4	n	10	10	100	8.22E-13
		3	n	10	5	50	1.03E-13
		4	n	30	12	360	3.83E-11
		4	y	25	10	250	1.28E-11
						23096	1.01E-05
						2.3096	1.01E-17
	m5	4	n	30	30	900	5.99E-10
		3	y	115	80	9200	6.4E-07
		3	y	16	15	240	1.14E-11
		3	y	20	11	220	8.75E-12
		3	y	28	20	560	1.44E-10
		3	y	50	16	800	4.21E-10
		3	n	11	5	55	1.37E-13
		4	n	45	31	1395	2.23E-09
		4	n	24	19	456	7.79E-11
		1	n	35	24	840	4.87E-10
		4	n	10	5	50	1.03E-13
						14716	2.62E-06
							0
	m6	4	n	35	22	770	3.75E-10
		4	n	68	28	1904	5.67E-09
		4	n	33	29	957	7.2E-10
		4	n	20	21	420	6.09E-11
		3	n	29	29	841	4.89E-10
		3	n	25	12	300	2.22E-11
		4	y	20	15	300	2.22E-11

		4	n	19	14	266	1.55E-11
		4	n	50	15	750	3.47E-10
		4	n	29	5	145	2.5E-12
		3	n	10	6	60	1.77E-13
		3	n	11	9	99	7.97E-13
		3	n	9	6	54	1.29E-13
		4	n	74	30	2220	8.99E-09
		4	n	40	15	600	1.77E-10
		4	n	40	22	880	5.6E-10
		3	n	55	40	2200	8.75E-09
		3	n	90	50	4500	7.49E-08
		3	y	54	25	1350	2.02E-09
		3	y	13	9	117	1.32E-12
		4	y	80	50	4000	5.26E-08
						22733	9.65E-06
							0
	m7	4	n	80	39	3120	2.5E-08
		4	n	24	10	240	1.14E-11
		4	n	20	7	140	2.25E-12
		4	n	95	45	4275	6.42E-08
		4	n	28	20	560	1.44E-10
		4	n	24	15	360	3.83E-11
		4	n	15	7	105	9.51E-13
		4	n	35	30	1050	9.51E-10
		4	n	40	30	1200	1.42E-09
		2	n	35	10	350	3.52E-11
		4	n	65	12	780	3.9E-10
		4	n	25	17	425	6.31E-11
		4	n	10	5	50	1.03E-13
		4	y	12	6	72	3.07E-13
		4	n	35	25	875	5.5E-10
		4	n	24	9	216	8.28E-12
		3	n	34	11	374	4.3E-11
		3	n	32	15	480	9.09E-11
						14672	2.59E-06
							0
	m8	4	n	153	90	13770	2.14E-06
		4	n	33	27	891	5.81E-10
		4	n	20	5	100	8.22E-13
		4	n	29	9	261	1.46E-11
		4	n	200	120	24000	1.14E-05
		4	n	46	25	1150	1.25E-09
		4	n	22	20	440	7E-11
		4	n	18	19	342	3.29E-11
		3	n	23	15	345	3.37E-11

		3	n	43	19	817	4.48E-10
		3	n	88	62	5456	1.33E-07
		3	n	25	18	450	7.49E-11
		3	n	22	19	418	6E-11
		3	n	35	32	1120	1.15E-09
		3	n	36	5	180	4.79E-12
		3	n	53	24	1272	1.69E-09
		3	n	54	34	1836	5.08E-09
		3	n	74	50	3700	4.16E-08
		4	y	19	12	228	9.74E-12
		1	n	27	15	405	5.46E-11
		4	n	6	4	24	1.14E-14
		4	n	24	23	552	1.38E-10
		3	n	14	14	196	6.19E-12
		4	n	27	25	675	2.53E-10
		3	n	26	15	390	4.87E-11
		4	n	27	27	729	3.18E-10
		4	n	20	5	100	8.22E-13
		4	n	32	6	192	5.81E-12
		4	n	36	16	576	1.57E-10
		4	n	8	7	56	1.44E-13
		4	n	21	5	105	9.51E-13
		4	n	15	15	225	9.36E-12
		4	n	7	6	42	6.09E-14
		4	n	14	5	70	2.82E-13
		3	n	14	6	84	4.87E-13
		3	n	25	6	150	2.77E-12
		3	n	9	8	72	3.07E-13
		2	n	36	19	684	2.63E-10
		4	n	9	5	45	7.49E-14
		4	n	29	16	464	8.21E-11
		4	n	38	16	608	1.85E-10
		4	n	17	11	187	5.37E-12
		4	n	27	23	621	1.97E-10
		4	n	25	15	375	4.33E-11
		4	n	13	10	130	1.8E-12
		3	n	37	17	629	2.04E-10
		3	n	15	5	75	3.47E-13
		3	n	16	6	96	7.27E-13
		3	n	11	9	99	7.97E-13
		3	n	9	5	45	7.49E-14
		4	n	15	20	300	2.22E-11
		4	n	20	5	100	8.22E-13
		4	n	22	16	352	3.58E-11
		4	n	17	10	170	4.04E-12

						66399	0.00024
							0
m9		1	n	80	76	6080	1.85E-07
		2	n	140	75	10500	9.51E-07
		4	n	22	10	220	8.75E-12
		4	n	26	19	494	9.9E-11
		4	n	40	35	1400	2.25E-09
		4	n	11	9	99	7.97E-13
		4	n	35	29	1015	8.59E-10
		4	n	15	10	150	2.77E-12
		4	n	11	10	110	1.09E-12
		4	n	15	11	165	3.69E-12
		4	n	12	2	24	1.14E-14
		4	n	39	20	780	3.9E-10
		4	n	25	10	250	1.28E-11
		4	n	7	6	42	6.09E-14
		1	n	50	35	1750	4.4E-09
		4	n	29	15	435	6.76E-11
						23514	1.07E-05
							0
30	4	2	n	55	60	3300	2.95E-08
				96	54	5184	1.14E-07
				59	50	2950	2.11E-08
				44	29	1276	1.71E-09
				145	250	36250	3.91E-05
				150	60	9000	5.99E-07
				98	70	6860	2.65E-07
				45	10	450	7.49E-11
				63	15	945	6.93E-10
						66215	0.000238
						6.6215	
				lithic type			number
				aphyric poorly vesic basalt			1
				aphyric dense basaltic agglutinate			2
				plagioclase porphyritic dense basalt			3
				aphyric, non vesic basalt			4
Table A1.20. Measurements of lithic clasts.							

length on transect (m)	height on face (m)	scour dip (°)	scour lineation (°)	face strike (°)	face dip (°)
1.6	0.5	58	350	300	58

1.6	3			336	60
5.8	1.2	33	42	300	33
8.2	0.9			018	20
28	0.5			328	56
31	0.3	29	20	002	77
35.7	0.5			320	57
37	0.5	53	39	292	53
37	3.2			004	28
35.7	3.2	28	92	021	45
41	3.6			021	51
43	0.5	51	106	007	21
44	1			339	29
56	0.5	21	74	004	25
56	1			360	45
59	2	29	61	001	25
59	4			302	18
65	0.5			310	29
75	1			022	31
79.5	1	42	116	022	42
85	0.5			300	44

Table A1.21. Measurements of scours at location y29.

tension gash length (mm)	distance along tension gash from its base	tension gash width (mm)	normalised width
60	10	10	0.25
	20	12	0.3
	30	21	0.525
	40	23	0.575
	50	40	1
	60	40	1
80	10	4	0.1333333333
	20	13	0.4333333333
	30	15	0.5
	40	17	0.5666666667
	50	17	0.5666666667
	60	30	1
	70	20	0.6666666667
	80	8	0.2666666667
22	4	2	1
	8	2	1
	16	2	1
	22	2	1

Table A1.22. Measurements of tension gashes at location y26.

length on transect (m)	height on face (m)	scour dip (°)	scour lineation (°)	face strike (°)	face dip (°)	max scour depth (mm)	tension gash width
1	0.5	42	236	130	42	5	
2	0.5	31	227	155	31	10	
3	0.5	35	221	142	35	10	
5	0.5	40	226	133	40	30	
1	1.5	16	248	142	16	10	
7.5	1.5	32	252	147	32	10	
8.5	1.5	19	244	142	19	3	10
9.5	1.5	32	226	159	32	5	8
11.5	1.5	28	226	148	28	8	
12.5	1.5	24	210	132	24	40	
14	1.5	24	222	140	24	10	
16.2	1.5	24	220	134	24	5	
17.4	1.5	24	228	128	22	10	
18.4	1.5	22	212	140	26	8	
24	1.5	26	240	160	31	0.5	
2	2.5	39	259	132	48	30	10
3	2.5	40	261	138	47	5	
4	2.5	37	245	132	37	30	
6.7	2.5	22	245	166	22	10	
7.7	2.5	22	250	160	22	5	
10.1	2.5	29	238	157	29	0.5	
11.2	2.5	30	226	169	30	4	
12	2.5	25	218	134	25	10	
13	2.5	36	215	146	36	10	
15	2.5	26	232	160	26	10	
18.7	2.5	28	225	160	28	3	
3.2	3.5	40	240	133	40	5	
12.9	3.5	25	256	160	25	10	
16.3	3.5	23	234	164	23	5	
17.3	3.5	20	236	150	20	50	
18.3	3.5	14	224	146	14	5	
6.3	4.5	28	261	168	28	3	
17.8	4.5	23	230	156	23		
18.8	4.5	16	227	131	16		
Table A1.23. Measurements of scours at location Y29.							

tension gash length (mm)	tension gash width (mm)	tension gash dip (°)	total unit thickness (mm)	vertical height of tension gash from unit base (mm)
--------------------------	-------------------------	----------------------	---------------------------	---

4	0.5	05	730	180
4	0.5	06		190
10	0.5	06		205
8	0.5	12		215
8	0.5	11		220
3	0.5	11		240
4	0.5	44		340
16	2	62		390
	1	28	650	110
	0.5	10		160
	0.5	12		162
	0.5	10		165
	1	14		172
	1	12		176
	1	16		178
	0.5	12		182
	1	18		188
	1	21		192
	1	11		196
	0.5	14		200
	1	03		208
	1	08		240
	0.5	10		253
	1	03		233
	4	24		273
Table A1.24. Measurements of tension gashes at location y26.				

length across crust (mm)	height of tension gash on crust (mm)	normalised distance across crust	tension gash length (mm)	tension gash width (mm)	tension gash strike (°)	tension gash dip (°)	crust strike (°)	crust dip (°)
960	200	0.208333333	30	4	264	62	096	55
	230	0.239583333	70	2	256	46	070	34
	260	0.270833333	70	6	068	90	070	24
	300	0.3125	85	5	075	45	066	30
	320	0.333333333	80	5	260	56	070	26
	400	0.416666667	45	10	250	70	072	52
	450	0.46875	15	8	238	82	072	41
	470	0.489583333	85	5	256	82	074	41
	500	0.520833333	340	15	252	67	064	41
	530	0.552083333	70	10	238	64	073	41
	535	0.557291667	15	5	258	78	082	41
	540	0.5625	115	10	252	45	080	41
	550	0.572916667	135	9	250	80	060	41
	560	0.583333333	85	25	282	40	055	41
	620	0.645833333	40	5	246	86	092	39
	660	0.6875	150	10	242	44	078	48
	680	0.708333333	130	5	250	68	078	36
	700	0.729166667	40	9	246	78	076	45
	720	0.75	150	10	248	62	072	56
	760	0.791666667	60	10	236	58	070	70
	780	0.8125	75	8	262	56	067	68
	850	0.885416667	200	30	254	84	062	6
	900	0.9375	115	10	52	68	052	26
	955	0.994791667	120	20	200	42	038	6
Table A1.25. Measurements of tension gashes at location y28.								

tension gash length (mm)	distance along tension gash from its base	tension gash width (mm)	normalised width	normalised height along tension gash
90	10	2	0.2	0.111111111
	20	4	0.4	0.222222222
	30	7	0.7	0.333333333
	40	9	0.9	0.444444444
	50	8	0.8	0.555555556
	60	9	0.9	0.666666667
	70	10	1	0.777777778
	80	8	0.8	0.888888889
	90	10	1	1
80	10	2	0.25	0.125
	20	1	0.125	0.25
	30	2	0.25	0.375
	40	7	0.875	0.5
	50	8	1	0.625
	60	8	1	0.75
	70	5	0.625	0.875
	80	6	0.75	1
Table A1.26. Measurements of tension gashes at location y28.				

height on tension gash on crustal transect (mm)	normalised distance across crust	tension gash width (mm)	transect length across unit crust (mm)
100	2.173913043	20	1230
170	3.695652174	30	
370	8.043478261	23	
400	8.695652174	2	
450	9.782608696	26	
530	11.52173913	20	
660	14.34782609	33	
690	15	8	
820	17.82608696	18	
750	16.30434783	3	
760	16.52173913	5	
890	19.34782609	3	
910	19.7826087	16	
920	20	7	
930	20.2173913	4	
970	21.08695652	3	
1120	24.34782609	8	
1130	24.56521739	6	
1140	24.7826087	4	
1210	26.30434783		
1230	26.73913043		

Table A1.27. Measurements of tension gashes at location y29.

transect length across unit crust (mm)	height of tension gash on crustal transect (mm)	normalised distance across crust	tension gash length (mm)	tension gash width (mm)
675	20	0.02962963	25	4
	30	0.044444444	60	5
	45	0.066666667	35	3
	60	0.088888889	60	2
	70	0.103703704	30	1
	80	0.118518519	25	1
	95	0.140740741	35	2
	115	0.17037037	55	2
	130	0.192592593	5	1
	195	0.288888889	35	2
	215	0.318518519	35	2
	235	0.348148148	10	2
	240	0.355555556	10	1
	250	0.37037037	35	1
	255	0.377777778	25	1
	270	0.4	70	4

	325	0.481481481	5	1
	350	0.518518519	10	0.5
	355	0.525925926	10	0.5
	357	0.528888889	10	0.5
	359	0.531851852	10	0.5
	461	0.682962963	10	0.5
	501	0.742222222	10	0.5
	511	0.757037037	10	0.5
	591	0.875555556	50	1
	616	0.912592593	40	2
	640	0.948148148	40	2
	665	0.985185185	40	2

Table A1.28. Measurements of tension gash distribution at Location Y29.

tension gash length (mm)	distance along tension gash from its base	tension gash width (mm)	normalised width
70	10	6	0.375
	20	16	1
	30	10	0.625
	40	7	0.4375
	50	11	0.6875
	60	12	0.75
80	10	4	0.4
	20	4	0.4
	30	8	0.8
	40	10	1
	50	8	0.8
50	10	8	0.5
	20	12	0.75
	30	13	0.8125
	40	15	0.9375
	50	16	1
13	4	3	0.375
	8	4	0.5
	13	8	1

Table A1.29. Measurements of tension gash lengths at location y29.

transect length across unit crust (mm)	height of tension gash on crustal transect (mm)	normalised distance across crust	tension gash length (mm)	tension gash width (mm)	tension gash strike (°)	tension gash dip (°)	crust strike (°)	crust dip (°)
2900	120	0.04137931		80	328	28	134	72
	220	0.075862069		6	348	32	340	05
	330	0.113793103		50	340	16	125	38
	365	0.125862069		30	310	43	144	47
	446	0.153793103			311	29	181	36
	740	0.255172414		14	007	58	162	53
	910	0.313793103		12	300	08	186	31
	960	0.331034483		14	040	42	152	44
	1270	0.437931034		16	056	36	154	38
	1460	0.503448276		16	020	39	138	28
	1740	0.6		16	001	31	160	40
	1765	0.60862069		6	330	58	139	42
	1950	0.672413793		8	348	44	152	33
	2460	0.848275862		40	286	43	134	48
	2755	0.95		8	296	44	118	31
	2900	1		30	314	61	129	57
	550	0.189655172		18	360	64	144	50
	655	0.225862069		16	286	58	136	13
	830	0.286206897		40	296	56	166	28
	870	0.3		4	010	36	159	56
	1335	0.460344828		24	346	08	146	32
	1365	0.470689655		16	341	31	115	26
	1405	0.484482759		5	358	52	122	48
	1715	0.59137931		3	310	30	130	35
	2580	0.889655172		5	340	29	180	33
	2675	0.922413793		13	360	68	129	15
2200	230	0.104545455		4	328	33	160	48
	340	0.154545455	110	3	032	30		
	370	0.168181818	90	1				
	390	0.177272727	50	4				
	500	0.227272727	50	2				
	600	0.272727273	175	10				
	670	0.304545455	110	10				
	750	0.340909091	115	5				
	910	0.413636364	150	20				
	970	0.440909091	120	3				
	1030	0.468181818	130	1				
	1040	0.472727273	200					
	1110	0.504545455	110					
	1200	0.545454545	140					
	1270	0.577272727	500					
	1340	0.609090909	2				080	
	1480		2					
	1530	0.695454545	160				002	

	1550	0.704545455	70				001	
	1600	0.727272727	375					
	1640	0.745454545	100				003	
	1700	0.772727273	130				010	
	1760	0.8	90				008	
	1860	0.845454545	340				010	
	1890	0.859090909	220					
	1940	0.881818182	570					
	2000	0.909090909	800				005	
	2100	0.954545455	800				100	

Table A1.30. Measurements of tension gashes at location y29.

transect length across crust (mm)	height on tension gash on crustal transect (mm)	normalised distance across crust	tension gash length (mm)	tension gash width (mm)	tension gash strike (°)	tension gash dip (°)	crust strike (°)	crust dip (°)
1300	100	0.076923077	105	8	282	38	123	68
	180	0.138461538	55	20	122	36	118	76
	290	0.223076923	270	80	131	03	316	76
	340	0.261538462	30	5				
	345	0.265384615	30	5				
	347	0.266923077	20	5			104	86
	348	0.267692308	20	4	110	36	104	86
	540	0.415384615	240		122	22	144	88
	690	0.530769231	130	3	178	39	350	82
	730	0.561538462	350	2	189	36	356	66
	800	0.615384615	400	40	193	36	016	62
	870	0.669230769	80	4	184	37	004	76
	910	0.7	200		216	27	045	70
	1010	0.776923077	280	5	220	80	014	51
	1140	0.876923077	360	40	196	48	348	56
	1275	0.980769231	2900	80	178	40	360	30

Table A1.31. Measurements of tension gashes at location y27.

transect length across unit crust (mm)	height on tension gash on crustal transect (mm)	normalised distance across crust	tension gash width (mm)	tension gash strike (°)	tension gash dip (°)	crust strike (°)	crust dip (°)
3500	400	0.114285714	50	306	29	146	31
	410	0.117142857	12	288	39	138	28
	540	0.154285714	50	330	42	126	22
	590	0.168571429	40	324	40	164	18
	630	0.18	5	295	42	127	64
	645	0.184285714	15	220	35	137	62
	670	0.191428571	15	308	35	146	48
	705	0.201428571	25	340	42	146	19
3200	60	0.01875	17	178	28	003	53
	250	0.078125	12	333	64	150	58
	350	0.109375	45	273	54	123	33
	395	0.1234375	50	339	20	153	45
	585	0.1828125	10	346	44	340	108
	775	0.2421875	10	326	23	156	58
	795	0.2484375	45	340	30	150	51
	855	0.2671875	25	346	30	152	37
	1105	0.3453125	5	357	07	138	46
	1175	0.3671875	10	360	32	144	31
	1295	0.4046875	30	346	15	124	12
Table A1.32. Measurements of tension gashes at location y29.							

transect length across unit crust (mm)	height on tension gash on crustal transect (mm)	normalised distance across crust	tension gash length (mm)	tension gash width (mm)	tension gash dip (°)	crust strike (°)	crust dip (°)
340	200	0.588235294	5	0.5	38	055	46
	215	0.632352941	13	0.5	41	055	46
	250	0.735294118	4	0.5	36	055	46
600	280	0.466666667	8	0.5	19	088	38
	360	0.6	4	0.5	20	088	38
	392	0.653333333	16	0.5	23	088	38

Table A1.33. Measurements of tension gashes at location y35.

tension gash length (mm)	distance along tension gash from its base	tension gash width (mm)	normalised width
140	10	3	0.078947368
	20	3	0.078947368
	30	3	0.078947368
	40	5	0.131578947
	50	2	0.052631579
	60	2	0.052631579
	70	10	0.263157895
	80	10	0.263157895
	90	13	0.342105263
	100	24	0.631578947
	110	29	0.763157895
	120	30	0.789473684
	130	32	0.842105263
	140	38	1
60	10	4	0.307692308
	20	6	0.461538462
	30	5	0.384615385
	40	11	0.846153846
	50	13	1
	60	13	1
300	10	2	0.015384615
	20	2	0.015384615
	30	2	0.015384615
	40	2	0.015384615
	50	2	0.015384615

	60	2	0.015384615
	70	4	0.030769231
	80	4	0.030769231
	90	8	0.061538462
	100	14	0.107692308
	110	130	1
	120	31	0.238461538
	140	55	0.423076923
	160	72	0.553846154
	180	114	0.876923077
	200	115	0.884615385
	300	110	0.846153846
100	10	0.5	0.015625
	20	1	0.03125
	30	1	0.03125
	40	16	0.5
	50	16	0.5
	60	20	0.625
	70	24	0.75
	80	32	1
	90	20	0.625
	100	20	0.625
50	10	4	0.363636364
	20	11	1
	30	8	0.727272727
	40	2	0.181818182
	50	1	0.090909091

Table A1.34. Measurements of tension gashes at location y37.

tension gash length (mm)	tension gash width (mm)	tension gash dip (°)	total unit thickness (mm)	vertical height of tension gash from unit base (mm)
135	3	30	1630	90
310		78		290
150	8	84		500
32	0.5	04		530
34	2	11		760
270	120	10		870
60	8	28		890
45	2	10		910

6	1	01		915
4	1	01		951
20	0.5	48		10
40	2	22		43
50	4	22		80
80	1	31		630
121	1	43		1030
70	1	32		1230
220	50	76		
	2	22	1480	10
	4	22		43
	1	31		80
	1	43		630
	1	32		1030
	50	76		1230

Table A1.35. Measurements of tension gashes at location y37.

transect length along base (mm)	distance along transect	tension gash length (mm)	distance along tension gash from its base	tension gash width (mm)	normali sed width
675	80	82	10	7	0.53846 1538
			20	7	0.53846 1538
			30	8	0.61538 4615
			40	10	0.76923 0769
			50	13	1
			60	2	0.15384 6154
			80	8	0.61538 4615
675	230	80	10	2	0.25
			30	4	0.5
			50	0	0
			70	8	1
			80	4	0.5
675	260	64	10	16	0.4
			20	40	1
			40	13	0.325
			60	8	0.2
675	350	50	10	2	0.2
			20	5	0.5

			40	10	1
675	515	100	10	2	0.4
			20	2	0.4
			30	1	0.2
			40	1	0.2
			50	1	0.2
			80	4	0.8
			100	5	1
675	575	80	10	1	1
			80	1	1
675	625	175	10	4	0.26666 6667
			20	10	0.66666 6667
			40	10	0.66666 6667
			60	10	0.66666 6667
			70	15	1
			80	8	0.53333 3333
675	665	20	10	4	0.66666 6667
			20	6	1
Table A1.36. Measurements of tension gashes at Location Y42.					

Appendix 2: Support Material for Chapter 4

image	area analysed (mm ²)	particle number	area (mm ²)	width (mm)	height (mm)	conduit
158	9522	1	37.69	117.376	81.358	L6
		2	26.932	6.904	5.639	
		3	4.03	1.764	3.184	
		4	55.439	12.083	6.713	
		5	21.383	5.524	5.715	
		6	12.646	4.143	5.984	
		7	81.298	10.625	11.584	
		8	10.352	4.066	3.567	
		9	154.451	13.656	21.289	
		10	36.763	8.861	6.137	
		11	16.214	4.833	5.063	
		12	33.201	6.751	7.135	
		13	16.828	5.6	4.45	
		14	75.486	10.779	11.546	
		15	25.034	4.028	9.398	
		16	168.373	13.425	24.127	
		17	43.099	5.754	10.165	
		18	11.908	3.567	4.718	
		19	92.052	11.277	14.001	
		20	162.392	13.387	15.267	
		21	90.909	11.469	11.277	
		22	31.998	7.71	7.748	
		23	27.049	6.981	5.178	
		24	23.152	6.866	5.677	
		25	184.412	14.998	17.338	
		26	32.126	5.984	8.746	
		27	208.01	17.453	18.412	
		28	68.386	11.469	12.198	
		29	38.001	6.137	8.094	
		30	6.349	3.644	2.57	
		31	156.699	24.357	12.773	
		32	3.687	2.11	2.992	
		33	11.059	4.219	3.836	
		34	55.629	6.981	11.009	
		35	3.515	2.033	2.647	
		36	9.798	5.946	3.299	
		sum	2036.35			
		area covered by lapilli (%)	21.38573829			
160	8715	1	90.428	113.076	77.958	L6
		2	36.867	10.876	4.94	

		3	9.651	2.74	5.396	
		4	36.619	9.589	7.347	
		5	296.258	21.254	20.382	
		6	15.047	5.729	3.861	
		7	24.393	5.562	6.808	
		8	41.704	8.759	5.562	
		9	259.978	22.873	19.552	
		10	125.327	17.061	12.993	
		11	94.851	10.046	20.05	
		12	96.823	9.755	13.948	
		13	25.837	6.766	4.94	
		14	39.512	7.057	9.714	
		15	26.921	5.895	6.434	
		16	64.283	8.136	10.834	
		17	7.036	3.57	3.279	
		18	10.244	3.653	4.151	
		19	36.069	8.136	6.227	
		20	41.945	9.838	7.015	
		21	21.667	5.978	5.23	
		22	66.874	8.427	12.121	
		23	1.73	1.577	1.826	
		24	22.215	6.102	5.562	
		25	24.722	5.313	7.846	
		26	82.638	8.717	14.944	
		27	7.063	2.574	4.317	
		28	43.201	7.597	8.136	
		29	95.329	11.457	12.37	
		30	9.093	4.359	3.113	
		31	19.782	9.921	3.072	
		32	2.7	1.785	2.449	
		33	5.356	2.532	3.03	
		34	57.124	7.597	10.253	
		35	32.24	5.645	8.344	
		36	9.326	4.566	2.781	
		37	24.374	4.815	6.393	
		38	16.615	6.185	4.815	
		39	7.628	3.819	3.321	
		40	25.608	6.6	5.77	
		41	22.043	6.061	5.396	
		sum	1977.121			
		area covered by lapilli (%)	22.68641423			
161	7328	1	4.005	103.931	0.039	L6
		2	56.376	11.638	8.208	
		3	51.353	10.328	8.516	

		4	11.633	5.241	2.813	
		5	18.258	5.511	4.817	
		6	14.74	3.892	5.125	
		7	12.602	5.01	3.776	
		8	24.425	5.125	6.782	
		9	6.815	2.967	3.661	
		10	89.082	14.913	9.017	
		11	7.094	2.736	3.854	
		12	52.413	8.863	9.518	
		13	41.724	8.17	7.669	
		14	12.361	6.204	2.967	
		15	6.167	2.736	3.198	
		16	26.938	8.748	5.125	
		17	25.808	5.395	6.744	
		18	124.719	14.181	11.946	
		19	28.311	5.125	10.25	
		20	8.191	3.276	3.237	
		21	27.823	7.283	5.934	
		22	26.766	5.665	8.131	
		23	17.128	5.164	4.701	
		24	14.811	4.586	4.316	
		25	28.378	5.934	6.166	
		26	8.883	4.316	2.967	
		27	10.607	5.202	3.699	
		28	66.461	9.364	9.827	
		29	158.826	14.258	16.108	
		30	3.077	2.582	2.235	
		31	5.783	2.389	3.738	
		32	16.298	5.626	4.239	
		33	26.939	6.281	5.395	
		34	7.146	3.661	2.967	
		35	135.975	17.418	11.291	
		36	15.551	5.279	4.701	
		37	19.107	5.164	5.511	
		38	46.142	8.748	8.285	
		39	31.525	6.358	7.514	
		40	9.18	4.509	2.89	
		41	17.349	4.855	4.894	
		sum	1316.77			
		area covered by lapilli (%)	17.96902293			
169	9473	1	46.517	116.552	81.281	L6
		2	349.205	27.931	18.128	
		3	9.789	3.793	4.335	
		4	695.94	33.695	29.261	

		5	59.725	10.69	9.458	
		6	28.474	6.207	7.192	
		7	30.804	8.374	6.502	
		8	186.675	19.261	19.458	
		9	355.854	17.537	26.502	
		10	4.567	2.069	3.448	
		11	27.276	6.453	6.552	
		12	55.328	10.591	8.67	
		13	10.961	3.645	4.68	
		14	9.755	3.793	3.744	
		15	139.659	16.207	13.448	
		16	43.918	8.128	7.734	
		17	97.986	9.507	16.305	
		18	290.323	20.887	20.69	
		19	92.645	13.744	13.005	
		20	14.946	6.453	3.103	
		21	316.819	20.148	22.167	
		22	28.297	7.192	7.389	
		23	37.596	7.143	7.586	
		24	9.233	3.793	3.448	
		25	2.245	1.626	2.217	
		sum	2944.537			
		area covered by lapilli (%)	31.08346881			
227	11245	1	97.443	19.796	9.059	L19
		2	57.865	11.705	10.992	
		3	7.301	2.85	4.427	
		4	56.417	9.873	8.092	
		5	14.811	4.478	4.885	
		6	15.702	6.26	5.598	
		7	6.467	2.748	3.359	
		8	89.321	14.504	11.552	
		9	26.543	5.751	7.735	
		10	17.409	6.107	5.038	
		11	30.563	6.921	6.463	
		12	4.351	3.104	1.985	
		13	24.798	6.616	5.242	
		14	62.281	11.145	9.567	
		15	24.606	6.056	5.649	
		16	8.761	3.868	3.053	
		17	10.888	3.308	4.478	
		18	21.869	6.972	4.326	
		19	42.01	7.888	7.837	
		20	12.084	4.173	4.02	
		21	57.816	9.517	8.804	

		22	26.334	5.547	5.852	
		23	18.52	5.293	5.089	
		24	19.605	3.868	6.463	
		25	22.827	5.7	5.903	
		26	54.861	7.481	10.331	
		27	3.527	1.883	2.799	
		28	3.126	2.087	2.188	
		29	5.775	4.02	2.036	
		30	47.324	12.417	7.125	
		31	190.111	24.987	12.57	
		32	37.001	8.55	7.074	
		sum	1118.317			
		area covered by lapilli (%)	9.945015562			
229	6182	1	3.212	0.084	76.076	L19
		2	70.721	10.97	8.565	
		3	26.849	5.443	7.468	
		4	10.294	5.148	2.827	
		5	12.097	4.262	4.219	
		6	170.537	16.582	17.848	
		7	10.189	3.038	4.135	
		8	20.6	5.57	5.738	
		9	3.635	3.038	1.772	
		10	4.278	3.038	1.941	
		11	72.082	13.038	13.418	
		12	8.012	3.713	2.785	
		13	1.606	1.435	1.772	
		14	3.536	2.11	2.363	
		15	12.838	5.316	3.629	
		16	58.52	12.278	10.928	
		17	5.512	2.954	2.405	
		18	15.799	5.401	4.262	
		19	3.865	2.658	2.321	
		20	7.408	3.586	2.827	
		21	15.738	9.241	3.544	
		sum	537.328			
		area covered by lapilli (%)	8.691814947			
231	9806	1	3.249	0.04	81.295	L19
		2	3.958	1.719	2.918	
		3	30.976	7.434	8.074	
		4	49.497	7.354	8.753	
		5	2.605	2.198	1.878	
		6	6.161	4.716	2.798	

		7	14.104	4.676	4.836	
		8	3.746	2.878	1.878	
		9	4.005	2.198	2.478	
		10	6.283	3.197	4.117	
		11	1.31	1.439	1.439	
		12	55.543	5.675	14.189	
		13	4.903	3.197	2.718	
		14	35.292	6.355	9.552	
		15	3.708	2.438	2.198	
		16	2.407	1.878	2.158	
		17	12.102	4.396	4.117	
		18	22.243	5.116	6.155	
		19	14.059	4.556	4.756	
		20	10.403	4.556	3.078	
		21	4.463	2.238	3.837	
		22	11.957	3.157	5.036	
		23	13.425	4.117	5.516	
		24	41.772	8.074	8.513	
		25	15.96	5.116	4.277	
		26	72.45	10.312	14.868	
		27	107.704	12.91	15.588	
		28	17.888	5.556	7.034	
		29	20.997	6.555	5.596	
		30	10.161	3.917	3.477	
		31	9.495	3.637	5.316	
		32	3.521	1.839	2.278	
		33	3.968	2.118	2.878	
		34	4.093	2.238	2.838	
		35	9.406	3.317	4.077	
		36	10.137	3.557	4.157	
		37	44.251	8.713	9.392	
		38	18.458	5.835	4.836	
		39	17.567	4.836	5.476	
		40	5.947	3.078	3.197	
		41	53.442	11.271	8.233	
		42	4.534	3.197	2.158	
		43	20.733	7.194	5.875	
		44	5.323	2.918	2.958	
		45	2.265	1.559	2.278	
		46	3.522	1.799	3.118	
		47	0.85	0.999	1.159	
		48	6.395	3.277	2.558	
		49	12.157	6.875	2.958	
		50	2.99	2.518	1.998	
		51	8.056	4.836	2.958	

		52	19.249	4.956	6.075	
		53	24.813	5.036	9.512	
		54	20.641	4.037	7.594	
		55	3.859	2.998	1.799	
		56	7.064	2.878	3.437	
		57	3.35	2.318	2.758	
		58	1.505	1.199	1.559	
		59	57.725	7.954	10.791	
		60	299.156	19.904	19.345	
		61	44.922	8.793	8.993	
		62	22.204	4.476	7.354	
		63	6.882	2.438	4.037	
		64	1.134	1.759	0.999	
		65	9.126	5.516	2.798	
		66	18.109	3.797	6.914	
		67	10.466	5.156	2.918	
		68	0.955	1.199	1.079	
		69	5.458	2.798	2.718	
		70	7.436	3.677	3.038	
		71	7.46	3.597	3.477	
		72	2.272	2.558	1.479	
		73	50.005	6.155	10.671	
		74	37.423	7.234	7.714	
		75	24.765	6.435	5.755	
		76	7.69	2.598	3.797	
		77	4.649	2.558	2.558	
		78	5.505	2.558	3.317	
		79	58.821	10.392	8.673	
		80	28.639	7.874	5.755	
		81	7.12	2.958	3.397	
		82	47.917	7.994	9.153	
		83	4.553	2.878	2.478	
		84	19.503	4.636	6.954	
		85	16.412	5.316	4.716	
		86	10.272	4.197	3.717	
		87	11.811	4.716	3.877	
		88	39.506	7.114	9.872	
		89	63.192	8.753	8.953	
		90	7.117	3.797	2.878	
		91	73.273	10.911	9.992	
		92	5.855	2.118	3.637	
		93	3.613	2.118	2.678	
		94	26.97	6.235	7.234	
		95	5.719	2.758	2.958	
		96	1.768	1.359	2.398	

		97	3.791	2.158	2.518	
		98	4.668	3.118	2.318	
		99	55.979	11.95	5.875	
		100	8.722	3.997	4.716	
		101	7.637	3.477	2.958	
		102	2.958	2.318	1.599	
		sum	2070.08			
		area covered by lapilli (%)	21.11034061			
232	8567	1	13.292	5.229	3.913	L19
		2	12.654	5.342	4.026	
		3	4.398	2.069	3.649	
		4	85.147	11.851	11.099	
		5	14.614	4.477	5.455	
		6	23.319	5.869	5.38	
		7	6.18	3.348	2.521	
		8	90.058	10.534	15.162	
		9	4.977	2.822	2.558	
		10	3.493	1.693	3.047	
		11	4.328	2.634	2.408	
		12	15.019	5.154	4.138	
		13	23.723	4.778	6.998	
		14	50.743	6.659	10.534	
		15	115.93	15.237	12.491	
		16	52.002	9.105	9.067	
		17	61.286	7.675	13.318	
		18	6.507	4.101	2.521	
		19	13.444	4.628	4.74	
		20	15.196	5.982	3.875	
		21	113.708	13.281	13.657	
		22	26.074	9.105	5.869	
		23	7.326	2.521	4.251	
		24	3.718	2.445	2.144	
		25	1.507	1.279	1.655	
		26	4.933	2.333	2.445	
		27	50.508	8.54	10.91	
		28	16.351	4.929	5.004	
		29	21.188	5.117	6.885	
		30	7.737	3.01	3.762	
		31	7.394	2.897	4.289	
		32	25.607	6.96	8.728	
		33	12.156	4.816	3.16	
		34	28.551	5.192	7.901	
		35	6.392	2.445	3.762	
		36	6.62	3.085	3.047	

		sum	956.08			
		area covered by lapilli (%)	11.16003268			
234	8591	1	41.332	8.917	7.958	L19
		2	77.788	10.458	12.333	
		3	11.628	3.458	4.792	
		4	23.55	5.458	6.5	
		5	7.524	3.208	3.667	
		6	4.076	2.458	2.792	
		7	2.432	1.917	2.333	
		8	11.043	3.5	4.875	
		9	14.674	4.667	5.833	
		10	1.729	1.625	1.625	
		11	19.127	6.5	5.5	
		12	8.599	2.542	4.458	
		13	11.017	3.875	4.208	
		14	5.583	3.083	2.75	
		15	107.899	15	10.083	
		16	16.41	4.083	5.875	
		17	19.243	3.958	5.792	
		18	3.91	2.833	2.375	
		19	3.556	2.542	1.833	
		20	2.078	1.5	1.708	
		21	8.698	3.292	4.167	
		22	6.236	2.625	2.958	
		23	36.476	6.708	8.083	
		24	4.149	3.25	2.125	
		25	14.493	4.042	4.542	
		26	1.123	0.958	1.833	
		27	5.913	3.583	2.5	
		28	1.498	1.5	1.792	
		29	4.21	2.917	2.375	
		30	6.462	4.875	2.333	
		31	39.191	5.542	10.833	
		32	1.457	1.292	1.917	
		33	7.222	2.458	4.083	
		34	3.316	2.083	2.458	
		35	1.776	1.625	1.708	
		36	11.128	3.958	5.125	
		37	75.498	9.458	10.417	
		38	2.88	2.208	1.917	
		39	6.927	2.708	3.708	
		40	53.632	11.708	10.708	
		41	6.05	2.667	3.208	
		42	4.302	2.292	2.625	

		43	0.771	1.208	0.833	
		44	2.965	2.5	1.833	
		45	2.924	1.583	2.542	
		46	34.66	6.792	8.375	
		47	4.208	2.167	3.375	
		48	44.175	8.708	7.458	
		49	15.901	6.167	4.875	
		50	11.911	3.5	4.917	
		51	6.106	3.5	3.25	
		52	17.962	5.333	5.833	
		53	2.979	2.875	1.5	
		54	2.061	1.583	2.042	
		55	36.411	7.75	8.083	
		56	151.983	13.125	17.958	
		57	3.337	2.417	2.042	
		58	19.172	7.125	4.417	
		59	4.901	2.333	2.75	
		60	98.17	13.375	10.333	
		61	44.312	7.625	8	
		62	5.382	2.375	3.167	
		63	1.068	1.042	1.333	
		64	1.542	1.208	1.917	
		65	0.84	1.292	0.917	
		66	52.316	14.875	7.125	
		67	117.974	11.417	13.542	
		68	1.076	1.208	1.333	
		69	4.082	2.083	2.542	
		70	4.198	2.375	2.667	
		71	18.472	4.292	6.333	
		72	154.734	20.792	13.833	
		73	0.703	0.875	1.208	
		74	2.99	2.292	1.542	
		75	2.302	1.583	2.042	
		76	3.562	2.583	1.958	
		77	4.74	3.125	2	
		78	2.472	1.833	2.25	
		79	2.135	1.708	1.917	
		80	3.736	1.833	3.292	
		81	1.429	1.5	1.208	
		82	13.632	4.708	5.333	
		83	0.877	1	1.333	
		84	10.556	3.792	3.917	
		85	4.8	2.292	3.083	
		86	103.72	10.958	13.042	
		87	19.477	4.708	5.333	

		88	2.165	1.917	1.792	
		89	11.314	4	5.125	
		90	8.653	3.458	3.792	
		91	4.644	4	1.667	
		92	11.465	4.583	4.875	
		93	17.316	4.792	5.792	
		94	1.05	1.583	1.083	
		95	11.745	3.542	5.583	
		96	7.139	3	3.292	
		97	11.898	3.292	5.667	
		98	14.431	5.625	3.417	
		99	8.283	3.875	3.125	
		100	1.005	1.292	1.208	
		101	10.095	4.042	3.125	
		102	98.118	12.167	12.333	
		103	4.667	2.25	2.875	
		104	23.705	5.792	6	
		105	2.392	2.5	1.292	
		106	90.807	11.958	10.5	
		107	8.589	4.208	3.25	
		108	61.134	10.167	7.625	
		109	1.49	1.375	1.708	
		110	2.835	2.833	1.625	
		111	16.745	4.875	4.375	
		sum	2171.244			
		area covered by lapilli (%)	25.27347224			
242	11189	1	24.386	127.023	88.092	L19
		2	117.167	11.247	14.911	
		3	51.276	13.69	8.55	
		4	68.209	10.331	9.669	
		5	12.703	5.852	3.003	
		6	123.204	13.944	14.148	
		7	104.299	15.522	9.924	
		8	18.308	4.326	6.463	
		9	12.807	4.936	3.613	
		10	47.047	8.804	8.092	
		11	11.463	5.598	3.461	
		12	36.007	6.819	7.532	
		13	165.191	15.369	14.656	
		14	21.687	5.751	5.242	
		15	49.772	8.601	8.499	
		16	56.845	7.888	12.621	
		17	48.156	9.72	6.718	
		18	14.48	5.954	4.02	

		19	12.872	4.885	4.122	
		20	2.927	1.578	2.646	
		21	141.8	12.417	15.929	
		22	40.081	5.496	10.891	
		23	25.075	6.514	5.954	
		24	16.907	5.445	5.7	
		25	11.615	5.344	3.613	
		26	93.786	7.634	14.249	
		27	12.411	5.751	3.003	
		28	29.75	4.936	7.379	
		sum	1370.231			
		area covered by lapilli (%)	12.24623291			
243	13812	1	271.074	142.209	97.126	L19
		2	6.579	3.379	2.723	
		3	8.885	3.732	3.227	
		4	116.965	15.179	11.8	
		5	30.005	9.228	6.102	
		6	1.879	1.815	1.715	
		7	1.991	1.664	1.462	
		8	20.998	5.951	5.093	
		9	22.997	8.069	4.539	
		10	1.33	1.362	1.362	
		11	0.712	1.362	0.857	
		12	2.271	2.824	1.513	
		13	148.117	18.154	14.776	
		14	1.574	1.664	1.261	
		15	10.795	4.589	4.639	
		16	59.975	9.128	9.531	
		17	1.213	1.362	1.462	
		18	14.559	4.085	6.051	
		19	2.022	2.168	1.412	
		20	23.521	5.345	6.001	
		21	0.445	0.958	0.857	
		22	41.716	7.564	8.018	
		23	11.683	4.387	4.186	
		24	1.17	1.412	1.412	
		25	2.711	1.866	2.168	
		26	45.526	9.632	7.615	
		27	11.82	3.833	4.438	
		28	111.406	15.482	11.195	
		29	1.933	1.311	1.563	
		30	19.508	5.749	5.648	
		31	15.368	6.354	4.639	
		32	20.385	6.354	5.043	

		33	15.96	3.53	6.556	
		34	63.716	12.355	12.758	
		35	2.08	2.017	1.765	
		36	1.828	1.462	2.118	
		37	86.181	14.876	16.087	
		38	12.199	3.883	3.984	
		39	3.064	1.967	2.471	
		40	32.06	6.001	7.564	
		41	1.973	2.118	1.362	
		42	21.303	6.657	5.043	
		43	77.553	8.321	15.885	
		44	5.951	2.421	3.681	
		45	3.115	2.068	2.269	
		46	0.778	1.059	1.059	
		47	3.487	2.521	2.017	
		48	6.289	2.37	3.833	
		49	8.557	3.026	4.942	
		50	23.605	8.321	4.589	
		51	68.82	9.43	10.842	
		52	480.201	21.836	38.477	
		53	86.957	9.632	11.8	
		54	6.264	3.127	2.572	
		55	2.904	2.168	2.219	
		56	75.094	9.027	15.431	
		57	81.372	10.893	14.523	
		58	18.447	6.404	5.144	
		59	5.401	2.521	3.076	
		60	4.814	2.572	3.177	
		61	7.103	2.925	3.227	
		62	4.501	2.673	2.168	
		63	4.544	1.967	3.127	
		64	2.523	2.521	1.462	
		65	8.873	4.337	2.874	
		66	39.702	8.169	8.926	
		67	7.164	4.942	2.622	
		68	12.293	3.833	5.144	
		69	12.985	5.194	4.186	
		70	240.783	16.793	19.213	
		71	64.703	11.699	7.968	
		72	47.552	7.363	9.632	
		73	27.035	7.816	4.74	
		74	0.926	1.765	0.958	
		75	1.274	1.362	1.362	
		76	2.566	1.462	2.32	
		77	43.644	7.766	8.069	

		78	9.824	4.085	3.984	
		79	47.255	7.01	9.178	
		80	8.334	3.53	4.387	
		81	12.522	4.186	4.841	
		82	11.423	5.648	3.127	
		83	3.624	2.269	2.32	
		84	8.166	3.631	3.48	
		85	2.235	1.916	1.765	
		86	1.121	1.261	1.715	
		87	1.292	1.462	1.311	
		88	36.91	9.279	7.11	
		89	30.28	8.825	5.799	
		90	2.116	1.462	1.916	
		91	5.47	3.984	2.32	
		92	7.571	2.521	4.085	
		93	18.374	7.11	4.438	
		94	5.76	2.723	3.328	
		95	5.198	3.631	2.572	
		96	9.453	4.034	2.975	
		97	79.218	13.868	8.825	
		98	5.625	3.429	2.521	
		99	15.551	5.345	4.387	
		100	36.447	6.858	7.816	
		101	13.501	5.093	3.58	
		102	28.281	6.354	6.909	
		103	66.775	10.59	9.329	
		104	10.134	4.892	2.975	
		105	39.239	8.119	7.564	
		106	23.058	5.245	6.404	
		107	16.41	4.539	5.598	
		108	13.949	5.396	4.337	
		109	16.273	6.203	3.681	
		110	9.544	3.379	3.933	
		111	61.794	10.136	8.169	
		112	3.148	1.765	2.421	
		113	57.267	9.884	9.934	
		114	3.413	2.219	2.572	
		115	4.527	2.572	2.572	
		116	36.35	5.951	9.329	
		117	33.962	8.119	6.657	
		118	9.806	3.933	3.227	
		119	3.011	2.521	1.614	
		120	9.852	5.245	3.026	
		121	4.539	2.421	2.723	
		122	15.757	5.093	5.043	

		123	97.999	13.162	10.439	
		124	5.638	2.673	2.975	
		125	51.169	8.926	9.38	
		126	29.644	7.867	5.295	
		127	30.186	7.514	8.27	
		128	23.765	5.799	5.698	
		129	16.563	6.051	4.438	
		130	7.077	2.774	3.782	
		sum	3865.677			
		area covered by lapilli (%)	27.98781494			

Table A2.1. Measurements of the lapilli impacted into the conduit walls.

Location	Unit	Lithofacies	Clast size (mm)	
			X	Y
L9	1	mLA	230	115
L9	1	mLA	108	50
L9	1	mLA	85	80
L9	1	mLA	330	160
L9	1	mLA	155	90
L9	1	mLA	100	30
L9	1	mLA	104	34
L9	1	mLA	75	54
L9	1	mLA	89	62
L9	1	mLA	131	110
L9	1	mLA	84	50
L9	1	mLA	95	70
L9	1	mLA	120	40
L9	1	mLA	130	75
L9	1	mLA	145	80
L9	1	mLA	120	109
L9	1	mLA	107	70
L9	1	mLA	140	60
L9	1	mLA	225	55
L9	1	mLA	108	55
L9	1	mLA	89	86
L9	1	mLA	69	26
L9	1	mLA	95	39
L9	1	mLA	84	44
L9	1	mLA	55	49
L9	1	mLA	126	70
L9	1	mLA	310	180
L9	1	mLA	110	85
L9	1	mLA	65	45
L9	1	mLA	310	180

L9	2	lensLA	100	20
L9	2	lensLA	70	30
L9	2	lensLA	49	10
L9	2	lensLA	43	34
L9	2	lensLA	82	24
L9	2	lensLA	42	40
L9	2	lensLA	50	21
L9	2	lensLA	75	70
L9	2	lensLA	30	25
L9	2	lensLA	35	11
L9	3	xsLA	145	55
L9	3	xsLA	210	100
L9	3	xsLA	79	50
L9	3	xsLA	42	33
L9	3	xsLA	96	26
L9	3	xsLA	42	24
L9	3	xsLA	22	21
L9	3	xsLA	21	20
L9	3	xsLA	35	23
L9	3	xsLA	42	20
L9	4	//bSp	527	58
L9	4	//bSp	1280	46
L9	4	//bSp	1763	36
L9	4	//bSp	2544	54
L9	4	//bSp	3149	22
L9	4	//bSp	668	53
L9	4	//bSp	1352	40
L9	4	//bSp	2424	25
L9	4	//bSp	3516	22
L15	1	(n)LA	110	85
L15	1	(n)LA	220	70
L15	1	(n)LA	135	50
L15	1	(n)LA	80	30
L15	1	(n)LA	90	50
L15	1	(n)LA	65	58
L15	1	(n)LA	100	85
L15	1	(n)LA	60	40
L15	1	(n)LA	80	70
L15	1	(n)LA	160	50
L15	2	xsLA	100	80
L15	2	xsLA	54	40
L15	2	xsLA	290	110
L15	2	xsLA	180	70
L15	2	xsLA	80	60
L15	2	xsLA	40	20

L15	2	xsLA	60	55
L15	2	xsLA	60	30
L15	2	xsLA	60	30
L15	2	xsLA	74	54
L15	3	(m)LA	160	50
L15	3	(m)LA	140	55
L15	3	(m)LA	48	27
L15	3	(m)LA	44	30
L15	3	(m)LA	55	35
L15	3	(m)LA	70	45
L15	3	(m)LA	80	30
L15	3	(m)LA	40	30
L15	3	(m)LA	42	30
L15	3	(m)LA	35	28
L14	1	mLA	144	133
L14	1	mLA	84	30
L14	1	mLA	82	35
L14	1	mLA	70	50
L14	1	mLA	130	35
L14	1	mLA	55	35
L14	1	mLA	85	26
L14	1	mLA	67	55
L14	1	mLA	36	24
L14	1	mLA	165	35
L14	2	lensLA	14	11
L14	2	lensLA	27	10
L14	2	lensLA	12	10
L14	2	lensLA	21	15
L14	2	lensLA	54	41
L14	2	lensLA	90	34
L14	2	lensLA	55	14
L14	2	lensLA	30	27
L14	2	lensLA	79	30
L14	2	lensLA	50	41
L14	3	(n)LA	440	160
L14	3	(n)LA	78	40
L14	3	(n)LA	290	120
L14	3	(n)LA	200	85
L14	3	(n)LA	160	120
L14	3	(n)LA	100	75
L14	3	(n)LA	100	60
L14	3	(n)LA	95	30
L14	3	(n)LA	65	40
L14	3	(n)LA	65	40
L14	4	xsLA	38	15

L14	4	xsLA	33	20
L14	4	xsLA	40	40
L14	4	xsLA	83	25
L14	4	xsLA	55	55
L14	4	xsLA	32	19
L14	4	xsLA	36	26
L14	4	xsLA	33	24
L14	4	xsLA	22	20
L14	4	xsLA	43	25
L14	5	(n)LA(f)	160	90
L14	5	(n)LA(f)	130	115
L14	5	(n)LA(f)	260	160
L14	5	(n)LA(f)	300	80
L14	5	(n)LA(f)	150	50
L14	5	(n)LA(f)	100	60
L14	5	(n)LA(f)	140	120
L14	5	(n)LA(f)	105	70
L14	5	(n)LA(f)	135	80
L14	5	(n)LA(f)	140	65
L10	1	(m)LA(f)	85	65
L10	1	(m)LA(f)	60	55
L10	1	(m)LA(f)	89	60
L10	1	(m)LA(f)	148	40
L10	1	(m)LA(f)	195	25
L10	1	(m)LA(f)	100	60
L10	1	(m)LA(f)	55	41
L10	1	(m)LA(f)	80	70
L10	1	(m)LA(f)	70	30
L10	1	(m)LA(f)	80	60
L8	1	lensLA	36	27
L8	1	lensLA	30	12
L8	1	lensLA	24	14
L8	1	lensLA	29	6
L8	1	lensLA	54	22
L8	1	lensLA	35	16
L8	1	lensLA	33	12
L8	1	lensLA	100	36
L8	1	lensLA	79	32
L8	1	lensLA	101	35
L8	2	(n)LA	210	200
L8	2	(n)LA	260	40
L8	2	(n)LA	170	55
L8	2	(n)LA	130	50
L8	2	(n)LA	59	49
L8	2	(n)LA	42	35

L8	2	(n)LA	85	29
L8	2	(n)LA	34	31
L8	2	(n)LA	175	75
L8	2	(n)LA	130	60
L4	1	(n)LA	480	130
L4	1	(n)LA	185	95
L4	1	(n)LA	165	55
L4	1	(n)LA	200	130
L4	1	(n)LA	295	180
L4	1	(n)LA	187	130
L4	1	(n)LA	230	120
L4	1	(n)LA	195	97
L4	1	(n)LA	170	60
L4	1	(n)LA	170	110
L4	2	(n)LA	130	36
L4	2	(n)LA	80	34
L4	2	(n)LA	48	28
L4	2	(n)LA	280	170
L4	2	(n)LA	54	11
L4	2	(n)LA	39	25
L4	2	(n)LA	33	20
L4	2	(n)LA	105	30
L4	2	(n)LA	54	19
L4	2	(n)LA	50	21
L3	1	mLA	119	69
L3	1	mLA	100	70
L3	1	mLA	198	70
L3	1	mLA	81	60
L3	1	mLA	105	33
L3	1	mLA	86	79
L3	1	mLA	90	76
L3	1	mLA	85	53
L3	1	mLA	142	105
L3	1	mLA	89	40
L3	2	mLA	276	170
L3	2	mLA	215	100
L3	2	mLA	145	125
L3	2	mLA	120	97
L3	2	mLA	155	70
L3	2	mLA	170	140
L3	2	mLA	115	60
L3	2	mLA	100	95
L3	2	mLA	89	66
L3	2	mLA	66	39
L5	1	mLA	125	50

L5	1	mLA	120	50
L5	1	mLA	155	40
L5	1	mLA	87	46
L5	1	mLA	78	55
L5	1	mLA	65	60
L5	1	mLA	85	60
L5	1	mLA	75	45
L5	1	mLA	61	25
L5	1	mLA	240	100
L5	2	mLA	420	84
L5	2	mLA	105	76
L5	2	mLA	80	40
L5	2	mLA	150	50
L5	2	mLA	127	57
L5	2	mLA	200	130
L5	2	mLA	170	55
L5	2	mLA	100	60
L5	2	mLA	119	70
L5	2	mLA	175	55
L7	1	//bSp	-	-
L11	1	//bSp	-	-
L21	1	mLA	-	-

Table A2.2. Measurements of juvenile clast sizes and lithofacies type.

Location	Unit	Unit thickness (m)	Av max clast size (mm)	Silicic volcanic ash abundance %
L9	1	1	140.7	20
L9	1	1	127.4	20
L9	1	1.1	131.3	20
L9	2	1.2	57.6	85
L9	3	1	73.4	25
L9	4	3.3	1913	8
L15	1	0.35	110	60
L15	2	0.2	99.8	55
L15	3	0.2	71.4	50
L14	1	0.6	91.8	45
L14	2	0.55	43.2	27
L14	3	0.4	159.3	75
L14	4	0.6	41.5	20
L14	5	0.75	162	60
L10	1	1.3	104	60
L8	1	1	52.1	55
L8	2	0.8	129.5	75
L4	1	1	227	60
L4	2	1.1	87.3	60

L3	1	1	109.5	60
L3	2	1.25	145.1	75
L5	1	1	109.1	60
L5	2	1.25	164.6	75
L11	1	1.1	3.25	<5
L7	1	3.2	1.1	10
L21	1	0.5	0.5	70
Table A2.3. Summary of unit thickness, average maximum clast size and Silicic volcanic ash abundance.				

Location	Cooling joint spacing in host lava flow (mm)					Mean
L16	250	85	170	70	150	150.3
	240	130	180	120	155	
	170	120	230	100	170	
	170	150	100	100	140	
	200	190	210	90	150	
	160	80	160	120		
L19	140	210	200			189.5
	125	270				
	250	190				
	260	150				
	150	140				
Table A2.4. Spacing of cooling joints in host lava flows.						

Location	photo	facies	%juvenile	mean juvenile abun	location	photo	facies	%juvenile	mean juvenile abund
L3	367	mLA	59		L14	47	lensLA	17	
	366		54			47		45	
	365		65			48		27	
	364		65			48		45	
	363		67			49		50	
	362		75			49		40	
	361		72			50		11	
	360		64			50		26	
	359		73			51		2	
	358		49			51		21	
	357		69			52		4	
	356		68			52		12	
	355		71	65		53		24	
L5	398	mLA	58			53		11	
	398		58			54		42	
	399		79			54		21	
	399		78			55		0	
	400		82			55		0	22
	400		79		wp191 L3	285		82	
	401		73			285		69	
	401		78			286		75	
	402		64			286		74	
	402		74			287		80	
	403		63			287		75	
	403		67			288		67	
	404		63			288		65	
	404		69			289		86	
	405		68			289		78	
	405		73			290		79	
	406		71			290		76	
	406		81			291		72	
	407		84			291		72	
	407		76	71.9		292		64	
						292		63	
						293		65	
						293		68	
						294		69	
						294		71	
						295		85	
						295		80	73
Table A2.5. Juvenile abundance calculated using IJ.									

Sample	Rock name	Date	Mineral	Count	%
WP199 PR40	Spatter	09-May	Tachylite	334	66.8
			Microlite	59	11.8
			Plag phenocryst	10	2
			Pyroxene phenocryst	5	1
			Palagonite	46	9.2
			Vesicle	42	8.4
			Silicic volcanic ash	4	0.8
Total Glass %					83.7
WP199 PR015	Sideromelane clasts	09-May	Sideromelane	256	64.1
			Microlite	78	19.5
			Plag phenocryst	14	3.5
			Pyroxene phenocryst	0	0
			Palagonite	27	6.7
			Vesicle	24	6.0
Total Glass %					70.0
WP199 PR41.2	Ventricular bomb	09-May	Sideromelane	11	2.3
			Microlite	101	21.9
			Plag phenocryst	23	5
			Pyroxene phenocryst	0	0
			Palagonite	70	15.2
			Vesicle	1	0.2
			Tachylite	254	55.2
Total Glass %					72.8
WP198 PR003.1	spatter	09-May	Sideromelane	6	1.2
			Microlite	78	15.6
			Plag phenocryst	7	1.4
			Pyroxene phenocryst	4	0.8
			Palagonite	17	3.4
			Vesicle	52	10.4
			Tachylite	336	67.2
Total Glass %					71.8
WP203 PR35	lava	09-May	Sideromelane		0
			Microlite	132	63.4
			Plag phenocryst	5	2.4
			Pyroxene phenocryst	11	5.2
			Palagonite	2	0.9
			Vesicle	0	0
			Tachylite	58	27.8
Total Glass %					28.8

WP199 PR41.1	Ventricular bomb	09-May	Sideromelane	26	5.1
			Microlite	92	18.3
			Plag phenocryst	12	2.3
			Pyroxene phenocryst	7	1.3
			Palagonite	84	16.7
			Vesicle	1	0.1
			Tachylite	280	55.7
Total Glass %					77.6
WP198 PR003.2	Spatter	09-May	Sideromelane	0	0
			Microlite	116	23.2
			Plag phenocryst	18	3.6
			Pyroxene phenocryst	1	0.2
			Palagonite	14	2.8
			Vesicle	58	11.6
			Tachylite	293	58.6
Total Glass %					61.4
WP190PR002.1	Cored bomb	09-May	Sideromelane		0
			Microlite	37	7.4
			Plag phenocryst	9	1.8
			Pyroxene phenocryst		0
			Palagonite	30	6.0
			Vesicle	211	42.2
			Tachylite	212	42.4
Total Glass %					48.49
WP204 PR005	sideromelane clasts	09-May	Sideromelane	80	56.3
			Microlite	24	16.9
			Plag phenocryst	2	1.4
			Pyroxene phenocryst	3	2.1
			Palagonite	30	21.1
			Vesicle	3	2.1
			Tachylite	0	0
Total Glass %					77.4
WP199 pr018	sideromelane clasts	09-May	Sideromelane	228	59.5
			Microlite	76	19.8
			Plag phenocryst	19	4.9
			Pyroxene phenocryst	2	0.5
			Palagonite	30	7.8
			Vesicle	28	7.3
			Tachylite	0	0

Total Glass %					67.3
WP196 PR43	Conduit wall	09-May	Sideromelane	0	0
			Microlite	145	29
			Plag phenocryst	17	3.4
			Pyroxene phenocryst	0	0
			Palagonite	24	4.8
			Vesicle	25	5
			Tachylite	289	57.8
Total Glass %					62.6
WP190 PR002	Lapilli	09-May	Sideromelane	0	0
			Microlite	18	6
			Plag phenocryst	6	2
			Pyroxene phenocryst	1	0.3
			Palagonite	2	0.6
			Vesicle	118	39.3
			Tachylite	155	51.6
Total Glass %					52.3
Table A2.6. Point count measurements of pyroclasts. Glass content corrected for vesicles and Silicic volcanic ash. Point counts conducted at 20X mag.					

Image name	Clast size (mm)		aspect ratio	Image name	Clast size (mm)		aspect ratio
	X	Y			X	Y	
wp 199 pr018 matrix fabric	0.7	0.6	0.85714286	wp204 pr 05 droplets	0.55	0.23	0.41818182
wp 199 pr018 matrix fabric	2.3	1.6	0.69565217	wp204 pr 05 droplets	0.32	0.14	0.4375
wp 199 pr018 matrix fabric	1.9	1.3	0.68421053	wp204 pr 05 pele	0.84	0.07	0.08333333
wp 199 pr018 matrix fabric	1.5	1.6	1.06666667	wp204 pr 05 pele1	1.56	0.21	0.13461538
wp 199 pr018 matrix fabric	2.2	0.5	0.22727273	wp204 pr 05 pele1	0.16	0.08	0.5
wp 199 pr018 matrix fabric	0.3	0.1	0.33333333	wp204 pr 05 quench edit	0.38	0.18	0.47368421
wp 199 pr018 matrix fabric	0.4	0.3	0.75	wp204 pr 05 quench edit	0.99	0.47	0.47474747
wp 199 pr018 matrix fabric	1	0.4	0.4	wp204 pr 05 quench edit	2.3	1	0.43478261
wp 199 pr018 matrix fabric	0.17	0.1	0.58823529	wp204 pr 05 quench edit	0.9	0.8	0.88888889
WP199 PR018 horiz fabric	2.32	1.15	0.49568966	wp204 pr 05 quench edit	1	0.98	0.98
WP199 PR018 horiz fabric	0.95	0.53	0.55789474	wp204 pr 05 quench edit	0.32	0.2	0.625
WP199 PR018 horiz fabric	0.77	0.51	0.66233766	wp204 pr 05 quench edit	0.76	0.19	0.25
WP199 PR018 horiz fabric	0.26	0.06	0.23076923	wp204 pr 05 quench edit	1.34	0.64	0.47761194
WP199 PR018 horiz fabric	0.88	0.72	0.81818182	wp204 pr 05 quench edit	0.52	0.12	0.23076923
WP199 PR018 horiz fabric	0.38	0.12	0.31578947	wp204 pr 05 quench edit	0.28	0.09	0.32142857
WP199 PR018 horiz fabric	1.84	0.42	0.22826087	wp204 pr 05 quench edit	0.43	0.11	0.25581395
WP199 PR018 horiz fabric	1.64	0.86	0.52439024	wp204 pr 05 quench edit	1.13	0.55	0.48672566
WP199 PR018 horiz fabric	1.51	1	0.66225166	wp204 pr 05 type edit	3.52	1.97	0.55965909
WP199 PR018 horiz fabric	0.94	0.45	0.4787234	wp204 pr 05 type edit	2.03	0.73	0.35960591
WP199 PR018 horiz fabric	1.38	0.51	0.36956522	wp204 pr 05 type edit	0.34	0.28	0.82352941
WP199 PR018 horiz fabric	0.79	0.4	0.50632911	wp204 pr 05 type edit	0.25	0.17	0.68
WP199 PR018 horiz fabric	1.01	1.42	1.40594059	wp204 pr 05 type edit	0.63	0.16	0.25396825
WP199 PR018 horiz fabric	0.36	0.13	0.36111111	wp204 pr 05 type edit	0.72	0.4	0.55555556
WP199 PR018 horiz fabric	0.48	0.26	0.54166667	wp204 pr005 ductile defm	0.52	0.35	0.67307692
WP199 PR018 horiz fabric	0.38	0.19	0.5	wp204 pr005 ductile defm	0.13	0.08	0.61538462
WP199 PR018 horiz fabric	0.17	0.12	0.70588235	wp204 pr005 elon	0.86	0.38	0.44186047
WP199 PR018 horiz fabric	0.09	0.06	0.66666667	wp204 pr005 mixed clasts	0.49	0.06	0.12244898
WP199 PR018 horiz fabric	0.23	0.07	0.30434783	wp204 pr005 mixed clasts	0.48	0.14	0.29166667
WP199 PR018 horiz fabric	0.29	0.14	0.48275862	wp204 pr005 mixed clasts	0.39	0.1	0.25641026
WP199 PR018 horiz fabric	0.2	0.13	0.65	wp204 pr005 mixed clasts	0.34	0.44	1.29411765
WP199 PR018 horiz fabric	0.22	0.11	0.5	wp204 pr005 mixed clasts	0.31	0.16	0.51612903
WP199 PR018 horiz fabric	0.09	0.12	1.33333333	WP190 PR02.1	1.39	0.93	0.66906475
WP199 PR018 horiz fabric	0.37	0.1	0.27027027	WP190 PR02.1	0.36	0.11	0.30555556
WP199 PR018 horiz fabric	0.14	0.04	0.28571429	WP190 PR02.1	0.43	0.14	0.3255814
WP199 PR018 various shapes	2.39	0.76	0.31799163	WP204 005.4	4.37	1.53	0.35011442
WP199 PR018 various shapes	1.07	0.55	0.51401869	WP204 005.4	0.067	0.17	2.53731343
WP199 PR018 various shapes	0.67	0.037	0.05522388	WP204 005.4	1.74	0.31	0.17816092
WP199 PR018 various shapes	0.38	0.24	0.63157895	WP204 005.4	1.61	0.28	0.17391304
WP199 PR018 various shapes	0.52	0.3	0.57692308	WP204 005.4	0.46	0.38	0.82608696
WP199 PR018 various shapes	1.39	0.69	0.49640288	WP204 005.4	0.37	0.2	0.54054054
WP199 PR018 various shapes	0.18	0.05	0.27777778	WP204 005.4	0.067	0.31	4.62686567
WP199 PR018 ves clast	4.6	3.61	0.78478261	WP204 005.4	0.43	0.1	0.23255814
WP199 PR018 ves clast	0.65	0.41	0.63076923	WP204 005.6	0.27	0.13	0.48148148

WP199 PR018 ves clast	0.11	0.11	1	WP204 005.6	1	0.3	0.3
wp199 pr18 curvi edit	3.2	1.35	0.421875	WP204 005.6	3.43	0.36	0.10495627
wp199 pr18 curvi edit	0.38	0.3	0.78947368	WP204 005.6	2.88	0.79	0.27430556
wp199 pr18 curvi edit	0.39	0.18	0.46153846				
wp199 pr18 curvi edit	0.96	0.85	0.88541667				
wp199 pr18 curvi edit	0.54	0.53	0.98148148				
wp199 pr18 curvi edit	0.66	0.19	0.28787879				
wp199 pr18 curvi1	0.92	0.91	0.98913043				
wp199 pr18 curvi1	0.85	5	5.88235294				
wp199 pr18 curvi1	0.38	0.1	0.26315789				
wp199 pr18 curvi1	1.11	0.83	0.74774775				
wp199 pr18 curvi1	1.19	0.65	0.54621849				
wp199 pr18 curvi1	0.85	0.21	0.24705882				
wp199 pr18 curvi1	0.44	0.21	0.47727273				
wp199 pr18 curvi1	1.01	0.61	0.6039604				
wp199 pr18 curvi1	0.25	0.2	0.8				
wp199 pr18 curvi1	0.59	0.14	0.23728814				
wp199 pr18 curvi1	0.19	0.1	0.52631579				
wp199 pr18 curvi1	0.36	0.11	0.30555556				
clast type mean dimension	0.932125	0.553148					
	0.80135	0.2095					
clast type abundance (%)	82.40741						
	18.69159						
clast type mean aspect ratio	0.593427						
	0.261434						

Table A2.7. Image analysis measurements of sideromelane ash.

Location	UTM Coordinates
Leitin rootless cones	500000/7097014
Búrfell rootless cones	402187/7098548
Pomeroy quarry	544082/5094205
Lava flow toward west of study area	615513/5095129
L18	615474/5095128
L19	615489/5095128
L20	577432/5094533
L21	577432/5094533
L22	577432/5094533
L23	577430/5094530
L17	639775/5126889
L16	639845/5126787
L1	639915/5126782
L2	639936/5126738
L12	640183/5126432
L4	640008/5126657
L3	640004/5126656
L5	640006/5126598
L7	639998/5126562
L8	640059/5126568
L9	640057/5126519
L11	640058/5126570
L6	640116/5126496
L10	640138/5126486
L13	640173/5126454
L14	640175/5126447
L15	640183/5126433
Table A2.8. UTM coordinates of study locations.	

	weight (g)	size (μm)	% contribution to Silicic volcanic ash	Φ	cumulative wt %
Silicic volcanic ash	0.0004	500	0.007355916	1	0.0004
	1.6593	250	30.51417853	2	1.6597
	1.8935	125	34.82106734	3	3.5532
	1.157	63	21.27698702	4	4.7102
	0.7276	<63	13.3804112	5.0115 88	5.4378
whole sample weight	6.0387				
juvenile weight	0.6009				
Table A2.9. Sorting of Silicic volcanic ash calculated by sieving.					

image	clast dimension (mm)		location	image	clast dimension (mm)		location
	x	y			x	y	
248	93	87	L20	47	37	22	L23
246	17	10	L20	47	35	15	L23
246	16	11	L20	47	54	40	L23
245	11	8	L20	49	43	23	L23
245	16	12	L20	158	16	15	L6
244	23	11	L20	158	14	5	L6
244	15	13	L20	159	37	22	L6
243	25	17	L20	159	44	37	L6
242	16	13	L20	160	17	14	L6
242	14	12	L20	160	16	10	L6
297	38	19	L19	161	15	12	L6
297	35	26	L19	161	15	12	L6
298	32	40	L19	161	14	10	L6
298	26	21	L19	161	15	12	L6
299	26	18	L19	162	13	6	L6
299	33	35	L19	192	212	94	L16
300	32	16	L19	192	230	85	L16
300	16	15	L19	192	240	96	L16
301	79	35	L19	193	116	54	L16
301	17	16	L19	193	150	77	L16
41	11	7	L23	194	170	54	L16
41	12	10	L23	194	71	30	L16
45	93	52	L23	195	197	28	L16
45	71	42	L23	195	185	17	L16

Table A2.10. Measurements of largest clasts in lithofacies mSp.

Weight of clast in air			Weight of clast and sheet in water			Ws water	Wc water	SG	Density
dry uncoated	coated	wet	clast wet	sheet dry weight	sheet %	sheet wet weight (g)	clast wet no sheet		
13.2	13.41	7.71	7.71	0.21	1.565996	0.120738	7.589261745	2.35	2352.632
12.15	12.44	7.41	7.41	0.29	2.33119	0.172741	7.237258842	2.47	2473.161
15.91	16.2	8.57	8.57	0.29	1.790123	0.153414	8.41658642	2.12	2123.198
18.68	19.04	11.05	11.05	0.36	1.890756	0.208929	10.84107143	2.38	2382.979
15.24	15.58	9.34	9.34	0.34	2.182285	0.203825	9.136174583	2.5	2496.795
11.04	11.31	6.63	6.63	0.27	2.387268	0.158276	6.471724138	2.42	2416.667
8.43	8.66	4.77	4.77	0.23	2.655889	0.126686	4.643314088	2.23	2226.221
21.5	21.98	12.55	12.55	0.48	2.183803	0.274067	12.27593267	2.33	2330.859
18.5	18.85	11.03	11.03	0.35	1.856764	0.204801	10.82519894	2.41	2410.486
16.22	16.69	10.03	10.03	0.47	2.816058	0.282451	9.747549431	2.51	2506.006
22.3	22.62	13.48	13.48	0.32	1.414677	0.190698	13.2893015	2.47	2474.836
15.47	15.84	8.89	8.89	0.37	2.335859	0.207658	8.682342172	2.28	2279.137
13.16	13.59	7.93	7.93	0.43	3.164091	0.250912	7.679087564	2.4	2401.06
17.31	17.71	10.12	10.12	0.4	2.258611	0.228571	9.891428571	2.33	2333.333
9.64	9.7	5	5	0.06	0.618557	0.030928	4.969072165	2.06	2063.83
17.77	18.13	10.36	10.36	0.36	1.985659	0.205714	10.15428571	2.33	2333.333
14.07	14.28	7.91	7.91	0.21	1.470588	0.116324	7.793676471	2.24	2241.758
19.22	19.64	10.89	10.89	0.42	2.138493	0.232882	10.65711813	2.24	2244.571
14.54	14.92	8.41	8.41	0.38	2.546917	0.214196	8.19580429	2.29	2291.859
15.01	15.15	8.79	8.79	0.14	0.924092	0.081228	8.708772277	2.38	2382.075
17.24	17.75	8.83	8.83	0.51	2.873239	0.253707	8.576292958	1.99	1989.91
20.02	20.33	11.92	11.92	0.31	1.52484	0.181761	11.73823906	2.42	2417.36
5.28	5.51	3.11	3.11	0.23	4.174229	0.129819	2.980181488	2.3	2295.833
10.38	10.64	6.3	6.3	0.26	2.443609	0.153947	6.146052632	2.45	2451.613
8.97	9.25	4.62	4.62	0.28	3.027027	0.139849	4.480151351	2	1997.84
18.01	18.32	10.54	10.54	0.31	1.69214	0.178352	10.36164847	2.35	2354.756
19.56	19.83	11.42	11.42	0.27	1.361573	0.155492	11.26450832	2.36	2357.907
13.45	13.76	8.32	8.32	0.31	2.252907	0.187442	8.13255814	2.53	2529.412
18.25	18.37	9.87	9.87	0.12	0.653239	0.064475	9.805525313	2.16	2161.176
11.69	12.03	6.09	6.09	0.34	2.826268	0.17212	5.917880299	2.03	2025.253
13.23	13.57	7.61	7.61	0.34	2.505527	0.190671	7.419329403	2.28	2276.846
14.28	14.54	8.57	8.57	0.26	1.788171	0.153246	8.416753783	2.44	2435.511
20.31	20.72	11.71	11.71	0.41	1.978764	0.231713	11.47828668	2.3	2299.667
23.86	24.27	14.43	14.43	0.41	1.689328	0.24377	14.18622991	2.47	2466.463
10.63	10.95	6.43	6.43	0.32	2.922374	0.187909	6.242091324	2.42	2422.566
14.08	14.52	7.09	7.09	0.44	3.030303	0.214848	6.875151515	1.95	1954.24
15.32	15.66	9.12	9.12	0.34	2.171137	0.198008	8.921992337	2.39	2394.495
14.21	14.49	7.08	7.08	0.28	1.932367	0.136812	6.943188406	1.96	1955.466
24.05	24.51	13.72	13.72	0.46	1.876785	0.257495	13.4625051	2.27	2271.548
23.92	24.32	14.37	14.37	0.4	1.644737	0.236349	14.13365132	2.44	2444.221
13.86	14.27	7.8	7.8	0.41	2.87316	0.224107	7.575893483	2.21	2205.564
6.65	6.87	3.27	3.27	0.22	3.202329	0.104716	3.165283843	1.91	1908.333
8.4	8.64	5.15	5.15	0.24	2.777778	0.143056	5.006944444	2.48	2475.645

15.21	15.51	8.92	8.92	0.3	1.934236	0.172534	8.747466151	2.35	2353.566
10.73	11.05	5.9	5.9	0.32	2.895928	0.17086	5.729140271	2.15	2145.631
17.28	17.66	9.84	9.84	0.38	2.151755	0.211733	9.628267271	2.26	2258.312
8.2	8.48	4.71	4.71	0.28	3.301887	0.155519	4.554481132	2.25	2249.337
13.47	13.75	6.25	6.25	0.28	2.036364	0.127273	6.122727273	1.83	1833.333
17.91	18.31	9.92	9.92	0.4	2.184599	0.216712	9.703287821	2.18	2182.36
20.06	20.47	11.94	11.94	0.41	2.002931	0.23915	11.70085002	2.4	2399.766
13.81	14.15	8.24	8.24	0.34	2.402827	0.197993	8.042007067	2.39	2394.247
13.57	13.91	7.42	7.42	0.34	2.444285	0.181366	7.238634076	2.14	2143.297
16.97	17.31	9.81	9.81	0.34	1.964183	0.192686	9.617313692	2.31	2308
10.67	10.97	6.44	6.44	0.3	2.734731	0.176117	6.263883318	2.42	2421.634
18.35	18.56	10.88	10.88	0.21	1.131466	0.123103	10.75689655	2.42	2416.667
10.74	10.98	5.62	5.62	0.24	2.185792	0.122842	5.49715847	2.05	2048.507
13.9	14.3	5.45	5.45	0.4	2.797203	0.152448	5.297552448	1.62	1615.819
6.81	7.22	4.09	4.09	0.41	5.67867	0.232258	3.857742382	2.31	2306.709
5.96	6.24	3.36	3.36	0.28	4.487179	0.150769	3.209230769	2.17	2166.667
16.69	17.06	9.48	9.48	0.37	2.168816	0.205604	9.274396249	2.25	2250.66
20.83	21.23	11.87	11.87	0.4	1.884126	0.223646	11.64635422	2.27	2268.162
11.39	11.65	4.95	4.95	0.26	2.23176	0.110472	4.839527897	1.74	1738.806
9.21	9.32	5.19	5.19	0.11	1.180258	0.061255	5.128744635	2.26	2256.659
9.41	9.94	5.35	5.35	0.53	5.331992	0.285262	5.064738431	2.17	2165.577
6.63	6.74	3.95	3.95	0.11	1.632047	0.064466	3.885534125	2.42	2415.771
13.23	13.52	7.89	7.89	0.29	2.14497	0.169238	7.720761834	2.4	2401.421
11.74	12.03	5.47	5.47	0.29	2.41064	0.131862	5.338137988	1.83	1833.841
24.62	24.97	13.58	13.58	0.35	1.401682	0.190348	13.38965158	2.19	2192.274
20.39	20.77	11.24	11.24	0.38	1.829562	0.205643	11.03435725	2.18	2179.433
11.01	11.34	6.7	6.7	0.33	2.910053	0.194974	6.505026455	2.44	2443.966
15.49	15.79	9.39	9.39	0.3	1.899937	0.178404	9.211595947	2.47	2467.188
15.58	15.64	9.32	9.32	0.06	0.383632	0.035754	9.284245524	2.47	2474.684
17.79	18.18	10.82	10.82	0.39	2.145215	0.232112	10.58788779	2.47	2470.109
11.22	11.48	5.55	5.55	0.26	2.264808	0.125697	5.424303136	1.94	1935.919
13.6	14.16	8.17	8.17	0.56	3.954802	0.323107	7.846892655	2.36	2363.94
22	22.32	12.23	12.23	0.32	1.433692	0.175341	12.0546595	2.21	2212.091
7.11	7.49	4.49	4.49	0.38	5.073431	0.227797	4.262202937	2.5	2496.667
6.71	6.99	2.34	2.34	0.28	4.005722	0.093734	2.246266094	1.5	1503.226
15.08	15.35	8.84	8.84	0.27	1.758958	0.155492	8.684508143	2.36	2357.911
15.36	15.7	8.84	8.84	0.34	2.165605	0.191439	8.64856051	2.29	2288.63
7.81	8.03	2.98	2.98	0.22	2.739726	0.081644	2.898356164	1.59	1590.099
6.41	6.67	2.68	2.68	0.26	3.898051	0.104468	2.575532234	1.67	1671.679
16.36	16.73	9.49	9.49	0.37	2.211596	0.20988	9.280119546	2.31	2310.773
6.03	6.27	3.33	3.33	0.24	3.827751	0.127464	3.202535885	2.13	2132.653
15.26	15.61	8.3	8.3	0.35	2.242152	0.186099	8.113901345	2.14	2135.431
11.43	11.78	6.64	6.64	0.35	2.971138	0.197284	6.442716469	2.29	2291.829
15.1	15.5	9.24	9.24	0.4	2.580645	0.238452	9.001548387	2.48	2476.038
9.06	9.34	5.64	5.64	0.28	2.997859	0.169079	5.470920771	2.52	2524.324

11.57	11.91	7.19	7.19	0.34	2.854744	0.205256	6.984743913	2.52	2523.305
15.36	15.7	7.91	7.91	0.34	2.165605	0.171299	7.738700637	2.02	2015.404
density range	density mean	vesicularity							
1503	2249.87492	16.67129927							
2529									
Table A2.11. Density measurements for the Ice Harbor lava core. Weight is in g, density in kg m ⁻³ , vesicularity in %.									

Weight of clast in air			Weight of clast and sheet in water			Ws water	Wc water	SG	Density
dry uncoated	coated	wet	clast wet	sheet dry weight	sheet %	sheet wet weight (g)	clast wet no sheet		
17.24	17.72	9.49	9.49	0.48	2.708804	0.257065463	9.23	2.15309842	2153.09842
9.1	9.55	4.43	4.43	0.45	4.712042	0.208743455	4.22	1.865234375	1865.234375
9.79	10.1	5.55	5.55	0.31	3.069307	0.170346535	5.38	2.21978022	2219.78022
10.33	10.69	4.37	4.37	0.36	3.367633	0.147165575	4.22	1.691455696	1691.455696
9.99	10.31	4.59	4.59	0.32	3.103783	0.142463628	4.45	1.802447552	1802.447552
14.25	14.66	7.69	7.69	0.41	2.796726	0.215068213	7.47	2.103299857	2103.299857
21.84	22.45	12.76	12.76	0.61	2.717149	0.346708241	12.4	2.316821465	2316.821465
8.84	9.26	5.18	5.18	0.42	4.535637	0.234946004	4.95	2.269607843	2269.607843
17.29	17.8	9.89	9.89	0.51	2.865169	0.283365169	9.61	2.250316056	2250.316056
9.25	9.63	4.15	4.15	0.38	3.946002	0.163759086	3.99	1.75729927	1757.29927
6.78	7.16	1.95	1.95	0.38	5.307263	0.10349162	1.85	1.37428023	1374.28023
10.46	11.05	4.98	4.98	0.59	5.339367	0.265900452	4.71	1.820428336	1820.428336
9.83	10.31	5.4	5.4	0.48	4.655674	0.251406402	5.15	2.099796334	2099.796334
10.69	11.11	6.55	6.55	0.42	3.780378	0.247614761	6.3	2.436403509	2436.403509
10.32	10.6	6.24	6.24	0.28	2.641509	0.164830189	6.08	2.431192661	2431.192661
15.25	15.69	9.22	9.22	0.44	2.804334	0.258559592	8.96	2.42503864	2425.03864
14.51	14.97	6.35	6.35	0.46	3.072812	0.19512358	6.15	1.736658933	1736.658933
20.72	21.28	12.51	12.51	0.56	2.631579	0.329210526	12.2	2.42645382	2426.45382
6.26	6.63	4.18	4.18	0.37	5.580694	0.233273002	3.95	2.706122449	2706.122449
16.46	16.97	10.35	10.35	0.51	3.005303	0.31104891	10	2.563444109	2563.444109
16.56	17.1	9.05	9.05	0.54	3.157895	0.285789474	8.76	2.124223602	2124.223602
14.24	14.85	8.11	8.11	0.61	4.107744	0.333138047	7.78	2.203264095	2203.264095
8.16	8.53	4.89	4.89	0.37	4.337632	0.212110199	4.68	2.343406593	2343.406593
11.88	12.39	7.13	7.13	0.51	4.116223	0.293486683	6.84	2.355513308	2355.513308
13.36	13.86	8.5	8.5	0.5	3.607504	0.306637807	8.19	2.585820896	2585.820896
9.98	10.37	6.87	6.87	0.39	3.760849	0.258370299	6.61	2.962857143	2962.857143
12.5	13.04	5.66	5.66	0.54	4.141104	0.234386503	5.43	1.766937669	1766.937669
22.68	23.27	12.66	12.66	0.59	2.535453	0.320988397	12.3	2.193213949	2193.213949
8.55	8.8	4.01	4.01	0.25	2.840909	0.113920455	3.9	1.837160752	1837.160752
13.61	14.12	7.17	7.17	0.51	3.611898	0.258973088	6.91	2.031654676	2031.654676
20.73	21.15	10.61	10.61	0.42	1.985816	0.210695035	10.4	2.006641366	2006.641366
15.52	16.02	9.08	9.08	0.5	3.121099	0.283395755	8.8	2.308357349	2308.357349
12.08	12.6	6.81	6.81	0.52	4.126984	0.281047619	6.53	2.176165803	2176.165803
5.87	6.17	4.02	4.02	0.3	4.862237	0.195461912	3.82	2.869767442	2869.767442
8.01	8.6	4.84	4.84	0.59	6.860465	0.332046512	4.51	2.287234043	2287.234043

7.97	8.42	4.61	4.61	0.45	5.344418	0.246377672	4.36	2.209973753	2209.973753
5.96	6.44	4.21	4.21	0.48	7.453416	0.31378882	3.9	2.887892377	2887.892377
4.85	5.15	3.14	3.14	0.3	5.825243	0.182912621	2.96	2.562189055	2562.189055
6.66	7.14	4.56	4.56	0.48	6.722689	0.306554622	4.25	2.76744186	2767.44186
5.95	6.27	3.83	3.83	0.32	5.103668	0.195470494	3.63	2.569672131	2569.672131
10.4	10.8	6.79	6.79	0.4	3.703704	0.251481481	6.54	2.693266833	2693.266833
6.76	7.07	2.6	2.6	0.31	4.384724	0.114002829	2.49	1.581655481	1581.655481
10	10.5	5.81	5.81	0.5	4.761905	0.276666667	5.53	2.23880597	2238.80597
10.7	11.07	7.31	7.31	0.37	3.342367	0.24432701	7.07	2.944148936	2944.148936
15.75	16.07	9.73	9.73	0.32	1.991288	0.193752334	9.54	2.534700315	2534.700315
15.99	16.5	9.67	9.67	0.51	3.090909	0.298890909	9.37	2.415812592	2415.812592
13.39	13.73	8.36	8.36	0.34	2.476329	0.207021122	8.15	2.55679702	2556.79702
13.15	13.64	6.7	6.7	0.49	3.592375	0.24068915	6.46	1.965417867	1965.417867
16.48	16.91	10.39	10.39	0.43	2.542874	0.264204613	10.1	2.593558282	2593.558282
5.86	6.24	3.02	3.02	0.38	6.089744	0.183910256	2.84	1.937888199	1937.888199
6.6	6.89	4.16	4.16	0.29	4.208999	0.17509434	3.98	2.523809524	2523.809524
10.99	11.56	6.84	6.84	0.57	4.930796	0.337266436	6.5	2.449152542	2449.152542
10.86	11.47	6.85	6.85	0.61	5.318221	0.364298169	6.49	2.482683983	2482.683983
24.36	24.95	13.93	13.93	0.59	2.364729	0.329406814	13.6	2.264065336	2264.065336
9.46	9.92	5.03	5.03	0.46	4.637097	0.233245968	4.8	2.028629857	2028.629857
14.29	14.95	7.8	7.8	0.66	4.414716	0.344347826	7.46	2.090909091	2090.909091
7.44	7.89	3.6	3.6	0.45	5.703422	0.205323194	3.39	1.839160839	1839.160839
4.1	4.27	2.51	2.51	0.17	3.981265	0.099929742	2.41	2.426136364	2426.136364
6.75	7.12	3.85	3.85	0.37	5.196629	0.200070225	3.65	2.177370031	2177.370031
18.88	19.34	11.17	11.17	0.46	2.37849	0.265677353	10.9	2.367197062	2367.197062
6.78	7.06	2.63	2.63	0.28	3.966006	0.104305949	2.53	1.593679458	1593.679458
7.17	7.48	3.52	3.52	0.31	4.144385	0.145882353	3.37	1.888888889	1888.888889
7.48	7.81	2.81	2.81	0.33	4.225352	0.118732394	2.69	1.562	1562
11.1	11.54	5.81	5.81	0.44	3.812825	0.22152513	5.59	2.013961606	2013.961606
15.21	15.7	7.27	7.27	0.49	3.121019	0.226898089	7.04	1.862396204	1862.396204
11.87	12.32	6.27	6.27	0.45	3.652597	0.229017857	6.04	2.036363636	2036.363636
11.85	12.35	7.86	7.86	0.5	4.048583	0.318218623	7.54	2.750556793	2750.556793
8.85	9.23	3.63	3.63	0.38	4.11701	0.149447454	3.48	1.648214286	1648.214286
6.51	6.84	2.19	2.19	0.33	4.824561	0.105657895	2.08	1.470967742	1470.967742
8.28	8.61	5.54	5.54	0.33	3.832753	0.212334495	5.33	2.804560261	2804.560261
15	15.33	8.91	8.91	0.33	2.152642	0.191800391	8.72	2.387850467	2387.850467
8.4	8.17	5.1	5.1	-0.23	-2.81518	-0.143574051	5.24	2.661237785	2661.237785
6.56	6.91	2.04	2.04	0.35	5.065123	0.103328509	1.94	1.41889117	1418.89117
11.42	11.67	5.9	5.9	0.25	2.142245	0.126392459	5.77	2.022530329	2022.530329
13.4	13.67	7.8	7.8	0.27	1.975128	0.154059985	7.65	2.32879046	2328.79046
5.51	5.85	3.25	3.25	0.34	5.811966	0.188888889	3.06	2.25	2250
12.21	12.61	6.89	6.89	0.4	3.172086	0.218556701	6.67	2.204545455	2204.545455
8.32	8.78	2.69	2.69	0.46	5.23918	0.140933941	2.55	1.441707718	1441.707718
6	6.13	2.68	2.68	0.13	2.120718	0.056835237	2.62	1.776811594	1776.811594
10.84	11.19	5.43	5.43	0.35	3.127793	0.169839142	5.26	1.942708333	1942.708333

11.74	12.14	4.9	4.9	0.4	3.294893	0.161449753	4.74	1.67679558	1676.79558
4.84	5.22	2.14	2.14	0.38	7.279693	0.155785441	1.98	1.694805195	1694.805195
7.08	7.5	4.22	4.22	0.42	5.6	0.23632	3.98	2.286585366	2286.585366
6.02	6.31	3.88	3.88	0.29	4.59588	0.178320127	3.7	2.596707819	2596.707819
4.46	4.74	2.06	2.06	0.28	5.907173	0.121687764	1.94	1.768656716	1768.656716
7.96	8.27	4.71	4.71	0.31	3.748489	0.176553809	4.53	2.323033708	2323.033708
7.65	7.94	4.36	4.36	0.29	3.652393	0.159244332	4.2	2.217877095	2217.877095
5.25	5.48	2.34	2.34	0.23	4.19708	0.098211679	2.24	1.74522293	1745.22293
8.04	8.43	4.48	4.48	0.39	4.626335	0.207259786	4.27	2.134177215	2134.177215
8.84	9.13	4.71	4.71	0.29	3.176342	0.149605696	4.56	2.06561086	2065.61086
density range	density mean	vesicularity							
1374	2179.842983	19.26507472							
2962									
st dev	378.0736607								

Table A2.12. Density measurements for the spatter bombs. Weight is in g, density in kg m⁻³, vesicularity in %.

Weight of clast in air			Weight of clast and sheet in water			Ws water	Wc water	SG	Density
dry uncoated	coated	wet	clast wet	sheet dry weight	sheet %	sheet wet weight (g)	clast wet no sheet		
8.76	9.16	4.93	4.93	0.4	4.366812	0.21528384	4.71	2.165484634	2165.484634
8.87	9.3	4.56	4.56	0.43	4.623656	0.21083871	4.35	1.962025316	1962.025316
2.97	4.32	2.41	2.41	1.35	31.25	0.753125	1.66	2.261780105	2261.780105
14.66	15.01	7.29	7.29	0.35	2.331779	0.169986676	7.12	1.944300518	1944.300518
9.02	9.54	3.43	3.43	0.52	5.450734	0.186960168	3.24	1.561374795	1561.374795
6.15	6.53	3.39	3.39	0.38	5.819296	0.197274119	3.19	2.079617834	2079.617834
6.69	7	3.04	3.04	0.31	4.428571	0.134628571	2.91	1.767676768	1767.676768
5.67	6.06	3.3	3.3	0.39	6.435644	0.212376238	3.09	2.195652174	2195.652174
3.55	3.8	1.82	1.82	0.25	6.578947	0.119736842	1.7	1.919191919	1919.191919
4.53	4.77	2.45	2.45	0.24	5.031447	0.12327044	2.33	2.056034483	2056.034483
14.49	14.93	6.93	6.93	0.44	2.947086	0.204233088	6.73	1.86625	1866.25
9.34	9.72	5.23	5.23	0.38	3.909465	0.204465021	5.03	2.16481069	2164.81069
7.03	7.47	3.32	3.32	0.44	5.890228	0.195555556	3.12	1.8	1800
9.08	9.54	5.43	5.43	0.46	4.821803	0.261823899	5.17	2.321167883	2321.167883
3.08	3.32	1.39	1.39	0.24	7.228916	0.100481928	1.29	1.720207254	1720.207254
8.2	8.67	3.58	3.58	0.47	5.420992	0.194071511	3.39	1.703339882	1703.339882
6.56	6.92	3.75	3.75	0.36	5.202312	0.195086705	3.55	2.1829653	2182.9653
9.86	10.07	5.48	5.48	0.21	2.085402	0.11428004	5.37	2.193899782	2193.899782
9.31	9.67	5.21	5.21	0.36	3.722854	0.193960703	5.02	2.168161435	2168.161435
10.55	10.9	5.01	5.01	0.35	3.211009	0.16087156	4.85	1.850594228	1850.594228
4.52	4.96	0.4	0.4	0.44	8.870968	0.035483871	0.36	1.087719298	1087.719298
10.44	10.82	3.47	3.47	0.38	3.512015	0.121866913	3.35	1.472108844	1472.108844
6.43	7.11	1.98	1.98	0.68	9.563994	0.189367089	1.79	1.385964912	1385.964912
7.38	7.88	1.91	1.91	0.5	6.345178	0.121192893	1.79	1.319932998	1319.932998
8.07	8.45	3.14	3.14	0.38	4.497041	0.141207101	3	1.5913371	1591.3371
7.93	8.47	2.21	2.21	0.54	6.375443	0.140897285	2.07	1.353035144	1353.035144

5.19	5.43	2.7	2.7	0.24	4.41989	0.119337017	2.58	1.989010989	1989.010989
7.49	8.06	2.93	2.93	0.57	7.07196	0.207208437	2.72	1.571150097	1571.150097
2.28	2.59	1.29	1.29	0.31	11.96911	0.154401544	1.14	1.992307692	1992.307692
3.03	3.45	1.06	1.06	0.42	12.17391	0.129043478	0.93	1.443514644	1443.514644
8.14	8.46	3.97	3.97	0.32	3.782506	0.150165485	3.82	1.884187082	1884.187082
3.76	4.09	1.44	1.44	0.33	8.06846	0.116185819	1.32	1.543396226	1543.396226
5.69	5.97	2.1	2.1	0.28	4.690117	0.098492462	2	1.542635659	1542.635659
6.66	7.07	2.73	2.73	0.41	5.799151	0.158316832	2.57	1.629032258	1629.032258
6.53	6.93	1.77	1.77	0.4	5.772006	0.102164502	1.67	1.343023256	1343.023256
7.23	7.59	2.08	2.08	0.36	4.743083	0.098656126	1.98	1.377495463	1377.495463
6.43	6.83	2.58	2.58	0.4	5.856515	0.151098097	2.43	1.607058824	1607.058824
5.66	5.95	1.85	1.85	0.29	4.87395	0.090168067	1.76	1.451219512	1451.219512
3.87	4.21	1.11	1.11	0.34	8.07601	0.089643705	1.02	1.358064516	1358.064516
9.92	10.32	4.24	4.24	0.4	3.875969	0.164341085	4.08	1.697368421	1697.368421
13.53	13.91	7.76	7.76	0.38	2.731848	0.211991373	7.55	2.261788618	2261.788618
2.88	3.16	0.64	0.64	0.28	8.860759	0.056708861	0.58	1.253968254	1253.968254
2.05	2.3	1.5	1.5	0.25	10.86957	0.163043478	1.34	2.875	2875
3.08	3.34	0.43	0.43	0.26	7.784431	0.033473054	0.4	1.147766323	1147.766323
6.29	6.71	2.31	2.31	0.42	6.259314	0.144590164	2.17	1.525	1525
7.68	8.02	2.82	2.82	0.34	4.239401	0.119551122	2.7	1.542307692	1542.307692
5.38	5.84	2.05	2.05	0.46	7.876712	0.161472603	1.89	1.540897098	1540.897098
5.76	6.11	2.3	2.3	0.35	5.728314	0.131751227	2.17	1.603674541	1603.674541
2.45	2.66	1.05	1.05	0.21	7.894737	0.082894737	0.97	1.652173913	1652.173913
3.49	3.7	1.63	1.63	0.21	5.675676	0.092513514	1.54	1.787439614	1787.439614
5.17	5.47	1.89	1.89	0.3	5.484461	0.103656307	1.79	1.527932961	1527.932961
3.62	3.92	1.1	1.1	0.3	7.653061	0.084183673	1.02	1.390070922	1390.070922
3.7	3.94	2.04	2.04	0.24	6.091371	0.124263959	1.92	2.073684211	2073.684211
3.68	3.89	2.02	2.02	0.21	5.398458	0.109048843	1.91	2.080213904	2080.213904
10.79	11.13	4.99	4.99	0.34	3.054807	0.152434861	4.84	1.812703583	1812.703583
4.31	4.4	1.46	1.46	0.09	2.045455	0.029863636	1.43	1.496598639	1496.598639
4.05	4.52	2.12	2.12	0.47	10.39823	0.220442478	1.9	1.883333333	1883.333333
3.41	3.66	1.94	1.94	0.25	6.830601	0.132513661	1.81	2.127906977	2127.906977
2.2	2.42	0.89	0.89	0.22	9.090909	0.080909091	0.81	1.581699346	1581.699346
3.75	3.96	2.14	2.14	0.21	5.30303	0.113484848	2.03	2.175824176	2175.824176
9.98	10.29	4.08	4.08	0.31	3.012634	0.122915452	3.96	1.657004831	1657.004831
7.71	8.1	3.74	3.74	0.39	4.814815	0.180074074	3.56	1.857798165	1857.798165
5.03	5.29	2.34	2.34	0.26	4.914934	0.115009452	2.22	1.793220339	1793.220339
7.13	7.37	3.4	3.4	0.24	3.256445	0.110719132	3.29	1.856423174	1856.423174
6.89	7.32	3.23	3.23	0.43	5.874317	0.189740437	3.04	1.789731051	1789.731051
6.05	6.64	2.46	2.46	0.59	8.885542	0.218584337	2.24	1.588516746	1588.516746
5.98	6.18	3.5	3.5	0.2	3.236246	0.113268608	3.39	2.305970149	2305.970149
5.97	6.32	3.41	3.41	0.35	5.537975	0.188844937	3.22	2.171821306	2171.821306
3.81	4.1	1.11	1.11	0.29	7.073171	0.078512195	1.03	1.371237458	1371.237458
4.96	5.63	2.45	2.45	0.67	11.90053	0.291563055	2.16	1.770440252	1770.440252
3.78	4.18	0.67	0.67	0.4	9.569378	0.064114833	0.61	1.190883191	1190.883191

8.75	9.23	3.78	3.78	0.48	5.200433	0.196576381	3.58	1.693577982	1693.577982
10.67	11.06	4.7	4.7	0.39	3.526221	0.165732369	4.53	1.738993711	1738.993711
7.2	7.61	3.39	3.39	0.41	5.387648	0.182641261	3.21	1.803317536	1803.317536
5.93	6.35	1	1	0.42	6.614173	0.066141732	0.93	1.186915888	1186.915888
5.79	6.14	2.52	2.52	0.35	5.700326	0.143648208	2.38	1.696132597	1696.132597
8.87	9.28	3.24	3.24	0.41	4.418103	0.143146552	3.1	1.536423841	1536.423841
4.26	4.91	0.61	0.61	0.65	13.23829	0.080753564	0.53	1.141860465	1141.860465
6.68	6.85	2.93	2.93	0.17	2.481752	0.072715328	2.86	1.74744898	1747.44898
7.84	8.29	2.64	2.64	0.45	5.428227	0.143305187	2.5	1.467256637	1467.256637
4.01	4.26	1.47	1.47	0.25	5.868545	0.086267606	1.38	1.52688172	1526.88172
5.82	6.53	1.17	1.17	0.71	10.87289	0.127212864	1.04	1.218283582	1218.283582
9.92	10.47	5.09	5.09	0.55	5.253104	0.267382999	4.82	1.946096654	1946.096654
6.06	6.36	1.79	1.79	0.3	4.716981	0.084433962	1.71	1.391684902	1391.684902
4	4.3	1.8	1.8	0.3	6.976744	0.125581395	1.67	1.72	1720
5.24	5.58	2.15	2.15	0.34	6.09319	0.131003584	2.02	1.626822157	1626.822157
3.84	4.22	1.2	1.2	0.38	9.004739	0.108056872	1.09	1.397350993	1397.350993
4.9	5.21	1.58	1.58	0.31	5.950096	0.094011516	1.49	1.435261708	1435.261708
4.92	5.24	1.05	1.05	0.32	6.10687	0.064122137	0.99	1.250596659	1250.596659
3.55	4.16	1.34	1.34	0.61	14.66346	0.196490385	1.14	1.475177305	1475.177305
density range	density mean	vesicularity							
1087	1713.524578	36.53612674							
2321									
st dev	333.9175475								
Table A2.13. Density measurements for the armoured bombs. Weight is in g, density in kg m ⁻³ , vesicularity in %.									

Weight of clast in air			Weight of clast and sheet in water			Ws water	Wc water	SG	Density
dry uncoated	coated	wet	clast wet	sheet dry weight	sheet %	sheet wet weight (g)	clast wet no sheet		
14.94	15.19	8.6	8.6	0.25	1.64582	0.141540487	8.458459513	2.30500	2305.007587
15.68	16.13	9.2	9.2	0.45	2.789833	0.2566646	8.9433354	2.32756	2327.561328
10.55	10.78	5.45	5.45	0.23	2.133581	0.116280148	5.333719852	2.02251	2022.514071
14.98	15.18	8.29	8.29	0.2	1.317523	0.109222661	8.180777339	2.20319	2203.193033
14.55	14.9	8.28	8.28	0.35	2.348993	0.194496644	8.085503356	2.250755	2250.755287
10.49	10.83	6.18	6.18	0.34	3.139428	0.19401662	5.98598338	2.329032	2329.032258
20.21	20.58	13.15	13.15	0.37	1.797862	0.236418853	12.91358115	2.769852	2769.851952
13.32	13.75	8.29	8.29	0.43	3.127273	0.259250909	8.030749091	2.518315	2518.315018
10.79	10.9	6.91	6.91	0.11	1.009174	0.069733945	6.840266055	2.73183	2731.829574
8.53	8.88	5.12	5.12	0.35	3.941441	0.201801802	4.918198198	2.361702	2361.702128
9.83	10.17	5.46	5.46	0.34	3.343166	0.182536873	5.277463127	2.159236	2159.235669
15.68	16.02	9.99	9.99	0.34	2.122347	0.212022472	9.777977528	2.656716	2656.716418
15.09	15.36	8.53	8.53	0.27	1.757813	0.149941406	8.380058594	2.248902	2248.901903
9.13	9.39	5.16	5.16	0.26	2.768903	0.142875399	5.017124601	2.219858	2219.858156
10.89	11.18	6.72	6.72	0.29	2.593918	0.17431127	6.54568873	2.506726	2506.726457
11.7	12.05	7.03	7.03	0.35	2.904564	0.204190871	6.825809129	2.400398	2400.398406
7.48	7.88	1.92	1.92	0.4	5.076142	0.097461929	1.822538071	1.322148	1322.147651
10.78	11.03	6.91	6.91	0.25	2.266546	0.156618314	6.753381686	2.677184	2677.184466
6.65	6.92	2.96	2.96	0.27	3.901734	0.115491329	2.844508671	1.747475	1747.474747
10.85	11.13	5.97	5.97	0.28	2.515723	0.150188679	5.819811321	2.156977	2156.976744
13.35	13.79	8.49	8.49	0.44	3.190718	0.270891951	8.219108049	2.601887	2601.886792
13.78	14.11	7.77	7.77	0.33	2.338767	0.181722183	7.588277817	2.225552	2225.55205
15.96	16.4	9.33	9.33	0.44	2.682927	0.250317073	9.079682927	2.319661	2319.660537
4.51	4.81	2.13	2.13	0.3	6.237006	0.132848233	1.997151767	1.794776	1794.776119
7.93	8.18	4.28	4.28	0.25	3.056235	0.130806846	4.149193154	2.097436	2097.435897
13.72	14.07	7.76	7.76	0.35	2.487562	0.193034826	7.566965174	2.229794	2229.793978
13.86	14.34	6.99	6.99	0.48	3.34728	0.233974895	6.756025105	1.95102	1951.020408
9.11	9.3	5.05	5.05	0.19	2.043011	0.103172043	4.946827957	2.188235	2188.235294
16.79	17.17	10.32	10.32	0.38	2.213162	0.228398369	10.09160163	2.506569	2506.569343
12.77	13.18	6.46	6.46	0.41	3.110774	0.200955994	6.259044006	1.96131	1961.309524
13.42	13.78	6.83	6.83	0.36	2.612482	0.178432511	6.651567489	1.982734	1982.733813
14.18	14.35	8.48	8.48	0.17	1.184669	0.10045993	8.37954007	2.444634	2444.633731
9.18	9.53	4.34	4.34	0.35	3.672613	0.159391396	4.180608604	1.836224	1836.223507
13.35	13.66	8.03	8.03	0.31	2.2694	0.182232796	7.847767204	2.426288	2426.287744
7.7	7.92	4.41	4.41	0.22	2.777778	0.1225	4.2875	2.25641	2256.410256
11.27	11.5	6.52	6.52	0.23	2	0.1304	6.3896	2.309237	2309.236948
13.43	13.78	7.39	7.39	0.35	2.539913	0.187699565	7.202300435	2.156495	2156.494523
9.63	9.96	4.58	4.58	0.33	3.313253	0.151746988	4.428253012	1.851301	1851.301115
8.38	8.75	5.41	5.41	0.37	4.228571	0.228765714	5.181234286	2.61976	2619.760479
13.98	14.45	8.66	8.66	0.47	3.252595	0.28167474	8.37832526	2.495682	2495.682211
6.84	7.07	4.21	4.21	0.23	3.253182	0.136958982	4.073041018	2.472028	2472.027972
12.72	13.26	7.41	7.41	0.54	4.072398	0.301764706	7.108235294	2.266667	2266.666667
12.55	13.05	7.24	7.24	0.5	3.831418	0.277394636	6.962605364	2.246127	2246.127367

9.71	10.12	6.5	6.5	0.41	4.051383	0.263339921	6.236660079	2.79558	2795.58011
9.12	9.52	5.64	5.64	0.4	4.201681	0.23697479	5.40302521	2.453608	2453.608247
8.91	9.16	5.72	5.72	0.25	2.729258	0.156113537	5.563886463	2.662791	2662.790698
10.77	11.11	6.73	6.73	0.34	3.060306	0.205958596	6.524041404	2.53653	2536.52968
13.35	13.83	8.24	8.24	0.48	3.470716	0.285986985	7.954013015	2.474061	2474.060823
6.84	7.24	3.89	3.89	0.4	5.524862	0.214917127	3.675082873	2.161194	2161.19403
11.3	11.76	6.8	6.8	0.46	3.911565	0.265986395	6.534013605	2.370968	2370.967742
6.79	7.29	4.28	4.28	0.5	6.858711	0.293552812	3.986447188	2.421927	2421.92691
11.13	11.56	6.85	6.85	0.43	3.719723	0.254801038	6.595198962	2.454352	2454.352442
14.19	14.43	7.93	7.93	0.24	1.663202	0.131891892	7.798108108	2.22	2220
8.67	9.1	5.79	5.79	0.43	4.725275	0.273593407	5.516406593	2.749245	2749.244713
18.11	18.61	10.56	10.56	0.5	2.686728	0.283718431	10.27628157	2.311801	2311.801242
5.26	5.58	3.32	3.32	0.32	5.734767	0.190394265	3.129605735	2.469027	2469.026549
7.76	8.22	3.48	3.48	0.46	5.596107	0.194744526	3.285255474	1.734177	1734.177215
6.65	7.04	3.99	3.99	0.39	5.539773	0.221036932	3.768963068	2.308197	2308.196721
5.5	5.82	3.08	3.08	0.32	5.498282	0.169347079	2.910652921	2.124088	2124.087591
16.01	16.41	10.23	10.23	0.4	2.437538	0.249360146	9.980639854	2.65534	2655.339806
11.08	11.57	6.26	6.26	0.49	4.235091	0.265116681	5.994883319	2.178908	2178.907721
5.91	6.46	4.22	4.22	0.55	8.513932	0.359287926	3.860712074	2.883929	2883.928571
5.89	6.3	2.77	2.77	0.41	6.507937	0.180269841	2.589730159	1.784703	1784.70255
3.79	4.18	2.02	2.02	0.39	9.330144	0.1884689	1.8315311	1.935185	1935.185185
2.14	2.31	1.19	1.19	0.17	7.359307	0.087575758	1.102424242	2.0625	2062.5
4.58	4.88	0.07	0.07	0.3	6.147541	0.004303279	0.065696721	1.014553	1014.553015
9.26	9.7	5.5	5.5	0.44	4.536082	0.249484536	5.250515464	2.309524	2309.52381
8.33	8.62	5.42	5.42	0.29	3.364269	0.182343387	5.237656613	2.69375	2693.75
14.51	14.77	9.51	9.51	0.26	1.760325	0.167406906	9.342593094	2.807985	2807.984791
13.41	13.78	8.59	8.59	0.37	2.685051	0.230645864	8.359354136	2.655106	2655.105973
15.84	16.41	9.65	9.65	0.57	3.473492	0.335191956	9.314808044	2.427515	2427.514793
12.67	13.1	7.88	7.88	0.43	3.282443	0.258656489	7.621343511	2.509579	2509.578544
16.97	17.53	10.08	10.08	0.56	3.194524	0.322007986	9.757992014	2.35302	2353.020134
11.72	12.05	6.68	6.68	0.33	2.738589	0.182937759	6.497062241	2.243948	2243.947858
17.81	18.31	10.79	10.79	0.5	2.730748	0.294647733	10.49535227	2.43484	2434.840426
11.35	11.92	5.95	5.95	0.57	4.781879	0.284521812	5.665478188	1.99665	1996.649916
11.95	12.36	7.39	7.39	0.41	3.317152	0.24513754	7.14486246	2.486922	2486.921529
14.69	15.2	8.97	8.97	0.51	3.355263	0.300967105	8.669032895	2.439807	2439.807384
7.65	8.02	3.26	3.26	0.37	4.613466	0.150399002	3.109600998	1.684874	1684.87395
16.68	17.15	10.31	10.31	0.47	2.740525	0.282548105	10.0274519	2.50731	2507.309942
11.14	11.44	4.95	4.95	0.3	2.622378	0.129807692	4.820192308	1.762712	1762.711864
9.14	9.51	5.18	5.18	0.37	3.890641	0.201535226	4.978464774	2.196305	2196.30485
16.73	17.23	9.69	9.69	0.5	2.901915	0.281195589	9.408804411	2.285146	2285.145889
13.36	13.73	5.89	5.89	0.37	2.694829	0.158725419	5.731274581	1.751276	1751.27551
12.22	12.52	6.37	6.37	0.3	2.396166	0.152635783	6.217364217	2.035772	2035.772358
7.07	7.44	4.25	4.25	0.37	4.973118	0.211357527	4.038642473	2.332288	2332.288401
9.17	9.52	5.98	5.98	0.35	3.676471	0.219852941	5.760147059	2.689266	2689.265537
7.8	8.32	4.48	4.48	0.52	6.25	0.28	4.2	2.166667	2166.666667

8.16	8.7	5.2	5.2	0.54	6.206897	0.322758621	4.877241379	2.485714	2485.714286
9.12	9.54	4.58	4.58	0.42	4.402516	0.20163522	4.37836478	1.923387	1923.387097
density range	density mean of 90	vesicularity							
1014	2278.858136	15.59784683							
2883									
St dev									
Table A2.14. Density measurements for the hypocrystalline lapilli. Weight is in g, density in kg m ⁻³ , vesicularity in %.									

photo	wp	facies	orange fragment dimension (mm)	axis	fragment area (mm ²)	area analysed (mm ²)	orange fragment %
1010619edit1	199	mLA	27.03	x	617.06787	10000	24.14903692
1010619edit1	199	mLA	22.829	y			
1010619edit1	199	mLA	18.664	x	294.23796		
1010619edit1	199	mLA	15.765	y			
1010619edit1	199	mLA	44.65	x	1259.9337		
1010619edit1	199	mLA	28.218	y			
1010619edit1	199	mLA	19.159	x	243.664162		
1010619edit1	199	mLA	12.718	y			
1010621edit1	199	mBr	0	x	0	10000	0
1010621crop3	199	mBr	0	y	0	10000	0
1010621edit2	199	mBr	14.292	x	240.8202	10000	4.048967
1010621edit2	199	mBr	16.85	y			
1010621edit2	199	mBr	17.738	x	164.0765		
1010621edit2	199	mBr	9.25	y			
1010621crop2	199	mBr	0	x	0	10000	0
1010624edit1	199	mBr		y		10000	0
1010629edit1	199	mBr	78.354	x	3448.35954	10000	51.4288006
1010629edit1	199	mBr	44.01	y			
1010629edit1	199	mBr	22.738	x	621.65692		
1010629edit1	199	mBr	27.34	y			
1010629edit1	199	mBr	27.78	x	1072.8636		
1010629edit1	199	mBr	38.62	y			
1010629edit2	199	mBr	96.636	x	6542.643744	10000	77.23632644
1010629edit2	199	mBr	67.704	y			
1010629edit2	199	mBr	28.458	x	699.21306		
1010629edit2	199	mBr	24.57	y			
1010629edit2	199	mBr	18.256	x	481.77584		
1010629edit2	199	mBr	26.39	y			
1010629edit3	199	mBr	43.171	x	1025.570276	10000	23.39864486
1010629edit3	199	mBr	23.756	y			
1010629edit3	199	mBr	36.091	x	643.791258		
1010629edit3	199	mBr	17.838	y			
1010629edit3	199	mBr	36.484	x	670.502952		
1010629edit3	199	mBr	18.378	y			
1010629edit4	199	mBr	25.828	x	809.96608	10000	8.0996608
1010629edit4	199	mBr	31.36	y			

1060629edit5	199	mBr	106.43	x	7604.4235	10000	76.044235
1060629edit5	199	mBr	71.45	y			
1010629edit6	199	mBr	70.65	x	7872.5295	10000	78.725295
1010629edit6	199	mBr	111.43	y			
1010630edit1	199	mLA	35.439	x	856.950459	10000	27.85823798
1010630edit1	199	mLA	24.181	y			
1010630edit1	199	mLA	24.365	x	295.815465		
1010630edit1	199	mLA	12.141	y			
1010630edit1	199	mLA	27.931	x	365.309549		
1010630edit1	199	mLA	13.079	y			
1010630edit1	199	mLA	12.278	x	157.195234		
1010630edit1	199	mLA	12.803	y			
1010630edit1	199	mLA	13.294	x	120.682932		
1010630edit1	199	mLA	9.078	y			
1010630edit1	199	mLA	37.895	x	747.2894		
1010630edit1	199	mLA	19.72	y			
1010630edit1	199	mLA	18.257	x	242.580759		
1010630edit1	199	mLA	13.287	y			
1010639edit	199	mLA	0	x	0	10000	0
1010639edit2	199	mLA	16.05	y	177.834	10000	1.77834
1010639edit2	199	mLA	11.08	x			
1010639edit4	199	mLA		y	0	10000	0
1010641edit1	199	mLA	21.1	x	280.841	10000	2.80841
1010641edit1	199	mLA	13.31	y			
1010641edit2	199	mLA	40.641	x	547.231065	10000	14.45516226
1010641edit2	199	mLA	13.465	y			
1010641edit2	199	mLA	12.958	x	138.171154		
1010641edit2	199	mLA	10.663	y			
1010641edit2	199	mLA	9.366	x	102.201792		
1010641edit2	199	mLA	10.912	y			
1010641edit2	199	mLA	16.015	x	657.912215		
1010641edit2	199	mLA	41.081	y			
1010641edit2	199	mLA	0	x	0	10000	0
1010641edit4	199	mLA	6.76	y	64.22	10000	0.6422
1010641edit4	199	mLA	9.5	x			
1010642edit1	199	mLA	15.81	y	255.9639	10000	2.559639
1010642edit1	199	mLA	16.19	x			
1010642edit2	199	mLA	17.75	y	253.2925	10000	2.532925
1010642edit2	199	mLA	14.27	x			
1010642edit3	199	mLA	0	y		10000	0
1010642edit4	199	mLA	0	x		10000	0
1010652edit2	199	lensLA	22.72	y	433.2704	10000	4.332704
1010652edit2	199	lensLA	19.07	x			
1010652edit1	199	lensLA		y			0
1010652edit3	199	lensLA	10.12	x	36.1284	10000	0.361284

1010652edit3	199	lensLA	3.57	y			
1010653edit1	199	lensLA		x			0
1010655edit1	199	lensLA	20.01	y	222.7113	10000	2.227113
1010655edit1	199	lensLA	11.13	x			
1010655edit2	199	lensLA		y	0	10000	0
1010655edit3	199	lensLA		x			
1010658edit1	199	lensLA		y	0	10000	0
1010658edit2	199	lensLA		x	0	10000	0
1010662edit1	199	lensLA		y	0	10000	0
1010648edit1	199	lensLA		x	0	10000	0
Table A2.15. Measurements of ventricular and globular bomb fragments in lithofacies lensLA, mSp and mLA.							

Appendix 3: Support Material for Chapter 5

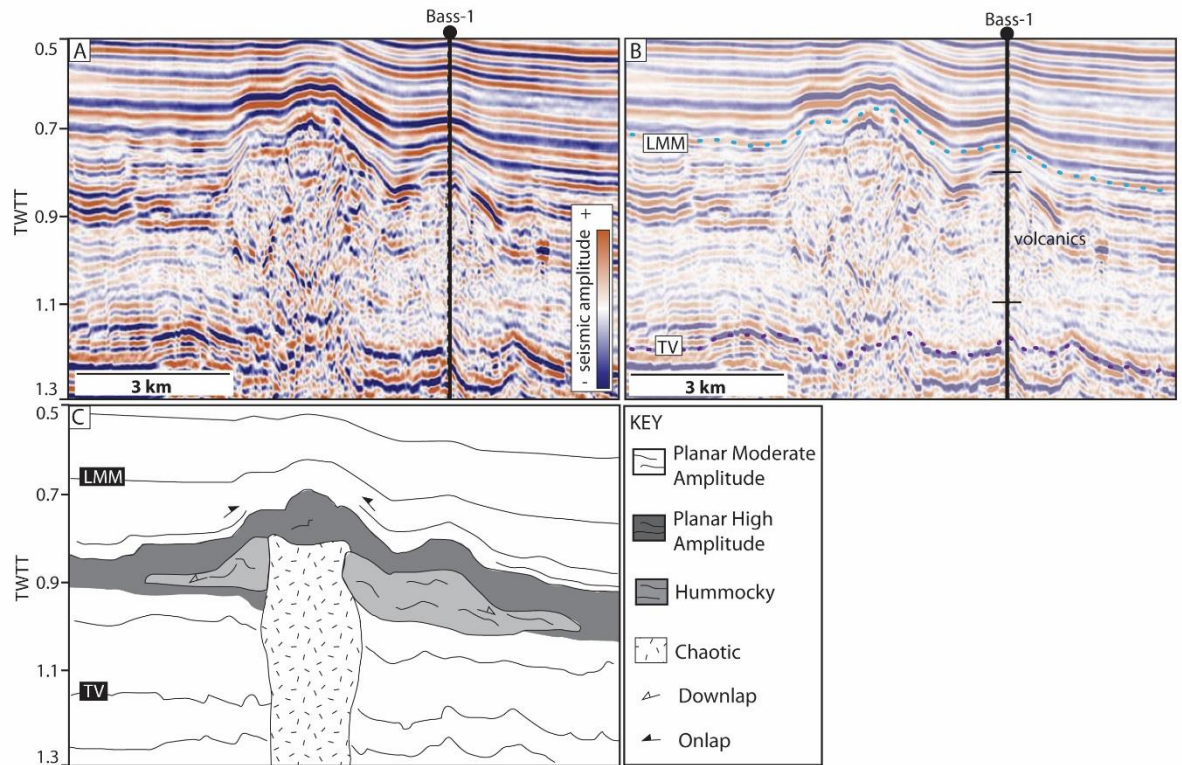


Figure A.1. Seismic section (A) and interpretations (B and C) of the cone-shaped edifice observed on the 2D seismic line between the Yolla and Labatt surveys. The edifice has identical internal facies to the edifices observed in the Labatt and Yolla surveys, although its morphology is somewhat different. Well data from King-1 indicates that the edifice is composed of volcanic rock. LMM=Lower Mid Miocene, TV= Top Volcanic.

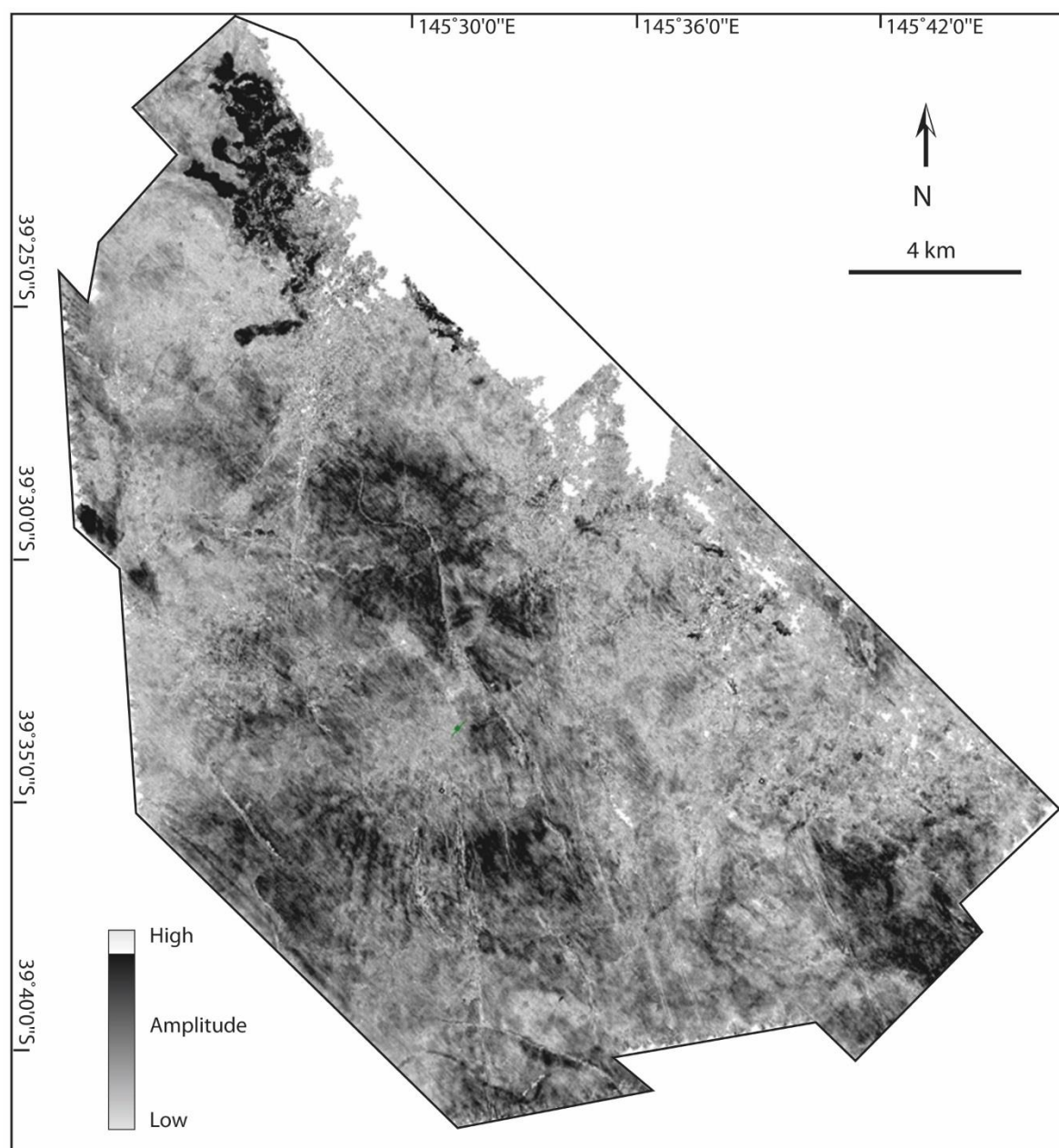


Figure A2. Amplitude map of the Lower Volcanic Horizon in the Labatt survey.

Vent number	Basal Diameter (m)	Crater Diameter (m)	Height/Depth (m)	Volume (km ³)	Height/diameter ratio	Vent type	Distribution	Flank dip (°)	Spacing to nearest neighbour (km)	Depth to underlying sill (m)
1	3743	955	319	1.15	0.085	Cratered	Chain 1	9	2863	-
2	3988	-	247	1.00	0.061	Flat	Chain 1	7	2863	-
3	3033	-	136	0.69	0.045	Pointed	Isolated	5	-	835
4	4851	382	382	1.36	0.078	Cratered	Chain 2	8	1817	1034
5	3177	-	523	1.11	0.164	Flat	Isolated	18	-	-
6	4276	408	203	1.02	0.047	Cratered	Chain 2	5	2208	-
7	3415	444	337	1.05	0.098	Cratered	Chain 2	11	2208	-
8	1673	-	167	0.49	0.100	Pointed	Isolated	11	-	-
9	2106	-	194	0.64	0.092	Flat	Clustered	10	-	-
10	1722	-	143	0.48	0.083	Flat	Clustered	9	-	546
11	1978	-	147	0.53	0.074	Flat	Clustered	8	-	495
12	1085	-	169	0.37	0.156	Flat	Clustered	17	-	494
13	1174	-	127	0.35	0.108	Flat	Clustered	12	-	660
14	-	1166	118	0.34	-	Pit crater	Clustered	-	-	-
15	-	900	81	0.25	-	Pit crater	Clustered	-	-	1172
16	-	1296	70	0.31	-	Pit crater	Clustered	-	-	1207
17	-	450	107	0.17	-	Pit crater	Clustered	-	-	-
18	-	341	98	0.14	-	Pit crater	Clustered	-	-	-
19	-	374	93	0.15	-	Pit crater	Clustered	-	-	1155
20	-	433	101	0.17	-	Pit crater	Clustered	-	-	-
21	-	382	122	0.16	-	Pit crater	Clustered	-	-	-
22	-	1027	75	0.27	-	Pit crater	Clustered	-	-	-
23	-	458	99	0.17	-	Pit crater	Clustered	-	-	-
24	-	549	118	0.21	-	Pit crater	Clustered	-	-	-
25	-	823	112	0.27	-	Pit crater	Clustered	-	-	-
26	-	350	101	0.14	-	Pit crater	Clustered	-	-	-
27	-	670	51	0.18	-	Pit crater	Clustered	-	-	-
28	-	499	103	0.18	-	Pit crater	Clustered	-	-	-
29	4500	1107	351	1.34	0.07	Cratered	Clustered?	8	-	-
30	1663	-	183	0.51	0.11	Pointed	Chain 3	12	843	-
31	1986	-	192	0.58	0.09	Pointed	Chain 3	10	1373	-
32	3246	-	280	0.91	0.08	Pointed	Chain 3	9	1843	-
33	1743	517	151	0.55	0.08	Pointed	Chain 3	9	843	-
34	2484	-	382	0.85	0.15	Pointed	Clustered	17	-	-

Table A3.1 Summary of measurements for vents described in this study. Vents 1–28 are found within the Labatt survey, 29 – 34 are within the Yolla survey.

Appendix 4: Material Published in Support of the Thesis*

*This manuscript was officially accepted into the Bulletin of Volcanology on the 21/07/15

DOI 10.1007/s00445-015-0958-3

Rootless cone eruption processes informed by dissected tephra deposits and conduits

P. Reynolds^{1*}, R. J. Brown¹, T. Thordarson², E.W. Llewellyn¹, K. Fielding³

¹Department of Earth Sciences, Durham University, Science Labs, Durham, DH1 3LE, UK

²Faculty of Earth Sciences and Nordvulk, University of Iceland, Sturlugata 7, 101 Reykjavík, Iceland

³Formerly at: Hess Corporation, Level 9, The Adelphi Building, 1-1 John Adam Street, London, WC2N 6AG, UK

*Corresponding author: peter.reynolds@durham.ac.uk, +447887863550

Abstract

Rootless cones result from the explosive interaction between lava flows and underlying water-saturated sediment or volcanoclastic deposits. Rootless explosions can represent a significant far-field hazard during basaltic eruptions, but there are few detailed studies of their deposits. A rootless cone field in the 8.5 Ma Ice Harbor flow field of the Columbia River Basalt Province, NW USA, is revealed by sections through rootless conduit and cone structures. The Ice Harbor lava flow hosting the rootless cones was emplaced across a floodplain or lacustrine environment that had recently been mantled by a layer of silicic volcanic ash from a major explosive eruption. Our observations indicate a two-stage growth model for the rootless cones: (1) initial explosions generated sediment-rich tephra emplaced by fallout and pyroclastic density currents; and (2) later weaker explosions that generated spatter-rich fountains. Variable explosive activity resulted in a wide range of pyroclast morphologies and vesicularities. Cross-sections through funnel-shaped conduits also show how the conduits were constructed and stabilised. The growth model is consistent with decreasing water availability with time, as inferred for rootless cones described in Iceland.

The Ice Harbor rootless cones provide further lithological data to help distinguish between rootless cone-derived tephra and tephra generated above an erupting dyke.

Keywords: rootless cones; basalt lava; pāhoehoe; Columbia River Basalt Province; lava-water interaction.

1. Introduction

Explosive interaction between water-logged sediments (or volcanoclastic deposits) and molten lava can result in the formation of rootless cones, also known as ‘pseudocraters’ (Fig. 1; Thorarinsson 1953). Rootless cones are present within flow fields where the lava advanced over lacustrine, marsh and fluvial environments (Fagents and Thordarson 2007; Hamilton et al. 2010a, 2010b). Explosions are driven by the interaction of molten lava with a water-saturated, unconsolidated substrate. Explosions initiated by interaction of molten lava with substrate pore water eject clasts composed of lava crust, disrupted liquid lava and substrate-derived sediment onto a stationary surface of an active lava flow, thereby building a cone. Similar rootless edifices, known as littoral cones, form when lava flows interact with seawater in a littoral environment (Moore and Ault 1965; Fisher 1968; Jurado-Chichay et al. 1996; Mattox and Mangan 1997; Jaeger et al. 2007). Rootless cone-like structures have also been observed on the surface of Mars near the Martian equator (Lanagan et al. 2001; Bruno et al. 2004; Fagents and Thordarson 2007; Hamilton et al. 2010a) and have been used to infer the former presence of fluids in the Martian substrate.

Two models for rootless eruptions have been proposed; one assuming static heat transfer and the other inferring dynamic heat transfer. The static heat transfer model infers rapid emplacement of lava above a water-logged substrate. Water trapped beneath the lava flow is converted to steam producing eruptions that are analogous to phreatic explosions (Thorarinsson 1951, 1953).

In contrast, the dynamic heat transfer model of Fagents and Thordarson (2007) argues that the explosive interactions are driven by physical (dynamic) mixing of the lava and the water-logged substrate. The model is based on observations that sediment from the substrate is physically mixed into the rootless cone deposits and found between the core and the rim in armoured bombs. Furthermore, the cones feature multiple layers of tephra, which increase upwards in grain size from coarse ash/fine lapilli to bomb-size clasts

(Fagents and Thordarson 2007; Hamilton et al. 2010). The presence of layering implies sustained eruptions (estimated to have lasted for hours to days; Thordarson and Höskuldsson 2008), maintained by quasi-steady input of molten lava to the explosion site.

During rootless cone activity on pāhoehoe lavas, initial sedimentation occurs from explosions that produce pyroclastic density currents (PDCs) that deposit broad, sheet-like platform deposits around the vent (Hamilton et al. 2010a). Later tephra jets and lava fountains deposit lapilli- to bomb-sized scoria and spatter that build a cone (Thordarson et al. 1998; Fagents and Thordarson 2007; Hamilton et al. 2010a). The deposits of rootless activity are usually unconsolidated, except in proximal regions (Hamilton et al. 2010a). Rootless cones vary from 1–40 m in height and 2–450 m in basal diameter. The cones are crudely bedded, inversely graded, and may contain layers of rheomorphic spatter. The degree of explosivity is thought to be controlled by the explosion site geometry, the rate of lava influx, and the amount and availability of external water. Tephra deposits within rootless cone fields can cover areas of up to 150 km² and may exhibit complex stratigraphic relationships (Fagents and Thordarson 2007; Hamilton et al. 2010a and references therein).

Despite the abundance of rootless cones (e.g. Greeley and Fagents 2001; Lanagan et al. 2001; Fagents et al. 2002; Bruno et al. 2004; Fagents and Thordarson 2007; Hamilton et al. 2010a, 2010b, 2010c, 2011; Keszthelyi and Jaeger 2014), there is little documentation of their constituent pyroclasts and the characteristics of their host lava flows (e.g. Melchior Larsen et al. 2006; Hamilton et al. 2010a; 2010 b). Furthermore, rootless cones are superficially similar to small scoria cones and spatter cones, both in size and componentry (e.g. Fagents and Thordarson 2007). They may also have a linear spatial arrangement, similar to that of edifices along a dyke (e.g. Hamilton et al. 2010a). The limited knowledge of the internal stratigraphy of rootless cones coupled with their similarity to other volcanic edifices means that it can be difficult to distinguish rootless tephra from tephra generated during dyke-fed eruptions. This is particularly the case in flood basalt provinces, where pyroclastic successions are usually poorly preserved and poorly exposed (e.g. Swanson et al. 1975; Reidel and Tolan 1992; Brown et al. 2014).

In this paper, we document a newly discovered rootless cone field within the 8.5 Ma Ice Harbor pāhoehoe lava flow field in the Columbia River Basalt Province (CRBP), USA. Erosional dissection allows us to examine the tephra deposits and conduits of the rootless cones. We use these features to inform on the nature of the explosions that created the

rootless cones and to help define criteria that distinguish the deposits of rootless cones from those of dyke-fed eruptions.

2. Geological setting of the Columbia River Basalt Province

Flood basalt volcanism in the NW USA initiated c. 17 m.y. ago in the Steens Mountain region, Oregon. Over the following ~11 m.y. the volume of erupted mafic magma exceeded $>210\,000\text{ km}^3$ across Oregon and Washington (now considered part of the CRBP; Camp et al. 2003; Reidel et al. 2013). Eruptions were fed by ~300 km-long dyke swarms from crustal magma chambers under east-central Oregon/west-central Idaho (Wolff et al. 2008; Ramos et al. 2013). Volcaniclastic rocks in the CRBP are generally scarce, although exceptionally preserved examples of proximal tephra deposits (Swanson et al. 1975; Reidel and Tolan 1992; Brown et al. 2014), hyaloclastite deposits (Tolan et al. 2002), inferred rootless deposits (Thordarson and Self 1998) and drowned rootless cones (Keszthelyi and Jaeger 2014) are known.

The rootless cone deposits in this study occur in the 8.5 Ma Ice Harbor Member (Fig. 2), which is composed of three pāhoehoe lava flow fields that are the youngest products ascribed to the CRBP (McKee et al. 1977; Swanson et al. 1979). The lavas have been divided into three chemically distinct types that were fed from a dyke system that was up to 90 km in length and on average $<15\text{ km}$ in width (Swanson et al. 1975). The lava flow field has a minimum volume of 1.2 km^3 (Swanson et al. 1975) and individual lava flows are typically $<15\text{ m}$ thick. The pāhoehoe lavas are interbedded with the Ellensburg Formation sediments – diatomaceous muds, lacustrine sands and silts, volcaniclastic silt, conglomerates, and silicic volcanic ash probably sourced from eruptions of volcanoes in the NW USA. These sediments record deposition both within extensive lava-dammed lakes and by ephemeral and established rivers (Schminke 1967; Smith 1988; Tolan et al. 2002).

3. Method

Field studies involved detailed sedimentary logging of tephra successions, lithofacies analysis, geological mapping and sampling. Locations were recorded using a handheld GPS unit with an accuracy of $\pm 5\text{ m}$. Petrographic characterisation was undertaken by optical microscopy on representative thin sections. Vesicle and clast dimensions and abundances were calculated using the image analysis software ImageJ (<http://imagej.nih.gov/ij/>) with

representative samples and outcrop photographs. The crystal content of the cone deposits was calculated by point-counting representative samples. Clast densities were calculated on clasts >16 mm across using the method of Houghton and Wilson (1989). Grain size was determined by sieving.

4. Ice Harbor rootless cone field

The Ice Harbor rootless cone field is composed of: 1) the substrate over which the lava flows were emplaced (silicic volcanic ash); 2) the host pāhoehoe lava flows; 3) rootless cone conduits within the lava flows; 4) rootless cone- and platform-forming tephra deposits. The cone field is inferred to have occupied an area of ≥ 1 km², based on the distribution of the conduits and associated tephra. The cone field is overlain by later Ice Harbor lava flows.

4.1 Volcanic ash substrate

The pre-eruption substrate beneath the Ice Harbor flow field does not crop out in the study area, and the nature of the substrate has been inferred from analysis of material incorporated into the rootless cone tephra deposits. This material is composed of white, silicic, volcanic ash and forms 10–85 vol. % of all rootless cone tephra deposits. The volcanic ash is well-sorted ($1.2 \sigma\Phi$) and individual particles are platy, angular or cusped in shape and occasionally preserve vesicles. The volcanic ash has a median diameter of <0.25 mm. Smaller particles are blade shaped, whilst coarser particles have complex morphologies and exhibit bubble junctures.

Interpretation

The silicic volcanic ash is interpreted as a pyroclastic fall deposit within the Ellensburg Formation (e.g. Schminke 1967). The monolithologic character of the volcanic ash and the absence of organic matter or detrital sediment indicate that the volcanic ash had not been substantially reworked and that burial by the Ice Harbor lava may have occurred shortly after fallout. We infer that the volcanic ash fell out onto a flood plain or shallow lake; common features across the plateau-like CRBP during the Miocene (e.g. Schminke 1967; Smith 1988; Tolan et al. 2002). These environments are conducive to the formation of

rootless cones (e.g. Thorarinsson 1951, 1953; Fagents and Thordarson 2007; Hamilton et al. 2010a, 2010b).

4.2 Ice Harbor lava flows

The rootless cone field crops out along the banks of the Snake River (Fig. 2). The flow field is composed of pāhoehoe sheet lobes that reach 8 m thick and exhibit the tripartite structure typical of pāhoehoe sheet lobes in the CRBP (e.g. Self et al. 1998; Thordarson and Self 1998). They have lower crusts that contain distorted pipe vesicles, massive, dense cores with columnar joints and vesicular upper crusts. The groundmass of the flows is composed of interstitial glass, and plagioclase and pyroxene microlites. Pyroxene and rare swallow-tail plagioclase phenocrysts and glomerocrysts 0.1–3 mm in diameter constitute 1–4 vol. % of the rock. Vesicles are partially filled with zeolite minerals. The Ice Harbor sheet lobes that contain the rootless cones have poorly vesicular cores and incipiently vesicular crusts (as defined by Houghton and Wilson 1989) that exhibit hackly, entablature-style joints spaced 11–21 cm apart.

Interpretation

We infer that inflation of the flows took several weeks, based on a lava upper crust thickness of ≥ 2 m and the relationship: $t = 164.8C^2$; where t = time in hours and C = crustal thickness in metres (see Hon et al. 1994). The presence of entablature-style jointing in the lava indicates that the flows were subjected to water enhanced cooling, implying emplacement in an environment where surface water was abundant (e.g. Long and Wood 1986). The swallow tail plagioclase microlites indicate that the lava cooled rapidly; this texture is also found in pillow lavas (e.g. Bryan 1972; Jafri and Charan 1992).

4.3 Rootless cone conduits

Cliffs along the Snake River reveal funnel-shaped, upward-flaring features in the Ice Harbor sheet lobes (Fig. 3). These features range from 1–4 m in diameter, are up to 4 m deep and have cross-sectional areas of 8–12 m². Their walls dip inwards $\sim 60^\circ$. All the funnels appear to terminate ≥ 0.5 m above the bases of the sheet lobes and sometimes form irregular, isolated cavities; these are likely 2D section effects (Fig. 3). Hackly cooling joints

spaced ~16 cm apart radiate away from the funnel walls and extend up to ~4 m into the surrounding lava core (Fig. 3).

The inner surfaces of the funnels are coated with ropey-textured and bread-crust spatter that is ≤ 6 cm thick. The spatter has a hypohyaline groundmass texture, contains sheared vesicles and has multiple chilled rinds. The surface of the spatter has angular, hypocrySTALLINE and hypohyaline clasts of upper lava crust embedded in it. These clasts cover 10–30% of each funnel wall. There is a patchy, heterogeneous distribution of silicic volcanic ash across the surfaces; typically $< 5\%$. These funnels are often partially filled with tephra with a similar composition to the overlying cone deposits (massive spatter bombs, mSp; see below).

Twelve of these features have been recognised along a 450 m transect (Fig. 2); five on the north bank of the river and seven on the south. The features are spaced 3–206 m apart with tephra deposits exposed above them. Exposures spaced less than 5 m apart may represent irregular sections through the same feature.

Interpretation

We interpret these funnel-shaped features as remnants of rootless conduits because they have spatter, angular lapilli and patches of silicic ash plastered onto their inner wall which can only have occurred via explosive interactions. They are also filled with lapilli- to bomb-sized tephra. These features distinguish them from features described within rubbly pāhoehoe flows (e.g. Duraiswami et al. 2008; Keszthelyi et al. 2009). Sheared vesicles and rope-like textures on the conduit wall result from rheomorphic flow of spatter. The funnel shape of the conduits and their radiating cooling joints are similar to features seen in rootless cones in Iceland (e.g. Hamilton et al. 2010a).

Based on the abundance of conduits and the possibility that some locations represent irregular cross sections through the same conduit (e.g. L16/17; L1/2/6; L12/13) we suggest that the flow field hosted at least eight rootless cones. Since the size of the conduits is proportional to the size of the overlying cone (e.g. Hamilton et al. 2010a), the cones were likely to have been ≥ 5 m in basal diameter.

4.4 Rootless cone tephra deposits

Proximal rootless platform and cone-forming deposits are widely exposed over a 450 m-long transect along the south bank of the Snake River, and are intermittently exposed along the north bank of the river (Fig. 2). The tephra deposits are composed of juvenile pyroclasts (described below), silicic volcanic ash and fragmented lava crust.

4.4.1 Juvenile pyroclast types

The tephra deposits contain four different pyroclast types derived from the fragmentation and modification of the host lava flow (Fig. 4; Table 1). These juvenile clasts are (1) sideromelane ash and lapilli of both blocky and fluidal morphologies; (2) hypocrySTALLINE bombs (with both ventricular and globular morphologies) and angular lapilli; (3) armoured scoria bombs and lapilli; and (4) spatter bombs. All clasts have hypohyaline to hypocrySTALLINE groundmasses and are mineralogically similar to the host lava. The pyroclasts are incipiently to poorly vesicular, ranging between 15–36% vesicles, and are non to incipiently welded. The density of pyroclasts ranges from 1700–2300 kg m⁻³. The pyroclast types and their occurrence is summarised in Table 1.

Interpretation

The density of the Ice Harbor rootless tephra is significantly higher than that of non-welded basaltic pyroclasts produced during dyke-fed eruptions (typically 240–1440 kg m⁻³; Houghton and Wilson 1989; Parcheta et al. 2013). This suggests that the pyroclasts were sourced from lava that had already degassed at the source fissure and during transport to the rootless cone site. The ventricular and globular bombs are atypical of the deposits of fissure eruptions (e.g. Valentine and Gregg 2008); they are interpreted as water-quenched globules of lava ejected from beneath the lava flow during explosive activity. These bombs were subsequently mechanically fragmented into angular lapilli upon eruption and deposition, enhanced by cooling contraction fractures. The spatter bombs are interpreted as proximal deposits from rootless lava fountains (e.g. as observed during the 1783–1785 Laki eruptions, see Thordarson et al. 1998). Recycling by intermittent fountains appears necessary to form the armoured bombs. The blocky sideromelane clasts indicate cooling-contraction granulation and/or mechanical fragmentation. The fluidal, elongate sideromelane clasts indicate ductile disruption of molten lava and are common components of deposits from magmatic volatile driven eruptions (e.g. Walker and Croasdale 1971),

phreatomagmatism (e.g. Zimanowski et al. 1997; Morrissey et al. 2000; Büttner et al. 2002) and peperite (see section 4.4.3; Skilling et al. 2002).

4.4.2 Pyroclastic lithofacies

The tephra deposits can be sub-divided into four lithofacies according to their componentry, grain size and depositional structures (Fig. 5; Table 2). In general the pyroclastic lithofacies appear moderately to very poorly sorted and are composed of juvenile clasts with <10–85 vol. % silicic volcanic ash. Lithofacies with the largest juvenile clasts tend to have the least silicic volcanic ash (Fig. 6). The lithofacies form proximal platform, cone or conduit-filling deposits. Sheet deposits are not found; these are commonly unconsolidated (Hamilton et al. 2010a). Contacts between the tephra deposits and underlying lavas are not exposed (Fig. 6).

Platform deposits include massive or normally graded lapilli-ash (m/nLAf), lenses of lapilli-ash (lensLA) and cross-stratified lapilli-ash (xsLA; Table 2; Fig. 5). These deposits are 1–5.5 m in thickness (Fig. 7) and are present beneath the parallel-bedded spatter (//bSp; Figs. 6 and 7). Pyroclasts within the deposits are dominantly of lapilli size. They are exposed over a ~600 m long transect. Bedding dips vary from 10–20°.

Cone deposits are composed of parallel-bedded spatter (//bSp; Table 2) that is 1–3 m thick (Fig. 6) and contains predominantly bomb-sized clasts. Deposits are exposed over a ~200 m long transect. The spatter varies from horizontally bedded to dipping up to 20°; whether this is towards or away from a conduit is unclear (Figs. 6 and 7).

The conduits are partially filled with massive spatter (mSp; Table 2) and are not observed in contact with overlying cone and/or platform deposits.

Interpretation

The Ice Harbor platform deposits are inferred to have been deposited from both PDCs and by fallout (e.g. Hamilton et al. 2010a). The occurrence of massive/normally graded lapilli-ash (m/nLAf), lenses of lapilli-ash (lensLA) and cross-stratified lapilli-ash (xsLA) beneath the spatter-rich deposits (e.g. //bSp) suggests that the platform was constructed prior to cone formation. Intermittent deposits of normally-graded lapilli ash (nLA) and cross-stratified lapilli-ash (xsLA; Fig. 6) overlying the spatter layers suggests that the cone field is composed of numerous overlapping cones formed in a sequence of rootless

eruptions (e.g. Fagents and Thordarson 2007). The thickness and spatial distribution of the exposures suggest that the tephra platforms were ~5 m thick and were likely to be laterally extensive over 100's of metres. Cone-forming and conduit-filling deposits of rootless cones commonly contain spatter-rich lithofacies (Hamilton et al. 2010a), as observed in this study. These coarse-grained deposits are produced as the explosivity of the eruptions decreases (Fagents and Thordarson 2007).

4.4.3 Lava-silicic volcanic ash interaction textures in tephra deposits

A variety of peperite-like textures are observed in the tephra deposits (Fig. 8). Fluidal textures include spatter bombs that inter-finger with the silicic volcanic ash and associated globular and elongate spatter lapilli and ash found intimately mixed with the silicic volcanic ash. Within 2 cm of the spatter, the silicic volcanic ash is often thermally altered, becoming dark in colour and fused (e.g. Schminke 1967). Where fused, the silicic volcanic ash contains vesicles ≤ 2 mm in diameter. Vesicles in the spatter also contain silicic ash. Blocky textures include jigsaw-fit bombs; these clasts have hairline fractures filled with silicic volcanic ash. Other bombs have rinds that are partially separated from their core, encapsulating a 2 mm-thick domain of silicic volcanic ash between rind and core. These domains contain mm-scale globules of lava.

Interpretation

Peperite-like textures indicate interaction between hot juvenile clasts and unconsolidated sediment (e.g. Skilling et al. 2002). Vesicles in the fused silicic volcanic ash indicate that gas was generated during interaction (e.g. Kokelaar 1982; Skilling 2002; Squire and McPhie 2002). Silicic ash-filled vesicles in the spatter indicate that the sediment was mobilised during interaction (e.g. Goto and McPhie 1996; Skilling 2002 and references there-in). The fluidal and blocky textures indicate variations in mechanical stress, movement of lava, lava-silicic ash density contrasts and variations in lava viscosity and clast size (e.g. Skilling et al. 2002; Squire and McPhie 2002). These textures may represent a failed phreatomagmatic fragmentation process formed beneath the lava flow (e.g. Busby-Spera and White 1987; Hooten and Ort 2002). The bombs with encapsulated silicic volcanic ash are interpreted as intrusions of lava into the underlying substrate. Lava

globules in the silicic volcanic ash domain indicate that the cores of these bombs were molten during intrusion.

5. Emplacement of the Ice Harbor rootless cones

We infer that the Ice Harbor lava flows traversed a lacustrine or floodplain environment (Fig. 9). The ground was mantled by a layer of silicic volcanic ash fall derived from a major explosive eruption. As the lava flows inflated they developed brittle basal crusts (Hon et al. 1994). These crusts were weakened by the development of cooling fractures (Thordarson and Self 1998) which created a zone of weakness along the base of the flows. Cracking and subsequent failure of the crust would have been facilitated by heterogeneous subsidence of the flows during inflation (e.g. Fagents and Thordarson 2007; Hamilton et al. 2010a). Failure of the basal crust allowed extrusion of lava, analogous to the axial cleft of a tumulus (e.g. Walker 1991; Rossi and Gudmundsson 1996; Hamilton et al. 2010a).

Extrusion of lava through the basal crust resulted in the intimate mixing of molten lava with the water-saturated silicic volcanic ash. This mixing of the lava and sediment is evidenced by the peperite-like textures and abundance of silicic volcanic ash (i.e. substrate) in the tephra deposits. Lava-substrate mixing was followed by explosions. These fragmented the lower lava crust and burst through the molten lava core creating transient conduits. The preservation of conduits requires the cooling and solidification of the conduit walls over time to prevent pressure-driven collapse of the walls between explosions. The presence of spatter lining the walls of the conduits indicates that they were stabilised from both material ejected during the explosions, as well as from the chilling of the molten lava core. Explosive activity deposited the massive/normally graded lapilli-ash (lithofacies m/nLA (f)) on top of the lava flow. Some of the pyroclastic material formed PDCs (depositing lithofacies lensLA and xsLA; Table 2). These processes constructed the tephra platforms.

Spatter-rich lithofacies (e.g. //bSp and mSp; Table 2) were produced during rootless lava fountaining and cap the rootless cone successions and fill some conduits. The coarse clast size of these lithofacies indicates decreasing explosivity as water availability declined. Explosions also embedded juvenile clasts and lava crust lithics into the hot and ductile conduit walls.

The presence of the cones on top of sheet lobes suggests that the cones developed repelled, non-aligned spatial distributions (e.g. Hamilton et al. 2010a, 2010b). The cones were likely to have formed in topographic lows where lava and water were most abundant, and in regions of enhanced substrate compressibility (Hamilton et al. 2010a, 2010b). Exposures do not allow determination of the symmetry of the cones (e.g. radial or elongate). Growth of the cones was terminated by the decreasing availability of ground water, or by water being prevented from gaining access to the explosion site. Continued cooling stabilised the conduit walls and over time cooling joints radiated out into the core (e.g. Fig. 9).

6. Comparison with other rootless cones

The deposits in this study are comparable with the platform and cone-building deposits of rootless cones in Iceland (e.g. Table 3; Fig. 10), which show a similar pattern of sediment-rich PDC deposits overlain by coarse-grained fall deposits. These PDC and fall deposits are composed of scoria lapilli and bombs, spatter bombs and clastogenic lava, all intimately mixed with silt- to cobble-sized sediment. The coarse grainsize of the platform deposits in this study relative to others described in Iceland (Hamilton et al. 2010a) may result from the proximity of the Ice Harbor tephra platforms to the explosion source, or from less efficient magma-water interaction. The substrate properties (e.g. grainsize distribution and thermal conductivity) may also have affected explosivity (e.g. Sohn 1996; White 1996). Furthermore, the properties of the substrate would have evolved during the eruptions, due to mixing of pyroclasts and silicic volcanic ash beneath the lava flow. However, the role of sediment properties in governing the explosivity of rootless eruptions is as-yet unknown.

7. Conclusions

The Ice Harbor tephra deposits provide insights into the construction and componentry of a rootless cone field. Cross sections of conduits suggest that ≥ 8 cones were present in a cone field ≥ 1 km² in area. Cone- and platform-forming deposits are composed of admixed juvenile clasts, clasts from the host lava flow and silicic volcanic ash from an earlier, major explosive eruption in NW USA. Construction of the cone field occurred through a combination of deposition from PDCs and lava fountaining. Explosivity decreased with

time as a result of decreasing water availability in the underlying silicic volcanic ash. This study demonstrates that the abundance of sediment (in this case, silicic volcanic ash) in the tephra, juvenile clast morphology and clast density are useful criteria for distinguishing between rootless tephra and tephra produced above an erupting dyke.

Acknowledgements

PR acknowledges a studentship funded by Hess Corporation as part of the Volcanic Margins Research Consortium. Reviewers Bernd Zimanowski and Laszlo Keszthelyi are thanked for their thoughtful input, as is associate editor Pierre-Simon Ross.

References

- Brown RJ, Blake S, Thordarson T, Self S (2014) Pyroclastic edifices record vigorous lava fountains during the emplacement of a flood basalt flow field, Roza Member, Columbia River Basalt Province, USA. *Geol Soc Am Bull* 126:875-891
- Bruno BC, Fagents S, Thordarson T, Baloga SM, Pilger E (2004) Clustering within rootless cone groups on Iceland and Mars: Effect of nonrandom processes. *J Geophys Res* 109:1991-2012
- Bryan WB (1972) Morphology of quench crystals in submarine basalts. *J Geophys. Res.* 77:5812-5819
- Busby-Spera CJ, White, JD (1987) Variation in peperite textures associated with differing host-sediment properties. *B Volcanol* 49:765-776
- Büttner R, Dellino P, La Volpe L, Lorenz V, Zimanowski B (2002) Thermohydraulic explosions in phreatomagmatic eruptions as evidenced by the comparison between pyroclasts and products from Molten Fuel Coolant Interaction experiments. *J. Geophys. Res.* 107:2277
- Camp VE, Ross ME, Hanson WE (2003) Genesis of flood basalts and Basin and Range volcanic rocks from Steens Mountain to the Malheur River Gorge, Oregon. *Geol Soc Am Bull* 115:105-128
- Duraiswami RA, Bondre NR, Managave S (2008) Morphology of rubbly pahoehoe (simple) flows from the Deccan Volcanic Province: Implications for style of emplacement. *J Volcanol Geotherm Res* 177:822-836
- Fagents SA, Thordarson T (2007) Rootless cones in Iceland and on Mars. In: Chapman M, Skilling IP (eds) *The Geology of Mars: Evidence from Earth-Based Analogues*. Cambridge University Press, pp 151–177
- Fagents SA, Lanagan P, Greeley R (2002) Rootless cones on Mars: a consequence of lava-ground ice interaction. *Geological Society, London, Special Publications* 202:295-317
- Fisher RV (1968) Puu Hou littoral cones, Hawaii. *Geologische Rundschau* 57:837-864
- Goto Y, McPhie J (1996) A Miocene basanite peperitic dyke at Stanley, northwestern Tasmania, Australia. *J Volcanol Geoth Res* 74:111-120
- Greeley R, Fagents SA (2001) Icelandic pseudocraters as analogs to some volcanic cones on Mars. *J. Geophys. Res.* 106:20527-20546

- Hamilton CW, Thordarson T, Fagents SA (2010a) Explosive lava–water interactions I: architecture and emplacement chronology of volcanic rootless cone groups in the 1783–1784 Laki lava flow, Iceland. *B Volcanol* 72:449-467
- Hamilton CW, Fagents SA, Thordarson T (2010b) Explosive lava–water interactions II: self-organization processes among volcanic rootless eruption sites in the 1783–1784 Laki lava flow, Iceland. *B Volcanol* 72:469-485
- Hamilton CW, Fagents SA, Wilson L (2010c), Explosive lava-water interactions in Elysium Planitia, Mars: Geologic and thermodynamic constraints on the formation of the Tartarus Colles cone groups, *J. Geophys. Res.* 115:1991-2012
- Hamilton CW, Fagents SA, Thordarson T (2011) Lava–ground ice interactions in Elysium Planitia, Mars: Geomorphological and geospatial analysis of the Tartarus Colles cone groups, *J. Geophys. Res.* 116:1991-2012
- Hon K, Kauahikaua J, Delinger R, Mackay K (1994) Emplacement and inflation of pahoehoe sheet flows: Observations and measurements of active lava flows on Kilauea Volcano, Hawaii. *Geol Soc Am Bull* 106:351-370
- Hooten JA, Ort MH (2002) Peperite as a record of early-stage phreatomagmatic fragmentation processes: an example from the Hopi Buttes volcanic field, Navajo Nation, Arizona, USA. *J Volcanol Geoth Res* 114:95-106
- Houghton BF, Wilson CJN (1989) A vesicularity index for pyroclastic deposits. *B Volcanol* 51:451-462
- Jaeger WL, Keszthelyi LP, McEwen AS, Dundas CM, Russell PS (2007) Athabasca Valles, Mars: A Lava-Draped Channel System. *Science* 317:1709-1711
- Jafri SH, Charan SN (1992) Quench textures in pillow basalt from the Andaman-Nicobar Islands, Bay of Bengal, India. *Proc. Indian Acad. Sci. (Earth Planet Sci)* 101:99-107
- Jurado-Chichay Z, Rowland S, Walker GL (1996) The formation of circular littoral cones from tube-fed pāhoehoe: Mauna Loa, Hawai'i. *B Volcanol* 57:471-482
- Keszthelyi LP, Jaeger WL (2014) A field investigation of the basaltic ring structures of the Channeled Scabland and the relevance to Mars. *Geomorph.* doi:10.1016/j.geomorph.2014.06.027
- Keszthelyi LP, Baker VR, Jaeger WL, Gaylord DR, Bjornstad BN, Greenbaum N, Self S, Thordarson T, Porat N, Zreda MG (2009) Floods of water and lava in the Columbia River Basin: Analogs for Mars. *Geol Soc Am Field Guides* 15:845-874.
- Kokelaar BP (1982) Fluidization of wet sediments during the emplacement and cooling of various igneous bodies. *J Geol Soc* 139:21-33
- Lanagan PD, McEwen AS, Keszthelyi LP, Thordarson T (2001) Rootless cones on Mars indicating the presence of shallow equatorial ground ice in recent times. *Geophys Res Lett* 28:2365-2367
- Long PE, Wood BJ (1986) Structures, textures, and cooling histories of Columbia River basalt flows. *Geol Soc Am Bull.* 9:1144-1155.
- Mattox TN, Mangan MT (1997) Littoral hydrovolcanic explosions: a case study of lava–seawater interaction at Kilauea Volcano. *J Volcanol Geoth Res* 75:1-17
- McKee E, Swanson D, Wright T (1977) Duration and volume of Columbia River basalt volcanism, Washington, Oregon and Idaho. In: *Geol. Soc. Am. Abstr. Programs.* pp 463-464
- Melchior Larsen L, Ken Pedersen A, Krarup Pedersen G (2006) A subaqueous rootless cone field at Niuluut, Disko, Paleocene of West Greenland. *Lithos* 92:20-32
- Moore JG, Ault WU (1965) Historic littoral cones in Hawaii. *Pacific science* XIX(3-11)

- Morrissey M, Zimanowski B, Wohletz KH, Buettner R (2000) Phreatomagmatic fragmentation. In: Sigurdsson H (ed) *Encyclopedia of volcanoes*, pp 431-445.
- Parcheta CE, Houghton BF, Swanson DA (2013) Contrasting patterns of vesiculation in low, intermediate, and high Hawaiian fountains: A case study of the 1969 Mauna Ulu eruption. *J Volcanol Geoth Res* 255:79-89
- Ramos FC, Wolff JA, Starkel W, Eckberg A, Tollstrup DL, Scott S (2013) The changing nature of sources associated with Columbia River flood basalts: Evidence from strontium isotope ratio variations in plagioclase phenocrysts. *Geol Soc Am Spec Pap* 497:231-257
- Reidel SP, Tolan TL (1992) Eruption and emplacement of flood basalt: An example from the large-volume Teepee Butte Member, Columbia River Basalt Group. *Geol Soc Am Bull* 104:1650-1671
- Reidel SP, Camp VE, Tolan TL, Martin BS (2013) The Columbia River flood basalt province: stratigraphy, areal extent, volume, and physical volcanology. *Geol Soc Am Spec Pap* 497:1-43
- Rossi MJ, Gudmundsson A (1996) The morphology and formation of flow-lobe tumuli on Icelandic shield volcanoes. *J Volcanol Geotherm Res* 72:291-308
- Schminke H-U (1967) Fused Tuff and P  perites in South-Central Washington. *Geol Soc Am Bull* 78:319-330
- Self S, Keszthelyi L, Thordarson T (1998) The importance of pahoehoe. *Annu. Rev. Earth Planet. Sci.* 26:81-110
- Simpson K, McPhie J (2001) Fluidal-clast breccia generated by submarine fire fountaining, Trooper Creek Formation, Queensland, Australia. *J Volcanol Geoth Res* 109:339-355
- Skilling IP, White JDL, McPhie J (2002) Peperite: a review of magma-sediment mingling. *J Volcanol Geoth Res* 114:1-17
- Smith GA (1988) Neogene synvolcanic and syntectonic sedimentation in central Washington. *Geol Soc Am Bull* 100:1479-1492
- Sohn YK (1996) Hydrovolcanic processes forming basaltic tuff rings and cones on Cheju Island, Korea. *Geol Soc Am Bull* 108:1199-1211
- Sumner JM, Blake S, Matela RJ, Wolff JA (2005) Spatter. *J Volcanol Geoth Res* 142(1-2):49-65
- Swanson DA, Wright TL, Helz RT (1975) Linear vent systems and estimated rates of magma production and eruption for the Yakima Basalt on the Columbia Plateau. *Am J Sci* 275:877-905
- Swanson D, Wright TL, Hooper PR, Bentley RD (1979) Revisions in stratigraphic nomenclature of the Columbia River Basalt Group. *U.S Geol Surv Bull* 1457 G1-G59
- Thorarinsson S (1951) Laxargljufur and Laxarhraun: a tephrochronological study. *Geograf Annal* 2:1-89
- Thorarinsson S (1953) The crater groups in Iceland. *B Volcanol* 14:3-44
- Thordarson T, Self S (1998) The Roza Member, Columbia River Basalt Group: A gigantic pahoehoe lava flow field formed by endogenous processes? *J. Geophys. Res.* 103:27411-27445
- Thordarson T, H  skuldsson    (2008) Postglacial volcanism in Iceland. *J  kull* 58:197-228.
- Thordarson T, Miller D, Larsen G (1998) New data on the Leidolfsfell cone group in South Iceland. *J  kull* 46: 3-15

- Tolan TL, Beeson MH, Lindsey KA (2002) The effects of volcanism and tectonism on the evolution of the Columbia River system. In: A Field Guide to Selected Localities in the South-western Columbia River Plateau and Columbia River Gorge of Washington and Oregon State. Northwest Geological Society
- Valentine GA, Gregg TKP (2008) Continental basaltic volcanoes – Processes and problems. *J Volcanol Geoth Res* 177:857-873
- Walker GPL (1991) Structure, and origin by injection of lava under surface crust, of tumuli, 'lava rises', 'lava-rise pits', and 'lava inflation clefts' in Hawaii. *B Volcanol* 53:546–558
- Walker GPL, Croasdale R (1971) Characteristics of some basaltic pyroclastics. *Bulletin Volcanologique*, 35:303-317
- White JDL (1996) Impure coolants and interaction dynamics of phreatomagmatic eruptions. *J Volcanol Geoth Res* 74:155-170
- Wolff J, Ramos F, Hart G, Patterson J, Brandon A (2008) Columbia River flood basalts from a centralized crustal magmatic system. *Nat Geo* 1:177-180
- Zimanowski B, Büttner R, Lorenz V, Häfele HG (1997) Fragmentation of basaltic melt in the course of explosive volcanism. *J Geophys Res* 102:803-814

Figure Captions

Fig. 1 Generalised structure of a rootless cone. The cones form on active lava flows. The conduits in the host lava flow are irregular funnels that widen upwards. The upper parts of the conduits are filled with tephra. Cooling joints in the host lava flow radiate from the conduit. Cone forming deposits are composed of lapilli- to bomb-sized material that is often reversely graded and formed by fallout. Platform and sheet deposits are formed by fallout and deposition from pyroclastic density currents. Adapted from Hamilton et al. (2010a)

Fig. 2 Location of the study area. **a** The CRBP in the NW USA, adapted from Brown et al. (2014). **b** Map of the area showing the Ice Harbor fissure as described by Swanson et al. (1975) and our field area on the banks of the Snake River. **c** Sites of the tephra and conduit deposits described in this study

Fig. 3 Field photographs and schematic diagrams showing the varying geometries of rootless conduits. **a** Field sketch showing the upper part of a funnel-shaped conduit at location 6 (UTM Nad83 zone 11T, 359 987 E/5 126 647 N). View to the southwest. **b** Field photograph of massive spatter (mSp) within the conduit in **a**, composed of spatter bombs,

silicic volcanic ash and hypocrySTALLINE lapilli. **c** Irregular lower part of a conduit in the lava flow at location 22 (UTM Nad83 zone 11T, 359 724 E/5 128 162 N) with cooling joints (white) radiating from the conduit/lava core contact (outlined). The ruler is 1 m. Inset **d** shows a close up of the conduit inner wall with embedded juvenile and lava crust lithic clasts. The ruler is 25 cm. Image **e** shows a cross section through the conduit wall, with hypohyaline lapilli embedded into the surface. **f** Interpretive sketch of e. **g** Plan view of a section of conduit wall, approximately 100 mm across, showing clasts that are inferred to have become embedded in the conduit wall during explosions (dashed outlines)

Fig. 4 Clast types recognised in this study. **a** Folded spatter bomb with embedded lapilli (dashed outline). Graticules on the scale card are 1 cm (UTM Nad83 zone 11T, 359 942 E/5 126 519 N). **b** Ventricular clast (outlined). The clast has an amoeboid shape with a hypohyaline rind approx. 10 mm thick that grades inwards into the core. Vesicles up to 8 cm in diameter (dashed outline) have angular shapes and give clasts their characteristic ventricular morphology (UTM Nad83 zone 11T, 359 942 E/5 126 519 N). **c** Globular bomb (outlined). The bombs have a sub-spherical shape and a black hypohyaline rind ~1 cm thick that becomes more orange in colour toward the core. Sub angular, dull black coloured basaltic lapilli (arrowed) are contained within the cores of the bombs. Cooling joints (dashed lines) penetrate from the clast margin up to 10 mm towards the core (UTM Nad83 zone 11T, 359 942 E/5 126 519 N). **d** Armoured bomb (solid outline) with 1 cm thick dense rind and vesicular core (dashed outline) (UTM Nad83 zone 11T, 360 015 E/5 126 664 N). **e** Sideromelane clast (arrowed) formed by fragmentation in a brittle state (arrowed). **f** Sideromelane clast (arrowed) formed by ductile disruption of molten lava

Fig. 5 Lithofacies found in the study area. **a** mLA with ventricular bomb (outlined) enclosing laminated silicic volcanic ash. Graticules on the scale card are 1 cm (UTM Nad83 zone 11T, 359 881 E/5 126 506 N) **b** lensLA with hypocrySTALLINE lapilli-rich lenses. Dashed white outlines indicate lenses (UTM Nad83 zone 11T, 359 868 E/5 126 485 N) **c** lensLA with silicic ash-rich lenses. White outlines indicate lenses (UTM Nad83 zone 11T, 359 868 E/5 126 485 N) **d** xsLA, white outlines indicate beds. The ruler is 25 cm long (UTM Nad83 zone 11T, 359 868 E/5 126 485 N) **e** //bSp, showing bedded spatter bombs. The ruler is 50 cm (UTM Nad 83 zone 11T, 359 942 E/5 126 519 N)

Fig. 6 Lithofacies logs of tephra deposits south of the river. Clast size is shown on the top axis with divisions at 32, 64, 128 and 256 mm (Location 9 uses 32, 64, 128, 256 and >1000 mm divisions). Silicic volcanic ash abundance (black squares; %) is shown across the bottom axis in 25% graticules. Logs are shown at relative altitudes. For locations of the sections see Fig. 2

Fig. 7 Photographs and interpretive pictures of Location 9 (UTM Nad 83 zone 11T, 359 942 E/5 126 519 N). **a, b** Outcrop of platform-forming admixed tephra and silicic volcanic ash. **c,d** Outcrop of cone-forming tephra composed of lithofacies //bSp

Fig. 8 Peperite-like textures produced by the interaction of juvenile clasts and silicic volcanic ash. **a** Fluidal peperite with elongate and globular clasts in lithofacies //bSp (UTM Nad 83 zone 11T, 359 942 E/5 126 519 N). **b** Blocky peperite with jigsaw-fit fractures (circled). Graticules are 1 cm (UTM Nad 83 zone 11T, 360 014 E/5 126 649 N). Thin section **c** and interpretive sketch **d** shows section of mingled spatter and silicic volcanic ash. The spatter clasts exhibit elongate and globular morphologies. The silicic ash is thermally altered and contains vesicles. Vesicles within the spatter clasts enclose silicic volcanic ash. Section of a ventricular bomb **e** and interpretive sketch **f** are also shown. The hypohyaline rind is spalling from the core and has encapsulated a domain of silicic volcanic ash. Fluidal basalt clasts are found within the silicic ash domain (arrowed) indicating that the core of the bomb was molten when the sediment was encapsulated

Fig. 9 Inferred eruption chronology for the cones. **a** Lava flow traverses wet ground and subsides heterogeneously into the underlying silicic volcanic ash. **b** Initial mingling of lava with the silicic ash results in the formation of globular and ventricular juveniles and peperite-like textures. **c** Interaction between molten lava and water saturated silicic volcanic ash results in explosive brecciation of the host lava flow and fragmentation of the globular and ventricular juveniles into lapilli and ash sized clasts. Episodic eruptions and dilute PDC's deposit poorly sorted juveniles and clasts sourced from the host lava flow, forming sheet and platform deposits (lithofacies m/nLA(f), lensLA, xsLA). Minor clast recycling may occur, producing armoured bombs. Substrate pore water is gradually depleted beneath

the lava flow. **d** Decreasing water availability results in less efficient fragmentation and lava fountains are generated. These fountains produce lithofacies that builds a cone. Lapilli are also impacted into the cooling conduit walls. **e** With time water availability decreases and eruptions cease. The lava flow may continue to inflate and deform the conduit. Post-eruption cooling of the lava promotes the formation of cooling joints that radiate from the conduit

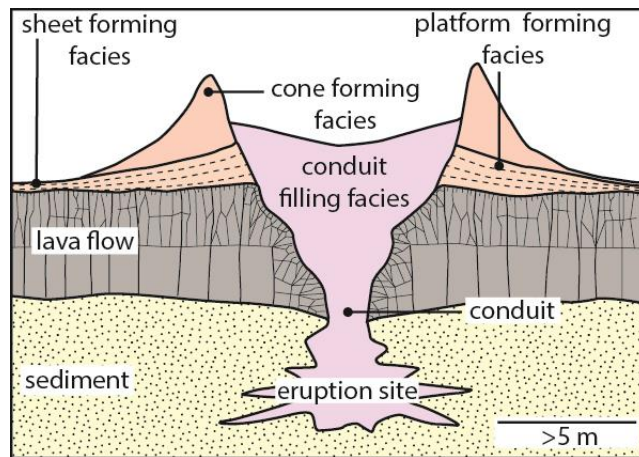
Fig. 10 Photographs of Leitin and Búrfell rootless cones in southern Iceland (UTM Nad 83, zone 27, 500 000 E/7 097 014 N; 402 187 E/7 098 548 N respectively). **a** Overlapping cone stratigraphies composed of crudely bedded spatter and scoria bombs and lapilli and clastogenic lava. The sequence is ~6 m thick. **b** Bomb-sized clast of sediment (outlined) within a sequence of scoria and spatter. The ruler is 40 cm long. **c** Sediment-rich pyroclastic density current deposit at the base of the cone forming stratigraphy. The reddish colour is given by the agglutinated sediment (inferred to be a lacustrine siltstone), not oxidation of the pyroclasts. The scale card is 120 mm long. **d** Bomb-sized, ventricular-type pyroclast (outlined) within the bedded spatter and scoria. The ruler is ~25 cm long. **e** Initial cone-forming fall deposit, composed of scoria lapilli. Beds often form inversely-graded couplets. The bed indicated is ~6 cm thick. Beds thickness and clast size increases up-section. **f** Cross section of the conduit wall, with lapilli sized pyroclasts agglutinated to the outer wall. Cooling joints (dashed lines) radiate from the contact and are perpendicular to the conduit contact. The arrow points towards the core of the lava flow. The ruler is 30 cm long. **g** A lava flow affected by rootless cone formation. The lava flow can be divided into a colonnade (CN) and an entablature (EN), and has an irregular upper contact that forms the rootless conduit. The lava is ~10 m thick

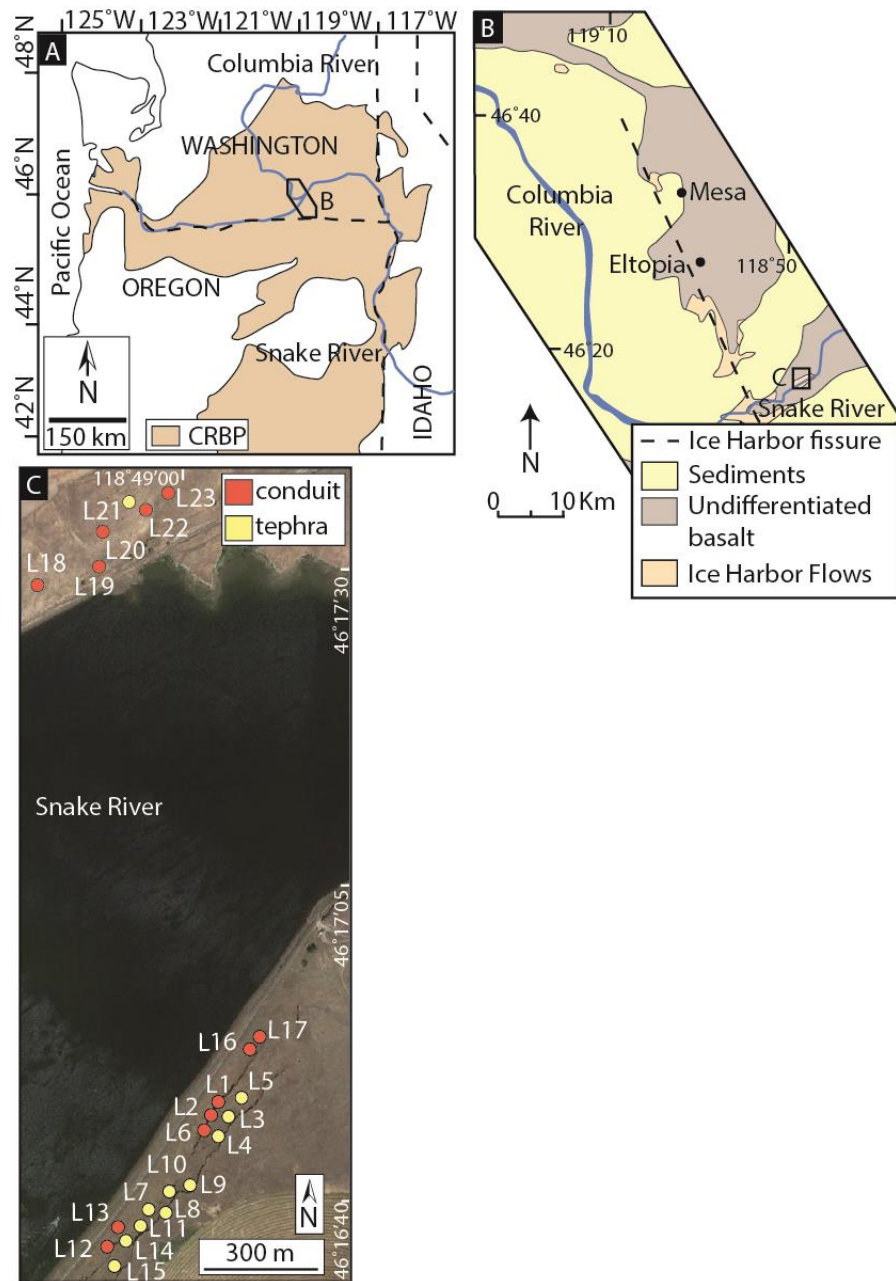
Table 1 Summary descriptions of pyroclast types

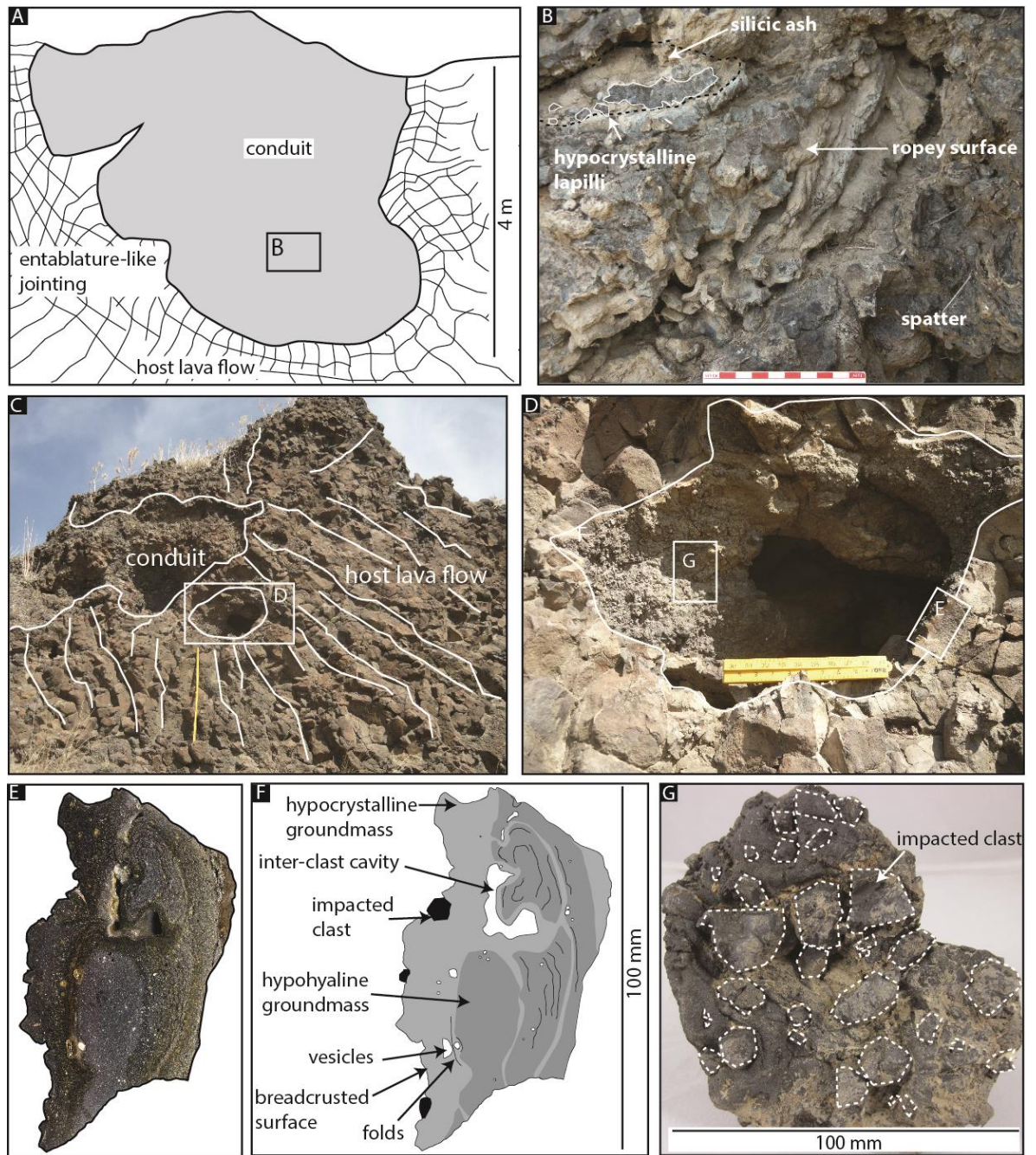
Table 2 Summary descriptions of cone-forming and conduit deposits

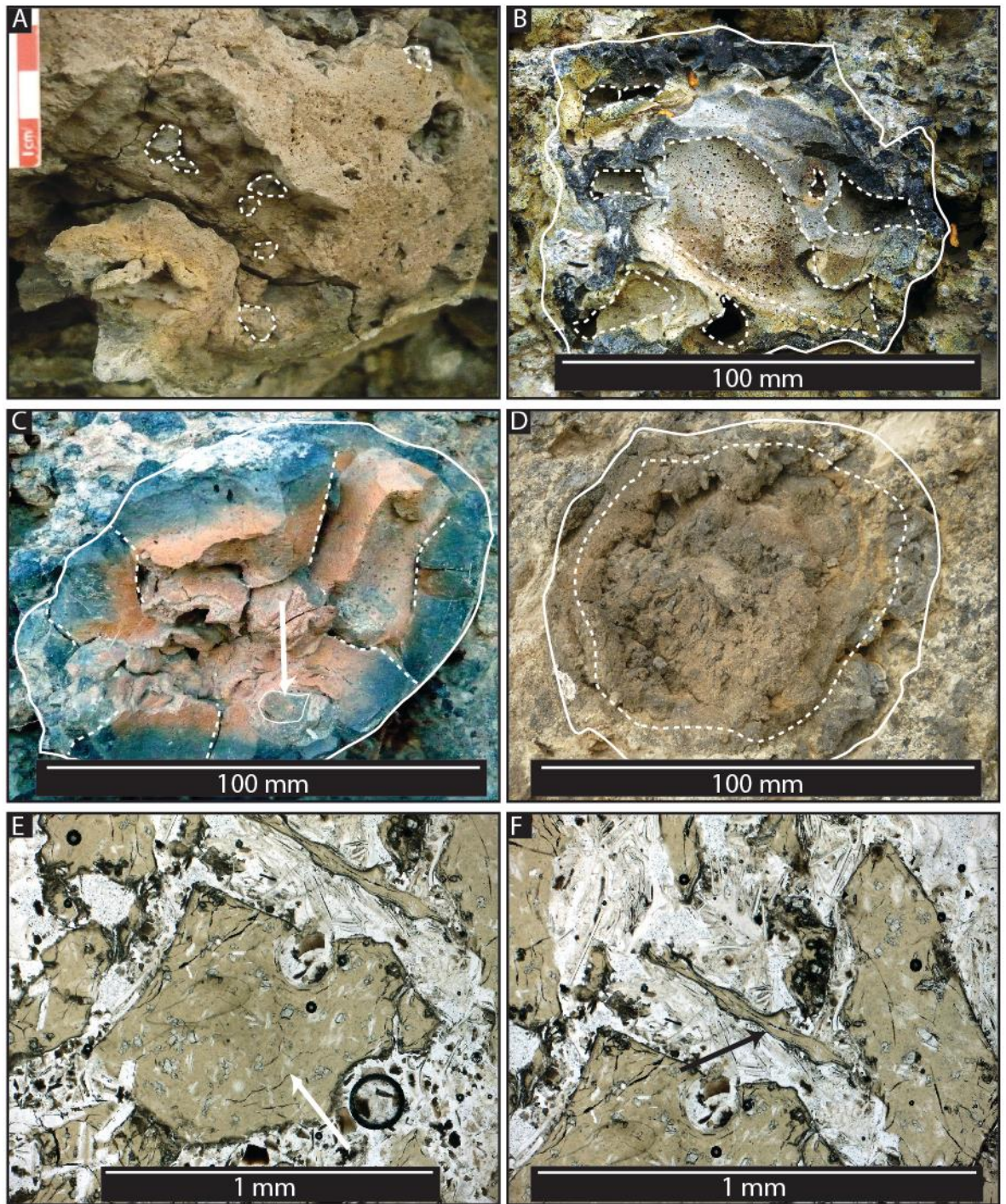
Table 3 Comparison of rootless and littoral cone structures using data from Simpson and McPhie (2001); Mattox and Mangan (1997); Moore and Ault (1965); Fisher (1968);

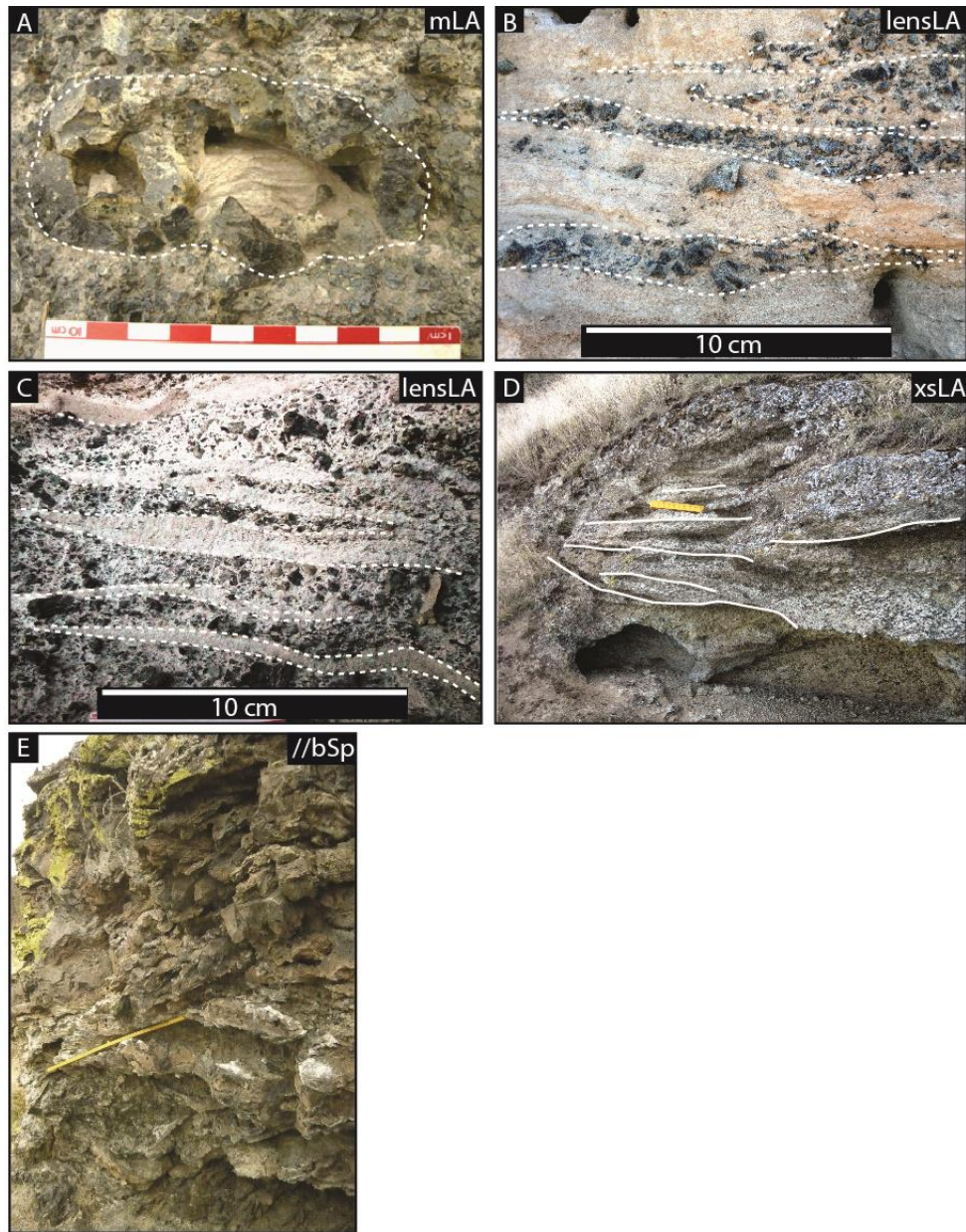
Hamilton et al. (2010a); Melchior Larsen et al. (2006); Jurado-Chichay et al. (1996); and this study



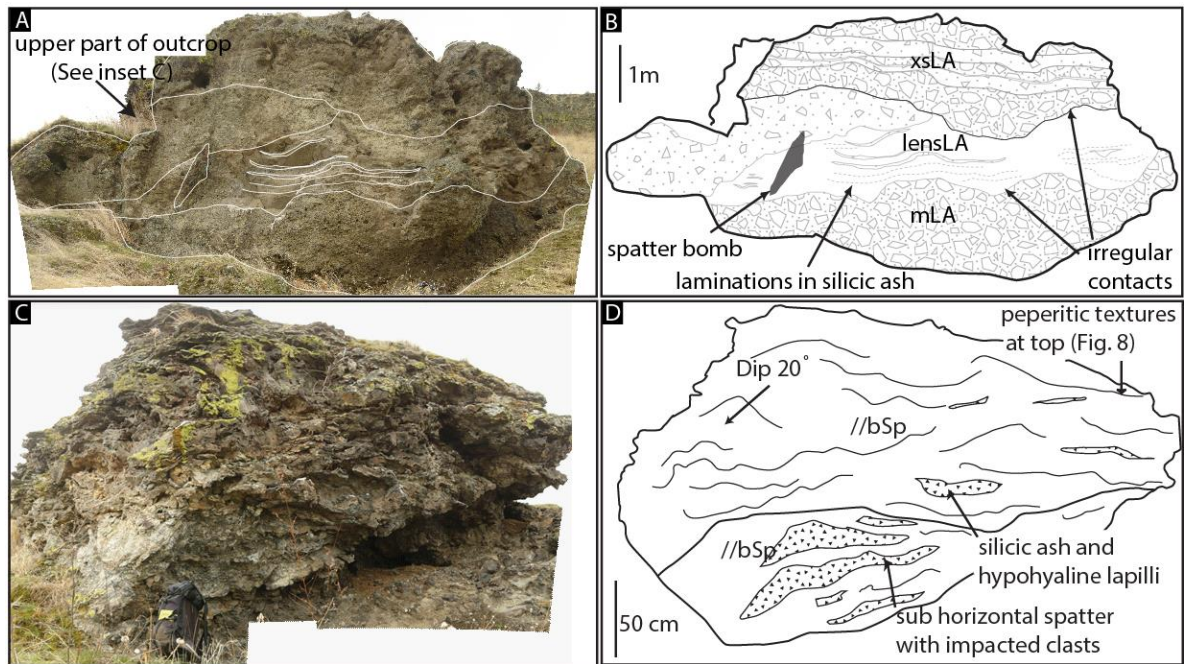


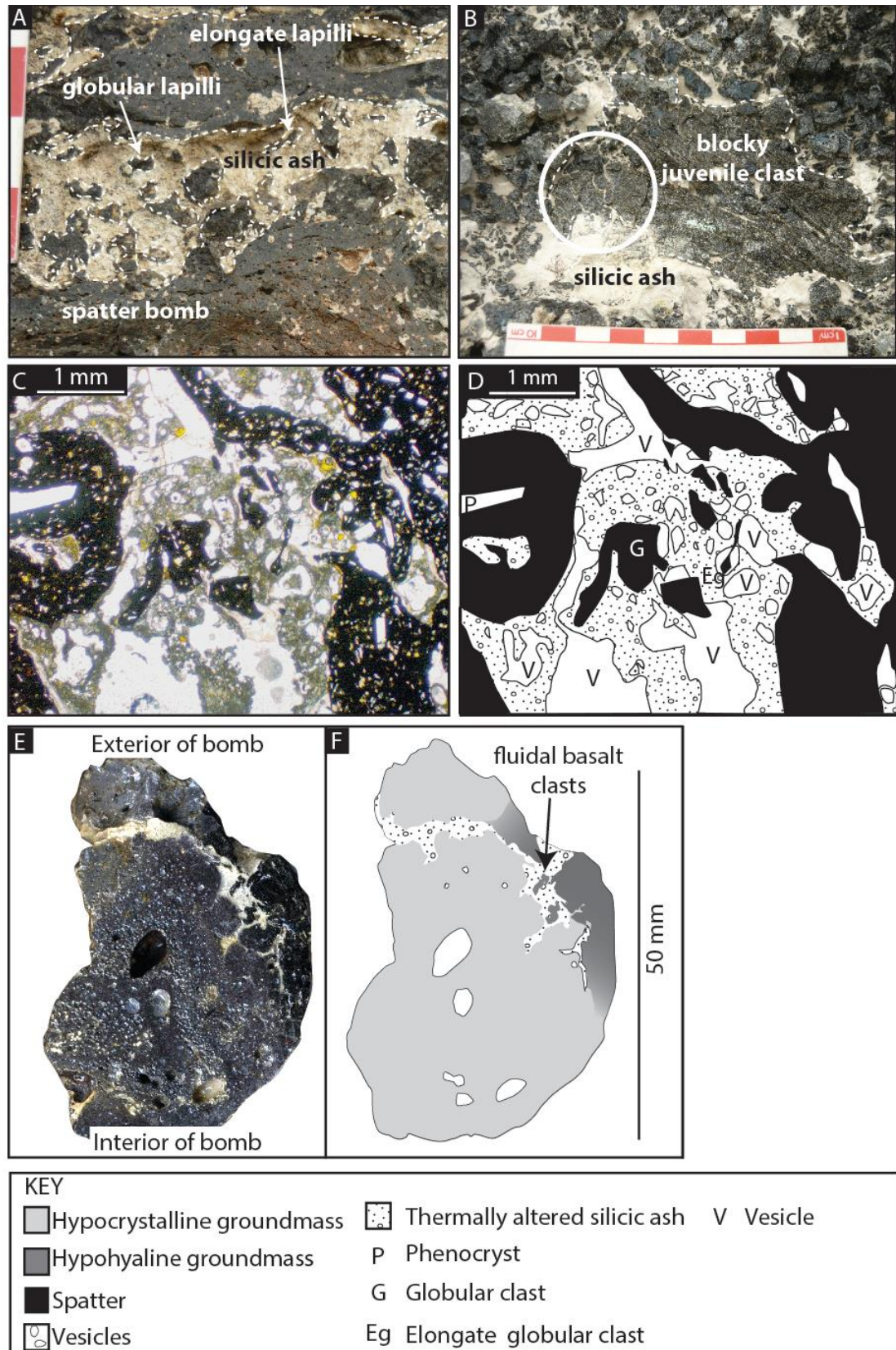


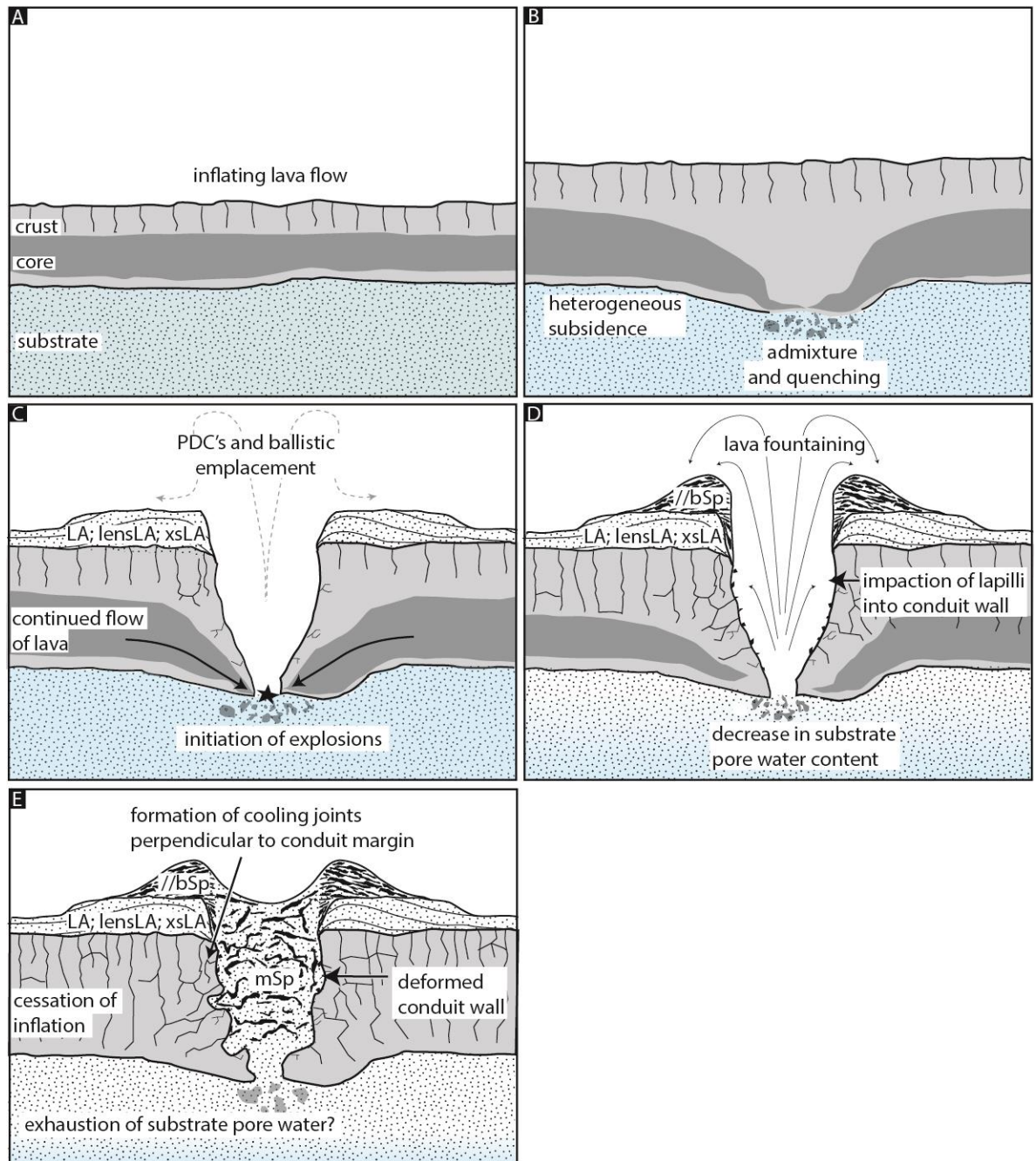


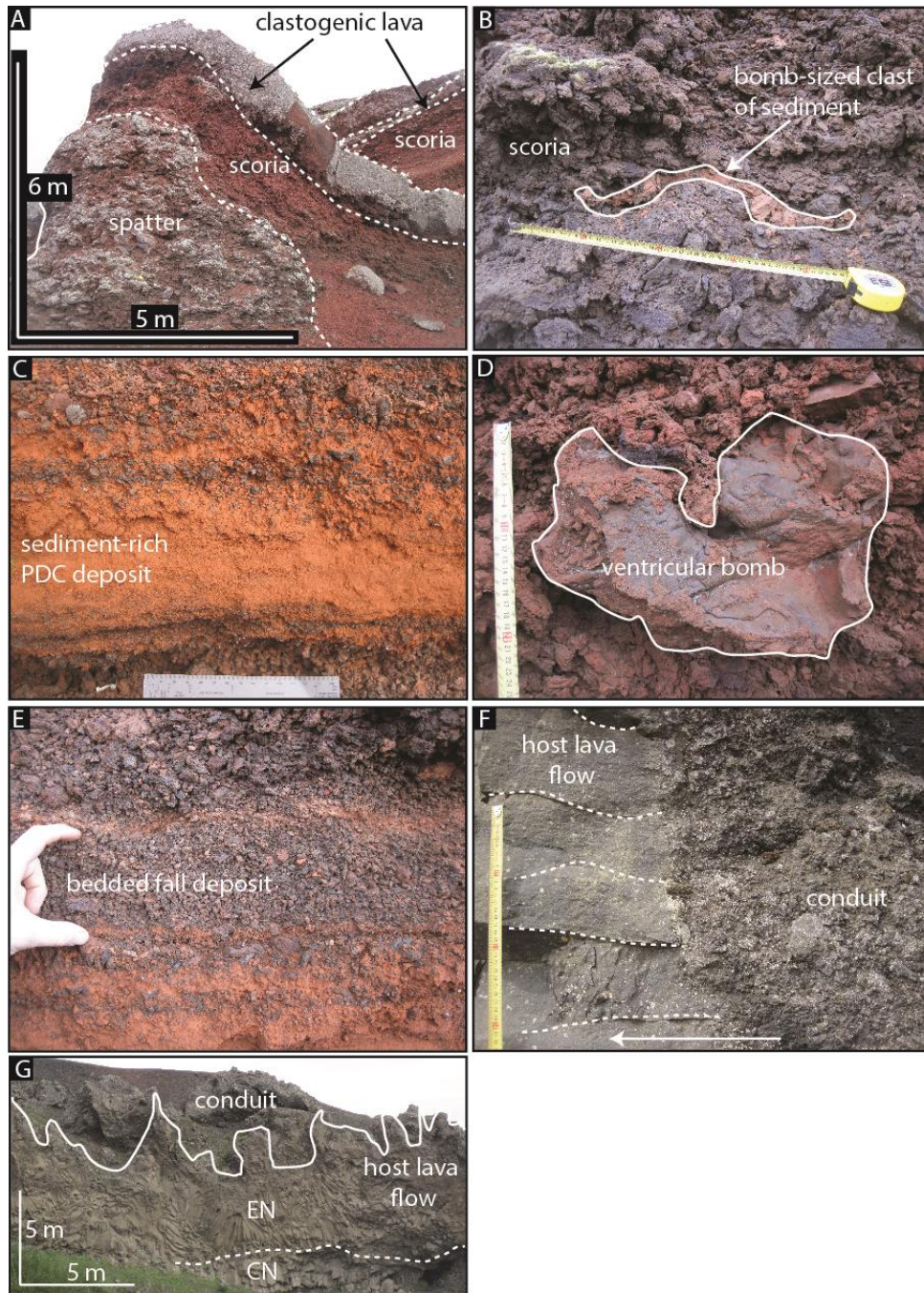












Juvenile clast type	Description	Mean density (kg m^{-3})	Mean vesicularity (%)	Mean crystallinity (%)	Interpretation
Spatter bombs	Lithology: Forms irregular bombs with fluidal and ropey exteriors Structure: Clast supported (<i>//bSp</i>); beds are parallel and dip 20°. Massive in lithofacies mSp. Occurrence: Tephra deposits; extending a maximum distance of ~70 m from source vent.	2200	19	31	Bombs indicate proximal fall deposition from a roofless lava fountain.
Hypocrystalline lapilli and ventricular or globular bombs	Lithology: Forming ventricular and globular shaped bombs frequently fragmented into blocky and equant clasts that occasionally preserve ropey textures on relict exterior surfaces; dominantly lapilli to bomb size; occasionally with radial fractures. Structure: Generally clast supported, occasionally matrix supported; forms cross stratified, massive and graded units (xsLA and m/nLA); also lenses and channels (lensLA).	2300	15	44	Clasts represent quenched globules of lava, ejected from beneath/within the host lava flow during tephra jetting. Bombs were mechanically fragmented into angular shapes upon eruption and deposition, and due to cooling contraction granulation.
Cored scoria bombs and lapilli	Occurrence: All tephra and conduit facies. Lithology: Black resinous rinds up to 10 mm thick and black scoriaceous cores; forming rounded bombs frequently fragmented into blocky and equant clasts; dominantly lapilli to bomb size. Structure: Clast-matrix supported; massive	1700	36	52	Produced by recycling of clasts in the conduit during intermittent and/or dry tephra jetting.
Blocky or fluidal sideromelane ash and lapilli	Occurrence: All tephra deposits. Lithology: Clast shapes vary from blocky and equant to fluidal and elongate. Structure: Varying from matrix to clast supported; massive (<i>//bSp</i> , mSp and xsLA), graded (m/nLA) and lenses and channels (lensLA).	-	-	28	Blocky and equant clasts indicate cooling contraction granulation and/or mechanical fragmentation; fluidal, elongate shapes indicate ductile disruption of magma. Bedding structures are interpreted to record deposition during the passage of density currents.

Table 1.

Lithofacies	Components	Description	Av. max clast size (mm)	% silicic ash	Interpretation
LA Sub facies: n (normal graded), m (massive) f (fabric)	Hypocrystalline lapilli and bombs, sideromelane ash, silicic volcanic ash, clasts of lava crust	Very poorly sorted, hypocrystalline lapilli with rare ash sized fragments; clast supported in silicic ash.	128	20–75	Platform forming deposit. The general lack of evidence for traction sedimentation in the juvenile clasts suggest proximal fall deposition, localised fabrics suggest a minor amount of lateral transport. The coarse nature of some deposits results from the ballistic emplacement of bombs.
lensLA	Hypocrystalline lapilli, sideromelane ash, silicic volcanic ash, clasts of lava crust	Lenses and channels of moderately well sorted, sideromelane and hypocrystalline lapilli; clast supported in silicic volcanic ash, and lenses and channels of substrate within sideromelane and hypocrystalline lapilli dominated rock. Irregular lower contact.	60	25–85	Platform forming deposit. Indicates deposition from dilute PDC. Erosion and transportation of material occurred in locally confined channels. Irregular lower contacts may suggest local erosion of underlying units.
xsLA	Hypocrystalline lapilli and bombs, sideromelane ash, silicic volcanic ash, clasts of lava crust	Cross stratified, moderately sorted sideromelane and hypocrystalline lapilli; clast supported in silicic volcanic ash; beds approximately 5 cm thick.	70	20–55	Platform forming deposit. Crude cross-bedding formed during deposition from PDC's, currents were locally erosive.
//bSp Sub facies: m (massive)	Spatter bombs, hypocrystalline lapilli, silicic volcanic ash, clasts of lava crust	Parallel-bedded spatter bombs with embedded angular hypocrystalline lapilli and silicic volcanic ash. Sub facies is massive.	>1000	<10	Cone forming deposit, sub facies (mSp) conduit fill deposit. Bomb beds indicate proximal fall deposition from rootless lava fountains. Large grain size indicates decreasing explosivity when water availability was decreasing towards the end of the eruptions.

Table 2.

Field area	Cone height (m)	Cone basal diameter (m)	Structure	Juvenile clast types	Environmental setting	Grading	Bedding	Deposition method	Substrate inclusions
Greenland	25	100–200	Fines upwards into ash layers rich in shale, largest clasts proximal, central sediment filled chimney	Pillows and pillow fragments up to 0.5 m size and glass-rich fluidal clasts at the base, yellow/brown sand-sized volcanic clasts at the top	Subaqueous lacustrine	Normal	Bedding seen as clast alignment, flanks dip 20°	(No data)	Partly consolidated shale; 10–20 vol. %
Iceland	1–35	2–450	Capped by spatter 1–2 m thick, inverse grading is common, occasionally with rheomorphic layers, form steep hornitos or broad cinder/tuff cones	Scoria and spatter, ash, lapilli and bombs	Lakes, marshes etc.	Inverse	<0.2 m thick beds of mud and ash, decimetre to metre thick beds of juveniles	PDC and fall	Common in lower sequences as beds, inclusions and coatings; no amounts given
Columbia River Ice Harbor lava flows	≥ 3	≥ 5	Substrate-rich tephra platforms at base, capped by spatter	Hypocrystalline ash and lapilli, spatter, cored, ventricular and globular bombs	Flood plain or shallow lake	Inverse	Decimetre to metre thick beds	PDC and fall	Common in all except uppermost beds, admixed with juvenile clasts; <10–85 vol. %
Hawaii	10–90	20–100's	Monomictic, variably welded and agglutinated, often form crescent shaped ridges at the shoreline	Scoria and spatter, ash, lapilli and cored bombs, Limu-o-Pele, lava crust lithics	Entry of lava into ocean	Normal and inverse	Massive to crudely bedded in proximal facies; poorly to moderately bedded in distal facies	Tephra jets, littoral lava fountains, lithic blasts, lava squeeze up and flow from cone, bubble bursts	(No data)

Table 3.